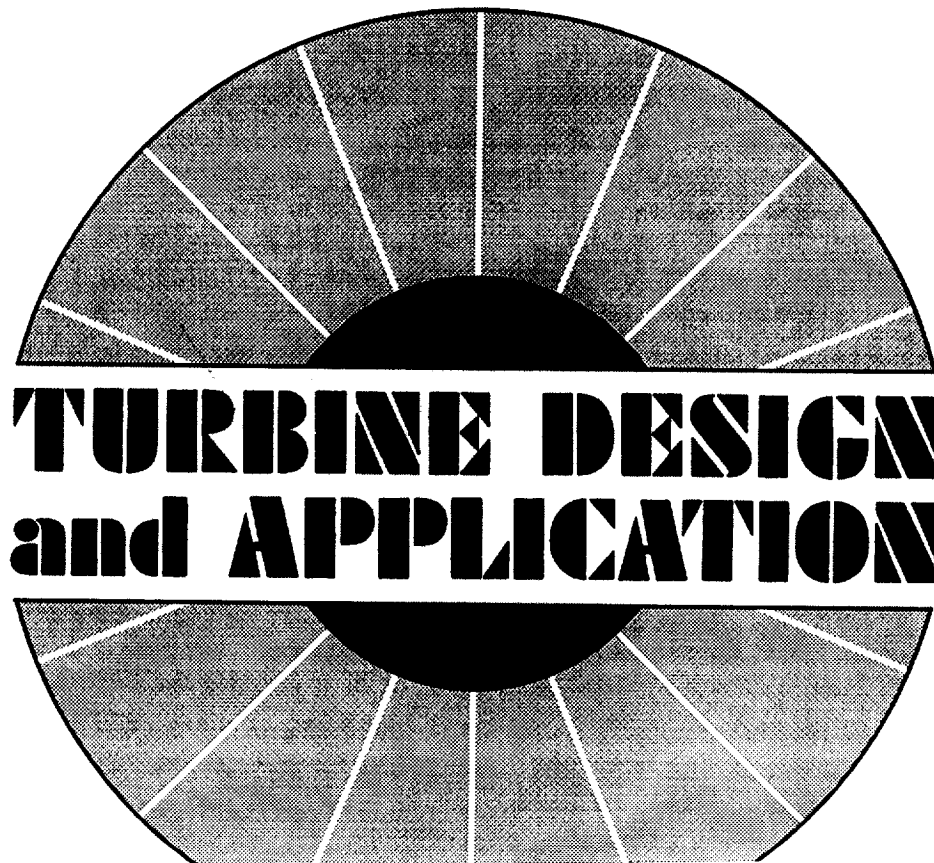


NASA SP-290

1N-07
41715
P-390



(NASA-SP-290) TURBINE DESIGN AND
APPLICATION (NASA) 390 p

N95-22341

Unclass

H1/07 0041715



NATIONAL AERONAUTICS AND SPACE ADMINISTRATION

TURBINE DESIGN and APPLICATION

Edited by Arthur J. Glassman
Lewis Research Center



Scientific and Technical Information Program—1994
NATIONAL AERONAUTICS AND SPACE ADMINISTRATION
Washington, DC

Available from the
NASA Center for AeroSpace Information
800 Elkridge Landing Road
Linthicum Heights, MD 21090-2934
Price Code: A17
Library of Congress Catalog Card Number: 94-67487

PREFACE

NASA has an interest in turbines related primarily to aeronautics and space applications. Airbreathing turbine engines provide jet and turboshaft propulsion, as well as auxiliary power for aircraft. Propellant-driven turbines provide rocket propulsion and auxiliary power for spacecraft. Closed-cycle turbine engines using inert gases, organic fluids, and metal fluids have been studied for providing long-duration electric power for spacecraft. Other applications of interest for turbine engines include land-vehicle (cars, trucks, buses, trains, etc.) propulsion power and ground-based electrical power.

In view of the turbine-system interest and efforts at Lewis Research Center, a course entitled "Turbine Design and Application" was presented during 1968-69 as part of the In-House Graduate Study Program. The course was somewhat revised and again presented in 1972-73. Various aspects of turbine technology were covered including thermodynamic and fluid-dynamic concepts, fundamental turbine concepts, velocity diagrams, losses, blade aerodynamic design, blade cooling, mechanical design, operation, and performance.

The notes written and used for the course have been revised and edited for publication. Such a publication can serve as a foundation for an introductory turbine course, a means for self-study, or a reference for selected topics.

Any consistent set of units will satisfy the equations presented. Two commonly used consistent sets of units and constant values are given after the symbol definitions. These are the SI units and the U.S. customary units. A single set of equations covers both sets of units by including all constants required for the U.S. customary units and defining as unity those not required for the SI units.

ARTHUR J. GLASSMAN

CONTENTS

CHAPTER	PAGE
<i>PREFACE</i>	iii
1. <i>THERMODYNAMIC AND FLUID-DYNAMIC CONCEPTS</i> by Arthur J. Glassman	1
BASIC CONCEPTS AND RELATIONS	1
APPLICATION TO FLOW WITH VARYING AREA	14
REFERENCES	19
SYMBOLS	20
2. <i>BASIC TURBINE CONCEPTS</i> by Arthur J. Glassman	21
TURBINE FLOW AND ENERGY TRANSFER	21
DIMENSIONLESS PARAMETERS	45
REFERENCES	62
SYMBOLS	63
GLOSSARY	65
3. <i>VELOCITY DIAGRAMS</i> by Warren J. Whitney and Warner L. Stewart	69
MEAN-SECTION DIAGRAMS	70
RADIAL VARIATION OF DIAGRAMS	84
COMPUTER PROGRAMS FOR VELOCITY-DIAGRAM STUDIES	95
REFERENCES	96
SYMBOLS	98
4. <i>BLADE DESIGN</i> by Warner L. Stewart and Arthur J. Glassman	101
SOLIDITY	102
BLADE-PROFILE DESIGN	118
REFERENCES	124
SYMBOLS	125
5. <i>CHANNEL FLOW ANALYSIS</i> by Theodore Katsanis	127
STREAM- AND POTENTIAL-FUNCTION ANALYSES	130
VELOCITY-GRADIENT ANALYSIS	147
REFERENCES	154
SYMBOLS	155
6. <i>INTRODUCTION TO BOUNDARY-LAYER THEORY</i> by William D. McNally	157
NATURE OF BOUNDARY LAYER	157
DERIVATION OF BOUNDARY-LAYER EQUATIONS	160
SOLUTION OF BOUNDARY-LAYER EQUATIONS	172
CONCLUDING REMARKS	188
REFERENCES	188
SYMBOLS	191

~~THIS PAGE BLANK NOT FILLED~~

PAGE IV INTENTIONALLY BLANK

7. <i>BOUNDARY-LAYER LOSSES</i> by Herman W. Prust, Jr.	193
BOUNDARY-LAYER PARAMETERS	195
BLADE-ROW LOSS COEFFICIENTS	201
BLADE-ROW LOSS CHARACTERISTICS	217
REFERENCES	221
SYMBOLS	223
8. <i>MISCELLANEOUS LOSSES</i> by Richard J. Roelke	225
TIP-CLEARANCE LOSS	225
DISK-FRICTION LOSS	231
PARTIAL-ADMISSION LOSSES	238
INCIDENCE LOSS	243
REFERENCES	246
SYMBOLS	247
9. <i>SUPERSONIC TURBINES</i> by Louis J. Goldman	249
METHOD OF CHARACTERISTICS	250
DESIGN OF SUPERSONIC STATOR BLADES	263
DESIGN OF SUPERSONIC ROTOR BLADES	266
OPERATING CHARACTERISTICS OF SUPERSONIC TURBINES	272
REFERENCES	277
SYMBOLS	278
10. <i>RADIAL-INFLOW TURBINES</i> by Harold E. Rohlik	279
OVERALL DESIGN CHARACTERISTICS	284
BLADE DESIGN	295
OFF-DESIGN PERFORMANCE	302
REFERENCES	305
SYMBOLS	306
11. <i>TURBINE COOLING</i> by Raymond S. Colladay	307
GENERAL DESCRIPTION	307
HEAT TRANSFER FROM HOT GAS TO BLADE	314
CONDUCTION WITHIN THE BLADE WALL	328
COOLANT-SIDE CONVECTION	330
FILM AND TRANSPIRATION COOLING	332
SIMILARITY	340
REFERENCES	345
SYMBOLS	347
12. <i>EXPERIMENTAL DETERMINATION OF AERO-</i> <i>DYNAMIC PERFORMANCE</i> by Edward M. Szanca and Harold J. Schum	351
TEST FACILITY AND MEASUREMENTS	352
TURBINE PERFORMANCE	374
REFERENCES	387
SYMBOLS	388

CHAPTER 1

Thermodynamic and Fluid-Dynamic Concepts

By Arthur J. Glassman

This chapter is intended to review some of the fundamental concepts of thermodynamics and compressible fluid mechanics. These are the concepts needed to analyze and understand the flow and energy-transfer processes occurring in a turbine. A more complete treatment of these subjects can be found in reference 1 and in many textbooks. Flow is assumed to be steady and one-dimensional for the purposes of this chapter.

Any consistent set of units will satisfy the equations presented. Two commonly used consistent sets of units and constant values are given after the symbol definitions. These are the SI units and the U.S. customary units. A single set of equations covers both sets of units by including all constants required for the U.S. customary units and defining as unity those not required for the SI units.

BASIC CONCEPTS AND RELATIONS

Equation of State

Before we can get very far with any kind of calculation involving gases, we must know how pressure, volume, and temperature are interrelated. The study of gases has resulted in certain laws and generalizations concerning their behavior. In discussing these laws of behavior, gases are referred to as being either ideal or real. The

ideal gas is only hypothetical and obeys various simplified laws that the real gas can only approach under certain conditions.

The ideal gas equation of state is

$$pv = \frac{R^*}{M_w} T \quad (1-1)$$

where

p absolute pressure, N/m²; lb/ft²

v specific volume, m³/kg; ft³/lb

R^* universal gas constant, 8314 J/(kg mole)(K); 1545 (ft)(lb)/(lb mole)(°R)

M_w molecular weight, kg/(kg mole); lb/(lb mole)

T absolute temperature, K; °R

The quantity R^*/M_w is often used as a single quantity such that

$$R = \frac{R^*}{M_w} \quad (1-2)$$

where R is the gas constant, in J/(kg)(K) or (ft)(lb)/(lb)(°R).

Density is often used instead of specific volume in the ideal gas law. Thus,

$$p = \frac{1}{v} RT = \rho RT \quad (1-3)$$

where ρ is density, in kg/m³ or lb/ft³.

In general, a real gas will approximate ideal behavior at low pressures or high temperatures, conditions under which the free space within the gas is large and the attractive forces between molecules are small. For gases which are above their critical temperatures, the ideal gas law may be accurate to within 5 percent up to pressures as high as 50 atmospheres, while for gases below their critical temperatures, deviations of 2 to 3 percent may appear at 1 atmosphere pressure.

Deviations of real gases from ideal behavior have resulted in the proposal of several hundred equations of state to express the p - v - T relation. None of these have been found universally satisfactory, and most are applicable only to a single gas over a limited range of temperature and pressure. Even the most useful of these equations are cumbersome to use and cannot be justified unless a high degree of accuracy is required.

The similarity in behavior of substances at equal values of reduced temperature (ratio of temperature, T , to critical temperature, T_c) and reduced pressure (ratio of pressure, p , to critical pressure, p_c) forms the basis of a relatively simple method for estimating real gas behavior. The method of general correlation is to incorporate a

correction term, called the compressibility factor, into the ideal gas law:

$$p = z\rho RT \quad (1-4)$$

where z is the compressibility factor.

The compressibility factor is a function of reduced temperature and reduced pressure, and is assumed to be independent of the nature of the gas. Values of compressibility factor as a function of reduced temperature and reduced pressure are presented in many texts and other sources. One of the charts from reference 2 is reproduced here as figure 1-1. This type of correlation is derived from an average of data for a large number of gases and is not in rigorous agreement with all the data for any one gas. The compressibility-factor correlation may be extended to gas mixtures if pseudocritical temperatures and pressures are used to calculate reduced temperatures and pressures. The pseudocritical properties are approximated by using the molal averages of the critical properties of the components.

Examination of figure 1-1 shows that there is a large region of state conditions where use of the ideal gas law would result in a large error. Fortunately, the conditions that we are concerned with in our calculations do not usually fall within this region. However, we should never take for granted that the ideal gas law is always valid. A quick determination of the compressibility factor can show the approximate error associated with use of the ideal gas law.

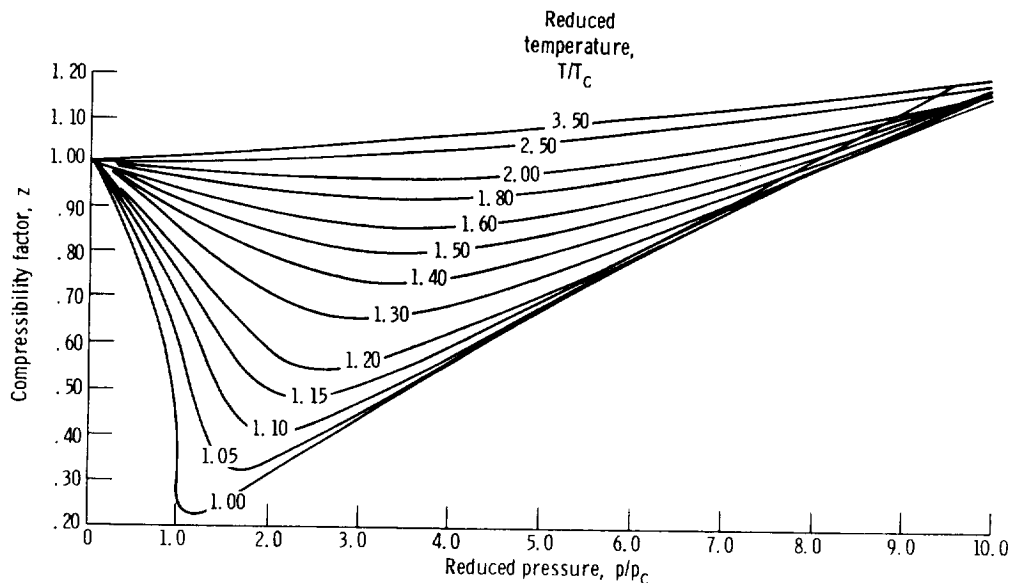


FIGURE 1-1.—Effect of reduced pressure and reduced temperature on compressibility factor. (Curves from ref. 2.)

Relation of Energy Change to State Conditions

In a flow process, the energy term associated with work and heat is the enthalpy h . For a one-phase system of constant chemical composition, enthalpy can be expressed as a function of temperature and pressure:

$$h = \text{fcn}(T, p) \quad (1-5)$$

where h is specific enthalpy, in J/kg or Btu/lb. A differential change in enthalpy can be expressed as

$$dh = \left(\frac{\partial h}{\partial T}\right)_p dT + \left(\frac{\partial h}{\partial p}\right)_T dp \quad (1-6)$$

The partial derivatives can be expressed in terms of determinable properties as follows. By definition,

$$c_p = \left(\frac{\partial h}{\partial T}\right)_p \quad (1-7)$$

where c_p is heat capacity at constant pressure, in J/(kg)(K) or Btu/(lb)(°R). One of the basic differential equations of thermodynamics is

$$dh = T ds + \frac{1}{J} v dp \quad (1-8)$$

where s is specific entropy, in J/(kg)(K) or Btu/(lb)(°R), and J is a conversion constant, 1 or 778 (ft)(lb)/Btu. Therefore, the partial derivative with respect to pressure at constant temperature is, as determined from equation (1-8),

$$\left(\frac{\partial h}{\partial p}\right)_T = T \left(\frac{\partial s}{\partial p}\right)_T + \frac{1}{J} v \quad (1-9)$$

One of the Maxwell relations states that

$$\left(\frac{\partial s}{\partial p}\right)_T = -\frac{1}{J} \left(\frac{\partial v}{\partial T}\right)_p \quad (1-10)$$

Substituting equations (1-7), (1-9), and (1-10) into equation (1-6) yields

$$dh = c_p dT + \frac{1}{J} \left[v - T \left(\frac{\partial v}{\partial T}\right)_p \right] dp \quad (1-11)$$

Equation (1-11) is the rigorous equation for a differential enthalpy change in terms of the state conditions, and the enthalpy change between two states is calculated rigorously as

$$\Delta h = \int_{T_1}^{T_2} c_p dT + \frac{1}{J} \int_{p_1}^{p_2} \left[v - T \left(\frac{\partial v}{\partial T} \right)_p \right] dp \quad (1-12)$$

If we now assume that the gas behaves according to the ideal gas law, we can set

$$v = \frac{RT}{p} \quad (1-13)$$

and

$$\left(\frac{\partial v}{\partial T} \right)_p = \frac{R}{p} \quad (1-14)$$

By using these last two equations in equation (1-12), the effect of pressure on enthalpy change is reduced to zero, and there remains

$$\Delta h = \int_{T_1}^{T_2} c_p dT \quad (1-15)$$

Empirical equations for c_p as a function of T are available in handbooks and textbooks for most gases of interest. If, for example,

$$c_p = a + bT + cT^2 \quad (1-16)$$

then integration of equation (1-15) yields

$$\Delta h = a(T_2 - T_1) + \frac{b}{2} (T_2^2 - T_1^2) + \frac{c}{3} (T_2^3 - T_1^3) \quad (1-17)$$

Although one might not want to use this type of expression for hand calculations, there is no reason to avoid it for computer calculations.

If it can be assumed that c_p is constant between temperatures T_1 and T_2 , then equation (1-15) becomes

$$\Delta h = c_p (T_2 - T_1) \quad (1-18)$$

This assumption is an excellent one for monatomic gases; for other gases, there is a significant variation in c_p with T . However, the use of some average value for c_p will give an approximation that should be within a few percent of the true value.

Relation of State Conditions for Constant Entropy Process

In a turbine, the heat loss is normally small, and the flow process usually can be assumed to be adiabatic. For adiabatic flow with no loss, there is no change in entropy. Therefore, the constant-entropy (isentropic) process is the ideal process for flow in the various parts of the turbine (inlet manifold, stator, rotor, and exit diffuser) as well as for the overall turbine. Actual conditions within and across the

turbine are usually determined from isentropic process calculations in conjunction with some efficiency or loss term. It is, therefore, necessary to be able to relate state conditions for an isentropic process.

For a one-phase system of constant chemical composition, entropy can be expressed as a function of temperature and pressure

$$s = \text{fcn}(T, p) \quad (1-19)$$

and a differential change in entropy can be expressed as

$$ds = \left(\frac{\partial s}{\partial T} \right)_p dT + \left(\frac{\partial s}{\partial p} \right)_T dp \quad (1-20)$$

From equations (1-8) and (1-7), we get

$$\left(\frac{\partial s}{\partial T} \right)_p = \frac{1}{T} \left(\frac{\partial h}{\partial T} \right)_p = \frac{c_p}{T} \quad (1-21)$$

Substituting equations (1-21) and (1-10) into equation (1-20) yields

$$ds = \frac{c_p}{T} dT - \frac{1}{J} \left(\frac{\partial v}{\partial T} \right)_p dp \quad (1-22)$$

For a constant-entropy process, $ds=0$ and

$$\int_{T_1}^{T_2} \frac{c_p}{T} dT = \frac{1}{J} \int_{p_1}^{p_2} \left(\frac{\partial v}{\partial T} \right)_p dp \quad (1-23)$$

Equation (1-23) is the rigorous, but not particularly useful, expression relating temperature and pressure conditions for an isentropic process.

If we assume ideal-gas-law behavior and substitute equation (1-14) into equation (1-23) and perform the integration, we get

$$\int_{T_1}^{T_2} \frac{c_p}{T} dT = \frac{1}{J} R \ln \frac{p_2}{p_1} \quad (1-24)$$

By using a relation such as equation (1-16), integration yields

$$\frac{1}{J} R \ln \frac{p_2}{p_1} = a \ln \frac{T_2}{T_1} + b(T_2 - T_1) + \frac{c}{2} (T_2^2 - T_1^2) \quad (1-25)$$

Like equation (1-17), equation (1-25) also is more suitable for use in a computer calculation than in a hand calculation.

With the additional assumption that c_p is constant between temperatures T_1 and T_2 , equation (1-24) becomes

$$Jc_p \ln \frac{T_2}{T_1} = R \ln \frac{p_2}{p_1} \quad (1-26)$$

and

$$\frac{p_2}{p_1} = \left(\frac{T_2}{T_1} \right)^{Jc_p/R} \quad (1-27)$$

But

$$\frac{Jc_p}{R} = \frac{\gamma}{\gamma-1} \quad (1-28)$$

where γ is the ratio of heat capacity at constant pressure to heat capacity at constant volume. Substitution of equation (1-28) into equation (1-27) yields the more familiar form

$$\frac{p_2}{p_1} = \left(\frac{T_2}{T_1} \right)^{\gamma/(\gamma-1)} \quad (1-29)$$

Where specific heat ratio γ is not constant, the use of an average value should give a reasonable approximation.

Conservation of Mass

The rate of mass flow through an area A can be expressed as

$$w = \rho AV \quad (1-30)$$

where

w rate of mass flow, kg/sec; lb/sec

A flow area, m²; ft²

V fluid velocity, m/sec; ft/sec

For a steady flow (and nonnuclear) process, the rate of mass flow across any section of the flow path must equal the rate of mass flow across any other section. That is,

$$\rho_1 A_1 V_1 = \rho_2 A_2 V_2 \quad (1-31)$$

This expresses the principle of conservation of mass, and equation (1-31) is referred to as the continuity equation.

Newton's Second Law of Motion

All conservation equations, theorems, etc., dealing with momentum are consequences of Newton's Second Law of Motion, which states that an unbalanced force that acts on a body will cause it to accelerate in the direction of the unbalanced force in such a manner that the force is proportional to the product of the mass and acceleration of the body.

Thus,

$$F = \frac{m}{g} a \quad (1-32)$$

where

F unbalanced force, N; lbf

m mass, kg; lbm

a acceleration, m/sec²; ft/sec²

g conversion constant, 1; 32.17 (lbm)(ft)/(lbf)(sec²)

But

$$a = \frac{dV}{dt} \quad (1-33)$$

where t is time, in seconds. Substituting equation (1-33) into equation (1-32) yields

$$F = \frac{m}{g} \frac{dV}{dt} \quad (1-34a)$$

Since the mass is constant, equation (1-34a) can also be written as

$$F = \frac{1}{g} \frac{d(mV)}{dt} \quad (1-34b)$$

Equation (1-34b) specifies that the unbalanced force acting on the fluid is equal to the rate of change of momentum (mV) with time. Since mass per increment of time is the mass flow rate, equation (1-34a) can also be written as

$$F = \frac{w}{g} dV \quad (1-35)$$

A useful relation, sometimes called the equation of motion, can be derived from second-law considerations. Consider an element of fluid as indicated in figure 1-2. Gravitational forces are assumed negligible. A frictional resistance (force) is indicated as R_f . The element of fluid is subjected to fluid-pressure and boundary-surface-pressure forces acting in the downstream direction and fluid-pressure and friction forces acting in the upstream direction. Therefore, the net force in the downstream direction is

$$F = pA + \left(p + \frac{dp}{2}\right)dA - (p + dp)(A + dA) - dR_f \quad (1-36)$$

Expanding, simplifying, and dropping second-order differentials yields

$$F = -Adp - dR_f \quad (1-37)$$

The mass of the element is

$$m = \rho A dx \quad (1-38)$$

Substituting equation (1-38) into equation (1-34) yields

$$F = \frac{\rho A dx}{g} \frac{dV}{dt} \quad (1-39)$$

Since

$$V = \frac{dx}{dt} \quad (1-40)$$

equation (1-39) can be written in the form

$$F = \frac{\rho A V}{g} dV \quad (1-41)$$

Equating (1-37) with (1-41) now yields

$$F = -Adp - dR_f = \frac{\rho A}{g} V dV \quad (1-42)$$

and

$$\frac{dp}{\rho} + \frac{V dV}{g} + \frac{dR_f}{\rho A} = 0 \quad (1-43)$$

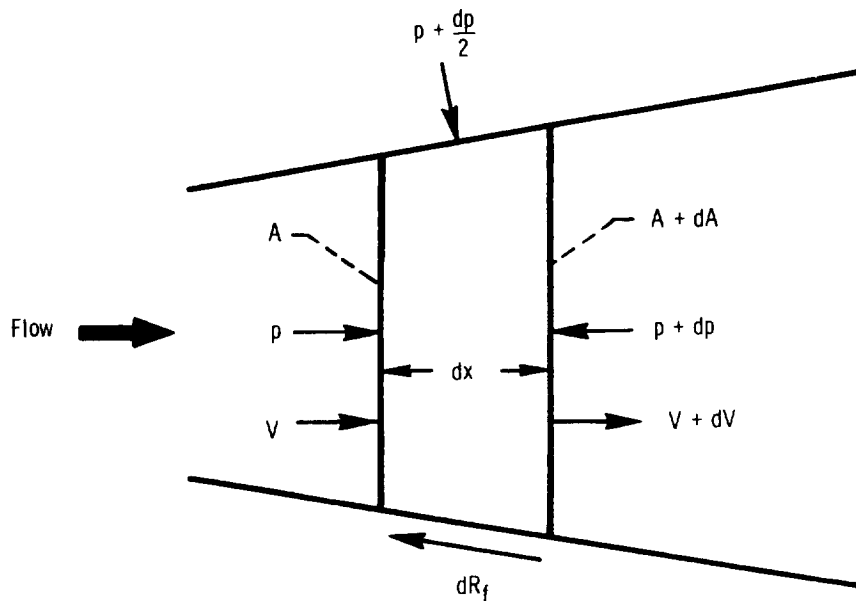


FIGURE 1-2.—Forces on an element of fluid.

If we now let

$$Jdq_f = \frac{dR_f}{\rho A} \quad (1-44)$$

where q_f is heat produced by friction, in J/kg or Btu/lb, we have

$$\frac{dp}{\rho} + \frac{VdV}{g} + Jdq_f = 0 \quad (1-45)$$

For isentropic flow, $dq_f = 0$.

Conservation of Energy

For a steady-flow (and nonnuclear) process, the energy entering a system or part of a system must equal the energy leaving that system or part of that system. If we can neglect chemical energy, electrical energy, etc., we still have to consider internal energy u , flow energy pv , kinetic energy $V^2/2g$, potential energy Z , heat q , and mechanical work W_s . Thus,

$$u_1 + \frac{p_1 v_1}{J} + \frac{V_1^2}{2gJ} + \frac{Z_1}{J} + q = u_2 + \frac{p_2 v_2}{J} + \frac{V_2^2}{2gJ} + \frac{Z_2}{J} + W_s \quad (1-46)$$

where

- u specific internal energy, J/kg; Btu/lb
- Z specific potential energy, J/kg; (ft) (lbf)/lbm
- q heat added to system, J/kg; Btu/lb
- W_s mechanical work done by system, J/kg; Btu/lb

For a gas system, the potential energy can be neglected. In addition, by definition

$$h = u + \frac{pv}{J} \quad (1-47)$$

Thus, equation (1-46) reduces to

$$h_1 + \frac{V_1^2}{2gJ} + q = h_2 + \frac{V_2^2}{2gJ} + W_s \quad (1-48)$$

Equation (1-48) is the basic form of the steady-flow energy balance as we will be using it.

Total Conditions

The sum of the enthalpy and the kinetic energy is always appearing in flow problems, and it is convenient to use it as a single quantity. Thus,

$$h' \equiv h + \frac{V^2}{2gJ} \quad (1-49)$$

where h' is total enthalpy, in J/kg or Btu/lb.

The concept of total enthalpy leads us to the concept of total temperature. Total temperature can be defined as the temperature that corresponds to the total enthalpy. The total-temperature concept is most useful when ideal-gas-law behavior and constant heat capacity can be assumed. In that case, according to equation (1-15),

$$h' - h = c_p(T' - T) \quad (1-50)$$

where T' is total temperature, in K or °R. Combining equation (1-50) with equation (1-49) yields

$$T' = T + \frac{V^2}{2gJc_p} \quad (1-51)$$

The total temperature T' can be thought of as the temperature attained when a gas at static temperature T and velocity V is brought to rest adiabatically. Thus, total temperature is also called stagnation temperature, and these two terms are used interchangeably.

The total, or stagnation, pressure can be regarded as the pressure of a fluid brought to rest isentropically from a velocity V and static pressure p . Since the relation between p' and p is isentropic, we can use equation (1-29) to write

$$\frac{p'}{p} = \left(\frac{T'}{T}\right)^{\gamma/(\gamma-1)} \quad (1-52)$$

where p' is total pressure, in N/m² or lb/ft².

With regard to the above-defined total conditions, certain points should be emphasized. The concept of total enthalpy is general, and its use involves no assumptions other than those associated with the energy balance as we have considered it. Total temperature, as will be seen, is a very useful convenience for easing the burden of calculation, but it is rigorous only for ideal-gas-law behavior and constant heat capacity. For systems involving chemical reaction or a phase change, the use of total temperature is not recommended. Total pressure, in addition to the assumptions associated with total temperature, involves an isentropic path between the static and total conditions.

Flow Process With No Heat and No Work

Let us now, in terms of total conditions, examine a process that occurs with neither heat transfer (adiabatic process) nor mechanical work. This process is the one that occurs (neglecting heat losses) in each part of the turbine (including the rotor, at constant radius, when

the velocities are expressed relative to the moving blade).

Substitution of equation (1-49) into equation (1-48) and rearrangement yields

$$h_2' - h_1' = q - W_s \quad (1-53)$$

The energy balance now looks something like the First Law of Thermodynamics for a flow process, as we were first exposed to it in college. If we set q and W_s equal to zero, we get

$$h_2' = h_1' \quad (1-54)$$

Therefore, for adiabatic flow with no work, total enthalpy remains constant. Further, from equations (1-18) and (1-50), it can be shown that total temperature also remains constant.

$$T_2' = T_1' \quad (1-55)$$

Note that the process does not have to be isentropic in order for total enthalpy and total temperature to remain constant.

Total pressure is another matter. From equations (1-22), (1-52), and (1-55) and the ideal-gas-law and constant-heat-capacity assumptions, it can be shown that for adiabatic flow with no work,

$$e^{\int ds/R} = \frac{p_1'}{p_2'} \quad (1-56)$$

Only for isentropic flow ($ds=0$), therefore, does total pressure remain constant. For flow with loss ($ds>0$), there is a decrease in total pressure.

Speed of Sound and Velocity Ratios

An important characteristic of gases is the speed of pressure-wave propagation or, as otherwise called, the speed of sound. From small-pressure-disturbance theory

$$a = \sqrt{g \left(\frac{\partial p}{\partial \rho} \right)} \quad (1-57)$$

where a is speed of sound, in m/sec or ft/sec.

From the ideal gas law and isentropic process relations, this reduces to

$$a = \sqrt{\gamma g R T} \quad (1-58)$$

The ratio of fluid velocity V to sound velocity a is an important factor in determining the flow characteristics of a gas. This ratio is called the Mach number M :

$$M = \frac{V}{a} \quad (1-59)$$

Mach number is a useful parameter not only for identifying flow-behavior regimes, but also for simplifying and generalizing certain expressions. Consider the relation of total temperature to static temperature, given in equation (1-51). Combining equations (1-58), (1-59), and (1-28) with equation (1-51) yields

$$\frac{T'}{T} = 1 + \frac{\gamma-1}{2} M^2 \quad (1-60)$$

Another velocity ratio often used is the ratio of fluid velocity to critical velocity

$$\frac{V}{V_{cr}} = \frac{V}{a_{cr}} \quad (1-61)$$

where V_{cr} is critical velocity, in m/sec or ft/sec, and a_{cr} is speed of sound at critical condition, in m/sec or ft/sec. The critical velocity is equal to the velocity of sound at the critical condition. The critical condition is that condition where $M=1$. Consequently, from equation (1-60), at the critical condition

$$T_{cr} = \frac{2}{\gamma+1} T' \quad (1-62)$$

and substitution of equation (1-62) into equation (1-58) yields

$$a_{cr} = \sqrt{\frac{2\gamma}{\gamma+1} gRT'} \quad (1-63)$$

Thus, in any flow process with constant total temperature (no heat and no work), the value of the critical velocity ($V_{cr}=a_{cr}$) remains constant for the entire process, while the value of the speed of sound (a) changes as the static temperature changes.

The ratio of fluid velocity to critical velocity is sometimes called the critical velocity ratio. Its use is often preferred over Mach number because the critical velocity ratio is directly proportional to velocity, while Mach number is not (since there is a square root of static temperature in the denominator).

The relation between static and total temperature in terms of the critical velocity ratio results from combining equations (1-61), (1-63), (1-28), and (1-51).

$$\frac{T}{T'} = 1 - \frac{\gamma-1}{\gamma+1} \left(\frac{V}{V_{cr}} \right)^2 \quad (1-64)$$

APPLICATION TO FLOW WITH VARYING AREA

The equations already presented are sufficient to analyze completely the flow through turbine passages, provided that there are no losses (flow is isentropic). Although there are losses in a turbine, we can use the loss-free process to learn something about the behavior of the flow in the varying-area passages (stator, rotor, and exit diffuser) of the turbine.

Effect of Flow Regime

We are going to examine the relations among pressure, velocity, area change, and Mach number. Proper manipulation of the previously presented equations yields the following equation for isentropic flow:

$$-(1-M^2) \frac{dV}{V} = \frac{1-M^2}{\gamma M^2} \frac{dp}{p} = \frac{dA}{A} \quad (1-65)$$

Equation (1-65) shows that (1) for all Mach numbers the change in velocity is opposite to the change in pressure and (2) the directions of the changes in velocity and pressure with changes in area depend on whether the Mach number is less than 1 (subsonic flow), equal to 1 (sonic flow), or greater than 1 (supersonic flow). By way of definition, let us specify that a nozzle is a varying-area passage in which static pressure decreases and a diffuser is a varying-area passage in which static pressure increases.

Let us examine the various cases from equation (1-65):

A. Subsonic flow ($M < 1$):1. Increasing pressure ($dp > 0$):

Velocity decreases ($dV < 0$) and area increases ($dA > 0$).

This is the subsonic diffuser.

2. Decreasing pressure ($dp < 0$):

Velocity increases ($dV > 0$) and area decreases ($dA < 0$).

This is the subsonic nozzle.

B. Supersonic flow ($M > 1$):1. Increasing pressure ($dp > 0$):

Velocity decreases ($dV < 0$) and area decreases ($dA < 0$).

This is the supersonic diffuser.

2. Decreasing pressure ($dp < 0$):

Velocity increases ($dV > 0$) and area increases ($dA > 0$).

This is the supersonic nozzle.

C. Sonic flow ($M = 1$):

Both increasing ($dp > 0$) and decreasing ($dp < 0$) pressure.

Area change must equal zero ($dA = 0$). Thus, the sonic, or critical, condition can occur only at the inlet, exit, or minimum-area section of a varying-area passage.

You may also want to note that in order to cross the critical condition ($M=1$) going either up or down in velocity, the flow passage must have a decreasing-area portion followed by an increasing-area portion.

Flow in Nozzles

Since we are concerned primarily with nozzle flow rather than diffuser flow in turbines, we will narrow the discussion to flow in nozzles. We will further limit the discussion to the case where the flow entering the nozzle is subsonic, since this is the case of most interest.

Convergent nozzle.—Let us first consider the simple convergent nozzle. This corresponds to the case A2 mentioned previously. Assume the nozzle is supplied with gas from a reservoir (zero velocity) where the gas is maintained at a static (and total) pressure p' and a static (and total) temperature T' . The exhaust, or outside, static pressure is designated as p_e and the static pressure right at the nozzle exit (in the throat) is designated as p_t . When p_e is a little less than p' , flow commences and the throat pressure p_t is equal to p_e . As p_e is progressively lowered, flow rate and velocity both increase, with p_t still equal to p_e . At some value of p_e , the velocity at the throat becomes equal to sonic velocity, and $M=1$ at the throat.

What happens if p_e is now lowered further? We have seen that a Mach number greater than 1 cannot be attained in a convergent nozzle. Therefore, the flow at the throat remains in the critical condition ($M=1$) no matter how much p_e is lowered. The static pressure in the throat remains at the critical pressure, which according to equations (1-62) and (1-29) is

$$p_t = p_{cr} = p' \left(\frac{2}{\gamma + 1} \right)^{\gamma/(\gamma-1)} \quad (1-66)$$

Once p_e is reduced below p_{cr} , the exhaust pressure has no effect on the flow within the nozzle. The gas expands from p' to $p_t = p_{cr}$ within the nozzle and then expands further from p_t to p_e outside the nozzle. The expansion process from p_t to p_e occurs with shocks (which occur with an increase in entropy and will be discussed a little later), and the isentropic equations are not valid for this part of the process.

The fact that the throat condition remains constant for nozzle pressure ratios (p'/p_e) greater than or equal to the critical pressure ratio (p'/p_{cr}) means that the nozzle mass flow rate also remains constant under these conditions. Thus, for a fixed upstream state, the mass flow rate reaches a maximum value when M becomes 1 at the throat and thereafter remains constant no matter to what value the exhaust pressure is reduced. The fact that this condition corresponds to maximum flow can be proven mathematically. A nozzle in

this condition is said to be choked.

Convergent-divergent nozzle.—Let us now consider the somewhat more involved case of the convergent-divergent nozzle. Again, assume the nozzle to be supplied with gas from the same reservoir maintained at pressure p' and temperature T' . Figure 1-3, showing plots of pressure ratio against nozzle length, will supplement this discussion. If the exhaust pressure p_e is a little less than p' (curve AB in fig. 1-3), flow commences with the lowest pressure occurring at the throat ($p_t < p_e$). In this case, the divergent section of the passage is acting as a subsonic diffuser. As p_e is progressively lowered (curve AC in fig. 1-3), the pressure p_t at the throat decreases and the velocity increases. Eventually, at some particular value of p_e , the throat velocity becomes equal to the sonic velocity, or $M_t=1$ (curve AD in fig. 1-3). Note that p_e is still higher than p_t , and the gas still diffuses subsonically

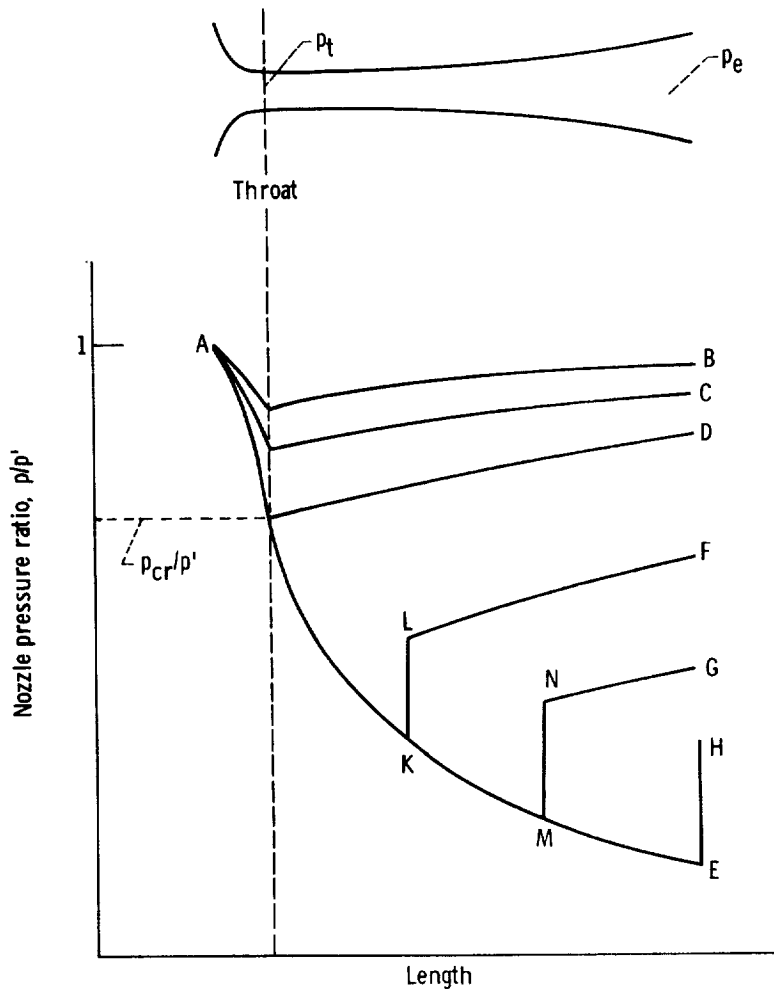


FIGURE 1-3.—Nozzle flow processes.

in the divergent section. Since the throat condition is now critical (with $p_t = p_{cr} < p_e$), we see that the nozzle pressure ratio (p'/p_e) required to achieve the critical condition in a convergent-divergent nozzle is less than the nozzle pressure ratio ($p'/p_e = p'/p_{cr}$) required to achieve the critical condition in a simple convergent nozzle.

If p_e is again lowered, the throat must remain at the critical condition because equation (1-65) showed us that the throat is the only place where the critical condition can exist. Thus, as with the convergent nozzle, the throat state remains constant, and the mass flow must remain constant at its maximum value. As long as the critical condition is maintained at the throat, the nozzle is choked and the convergent part of the nozzle continues to behave independently of the conditions beyond the throat.

If the flow is to be supersonic and isentropic throughout the divergent part of the nozzle, then for any given ratio of throat area to discharge area, only one exhaust pressure p_e will satisfy the conservation of mass and energy, as well as the isentropic process, relations. This case is represented in figure 1-3 by curve AE, which shows pressure falling continuously. It is unreasonable to assume that flow is impossible between the values of p_e that allow either isentropic subsonic diffusion to some $p_e > p_t$ (curve AD, fig. 1-3) or isentropic supersonic expansion to some $p_e < p_t$ (curve AE, fig. 1-3). The flow that does take place, therefore, cannot be isentropic.

Observing the gas flow under these nonisentropic conditions by optical means reveals that surfaces of abrupt density changes occur in the flow. These apparent discontinuities in the flow are shock waves. Shock waves are of very small thickness, and the fluid state changes may be considered as occurring instantaneously. Total temperature across a shock remains constant but, even though there is a rise in static pressure, there is a loss in total pressure because the process occurs with an increase in entropy. Shocks may be strong or weak. Strong shocks occur normal to the flow (and are thus called normal shocks) and result in subsonic velocities downstream of the shock. Weak shocks occur at some small angle with respect to the flow direction (and are thus called oblique shocks), and the velocity downstream of the shock remains supersonic, but the Mach number is less than that upstream of the shock.

Let us now complete the discussion of convergent-divergent nozzles for the region of pressure ratios between points D and E in figure 1-3. If the exhaust pressure p_e is reduced a little below the value at point D, a normal shock occurs at some point in the divergent part of the nozzle, and the pressure rises instantaneously to a value such that isentropic subsonic diffusion occurs from the shock plane to the nozzle

exit. The flow process in this case is illustrated by the path AKLF, with AK being an isentropic expansion, KL being the normal shock, and LF being the isentropic diffusion. As p_e is reduced further, the normal shock moves toward the nozzle exit, and the flow process is represented by a path such as AMNG. At some value of p_e corresponding to point H, the normal shock will be right at the nozzle exit, and the flow path in the nozzle is AEH.

For values of p_e between points H and E, a normal shock cannot occur because it is too strong and would result in a static pressure higher than p_e . In this case, the weaker oblique shock occurs at the nozzle exit, with the shock becoming weaker as p_e approaches point E. When p_e corresponds to point E, as mentioned previously, the nozzle flow is again completely isentropic. For lower values of p_e , the final expansion from the nozzle-exit static pressure to p_e occurs outside the nozzle in a nonisentropic manner.

It should be pointed out that the previous discussion and the processes shown in figure 1-3 are idealized. In actuality, the shock effects do not occur exactly instantaneously and the pressure rise, although abrupt, takes place over a finite distance. Also, real-fluid considerations may produce effects that make the subsonic flow downstream of a shock different from isentropic. The general processes, however, are qualitatively similar to those shown in figure 1-3.

Thermodynamic-Property and Flow-Function Tables and Charts

In order to facilitate thermodynamic and flow calculations, many sets of tables and charts have been constructed and published in books and reports. Some of these are listed as references 3 to 7.

Thermodynamic properties of air and its combustion products as functions of temperature are presented in references 3 and 4. These charts and tables include the variation in heat capacity with temperature. The thermodynamic properties of air and also the individual components of air and its combustion products (nitrogen, oxygen, carbon dioxide, water vapor, and argon) are presented in references 4 and 5. Compressibility factors are also presented in reference 5. The properties presented in reference 5 include the effect of pressure, as well as temperature.

Isentropic compressible-flow functions (T/T' , p/p' , ρ/ρ' , A/A_{cr} , and others) as functions of Mach number are presented in references 4, 6, and 7 for various values of heat-capacity ratio. Also included are tables and charts for normal and oblique shock calculations. Reference 6 presents a listing of compressible flow function and shock function equations in terms of both Mach number and critical velocity ratio.

REFERENCES

1. KUNKLE, JOHN S.; WILSON, SAMUEL D.; AND COTA, RICHARD A.; ED: Compressed Gas Handbook. NASA SP-3045, 1969.
2. NELSON, L. C.; AND OBERT, E. F.: How to Use the New . . . Generalized Compressibility Charts. Chem. Eng., vol. 61, no. 7, July 1954, pp. 203-208.
3. ENGLISH, ROBERT E.; AND WACHTL, WILLIAM W.: Charts of Thermodynamic Properties of Air and Combustion Products from 300° to 3500° R. NACA TN 2071, 1950.
4. KEENAN, JOSEPH H.; AND KAYE, JOSEPH: Gas Tables. John Wiley and Sons, Inc., 1948.
5. HILSEN RATH, JOSEPH; BECKETT, CHARLES W.; BENEDICT, WILLIAM S.; FANO, LILLA; HOGE, HAROLD J.; MASI, JOSEPH F.; NUTTALL, RALPH L.; TOULOUKIAN, YERAM S.; AND WOOLLEY, HAROLD W.: Tables of Thermal Properties of Gases Comprising Tables of Thermodynamics and Transport Properties of Air, Argon, Carbon Dioxide, Carbon Monoxide, Hydrogen, Nitrogen, Oxygen, and Steam. NBS Circular 564, National Bureau of Standards, Nov. 1, 1955.
6. AMES RESEARCH STAFF: Equations, Tables, and Charts for Compressible Flow. NACA Rep. 1135, 1953.
7. LEWIS LABORATORY COMPUTING STAFF: Tables of Various Mach Number Functions for Specific-Heat Ratios from 1.28 to 1.38. NACA TN 3981, 1957.

SYMBOLS

A	flow area, m^2 ; ft^2
a	{acceleration, m/sec^2 ; ft/sec^2 speed of sound, m/sec ; ft/sec
a, b, c	general constants for polynomial, eq. (1-16)
c_p	heat capacity at constant pressure, $J/(kg)(K)$; $Btu/(lb)(^\circ R)$
F	unbalanced force, N ; lb
g	conversion constant, 1; 32.17 $(lbm)(ft)/(lbf)(sec^2)$
h	specific enthalpy, J/kg ; Btu/lb
J	conversion constant, 1; 778 $(ft)(lb)/Btu$
M	Mach number, defined by eq. (1-59)
M_w	molecular weight, $kg/(kg\ mole)$; $lb/(lb\ mole)$
m	mass, kg ; lb
p	absolute pressure, N/m^2 ; lb/ft^2
q	heat added to system, J/kg ; Btu/lb
q_f	heat produced by friction, J/kg ; Btu/lb
R	gas constant, $J/(kg)(K)$; $(ft)(lbf)/(lbm)(^\circ R)$
R_f	frictional resistance force, N ; lb
R^*	universal gas constant, 8314 $J/(kg\ mole)(K)$; 1545 $(ft)(lbf)/(lb\ mole)(^\circ R)$
s	specific entropy, $J/(kg)(K)$; $Btu/(lb)(^\circ R)$
T	absolute temperature, K ; $^\circ R$
t	time, sec
u	specific internal energy, J/kg ; Btu/lb
V	fluid absolute velocity, m/sec ; ft/sec
v	specific volume, m^3/kg ; ft^3/lb
W_s	mechanical work done by system, J/kg ; Btu/lb
w	mass flow rate, kg/sec ; lb/sec
x	length, m ; ft
Z	specific potential energy, J/kg ; $(ft)(lbf)/lbm$
z	compressibility factor, defined by eq. (1-4)
γ	ratio of heat capacity at constant pressure to heat capacity at constant volume
ρ	density, kg/m^3 ; lb/ft^3
Subscripts:	
c	critical state condition
cr	critical flow condition ($M=1$)
e	exhaust
t	throat
Superscript:	
'	absolute total state

CHAPTER 2

Basic Turbine Concepts

By Arthur J. Glassman

This chapter introduces turbine geometric, flow, energy-transfer, efficiency, and performance characteristics primarily by means of definitions, diagrams, and dimensionless parameters. Terms referring to the blades and blading geometry are defined in the GLOSSARY, at the end of this chapter.

TURBINE FLOW AND ENERGY TRANSFER

Analysis Coordinate System

An analysis of the flow and energy-transfer processes within a turbine requires some convenient coordinate system. For fluid flowing through a turning wheel, a logical system consists of one coordinate directed parallel to the axis of rotation, one coordinate directed radially through the axis of rotation, and one coordinate directed tangentially to the rotating wheel. These are the axial, radial, and tangential directions indicated in figure 2-1.

These three coordinates form three planes. Analysis of flow in the radial-axial plane depicts the circumferentially-averaged (or blade-to-blade average) radial and axial variation of the desired flow parameters. For many types of calculations, we can ignore the circumferential (or blade-to-blade) variation of parameter values and just use average values. Such a calculation is called an axisymmetric analysis.

Calculations made in the axial-tangential or radial-tangential planes are usually at some constant value (rather than for average conditions) of the third coordinate. Velocity diagram, as well as blade-to-blade velocity-variation, calculations are usually made in these planes. When

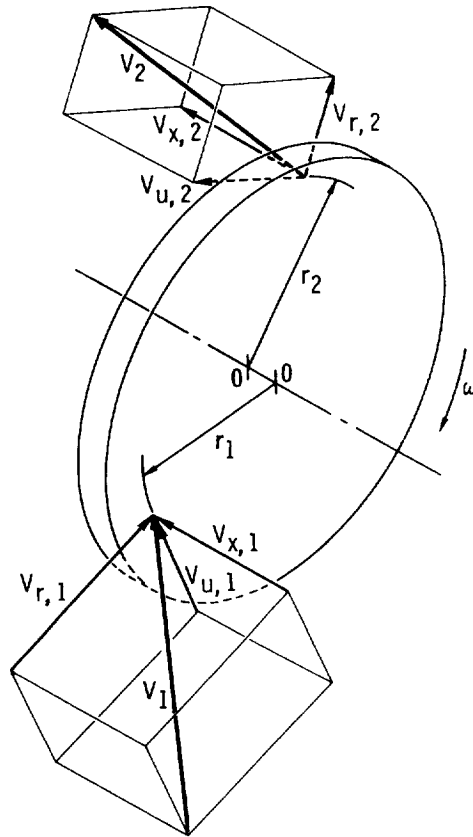


FIGURE 2-1.—Velocity components for a generalized rotor.

flow is predominantly radial, such as at the inlet to a radial-flow turbine, the radial-tangential plane is used. When flow is predominantly axial, such as in an axial-flow turbine, the axial-tangential plane is used.

Velocity Vectors and Diagrams

One of the most, if not the most, important variables that we will be concerned with in the analysis of turbine flow and energy transfer is the fluid velocity and its variation in the different coordinate directions. To assist us in making these analyses and in depicting blading shapes and types, we use velocity-vector diagrams.

For flow in and across the stators, the absolute velocities are of interest. For flow in and across the rotors, velocities must be considered relative to the rotating blade. In terms of relative velocities and other relative parameters to be discussed later in this chapter, flow in a rotating blade row can be analyzed in a manner similar to the analysis of flow in a stationary passage.

Velocity-diagram calculations are made at locations upstream and downstream of the various blade rows or at just infinitesimal distances inside the blade rows. In making the velocity diagrams, the circumferential variations in flow are not considered. The velocity vectors represent the circumferential average of the flow.

The velocity diagram shows both the absolute and the relative velocities. In making the velocity diagram, note that

$$\text{Relative velocity} = \text{Absolute velocity} - \text{Blade velocity} \quad (2-1)$$

or

$$\vec{W} = \vec{V} - \vec{U} \quad (2-2)$$

where

\vec{W} relative velocity vector

\vec{V} absolute velocity vector

\vec{U} blade velocity vector

Since blade velocity is always in the tangential direction, we need only consider the magnitude, that is, the blade speed. So, we can write

$$\vec{W} = \vec{V} - U \quad (2-3)$$

The velocity diagram in figure 2-2 represents equation (2-3) and also shows the components of the absolute and relative velocities. Assuming this velocity diagram to be drawn in an axial-tangential plane, the absolute and relative velocities can be expressed in terms of their

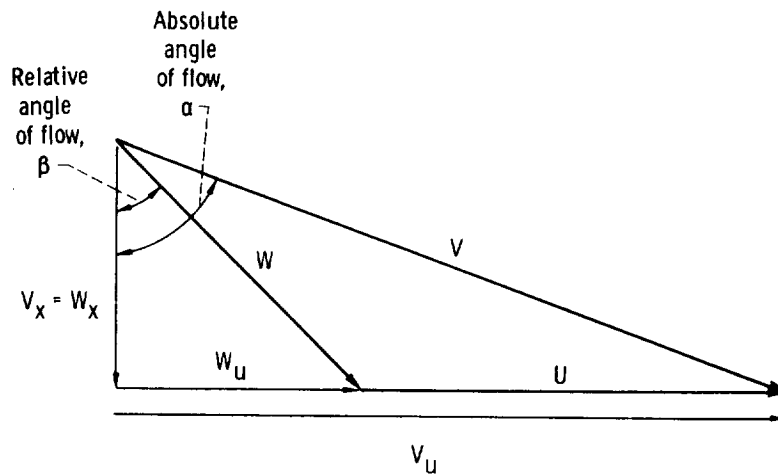


FIGURE 2-2.—Typical velocity-vector diagram having tangential components of absolute and relative velocities in the same direction.

components in the axial and tangential directions as

$$V^2 = V_x^2 + V_u^2 \quad (2-4)$$

and

$$W^2 = W_x^2 + W_u^2 \quad (2-5)$$

where

- V magnitude of \vec{V} , m/sec; ft/sec
- V_x axial component of absolute velocity, m/sec; ft/sec
- V_u tangential component of absolute velocity, m/sec; ft/sec
- W magnitude of \vec{W} , m/sec; ft/sec
- W_x axial component of relative velocity, m/sec; ft/sec
- W_u tangential component of relative velocity, m/sec; ft/sec

If this diagram (fig. 2-2) were drawn in the radial-tangential plane, the values marked as axial components would be radial components. From figure 2-2, we see that we can write

$$W_u = V_u - U \quad (2-6)$$

A sign convention must be established for the angles and the tangential components of velocity, since not all velocity diagrams are of the exact same geometrical shape as the example diagram shown in figure 2-2. We could have, for example, the velocity diagram shown in figure 2-3. In this instance, the tangential components and flow angles of the absolute and relative velocities are directed in opposite directions, and it is not obvious that equation (2-6) is valid. Therefore, we will adopt and stick with the convention that

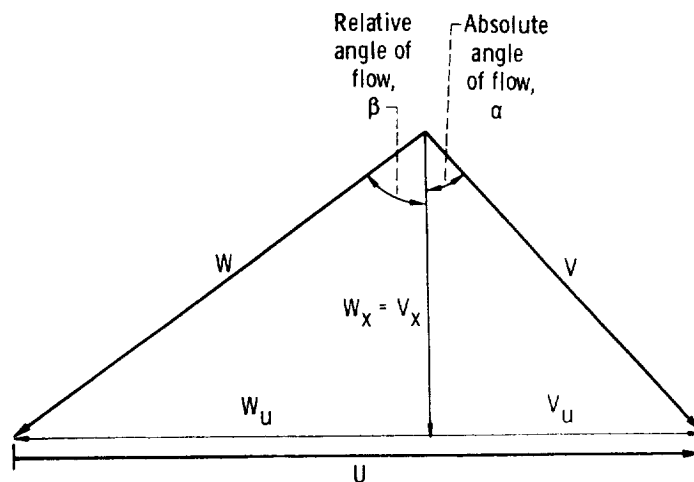


FIGURE 2-3.—Typical velocity-vector diagram having tangential components of absolute and relative velocities in opposite directions.

all angles and tangential components of velocity are positive if they are in the direction of the blade velocity and are negative if they are in the direction opposite to the blade velocity. With this convention, we can now see that equation (2-6) remains valid for the velocity diagram shown in figure 2-3, where a small positive value of V_u minus a larger positive value of U yields a negative value for W_u .

Not all turbine analysts use the above convention for all cases. Some use the above convention at a location immediately upstream of a rotor and then switch positive and negative directions at locations immediately downstream of a rotor. In many cases this avoids working with negative values. Also, many analysts work with angles defined with respect to the tangential direction rather than the axial direction as we are using. Therefore, if you should have occasion to use velocity-diagram information generated by someone else, make sure that you are aware of the convention used in generating this information.

Energy Transfer

The basic energy-transfer relation for all turbomachines is relatively simple and is only a form of Newton's Second Law of Motion as applied to a fluid traversing a rotor. Figure 2-1 represents a rotor of a generalized turbomachine, with 0-0 the axis of rotation and ω the angular velocity. Fluid enters the rotor at point 1, passes through the rotor by any path, and is discharged at point 2. The directions of the fluid at points 1 and 2 are at any arbitrary angle, and points 1 and 2 are at any radii r_1 and r_2 . A condition of steady state is assumed. Further, the velocity vectors at the inlet and the outlet are regarded as representing the average values for the mass of flow being considered.

The inlet and outlet velocity vectors can be resolved into the three mutually perpendicular components discussed previously. The change in magnitude of the axial velocity components through the rotor gives rise to an axial force, which must be taken by a thrust bearing. The change in magnitude of the radial velocity components gives rise to a radial bearing load. Neither the axial nor the radial velocity components have any effect on the angular motion of the rotor (except for the effect of bearing friction). It is the change in magnitude and radius of the tangential components of velocity that corresponds to a change in angular momentum of the fluid and results in the desired energy transfer.

Net rotor torque is equal to the difference between the inlet and outlet products of tangential force times radius, or

$$\tau = (F_u r)_1 - (F_u r)_2 \quad (2-7)$$

TURBINE DESIGN AND APPLICATION

where

τ net torque, N-m; lb-ft
 F_u tangential force, N; lb
 r radius, m; ft

Applying equation (1-34) in the tangential direction, integrating from $V=0$ at $t=0$ to $V=V$ at $t=t$, and setting $w=m/t$ yields

$$F_u = \frac{w}{g} V_u \quad (2-8)$$

where

w rate of mass flow, kg/sec; lb/sec
 g conversion constant, 1; 32.17 (lbm)(ft)/(lbf)(sec²)

Substituting equation (2-8) into (2-7) then yields

$$\tau = \frac{w}{g} V_{u,1} r_1 - \frac{w}{g} V_{u,2} r_2 = \frac{w}{g} (V_{u,1} r_1 - V_{u,2} r_2) \quad (2-9)$$

Power (rate of energy transfer) is equal to the product of torque and angular velocity:

$$P = \frac{\tau \omega}{J} = \frac{w}{gJ} \omega (r_1 V_{u,1} - r_2 V_{u,2}) \quad (2-10)$$

where

P net power, W; Btu/sec
 ω angular velocity, rad/sec
 J conversion constant, 1; 778 (ft)(lb)/Btu

Since

$$r\omega = U \quad (2-11)$$

we can write

$$P = \frac{w}{gJ} (U_1 V_{u,1} - U_2 V_{u,2}) \quad (2-12)$$

But

$$P = w \Delta h' \quad (2-13)$$

where h' is total enthalpy, in J/kg or Btu/lb. Substituting equation (2-13) into equation (2-12) yields

$$\Delta h' = \frac{1}{gJ} (U_1 V_{u,1} - U_2 V_{u,2}) \quad (2-14)$$

where $\Delta h'$ is here defined as $h'_1 - h'_2$.

Equation (2-14) is the basic work equation for all forms of turbomachines and is called the Euler equation. All the energy transfer between the fluid and the rotor must be accounted for by the difference between the two UV_u terms. The way equation (2-14) is stated, it

can be seen that $\Delta h'$ must be positive for a turbine. This is consistent with the energy balance, equation (1-46), where work done by the fluid is defined as positive.

It is useful to transform the Euler equation into another form. This will be done with the aid of figure 2-4, which shows an axial-flow turbine blade section along with the velocity diagrams for the inlet and outlet. The velocity diagrams are in axial-tangential planes. There is assumed to be no radial component of velocity at either the inlet or the outlet locations, although these locations are not necessarily at the same radius. Actually, the following derivation also can be made for a general three-dimensional case.

From equations (2-4) and (2-5), we get

$$V_x^2 = V^2 - V_u^2 \tag{2-15}$$

and

$$W_x^2 = W^2 - W_u^2 \tag{2-16}$$

Substituting equation (2-6) into (2-16) gives

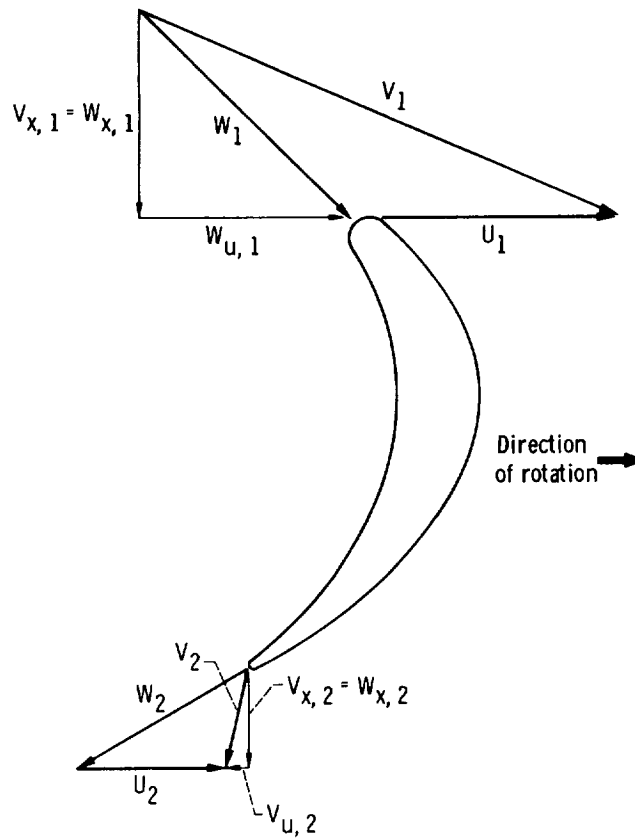


FIGURE 2-4.—Rotor section with inlet- and exit-velocity-vector diagrams.

$$W_x^2 = W^2 - (V_u - U)^2 \quad (2-17)$$

Since $V_x = W_x$, combining equations (2-15) and (2-17) yields

$$V^2 - V_u^2 = W^2 - V_u^2 + 2UV_u - U^2 \quad (2-18)$$

Therefore,

$$UV_u = \frac{1}{2} (V^2 + U^2 - W^2) \quad (2-19)$$

Now, adding subscripts for inlet and outlet yields

$$U_1 V_{u,1} = \frac{1}{2} (V_1^2 + U_1^2 - W_1^2) \quad (2-20)$$

$$U_2 V_{u,2} = \frac{1}{2} (V_2^2 + U_2^2 - W_2^2) \quad (2-21)$$

Inserting these values into the Euler equation (eq. (2-14)) finally yields

$$\Delta h' = \frac{1}{2gJ} (V_1^2 - V_2^2 + U_1^2 - U_2^2 + W_2^2 - W_1^2) \quad (2-22)$$

Equation (2-22) is an alternative form of the basic energy-transfer relation.

By definition,

$$\Delta h' = h'_1 - h'_2 = h_1 + \frac{V_1^2}{2gJ} - h_2 - \frac{V_2^2}{2gJ} \quad (2-23)$$

Therefore, comparison of equation (2-22) with equation (2-23) shows that

$$\Delta h = h_1 - h_2 = \frac{1}{2gJ} (U_1^2 - U_2^2 + W_2^2 - W_1^2) \quad (2-24)$$

Thus, the U^2 and W^2 terms of equation (2-22) represent the change in static enthalpy across the rotor, while the V^2 terms represent the change in absolute kinetic energy across the rotor. These three pairs of terms are sometimes referred to as the components of energy transfer.

Blade Loading

As mentioned previously, it is the change in the tangential momentum of the fluid that results in the transfer of energy from the fluid to the rotor. The following discussion and figure 2-5 concern the cause of this change in tangential momentum and the way in which the energy is actually transferred to the wheel.

As the fluid flows through the curved passage between each pair of blades, a centrifugal force acts on it in the direction of the pressure

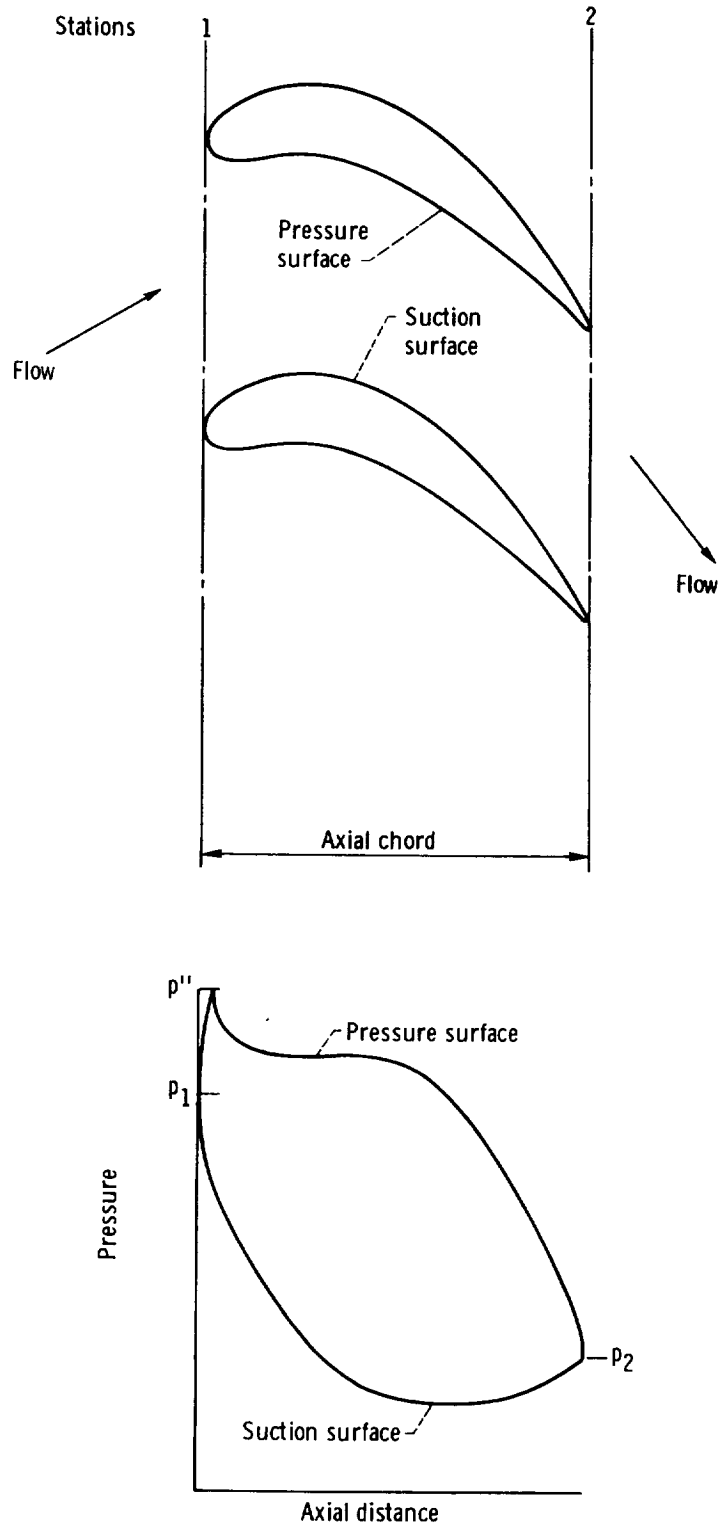


FIGURE 2-5.—Blade row with surface static-pressure distribution.

(concave) surface. Since the fluid is constrained and, therefore, not free to move in the direction of the centrifugal force, a pressure force must be established to balance the centrifugal force and turn the fluid through its curved path. The pressure force is directed normal to the flow and toward the suction (convex) surface. Thus, the pressure in the passage is highest at the pressure surface and lowest at the suction surface.

The resulting distribution of static pressure on the blade surfaces is illustrated in figure 2-5, where pressure is plotted against axial distance. At or near the blade leading edge there is a stagnation point where the velocity becomes zero and the pressure reaches its stagnation value. The stagnation point is the dividing point for the fluid flowing around to the two sides of the blade. From the stagnation point, the pressure along the blade surfaces decreases toward the blade trailing edge. On the suction surface, the static pressure will often decrease below the exit pressure and then increase back up to the exit pressure.

The pressure-distribution curve illustrated in figure 2-5 is called the blade-loading diagram. The area between the curves represents the blade force acting in the tangential direction.

Relative Conditions

Flow in a rotating passage can be analyzed in a manner similar to flow in a stationary passage by considering conditions relative to the moving passage. Let us first define relative total enthalpy in a manner similar to the definition of absolute total enthalpy.

$$h'' \equiv h + \frac{W^2}{2gJ} \quad (2-25)$$

where h'' is relative total enthalpy, in J/kg or Btu/lb. Now let us examine what happens to relative total enthalpy as the fluid flows through the rotor. If in equation (2-24) we substitute for W^2 according to equation (2-25), we get

$$h_2'' - h_1'' = \frac{U_2^2 - U_1^2}{2gJ} \quad (2-26)$$

Therefore, we see that the relative total enthalpy of the fluid flowing through the rotor changes only if there is a change in the blade speed. For purely axial flow, where there is no change in radius and, consequently, no change in blade speed, the relative total enthalpy remains constant for the rotor flow process.

We can also define a temperature that corresponds to relative total enthalpy. This is called the relative total temperature, T'' . When

ideal-gas-law behavior and constant heat capacity can be assumed, we can write

$$h'' - h = c_p(T'' - T) \quad (2-27)$$

where

c_p heat capacity at constant pressure, J/(kg)(K); Btu/(lb)(°R)

T absolute temperature, K; °R

Combining equation (2-27) with equation (2-25) then yields

$$T'' = T + \frac{W^2}{2gJc_p} \quad (2-28)$$

From equation (1-51) and equation (2-28), we see that the absolute and relative total temperatures are related as follows:

$$T' - T'' = \frac{V^2 - W^2}{2gJc_p} \quad (2-29)$$

For the rotor flow process, we can write

$$h_2'' - h_1'' = c_p(T_2'' - T_1'') \quad (2-30)$$

Combining this with equation (2-26) shows that

$$T_2'' - T_1'' = \frac{U_2^2 - U_1^2}{2gJc_p} \quad (2-31)$$

Therefore, relative total temperature, like relative total enthalpy, depends only on blade speed and remains constant for purely axial flow through a rotor.

Relative total pressure can be defined as the pressure of a fluid brought to rest isentropically from a relative velocity W and a static pressure p . Therefore,

$$\frac{p''}{p} = \left(\frac{T''}{T}\right)^{\gamma/(\gamma-1)} \quad (2-32)$$

where

p'' relative total pressure, N/m²; lb/ft²

γ ratio of heat capacity at constant pressure to heat capacity at constant volume

From this equation and equation (1-52), we also see that

$$\frac{p''}{p'} = \left(\frac{T''}{T'}\right)^{\gamma/(\gamma-1)} \quad (2-33)$$

For the rotor flow process, relative total pressure can increase, decrease, or remain constant, depending on the change in relative total temperature and on the losses. For purely axial flow, relative total

pressure will remain constant only if the flow is isentropic; otherwise, it must decrease.

We can define a relative Mach number M_{rel} as

$$M_{rel} = \frac{W}{a} \quad (2-34)$$

and a relative critical velocity as

$$W_{cr} = a_{cr,rel} = \sqrt{\frac{2\gamma}{\gamma+1} gRT''} \quad (2-35)$$

where

W_{cr} critical velocity, m/sec; ft/sec

$a_{cr,rel}$ speed of sound at relative critical condition, m/sec; ft/sec

R gas constant, J/(kg)(K); (ft)(lb)/(lb)(°R)

Then, in a manner similar to the way we derived equations (1-60) and (1-64), we can get

$$\frac{T''}{T} = 1 + \frac{\gamma-1}{2} M_{rel}^2 \quad (2-36)$$

and

$$\frac{T}{T''} = 1 - \frac{\gamma-1}{\gamma+1} \left(\frac{W}{W_{cr}} \right)^2 \quad (2-37)$$

Reaction

The fraction of total energy transfer (change in absolute total enthalpy) that is obtained by a change in static enthalpy is one important way of classifying a turbine stage. The change in kinetic energy as a fraction of the exit kinetic energy is one important way of classifying a blade row. The parameter used in both cases is the degree of reaction, or more simply, the reaction. Reaction is used for classifying types of velocity diagrams, and it is also an important parameter for correlating losses.

Stage reaction.—Stage reaction is defined as the change in static enthalpy across the rotor as a fraction of the change in absolute total enthalpy across the stage. Note that the change in absolute total enthalpy across the stage is the same as the change in absolute total enthalpy across the rotor, since total enthalpy remains constant through the stator. According to the above definition of stage reaction, we can write

$$R_{stg} = \frac{h_1 - h_2}{h_1' - h_2'} \quad (2-38)$$

where R_{stg} is stage reaction, and the subscripts 1 and 2 refer to conditions upstream and downstream of the rotor, respectively.

The preceding equation for reaction can be expressed in terms of velocities. Substituting equations (2-22) and (2-24) into equation (2-38) yields

$$R_{st} = \frac{(U_1^2 - U_2^2) + (W_2^2 - W_1^2)}{(V_1^2 - V_2^2) + (U_1^2 - U_2^2) + (W_2^2 - W_1^2)} \quad (2-39)$$

Reaction can be positive, negative, or zero, depending on the values of $(U_1^2 - U_2^2)$ and $(W_2^2 - W_1^2)$.

Zero reaction is one important value that characterizes a particular stage design. If $R_{st} = 0$, there is no change in static enthalpy in the rotor, and all the work done by the stage is a result of the change in absolute kinetic energy across the stage. This stage is called an impulse stage. In the general case where the fluid enters and leaves the rotor at different radii, an impulse stage may result from having a change of static enthalpy in one direction contributed by the centrifugal (U^2) effect and an equal change in the other direction contributed by the relative-velocity effect. For purely axial flow, any change in static enthalpy must be caused by a change of relative velocity only. Thus, an axial-flow impulse stage must have $W_1 = W_2$.

Some people define impulse on the basis of no change in static pressure in the rotor rather than no change in static enthalpy. This definition in terms of static pressure is approximately the same as that used herein. The difference is due to losses. For isentropic flow, the definitions exactly coincide.

Simple examples of impulse turbines are the child's pinwheel, the windmill, or the paddle wheel operated by the impingement of a fluid from a stationary nozzle. A simple example of a reaction turbine is the lawn sprinkler that ejects the water from nozzles, thus causing rotation.

Blade-row reaction.—Blade-row reaction is defined as the kinetic energy developed within the blade row as a fraction of the kinetic energy at the blade-row exit. These are the kinetic energies relative to that blade row. For a stator or axial-flow rotor, the change in kinetic energy corresponds to the change in static enthalpy. Therefore, blade-row reaction represents an effect similar to that represented by stage reaction.

For a stator blade row, reaction is defined as

$$R_{st} = \frac{V_1^2 - V_0^2}{V_1^2} = 1 - \frac{V_0^2}{V_1^2} \quad (2-40)$$

where R_{st} is stator reaction. For a rotor blade row, reaction is defined as

$$R_{r,0} = \frac{W_2^2 - W_1^2}{W_2^2} = 1 - \frac{W_1^2}{W_2^2} \quad (2-41)$$

where $R_{r,0}$ is rotor reaction. The subscripts 0, 1, and 2 refer to conditions upstream of the stator, downstream of the stator, and downstream of the rotor, respectively.

In some literature, the blade-row reaction is defined in terms of velocities instead of kinetic energies. This definition is similar to equations (2-40) and (2-41) except that the velocities appear to the first power rather than squared (i.e., V rather than V^2).

Turbine Expansion Process

For all adiabatic expansion processes, the maximum energy transformation (development of kinetic energy) or energy transfer (development of mechanical work) for a given pressure ratio is obtained when the process is isentropic. This can be proven from the previously presented equations (but we will not do it here), and we will illustrate this fact graphically a little later in this discussion. With the ideal-gas-law and constant-heat-capacity assumptions, we have previously shown that energies and energy changes can be represented by temperatures and temperature changes. Therefore, with temperature, pressure, and entropy all being variables of interest, we can conveniently represent the ideal (isentropic) and actual expansion processes in a turbine by means of a temperature-entropy diagram.

The temperature-entropy diagram is a plot of temperature against entropy for lines of constant pressure. Since entropy increases with increasing temperature and decreasing pressure, as can be seen from

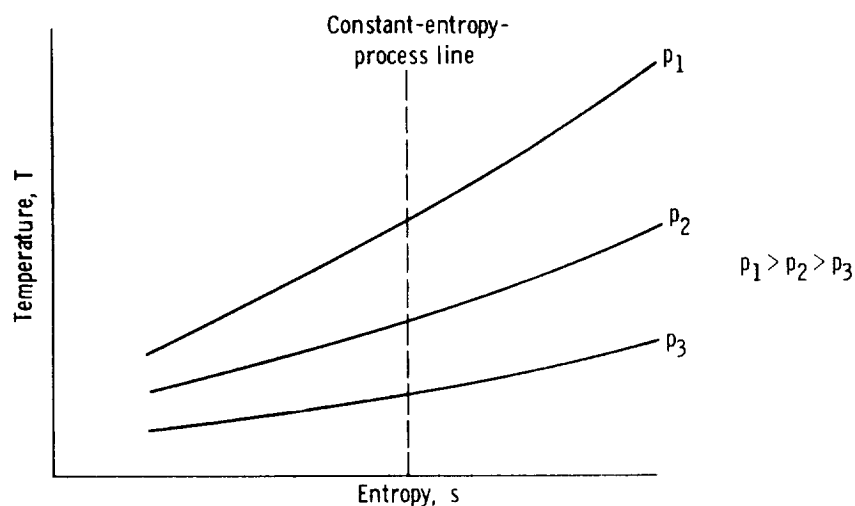
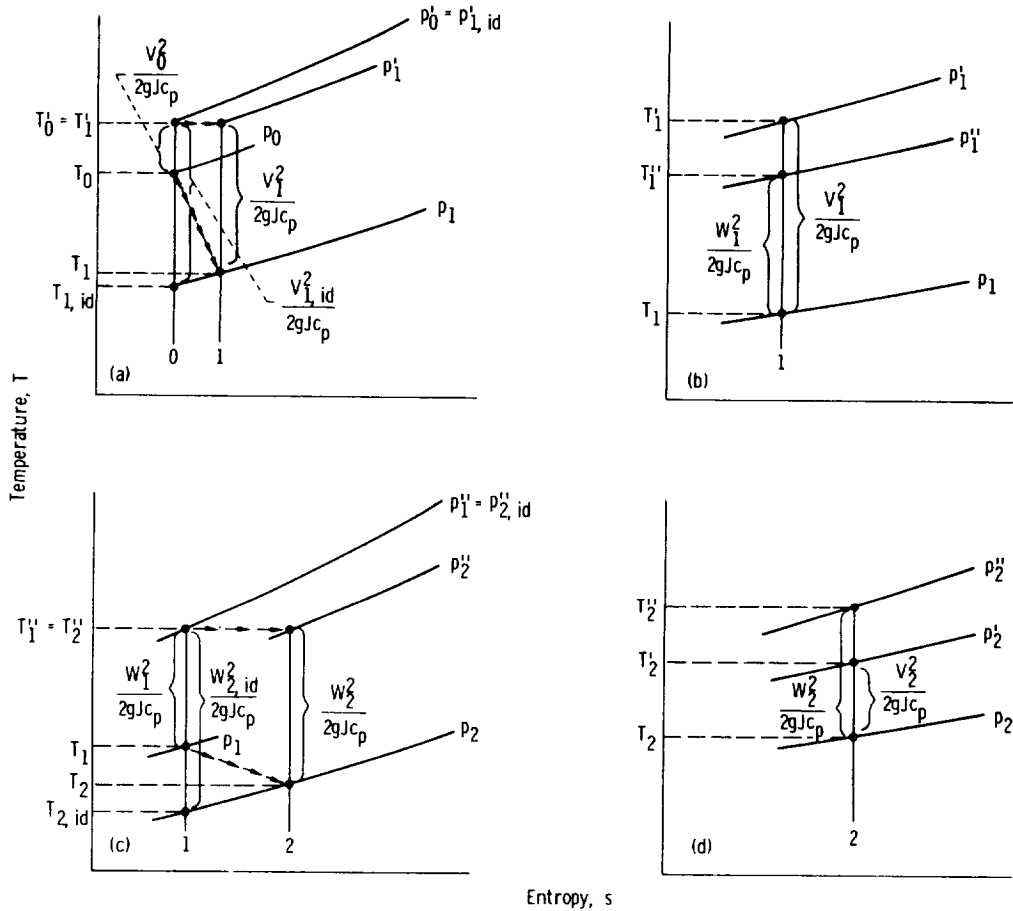


FIGURE 2-6.—Typical temperature-entropy diagram.

the discussion of the constant-entropy-process thermodynamics in chapter 1, a temperature-entropy, or T - s , diagram looks like the example shown in figure 2-6. A constant-entropy process is represented by a vertical line. At increasing values of temperature and entropy, the pressure curves diverge; therefore, at increasing values of constant entropy, the temperature difference between any two given pressure curves is also increasing.

For the purposes of clarity, the turbine expansion process will be divided into four steps, with each shown in a separate T - s diagram. These four diagrams will then be combined into a single diagram. The four diagrams represent the stator expansion process (fig. 2-7(a)), the relation between absolute and relative conditions at the stator



(a) Expansion process across stator. (b) Relation between absolute and relative conditions at stator exit.
 (c) Expansion process across rotor. (d) Relation between relative and absolute conditions at rotor exit.

FIGURE 2-7.—Temperature-entropy diagrams for flow-process steps of an axial-flow turbine.

exit (fig. 2-7(b)), the rotor expansion process relative to the moving blades (fig. 2-7(c)), and the relation between relative and absolute conditions at the rotor exit (fig. 2-7(d)).

Figure 2-7(a) shows the expansion process across the stator. The four constant-pressure curves represent the static and absolute total pressures before and after the expansion. The kinetic energy at each state is represented by the vertical distance between the static state point and the total state point in accordance with equation (1-51). If the expansion process were isentropic, the final state would be that indicated by the subscript $1,id$. The actual process proceeds from state 0 to state 1 with a small increase in entropy, as indicated by the small arrows. It can be noted that the kinetic energy developed by the actual process is less than would be developed by the ideal process.

As mentioned previously, we analyze flow through the rotor in terms of relative conditions. Figure 2-7(b) shows the relation between the absolute and relative total states at the stator exit. These states are related isentropically, and the absolute and relative kinetic energies and total temperatures are indicated in the figure.

The expansion process across the rotor is shown in figure 2-7(c) in terms of the relative conditions. The four constant-pressure curves represent the static and relative total pressures before and after the expansion. For simplicity, axial flow is assumed, so that $T_1'' = T_2''$. If the expansion were isentropic, the final state would be that indicated by the subscript $2,id$. The actual process proceeds from state 1 to state 2, as indicated by the small arrows, with an increase in entropy. Here again it can be noted that the relative kinetic energy developed by the actual process is less than would be developed by an ideal process.

The relation between the relative and absolute total states at the rotor exit is shown in figure 2-7(d). These states are related isentropically, and the relative and absolute kinetic energies at the stage exit are indicated.

The four diagrams of figure 2-7 are now combined into one diagram shown as figure 2-8. The static, absolute total, and relative total state processes for the turbine expansion are indicated by the arrows through the appropriate state points. For the time being, ignore the enthalpy differences indicated on the right of the figure. Note that the point $(p_2, T_{2,id})$, which is on the state 1 constant-entropy line in figure 2-7(c), is not the same point as indicated in figure 2-8, where it is on the state 0 constant-entropy line. In figure 2-7(c), the subscript $2,id$ refers to the ideal expansion across the rotor alone. In figure 2-8, the subscript $2,id$ refers to the ideal expansion across the entire stage (both stator and rotor). The meaning of the subscript $2,id$

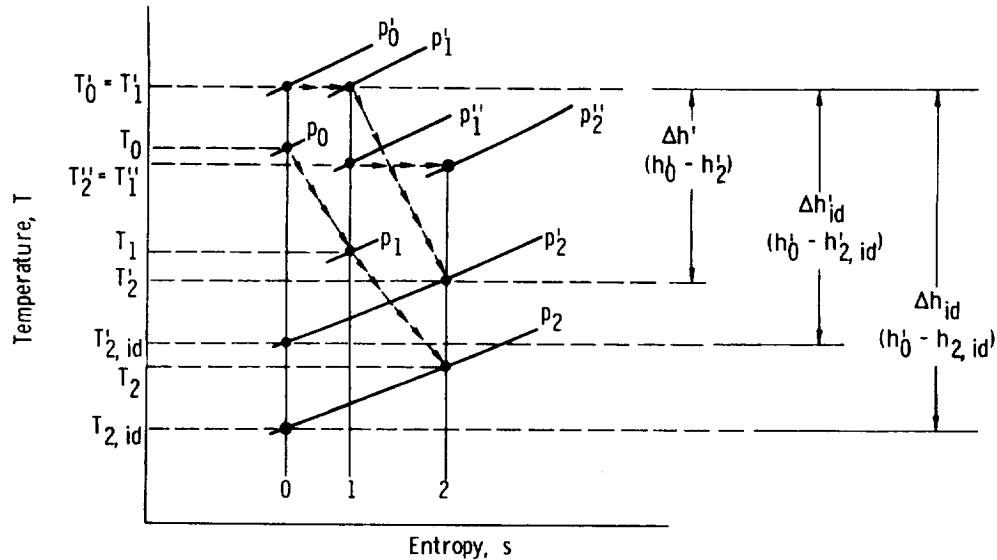


FIGURE 2-8.—Temperature-entropy diagram for a stage of an axial-flow turbine.

is, therefore, ambiguous but is commonly used in both senses. It is obvious from figure 2-8 that the work obtained from the real turbine process (as represented by $T'_0 - T'_2$) is less than the work that could be obtained from an ideal turbine process (as represented by $T'_0 - T'_{2, id}$).

Blade-Row Efficiency

Since turbine blade rows do not operate isentropically, we need a parameter to express blade-row performance. One common parameter used for this purpose is blade-row efficiency, which is defined as the actual exit kinetic energy divided by the ideal exit kinetic energy of the blade row. For the stator,

$$\eta_{st} = \frac{V_1^2}{V_{1, id}^2} \quad (2-42)$$

where η_{st} is stator efficiency. The relation between V_1^2 and $V_{1, id}^2$ is indicated in figure 2-7(a). By applying equations (1-51), (1-52), and (1-55), we get

$$V_{1, id}^2 = 2gJc_p T'_0 \left[1 - \left(\frac{p_1}{p_0} \right)^{(\gamma-1)/\gamma} \right] \quad (2-43)$$

For the rotor

$$\eta_{ro} = \frac{W_2^2}{W_{2, id}^2} \quad (2-44)$$

where η_{ro} is rotor efficiency. The relation between W_2^2 and $W_{2, id}^2$ is indicated in figure 2-7(c). For purely axial flow,

$$W_{2, id}^2 = 2gJc_p T_1'' \left[1 - \left(\frac{p_2}{p_1} \right)^{(\gamma-1)/\gamma} \right] \quad (2-45)$$

Thus, with inlet conditions and efficiency known for a given blade row, it is possible to calculate exit velocity for a specified exit static pressure. Blade-row performance in terms of kinetic energy is sometimes expressed as a loss rather than as an efficiency, as

$$e = 1 - \eta \quad (2-46)$$

where e is the kinetic-energy loss coefficient.

Blade-row performance also can be expressed in terms of a loss in total pressure. Several coefficients of this type have been used, each differing by the normalizing parameter used to make the coefficient dimensionless. Inlet total pressure, exit ideal dynamic head, and exit actual dynamic head have all been used for this purpose as follows:

Stator:	Axial rotor:	
$Y_{st} = \frac{p_0' - p_1'}{p_0'}$	$Y_{ro} = \frac{p_1'' - p_2''}{p_1''}$	(2-47a)

$Y'_{st} = \frac{p_0' - p_1'}{p_0' - p_1'}$	$Y'_{ro} = \frac{p_1'' - p_2''}{p_1'' - p_2}$	(2-47b)
---	---	---------

$Y''_{st} = \frac{p_0' - p_1'}{p_1' - p_1}$	$Y''_{ro} = \frac{p_1'' - p_2''}{p_2'' - p_2}$	(2-47c)
---	--	---------

where Y , Y' , and Y'' are total-pressure loss coefficients. Relations between the kinetic-energy loss coefficient and the various total-pressure loss coefficients can be derived. These relations are not simply stated, and they involve a Mach number dependency.

Turbine and Stage Efficiencies

Turbine or stage energy transfer is maximum when the expansion process is isentropic. Since the process is never isentropic, we need a parameter for expressing turbine or stage performance. The parameter that we use is the turbine or stage efficiency, which is defined as the ratio of actual energy transfer to ideal (isentropic) energy transfer. This efficiency is known as the isentropic or adiabatic efficiency. The several different ways that we can apply the above definition are discussed in the sections to follow.

Overall efficiency.—Overall efficiency refers to the overall turbine or stage process. It is the ratio of actual energy transferred in the turbine or stage to the ideal energy transfer based on isentropic flow from the turbine or stage inlet condition to the exit pressure. Note that we are discussing aerodynamic efficiency and are not, at present,

considering mechanical inefficiencies due to items such as bearing and seal friction.

We will define actual energy transfer as the shaft work done by the turbine. This definition is the one used by most people; occasionally, however, actual energy transfer is defined as shaft work plus exit kinetic energy. Actual energy transfer as defined herein is the decrease in absolute total enthalpy across the turbine or stage, and this is indicated in figure 2-8.

Now we must consider whether to define the ideal energy available to do work on the basis of static or total conditions. At the inlet, the total state is always used because the inlet kinetic energy is available for conversion to shaft work. At the turbine or stage exit, static conditions are sometimes used and total conditions are sometimes used. If the turbine exhaust-flow kinetic energy is dissipated, as in a plenum, then the exit kinetic energy is just wasted. This wasted kinetic energy could have been put to use if it could have been converted to shaft work in the turbine. In such a case, we use the exit static state for the computation of ideal work because it would be desirable to expand down to the exit static state with zero exit kinetic energy. In this desirable ideal case, the exit total state would equal the exit static state.

If we were considering a multistage turbine in the above situation, the kinetic energy from only the last stage would be considered as a loss. The kinetic energies leaving the other stages are not wasted, but are carried over to the next stage, where they may be converted to shaft work. Thus, the last stage is rated on the basis of its exit static condition, while the other stages are rated on the basis of their exit total conditions.

In cases where the turbine-exit kinetic energy serves a useful purpose, the entire turbine is rated on the basis of ideal work computed from the exit total state conditions. The most obvious example of this case is the jet-engine turbine. Here the gas must be expanded to a high velocity before leaving the engine, and, therefore, a high velocity leaving the turbine is not a waste.

The efficiency based on the ideal work available between the inlet total and exit static conditions is called the static efficiency. The efficiency based on the ideal work available between the inlet total and exit total conditions is called the total efficiency. The conditions represented by the ideal enthalpy decrease for each of these cases are indicated in figure 2-8. It can be seen that the ideal work based on the exit total condition must be less (as long as there is some exit kinetic energy) than that based on the exit static condition. Thus, total efficiency is always higher than static efficiency, with the difference between the two increasing with increasing exit kinetic energy.

Overall turbine efficiency $\bar{\eta}$ and stage efficiency η_{stg} are defined by similar equations. The subscripts *in* and *ex* are used to denote turbine inlet and exit conditions, instead of the subscripts 0 and 2 used for the stage. Overall turbine static efficiency can be expressed as

$$\bar{\eta} = \frac{\overline{\Delta h'}}{\overline{\Delta h'_{id}}} = \frac{h'_{in} - h'_{ex}}{h'_{in} - h'_{id,ex}} \quad (2-48a)$$

For the ideal-gas-law and constant-heat-capacity assumptions, this reduces to

$$\bar{\eta} = \frac{T'_{in} - T'_{ex}}{T'_{in} \left[1 - \left(\frac{p'_{ex}}{p'_{in}} \right)^{(\gamma-1)/\gamma} \right]} \quad (2-48b)$$

Overall turbine total efficiency is expressed as

$$\bar{\eta}' = \frac{\overline{\Delta h'}}{\overline{\Delta h'_{id}}} = \frac{h'_{in} - h'_{ex}}{h'_{in} - h'_{id,ex}} \quad (2-49a)$$

For the ideal-gas-law and constant-heat-capacity assumptions, this reduces to

$$\bar{\eta}' = \frac{T'_{in} - T'_{ex}}{T'_{in} \left[1 - \left(\frac{p'_{ex}}{p'_{in}} \right)^{(\gamma-1)/\gamma} \right]} \quad (2-49b)$$

Stage total and static efficiencies are similarly defined but with the appropriate subscripts.

Relation of turbine efficiency to stage efficiency.—The overall turbine efficiency is useful as a measure of the overall performance of the turbine. However, it is not a true indication of the efficiency of the stages comprising the turbine. There is an inherent thermodynamic effect hidden in the overall turbine efficiency expression. If equation (2-48b) or (2-49b) were written for a stage, it could be seen that for a given stage pressure ratio and stage efficiency, the energy transfer, which for a stage would be $(T'_0 - T'_2)$, is proportional to the temperature of the gas entering the stage. For a turbine, as can be seen from figure 2-8, the losses of one stage appear in the form of a higher temperature gas entering the following stage ($T_2 > T_{2,id}$). This following stage is then capable of delivering additional work. Therefore, even though all the individual stages may have the same stage efficiency, the overall turbine efficiency still depends on the pressure ratio and the number of stages.

This effect can be shown by means of a temperature-entropy diagram, such as figure 2-9. The solid vertical line 0-2,*id* represents

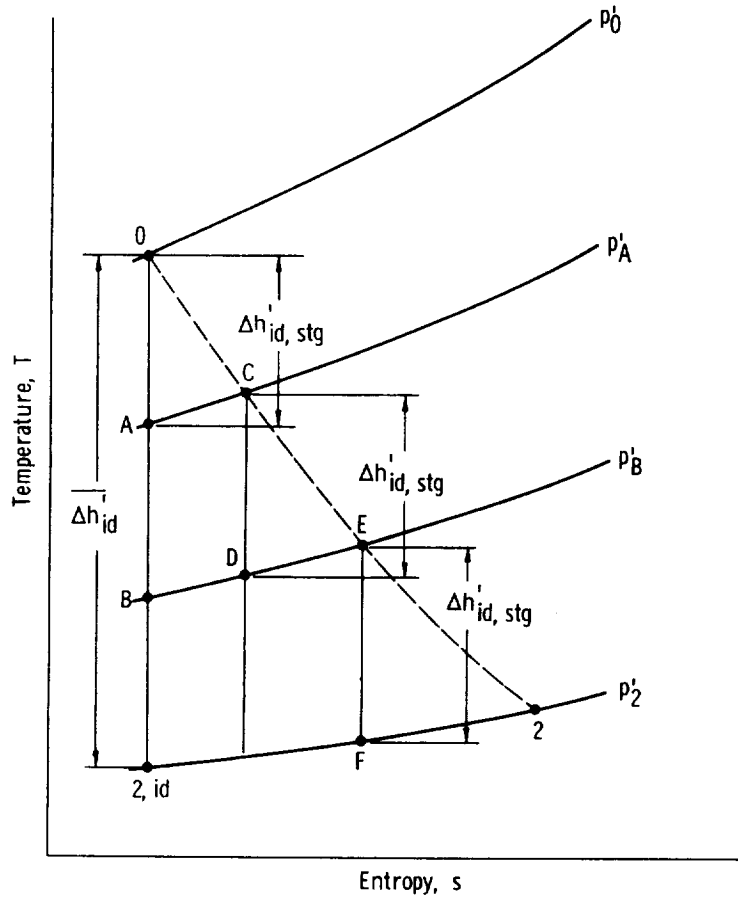


FIGURE 2-9.—Temperature-entropy diagram showing reheat effect in a multistage turbine.

isentropic expansion from inlet pressure p'_0 to exit pressure p'_2 . The dashed line 0-2 represents the process of overall turbine efficiency $\bar{\eta}'$ taking place in three stages, each having the same stage efficiency η'_{stg} .

The actual work obtained from each stage is $\eta'_{stg} \Delta h'_{id, stg}$, where $\Delta h'_{id, stg}$ is the ideal work for a stage. As mentioned previously, the difference of temperature between lines of constant pressure increases with increasing values of entropy. Hence, for the second stage (p'_A to p'_B), the isentropic work represented by the line C-D is greater than that represented by A-B. Thus, the isentropic work for this stage is greater by virtue of the inefficiency of the previous stage and, for constant stage efficiency, the actual work will be greater. Similarly, E-F is greater than B-2, *id*. With lines 0-A, C-D, and E-F representing the ideal work for the three stages, and $\Sigma \Delta h'_{id, stg}$ representing the sum of these, it can be seen that $\Sigma \Delta h'_{id, stg}$ is greater than $\bar{\Delta h}'_{id}$, which is the turbine ideal work represented by the sum of 0-A, A-B, and B-2, *id*.

The total actual turbine work obtained from the expansion from p'_0 to p'_2 can be represented by either $\bar{\eta}' \bar{\Delta h}'_{id}$ or $\eta'_{stg} \Sigma \Delta h'_{id, stg}$, and these two values must be equal. Thus,

$$\bar{\eta}' \bar{\Delta h}'_{id} = \eta'_{stg} \Sigma \Delta h'_{id, stg} \quad (2-50)$$

or

$$\frac{\bar{\eta}'}{\eta'_{stg}} = \frac{\Sigma \Delta h'_{id, stg}}{\bar{\Delta h}'_{id}} \quad (2-51)$$

Since $\Sigma \Delta h'_{id, stg} > \bar{\Delta h}'_{id}$, the turbine overall isentropic efficiency is greater than the stage isentropic efficiencies, or $\bar{\eta}' > \eta'_{stg}$.

This effect in turbines is called the "reheat" effect. This must not be confused with the process of adding heat from an external source between stages, which is also called "reheat".

The equation for calculating overall turbine efficiency for several stages of constant stage pressure ratio p'_2/p'_0 and constant stage efficiency η'_{stg} is

$$\bar{\eta}' = \frac{1 - \left\{ 1 - \eta'_{stg} \left[1 - \left(\frac{p'_2}{p'_0} \right)^{(\gamma-1)/\gamma} \right] \right\}^n}{1 - \left(\frac{p'_2}{p'_0} \right)^{n(\gamma-1)/\gamma}} \quad (2-52)$$

where n is the number of stages. The derivation of this equation can be found in reference 1.

The fact that stage efficiency differs from turbine efficiency, depending on the pressure ratio, raises an important consideration. A comparison of turbine efficiencies of two machines of different pressure ratios is not a true comparison of their aerodynamic behavior, as the one of higher pressure ratio is helped by the reheat effect. It would be desirable to be able to express a true aerodynamic efficiency for a turbine. In order to eliminate all reheat effect, this would have to be the efficiency of an infinitesimally small stage.

Infinitesimal-stage efficiency.—Starting from pressure p and temperature T , suppose a gas is expanded to pressure $(p-dp)$ and temperature $(T-dT)$, where dT is the increment of temperature for an infinitesimal stage of isentropic efficiency η_p . By using the isentropic-efficiency definition, we write

$$dT = \eta_p T \left[1 - \left(\frac{p-dp}{p} \right)^{(\gamma-1)/\gamma} \right] \quad (2-53)$$

and

$$\frac{dT}{T} = \eta_p \left[1 - \left(1 - \frac{dp}{p} \right)^{(\gamma-1)/\gamma} \right] \quad (2-54)$$

These equations are not quite rigorously in accord with the isentropic-efficiency definition. Some authors ignore the fact that the actual work differential should be proportional to the total-temperature differential rather than the static-temperature differential. Other authors make the assumption that there is no change in kinetic energy across the infinitesimal stage, so that $dT' = dT$. However, it always seems to be the static temperature that is used in the infinitesimal-efficiency expression.

Using the series expansion approximation $(1+x)^n = 1+nx$ for evaluation of equation (2-54) yields

$$\frac{dT}{T} = \eta_p \frac{\gamma-1}{\gamma} \frac{dp}{p} \quad (2-55)$$

Integrating between the turbine inlet and exit yields

$$\eta_p = \frac{\ln \frac{T_{in}}{T_{ex}}}{\frac{\gamma-1}{\gamma} \ln \frac{p_{in}}{p_{ex}}} \quad (2-56)$$

Equation (2-56) can be written as

$$\frac{T_{in}}{T_{ex}} = \left(\frac{p_{in}}{p_{ex}} \right)^{\eta_p [(\gamma-1)/\gamma]} \quad (2-57)$$

The infinitesimal-stage efficiency η_p is supposedly the true aerodynamic efficiency, exclusive of the effect of pressure ratio. This efficiency is also known as the polytropic efficiency. This name arises from the method of expressing an irreversible process path as $pv^n = \text{constant}$, where n is called the polytropic exponent, and the process is called a polytropic process. Substituting for v from the ideal gas law, we get for the polytropic process

$$\frac{T_{in}}{T_{ex}} = \left(\frac{p_{in}}{p_{ex}} \right)^{(n-1)/n} \quad (2-58)$$

Equations (2-57) and (2-58) are very similar, and if the turbine process were to be expressed as a polytropic process, then we could relate polytropic efficiency and the polytropic exponent as

$$\frac{n-1}{n} = \eta_p \frac{\gamma-1}{\gamma} \quad (2-59)$$

If we neglect inlet and exit kinetic energies for the overall turbine

TURBINE DESIGN AND APPLICATION

process, we can relate turbine overall efficiency to polytropic efficiency. Actual temperature drop could be expressed as

$$T_{in} - T_{ex} = \bar{\eta} T_{in} \left[1 - \left(\frac{p_{ex}}{p_{in}} \right)^{(\gamma-1)/\gamma} \right] \quad (2-60)$$

or

$$T_{in} - T_{ex} = T_{in} \left\{ 1 - \left(\frac{p_{ex}}{p_{in}} \right)^{\eta_p [(\gamma-1)/\gamma]} \right\} \quad (2-61)$$

Equating (2-60) with (2-61) then yields

$$\bar{\eta} = \frac{1 - \left(\frac{p_{ex}}{p_{in}} \right)^{\eta_p [(\gamma-1)/\gamma]}}{1 - \left(\frac{p_{ex}}{p_{in}} \right)^{(\gamma-1)/\gamma}} \quad (2-62)$$

This relation is illustrated in figure 2-10. The two efficiencies approach each other as pressure ratio and efficiency each approach unity. However, at higher pressure ratios, especially at lower efficiency levels, the two efficiencies can differ significantly.

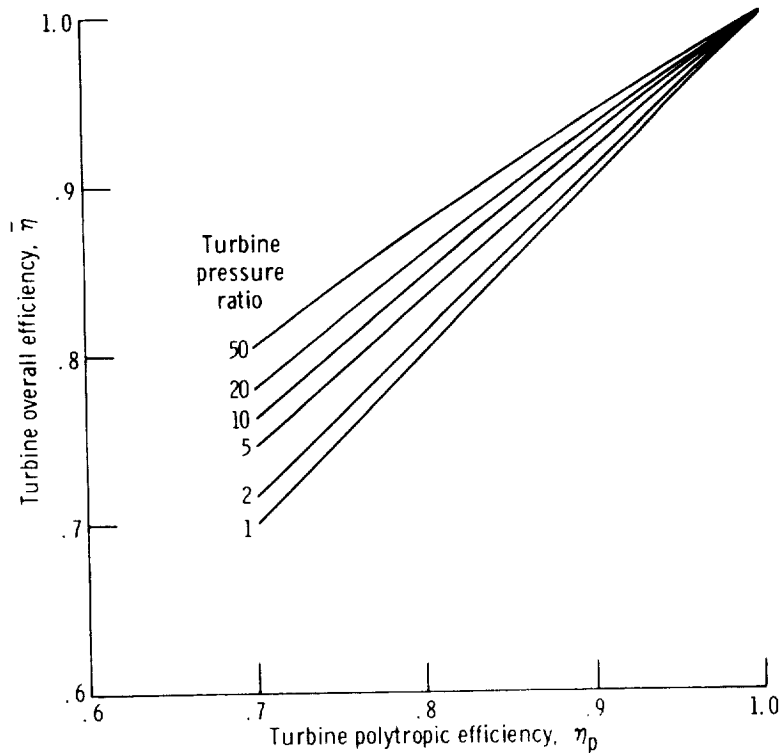


FIGURE 2-10.—Relation between turbine overall and polytropic efficiencies. Specific heat ratio γ , 1.4.

DIMENSIONLESS PARAMETERS

Dimensionless parameters serve to classify velocity diagrams, classify turbine geometry, and correlate turbine performance. A number of the more commonly used dimensionless parameters are introduced and discussed in this section. The basis for the use of dimensionless parameters is dimensional analysis.

Dimensional Analysis

Dimensional analysis is a procedure that allows a group of variables comprising a physical relation to be arranged so that they throw some light on the nature of the relation. It is a procedure for grouping the variables into a smaller number of dimensionless groups, each containing two or more variables. The number of such groups will be the minimum necessary to include all the variables at least once and to represent the physical relation between them. The basis of dimensional analysis as a formal procedure is the π -Theorem, which states that a complete physical equation may be expressed in the form of a number of terms, each term representing a product of powers of some of the variables and forming a dimensionless group. The formal procedure for obtaining the dimensionless groups from the pertinent variables is presented in many texts, including reference 1, which served as the basis for this discussion.

Application of dimensional analysis to the general problem of fluid flow yields considerable insight into the nature of the basic physical relations. The resultant dimensionless terms represent ratios of dimensions, ratios of forces, and ratios of velocities. The geometrical term implies that shape (as a ratio of linear dimensions), rather than the actual magnitude of each linear dimension by itself, is a controlling factor. Another term expresses the ratio of the force due to the change of pressure in the fluid to the inertia force due to the motion of the fluid. This is a basic flow parameter characteristic of an analysis based on an ideal fluid. There are other dimensionless groups, based on various attributes of a real fluid, that modify the ideal relations. These include the Reynolds number, which expresses the effect of viscous forces; the Weber number, which expresses surface-tension effects; an elasticity parameter (which for a gas reduces to the Mach number), which expresses compressibility effects; and the Froude number, which expresses gravitational effects. Of these terms expressing real fluid effects, in general, the Reynolds and Mach numbers are the significant parameters for gas flow.

The concept of dimensionless groups as ratios of geometric, kinematic, and dynamic quantities leads to the idea of similarity or similitude. If two operating conditions are such that all the dimen-

sionless terms have the same value, regardless of the individual values of the separate variables, then exactly similar physical conditions are obtained. Complete physical similarity implies (1) geometric similarity, which means that the linear dimension ratios are everywhere the same; (2) kinematic similarity, which means that the velocity ratios are the same; and (3) dynamic similarity, which means that the ratios of the different forces are the same. It is doubtful whether complete physical similarity is ever attained, but for most practical purposes it can be approached sufficiently closely to be of great utility. One use of similarity is the operation of models of smaller linear scale so that relatively inexpensive experiments can be performed with the results applicable to the full-size machine. Another use of similarity involves the operation of machines with the fluid at or near ambient conditions rather than at some severe design condition.

Turbomachine Operational Parameters

Application of dimensional analysis to the general problem of fluid flow results in the previously mentioned set of parameters. These parameters are important for the detailed examination of flow within the blade rows of turbomachines. In addition, dimensional analysis has great utility in the analysis of the overall operational characteristics. For any turbomachine, we are interested in the relation of head (for compressible flow, this relates to ideal work), flow rate, and power in conjunction with size, speed, and the properties of the fluid. The following variables are used to demonstrate some of the more important relations:

- Volume flow rate, Q , m³/sec or ft³/sec
- Head, H , J/kg or (ft)(lbf)/lbm
- Power, P , W or Btu/sec
- Rotative speed, N , rad/sec or rev/min
- Characteristic linear dimension, D , m or ft
- Fluid density, ρ , kg/m³ or lb/ft³
- Fluid viscosity, μ , (N)(sec)/m² or lbm/(ft)(sec)
- Fluid elasticity, E , N/m² or lbf/ft²

From these variables, five dimensionless groups can be formed. If we drop the dimensional conversion constants in order to ease the manipulation, the five dimensionless groups can be expressed as

$$\frac{Q}{ND^3} = \text{fcn} \left(\frac{H}{N^2 D^2}, \frac{P}{\rho N^3 D^5}, \frac{\rho N D^2}{\mu}, \frac{E}{\rho N^2 D^2} \right) \quad (2-63)$$

The capacity, or flow rate, is expressed in dimensionless form by Q/ND^3 , which is called the capacity coefficient. It can be further

represented as

$$\frac{Q}{ND^3} \propto \frac{VA}{ND^3} \propto \frac{VD^2}{ND^3} \propto \frac{V}{ND} \propto \frac{V}{U} \quad (2-64)$$

Thus, the capacity coefficient is equivalent to V/U , and a given value of Q/ND^3 implies a particular relation of fluid velocity to blade speed or, in kinematic terms, similar velocity diagrams.

The head is expressed in dimensionless form by H/N^2D^2 , which is called the head coefficient. This can be represented as

$$\frac{H}{N^2D^2} \propto \frac{H}{U^2} \quad (2-65)$$

Thus, a given value of H/N^2D^2 implies a particular relation of head to rotor kinetic energy, or dynamic similarity.

The term $P/\rho N^3D^5$ is a power coefficient. It represents the actual power and thus is related to the capacity and head coefficients, as well as to the efficiency.

The term $\rho ND^2/\mu$ is the Reynolds number, or viscous effect coefficient. Its effect on overall turbine performance, while still important, can be regarded as secondary. The Reynolds number effect will be discussed separately later in this chapter.

The term $E/\rho N^2D^2$ is the compressibility coefficient. Its effect depends on the level of Mach number. At low Mach number, where the gas is relatively incompressible, the effect is negligible or very secondary. As Mach number increases, the compressibility effect becomes increasingly significant.

Velocity-Diagram Parameters

We have seen that the ratio of fluid velocity to blade velocity and the ratio of fluid energy to blade energy are important factors required for achieving similarity in turbomachines. Since completely similar machines should perform similarly, these factors become important as a means for correlating performance. Since the factors V/U and H/U^2 are related to the velocity diagrams, factors of this type are referred to as velocity-diagram parameters.

Several velocity-diagram parameters are commonly used in turbine work. Most of these are used primarily with respect to axial-flow turbines. One of these parameters is the speed-work parameter

$$\lambda = \frac{U^2}{gJ\Delta h'} \quad (2-66)$$

The reciprocal of the speed-work parameter is also often used, and it

is referred to as the loading factor or loading coefficient

$$\psi = \frac{1}{\lambda} = \frac{gJ\Delta h'}{U^2} \quad (2-67)$$

For an axial-flow turbine, we can write

$$\Delta h' = \frac{U\Delta V_u}{gJ} \quad (2-68)$$

Therefore, equations (2-66) and (2-67) can be expressed as

$$\lambda = \frac{1}{\psi} = \frac{U}{\Delta V_u} \quad (2-69)$$

Another parameter often used is the blade-jet speed ratio

$$\nu = \frac{U}{V_j} \quad (2-70)$$

where V_j is the jet, or spouting, velocity, in m/sec or ft/sec. The jet, or spouting, velocity is defined as the velocity corresponding to the ideal expansion from inlet total to exit static conditions across the stage or turbine. That is,

$$V_j^2 = 2gJ\Delta h_{id} \quad (2-71)$$

Substitution of equation (2-71) back into equation (2-70) yields

$$\nu = \frac{U}{\sqrt{2gJ\Delta h_{id}}} \quad (2-72)$$

A relation between the blade-jet speed ratio and the speed-work parameter can be obtained by use of equations (2-66) and (2-72) and the static efficiency definition

$$\eta = \frac{\Delta h'}{\Delta h_{id}} \quad (2-73)$$

The resultant relation is

$$\nu = \sqrt{\frac{\lambda\eta}{2}} \quad (2-74)$$

This shows that if efficiency is a function of one of these parameters it must also be a function of the other. While the speed-work parameter is directly related only to the actual velocity diagram, the blade-jet speed ratio is related to the velocity diagram and to the efficiency.

Another frequently used velocity-diagram parameter is the flow

factor, or flow coefficient

$$\varphi = \frac{V_r}{U} \quad (2-75)$$

The flow coefficient can be related to the loading coefficient as follows:

$$\varphi = \frac{V_r}{U} = \left(\frac{V_r}{V_{u,1}} \right) \left(\frac{V_{u,1}}{\Delta V_u} \right) \left(\frac{\Delta V_u}{U} \right) \quad (2-76)$$

By using equation (2-69) and the velocity-diagram geometry, we get

$$\varphi = \psi \cot \alpha_1 \left(\frac{V_{u,1}}{\Delta V_u} \right) \quad (2-77)$$

The term $V_{u,1}/\Delta V_u$ cannot be completely generalized. However, for specific types of velocity diagrams, such as will be discussed in the next chapter, this term becomes a function of loading coefficient alone (a different function for each type of velocity diagram). Therefore, for each of the different types of velocity diagrams, the flow coefficient can be expressed in terms of the loading coefficient and the stator exit angle.

It is thus seen that these four velocity-diagram parameters are related to each other. In addition, efficiency can be related to these parameters. This will be shown for an idealized specific case in the next section and for a somewhat more general real case in the next chapter. Where a particular type of velocity diagram is specified, only one of the velocity-diagram parameters is required for correlating efficiency. We at Lewis generally use the speed-work parameter or the blade-jet speed ratio. For a more general efficiency correlation, two of these parameters are required. One parameter must be the flow coefficient, and the other is usually the loading coefficient.

Relation of Efficiency to Velocity-Diagram Parameters

We will now show for an idealized specific case how static efficiency can be related mathematically to the blade-jet speed ratio. Assume that we have a single axial-flow ($U_1=U_2$) impulse ($W_1=W_2$) stage with constant axial velocity ($V_{x,1}=V_{x,2}$). A velocity diagram for a stage of this type is shown in figure 2-11. Further assume that flow through this turbine stage is isentropic (total efficiency $\eta'=1$). The only loss, therefore, is exit kinetic energy. The static efficiency definition is

$$\eta = \frac{h'_0 - h'_2}{h'_0 - h'_{2,ia}} = \frac{\Delta h'}{\Delta h'_{ia}} \quad (2-78)$$

Substitution of equation (2-68) into equation (2-78) yields

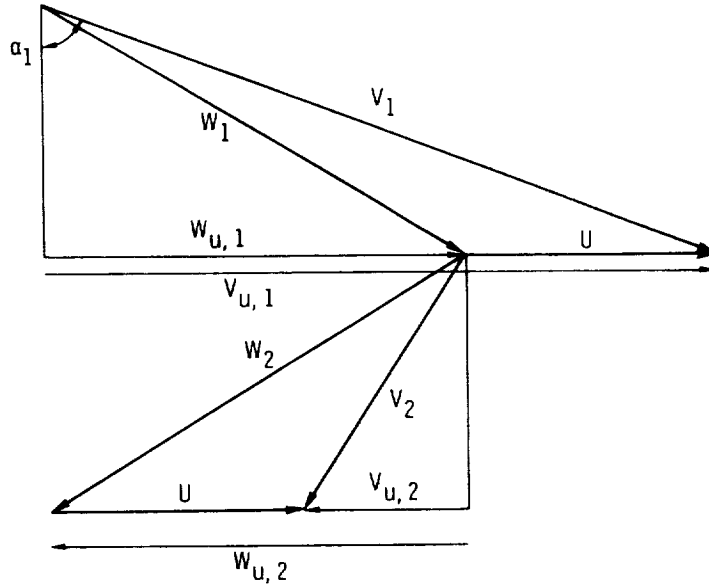


FIGURE 2-11.—Velocity-vector diagram for an axial-flow, impulse stage.

$$\eta = \frac{U \Delta V_u}{g J \Delta h_{id}} \quad (2-79)$$

The change in fluid tangential velocity is

$$\Delta V_u = V_{u,1} - V_{u,2} \quad (2-80)$$

From the assumptions ($W_1 = W_2$) and ($W_{x,1} = W_{x,2}$) and the sign convention we adopted,

$$W_{u,2} = -W_{u,1} \quad (2-81)$$

From equations (2-6), (2-81), and (2-80), we get

$$V_{u,2} = W_{u,2} + U = -W_{u,1} + U = -(V_{u,1} - U) + U = -V_{u,1} + 2U \quad (2-82)$$

and

$$\Delta V_u = V_{u,1} - V_{u,2} = V_{u,1} - (-V_{u,1} + 2U) = 2V_{u,1} - 2U \quad (2-83)$$

From the velocity-diagram geometry

$$V_{u,1} = V_1 \sin \alpha_1 \quad (2-84)$$

Since flow is isentropic and the turbine stage is of the impulse type ($h_{2, id} = h_2 = h_1$),

$$V_1 = \sqrt{2gJ\Delta h_{id}} \quad (2-85)$$

Substitution of equations (2-84) and (2-85) into equation (2-83)

yields

$$\Delta V_u = 2 \sin \alpha_1 \sqrt{2gJ\Delta h_{id}} - 2U \quad (2-86)$$

Substitution of equation (2-86) back into equation (2-79) yields

$$\eta = \frac{4U \sin \alpha_1}{\sqrt{2gJ\Delta h_{id}}} - \frac{4U^2}{2gJ\Delta h_{id}} \quad (2-87)$$

Now using the definition of blade-jet speed ratio from equation (2-72) finally yields

$$\eta = 4\nu \sin \alpha_1 - 4\nu^2 \quad (2-88)$$

Equation (2-88) shows that for this particular case and any constant stator exit angle, static efficiency is a function of blade-jet speed ratio only. The variation is parabolic and is illustrated in figure 2-12 for an example with a stator exit angle of 70° . A maximum efficiency of 0.88 is reached at a blade-jet speed ratio of 0.47. The optimum blade-jet speed ratio can be found mathematically by differentiating equation (2-88) and setting the derivative equal to zero:

$$\nu_{opt} = \frac{\sin \alpha_1}{2} \quad (2-89)$$

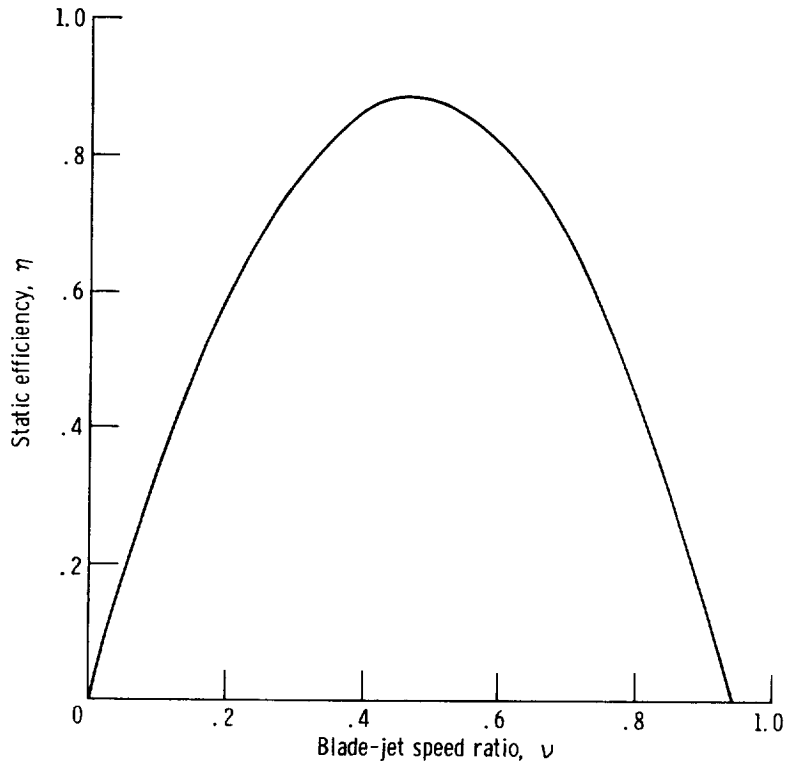


FIGURE 2-12.—Effect of blade-jet speed ratio on static efficiency of an isentropic, axial-flow, impulse stage. Stator exit angle, 70° .

Since the stator exit angle is normally in the range of 60° to 80° , where the sine of the angle does not vary greatly, the optimum blade-jet speed ratio for most cases of interest with a turbine of this type would be in the range of 0.4 to 0.5.

Equation (2-88) and figure 2-12 are, of course, very idealized and specific. While the levels and values for a real case will differ from the ideal case, the basic parabolic trend should remain the same; and, indeed, it does. We find that for a real case, blade-jet speed ratio is a very good correlating parameter for both static and total efficiency. Likewise, so are the other velocity-diagram parameters.

Design Parameters

The operation of dimensional analysis on the variables relating to turbomachines led to the dimensionless parameters shown in equation (2-63). This does not, however, exhaust the number of dimensionless parameters that are possible. A parameter not having the linear dimension D would be desirable because values of the remaining variables would apply to a range of geometrically similar turbomachines of all sizes. Also, a parameter not having rotative speed N would be desirable because, in this case, values of the remaining variables would apply to a turbomachine at all rotative speeds.

Such parameters can be found by combining two of the previous groups. The parameter that excludes D is known as the specific speed N_s , and is found as

$$N_s = \left(\frac{Q}{ND^3} \right)^{1/2} \left(\frac{N^2 D^2}{H} \right)^{3/4} = \frac{NQ^{1/2}}{H^{3/4}} \quad (2-90)$$

When used for a turbine, the volume flow rate is taken at the stage exit or turbine exit. Thus,

$$N_s = \frac{NQ_{ex}^{1/2}}{H^{3/4}} \quad (2-91)$$

The parameter that excludes N is known as the specific diameter D_s , and is found as

$$D_s = \left(\frac{H}{N^2 D^2} \right)^{1/4} \left(\frac{ND^3}{Q} \right)^{1/2} = \frac{DH^{1/4}}{Q^{1/2}} \quad (2-92)$$

With the volume flow rate taken at the stage exit or turbine exit,

$$D_s = \frac{DH^{1/4}}{Q_{ex}^{1/2}} \quad (2-93)$$

Commonly, but not exclusively, the values for these parameters are quoted with rotative speed N in revolutions per minute, exit

volume flow rate Q_{ex} in cubic feet per second, ideal work, or head, H in foot-pounds per pound, and diameter D in feet. With this set of units, specific speed and specific diameter are not truly dimensionless because the units are not consistent. The head H is usually taken to be the total-to-total value ($\Delta h'_{id}$), but sometimes, for convenience, it is specified as the total-to-static value (Δh_{id}).

Specific speed and specific diameter can be related to the previously presented velocity diagram parameters. The blade speed is

$$U = \frac{\pi ND}{K} \quad (2-94)$$

where K is the dimensional constant (2π rad/rev or 60 sec/min). The head is

$$H = J\Delta h'_{id} = J\Delta h_{id} \left(\frac{\eta}{\eta'} \right) \quad (2-95)$$

Combining equations (2-91), (2-93), and (2-72) with equations (2-94) and (2-95) yields

$$N_s D_s = \frac{K}{\pi} \sqrt{\frac{2g\eta'}{\eta}} \nu \quad (2-96)$$

The ratio of total efficiency to static efficiency appears because of the differing definitions of ideal work used in defining the various parameters. Some authors prefer to use the same ideal work definition in all cases, thus eliminating the efficiency ratio from equation (2-96).

The parameter interrelation can be expressed in terms of the speed-work parameter by substituting equation (2-74) into equation (2-96)

$$N_s D_s = \frac{K}{\pi} \sqrt{g\eta'\lambda} \quad (2-97)$$

Specific speed and specific diameter can also be related to the flow coefficient. The exit volume flow rate is

$$Q_{ex} = A_{ex} V_x \quad (2-98)$$

where A_{ex} is the exit flow area, in m^2 or ft^2 . Combining equations (2-91), (2-93), (2-94), and (2-75) with equation (2-98) yields

$$N_s D_s^3 = \frac{KD^2}{\pi\varphi A_{ex}} \quad (2-99)$$

Since specific speed and specific diameter are related to the velocity-diagram parameters, which can be used to correlate efficiency, then

specific speed and specific diameter can also be used to correlate efficiency.

Specific speed and specific diameter contain variables that the velocity-diagram parameters do not. These are diameter and volume flow rate, and their use leads to terms, such as D^2/A_{ex} appearing in equation (2-99), that imply shape. Thus, specific speed and specific diameter are sometimes referred to as shape parameters. They are also sometimes referred to as design parameters, since the shape will often dictate the type of design to be selected.

Overall Parameters

The dimensionless parameters that we have been discussing can be applied to a stage or to the entire turbine. When applied to a stage, these are the similarity parameters that represent similar conditions for equal values and thus can be used to correlate efficiency. When applied to the overall turbine, some of these parameters help identify the type of design that might be most appropriate and serve as a rapid means for estimating the number of required stages.

The following are the most commonly encountered overall parameters:

Overall specific speed

$$\bar{N}_s = \frac{NQ_{ex}^{1/2}}{\bar{H}^{3/4}} \quad (2-100)$$

Overall specific diameter

$$\bar{D}_s = \frac{D_{av}\bar{H}^{1/4}}{Q_{ex}^{1/2}} \quad (2-101)$$

Overall speed-work parameter

$$\bar{\lambda} = \frac{U_{av}^2}{gJ\Delta\bar{h}'} \quad (2-102)$$

Overall blade-jet speed ratio

$$\bar{v} = \frac{U_{av}}{(2gJ\Delta\bar{h}_{id})^{1/2}} \quad (2-103)$$

The subscript *av* refers to some average condition, and the superscript ($\bar{\quad}$) refers to the value for the entire turbine.

Of these overall parameters, specific speed perhaps is most significant because its value is almost always determined by application considerations only, while the values for the other parameters generally depend on the nature of the evolved geometry. Equation (2-100) for overall specific speed can be restated to show the considerations that contribute to the value of overall specific speed. Let

$$Q_{ex} = wv_{ex} \quad (2-104)$$

where v_{ex} is specific volume at exit, in m^3/sec or ft^3/lb . Also, let mass flow rate be expressed as

$$w = \frac{J\bar{P}}{\eta'H} \tag{2-105}$$

Then, substitution of equations (2-104) and (2-105) into equation (2-100) yields

$$\bar{N}_s = \frac{1}{\eta'} \left(\frac{v_{ex}}{H^{5/2}} \right)^{1/2} \left(N\sqrt{J\bar{P}} \right) \tag{2-106}$$

Thus, the overall specific speed can be expressed as the product of three terms. The first term reflects expected performance, which can be reasonably estimated. The second term depends only on the specified gas and the thermodynamic cycle conditions. This second term is useful for evaluating the effects that different fluids (in cases where a choice is available) have on the turbine. The third term is dictated by the application. Often, both rotative speed and power are specified; in other cases, the product $N\sqrt{J\bar{P}}$, rather than the individual values of N and \bar{P} , is established by the application.

The manner in which the overall specific speed influences the tur-

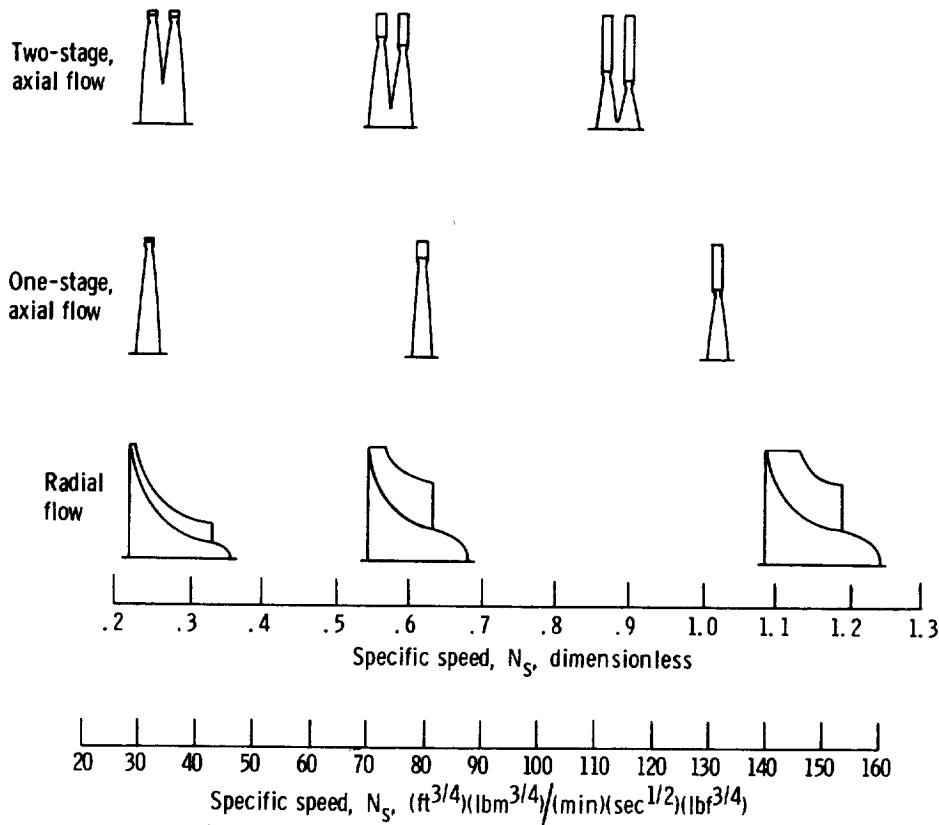


FIGURE 2-13.—Effect of specific speed on turbine-blade shape.

bine passage shape is illustrated in figure 2-13 for a radial-flow turbine and for one- and two-stage, axial-flow, example turbines. The ratio of hub radius to tip radius decreases with increasing specific speed. For the axial-flow turbines, increasing the number of stages decreases the radius ratio. Thus, the overall specific speed for any application indicates the type or types of design that will be required.

The values of some of the overall parameters give us a rapid approximation of the number of stages required for a given application. Dividing equation (2-100) for overall specific speed by equation (2-91) for stage specific speed yields

$$\frac{\bar{N}_s}{N_s} = \left(\frac{Q_{ex}}{Q_{ex, stag}} \right)^{1/2} \left(\frac{H}{\bar{H}} \right)^{3/4} \quad (2-107)$$

If we neglect the reheat effect, which is small, and assume equal head change per stage, we can write

$$\bar{H} = nH \quad (2-108)$$

Further, if the expansion ratio is not too large, we can neglect the compressibility effect and assume that $Q_{ex} = Q_{ex, stag}$. Substitution of these last two conditions into equation (2-107) and rearrangement yields

$$n = \left(\frac{N_s}{\bar{N}_s} \right)^{4/3} \quad (2-109)$$

Since stage specific speed is a correlating parameter for efficiency, experience can tell us a reasonable value of stage specific speed to assume in order to achieve a given level of efficiency. Thus, with stage specific speed assumed and overall specific speed known from the application requirement, equation (2-109) gives us an estimate for number of stages. The effect of compressibility on this estimate is discussed in reference 2, where a compressibility correction is presented.

A similar type of estimate for number of stages is often obtained from the overall speed-work parameter and an assumed value for the stage speed-work parameter. Knowledge of a value for the overall speed-work parameter, however, requires a knowledge of the blade speed. Often, a reasonable value of blade speed can be selected on the basis of stress considerations. Or, blade speed may be varied parametrically if desired. Dividing equation (2-66) for stage speed-work parameter by equation (2-102) for overall speed-work parameter, assuming a constant blade speed for the turbine ($U^2 = U_{av}^2$), and assuming equal work per stage,

$$\bar{\Delta h}' = n\Delta h' \quad (2-110)$$

yields

$$n = \frac{\lambda}{\lambda} \quad (2-111)$$

Equations (2-109) and (2-111) are particularly useful for parametric studies associated with preliminary system analyses.

Performance Specification Parameters

The turbomachinery parameters presented in equation (2-63) are perfectly correct for compressible flow machines. Another choice of variables, however, is often preferred for expressing nondimensional performance. The mass flow rate w is preferred to the volume flow rate Q because for any significant degree of expansion, Q changes considerably throughout the turbine, while w remains constant. Change of pressure expressed as pressure ratio is preferred to H , which for compressible flow depends on both pressure ratio and initial temperature. Instead of power P , the preferred term to express actual work is the specific work or drop in total enthalpy $\Delta h'$. Since ideal work depends on the initial temperature as well as on the pressure ratio, we include initial temperature as another variable. Since Mach number depends on temperature, introduction of temperature is equivalent to introducing elasticity. Rotative speed N and a characteristic dimension D are still of interest. The fluid properties are included as gas constant R , which implies a molecular weight, and viscosity μ . For simplicity here, the specific heat ratio γ is assumed constant.

Now, operating with the variables

$$w = \text{fcn}(\Delta h', p'_{in}, p'_{ex}, T'_{in}, N, D, R, \mu) \quad (2-112)$$

dimensional analysis produces the following:

$$\frac{w\sqrt{RT'_{in}}}{p'_i D^2} = \text{fcn}\left(\frac{\Delta h'}{RT'_{in}}, \frac{ND}{\sqrt{RT'_{in}}}, \frac{p'_{in}}{p'_{ex}}, \frac{w}{\mu D}\right) \quad (2-113)$$

If the specific heat ratio had not been assumed constant, there would be some complicated, but second-order, terms modifying the flow, work, and speed terms.

Let us operate on some of the above terms to see what significance we can get out of them. The mass-flow parameter may be transformed by using the continuity equation, the ideal-gas law, and the proportionality $A \propto D^2$, so that

$$w = AV\rho = AV \frac{p}{RT} \propto D^2 V \frac{p}{RT} \propto D^2 V \frac{p'_{in}}{RT'_{in}} \quad (2-114)$$

Substitution of this relation into the mass flow parameter of equation (2-113) yields

$$\frac{w\sqrt{RT'_{in}}}{p'_1 D^2} \propto \frac{D^2 V p'_{in} \sqrt{RT'_{in}}}{RT'_{in} p'_{in} D^2} \propto \frac{V}{\sqrt{RT'_{in}}} \propto \frac{V}{a_{cr}} \quad (2-115)$$

Thus, the mass flow rate is represented nondimensionally by the ratio of actual mass flow rate to the mass flow rate when the velocity equals the critical, or sonic, velocity.

The speed parameter may be transformed as

$$\frac{ND}{\sqrt{RT'_{in}}} \propto \frac{U}{\sqrt{RT'_{in}}} \propto \frac{U}{a_{cr}} \quad (2-116)$$

Thus, the rotative speed is represented nondimensionally by the ratio of rotor-blade velocity to critical velocity, which is a kind of rotor Mach number. Division of the mass-flow parameter by the speed parameter gives V/U , the kinematic condition of similarity. The implication of this analysis is that for similarity, not only must the fluid have a certain Mach number, but the rotor must also have a certain fixed velocity with respect to the critical velocity. For a given machine of fixed dimensions, therefore, the rotative speed is not a singular variable as for incompressible flow, but becomes associated with the temperature of the fluid. All variables must be expressed in dimensionless form in order for the effect of varying inlet temperature to be correlated.

For a given gas, the dimensionless parameters presented as equation (2-113) can be expressed as

$$\frac{w\sqrt{T'_{in}}}{p'_{in} D^2} = \text{fcn} \left(\frac{\Delta h'}{T'_{in}}, \frac{ND}{\sqrt{T'_{in}}}, \frac{p'_{in}}{p'_{ex}}, \frac{w}{\mu D} \right) \quad (2-117)$$

For a given gas in a given turbine, the parameters further reduce to

$$\frac{w\sqrt{T'_{in}}}{p'_{in}} = \text{fcn} \left(\frac{\Delta h'}{T'_{in}}, \frac{N}{\sqrt{T'_{in}}}, \frac{p'_{in}}{p'_{ex}}, \frac{w}{\mu} \right) \quad (2-118)$$

Depending on the particular case, the parameters presented in equations (2-113), (2-117), or (2-118) can be used to express turbine performance.

Equivalent Conditions

It is very useful to report performance under standard conditions of temperature and pressure and sometimes of fluid molecular weight and specific heat ratio. This is done in order that results obtained at

different conditions may be directly and readily compared and also easily used to determine performance for any condition we desire. The following are the standard conditions usually used: atmospheric pressure, 101 325 N/m² abs or 14.696 psia; temperature, 288.2 K or 518.7° R; molecular weight, 29.0; and specific heat ratio, 1.4. These are known as NACA standard conditions, or NACA standard air. The performance variables of flow, work, and speed expressed on the basis of these standard conditions are known as equivalent conditions.

Let us use the parameters of equation (2-113) but with diameter constant. With the subscript *std* denoting standard conditions and the subscript *eq* denoting equivalent conditions, the similarity conditions can then be expressed as

$$\frac{w\sqrt{RT'_{in}}}{p'_{in}} = \frac{w_{eq}\sqrt{R_{std}T'_{std}}}{p'_{std}} \quad (2-119)$$

$$\frac{\Delta h'}{RT'_{in}} = \frac{\Delta h'_{eq}}{R_{std}T'_{std}} \quad (2-120)$$

$$\frac{N}{\sqrt{RT'_{in}}} = \frac{N_{eq}}{\sqrt{R_{std}T'_{std}}} \quad (2-121)$$

Rearrangement of these equations then yields for the equivalent conditions

$$w_{eq} = w \frac{\sqrt{RT'_{in}}}{\sqrt{R_{std}T'_{std}}} \frac{p'_{std}}{p'_{in}} \quad (2-122)$$

$$\Delta h'_{eq} = \Delta h' \frac{R_{std}T'_{std}}{RT'_{in}} \quad (2-123)$$

$$N_{eq} = N \frac{\sqrt{R_{std}T'_{std}}}{\sqrt{RT'_{in}}} \quad (2-124)$$

As you may recall, we started off the discussion of these parameters by assuming constant specific heat ratio for all conditions. This is not always the case, since specific heat ratio can change with temperature and fluid. Let us now add a specific-heat-ratio effect into the above parameters. The specific-heat-ratio corrections that are commonly used do not yield similarity under all conditions, but only at critical (sonic) velocity. However, the terms that are left out depend on both specific heat ratio and Mach number, are cumbersome to work with, and have only a very small effect on equivalent conditions. With the commonly used specific-heat-ratio terms, the equivalent conditions are expressed as

$$w_{eq} = w \sqrt{\left(\frac{V_{cr}}{V_{cr, std}}\right)^2 \left(\frac{p'_{std}}{p'_{in}}\right)^\epsilon} \quad (2-125)$$

$$\Delta h'_{eq} = \Delta h' \left(\frac{V_{cr, std}}{V_{cr}}\right)^2 \quad (2-126)$$

$$N_{eq} = N \sqrt{\left(\frac{V_{cr, std}}{V_{cr}}\right)^2} \quad (2-127)$$

where

$$\epsilon = \frac{\gamma_{std} \left(\frac{2}{\gamma_{std} + 1}\right)^{\gamma_{std}/(\gamma_{std} - 1)}}{\gamma \left(\frac{2}{\gamma + 1}\right)^{\gamma/(\gamma - 1)}} \quad (2-128)$$

and, as you recall,

$$V_{cr}^2 = \frac{2\gamma}{\gamma + 1} gRT' \quad (2-129)$$

Therefore, for constant specific heat ratio, equations (2-125) to (2-127) reduce to equations (2-122) to (2-124).

Finally, we define

$$\theta = \left(\frac{V_{cr}}{V_{cr, std}}\right)^2 \quad (2-130)$$

and

$$\delta = \frac{p'_{in}}{p'_{std}} \quad (2-131)$$

The equivalent conditions are then expressed as

$$w_{eq} = w \frac{\sqrt{\theta}}{\delta} \epsilon \quad (2-132)$$

$$\Delta h'_{eq} = \frac{\Delta h'}{\theta} \quad (2-133)$$

$$N_{eq} = \frac{N}{\sqrt{\theta}} \quad (2-134)$$

One point that can be seen from these similarity equations is that operation at temperatures greater than standard will cause a reduction of both actual mass flow and equivalent speed. Both of these factors reduce the output of a powerplant. A well-known example of this effect is the reduction in takeoff performance of jet aircraft on hot days.

Reynolds Number Effect

The effect of viscosity in the form of Reynolds number was shown to be one of the dimensionless parameters affecting turbomachine

performance. While its effect is secondary, it is still important. The effect of Reynolds number on turbine efficiency is usually correlated in the following manner:

Expressing efficiency as

$$\eta' = \frac{\Delta h'_{id} - \Delta h'_{loss}}{\Delta h'_{id}} = 1 - \frac{\Delta h'_{loss}}{\Delta h'_{id}} \quad (2-135)$$

we can write

$$1 - \eta' = \frac{\Delta h'_{loss}}{\Delta h'_{id}} \quad (2-136)$$

If we assume that the only loss is friction loss,

$$\Delta h'_{loss} \propto f \left(\frac{L}{D} \right) V^2 \quad (2-137)$$

where f is the friction factor, and L is the characteristic flow-path length. For turbulent flow,

$$f \propto \frac{1}{Re^{0.2}} \quad (2-138)$$

where Re is the Reynolds number. Substituting equations (2-138) and (2-137) into equation (2-136) yields

$$1 - \eta' \propto \frac{1}{Re^{0.2}} \left(\frac{L}{D} \right) \left(\frac{V^2}{\Delta h'_{id}} \right) \quad (2-139)$$

Adding subscripts for conditions 1 and 2 to equation (2-139) and dividing the equation for condition 1 by the equation for condition 2 yield

$$\frac{1 - \eta'_1}{1 - \eta'_2} = \frac{\left(\frac{1}{Re_1^{0.2}} \right) \left(\frac{L_1}{D_1} \right) \left(\frac{V_1^2}{\Delta h'_{1, id}} \right)}{\left(\frac{1}{Re_2^{0.2}} \right) \left(\frac{L_2}{D_2} \right) \left(\frac{V_2^2}{\Delta h'_{2, id}} \right)} \quad (2-140)$$

Since for geometric similarity $L_1/D_1 = L_2/D_2$ and for dynamic similarity $V_1^2/\Delta h'_{1, id} = V_2^2/\Delta h'_{2, id}$, equation (2-140) reduces to

$$\frac{1 - \eta'_1}{1 - \eta'_2} = \left(\frac{Re_2}{Re_1} \right)^{0.2} \quad (2-141)$$

This is an ideal correlation. Actually, it has been found that the exponent for this type of correlation is not 0.2, but usually varies in the range of 0.1 to 0.2, depending on the machine. This occurs because all the losses are not viscous losses, and the fraction of total loss attributable to viscous loss varies between machines. In view of this, another suggested type of correlation is

$$\frac{1-\eta_1'}{1-\eta_2'} = A + B \left(\frac{Re_2}{Re_1} \right)^{0.2} \quad (2-142)$$

where A and B are fractions such that $A+B=1$. In equation (2-142) the exponent is maintained at 0.2 to reflect the viscous loss exponent, and the coefficients A and B serve to represent the fact that not all loss is viscous loss. Recent turbine tests here at Lewis, as well as the discussion presented in reference 1, indicate that values of about 0.3 to 0.4 for A and corresponding values of 0.7 to 0.6 for B seem to be a good compromise for correlating Reynolds number effects.

REFERENCES

1. SHEPHERD, D. G.: Principles of Turbomachinery. Macmillan Co., 1956.
2. GLASSMAN, ARTHUR J.; AND STEWART, WARNER L.: Use of Similarity Parameters for Examination of Geometry Characteristics of High-Expansion-Ratio Axial-Flow Turbines. NASA TN D-4248, 1967.

SYMBOLS

A	{flow area, m^2 ; ft^2 Reynolds number correlation coefficient in eq. (2-142)
a	speed of sound, m/sec ; ft/sec
B	Reynolds number correlation coefficient in eq. (2-142)
c_p	heat capacity at constant pressure, $J/(kg)(K)$; $Btu/(lb)(^\circ R)$
D	diameter, m ; ft
D_s	specific diameter, dimensionless; $(sec^{1/2})(lbf^{1/4})/(ft^{1/4})(lbm^{1/4})$
E	modulus of elasticity, N/m^2 ; lb/ft^2
e	kinetic energy loss coefficient, defined by eq. (2-46)
F	force, N ; lb
f	friction factor
g	conversion constant, 1; $32.17 (lbm)(ft)/(lbf)(sec^2)$
H	head, J/kg ; $(ft)(lbf)/lbm$
h	specific enthalpy, J/kg ; Btu/lb
J	conversion constant, 1; $778 (ft)(lb)/Btu$
K	conversion constant, 2π rad/rev; 60 sec/min
L	characteristic length, m ; ft
M	Mach number
N	rotative speed, rad/sec ; rev/min
N_s	specific speed, dimensionless; $(ft^{3/4})(lbm^{3/4})/(min)(sec^{1/2})(lbf^{3/4})$
n	{number of stages polytropic exponent
P	power, W ; Btu/sec
p	absolute pressure, N/m^2 ; lb/ft^2
Q	volume flow rate, m^3/sec ; ft^3/sec
R	{gas constant, $J/(kg)(K)$; $(ft)(lbf)/(lbm)(^\circ R)$ reaction
Re	Reynolds number
r	radius, m ; ft
T	absolute temperature, K ; $^\circ R$
U	blade speed, m/sec ; ft/sec
V	absolute velocity, m/sec ; ft/sec
V_j	ideal jet speed (defined by eq. (2-71)), m/sec ; ft/sec
v	specific volume, m^3/kg ; ft^3/lb
W	relative velocity, m/sec ; ft/sec
w	mass flow rate, kg/sec ; lb/sec
Y	} total-pressure loss coefficient, defined by eqs. (2-47)
Y'	
Y''	
α	fluid absolute angle measured from axial or radial direction, deg
β	fluid relative angle measured from axial or radial direction, deg

TURBINE DESIGN AND APPLICATION

γ	ratio of heat capacity at constant pressure to heat capacity at constant volume
δ	ratio of inlet total pressure to NACA standard pressure
ϵ	function of specific heat ratio, defined by eq. (2-128)
η	efficiency
θ	squared ratio of critical velocity based on turbine inlet temperature to critical velocity based on NACA standard temperature
λ	speed-work parameter, defined by eq. (2-66)
μ	viscosity, (N)(sec)/m ² ; lb/(ft)(sec)
ν	blade-jet speed ratio, defined by eq. (2-72)
ρ	density, kg/m ³ ; lb/ft ³
τ	torque, N-m; lb-ft
φ	flow coefficient, defined by eq. (2-75)
ψ	loading coefficient, defined by eq. (2-67)
ω	angular velocity, rad/sec

Subscripts:

<i>av</i>	average
<i>cr</i>	critical condition ($M=1$)
<i>eq</i>	equivalent
<i>ex</i>	exit
<i>id</i>	ideal
<i>in</i>	inlet
<i>loss</i>	loss
<i>opt</i>	optimum
<i>p</i>	polytropic
<i>r</i>	radial component
<i>rel</i>	relative
<i>ro</i>	rotor
<i>st</i>	stator
<i>std</i>	NACA standard condition
<i>stg</i>	stage
<i>u</i>	tangential component
<i>x</i>	axial component
0	at stator inlet
1	at stator exit or rotor inlet
2	at rotor exit

Superscripts:

→	vector quantity
—	overall turbine
'	absolute total state
''	relative total state

GLOSSARY

The terms defined herein are illustrated in figure 2-14.

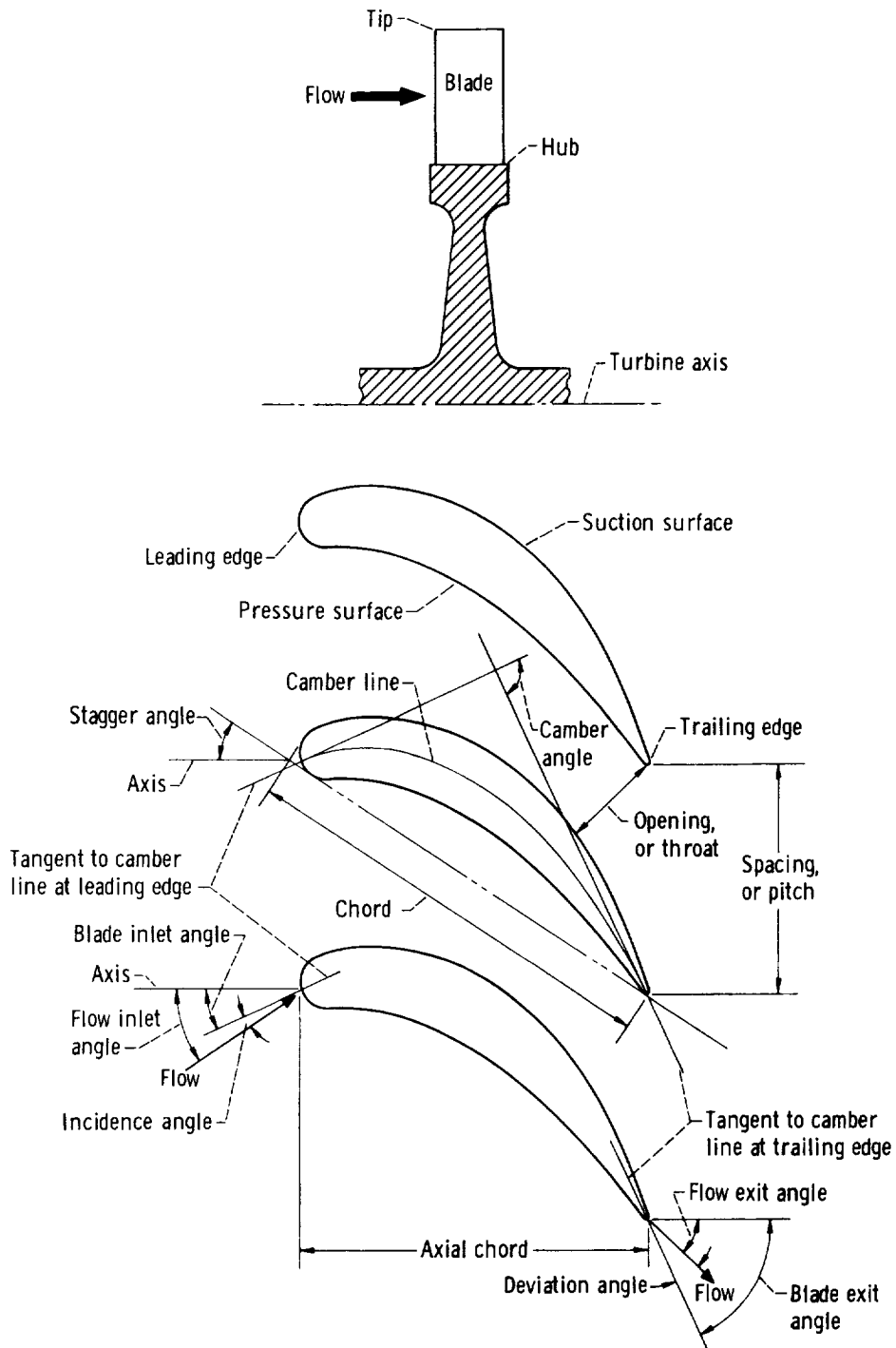


FIGURE 2-14.—Blade terminology.

- aspect ratio.** The ratio of the **blade height** to the **chord**.
- axial chord.** The length of the projection of the blade, as set in the turbine, onto a line parallel to the turbine axis. It is the axial length of the blade.
- axial solidity.** The ratio of the **axial chord** to the **spacing**.
- blade exit angle.** The angle between the tangent to the **camber line** at the **trailing edge** and the turbine axial direction.
- blade height.** The radius at the **tip** minus the radius at the **hub**.
- blade inlet angle.** The angle between the tangent to the **camber line** at the **leading edge** and the turbine axial direction.
- bucket.** Same as **rotor blade**.
- camber angle.** The external angle formed by the intersection of the tangents to the **camber line** at the **leading** and **trailing edges**. It is equal to the sum of the angles formed by the **chord line** and the **camber-line** tangents.
- camber line.** The mean line of the blade profile. It extends from the **leading edge** to the **trailing edge**, halfway between the **pressure surface** and the **suction surface**.
- chord.** The length of the perpendicular projection of the blade profile onto the **chord line**. It is approximately equal to the linear distance between the **leading edge** and the **trailing edge**.
- chord line.** If a two-dimensional blade section were laid convex side up on a flat surface, the **chord line** is the line between the points where the front and the rear of the blade section would touch the surface.
- deflection.** The total turning angle of the fluid. It is equal to the difference between the **flow inlet angle** and the **flow exit angle**.
- deviation angle.** The **flow exit angle** minus the **blade exit angle**.
- flow exit angle.** The angle between the fluid flow direction at the blade exit and the turbine axial direction.
- flow inlet angle.** The angle between the fluid flow direction at the blade inlet and the turbine axial direction.
- hub.** The innermost section of the blade.
- hub-tip ratio.** Same as **hub- to tip-radius ratio**.
- hub- to tip-radius ratio.** The ratio of the hub radius to the tip radius.
- incidence angle.** The **flow inlet angle** minus the **blade inlet angle**.
- leading edge.** The front, or nose, of the blade.
- mean section.** The blade section halfway between the **hub** and the **tip**.
- nozzle blade.** Same as **stator blade**.
- pitch.** The distance in the direction of rotation between corresponding points on adjacent blades.
- pressure surface.** The concave surface of the blade. Along this surface, pressures are highest.
- radius ratio.** Same as **hub- to tip-radius ratio**.

root. Same as **hub**.

rotor blade. A rotating blade.

solidity. The ratio of the **chord** to the **spacing**.

spacing. Same as **pitch**.

stagger angle. The angle between the **chord line** and the turbine axial direction.

stator blade. A stationary blade.

suction surface. The convex surface of the blade. Along this surface, pressures are lowest.

tip. The outermost section of the blade.

trailing edge. The rear, or tail, of the blade.

CHAPTER 3

Velocity Diagrams

By Warren J. Whitney and
Warner L. Stewart

As indicated in chapter 2, one of the most important variables to be considered in the design or analysis of turbines is the velocity of the fluid as it passes from one blade row to the next. The absolute and relative velocities and their relation to the speed of the blade row are universally described through the use of velocity diagrams. Once the overall design requirements of flow, work, and rotative speed are established, the next step is the evolution of the velocity diagrams. Their relation to the required blading geometry is very important in that these diagrams specify the flow angles and velocities that the blading is required to produce. In addition, the velocity diagrams significantly affect the efficiency level expected from the turbine.

The general methods for constructing velocity diagrams and relating them to the work and flow capacity of the turbine were discussed in chapter 2. Various dimensionless parameters associated with the velocity diagram were also presented in chapter 2, and their relation to turbine efficiency was illustrated by an idealized case. This chapter is devoted entirely to the subject of velocity diagrams. The first part of this chapter concerns a single diagram that can be considered representative of the average flow conditions for the stage. Usually, the conditions at the blade mean radius are used. The second part of this chapter is devoted to the radial variations in the diagrams that result from the balance of forces in the radial direction and from the variation in blade speed with radius. Only axial-flow turbines are considered in this chapter.

MEAN-SECTION DIAGRAMS

In this section, the velocity diagrams occurring at the mean section (halfway between hub and tip) are assumed to represent the average conditions encountered by the turbine. The different types of diagrams, their relation to stage efficiency, and their selection when staging is required are discussed.

In review, figure 3-1 shows an illustrative stage velocity diagram indicating the vector relations described in chapter 2 and the nomenclature. Assuming no change in mean radius through the stage, equation (2-14) can be written as

$$\Delta h' = \frac{U \Delta V_u}{gJ} \quad (3-1)$$

where

- h' total enthalpy, J/kg; Btu/lb
- U blade speed, m/sec; ft/sec
- V_u tangential component of velocity, m/sec; ft/sec
- g conversion constant, 1; 32.17 (lbm)(ft)/(lbf)(sec²)
- J conversion constant, 1; 778 (ft)(lb)/Btu

This equation relates the stage specific work to the velocity diagram. The axial component of the velocity vector is related to the flow rate, state conditions, and the area by the relation

$$V_x = \frac{w}{\rho A_{an}} \quad (3-2)$$

where

- V_x axial component of velocity, m/sec; ft/sec
- w mass flow rate, kg/sec; lb/sec
- ρ density, kg/m³; lb/ft³
- A_{an} annulus area, m²; ft²

Flow angles are key velocity-diagram parameters because they not only link the axial and swirl velocities (the tangential component of the absolute velocity is often referred to as the swirl velocity) but also affect the expected efficiency and blading geometry. In addition, dimensionless parameters are used in association with velocity-diagram studies because the parameter values can be related to the diagram shape. Such parameters were discussed in chapter 2 and include the speed-work parameter, which can be expressed in several ways, such as

$$\lambda = \frac{U^2}{gJ\Delta h'} = \frac{U}{\Delta V_u} = \frac{gJ\Delta h'}{\Delta V_u^2} \quad (3-3)$$

The speed-work parameter is used in this chapter because diagram

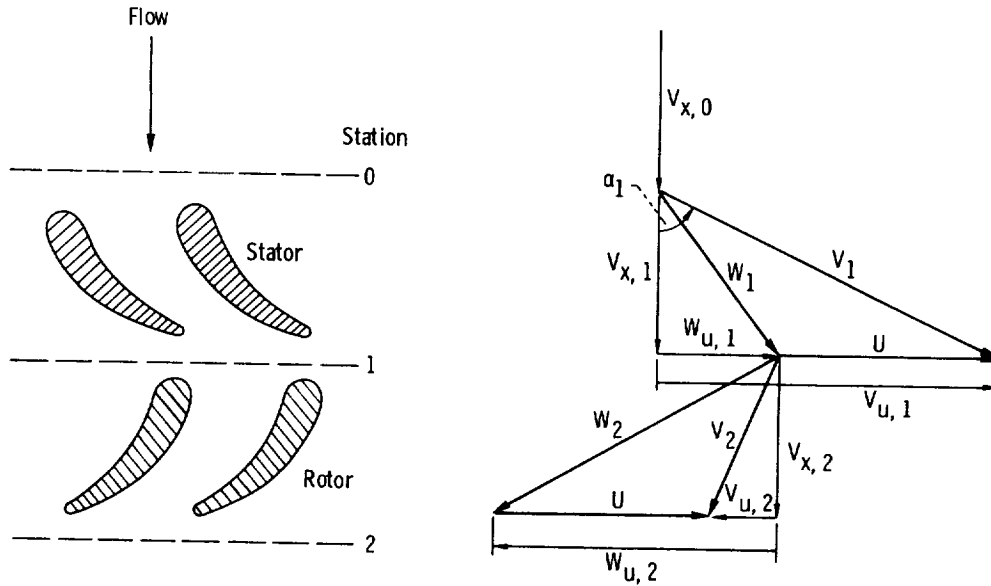


FIGURE 3-1.—Velocity-vector diagrams and nomenclature.

types are related to the swirl distribution and it is convenient to normalize the diagram velocities by ΔV_u .

Velocity-Diagram Types

After the overall design requirements are established, the velocity diagrams can be evolved. Velocity diagrams have different sizes and shapes depending on the diagram type and the value of the speed-work parameter. Diagram type refers to some physical constraint imposed on the diagram. Diagram shape determines the values of performance-related parameters, such as stage reaction and swirl split between the stator exit ($V_{u,1}$) and the rotor exit ($V_{u,2}$). The following three common types of diagrams and their reaction and swirl characteristics are discussed in this section:

- (1) Zero-exit-swirl diagram ($V_{u,2}=0$)
- (2) Rotor-impulse diagram ($W_1=W_2$)
- (3) Symmetrical diagram ($V_1=W_2$ and $V_2=W_1$)

These three diagrams for several values of speed-work parameter are shown in figure 3-2.

Zero-exit-swirl diagram.—In many cases, either the entire exit velocity head or the swirl component thereof represents a loss in efficiency. The zero-exit-swirl diagram, where

$$\frac{V_{u,1}}{\Delta V_u} = 1 \tag{3-4a}$$

and

Speed-work parameter	Diagram type		
	Zero exit swirl	Impulse	Symmetrical
0.25			
0.5			
1.0			

FIGURE 3-2.—Effects of speed-work parameter and diagram type on shape of stage velocity-vector diagram.

$$\frac{V_{u,2}}{\Delta V_u} = 0 \tag{3-4b}$$

can be used to reduce such loss.

For an axial-flow rotor ($U_1=U_2$) having constant axial velocity ($V_{x,1}=V_{x,2}$), the definition of stage reaction presented in equation (2-39) reduces to

$$R_{stg} = \frac{W_{u,2}^2 - W_{u,1}^2}{V_{u,1}^2 - V_{u,2}^2 + W_{u,2}^2 - W_{u,1}^2} \tag{3-5}$$

where

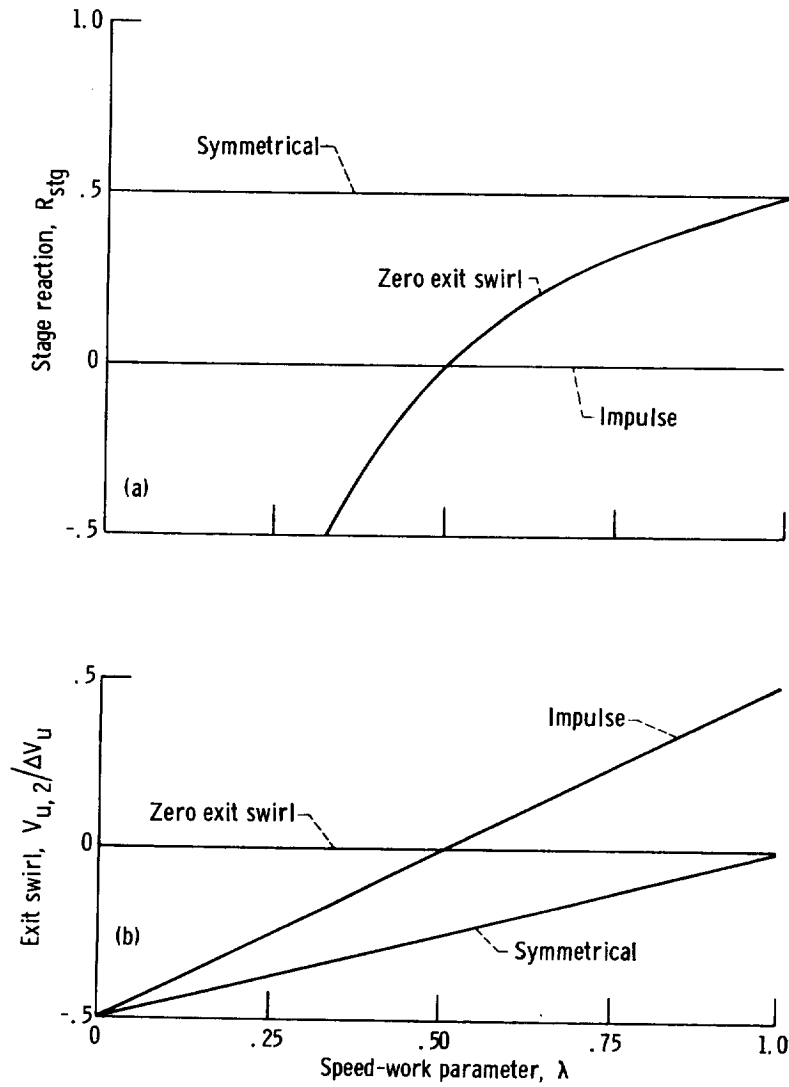
R_{stg} stage reaction

W_u tangential component of relative velocity, m/sec; ft/sec

By using equation (2-6) and equations (3-3) and (3-4), equation (3-5) can be expressed as

$$R_{stg} = 1 - \frac{1}{2\lambda} \tag{3-6}$$

This equation is plotted in figure 3-3(a). At $\lambda=1$, the reaction is 0.5, which indicates a conservative diagram. At $\lambda=0.5$, the reaction is zero, which indicates an impulse rotor. Below $\lambda=0.5$, negative reaction is encountered. For example, at $\lambda=0.33$, the reaction is -0.5 , which, as can be shown, represents a substantial decrease in velocity and increase in static pressure across the rotor. Because of



(a) Reaction.
 (b) Exit swirl.

FIGURE 3-3.—Effects of speed-work parameter and velocity-vector diagram type on reaction and exit swirl.

potentially high losses, such high negative reactions are usually avoided; therefore, zero-exit-swirl diagrams are seldom used for $\lambda < 0.5$. Figure 3-2 presents the zero-exit-swirl diagrams for the positive-reaction, impulse, and negative-reaction cases.

Impulse diagram.—For this case, $W_1 = W_2$ and the equation for stage reaction reduces to

$$R_{stg} = 0 \tag{3-7}$$

From equation (2-6), equation (3-3), and the assumption of constant axial velocity, the rotor inlet and exit swirl velocities can be expressed

as

$$\frac{V_{u,1}}{\Delta V_u} = \lambda + 0.5 \quad (3-8a)$$

and

$$\frac{V_{u,2}}{\Delta V_u} = \lambda - 0.5 \quad (3-8b)$$

The exit swirl characteristics are shown in figure 3-3(b). Positive swirls are encountered at λ values greater than 0.5, and negative swirls are obtained at λ values less than 0.5. At $\lambda=0.5$, the impulse and zero-exit-swirl cases coincide. These effects are illustrated in figure 3-2. Because swirl velocity leaving a turbine is a loss and because positive swirl decreases stage work, impulse diagrams are seldom, if ever, used when λ is greater than 0.5.

Symmetrical diagram.—A third type of diagram commonly used is one in which the stator-exit- and rotor-exit-velocity triangles are specified to have the same shape. In terms of velocities,

$$V_1 = W_2 \quad (3-9a)$$

and

$$V_2 = W_1 \quad (3-9b)$$

Under this condition, the equation for stage reaction reduces to

$$R_{stg} = \frac{1}{2} \quad (3-10)$$

From equation (2-6), equation (3-3), and the assumption of constant axial velocity, the swirl velocity components can be expressed as

$$\frac{V_{u,1}}{\Delta V_u} = \frac{\lambda + 1}{2} \quad (3-11a)$$

and

$$\frac{V_{u,2}}{\Delta V_u} = \frac{\lambda - 1}{2} \quad (3-11b)$$

These reaction and swirl characteristics are shown in figure 3-3, with typical diagrams illustrated in figure 3-2. The symmetrical diagram is the same as the zero-exit-swirl diagram at $\lambda=1$. As the value of λ decreases, the exit swirl increases, but the reaction remains constant at 0.5. This good reaction is conducive to high total efficiency, making this type of diagram attractive for stages where exit swirl is not a loss (e.g., the front and middle stages of a multistage turbine).

Stage Efficiency

A significant aspect of a turbine design is the expected efficiency.

The efficiency is an important function of, among other things, the type of velocity diagram used and the pressure distribution on the blade surface. Therefore, the diagram selection is greatly dependent on the efficiency requirements of the intended application. Some basic relations between diagram parameters and efficiency are presented and used herein to point up some of the more important effects. References 1 and 2 are used as a basis for this development.

As presented in chapter 2, turbine stage static efficiency can be written as

$$\eta = \frac{\Delta h'}{\Delta h_{id}} \quad (3-12)$$

where

η stage static efficiency

$\Delta h'$ stage work, J/kg; Btu/lb

Δh_{id} stage ideal work based on ratio of inlet total pressure to exit static pressure, J/kg; Btu/lb

Expressing ideal work in terms of actual work plus losses yields

$$\eta = \frac{\Delta h'}{\Delta h' + L_{st} + L_{ro} + \frac{V_2^2}{2gJ}} \quad (3-13)$$

where

L_{st} stator loss, J/kg; Btu/lb

L_{ro} rotor loss, J/kg; Btu/lb

$V_2^2/2gJ$ stage leaving loss, J/kg; Btu/lb

The equation for total efficiency η' is the same except for the elimination of the stage leaving loss, $V_2^2/2gJ$. Substituting equation (3-3) into equation (3-13) yields

$$\eta = \frac{\lambda}{\lambda + \frac{gJ(L_{st} + L_{ro})}{\Delta V_u^2} + \frac{1}{2} \frac{V_2^2}{\Delta V_u^2}} \quad (3-14)$$

In relating the stator and rotor losses to the diagram parameters, it was assumed that the losses were proportional to the average kinetic energy across the blade rows. That is,

$$L_{st} = K_{st} \frac{V_0^2 + V_1^2}{2gJ} \quad (3-15a)$$

and

$$L_{ro} = K_{ro} \frac{W_1^2 + W_2^2}{2gJ} \quad (3-15b)$$

where K is constant of proportionality.

Equations (3-14) and (3-15) serve as the basis for estimating efficiency. The exact nature of the assumptions and equations can be found in references 1 and 2. Briefly, the procedure for estimating efficiency is as follows:

- (1) The velocities are expressed in terms of their tangential and axial components.
- (2) The tangential components are expressed in terms of the speed-work parameter according to the diagram type being considered (eq. (2-6) and eq. (3-4), (3-8), or (3-11)).
- (3) The axial components are evaluated by means of an application-related mass-flow assumption or by relating them to the tangential components by an angle assumption.
- (4) The values for the constant of proportionality are selected on the basis of previous test experience.
- (5) Efficiency curves can then be generated over a range of speed-work parameter for the various diagram types.

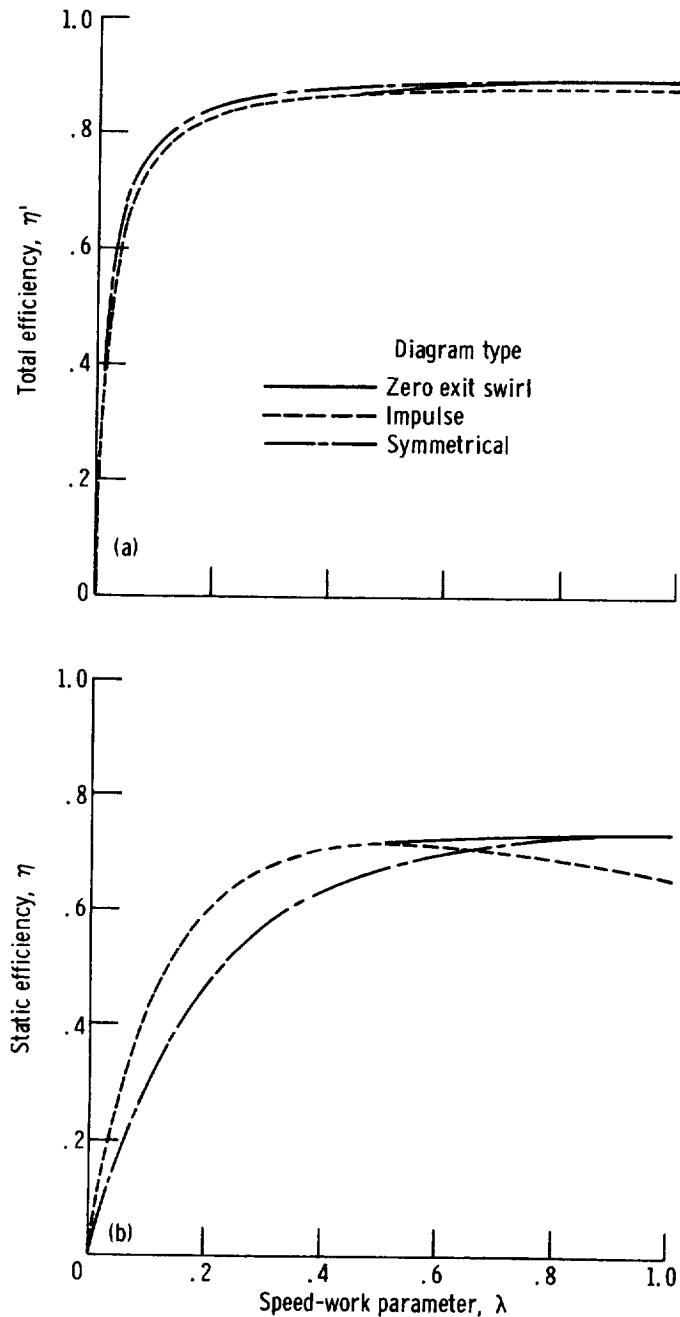
The total- and static-efficiency characteristics as obtained from reference 2 by the above method are presented in figure 3-4. The curves presented for the symmetrical diagram are actually for the diagram that analytically yields maximum total efficiency. This diagram, as determined in reference 2, approximates the symmetrical diagram, and the associated efficiency characteristics are representative of those for a symmetrical diagram. The curves for the zero-exit-swirl diagram were not obtained for λ values less than 0.5 because of the undesirable negative reaction in that region.

The total efficiency characteristics are presented in figure 3-4(a). For each diagram type, the highest efficiency occurs at a speed-work parameter, λ , value of 1. The symmetrical-diagram efficiency is slightly higher than the impulse-diagram efficiency for all values of λ . The zero-exit-swirl-diagram efficiency is equal to the symmetrical-diagram efficiency at $\lambda=1$, is equal to the impulse-diagram efficiency at $\lambda=0.5$, and, although not shown, becomes less than either of the other two for λ values less than 0.5. Between $\lambda=1$ and $\lambda=0.5$, the efficiency curves are rather flat. As λ is reduced below 0.5, efficiency decreases more rapidly.

High total efficiencies, therefore, are achievable with any of these diagram types for λ values greater than about 0.5. Even where total, rather than static, efficiency is the criterion of merit, however, the designer must still consider aspects such as the previously discussed exit swirls and the three-dimensional effects, to be discussed later in this chapter, before a diagram type is selected.

The static efficiency characteristics are presented in figure 3-4(b). The static efficiency is substantially lower than the total efficiency because the exit velocity head represents a loss. The highest static

efficiency for λ values less than 0.5 is obtained with the impulse diagram, and for λ values greater than 0.5, with the zero-exit-swirl diagram. For the impulse diagram, the efficiency is a maximum at $\lambda=0.5$, where there is no exit swirl. For the symmetrical diagram,



(a) Total efficiency.

(b) Static efficiency.

FIGURE 3-4.—Effects of speed-work parameter and velocity-vector diagram type on efficiency. (Curves from ref. 2.)

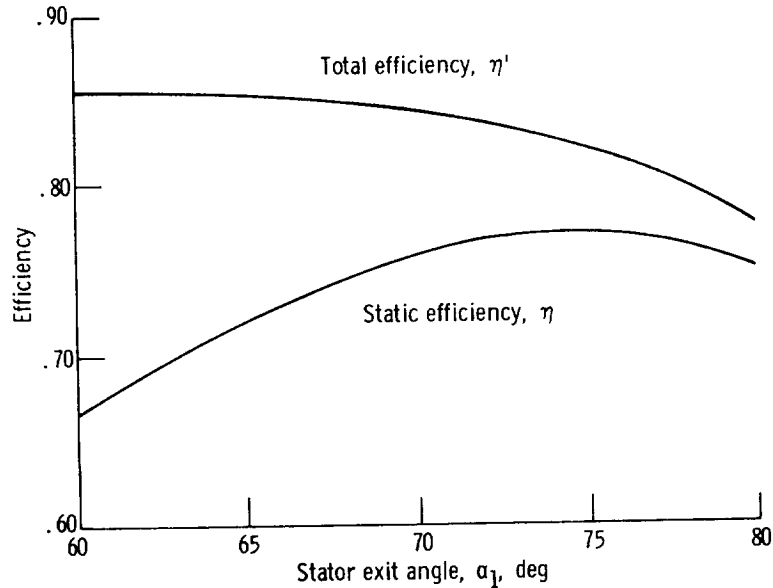


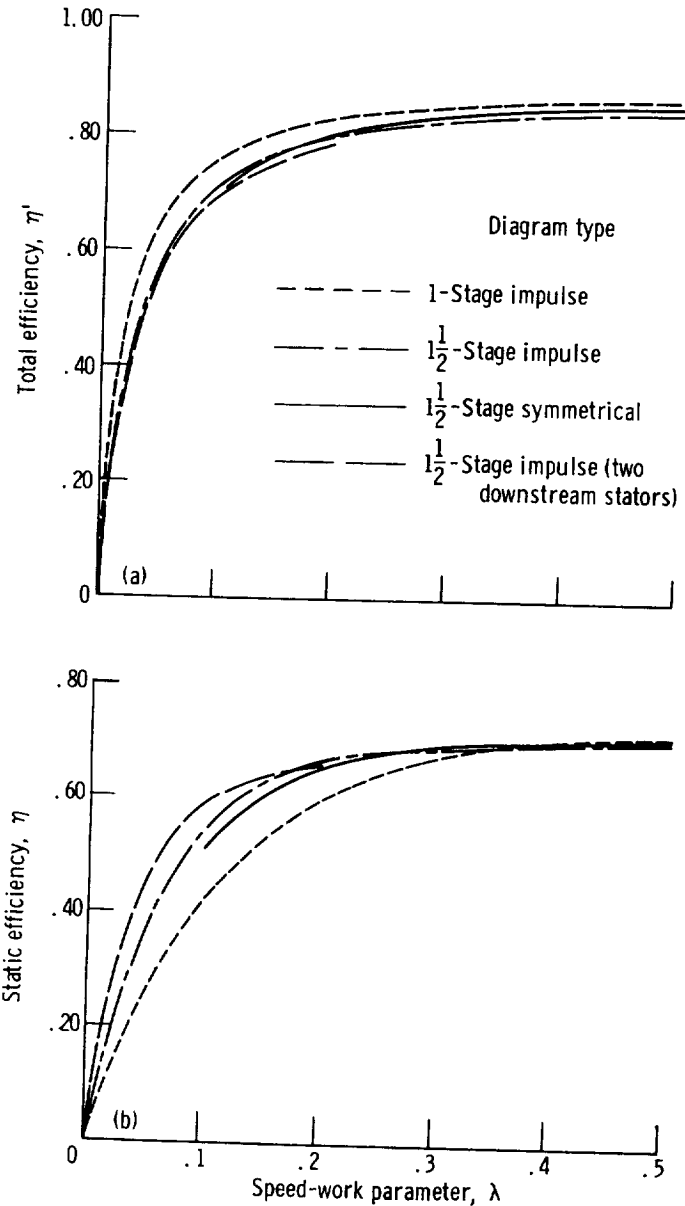
FIGURE 3-5.—Effect of stator exit angle on stage efficiency. Speed-work parameter λ , 0.5. (Curves from ref. 1.)

the efficiency is a maximum at $\lambda=1$, where there is no exit swirl. The zero-exit-swirl-diagram efficiency is highest at $\lambda=1$, but decreases very little as λ is reduced to 0.5.

Efficiency is affected not only by the speed-work parameter and diagram type but also by the velocity through-flow component V_x , which is related to the flow angles. An example of this effect can be obtained from reference 1. Figure 3-5, which is taken from reference 1, shows the total and static efficiencies as functions of stator exit angle. It is evident that the best angle depends upon which efficiency is to be maximized. If maximum total efficiency is desired, the stator exit angle should be about 60° . If maximum static efficiency is desired, a stator exit angle of about 75° is indicated. However, complete freedom of selection of this angle does not always exist since it affects the through-flow component of velocity and, therefore, the annulus area. The rotor stress level is also influenced by the annulus area and, hence, could influence the angle selection.

It has been shown that at low values of speed-work parameter, large exit swirls are encountered, with associated reductions in static efficiency. One means of increasing the static efficiency is through the use of downstream stators, which remove the swirl and diffuse the flow back to axial. The efficiency characteristics of such turbines (ref. 3) are presented in figure 3-6. In this figure, the turbines with downstream stators are referred to as $1\frac{1}{2}$ -stage turbines. Figure 3-6(a) shows that the total efficiencies of the $1\frac{1}{2}$ -stage turbines are lower

than those of the 1-stage impulse turbines. These lower total efficiencies are due to the additional friction losses of the downstream stators. Because of this additional friction loss, the $1\frac{1}{2}$ -stage turbine achieves no gain in static efficiency over that of the 1-stage turbine until the value of λ is below approximately 0.35 (fig. 3-6(b)). For λ values below about 0.35, substantial gains in static efficiency can be achieved through use of downstream stators.

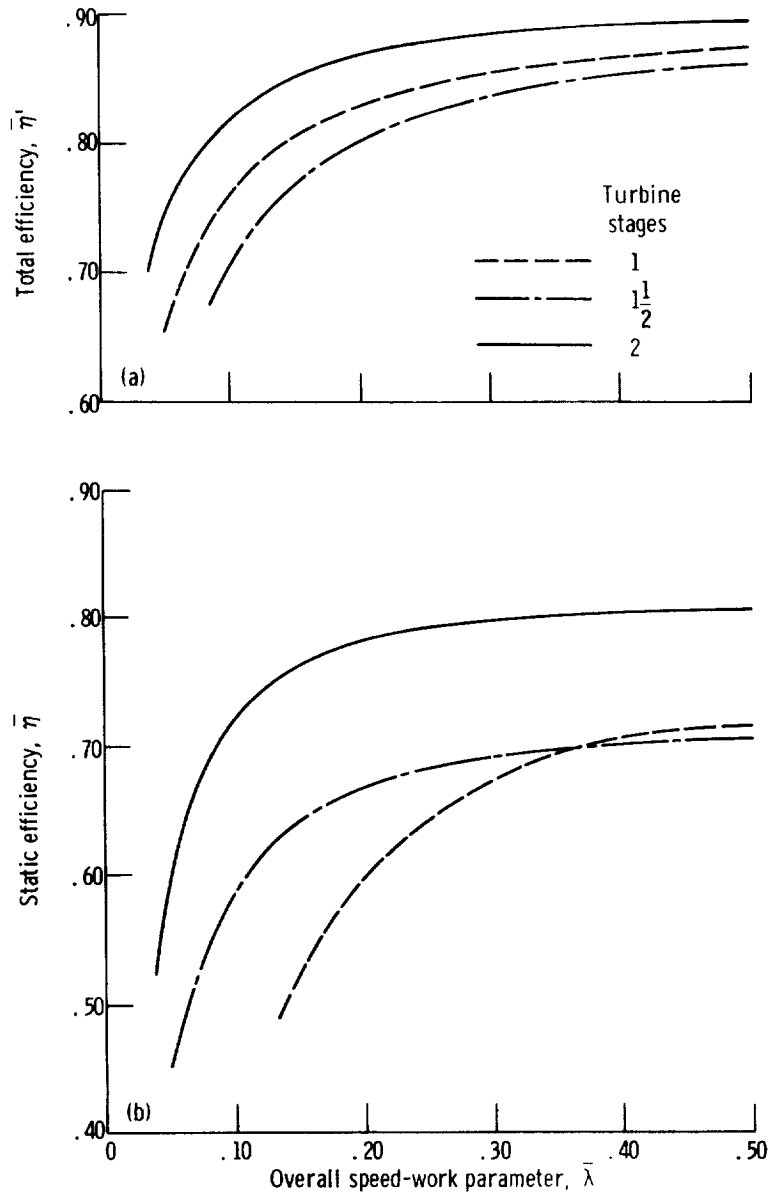


(a) Total efficiency.
 (b) Static efficiency.

FIGURE 3-6.—Effect of downstream stator on efficiency. (Curves from ref. 3.)

Multistage Turbine Efficiency

When the turbine requirements are such that the speed-work parameter is quite low and high efficiencies are still desired, multistage turbines are used, and the required work is split amongst the various stages.



(a) Total efficiency.

(b) Static efficiency.

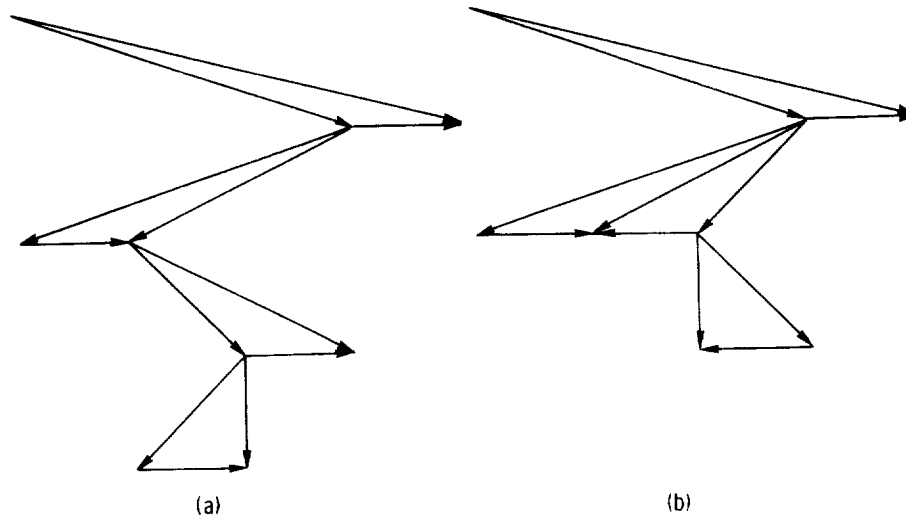
FIGURE 3-7.—Comparison of efficiencies of 1-, 1½-, and 2-stage turbines. (Curves from ref. 4.)

Two-stage turbines.—The addition of a second stage to a 1-stage turbine results in about doubling the average stage λ value through the reduction of stage work. As shown previously, an increase in stage λ is accompanied by an increase in stage efficiency. In addition, with two stages it becomes possible to adjust the stage work split and the exit swirls so as to maximize efficiency.

A study of the efficiency characteristics of 2-stage turbines is presented in reference 4. The efficiencies of 1-, 1½-, and 2-stage turbines (from ref. 4) are compared in figure 3-7. At an overall speed-work parameter, $\bar{\lambda}$, of 0.50, the 2-stage turbine has a 2-percentage-point-higher total efficiency and a 9-percentage-point-higher static efficiency than the 1-stage turbine. As $\bar{\lambda}$ is reduced to 0.15, the difference between the 2- and 1-stage efficiencies increases to 5 percentage points for total efficiency and 24 percentage points for static efficiency. The smaller difference between total and static efficiencies for the 2-stage turbine than for the 1-stage turbine occurs because the leaving loss for the 2-stage turbine is a much smaller fraction of the total work output.

The 2-stage turbine efficiencies presented in figure 3-7 are the maximum values obtained by varying stage work split and exit swirl while imposing good diagram criteria of no positive exit swirl and no negative reaction. At $\bar{\lambda}=0.5$, efficiency is maximized with a 50:50 work split and symmetrical zero-exit-swirl diagrams for each stage. As $\bar{\lambda}$ is reduced, maximum efficiency is achieved with zero exit swirl maintained in the second stage and an increasing fraction of the work produced by the first stage. At $\bar{\lambda}=0.125$, the optimum work split has increased to 75:25. The associated diagram features impulse first and second stages as well as an impulse second-stage stator. This type of diagram is illustrated in figure 3-8(a) and represents a type of turbine known as velocity compounded. In general, a velocity-compounded turbine is a two-stage (or three-stage) turbine in which all expansion (fluid velocity increase) is achieved in the first stator and all subsequent blade rows merely turn the flow with no change in velocity. As $\bar{\lambda}$ is reduced below 0.125, the velocity-compounded condition is maintained, but with increasing exit swirl and decreasing first-stage work fraction.

Figure 3-8(b) illustrates the velocity diagram for another type of two-stage turbine, the counterrotating turbine without a second-stage stator. The diagram shown is again for the $\bar{\lambda}=0.125$ case with zero exit swirl and with both blade speeds equal. A study of the efficiency characteristics of this type of turbine was made in reference 5. Efficiencies higher than those for conventional two-stage turbines were obtained because of the elimination of one blade row. Because the second-stage work depends upon the swirl leaving the first stage, the



(a) Velocity-compounded turbine. (b) Counterrotating turbine.
 FIGURE 3-8.—Velocity-vector diagrams for special types of 2-stage turbines.
 Overall speed-work parameter $\bar{\lambda}$, 0.125.

second stage, in general, would be a low-work stage (work split is 75:25 for the illustrated diagram). The efficiencies and work splits are also functions of the blade-speed ratio. Because of their high efficiency potential at low $\bar{\lambda}$ levels and their compactness due to the lack of a blade row, counterrotating turbines are being utilized in such advanced applications as direct-lift engines for V/STOL aircraft.

n-stage turbines.—In many applications the combination of work and speed requirements dictates the use of turbines in which considerably more than two stages are required. Such applications include fan-drive turbines, vapor turbines used for power production, and turbopump turbines for nuclear hydrogen rockets.

The efficiency characteristics of multistage turbines composed of impulse stages (for $\lambda \leq 0.5$) or zero-exit-swirl stages (for $\lambda \geq 0.5$) are examined in reference 6. Equal stage work and constant stage blade speed were assumed. Overall and stage speed-work parameters are related (derived as eq. (2-111)) as

$$\lambda = n\bar{\lambda} \quad (3-16)$$

where n is the number of stages. Total efficiency for a first stage (stator-inlet velocity is axial) and total and static efficiencies for a general stage (intermediate or last stage, where stator inlet velocity is equal to stage exit velocity) were obtained as functions of λ . Overall efficiencies were then obtained from the stage efficiencies. For overall static efficiency, neglecting the reheat effect discussed in chapter 2,

$$\bar{\eta} = \frac{n\Delta h'}{\Delta h'_{id,a} + (n-2)\Delta h'_{id,i} + \Delta h'_{id,t}} \quad (3-17)$$

where

$\Delta h'_{id,a}$ first-stage ideal work based on ratio of inlet total pressure to exit total pressure, J/kg; Btu/lb

$\Delta h'_{id,i}$ general-stage ideal work based on ratio of inlet total pressure to exit total pressure, J/kg; Btu/lb

$\Delta h'_{id,t}$ general-stage ideal work based on ratio of inlet total pressure to exit static pressure, J/kg; Btu/lb

This equation neglects the reheat effect, which reference 6 shows to be small. By using the stage-efficiency definition, equation (3-17) becomes

$$\bar{\eta} = \frac{n}{\frac{1}{\eta'_a} + \frac{n-2}{\eta'_i} + \frac{1}{\eta'_t}} \quad (3-18)$$

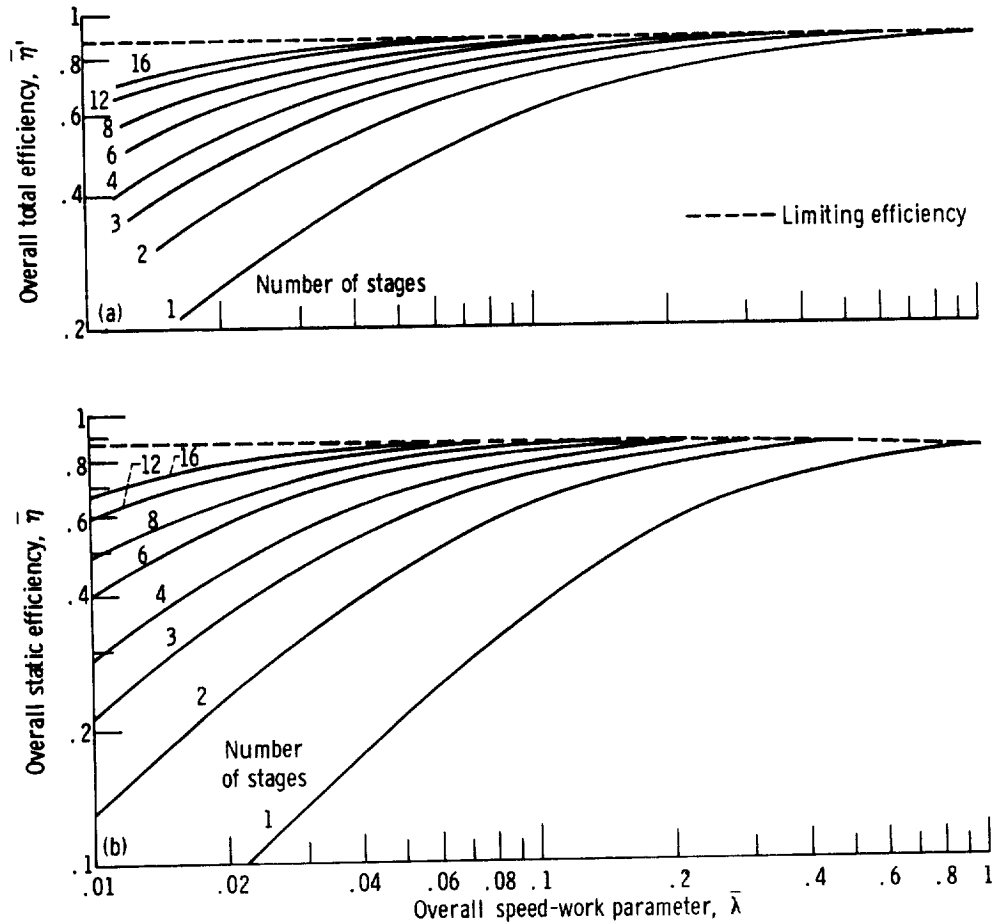
Overall total efficiency differs only in that the last stage is evaluated on the basis of stage total efficiency. Therefore,

$$\bar{\eta}' = \frac{n}{\frac{1}{\eta'_a} + \frac{n-1}{\eta'_i}} \quad (3-19)$$

The multistage efficiency characteristics obtained in this manner are presented in figure 3-9, which was obtained from reference 6. Figure 3-9(a) shows total efficiency as a function of $\bar{\lambda}$. The limiting efficiency (in this case, 0.88) is reached when all stages are at $\lambda=1$. This level of efficiency, as well as all those described herein, is a function of many other factors (stator angle, Reynolds number, blade aspect ratio, blade solidity, etc.) in addition to diagram shape and may vary upward or downward from the indicated value. The variations in efficiency with varying diagrams are, however, the concern here. This figure illustrates that at low $\bar{\lambda}$ values (0.1 or less), either large increases in the number of stages are required to achieve high total efficiencies or, if some restriction on the number of stages is imposed, lower efficiencies must be expected. The static efficiencies shown in figure 3-9(b) show similar trends, although at lower levels because of the leaving loss.

Another commonly used method of presenting turbine performance in terms of diagram parameters is to plot efficiency as a function of overall blade-jet speed ratio. This parameter was described in chapter 2 (eq. (2-72)) as the ratio of the blade speed to a velocity corresponding to the kinetic energy associated with the total-to-static pressure ratio across the turbine. Blade-jet speed ratio is related to speed-work

TURBINE DESIGN AND APPLICATION



(a) Total efficiency.

(b) Static efficiency.

FIGURE 3-9.—Overall efficiency characteristics. (Curves from ref. 6.)

parameter and efficiency according to equation (2-74).

From the discussions in this section, it is clear that the selections of the number of stages and velocity diagram type have an important effect on the expected efficiency level and are very dependent upon the specific work (actual or ideal) imposed and blade speed utilized. In an actual design, the final selection of the turbine diagrams must represent a compromise among such design goals as performance (dictated by the cycle requirements), structural integrity (related to component life), compactness, and weight.

RADIAL VARIATION OF DIAGRAMS

In the first half of this chapter, a single velocity diagram was assumed to represent average conditions over the entire blade span. In a turbine having a relatively high hub- to tip-radius ratio (about

0.85 or greater), such an assumption is reasonable. In the case of lower hub- to tip-radius ratios, however, substantial variations in the velocity diagrams are encountered, and the mean-section diagrams may or may not represent the average flow conditions for the entire blade span. The radial variations in diagrams are due to the radial variation in blade speed and the balance of forces that must exist in the flow. The considerations that were described for the mean section diagrams must also be applied to the end regions, which become very important in the final diagram selection. This section will consider the radial variations in flow conditions and their effect on the velocity diagrams.

Radial Equilibrium

Consider an element of fluid in the turbine flow field, as in figure 3-10(a). When there is a tangential component of velocity, the resulting circumferential flow (fig. 3-10(b)) must be maintained by a pressure force. The pressure force serves to balance the centrifugal force acting on the fluid and to keep the fluid moving along its curved path. When the through-flow path (streamline) is curved (fig. 3-10(c)), the force required to maintain the flow along this curved path must be accounted for as part of the net pressure force. Any linear acceleration of the flow must have an associated pressure force, part of which is in the radial direction if the streamline is inclined from horizontal. The balance of forces required to account for these factors is termed radial equilibrium.

The radial equilibrium will now be formulated mathematically. The pressure forces acting on an element of fluid are indicated in figure 3-10(b). Fluid weight is neglected. If unit length is assumed in the x direction, the net pressure force (directed radially inward) is

$$F_{p, net} = (p + dp)(r + dr)d\theta - prd\theta - 2 \left(p + \frac{dp}{2} \right) dr \sin \frac{d\theta}{2} \tag{3-20a}$$

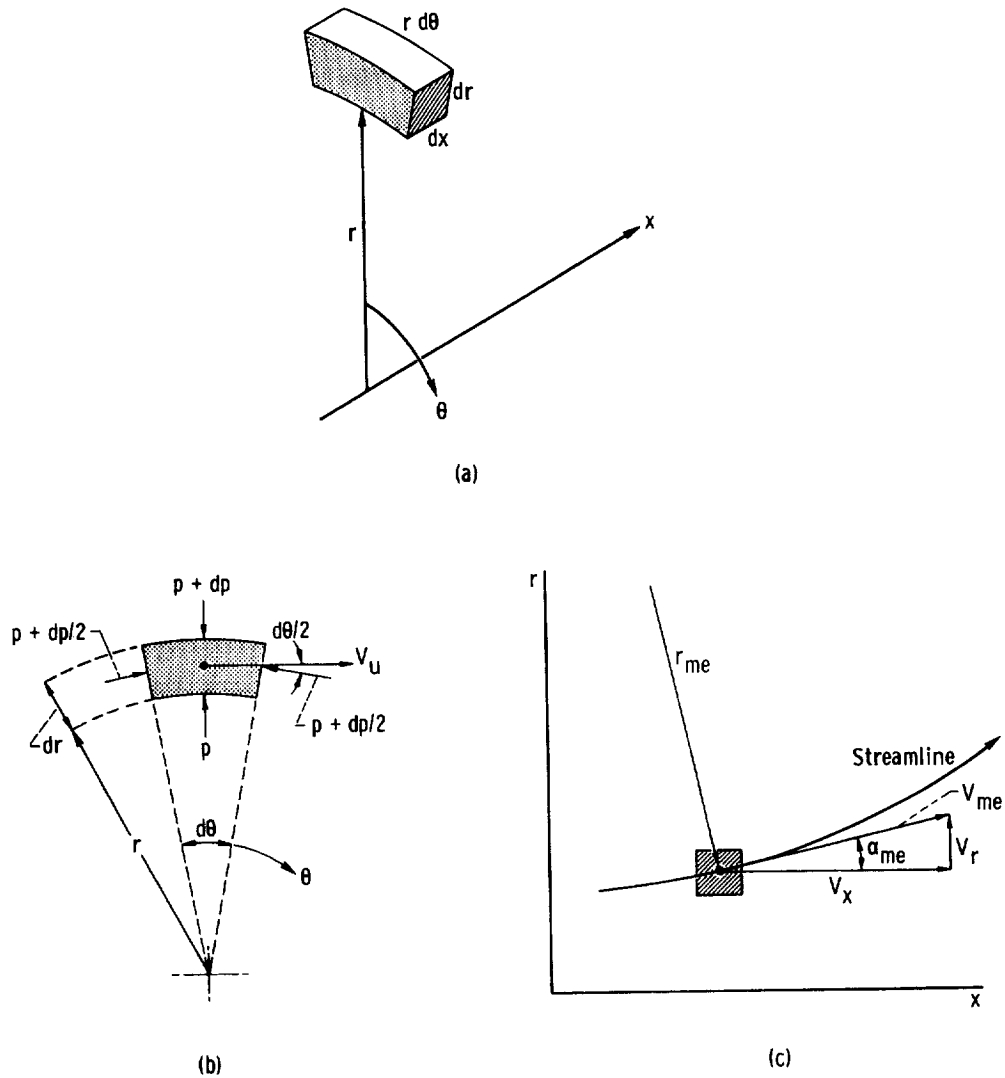
where

- $F_{p, net}$ net inward pressure force, N; lb
- p static pressure, N/m²; lb/ft²
- θ angle of rotation, rad
- r radius of rotation, m; ft

Neglecting higher-order terms (product of three differentials) and setting $\sin (d\theta/2) = d\theta/2$ yields

$$F_{p, net} = rdpd\theta \tag{3-20b}$$

The mass m of the fluid being acted on by the pressure force is



(a) Element of fluid in turbine flow field. (b) Rotation plane ($r-\theta$). (c) Meridional plane ($r-x$).
 FIGURE 3-10.—Radial equilibrium factors.

$$m = \rho[\pi(r + dr)^2 - \pi r^2] \frac{d\theta}{2\pi} \quad (3-21a)$$

which reduces to

$$m = \rho r dr d\theta \quad (3-21b)$$

The net pressure force results from the three factors mentioned previously. To balance the centrifugal force associated with circumferential flow, the radial pressure force is

$$F_{p,c} = \frac{m}{g} \frac{V_u^2}{r} = \frac{\rho r dr d\theta}{g} \frac{V_u^2}{r} = \frac{\rho}{g} V_u^2 dr d\theta \quad (3-22)$$

The radial component of the pressure force required to balance the centrifugal force associated with flow along the meridional streamline is

$$F_{p,r} = -\frac{m}{g} \frac{V_{me}^2 \cos \alpha_{me}}{r_{me}} = -\frac{\rho r dr d\theta}{g} \frac{V_{me}^2}{r_{me}} \cos \alpha_{me} \quad (3-23)$$

where

V_{me} velocity along meridional streamline, m/sec; ft/sec

r_{me} radius of curvature of meridional streamline, m; ft

α_{me} angle of inclination of meridional streamline, deg

The positive directions for streamline curvature and inclination angle are as indicated in figure 3-10(c). The minus sign in equation (3-23) indicates that the balancing pressure force is directed outward in this case. The radial component of the pressure force required to produce the linear acceleration along the meridional streamline is

$$F_{p,t} = -\frac{m}{g} \frac{dV_{me}}{dt} \sin \alpha_{me} = -\frac{\rho r dr d\theta}{g} \frac{dV_{me}}{dt} \sin \alpha_{me} \quad (3-24)$$

Setting the net radial pressure force (eq. (3-20(b))) equal to the various components (eqs. (3-22), (3-23), and (3-24)) yields

$$\frac{g}{\rho} \frac{dp}{dr} = \frac{V_u^2}{r} - \frac{V_{me}^2}{r_{me}} \cos \alpha_{me} - \frac{dV_{me}}{dt} \sin \alpha_{me} \quad (3-25)$$

Equation (3-25) is the radial equilibrium equation and includes all contributing factors. It is, however, not convenient to use in its complete form. For axial flow (or near-axial flow), the meridional streamline curvatures ($1/r_{me}$) and inclination angles (α_{me}) are both quite small. Therefore, the last two terms on the right side of equation (3-25) are small as compared to the first (rotational) term and can often be neglected. Thus, we can write

$$\frac{g}{\rho} \frac{dp}{dr} = \frac{V_u^2}{r} \quad (3-26)$$

The approximation represented by equation (3-26) has become known as "simple" radial equilibrium.

Radial Variations in Velocity

In order to illustrate the nature of the radial variations in velocity, those effects that are usually second order will be neglected, and certain other simplifying assumptions will be made. If streamline slope is assumed to be zero, there is no radial component of velocity, and the total enthalpy definition (eq. (1-49)) can be written as

$$h' = h + \frac{V_u^2}{2gJ} + \frac{V_x^2}{2gJ} \quad (3-27)$$

Differentiating with respect to radius and using equation (1-8) to substitute for dh (and since $\rho=1/v$) yields

$$\frac{dh'}{dr} = T \frac{ds}{dr} + \frac{1}{J\rho} \frac{dp}{dr} + \frac{1}{2gJ} \frac{d(V_u^2)}{dr} + \frac{1}{2gJ} \frac{d(V_x^2)}{dr} \quad (3-28)$$

If the flow entering the turbine is radially uniform, then the total enthalpy at the first-stator exit is radially constant. Further, if the stator loss is radially constant, then the entropy at the first-stator exit is also radially constant. The rotor, as will be discussed later in this chapter, may or may not have radially constant work (total enthalpy) extraction and probably does not have radially constant loss. At any place in the turbine, therefore, radial gradients in total enthalpy and entropy depend on the uniformity of the inlet flow, the gradients imposed by the various blade rows, and the gradient damping due to radial mixing.

For simplicity, it is here assumed that the total enthalpy and the entropy are radially constant. With these assumptions and with equation (3-26), the "simple" radial equilibrium expression, substituted into equation (3-28), we get

$$\frac{V_u^2}{r} + \frac{1}{2} \frac{d(V_u^2)}{dr} + \frac{1}{2} \frac{d(V_x^2)}{dr} = 0 \quad (3-29)$$

In order to solve this equation, it is necessary to independently specify a relation between V_u or V_x and r or between V_u and V_x . Most often, a variation of swirl velocity with radius has been specified as

$$V_u = Kr^N \quad (3-30a)$$

or, in terms of mean-section conditions,

$$\frac{V_u}{V_{u,m}} = \left(\frac{r}{r_m}\right)^N \quad (3-30b)$$

Substituting equation (3-30b) and its differential form into equation (3-29) and then integrating between the limits of r_m and r yields

$$\frac{V_x}{V_{x,m}} = \left\{ 1 - \tan^2 \alpha_m \left(\frac{N+1}{N}\right) \left[\left(\frac{r}{r_m}\right)^{2N} - 1 \right] \right\}^{1/2} \quad (3-31)$$

where α_m is the absolute flow angle at the mean radius. Equation (3-31) is not valid for the special case of $N=0$ (constant V_u). For this

special case, integration of equation (3-29) yields

$$\frac{V_z}{V_{z,m}} = \left[1 - 2 \tan^2 \alpha_m \ln \frac{r}{r_m} \right]^{1/2} \quad (3-32)$$

A case of interest not covered by equation (3-30b) is that where the absolute flow angle is radially constant. In this case, $V_u = V_z \tan \alpha$, and equation (3-29) integrates to

$$\frac{V_u}{V_{u,m}} = \frac{V_z}{V_{z,m}} = \left(\frac{r}{r_m} \right)^{-\sin^2 \alpha} \quad (3-33)$$

The radial variations in swirl velocity, axial velocity, and flow angle, as computed from the above equations, are presented in figure 3-11 for a mean radius flow angle of 60° . The radial variations in axial velocity and flow angle are largely dependent on the specified swirl

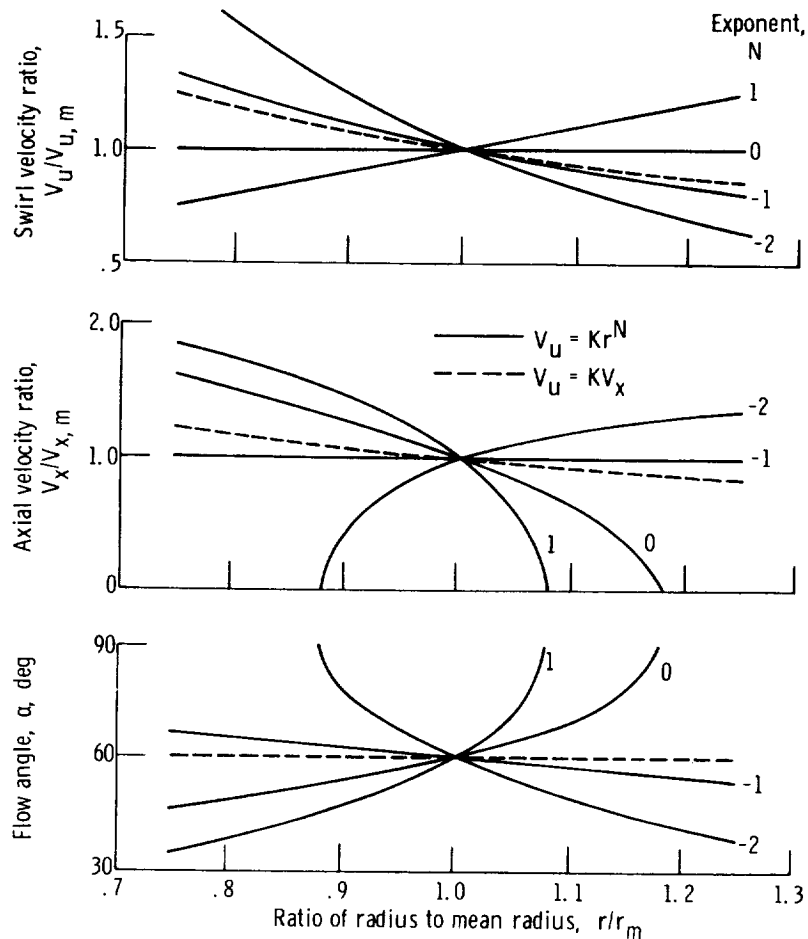


FIGURE 3-11.—Radial variations of velocity and flow angle. Mean-section flow angle α_m , 60° .

velocity variation (value of N). As the swirl distribution exponent N increases or decreases from a value of -1 , the changes in axial velocity and flow angle with changing radius become more pronounced. As seen, the axial velocities and flow angles associated with certain values of N cannot be obtained with all blade lengths. The range of N that can be used for design purposes becomes larger as the blades become shorter (values of r_h/r_m and r_t/r_m closer to 1). The effects of the radial variations illustrated in figure 3-11 on stage velocity diagrams are discussed in subsequent sections of this chapter.

Free-Vortex Diagrams

When a value of -1 is used for the exponent N in equation (3-30a), then

$$rV_u = K \quad (3-34)$$

This is the condition for flow in a free vortex, and a turbine designed for such a swirl distribution is referred to as a free-vortex design, or a free-vortex turbine.

The free-vortex design is used in the vast majority of axial-flow turbines in which radial variation of the diagram is accounted for. If this condition is specified at both the stator and rotor outlets, then there is no radial variation in specific work, $\Delta(UV_u)$, because the UV_u products both entering and leaving the rotor are radially constant. Thus, the specific work computed from the mean-section diagram is valid for the entire flow. Further, if $N = -1$ in equation (3-31), the axial velocity V_x is radially constant. Thus, the radial variation in mass flow per unit area (ρV_x) is small, and the mass flow rate obtained from the mean-section velocity diagram can be used to represent the entire flow within an accuracy of 0.1 percent in most cases. This design simplicity is one of the main reasons for the wide use of free-vortex designs for axial-flow turbines.

An example set of velocity diagrams for a free-vortex design is shown in figure 3-12 for the hub, mean, and tip sections of a blade with a radius ratio of 0.6. The radial variation in the diagram shape is considerable. The mean-section diagram for this example is a symmetrical zero-exit-swirl diagram having a speed-work parameter λ_m of 1. The associated hub diagram is nearly an impulse diagram ($\lambda_h = 0.56$), while the tip diagram is very conservative, with high reaction ($\lambda_t = 1.56$). Thus, for a free-vortex swirl distribution, the hub section is the critical section from an aerodynamic standpoint (lowest efficiency). Therefore, special care must be taken when selecting the mean-section diagram, especially for low-radius-ratio blades, in order to ensure satisfactory diagrams at the hub section. A

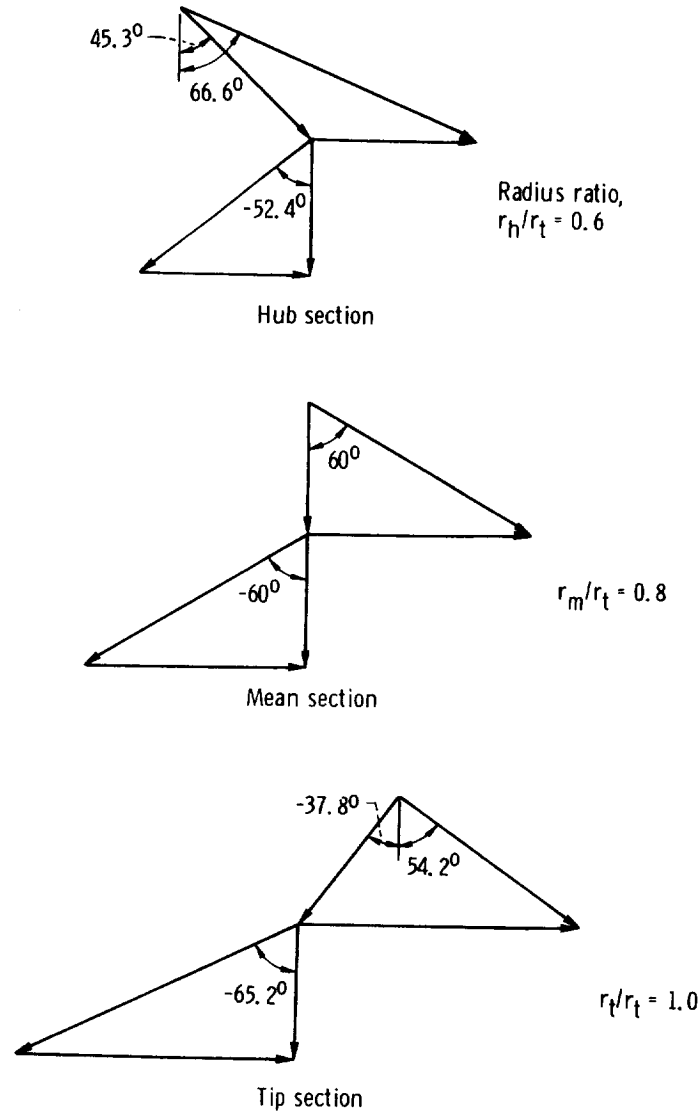


FIGURE 3-12.—Radial variation of velocity-vector diagrams for free-vortex flow. Stator mean-section exit angle α_m , 60° ; mean-section speed-work parameter λ_m , 1.

very high reaction tip diagram can also be troublesome because it increases leakage across the blade tip clearance space.

Another potential problem is that of rotor-blade twist. There is a considerable radial variation in rotor inlet angle. For the case illustrated in figure 3-12, the rotor inlet angle varies from 45° at the hub to -38° at the tip, a variation of 83° . This results in a blade having an overhanging tip section, thus causing some fabrication problems and bending stresses. The positioning of the hub and tip sections of such a blade is illustrated in figure 3-13.

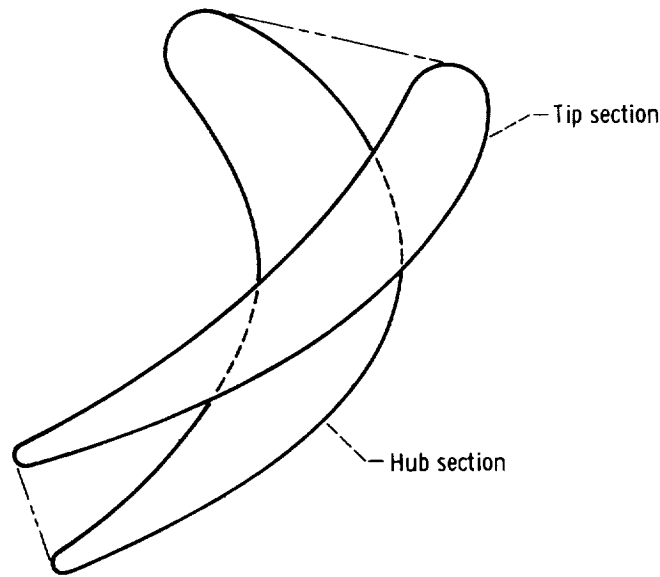


FIGURE 3-13.—Relative positioning of hub and tip sections of free-vortex turbine.

Non-Free-Vortex Diagrams

Free-vortex designs are so commonly used that all other designs are often classified under the common heading of non-free vortex. The non-free-vortex designs are used in an attempt to alleviate some of the potential disadvantages associated with the free-vortex design. Illustrated in figure 3-14 are the radial variations in diagrams for the cases having the velocity variations illustrated in figure 3-11. The super-vortex ($N = -2$) design, the constant-swirl ($N = 0$) design, the wheel-flow, or solid-rotation, ($N = 1$) design, and the constant-flow-angle design are compared with the free-vortex ($N = -1$) design. The mean-section diagrams, which are at a radius ratio r/r_m of 1, are the same for all cases. Also shown are diagrams at radius ratios r/r_m of 0.75, 0.889, 1.111, and 1.25. For a blade with a hub- to tip-radius ratio of 0.6, the r/r_m values of 0.75 and 1.25 correspond to the hub and tip sections, respectively. For a blade with a hub- to tip-radius ratio of 0.8, the r/r_m values of 0.889 and 1.111 correspond to the hub and tip sections, respectively. As the blade hub- to tip-radius ratio decreases, any particular value of r/r_m corresponds to a blade section relatively closer to the mean section. There are, of course, no diagrams to show in figure 3-14 for those particular cases for which, as shown in figure 3-11, no real values exist for axial velocity.

At any radius ratio, the rotor exit diagrams are the same for all the swirl distributions. This is due to the selected mean-section diagram having zero exit swirl ($\alpha_{2,m} = 0$).

The constant-flow-angle diagrams are quite similar to the free-

Ratio of radius to mean radius, r/r_m	Radial swirl distribution				
	Super vortex ($N = -2$)	Free vortex ($N = -1$)	Constant swirl ($N = 0$)	Wheel flow ($N = 1$)	Constant flow angle
1.250			(a)	(a)	
1.111				(a)	
1.000					
0.889					
0.750	(a)				

^aNo real value for axial velocity.

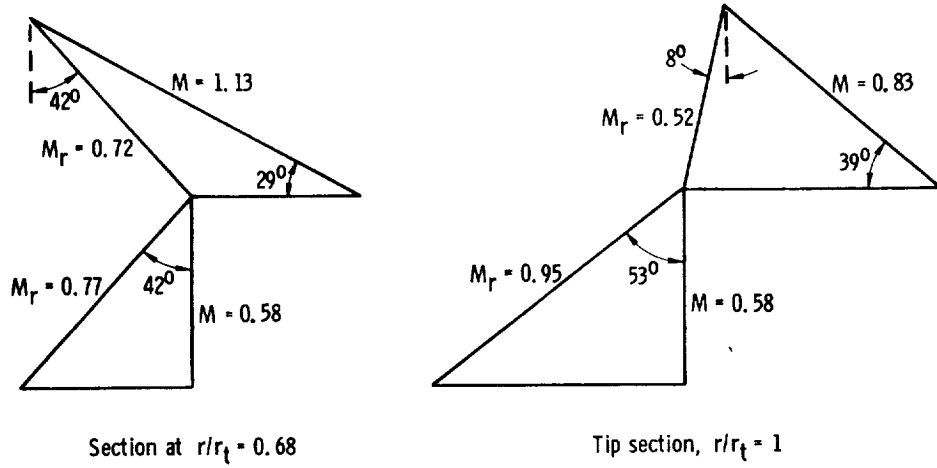
FIGURE 3-14.—Radial variation of velocity-vector diagrams for various swirl distributions.

vortex diagrams and, therefore, present the same problems of high rotor-blade twist and low hub reaction. A possible advantage is that the constant-flow-angle stator has no twist, while the free-vortex stator has a small amount of twist (about 12°).

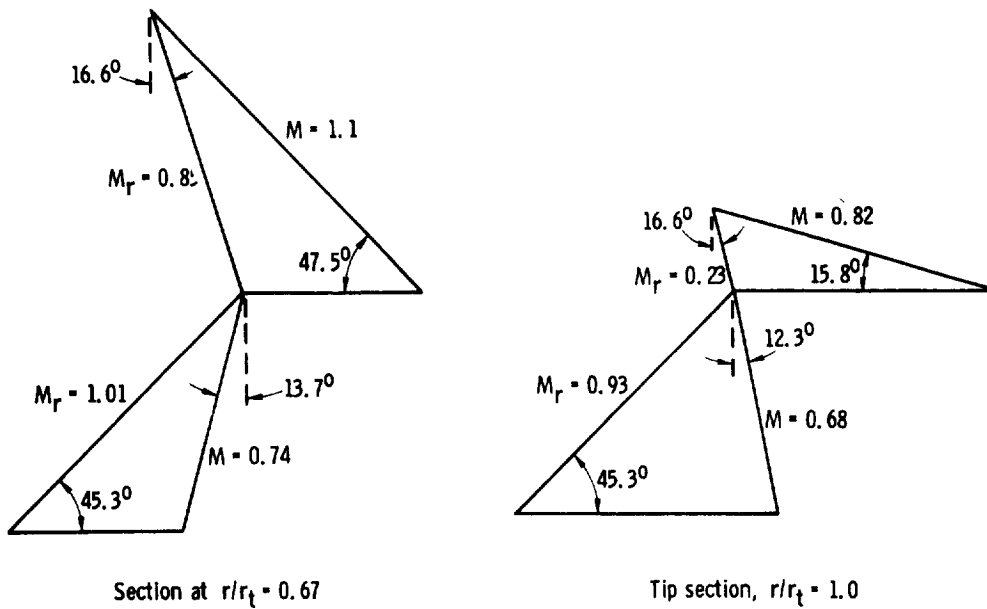
The super-vortex ($N = -2$) diagrams appear to have no advantage of any sort. The blade twist is more severe than for the free-vortex case. The radial variation of stator-exit axial velocity is large and cannot be sustained (V_x becomes imaginary) on blades with hub- to tip-radius ratios much below 0.8.

The constant-swirl ($N = 0$) and wheel-flow ($N = 1$) diagrams do alleviate the blade-twist and hub-reaction problems of the free-vortex design. However, here too the radial variation in axial velocity is large and cannot be sustained on blades with hub- to tip-radius ratios below about 0.70 for the constant-swirl ($N = 0$) design and below about 0.85 for the wheel-flow ($N = 1$) design. In addition, the hub absolute and relative velocities at the stator exit are higher for these designs than for the free-vortex design. For relatively high Mach number turbines, these higher flow velocities could cause higher losses than those of a free-vortex design.

TURBINE DESIGN AND APPLICATION



(a)



(b)

(a) Free-vortex turbine.

(b) Nontwisted turbine.

FIGURE 3-15.—Comparison of velocity-vector diagrams of free-vortex and nontwisted turbines. (Diagrams from ref. 9.)

A design procedure for rotor blades of constant inlet and exit angle, termed a "nontwisted" design, is presented in reference 7. Such a design completely eliminates twist in the rotor, which, therefore, should be easy to fabricate. References 8 and 9 contain experimental results comparing free-vortex designs with nontwisted designs. The design velocity diagrams used for the study of reference 9 are shown in figure 3-15. A large radial variation in axial velocity at the stator exit is also present in this nontwisted design. The stator-exit conditions correspond closely to a swirl-distribution-exponent (N) value of $\frac{1}{4}$. Although rotor twist is eliminated, stator twist has increased from 10° for the free-vortex design to more than 30° for the nontwisted design. At the rotor exit, the swirl is negative at the hub and positive at the tip. The relative blade-inlet Mach number at the hub is higher for the nontwisted design (0.85) than for the free-vortex design (0.72). However, the reaction at the hub of the nontwisted design is improved over that of the free-vortex turbine. The two turbines have about the same efficiency.

The non-free-vortex designs all feature radial variation in specific work and, because of the radial gradient in axial velocity, radial variation in mass flow rate per unit area. Thus, the mean-section conditions may not represent true average conditions, and considerable error may occur if such a turbine is designed on the basis of the mean-section flow conditions. A non-free-vortex turbine should be designed by integrating the flow conditions between hub and tip in order to compute work and flow rate. The proper design of a non-free-vortex turbine is, therefore, much more complex than the design of a free-vortex turbine. With computerized design procedures, however, this additional complexity is no real disadvantage.

As seen from this discussion, the use of non-free-vortex designs to alleviate the rotor-twist and hub-reaction problems associated with free-vortex designs results in other problems such as higher hub Mach numbers, increased stator twist, and increased design complexity. It has been shown that large deviations from free-vortex designs cannot be sustained over all blade spans. However, small deviations from free-vortex designs, as reported in reference 10, have been used to obtain improved turbine performance.

COMPUTER PROGRAMS FOR VELOCITY-DIAGRAM STUDIES

This chapter has presented some of the basic aspects of velocity-diagram selection, including diagram types, their relation to efficiency, staging, and radial variations. It is evident that the determination of the best diagrams and number of stages for a given application requires

many considerations. If it is desired to include non-free-vortex designs, meridional-streamline curvature effects, and radial variation in efficiency, then such analyses are out of the realm of hand calculation. Therefore, computer programs have been evolved to perform such tasks.

One such computer program is described in references 11 and 12. The program includes consideration of streamline-curvature effects in the radial equilibrium equation and radial gradients in enthalpy and entropy in determining radial variations in flow. In addition, it not only allows for blade loss as an input but also includes an internal loss correlation using the information from reference 13 as a basis. This program uses stator exit swirl distribution and rotor work (which reflects rotor exit swirl) distribution as inputs. However, for many values and combinations of these input specifications, either there is no real solution for meridional velocity ($V_{me} = V_x / \cos \alpha_{me}$) or the computer cannot find the solution because of a large variation in dependent variable (meridional velocity) with small variations in independent variable (swirl velocity). The existence of these conditions is indicated by figure 3-11.

This problem has resulted in a program modification, as reported in reference 14, wherein the radial variation in meridional velocity instead of swirl velocity is used as input. The modified program has proven very successful and shows that valid turbine designs can be generated with any reasonable variation in meridional velocity.

REFERENCES

1. STEWART, WARNER L.: A Study of Axial-Flow Turbine Efficiency Characteristics in Terms of Velocity Diagram Parameters. Paper 61-WA-37, ASME, Dec. 1961.
2. STEWART, WARNER L.: Analytical Investigation of Single-Stage-Turbine Efficiency Characteristics in Terms of Work and Speed Requirements. NACA RM E56G31, 1956.
3. WINTUCKY, WILLIAM T.; AND STEWART, WARNER L.: Analysis of Efficiency Characteristics of a Single-Stage Turbine with Downstream Stators in Terms of Work and Speed Requirements. NACA RM E56J19, 1957.
4. STEWART, WARNER L.; AND WINTUCKY, WILLIAM T.: Analysis of Two-Stage-Turbine Efficiency Characteristics in Terms of Work and Speed Requirements. NACA RM E57F12, 1957.
5. WINTUCKY, WILLIAM T.; AND STEWART, WARNER L.: Analysis of Two-Stage Counterrotating Turbine Efficiencies in Terms of Work and Speed Requirements. NACA RM E57L05, 1958.
6. STEWART, WARNER L.: Analytical Investigation of Multistage-Turbine Efficiency Characteristics in Terms of Work and Speed Requirements. NACA RM E57K22b, 1958.

7. SLIVKA, WILLIAM R.; AND SILVERN, DAVID H.: Analytical Evaluation of Aerodynamic Characteristics of Turbines with Nontwisted Rotor Blades. NACA TN 2365, 1951.
8. HEATON, THOMAS R.; SLIVKA, WILLIAM R.; AND WESTRA, LEONARD F.: Cold-Air Investigation of a Turbine with Nontwisted Rotor Blades Suitable for Air Cooling. NACA RM E52A25, 1952.
9. WHITNEY, WARREN J.; STEWART, WARNER L.; AND MONROE, DANIEL E.: Investigation of Turbines for Driving Supersonic Compressors. V-Design and Performance of Third Configuration with Nontwisted Rotor Blades. NACA RM E53G27, 1953.
10. DORMAN, T. E.; WELNA, H.; AND LINDLAUF, R. W.: The Application of Controlled-Vortex Aerodynamics to Advanced Axial Flow Turbines. J. Eng. Power, vol. 90, no. 3, July 1968, pp. 245-250.
11. CARTER, A. F.; PLATT, M.; AND LENHERR, F. K.: Analysis of Geometry and Design Point Performance of Axial Flow Turbines. I-Development of the Analysis Method and the Loss Coefficient Correlation. NASA CR-1181, 1968.
12. PLATT, M.; AND CARTER, A. F.: Analysis of Geometry and Design Point Performance of Axial Flow Turbines. II-Computer Program. NASA CR-1187, 1968.
13. SMITH, S. F.: A Simple Correlation of Turbine Efficiency. J. Roy. Aeron. Soc., vol. 69, no. 655, July 1965, pp. 467-470.
14. CARTER, A. F.; AND LENHERR, F. K.: Analysis of Geometry and Design-Point Performance of Axial-Flow Turbines Using Specified Meridional Velocity Gradients. NASA CR-1456, 1969.

SYMBOLS

<i>A</i>	flow area, m ² ; ft ²
<i>F_p</i>	pressure force, N; lb
<i>g</i>	conversion constant, 1; 32.17 (lbm)(ft)/(lbf)(sec ²)
<i>h</i>	specific enthalpy, J/kg; Btu/lb
<i>J</i>	conversion constant, 1; 778 (ft)(lb)/Btu
<i>K</i>	proportionality constant
<i>L</i>	loss, J/kg; Btu/lb
<i>m</i>	mass, kg; lb
<i>N</i>	swirl distribution exponent
<i>n</i>	number of stages
<i>p</i>	pressure, N/m ² ; lb/ft ²
<i>R</i>	reaction
<i>r</i>	radius, m; ft
<i>s</i>	specific entropy, J/(kg)(K); Btu/(lb)(°R)
<i>T</i>	temperature, K; °R
<i>U</i>	blade speed, m/sec; ft/sec
<i>V</i>	absolute velocity, m/sec; ft/sec
<i>v</i>	specific volume, m ³ /kg; ft ³ /lb
<i>W</i>	relative velocity, m/sec; ft/sec
<i>w</i>	mass flow rate, kg/sec; lb/sec
<i>α</i>	fluid absolute flow angle, deg
<i>η</i>	efficiency
<i>θ</i>	angle of rotation, deg
<i>λ</i>	speed-work parameter
<i>ρ</i>	density, kg/m ³ ; lb/ft ³

Subscripts:

<i>a</i>	first stage
<i>an</i>	annulus
<i>c</i>	component due to circumferential flow
<i>h</i>	hub
<i>i</i>	general stage
<i>id</i>	ideal
<i>l</i>	component due to linear acceleration
<i>m</i>	mean section
<i>me</i>	meridional
<i>net</i>	net
<i>r</i>	radial component
<i>ro</i>	rotor
<i>s</i>	component due to streamline curvature
<i>st</i>	stator
<i>stg</i>	stage

VELOCITY DIAGRAMS

t	tip
u	tangential component
x	axial component
0	at stator inlet
1	at stator exit or rotor inlet
2	at rotor exit

Superscripts:

—	overall turbine
'	absolute total state

CHAPTER 4

Blade Design

By Warner L. Stewart and
Arthur J. Glassman

The design of a turbine consists of three major steps. The first is the determination of the overall requirements of flow, work, and speed. These are usually established by the particular application. The second step is the evolution of velocity diagrams consistent with the desired efficiency and/or number of stages. This was discussed in chapter 3. The third step is the design of the blading that will produce the flow angles and velocities required by the velocity diagrams. This step involves the determination of the size, shape, and spacing of the blades.

This chapter covers some of the more important aspects of blade design. The height of the blade is set by the overall requirements of flow, speed, and inlet state conditions and the selected velocity diagram, which dictates the fluid state conditions throughout the turbine. The blade chord is usually selected to be a minimum value consistent with mechanical considerations. The chord must be long enough to allow accurate fabrication and assure structural integrity during operation. The selection of blade spacing, which can be expressed nondimensionally as solidity (ratio of chord to spacing) or axial solidity (ratio of axial chord to spacing), involves many considerations that will be discussed in the first part of this chapter. Blade profile design, which includes blade exit and inlet geometries as well as the connecting surface profiles, is then discussed in the last part of this chapter. Channel flow theory, which is the basis for the analytical procedures used to accomplish the profile design, is discussed in the next chapter.

~~REMOVED~~ MADE BLANK NOT FILLED

PAGE 100 INTENTIONALLY BLANK

SOLIDITY

One of the important aspects of turbine blading design is the selection of the blade solidity, which is the ratio of chord or axial chord to spacing. A minimum value is usually desired from the standpoint of reducing weight, cooling flow, and cost. However, chord reduction is limited by mechanical considerations, and increased spacing eventually results in decreased blade efficiency due to separated flow. This section will concern itself with the aerodynamic factors affecting solidity selection. The discussion will include the effect of velocity diagram requirements on solidity and the relation between blade loading and solidity. Also included will be a description of advanced blading concepts that are being studied for use to suppress separation and thereby reduce the permissible solidity.

Effect of Velocity Diagrams on Solidity

Figure 4-1 shows a typical set of blade inlet and exit diagrams as well as the static-pressure distribution around a blade. The velocities in this figure are shown as absolute velocities. The discussion in this chapter pertains to rotor blade rows as well as to stator blade rows. When referring to a rotor, we must use relative rather than absolute velocities in the equations and figures. Since in this chapter we are concerned with blade rows rather than with stages, the angle convention will differ slightly from that used in previous chapters. The exit tangential-velocity component and flow angle are taken as negative values. The inlet values are positive if the inlet and exit tangential-velocity components are in opposite directions, and negative if in the same direction.

If one considers the two-dimensional flow through a passage of unit height between two blades, then the tangential force exerted by the fluid as it flows from blade inlet (subscript 1) to exit (subscript 2) is

$$F_u = \frac{1}{g} s \rho_2 V_{x,2} (V_{u,1} - V_{u,2}) \quad (4-1)$$

where

F_u	tangential force, N; lb
g	conversion constant, 1; 32.17 (lbm) (ft)/(lbf) (sec ²)
s	blade spacing, m; ft
ρ	density, kg/m ³ ; lb/ft ³
V_x	axial component of velocity, m/sec; ft/sec
V_u	tangential component of velocity, m/sec; ft/sec

This tangential force exerted by the fluid must be the same as the force due to the static-pressure distribution around the blade, as was discussed in chapter 2. The lower part of figure 4-1 shows a typical static-pressure

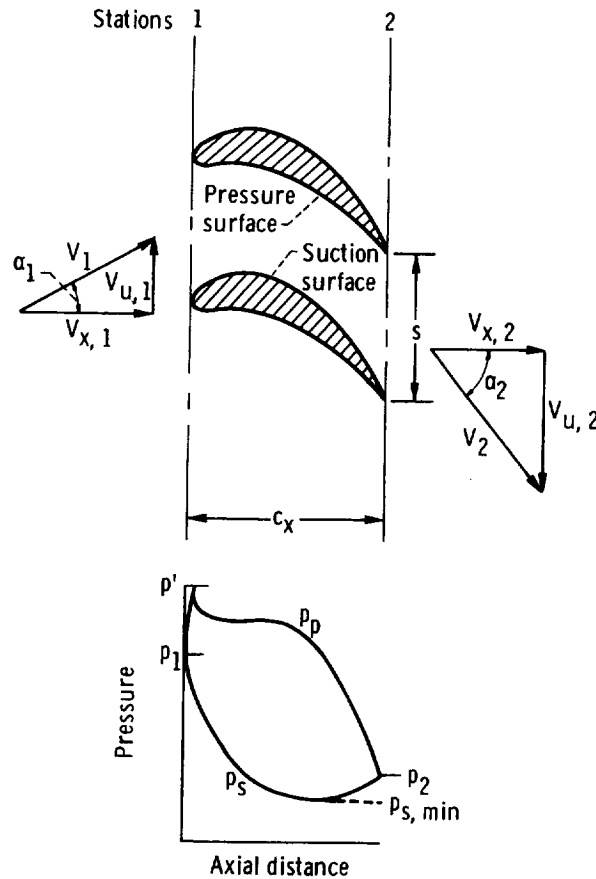


FIGURE 4-1.—Typical blade-row velocity diagrams and surface static-pressure distribution.

distribution around the blade row as a function of axial distance. The area between the two curves represents the total blade force acting on the flow in the tangential direction. Thus,

$$F_u = c_x \int_0^1 (p_p - p_s) d\left(\frac{x}{c_x}\right) \quad (4-2)$$

where

- c_x axial chord, m; ft
- p_p pressure-surface static pressure, N/m²; lb/ft²
- p_s suction-surface static pressure, N/m²; lb/ft²
- x axial distance, m; ft

The axial solidity, σ_x , is

$$\sigma_x = \frac{c_x}{s} \quad (4-3)$$

Substituting equations (4-1) and (4-2) into equation (4-3) then yields

$$\sigma_x = \frac{\rho_2 V_{x,2} (V_{u,1} - V_{u,2})}{g \int_0^1 (p_p - p_s) d\left(\frac{x}{c_x}\right)} \quad (4-4)$$

At this point, we introduce two tangential loading coefficients that have been used to relate the actual blade loading to an ideal blade loading. The first is the widely used coefficient introduced by Zweifel (ref. 1). This coefficient is based on an ideal loading that assumes (1) the static pressure on the pressure surface to be constant and equal to the inlet total pressure and (2) the static pressure on the suction surface to be constant and equal to the exit static pressure. In equation form,

$$\psi_z = \frac{\int_0^1 (p_p - p_s) d\left(\frac{x}{c_x}\right)}{p_1' - p_2} \quad (4-5)$$

where

ψ_z Zweifel loading coefficient
 p_1' inlet total pressure, N/m²; lb/ft²
 p_2 exit static pressure, N/m²; lb/ft²

The second coefficient is similarly defined except that the assumed constant static pressure on the suction surface is equal to the minimum value of static pressure (see fig. 4-1) on that surface. This loading coefficient can never exceed a value of 1, and for all practical purposes, it must always be less than 1. The Zweifel coefficient, on the other hand, can exceed a value of 1. In equation form, this second loading coefficient ψ is defined as

$$\psi = \frac{\int_0^1 (p_p - p_s) d\left(\frac{x}{c_x}\right)}{p_1' - p_{s,min}} \quad (4-6)$$

where $p_{s,min}$ is the minimum static pressure on the suction surface in N/m² or lb/ft².

The velocity components in terms of velocity and flow angle are expressed as

$$V_u = V \sin \alpha \quad (4-7)$$

and

$$V_x = V \cos \alpha \quad (4-8)$$

where

V fluid velocity, m/sec; ft/sec
 α fluid flow angle, deg

Substituting equations (4-5) or (4-6), (4-7), and (4-8) into equation (4-4) and using the trigonometric relation $\sin 2\alpha = 2 \sin \alpha \cos \alpha$ yields

$$\sigma_x = \left(\frac{\frac{1}{2g} \rho_2 V_2^2}{p_1' - p_{s,min}} \right) \frac{(K-1) \sin 2\alpha_2}{\psi} = \left(\frac{\frac{1}{2g} \rho_2 V_2^2}{p_1' - p_2} \right) \frac{(K-1) \sin 2\alpha_2}{\psi_z} \quad (4-9)$$

where K is the ratio of tangential velocity component ($V_{u,1}$) at the blade inlet to that ($V_{u,2}$) at the blade exit.

Derivation of incompressible-flow relations.—Relations involving solidity, velocity diagrams, and loading are usually evolved by assuming incompressible flow with no loss. With this assumption, density ρ is constant, and Bernoulli's equation

$$p' = p + \frac{1}{2g} \rho V^2 \quad (4-10)$$

can be used. Substituting equation (4-10) into equation (4-9) yields

$$\sigma_x = \frac{(K-1) \sin 2\alpha_2}{\psi \left(\frac{V_{max}^2}{V_2^2} \right)} = \frac{(K-1) \sin 2\alpha_2}{\psi_z} \quad (4-11)$$

where V_{max} is the velocity on the suction surface where $p = p_{s,min}$.

Let us now define a suction-surface diffusion parameter D_s as

$$D_s \equiv \frac{V_{max}^2}{V_2^2} \quad (4-12)$$

Many parameters of this type have been used to represent a measure of the deceleration of the flow on the suction surface. This deceleration is an indication of the susceptibility of the flow on the blade to separate. Using this definition (eq. (4-12)) in equation (4-11) yields

$$\sigma_x = \frac{(K-1) \sin 2\alpha_2}{\psi D_s} = \frac{(K-1) \sin 2\alpha_2}{\psi_z} \quad (4-13)$$

Equation (4-13) shows that the solidity parameter $\sigma_x \psi D_s$ or $\sigma_x \psi_z$ is constant for each particular velocity-diagram requirement. Since loading coefficient ψ , which cannot exceed a value of 1, does not vary greatly, it can be seen that decreasing solidity results primarily in increased suction-

surface diffusion (higher D_s), the consequence of which will be discussed later in this chapter. The solidity parameter is plotted against the tangential velocity ratio K for several values of exit flow angle in figure 4-2(a). A value of $K=0$ represents a reaction blade with axial inlet, a value of $K=-1$ represents an impulse blade, and a value of $K < -1$ represents a negative reaction blade. Positive values of K represent inlet and exit tangential velocities in the same direction and are encountered primarily in the tip sections of rotor blades. As seen from equation (4-13), solidity parameter is equal to zero for all exit angles for $K=1$. This represents the case where there is no turning of the flow. The solidity parameter increases with decreasing K values. Thus, if excessive suction-surface diffusion is to be avoided, solidity must increase as the velocity diagrams move from reaction toward impulse. It can be seen that for any given value of K , a maximum value of solidity parameter is obtained with an exit angle of 45° .

Equation (4-13) can be modified to a function of the inlet and exit angles to yield the equation derived in reference 1.

$$\sigma_x = \frac{2 \cos \alpha_2}{\psi_z \cos \alpha_1} \sin (\alpha_1 - \alpha_2) \quad (4-14)$$

For brevity, this is expressed only in terms of the coefficient ψ_z . Equation (4-14) shows that the solidity parameter $\sigma_x \psi_z$ can be expressed in terms of the flow angles only. Solidity parameter is plotted against exit flow angle for several values of the inlet flow angle in figure 4-2(b). For a given exit angle, solidity parameter increases with increasing inlet angle. In the region of most interest ($\alpha_1 > 0^\circ$, $\alpha_2 < -45^\circ$), solidity parameter for each inlet angle decreases with decreasing exit angle.

A third relation can be evolved, this one in terms of blade reaction R , which was defined in chapter 2 as

$$R \equiv 1 - \frac{V_1^2}{V_2^2} \quad (4-15)$$

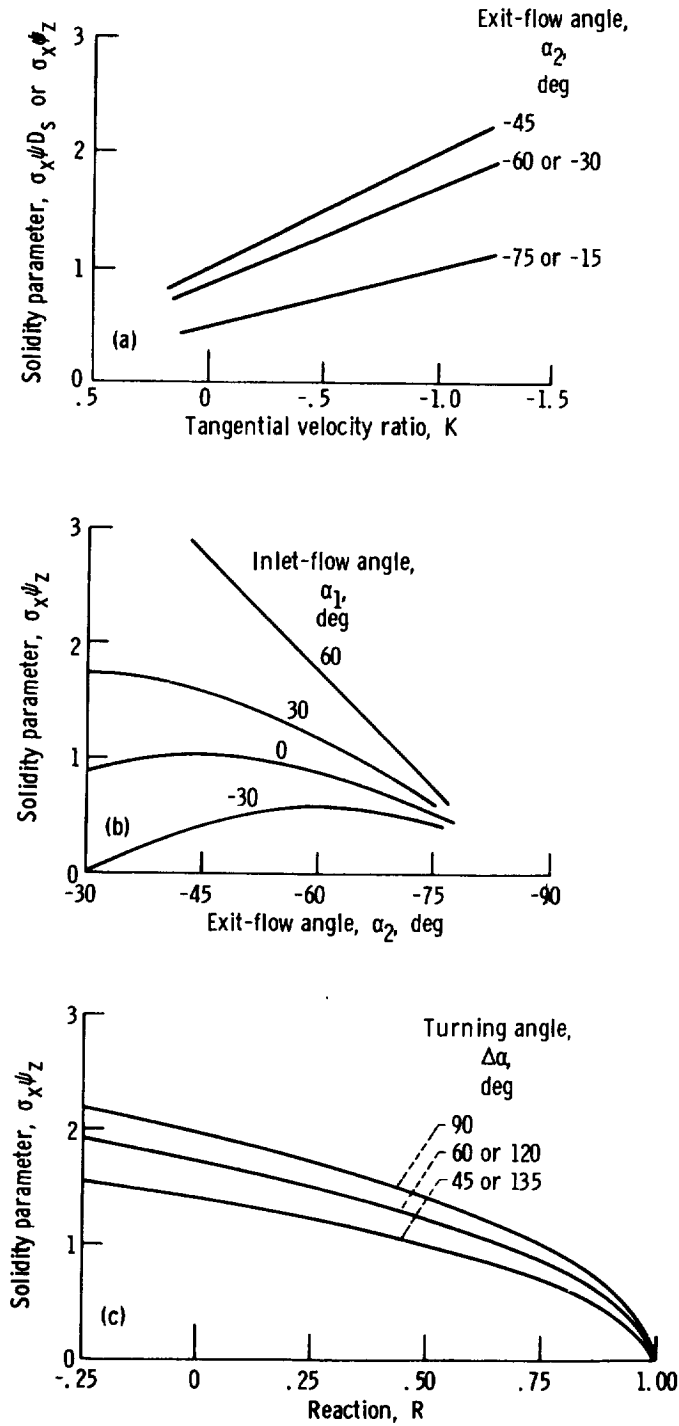
Substituting equation (4-8) into equation (4-15) yields

$$R = 1 - \left(\frac{\cos \alpha_2}{\cos \alpha_1} \right)^2 \quad (4-16)$$

for the two-dimensional, incompressible-flow case, where $V_{x,1} = V_{x,2}$. Substitution of equation (4-16) back into equation (4-14) then yields

$$\sigma_x = \frac{2}{\psi_z} \sqrt{1-R} \sin \Delta\alpha \quad (4-17)$$

where $\Delta\alpha$ is $\alpha_1 - \alpha_2$.



(a) Effect of tangential-velocity ratio and exit-flow angle.
 (b) Effect of exit- and inlet-flow angles.
 (c) Effect of reaction and turning angle.

FIGURE 4-2.—Effect of velocity diagrams on solidity.

Equation (4-17) expresses the solidity parameter in terms of blade reaction and turning angle. The solidity parameter is plotted against reaction for several values of turning angle in figure 4-2(c). It can be seen that, as indicated previously, the solidity parameter decreases with increasing reaction. The solidity parameter is a maximum for a turning angle of 90° and varies little with turning unless very high or very low turnings are used.

Radial variation.—Chapter 3 discussed the radial variations in velocity diagrams that must occur in order to satisfy both the varying blade speed and radial equilibrium. Since axial solidity was shown to vary with varying velocity diagrams, there will be a radial variation in the desired value of axial solidity. The nature of this radial variation will be illustrated by an example. Consider a single-stage turbine having axial inlet and exit flows (zero inlet and exit swirls), constant axial velocities, a constant hub-to-tip-radius ratio of 0.7, an impulse rotor hub with a stator-hub exit flow angle of -70° , and free-vortex swirl distribution. For this case, the flow angles at the hub and tip and the corresponding solidity-parameter values computed from equation (4-14) are shown in the following table:

	Stator			Rotor		
	Inlet angle, deg	Exit angle, deg	Solidity parameter, $\sigma_x \psi_z$	Inlet angle, deg	Exit angle, deg	Solidity parameter, $\sigma_x \psi_z$
Hub	0	-70	0.64	54	-54	1.90
Tip	0	-62	.83	-2	-63	.79

Note again that the angle convention being used in this chapter is somewhat different from that of previous chapters. Herein, stator exit angles are negative. Assume that the loading coefficient ψ_z is to be maintained constant radially. This is a reasonably desirable condition, and the assumption enables us to proportion solidity directly to the solidity parameter.

Let us now determine how the hub and tip values of solidity parameter shown in the preceding table can be made physically consistent. The axial solidity variation in any blade row must be inversely proportional to radius (because blade spacing is directly proportional to radius) and

directly proportional to axial chord. For the stator, the axial solidity parameter at the hub is 0.64. If axial chord were held constant, then the corresponding tip value of the axial solidity parameter would be $0.64 \times 0.7 = 0.45$, which is almost half of the desired value of 0.83. Therefore, a considerable axial taper from tip to hub is often used so that the axial chord can increase with radius and yield the higher solidities desired at the tip.

In the case of the rotor, the axial solidity parameter at the hub is 1.90. If axial chord were held constant, then the corresponding tip value of the axial solidity parameter would be $1.90 \times 0.7 = 1.33$, which is still larger than the desired value of 0.79. Therefore, axial taper from hub to tip is often used in rotor blades so that axial chord can decrease with increasing radius and yield the lower solidities desired at the tip. Taper from hub to tip in the rotor is not only aerodynamically desirable, but is also mechanically desirable from the standpoint of reducing blade stress. To simplify fabrication in many cases, especially for smaller turbines, axial taper is not used, and there results a radial variation in loading coefficient. With the axial solidity selected on the basis of the mean-section velocity diagrams, this radial variation in loading coefficient in many cases, especially those where the blading is not highly loaded, will not have a severe effect on turbine performance.

Effect of compressibility.—The term

$$\frac{\frac{1}{2g} \rho_2 V_2^2}{p_1' - p_{s,min}}$$

in equation (4-9) reduces to $1/D_s$ for incompressible flow conditions, as shown by equation (4-13). For a compressible flow case having the same loading coefficient ψ as for incompressible flow, division of equation (4-9) by equation (4-13) yields

$$\frac{\sigma_x}{\sigma_{x,inc}} = \frac{\frac{1}{2g} \rho_2 V_2^2 D_s}{p_1' - p_{s,min}} \quad (4-18)$$

where $\sigma_{x,inc}$ is the incompressible flow value as determined from an equation such as (4-13), (4-14), or (4-17). By introducing the relations between critical velocity ratio, density, and pressure (eqs. (1-3), (1-52), (1-61), (1-63), and (1-64)) and using the definition of D_s (eq. (4-12)), equation (4-18) is modified to

$$\frac{\sigma_x}{\sigma_{x,inc}} = \frac{\frac{\gamma}{\gamma+1} \left[1 - \frac{\gamma-1}{\gamma+1} \left(\frac{V}{V_{cr}} \right)_2^2 \right]^{1/(\gamma-1)} \left(\frac{V}{V_{cr}} \right)_2^2 D_s}{1 - \left[1 - \frac{\gamma-1}{\gamma+1} \left(\frac{V}{V_{cr}} \right)_2^2 \right]^{\gamma/(\gamma-1)}} \quad (4-19)$$

where

γ ratio of specific heat at constant pressure to specific heat at constant volume

V_{cr} critical velocity, m/sec; ft/sec

Then, by using binomial expansion and by neglecting the secondary terms, equation (4-19) can be approximated as

$$\frac{\sigma_x}{\sigma_{x,inc}} = 1 - \frac{\left(\frac{V}{V_{cr}} \right)_2^2}{\gamma+1} + \frac{D_s \left(\frac{V}{V_{cr}} \right)_2^2}{2(\gamma+1)} \quad (4-20)$$

The approximation represented by equation (4-20) is quite good for $(V/V_{cr})_2$ values up to about 1. The solidity ratio $\sigma_x/\sigma_{x,inc}$ is plotted against suction-surface diffusion parameter for several values of critical velocity ratio in figure 4-3. The compressibility effect becomes more pronounced as D_s either increases or decreases from a value of 2. At $D_s=2$, there is no compressibility effect for any value of $(V/V_{cr})_2$. For D_s values of less than 2, the required solidity decreases with increasing values of $(V/V_{cr})_2$.

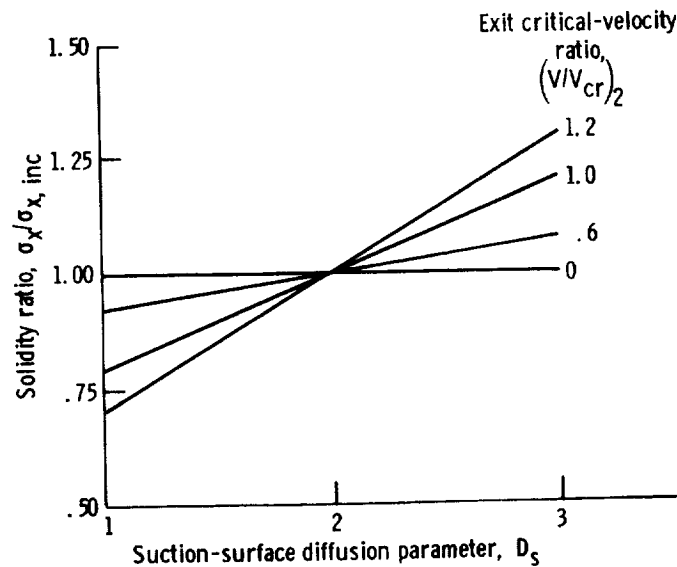


FIGURE 4-3.—Effect of compressibility on axial solidity.

For D_s values of more than 2, a region that is only of academic interest because it is beyond the limits of good design practice, the solidity ratio increases with increasing $(V/V_{cr})_2$. Experience has shown that D_s values should be maintained below about 2 to avoid excessive losses.

Relation of Loss to Solidity

It is well recognized that the loading of a turbine blade or of a compressor blade is an important function of both solidity and reaction. Correlation of blade loss with a compressor diffusion parameter was described in reference 2 and is used widely within the compressor field. This parameter includes two terms, one reflecting reaction and the second reflecting turning and solidity. An analogous diffusion parameter was evolved for the case of the turbine in reference 3, where an overall diffusion parameter is defined as the ratio of the sum of the decelerations in kinetic energy on the suction and pressure surfaces to the exit kinetic energy. If it is assumed that the pressure surface minimum velocity is low enough to neglect ($V_{p,min}=0$), then the overall diffusion parameter is defined as

$$D \equiv \frac{V_{max}^2 - V_2^2 + V_1^2}{V_2^2} \quad (4-21)$$

With the use of the definitions of D_s (eq. (4-12)) and R (eq. (4-15)), equation (4-21) reduces to

$$D = D_s - R \quad (4-22)$$

As seen from equation (4-13),

$$\psi_z = \psi D_s \quad (4-23)$$

Substitution of equations (4-23) and (4-14) into equation (4-22) then yields

$$D = \frac{2 \cos \alpha_2}{\sigma_x \psi \cos \alpha_1} \sin \Delta \alpha - R \quad (4-24)$$

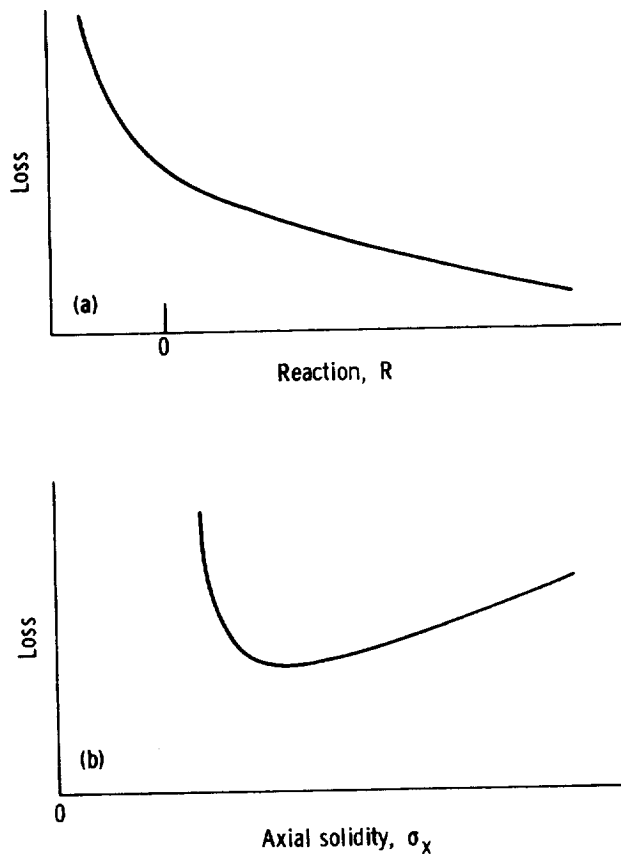
This relation is like that for compressors, with the two terms involving reaction and solidity.

Attempts have been made to correlate turbine blade loss with both overall (ref. 4) and suction-surface (ref. 5) diffusion parameters. A definite trend of increasing loss with increasing diffusion was established, but complete correlation could not be obtained. Such a correlation of blade loss with diffusion parameter alone would not be expected, since different values of reaction and solidity giving the same value of D do not give the same loss.

Consider first the effect of reaction on loss, as shown qualitatively in figure 4-4(a). As reaction is reduced from a relatively high value near

unity, there occurs a gradual increase in blade loss. Further reductions in reaction to negative values cause the loss to increase rapidly. This variation in loss with reaction is caused by the change in boundary-layer characteristics (which are discussed in chapter 6) as the nature of the flow varies from highly accelerating to diffusing. The negative reaction regime, although desired in many applications, is usually avoided because of the high loss encountered when conventional blading is used.

The effect of solidity on loss is indicated in figure 4-4(b). A minimum loss occurs at some optimum solidity. As solidity increases, the amount of frictional surface area per unit flow is increasing. As solidity is reduced, on the other hand, the loss per unit surface area is increasing because of the increased surface diffusion required. A minimum loss occurs as a result of these opposing factors. The value of the suction-surface diffusion



(a) Reaction.

(b) Solidity.

FIGURE 4-4.—Loss trend with reaction and solidity.

parameter corresponding to the optimum solidity is a function of many factors such as Reynolds number, shape of suction surface velocity distribution, and rate of turning. In general, as mentioned previously, values not exceeding about 2.0 are used.

Selection of Optimum Solidity

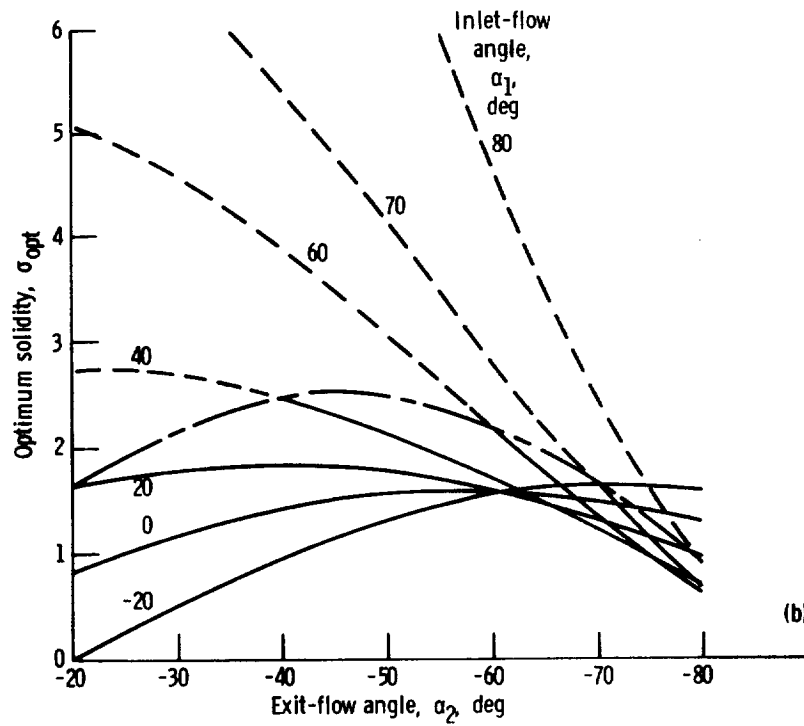
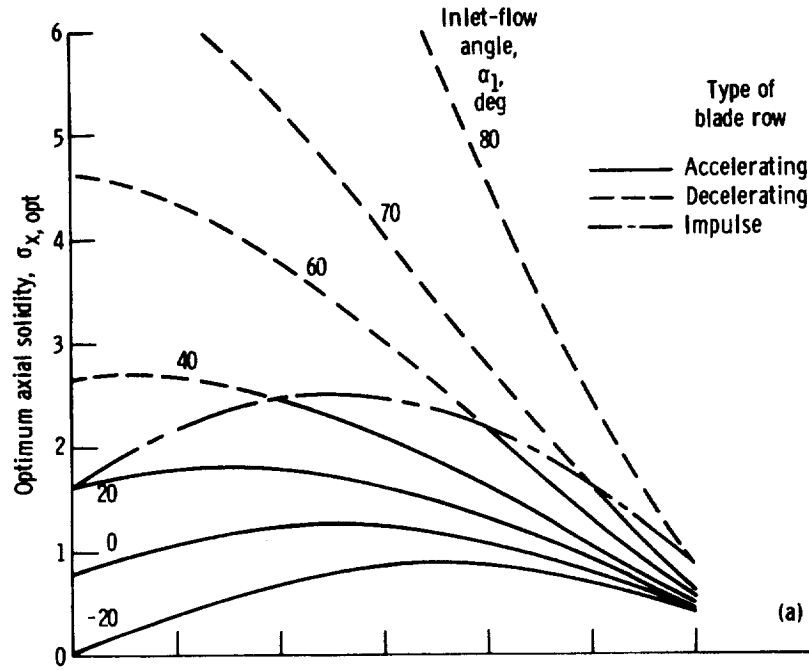
Both analytical and experimental attempts have been made to identify optimum solidity. According to reference 1, minimum loss occurs when the Zweifel loading coefficient ψ_z is equal to 0.8. By using this value in equation (4-14), optimum axial solidity can be determined as a function of the blade-row inlet and exit flow angles, and this is plotted in figure 4-5(a) for a wide range of angles. The dashed (long-short) curve represents the locus of points for impulse blading.

In order to determine the optimum values in terms of actual solidity, it is necessary to determine the stagger angle α_s , because

$$\sigma \approx \frac{\sigma_z}{\cos \alpha_s} \quad (4-25)$$

An analytical blade model was used in reference 6 to relate stagger angle to the flow angles and the axial solidity. Thus, optimum values of actual solidity were obtained as a function of inlet and exit angles, as shown in figure 4-5(b). The authors of reference 6 compared an optimum solidity determined in this way with the data of reference 7, where efficiency was measured with four different rotor solidities, as shown here in figure 4-6. The solidity determined as optimum in reference 6 from a figure such as figure 4-5(b) is seen to be quite close to that yielding maximum efficiency for this case.

Loss coefficients based on cascade data are presented in reference 8 as a function of pitch/chord ratio (inverse of solidity) and exit angle for reaction blades ($\alpha_1 = 0$) and impulse blades ($\alpha_1 = -\alpha_2$). These coefficients, in relative terms, are replotted here in figure 4-7 against solidity for various exit angles. These curves indicate the importance of selecting optimum solidity. For the larger (more negative) values of exit angle, the curves are rather flat in the region of minimum loss, and some deviation in solidity from optimum does not cause any significant increase in loss. As the exit angle gets smaller, the minimum loss region becomes more pronounced and the loss penalties become more severe as solidity departs from the optimum value. It must be recognized that curves such as those of figure 4-7 are usually obtained by using a given blade shape and varying the spacing. Thus, the blade shape and resultant velocity distribution cannot be optimized for each solidity, and the significance of such a correlation is somewhat clouded.



(a) Axial solidity.

(b) Actual solidity.

FIGURE 4-5.—Effect of inlet and exit angles on optimum solidity. Zweifel loading coefficient $\psi_z = 0.8$.

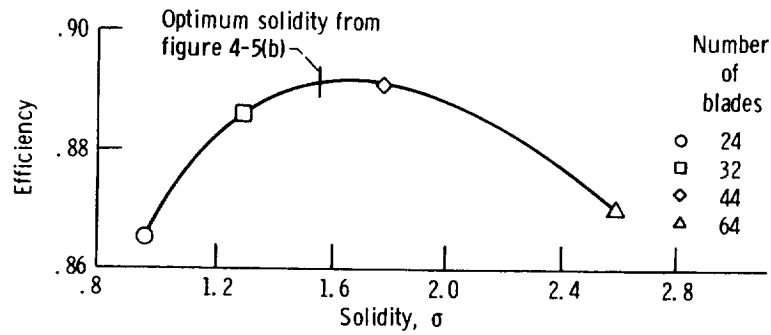


FIGURE 4-6.—Variation of efficiency with solidity for four turbines of reference 7.

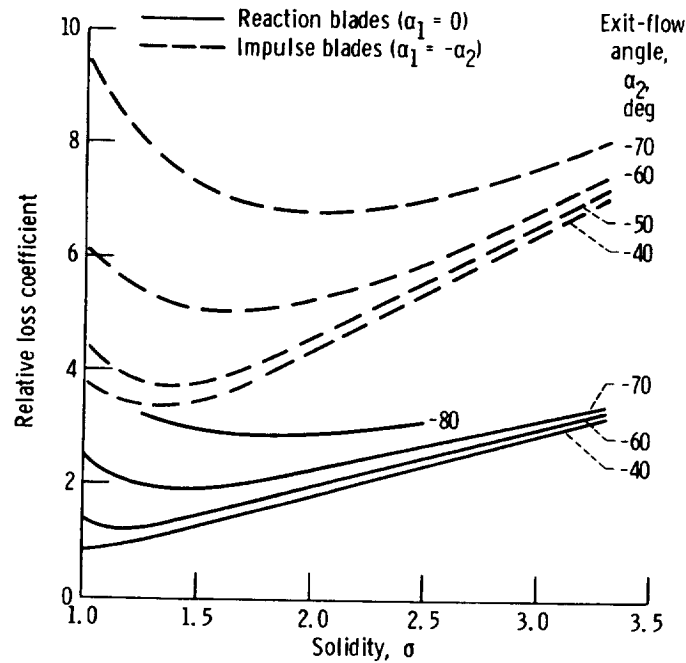


FIGURE 4-7.—Effect of solidity and exit angle on blade-loss coefficient.

The optimum solidities obtained from the cascade results shown in figure 4-7 are plotted against exit angle in figure 4-8 and are compared with those obtained analytically and shown in figure 4-5(b). It is obvious that agreement between the experimental and the analytical results is not good for most exit-angle values. Although the experimental and the analytical curves do cross each other for both the reaction ($\alpha_1 = 0$) blading and the impulse ($\alpha_1 = -\alpha_2$) blading, the indicated variations in optimum solidity with exit angle are just not similar. All that can be said at this time is that the analytical results involve many assumptions, the experimental results pertain to one particular blade profile, and there are many factors that act to determine optimum solidity in a manner that we do

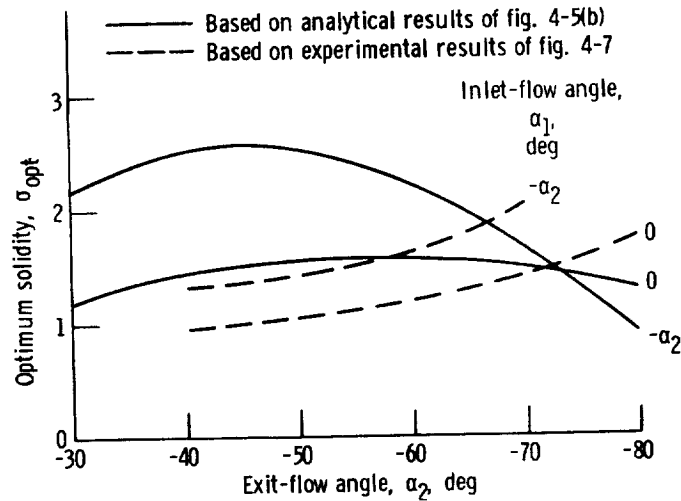


FIGURE 4-8.—Comparison of optimum solidities.

not yet fully understand. Analytical results, such as those of figure 4-5, are more frequently used to determine optimum solidity than are experimental results, such as those shown in figure 4-7. Current design practice is to use ψ_z values of 0.9 to 1.0, which is slightly higher than the 0.8 recommended in reference 1.

Ultralow-Solidity Blading

In the past, the limitation to reductions in solidity has been separation occurring on the suction surface of the blade. To achieve lower solidities, some modification in blade concept must be utilized such that separation is suppressed and the associated high losses do not occur.

The treatment of the boundary layer in the region of separation is one approach to reduced solidity. Such treatments could include removing the boundary layer by suction, energizing the boundary layer by blowing, or increasing the turbulence of the boundary layer by use of turbulators on the blade. Certain of these concepts have been explored with marginal success. Two alternate blade concepts that have, perhaps, better potential are the tandem and jet-flap blades, which are illustrated in figure 4-9. Studies applying the boundary-layer treatment concepts as well as the alternate blade concepts to stator blades and rotor blades are summarized in references 9 and 10, respectively. Cascade tests of low-solidity plain, tandem, and jet-flap blades are presented in references 11 to 14. Turbine test results with low-solidity tandem and jet-flap rotors are presented in references 15 and 16, respectively.

The tandem blade operates on the principle that, although a high value of suction-surface diffusion is utilized (perhaps 2), the front foil is terminated at about the point of separation. The remaining diffusion then

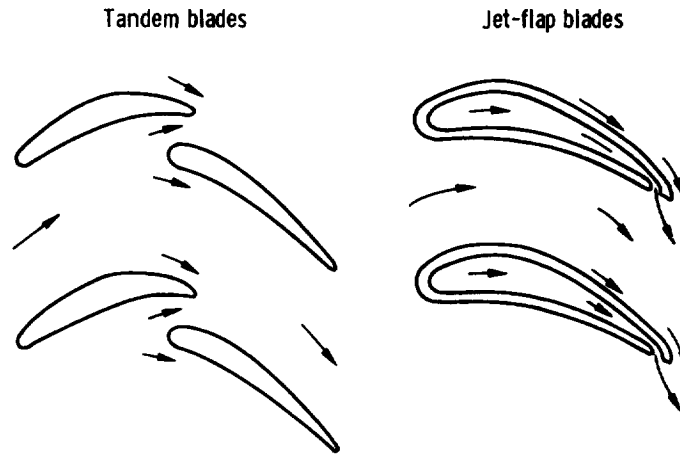


FIGURE 4-9.—Low-solidity blading concepts.

takes place on the rear foil with a clean boundary layer and with perhaps 20 to 30 percent of the mainstream air going through the slot.

The jet-flap blade operates with a secondary air stream jetting out the trailing edge perpendicular to the main stream. This jet moves the rear stagnation point around the trailing edge, thereby substantially increasing the lift. In addition, the jet delivers some force to the blade through its own momentum. Figure 4-10 shows experimental velocity distributions

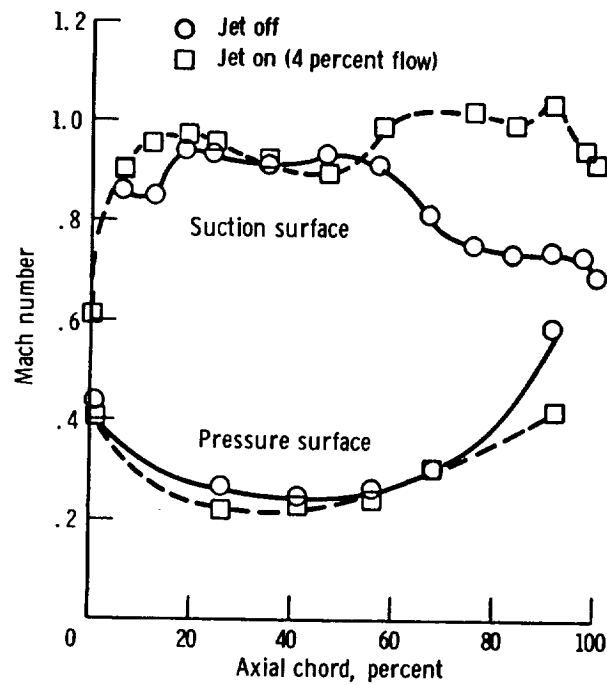


FIGURE 4-10.—Jet-flap experimental velocity distributions.

around one such blade with the jet off and on. With the jet on, there is no longer a requirement for the velocities on the suction and pressure surfaces to be equal at the blade trailing edge. The loading diagram now approaches a rectangular shape, with the load coefficient ψ more closely approaching unity. Also, the diffusion on the suction surface is substantially reduced, thus suppressing the tendency to separate.

Both the jet-flap-blade and the tandem-blade concepts offer the potential for solidity reductions. The jet flap, however, will probably be considered only for applications where a secondary air flow is required for other purposes, such as blade cooling.

BLADE-PROFILE DESIGN

After the blade chord length has been selected and the blade spacing determined from solidity considerations, the blade itself must be designed. This involves determination of the inlet and exit geometries and the connecting surface profiles. The inlet and exit parts of the blade must be designed to provide a smooth, efficient transition between the blade channel and the free stream. The surface profiles connecting the inlet and exit must provide the required flow turning with minimum loss.

Exit

Consideration of the blade exit section includes the trailing edge, the throat, and the suction surface between the throat and the trailing edge.

Trailing edge.—In the design of turbines, it is wise to utilize the smallest trailing edge consistent with mechanical considerations. As shown in reference 17, an increase in trailing-edge thickness causes an increase in the blade loss. This effect is discussed further as part of the turbine-loss discussion in chapter 7. In addition, trailing-edge thickness also has a significant effect on the flow blockage in the blade exit region.

Consideration of the blockage effect will be made with the use of figure 4-11, which shows example blade sections with the nomenclature used. A new exit-velocity diagram is constructed at station $2a$, which is located just within the blade trailing-edge region. The reduced area due to the trailing-edge blockage results in a higher velocity at station $2a$ than at station 2, which is located just beyond the blade trailing-edge region. The equations that have been used to obtain this “within-the-blade” diagram at $2a$ include conservation of tangential momentum:

$$V_{u,2a} = V_{u,2} \quad (4-26)$$

and continuity:

$$(\rho V_x)_{2a} \left(1 - \frac{t}{s \cos \alpha_{2a}} \right) = (\rho V_x)_2 \quad (4-27)$$

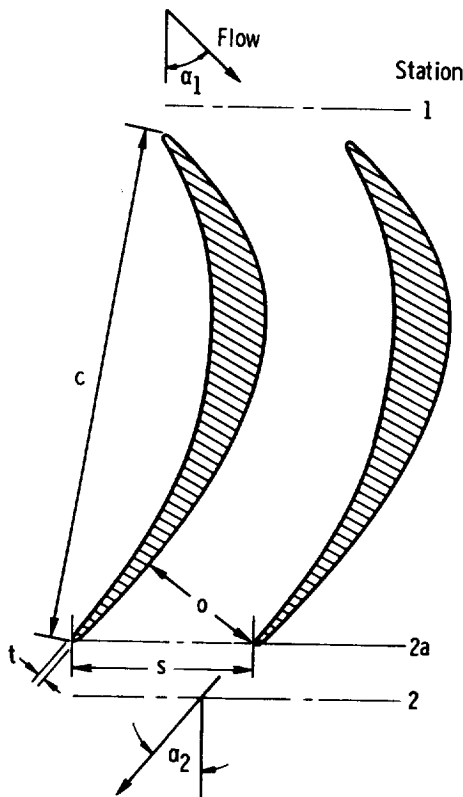


FIGURE 4-11.—Blade section and nomenclature.

where t is the trailing-edge thickness, in meters or feet. The flow angle α_{2a} is determined from equations (4-26) and (4-27) by assuming the flow between stations $2a$ and 2 to be either incompressible (since the changes are usually small) or isentropic. The blade must be designed to have an exit angle of α_{2a} in order to produce a velocity-diagram angle α_2 at station 2 outside the blade row.

The Mach number at station $2a$ can also be determined from the preceding equations and assumptions. Because the angle α_2 is often large (65° or greater) and the flow Mach number at the blade exit (station 2) is often specified to be in the high subsonic region, the trailing-edge blockage can cause station $2a$ to become choked. It is, therefore, important to determine whether choking inside the blade row will occur such that the design flow rate cannot be obtained.

Throat.—Since, in general, a turbine blade row operates as a nozzle, with the flow accelerating up to the throat, or minimum area, the determination of the throat opening o (see fig. 4-11) becomes a rather critical aspect of the design procedure. One technique used successfully to give this dimension makes use of the “inside-the-trailing-edge” velocity diagram. If one assumes no change in flow conditions and a straight suction surface

between the throat and station $2a$, then the throat dimension can be obtained from the velocity diagram at station $2a$ by using the following equation:

$$\frac{o}{s} = \left(1 - \frac{t}{s \cos \alpha_{2a}}\right) \cos \alpha_{2a} \quad (4-28)$$

where o is the throat opening, in meters or feet.

If it is assumed that the velocity and loss do not change between the throat and the "free-stream" station 2, then

$$\frac{o}{s} = \cos \alpha_2 \quad (4-29)$$

When this method is used, the effect of trailing-edge thickness changes the angle of the throat position but not its length. Both methods (eqs. (4-28) and (4-29)) give similar throat dimensions. Reference 8 compares measured exit-flow angles with those predicted by equation (4-29). This comparison indicates close agreement at exit angles greater than 60° and deviations of up to 5° for exit angles down to 35° . This deviation could be due to lower solidities as well as larger gradients that would occur across the throat.

The throat-opening dimension as determined from equation (4-28) or (4-29) applies to the case where the blade-row exit flow is subsonic. If the flow within the blade row expands to a supersonic velocity, then this computed throat dimension must be modified to account for expansion from the sonic condition at the throat to the supersonic condition at the exit. For exit Mach numbers greater than about 1.3, the choking section (throat) must be located back within the channel such that a convergent-divergent passage is obtained. For low supersonic Mach numbers (up to, perhaps, 1.3), it has been found that satisfactory performance can be achieved if the throat is still located at the exit of the channel, and the additional flow expansion occurs downstream from the throat. In this case, the required channel exit dimension o would be computed by the following equation:

$$o = o_{ss} \left(\frac{A_{cr}}{A_{ss}} \right) \quad (4-30)$$

where

- o_{ss} throat opening computed from equation (4-28) or (4-29) for supersonic velocity, m; ft
- A_{cr} flow area for sonic flow, m^2 ; ft^2
- A_{ss} flow area for supersonic flow, m^2 ; ft^2

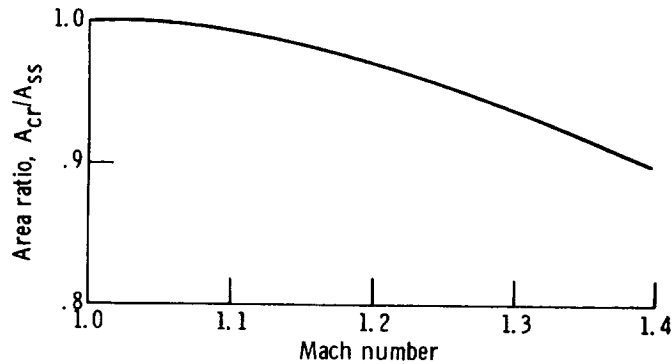


FIGURE 4-12.—Variation in flow area with supersonic flow Mach number.

This area correction, with assumed isentropic flow between throat and exit, is shown in figure 4-12.

Suction surface downstream from throat.—The selection of the type of surface between the throat and trailing edge on the suction surface must be made from such considerations as structural integrity in the trailing-edge region, Mach number level and associated losses, desired level of suction-surface diffusion (D_s), and blade surface area resulting from the design.

A “straight back” design is used when low values of D_s (approximately unity) are specified and long trailing edges are permissible. High subsonic or transonic blading, as would be indicated by the discussion in the next paragraph, uses this type of surface in order to prevent flow acceleration on the tail of the blade and keep the associated losses low. Principal problems with a straight surface are that the low D_s values preclude low-solidity designs and the long trailing edge can become structurally flimsy.

Most conventional gas-turbine blading utilizes some amount of curvature between the throat and trailing-edge region. This permits some diffusion and additional loading on the tail of the blade, and it adds considerably to the structural integrity of the blade by introducing a wedge angle at the exit. If conventionally loaded blading is used, the effect of this curved surface on loss is not great. As indicated by figure 4-13 (which is from ref. 8), if the exit-flow Mach number is less than 0.8, the curvature effect is small. At higher exit Mach numbers (greater than 0.8), the effect on loss can become severe. Therefore, design curvatures should be lower in the higher Mach number regions. The type of curvature selected for the suction surface between the throat and trailing edge has an effect on the suction-surface velocity distribution. In general, the velocity distribution is improved if the curvature decreases from throat to trailing edge instead of remaining constant.

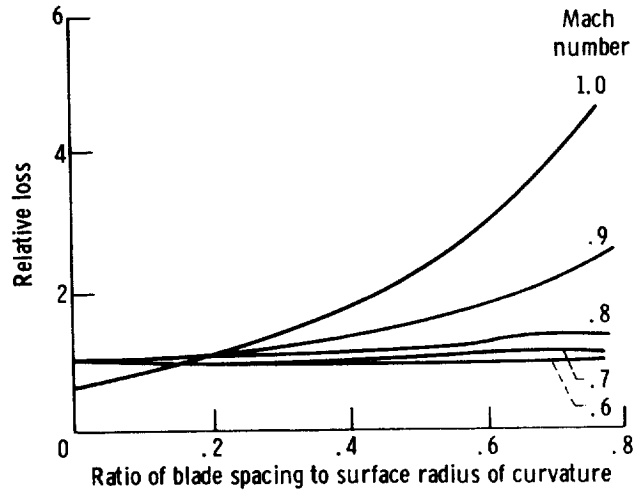


FIGURE 4-13.—Variation of profile loss with Mach number and surface curvature between throat and exit (from ref. 8).

Inlet

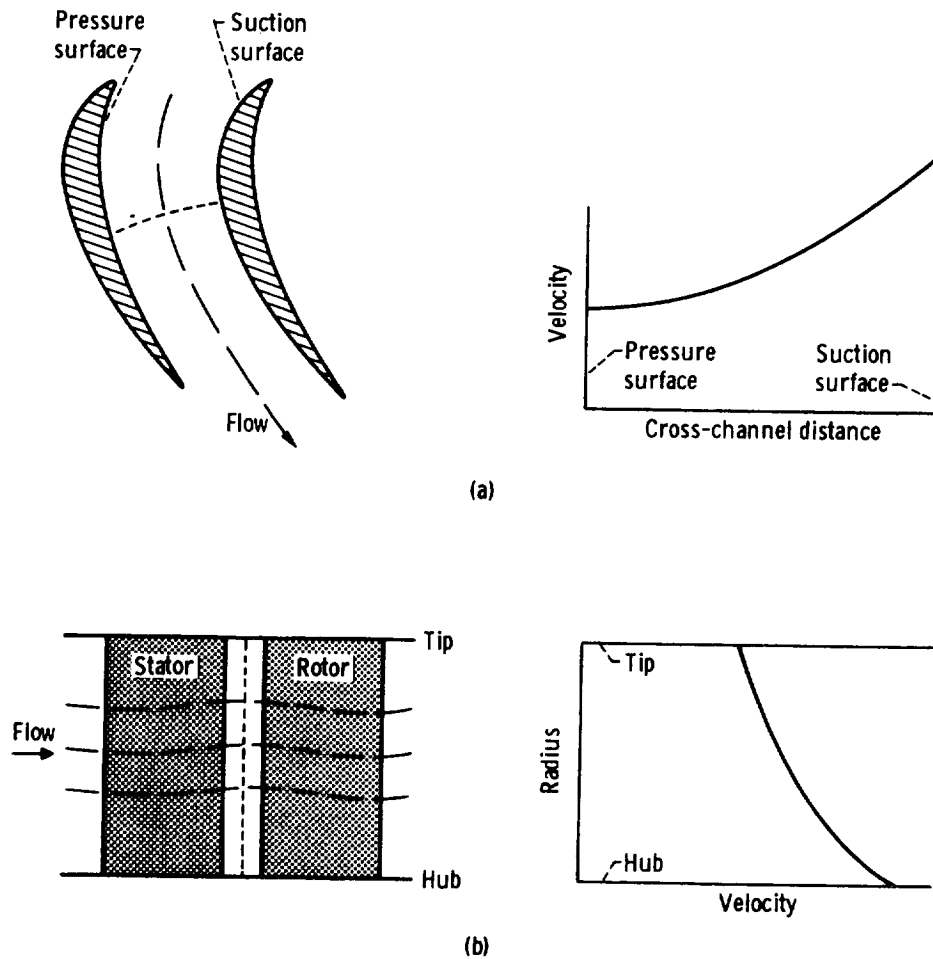
The leading-edge geometry of a turbine blade row is usually less critical than the exit-region geometry. At the blade inlet, a relatively large leading-edge radius can usually be used, because the Mach number is generally low at the inlet and then increases through the blade row. The leading edge becomes a serious concern for low-reaction blading and high Mach number blading. In the case of low-reaction blading, excessively high velocities in the inlet region can lead to high values of suction-surface diffusion and a tendency toward increased losses. With high inlet Mach numbers, care must be taken that the area contraction is not so severe as to choke the blade at the inlet. Equations (4-26) and (4-27), which were used for the blade exit, can also be used to determine a blade-inlet opening and "within-the-blade" flow angle and Mach number to check for blade-inlet choking.

Although circular leading edges are usually specified, this is arbitrary and could limit the freedom of velocity-distribution selection in the leading-edge region. The large curvatures associated with circular leading edges can result in undesirable velocity peaks on both the suction- and pressure-surface portions of the leading edge. Other geometries, such as ellipses, which permit variations in curvature around the leading edge, can be used to minimize or eliminate the velocity peaks.

Blade-Surface Profile

Once the leading- and trailing-edge geometries have been selected, the task remaining is to join them with a profile that yields the required flow

turning and a satisfactory velocity distribution around the blade. The design procedure must describe the flow conditions through the blade rows to an accuracy sufficient to impose design controls (e.g., diffusion limits). Two of the major flow considerations are illustrated in figure 4-14. Velocity gradients occur across the channel from the suction to the pressure surface as a result of the static-pressure difference required to turn the flow. Radial variations in streamline position and, therefore, velocity occur as a result of radial-equilibrium considerations. Since both of these factors influence the blade-surface velocity distribution, the design procedures used should be at least of a quasi-three-dimensional nature. The channel flow analysis theory that serves as the basis for these design procedures and the computer programs available to perform the computations are discussed in the next chapter.



(a) Cross-channel variation.

(b) Radial variation.

FIGURE 4-14.—Turbine blade-row velocity variations.

REFERENCES

1. ZWEIFEL, O.: The Spacing of Turbo-Machine Blading, Especially with Large Angular Deflection. *Brown Boveri Rev.*, vol. 32, no. 12, Dec. 1945, pp. 436-444.
2. LIEBLEIN, SEYMOUR; SCHWENK, FRANCIS C.; AND BRODERICK, ROBERT L.: Diffusion Factor for Estimating Losses and Limiting Blade Loadings in Axial-Flow-Compressor Blade Elements. NACA RM E53D01, 1953.
3. STEWART, WARNER L.; GLASSMAN, ARTHUR J.; AND VANCO, MICHAEL R.: Examination of Axial-Flow Turbine Blade-Loading Characteristics Using Diffusion Parameters. Paper 67-WA/GT-8, ASME, Nov. 1967.
4. STEWART, WARNER L.; WHITNEY, WARREN J.; AND MISER, JAMES W.: Use of Effective Momentum Thickness in Describing Turbine Rotor-Blade Losses. NACA RM E56B29, 1956.
5. WONG, ROBERT Y.; AND STEWART, WARNER L.: Correlation of Turbine-Blade-Element Losses Based on Wake Momentum Thickness with Diffusion Parameter for a Series of Subsonic Turbine Blades in Two-Dimensional Cascade and for Four Transonic Turbine Rotors. NACA RM E55B08, 1955.
6. MISER, JAMES W.; STEWART, WARNER L.; AND WHITNEY, WARREN J.: Analysis of Turbomachine Viscous Losses Affected by Changes in Blade Geometry. NACA RM E56F21, 1956.
7. HELLER, JACK A.; WHITNEY, ROSE L.; AND CAVICCHI, RICHARD H.: Experimental Investigation of a Conservatively Designed Turbine at Four Rotor-Blade Solidities. NACA RM E52C17, 1952.
8. AINLEY, D. G.; AND MATHIESON, G. C. R.: An Examination of the Flow and Pressure Losses in Blade Rows of Axial-Flow Turbines. Rep. R&M 2891, Aeronautical Research Council, Gt. Britain, 1955.
9. BETTNER, JAMES L.; AND NOSEK, STANLEY M.: Summary of Tests on Two Highly Loaded Turbine Blade Concepts in Three-Dimensional Cascade Sector. Paper 69-WA/GT-5, ASME, Nov. 1969.
10. LUEDERS, H. G.; AND ROELKE, R. J.: Some Experimental Results of Two Concepts Designed to Increase Turbine Blade Loading. *J. Eng. Power*, vol. 92, no. 2, Apr. 1970, pp. 198-206.
11. STABE, ROY G.: Design and Two-Dimensional Cascade Test of Turbine Stator Blade with Ratio of Axial Chord to Spacing of 0.5. NASA TM X-1991, 1970.
12. NOSEK, STANLEY M.; AND KLINE, JOHN F.: Two-Dimensional Cascade Investigation of a Turbine Tandem Blade Design. NASA TM X-1836, 1969.
13. NOSEK, STANLEY M.; AND KLINE, JOHN F.: Two-Dimensional Cascade Test of a Jet-Flap Turbine Rotor Blade. NASA TM X-2183, 1971.
14. STABE, ROY G.: Design and Two-Dimensional Cascade Test of a Jet-Flap Turbine Stator Blade with Ratio of Axial Chord to Spacing of 0.5. NASA TM X-2426, 1971.
15. BETTNER, JAMES L.: Design and Experimental Results of a Highly Loaded, Low Solidity Tandem Rotor. NASA CR-1803, 1971.
16. BETTNER, JAMES L.: Design and Experimental Results of a Highly Loaded, Low Solidity, Jet Flap Rotor. NASA CR-1968, 1972.
17. PRUST, HERMAN W., JR.; AND HELON, RONALD M.: Effect of Trailing-Edge Geometry and Thickness on the Performance of Certain Turbine Stator Blading. NASA TN D-6637, 1972.

SYMBOLS

A	flow area, m^2 ; ft^2
c	chord, m ; ft
D	diffusion parameter
F	force, N ; lb
g	conversion constant, 1; 32.17 (lbm) (ft)/(lbf) (sec ²)
K	ratio of inlet to exit tangential components of velocity ($V_{u,1}/V_{u,2}$)
o	throat opening, m ; ft
p	absolute pressure, N/m^2 ; lb/ft^2
R	reaction
s	blade spacing, m ; ft
t	trailing-edge thickness, m ; ft
V	absolute velocity, m/sec ; ft/sec
x	axial distance, m ; ft
α	fluid absolute angle from axial direction, deg
α_s	blade stagger angle from axial direction, deg
γ	ratio of specific heat at constant pressure to specific heat at constant volume
ρ	density, kg/m^3 ; lb/ft^3
σ	solidity
ψ	loading coefficient defined by equation (4-6)
ψ_z	loading coefficient defined by equation (4-5)

Subscripts:

cr	critical
inc	incompressible
max	maximum value
min	minimum value
opt	optimum
p	pressure surface
s	suction surface
ss	supersonic
u	tangential component
x	axial component
1	blade row inlet
2	blade row exit
2a	within trailing edge of blade row

Superscript:

'	absolute total state
---	----------------------

CHAPTER 5

Channel Flow Analysis

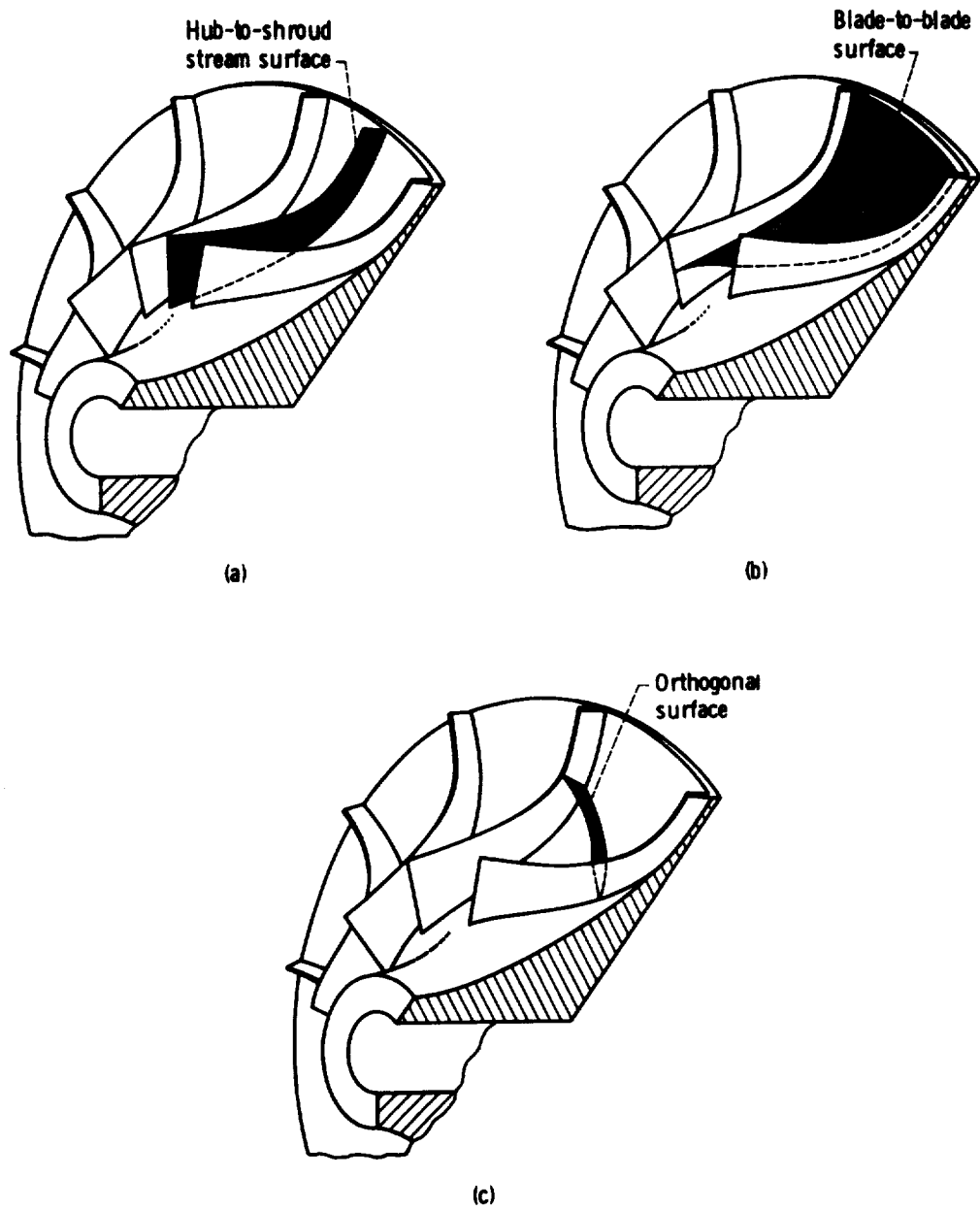
By Theodore Katsanis

The design of a proper blade profile, as indicated in the last section of chapter 4, requires calculation of the blade-row flow field in order to determine the velocities on the blade surfaces. This chapter presents the analysis theory for several methods used for this calculation and also discusses associated computer programs that were developed at NASA Lewis Research Center.

The actual velocity distribution throughout a blade-row flow field cannot be calculated at this time because of the extreme complexity of nonsteady, viscous, three-dimensional flow through geometrically complex passages. To calculate a theoretical velocity distribution, therefore, certain simplifying assumptions must be made. The three-dimensional flow is simplified to flow on or through various two-dimensional surfaces. Such surfaces are illustrated in figure 5-1 for the case of a radial-inflow turbine. Similar surfaces are used for an axial-flow turbine. A flow solution on the mean hub-to-shroud stream surface (commonly called the meridional surface), shown in figure 5-1(a), does not yield blade-surface velocities directly, but provides information required for the blade-to-blade surface (fig. 5-1(b)) and orthogonal surface (fig. 5-1(c)) solutions, which yield the desired blade-surface velocities.

There are two parts to a method of analysis to obtain a velocity distribution over one of these surfaces. The first part is the mathematical formulation of the problem, and the second part is the numerical solution of the mathematical problem. For the mathematical formulation of the problem, we will discuss stream- and potential-function methods and velocity-gradient (stream-filament) methods. The stream- and potential-

TURBINE DESIGN AND APPLICATION



(a) Hub-to-shroud stream surface.

(b) Blade-to-blade surface.

(c) Orthogonal surface across flow passage.

FIGURE 5-1.—Surfaces used for velocity-distribution calculations.

function methods will be described relative to the blade-to-blade surface solution. A similar type of analysis can be made for the meridional surface. The velocity-gradient equation to be presented is general and can be used for solutions on any of the surfaces.

The following assumptions are made in deriving the various methods of analysis discussed herein:

(1) The flow is steady relative to the blade. This means that the surface velocity at any given point on the blade does not vary with time. Thus, if the blade is rotating, the flow would not be steady relative to a fixed coordinate system.

(2) The fluid obeys the ideal-gas law

$$p = \rho RT \quad (5-1)$$

where

p	absolute pressure, N/m ² ; lb/ft ²
ρ	density, kg/m ³ ; lb/ft ³
R	gas constant, J/(kg) (K); (ft) (lbf)/(lbm) (°R)
T	absolute temperature, K; °R

or is incompressible ($\rho = \text{constant}$).

(3) The fluid is nonviscous. A nonviscous fluid has no boundary layer. The blade-surface velocity is calculated, therefore, as if the free stream extends to the blade surface.

(4) The fluid has a constant heat capacity.

(5) The flow is isentropic.

(6) The total temperature and total pressure are uniform across the inlet.

(7) For the stream- and potential-function analyses, the additional assumption is made that the flow is absolutely irrotational. Therefore,

$$\text{curl } \mathbf{V} = \nabla \times \mathbf{V} = \mathbf{0} \quad (5-2)$$

where \mathbf{V} is the absolute velocity vector. Intuitively, this means that particles do not change their *absolute* orientation with time, although their shape may change. For example, figure 5-2 shows a hypothetical particle at times t and $t + \Delta t$. In the absolute frame of reference, the particle changes its location and shape at a later instant of time, but the net rotation is zero. Of course, in a frame of reference relative to the blade, the particle has rotated, because the frame of reference has rotated.

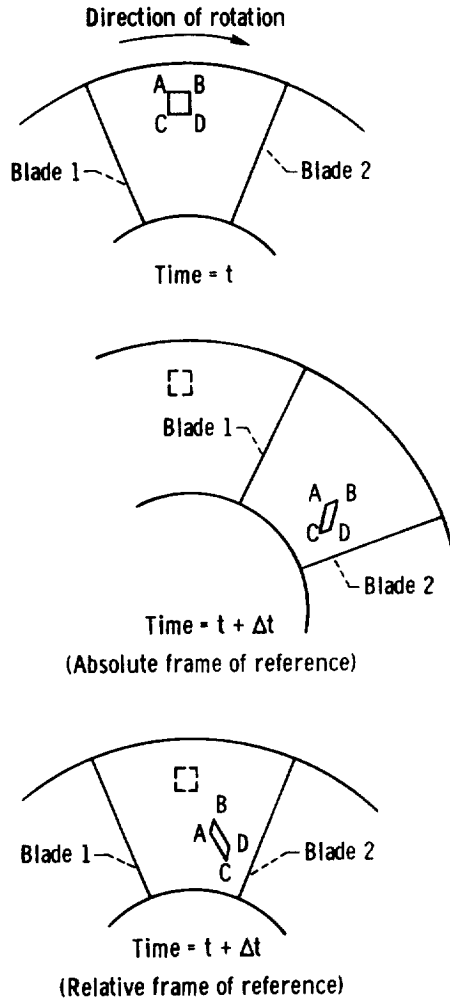


FIGURE 5-2.—Absolutely irrotational flow.

Some numerical techniques for solving the mathematical equations will also be discussed. However, it must be emphasized that there are many techniques for solving these equations, and we will discuss only a few. An excellent theoretical discussion of flow in two-dimensional cascades is given in Chapter IV of reference 1.

STREAM- AND POTENTIAL-FUNCTION ANALYSES

Stream-Function Method

The stream function can be defined several ways, but perhaps the simplest is in terms of streamlines. Suppose we consider two blades of a cascade as shown in figure 5-3. It is assumed that there is two-dimensional

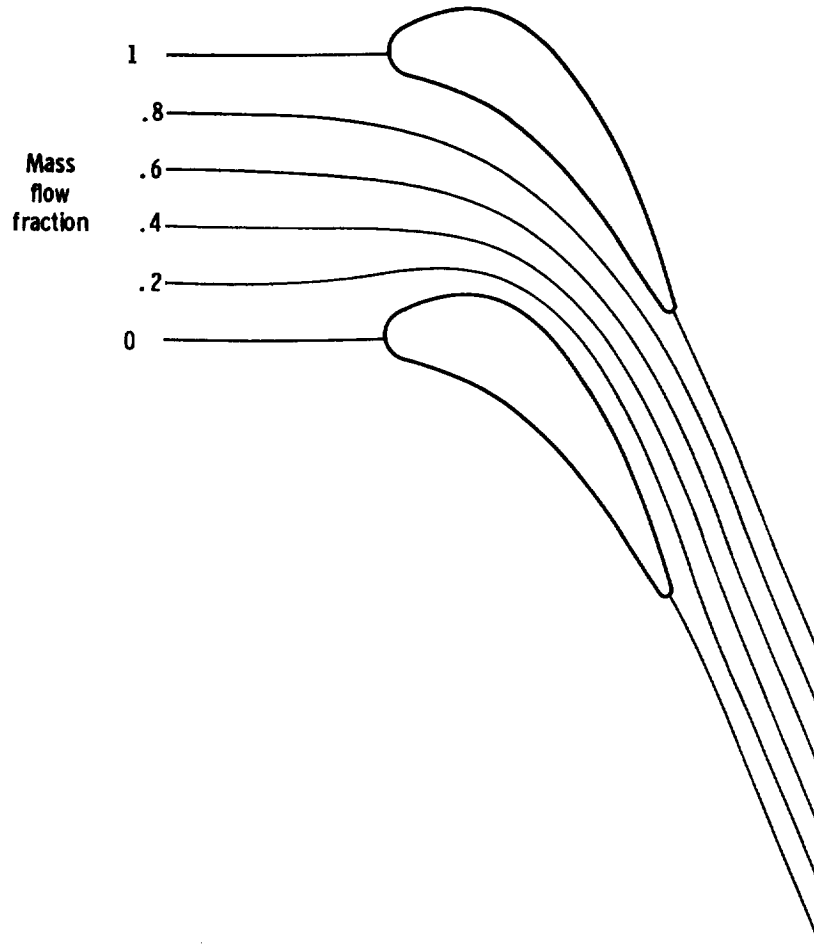


FIGURE 5-3.—Streamlines for a stator cascade.

axial flow here, so that the radius r from the centerline is constant and there is no variation of the flow in the radial direction. There may be rotation about the centerline.

Shown in figure 5-3 are a number of streamlines. The mass flow between the blades is w . The number by each streamline indicates the fraction of w passing between the upper surface of the lower blade and the given streamline. Thus, the upper surface (which is a streamline) has the value 0, and the lower surface of the upper blade has the value of 1, while the remaining streamlines have values between 0 and 1. Note that a value can be associated with any point in the passage. This value is called the stream-function value and can be used to define the stream function.

It will be recalled that mass flow can be calculated for a one-dimensional (or uniform) flow by

$$w = \rho VA \quad (5-3)$$

where

- w rate of mass flow, kg/sec; lb/sec
- V fluid absolute velocity, m/sec; ft/sec
- A flow area normal to the direction of the velocity V , m²; ft²

This can be extended to a varying flow by using an integral expression:

$$w = \int_A \rho V dA \quad (5-4)$$

Since this stream-function analysis applies to both stationary and rotating cascades (blade rows), the fluid velocity will be expressed in terms of relative velocity W , which for a stationary blade row reduces to absolute velocity V . We will assume that our cascade has a uniform height b . Then, the mass flow $w_{1,2}$ between any two points Q_1 and Q_2 in the passage (see fig. 5-4) can be calculated by

$$w_{1,2} = \int_{Q_1}^{Q_2} \rho W_n b dq \quad (5-5)$$

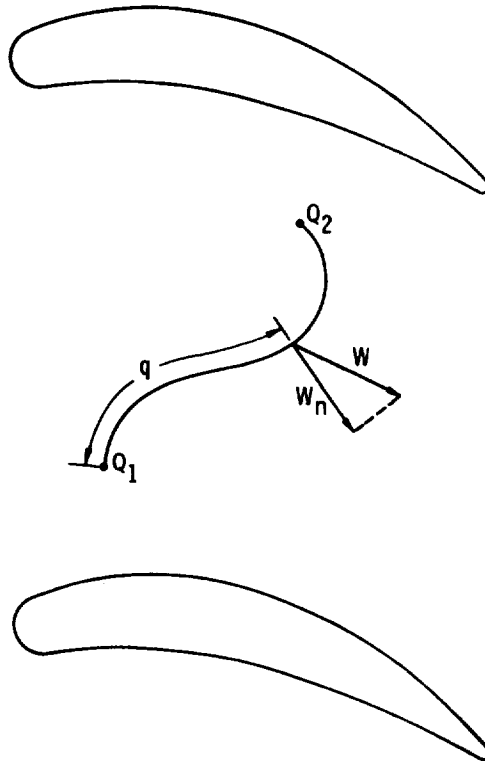


FIGURE 5-4.—Arbitrary curve joining two points in flow passage.

where W_n is the relative velocity component in the direction of the right-hand normal of the line going from Q_1 to Q_2 . This sign convention means that $w_{1,2}$ will be negative if Q_2 is below a streamline passing through Q_1 . The integral is a line integral between the points Q_1 and Q_2 and is independent of path for steady flow relative to the cascade.

With the use of equation (5-5), an analytical expression can be written for the stream function u at a point (x, y) :

$$u(x, y) = \frac{\int_{Q_0}^{(x,y)} \rho W_n b dq}{w} \quad (5-6)$$

where Q_0 is any point on the upper surface of the lower blade, and the integral is taken along any curve between Q_0 and (x, y) . This is indicated in figure 5-5.

Since the integral in equation (5-6) is independent of path, it is relatively easy to calculate the partial derivatives of u . For example, we will calculate $\partial u / \partial x$ at the point (x, y) . Let $x_0 < x$ such that the point (x_0, y) is still in the flow passage, as shown in figure 5-6. Then

$$u(x, y) = \frac{\int_{C_1} \rho W_n b dq + \int_{C_2} \rho W_n b dq}{w} \quad (5-7)$$

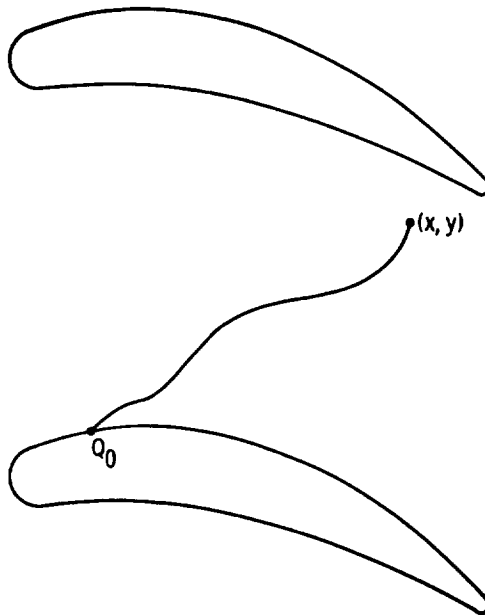


FIGURE 5-5.—Curve joining (x, y) with a point on the upper surface of the lower blade.

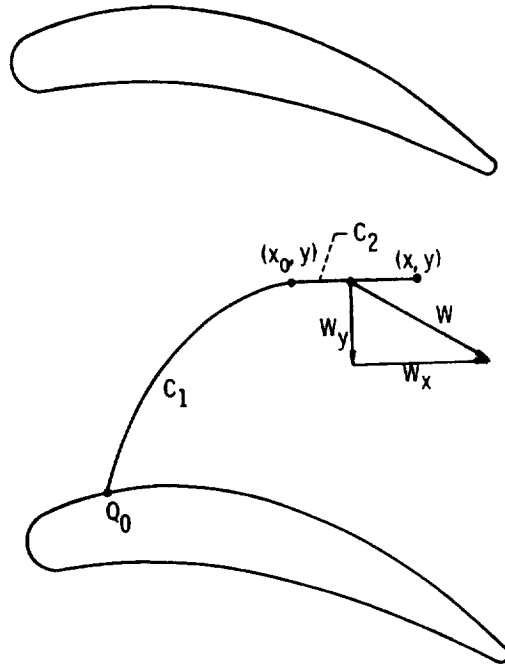


FIGURE 5-6.—Curve joining horizontal line through (x, y) with a point on the upper surface of the lower blade.

where C_1 is an arbitrary curve between Q_0 and (x_0, y) , and C_2 is a horizontal line between (x_0, y) and (x, y) . The integral along C_1 does not depend on x . Along C_2 , we have $W_n = -W_y$ and $dq = dx$. Hence,

$$\frac{\partial u}{\partial x}(x, y) = -\frac{\partial}{\partial x} \int_{x_0}^x \frac{\rho W_y b}{w} dx \quad (5-8)$$

or

$$\frac{\partial u}{\partial x} = -\frac{\rho W_y b}{w} \quad (5-9)$$

In a similar manner, we can calculate

$$\frac{\partial u}{\partial y} = \frac{\rho W_x b}{w} \quad (5-10)$$

Now we will make use of the fact that the flow is absolutely irrotational. From the definition of the curl operator and the above assumption,

$$\text{curl } \mathbf{V} = \left(\frac{\partial V_z}{\partial y} - \frac{\partial V_y}{\partial z} \right) \mathbf{i} + \left(\frac{\partial V_x}{\partial z} - \frac{\partial V_z}{\partial x} \right) \mathbf{j} + \left(\frac{\partial V_y}{\partial x} - \frac{\partial V_x}{\partial y} \right) \mathbf{k} = \mathbf{0} \quad (5-11)$$

where \mathbf{i} , \mathbf{j} , and \mathbf{k} are the unit vectors in the x , y , and z directions, respec-

tively, and V_x , V_y , and V_z are the absolute velocity components (in m/sec or ft/sec) in the x , y , and z directions, respectively. Since we are considering two-dimensional flow only,

$$V_z = 0 \quad (5-12)$$

and

$$\frac{\partial V_x}{\partial z} = \frac{\partial V_y}{\partial z} = 0 \quad (5-13)$$

Hence, equation (5-11) requires only that

$$\frac{\partial V_y}{\partial x} = \frac{\partial V_x}{\partial y} \quad (5-14)$$

Since

$$V_x = W_x \quad (5-15)$$

and

$$V_y = W_y + \omega r \quad (5-16)$$

where ω is the angular speed (in rad/sec) and the radius r is constant, equation (5-14) can be expressed in terms of relative velocities as

$$\frac{\partial W_y}{\partial x} = \frac{\partial W_x}{\partial y} \quad (5-17)$$

Actually, the flow is irrotational with respect to the moving coordinates in this particular case. Now, from equations (5-10) and (5-9),

$$W_x = \frac{w}{\rho b} \frac{\partial u}{\partial y} \quad (5-18)$$

$$W_y = -\frac{w}{\rho b} \frac{\partial u}{\partial x} \quad (5-19)$$

Substituting equations (5-18) and (5-19) into equation (5-17) yields

$$\frac{\partial}{\partial x} \left(\frac{1}{\rho} \frac{\partial u}{\partial x} \right) + \frac{\partial}{\partial y} \left(\frac{1}{\rho} \frac{\partial u}{\partial y} \right) = 0 \quad (5-20)$$

since w and b are both constant.

For incompressible flow, ρ is constant, and

$$\nabla^2 u = \frac{\partial^2 u}{\partial x^2} + \frac{\partial^2 u}{\partial y^2} = 0 \quad (5-21)$$

which is Laplace's equation. Any function satisfying Laplace's equation is called a harmonic function. There is a great deal of theory concerning

harmonic functions that is related to the theory of analytic functions of complex variables.

The important thing to know here is that there are a tremendous number of functions that satisfy equation (5-21), and we must find a solution that satisfies certain boundary conditions. The solution to either Laplace's equation (5-21) or equation (5-20) will be determined by specifying two things: (1) a finite region, and (2) a boundary condition along the entire boundary of the region.

The first thing that must be specified is the solution region. A typical two-dimensional cascade is shown in figure 5-7. Since the flow is the same in every passage, we can consider a finite solution region as shown in figure 5-8. It is assumed that AH is sufficiently far upstream so that the flow is uniform along this part of the boundary and that the flow angle β_{in} is known. Similarly, it is assumed that the flow is uniform along DE, and that the flow angle β_{out} is known. From the way the stream function was defined, we can specify boundary conditions on the entire boundary ABCDEFGHA. Along BC, $u=0$; and along FG, $u=1$. Along AB, HG, CD, and FE, a periodic condition exists; that is, the value of u along HG and FE is exactly 1 greater than it is along AB and CD. Along AH and DE, $\partial u/\partial \eta$ is known, where η is the distance in the direction of the outer normal.

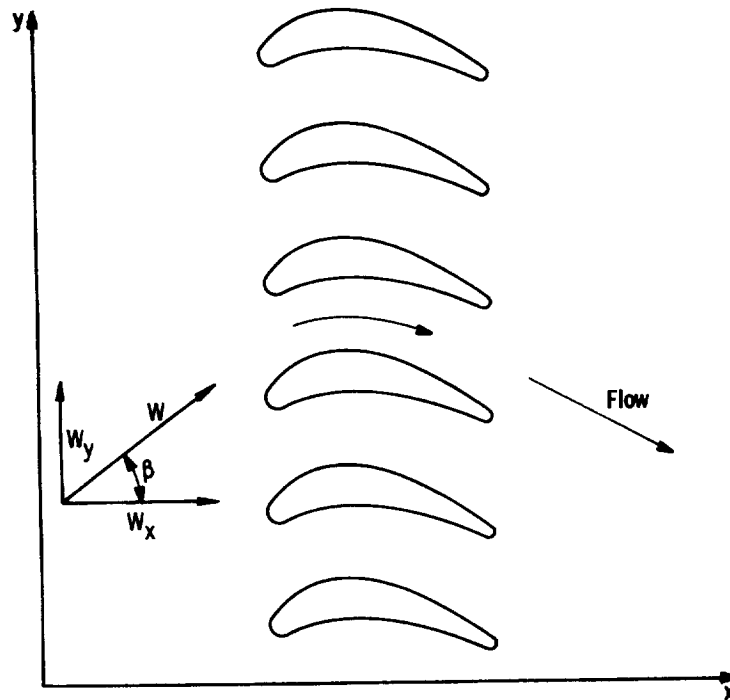


FIGURE 5-7.—Two-dimensional infinite cascade.

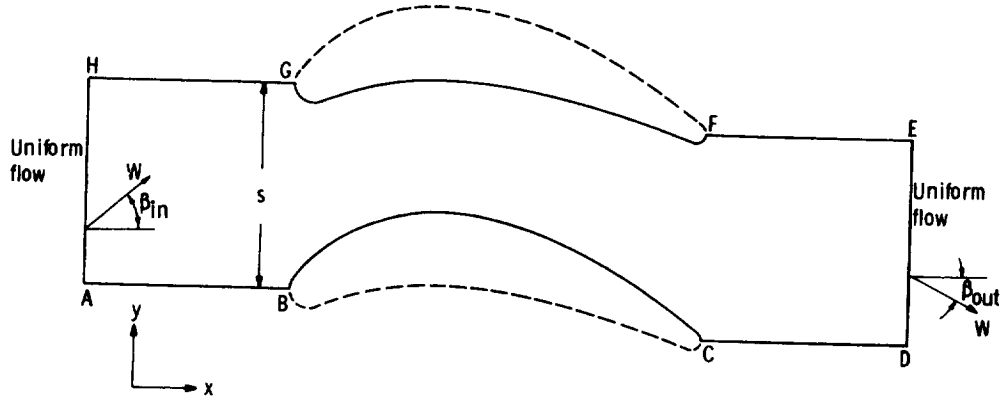


FIGURE 5-8.—Finite solution region.

Consider the differential of u in the direction of the velocity W :

$$du = \frac{\partial u}{\partial x} dx + \frac{\partial u}{\partial y} dy = 0 \quad (5-22)$$

The differential is 0 because the stream function is constant along a streamline, and the velocity vector must be tangent to a streamline. Along AH,

$$\frac{\partial u}{\partial \eta} = -\frac{\partial u}{\partial x} \quad (5-23)$$

and substitution from equation (5-22) yields

$$\frac{\partial u}{\partial \eta} = \frac{\partial u}{\partial y} \frac{dy}{dx} \quad (5-24)$$

However,

$$\frac{dy}{dx} = \tan \beta \quad (5-25)$$

Further, $\partial u / \partial y$ is constant along AH, since it is assumed that the flow is uniform there. Therefore,

$$\frac{\partial u}{\partial y} = \frac{[u(H) - u(A)]}{s} = \frac{1}{s} \quad (5-26)$$

where s is the blade spacing in the y direction. Substituting equations (5-25) and (5-26) in equation (5-24) gives along AH

$$\left(\frac{\partial u}{\partial \eta} \right)_{in} = \frac{\tan \beta_{in}}{s} \quad (5-27)$$

Similarly, along DE, one can calculate

$$\left(\frac{\partial u}{\partial \eta}\right)_{out} = -\frac{\tan \beta_{out}}{s} \quad (5-28)$$

We now have a boundary condition along the entire boundary of the region shown in figure 5-8. These boundary conditions will always determine a unique solution to Laplace's equation (5-21). For compressible flow (eq. (5-20)), a unique solution is always determined if the flow is strictly subsonic throughout the region.

There are numerous techniques for solving equation (5-20) or (5-21). After the stream function is obtained, blade-surface velocities and velocities throughout the passage can be obtained by differentiation of the stream function. This is what is known as the direct problem. A method of solving this problem will be discussed later. The indirect, or inverse, problem is to specify a desired velocity distribution on the blade surface and from this determine a blade shape that will give this velocity distribution. This will not be discussed here.

Potential-Function Method

For two-dimensional irrotational flow, a potential function can be defined. If lines of equal potential are drawn, they will be orthogonal to streamlines. The potential function will not be defined in the same detail as the stream function, but the main properties and relations will be given. If the potential function Φ exists (i.e., the flow is irrotational), then it can be defined so that

$$\frac{\partial \Phi}{\partial x} = V_x \quad (5-29)$$

and

$$\frac{\partial \Phi}{\partial y} = V_y \quad (5-30)$$

We will refer to absolute velocities here, since we must have flow irrotational relative to the coordinate system used. This, coupled with the assumption of absolute irrotational flow, implies that the coordinate system does not rotate. This does not exclude use of the potential function for pure axial flow, since the rotation has no effect if there is no change in radius; that is, the flow is actually irrotational with respect to the blades, as we saw in the discussion of the stream function.

From the continuity relationship for steady flow,

$$\frac{\partial(\rho V_x)}{\partial x} + \frac{\partial(\rho V_y)}{\partial y} = 0 \quad (5-31)$$

Substituting equations (5-29) and (5-30) in equation (5-31) yields

$$\frac{\partial}{\partial x} \left(\rho \frac{\partial \Phi}{\partial x} \right) + \frac{\partial}{\partial y} \left(\rho \frac{\partial \Phi}{\partial y} \right) = 0 \quad (5-32)$$

If the flow is incompressible, ρ is constant, and

$$\nabla^2 \Phi = \frac{\partial^2 \Phi}{\partial x^2} + \frac{\partial^2 \Phi}{\partial y^2} = 0 \quad (5-33)$$

So, the potential function satisfies Laplace's equation. Thus, for incompressible, irrotational flow, both the stream function and the potential function satisfy the same differential equation (Laplace's equation). The difference lies in the boundary conditions.

We can consider the same solution region shown in figure 5-8. We can specify boundary conditions over the entire boundary as follows: Along BC and FG,

$$\frac{\partial \Phi}{\partial \eta} = V_n = 0 \quad (5-34)$$

where V_n is the velocity normal to the blade surface. Along AH,

$$\left(\frac{\partial \Phi}{\partial \eta} \right)_{in} = - (V_x)_{in} \quad (5-35)$$

and along DE,

$$\left(\frac{\partial \Phi}{\partial \eta} \right)_{out} = (V_x)_{out} \quad (5-36)$$

The inlet and outlet axial velocities are given by the equations

$$(V_x)_{in} = \frac{w}{\rho_{in} b s} \quad (5-37)$$

and

$$(V_x)_{out} = \frac{w}{\rho_{out} b s} \quad (5-38)$$

Along AB, GH, CD, and EF, a periodic condition exists. Since the flow is uniform along AH,

$$\left(\frac{\partial \Phi}{\partial y} \right)_{in} = \frac{[\Phi(H) - \Phi(A)]}{s} = (V_v)_{in} \quad (5-39)$$

Substituting

$$V_v = V_x \tan \beta \quad (5-40)$$

into equation (5-39) yields

$$\Phi(H) = \Phi(A) + s(V_x)_{in} \tan \beta_{in} \quad (5-41)$$

Because of the periodicity, Φ is exactly $s(V_x)_{in} \tan \beta_{in}$ greater along HG than along AB. Similarly, at the outlet,

$$\Phi(E) = \Phi(D) + s(V_x)_{out} \tan \beta_{out} \quad (5-42)$$

Equation (5-42) gives the difference in Φ along the lines FE and CD.

This completes the boundary conditions for equation (5-32) or (5-33). The boundary conditions, however, do not determine a unique solution, but only a solution within an arbitrary additive constant. If the value of Φ is specified at one point, these boundary conditions will determine a unique solution to equation (5-33) for incompressible flow, or to equation (5-32), for strictly subsonic compressible flow throughout the region.

As for the stream function, there are numerous methods for solving equation (5-32) or (5-33) subject to the preceding or equivalent boundary conditions. A method for solving the inverse problem of specifying the velocity distribution to determine the blade shape is described in references 2 and 3.

Choice of Stream- or Potential-Function Method

If the flow is steady, irrotational, and incompressible, there is little to choose between the stream function and the potential function. In this case, the choice is made on the basis of ease of solution for the boundary conditions (the differential equation is the same: Laplace's equation). However, if any of the three assumptions (steady, irrotational, or incompressible flow) is not applicable, then we may be restricted as to the choice of stream function or potential function.

The existence of the stream function is proven from the continuity equation. For the stream function to be defined, the mass flow crossing a line between two points must be independent of path. This requires that the flow be either incompressible or steady. Some additional assumption is necessary for the flow to be unique. We used the assumption that the flow was absolutely irrotational, which turned out to be irrotational relative to the blade for the axial-flow case considered. However, other assumptions could be made for other problems. Another restriction on the stream function is that it can be defined only for two-dimensional flow. This can easily be seen since the stream function is defined as a percentage of mass flow between two points, and this is meaningless in three dimensions.

The existence of the potential function can be shown if the flow is irrotational relative to the given coordinate system. This is necessary

because we must have equality of mixed second partial derivatives; that is, if

$$\frac{\partial^2 \Phi}{\partial x \partial y} = \frac{\partial^2 \Phi}{\partial y \partial x} \quad (5-43)$$

then

$$\frac{\partial}{\partial x} V_y = \frac{\partial}{\partial y} V_x \quad (5-44)$$

and the flow must be irrotational. A similar situation exists in three-dimensional flow; that is, the potential function exists only if the flow is irrotational with respect to the coordinate system being used. Finally, an assumption must be made to assure a unique solution. This can be done by using the continuity equation.

Finite-Difference Solution for Stream-Function Method

As stated before, there are many ways of solving various problems posed by stream-function or potential-function theory. We will consider in further detail the finite-difference solution of the direct problem for the stream function for the simplest case of steady, incompressible, irrotational flow. In this case, we must solve Laplace's equation subject to the boundary conditions discussed in the section on the stream function. The method of solution for the potential function is quite similar, but with a lower rate of convergence for the finite difference solution.

The first step is to establish a rectangular grid of mesh points in the region shown in figure 5-8. A typical grid is shown in figure 5-9. Then a finite-difference approximation to Laplace's equation (eq. (5-21)) can be written at each mesh point where the stream function is unknown. A typical mesh point with four neighboring mesh points is shown in figure 5-10. The point in consideration is labeled 0, and the four neighboring points are labeled 1 to 4, as shown. The distance between points 1 and 0 is denoted h_1 , and similarly, the other distances are h_2 , h_3 , and h_4 as indicated in figure 5-10. The value of u at points 0 to 4 are labeled u_0 to u_4 , respectively. With the use of a Taylor series expansion for u in the x - and y -directions, equation (5-21) can be approximated by using only values of u at mesh points. (Further explanation of this is given in ch. 6 of ref. 4.) When this is done, the following expression is obtained:

$$\left[\frac{2u_1}{h_1(h_1+h_2)} + \frac{2u_2}{h_2(h_1+h_2)} - \frac{2u_0}{h_1 h_2} \right] + \left[\frac{2u_3}{h_3(h_3+h_4)} + \frac{2u_4}{h_4(h_3+h_4)} - \frac{2u_0}{h_3 h_4} \right] = 0 \quad (5-45)$$

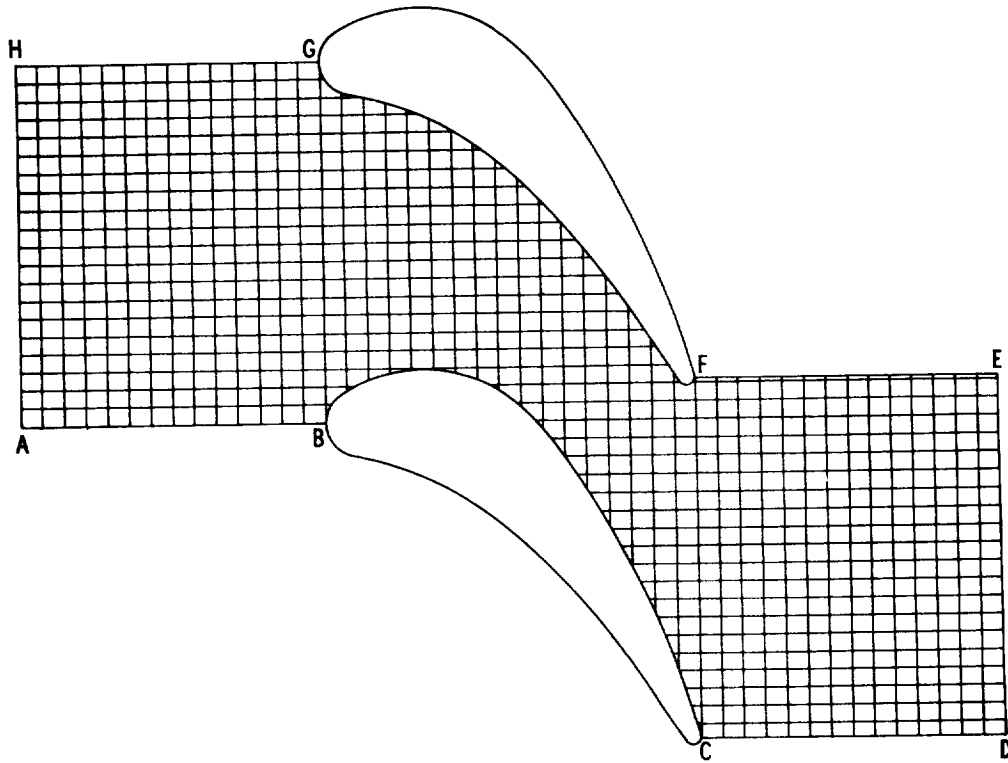


FIGURE 5-9.—Mesh used for a finite-difference solution.

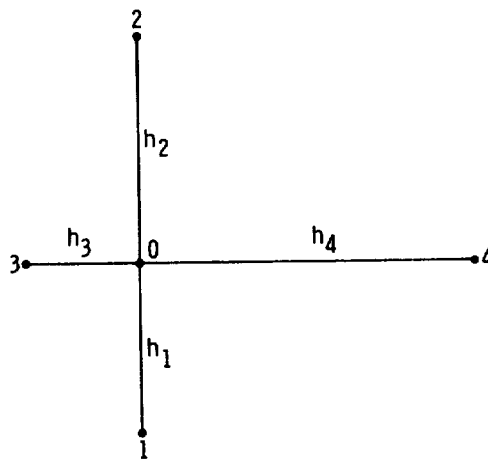


FIGURE 5-10.—Notation for adjacent mesh points and mesh spaces.

Solving equation (5-45) for u_0 yields the expression

$$u_0 = \sum_{i=1}^4 a_i u_i \quad (5-46)$$

where

$$a_1 = \frac{h_3 + h_4}{a_0 h_1} \quad (5-47)$$

$$a_2 = \frac{h_3 + h_4}{a_0 h_2} \quad (5-48)$$

$$a_3 = \frac{h_1 + h_2}{a_0 h_3} \quad (5-49)$$

$$a_4 = \frac{h_1 + h_2}{a_0 h_4} \quad (5-50)$$

$$a_0 = (h_3 + h_4) \left(\frac{1}{h_1} + \frac{1}{h_2} \right) + (h_1 + h_2) \left(\frac{1}{h_3} + \frac{1}{h_4} \right) \quad (5-51)$$

Equation (5-46) holds at every interior mesh point. If one of the neighboring points is on a blade surface, then the value of u at that point can be used. At other points along the boundary, equation (5-46) cannot be used, but the boundary conditions can be used to obtain alternate equations at these points. For example, along the upstream boundary AH in figure 5-9, $\partial u / \partial \eta$ is given by equation (5-27). If point 0 is on line AH, then, a finite difference approximation gives

$$u_0 = u_4 + h_4 \left(\frac{\tan \beta_{in}}{s} \right) \quad (5-52)$$

Similarly, if point 0 is on line DE,

$$u_0 = u_3 - h_3 \left(\frac{\tan \beta_{out}}{s} \right) \quad (5-53)$$

For the points along AB and CD, equations can be derived by using the periodic boundary condition. If the point 0 (fig. 5-11) is on the boundary between A and B, the point 1 is outside the boundary. However, it is known that $u_1 = u_{1,s} - 1$, where the point 1,s is a distance s above point 1 in the y -direction, as shown in figure 5-11. Substituting this

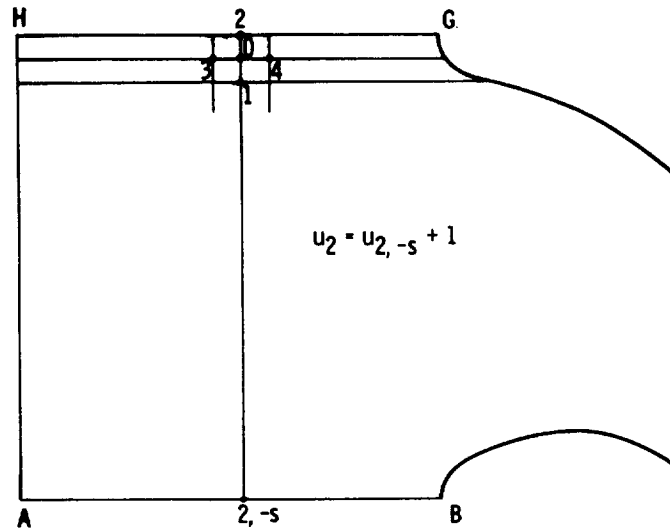


FIGURE 5-11.—Mesh point on line AB.

condition in equation (5-46) gives

$$u_0 = a_1 u_{1,s} + \sum_{i=2}^4 a_i u_i - a_1 \quad (5-54)$$

This equation holds along CD (fig. 5-8) also.

The points along HG need not be considered, since they are just 1 greater than the corresponding point along AB. The equation for the first mesh line below HG, therefore, must be modified, since point 2 is on line HG. In this case, $u_2 = u_{2,-s} + 1$, where the point 2, -s is a distance s below point 2 in the negative y-direction, as indicated in figure 5-12. Substituting this condition in equation (5-46) gives

$$u_0 = a_1 u_1 + a_2 u_{2,-s} + a_3 u_3 + a_4 u_4 + a_2 \quad (5-55)$$

This equation also applies to the first mesh line below FE (fig. 5-8).

One of equations (5-46) or (5-52) to (5-55) can be applied to each mesh point for which the stream function is unknown in the region of interest to give the same number of linear equations as there are unknowns. These points where the stream function is unknown will be referred to simply as unknown mesh points.

Suppose that there are n unknown mesh points. We then have n equations in n unknowns. The points can be numbered consecutively from 1 to n. The values of u will then be u_1 at the first point, u_2 at the second point, and so forth up to u_n at the last point. At each point, one equation will apply. The equation at a typical point, i, could be written

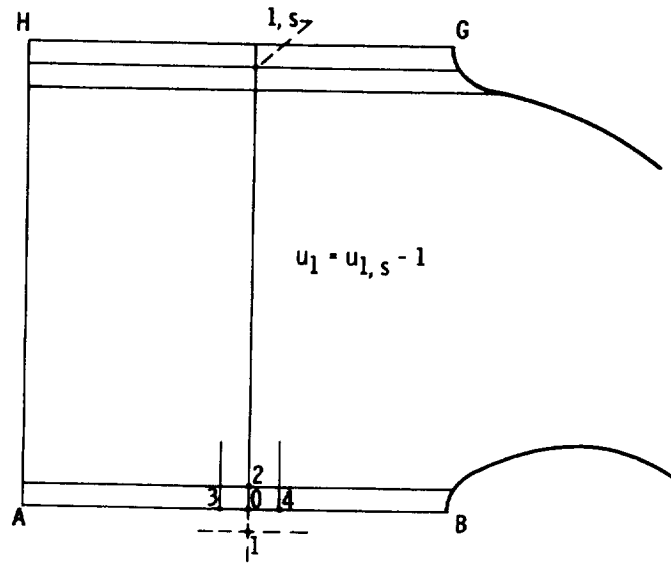


FIGURE 5-12.—Mesh point on first line below HG.

$$\sum_{j=1}^n a_{ij}u_j = k_i \tag{5-56}$$

The values of the a_{ij} are determined by one of equations (5-47) through (5-55). All but five, at most, of the a_{ij} are zero, and the $a_{ii} = -1$. The value of k_i is always zero, except for the outermost unknown points around the boundary. It can be shown that the a_{ij} matrix is always non-singular; hence there is always a unique solution for the u_j .

A numerical solution to equation (5-56) can be obtained by iterative techniques. These techniques are particularly valuable in solving systems of linear equations of this type; that is, where there are a large number of unknowns, but few terms in each equation. Storage requirements are small, and roundoff error is minimized with iterative methods. To start the iteration, an initial estimate of u at every unknown mesh point is required. The simplest iterative procedure is relaxation. This consists of changing the estimated value of u at each point in succession so as to satisfy the equation for that point. After this is done at every point, the procedure is repeated until there is negligible change in the values of u . The procedure is simple and it always converges for this problem. However, the convergence rate is extremely slow, so that excessive computer time is required. The convergence can be accelerated greatly by increasing the change in u at each iteration by a factor ω , called the overrelaxation factor. When $\omega = 1$, the procedure is straight relaxation, and when $\omega > 1$, it is overrelaxation. It is proven in reference 4 that overrelaxation (or underrelaxation) is convergent if $0 < \omega < 2$. However, the greatest rate of convergence occurs when $1 < \omega < 2$. In fact, there is an optimum value of ω

between 1 and 2 which gives the most rapid convergence. This optimum overrelaxation factor can be calculated as explained in reference 4.

To give an explicit expression for the overrelaxation procedure, we will use a superscript on the u_i . That is, u_i^m is the m^{th} iterate of u_i . The initial estimates are denoted u_i^0 and may be any value. For example, an initial estimate of $u_i^0=0$ is satisfactory. Then, if u_i^m is known for all i , we can calculate u_i^{m+1} , for $i=1, 2, \dots, n$ in succession by

$$u_i^{m+1} = u_i^m + \omega \left\{ - \sum_{j=1}^{i-1} a_{ij} u_j^{m+1} - \sum_{j=i+1}^n a_{ij} u_j^m + k_i - u_i^m \right\} \quad (5-57)$$

After a solution for u is obtained by overrelaxation (or any other method), it is necessary to calculate the velocities with the use of equations (5-9) and (5-10) as

$$W_x = \frac{w \left(\frac{\partial u}{\partial y} \right)}{\rho b} \quad (5-58)$$

and

$$W_y = - \frac{w \left(\frac{\partial u}{\partial x} \right)}{\rho b} \quad (5-59)$$

The partial derivatives $\partial u/\partial x$ and $\partial u/\partial y$ must be estimated from the calculated discrete values of u_i . This can be readily done, either by finite differences, or by fitting a smooth curve, such as a spline curve, through the points. The resultant velocity is calculated from the two components at unknown mesh points. On the blade surface, the velocity is calculated from one component and the blade tangent angle.

Computer Programs for Stream-Function Analyses

As can be seen, the solution of Laplace's equation and the calculation of velocities is a lengthy calculation procedure which is best done by computer. Several computer programs have been written at the NASA Lewis Research Center for the analysis of flow through turbomachine blading by stream-function methods. Most of these programs are for blade-to-blade analysis (region shown in fig. 5-9). The program called TURBLE, which is described in reference 5, can be used to analyze axial, radial, or mixed flow. In accordance with the constraints associated with the stream-function method, the flow must be subsonic throughout the entire solution region. The TSONIC program, described in reference 6, super-

sedes TURBLE in that it performs all the same calculations and, in addition, extends the solution to transonic (local supersonic velocities) flow problems. Transonic solutions are obtained by using a velocity-gradient equation of the type described in the next section to extend a preliminary (lower mass flow rate) subsonic stream-function solution. A program called TANDEM, which is described in reference 7, can be used to analyze flow in tandem or slotted blade rows or blade rows with splitters. Another program, called MAGNFY and described in reference 8, obtains a detailed solution in the leading- or trailing-edge regions of any blade or in the slot region of tandem or slotted blades. The TANDEM and MAGNFY programs are restricted to subsonic flow.

Flow in the meridional plane (mean hub-to-shroud flow surface, as indicated by fig. 4-14(b) or fig. 5-1(a)), of any axial- or mixed-flow turbomachine can be analyzed by a program called MERIDL, which is described in references 9 and 10. Transonic solutions can be obtained by the use of a velocity-gradient equation to extend a preliminary subsonic stream-function solution.

VELOCITY-GRADIENT ANALYSIS

As indicated previously, the stream-function and potential-function methods of analysis are limited to solutions that are entirely subsonic within the computation region. By use of a velocity-gradient equation and additional assumptions, however, the subsonic solution can be extended to give an approximate solution in the transonic flow regime. It is also possible to use a velocity-gradient method of analysis alone to obtain subsonic, transonic, or supersonic solutions without assumptions other than the basic ones indicated earlier. The velocity-gradient analysis is often called a stream-filament analysis because the velocity-gradient equation involves the streamline, or stream-filament, curvature and position.

A velocity-gradient method of analysis can only give solutions within a guided passage; that is, a passage where both ends of all streamline orthogonals intersect a solid boundary. Therefore, the usefulness of this method depends on the degree of flow guidance provided by the turbine blades. For a well-guided passage (high solidity and/or small angles), such as shown in figure 4-11, most of the suction surface is within the guided region, and the associated surface velocity distribution can be well defined. On the other hand, for a low-solidity blade row, such as that shown in figure 5-9, less than half of the suction surface is within the guided region, and surface velocities can be computed only on the front half of the suction surface. In this latter case, the stream-function analysis must be used if better definition of the suction-surface velocity distribution is required.

Method

The idea of a velocity-gradient method can be demonstrated by considering a simple case. Suppose we have two-dimensional flow through a narrow passage as shown in figure 5-13. We assume the height of the passage to be b , and the width d . If the mass flow is known, the average velocity can be calculated approximately from continuity by

$$W_{avg} = \frac{w}{\rho b d} \quad (5-60)$$

However, there is a variation in velocity across the width of the passage, and in turbomachinery it is this velocity difference we are interested in. With a force-equilibrium equation, by balancing centrifugal force against the pressure gradient as was done in chapter 3 for consideration of radial equilibrium, it can be shown that

$$\frac{dW}{dq} = \frac{W}{r_c} \quad (5-61)$$

where q is the distance from the suction (convex) surface, and r_c is the radius of curvature for the streamline. The sign convention for r_c is important; r_c is positive if it is concave upward, and negative if it is concave downward. For the simple case shown in figure 5-13, equation (5-61) can be integrated along a radial line by assuming the streamline radius of curvature to be equal in magnitude to the passage radius. There results, for integration from the inner radius to any point in the passage,

$$\frac{W}{W_s} = \frac{r_s}{r} \quad (5-62)$$

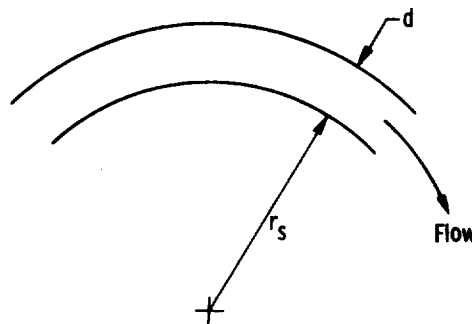


FIGURE 5-13.—Flow through a curved passage.

where

- W_s relative velocity on inner, or suction, surface, m/sec; ft/sec
 r_s radius of inner, or suction, surface, m; ft
 r radius of passage, m; ft

The mass flow through the passage is expressed as

$$w = \int_{r_s}^{r_s+d} \rho W b \, dr \quad (5-63)$$

and substitution of equation (5-62) into (5-63) and integration, with constant density assumed, yields

$$W_s = \frac{w}{\rho b r_s \ln \left(1 + \frac{d}{r_s} \right)} \quad (5-64)$$

In a similar manner, the outer, or pressure, surface velocity can be computed as

$$W_p = \frac{w}{\rho b r_s \left(1 + \frac{d}{r_s} \right) \ln \left(1 + \frac{d}{r_s} \right)} \quad (5-65)$$

Thus, an estimate of the blade-surface velocities can be obtained simply by using equation (5-62), which is a velocity-gradient equation. We are not necessarily restricted to two-dimensional flow. If there were some variation of velocity in the height of the passage, a velocity gradient could be calculated in that direction also.

We will now consider a very general velocity-gradient equation. Since we are interested in turbomachinery, we will use a rotating cylindrical coordinate system with radius r , angle θ , and axis x , as shown in figure 5-14. Also indicated are the velocity components, W_r , W_x , and W_θ . The meridional component W_m is the resultant of W_r and W_x . The meridional plane is a plane containing the x axis. Also shown in figure 5-14 are α , the angle between W_m and the x axis, and β , the angle between W and the meridional plane. The following relations hold for the components:

$$W_\theta = W \sin \beta \quad (5-66)$$

$$W_m = W \cos \beta \quad (5-67)$$

$$W_r = W_m \sin \alpha \quad (5-68)$$

$$W_x = W_m \cos \alpha \quad (5-69)$$

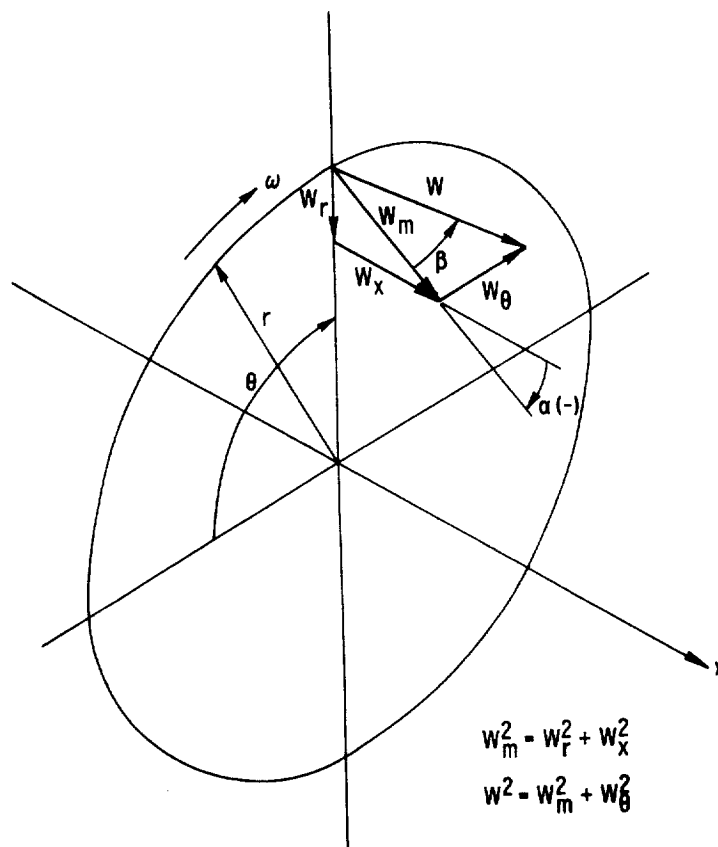


FIGURE 5-14.—Cylindrical coordinate system and velocity components.

In addition to the r -, θ -, and x -coordinate, it is convenient to use an m -coordinate. The m -coordinate is the distance along a meridional streamline, as shown in figure 5-15. The m -distance is less than the true streamline distance if the angle $\beta \neq 0$. The meridional streamline is the projection of a streamline in the meridional plane; that is, the θ -coordinate is neglected. The curvature of the meridional streamline is $1/r_c$, where r_c is the radius of curvature of the meridional streamline. The sign of r_c is positive if the streamline is concave upward.

We want the velocity gradient along an arbitrary curve. Let q be the distance along this curve. For the case of constant total temperature and constant angular momentum (rV_u) at the inlet,

$$\frac{dW}{dq} = a \frac{dr}{dq} + b \frac{dx}{dq} + c \frac{d\theta}{dq} \quad (5-70)$$

where

$$a = \frac{W \cos \alpha \cos^2 \beta}{r_c} - \frac{W \sin^2 \beta}{r} + \sin \alpha \cos \beta \frac{dW_m}{dm} - 2\omega \sin \beta \quad (5-71)$$

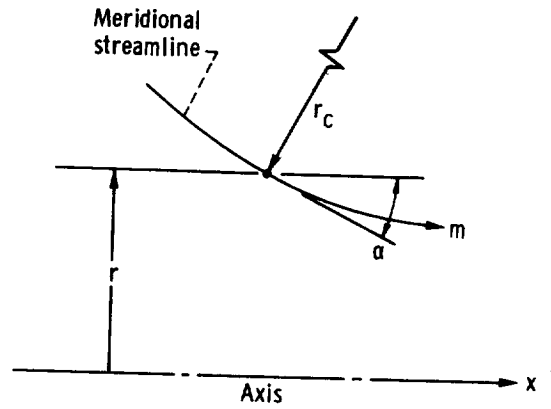


FIGURE 5-15.—The m -coordinate.

$$b = -\frac{W \sin \alpha \cos^2 \beta}{r_c} + \cos \alpha \cos \beta \frac{dW_m}{dm} \quad (5-72)$$

$$c = W \sin \alpha \sin \beta \cos \beta + r \cos \beta \left(\frac{dW_\theta}{dm} + 2\omega \sin \alpha \right) \quad (5-73)$$

These equations are derived as equations (B13) and (B14) of reference 11. In using any velocity-gradient equation, it is necessary to solve a differential equation involving streamline-geometry parameters, such as curvature, α , and β . These are not known precisely in advance. However, for a guided channel, these parameters can be estimated reasonably well.

A great number of special cases can be obtained from equations (5-70) to (5-73). For example, suppose we have an annular passage with no blades, as shown in figure 5-16, and no velocity component in the tangential (θ) direction (into page). We can calculate dW/dn , where n is the distance normal to the streamline. Let $q=n$ in equation (5-70). Since $W_\theta=0$, then $d\theta/dn=0$ and $\beta=0$. Further, from figure 5-16, it can be

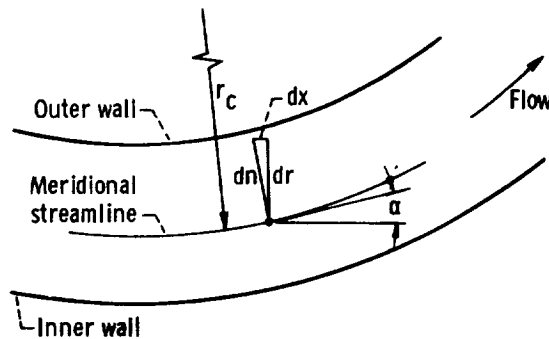


FIGURE 5-16.—Annular passage with no blades.

seen that $dr/dn = \cos \alpha$ and $dx/dn = -\sin \alpha$. Then, from equations (5-70) to (5-73),

$$\frac{dW}{dn} = \frac{W}{r_c} \quad (5-74)$$

Thus, for this case, equation (5-70) reduces to the simple form of equation (5-61).

Computer Programs

Several computer programs for the analysis of flow through turbomachine blading by velocity-gradient methods have been written at the NASA Lewis Research Center. One that was used for many years is the CTTD program, which is described in reference 12 and is limited to axial-flow turbines. This program has now been superseded by the more general and easier to use CHANEL program, which is described in reference 13. The CHANEL program can be used to analyze axial-, radial-, or mixed-flow turbines or compressors. Velocity-gradient equations are used to determine velocity variations both from hub to tip along meridional-streamline orthogonals and from blade to blade along hub-, mean-, and tip-streamline orthogonals. This results in a flow solution for an orthogonal surface, as illustrated in figure 5-17, which satisfies a specified mass flow rate. Computations are made for a number of these surfaces along the blade passage. This program can also be used to compute the maximum (choking) mass flow rate for the channel. The program gives good results for medium- to high-solidity blading. As indicated previously, more definition than can be provided by this program may be needed for low-solidity blading, because solutions can only be obtained for fully guided sections of the passage.

Velocity-gradient methods have also been used to obtain meridional-plane and blade-to-blade plane solutions. The basic method for a meridional-plane analysis for mixed-flow centrifugal impellers is presented in reference 14, which uses the velocity-gradient equation along streamline orthogonals. Since the orthogonal lengths are not known in advance, it was more convenient to base a computer program on the use of the velocity-gradient equation along fixed straight lines, which were called quasi-orthogonals. Such programs for meridional-plane analysis are presented in reference 11 for a radial-inflow turbine impeller and in reference 15 for backward-swept or radial impellers and vaned diffusers of centrifugal compressors. A program for a blade-to-blade plane analysis that uses quasi-orthogonals for a radial-inflow turbine impeller is described in reference 16.

A further use of the velocity-gradient equation, as mentioned previously in this chapter, is to extend a subsonic stream-function solution to

obtain local supersonic velocities. The subsonic solution is used to obtain the flow angles and streamline curvatures required for the velocity-gradient equation. Programs for transonic-flow solutions based on this method are presented in references 9 and 10 for a meridional solution and in reference 6 for a blade-to-blade solution.

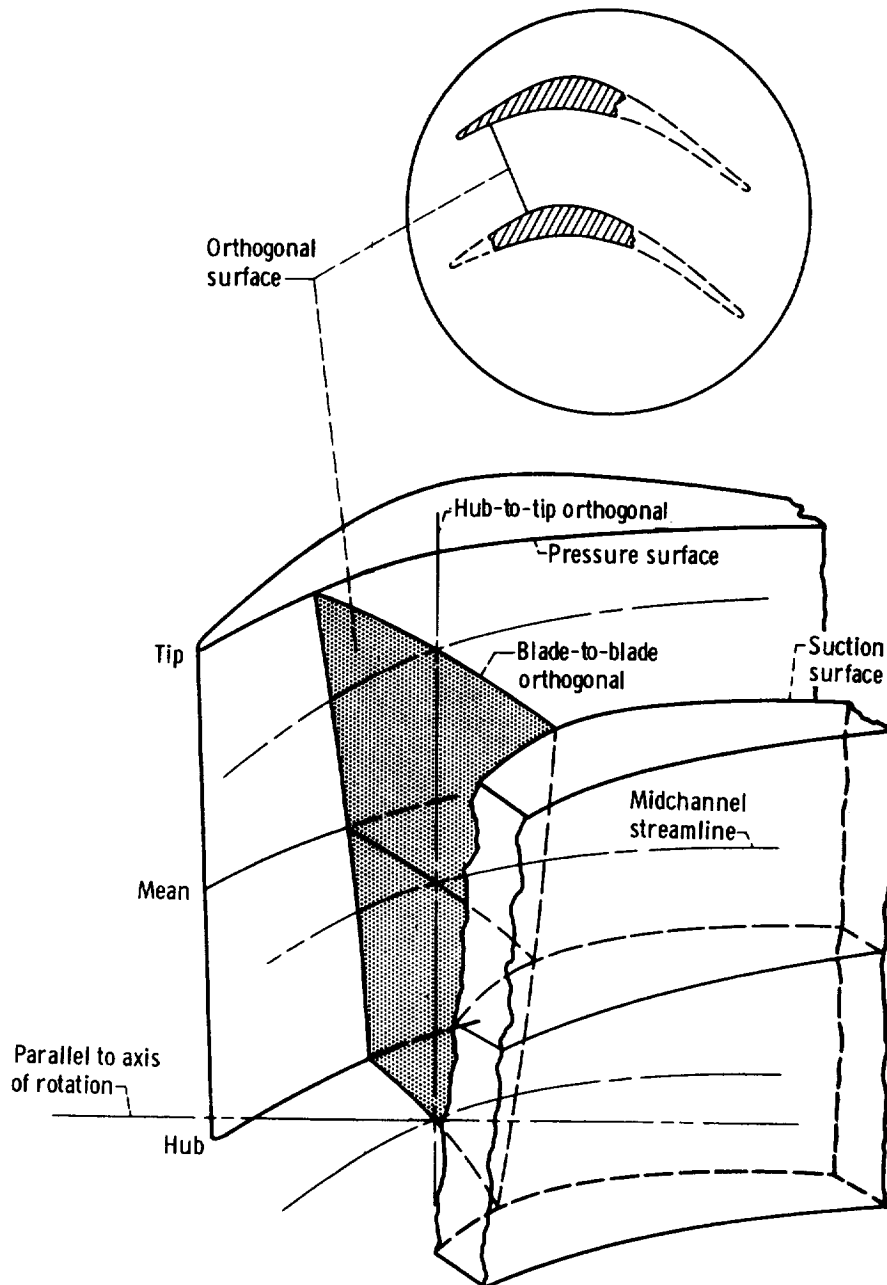


FIGURE 5-17.—Turbine blades with three-dimensional orthogonal surface across flow passage.

REFERENCES

1. JOHNSEN, IRVING A.; AND BULLOCK, ROBERT O., EDS.: Aerodynamic Design of Axial-Flow Compressors. NASA SP-36, 1965.
2. COSTELLO, GEORGE R.: Method of Designing Cascade Blades with Prescribed Velocity Distributions in Compressible Potential Flows. NACA Rep. 978, 1950.
3. COSTELLO, GEORGE R.; CUMMINGS, ROBERT L.; AND SINNETTE, JOHN T., JR.: Detailed Computational Procedure for Design of Cascade Blades with Prescribed Velocity Distributions in Compressible Potential Flows. NACA Rep. 1060, 1952.
4. VARGA, RICHARD S.: Matrix Iterative Analysis. Prentice-Hall, Inc., 1962.
5. KATSANIS, THEODORE; AND McNALLY, WILLIAM D.: Revised FORTRAN Program for Calculating Velocities and Streamlines on a Blade-to-Blade Stream Surface of a Turbomachine. NASA TM X-1764, 1969.
6. KATSANIS, THEODORE: FORTRAN Program for Calculating Transonic Velocities on a Blade-to-Blade Stream Surface of a Turbomachine. NASA TN D-5427, 1969.
7. KATSANIS, THEODORE; AND McNALLY, WILLIAM D.: FORTRAN Program for Calculating Velocities and Streamlines on a Blade-to-Blade Stream Surface of a Tandem Blade Turbomachine. NASA TN D-5044, 1969.
8. KATSANIS, THEODORE; AND McNALLY, WILLIAM D.: FORTRAN Program for Calculating Velocities in a Magnified Region on a Blade-to-Blade Stream Surface of a Turbomachine. NASA TN D-5091, 1969.
9. KATSANIS, THEODORE; AND McNALLY, WILLIAM D.: FORTRAN Program for Calculating Velocities and Streamlines on the Hub-Shroud Mid-Channel Flow Surface of an Axial- or Mixed-Flow Turbomachine. I—User's Manual. NASA TN D-7343, 1973.
10. KATSANIS, THEODORE; AND McNALLY, WILLIAM D.: FORTRAN Program for Calculating Velocities and Streamlines on the Hub-Shroud Mid-Channel Flow Surface of an Axial- or Mixed-Flow Turbomachine. II—Programmer's Manual. NASA TN D-7344, 1974.
11. KATSANIS, THEODORE: Use of Arbitrary Quasi-Orthogonals for Calculating Flow Distribution in the Meridional Plane of a Turbomachine. NASA TN D-2546, 1964.
12. KATSANIS, THEODORE; AND DELLNER, LOIS T.: A Quasi-Three-Dimensional Method for Calculating Blade-Surface Velocities for an Axial Flow Turbine Blade. NASA TM X-1394, 1967.
13. KATSANIS, THEODORE: FORTRAN Program for Quasi-Three-Dimensional Calculation of Surface Velocities and Choking Flow for Turbomachine Blade Rows. NASA TN D-6177, 1971.
14. HAMRICK, JOSEPH T.; GINSBURG, AMBROSE; AND OSBORNE, WALTER M.: Method of Analysis for Compressible Flow Through Mixed-Flow Centrifugal Impellers of Arbitrary Design. NACA Rep. 1082, 1952.
15. VANCO, MICHAEL R.: FORTRAN Program for Calculating Velocities in the Meridional Plane of a Turbomachine. I—Centrifugal Compressor. NASA TN D-6701, 1972.
16. KATSANIS, THEODORE: Use of Arbitrary Quasi-Orthogonals for Calculating Flow Distribution on a Blade-to-Blade Surface in a Turbomachine. NASA TN D-2809, 1965.

SYMBOLS

A	flow area, m^2 ; ft^2
a_i	coefficients for equation (5-46)
b	cascade height, m; ft
d	passage width, m; ft
h	distance between mesh points, m; ft
k_i	constant in equation (5-56)
m	distance along meridional streamline, m; ft
n	distance normal to streamline, m; ft
p	absolute pressure, N/m^2 ; lb/ft^2
q	distance along arbitrary curve, m; ft
R	gas constant, $J/(kg)(K)$; $(ft)(lbf)/(lbm)(^{\circ}R)$
r	radius, m; ft
s	blade spacing, m; ft
T	absolute temperature, K; $^{\circ}R$
t	time, sec
u	stream function
V	absolute velocity, m/sec; ft/sec
W	relative velocity, m/sec; ft/sec
w	mass flow rate, kg/sec; lb/sec
α	fluid absolute angle of inclination from axial direction in the meridional plane, deg
β	fluid flow angle, relative to blades, out of the meridional plane (in the tangential direction), deg
η	distance in direction of outer normal to cascade boundary, m; ft
θ	angular distance in direction of rotation, rad
ρ	density, kg/m^3 ; lb/ft^3
Φ	potential function
ω	{ angular velocity, rad/sec overrelaxation factor

Subscripts:

c	curvature
in	inlet
m	meridional component
n	component normal to streamline
out	outlet
p	pressure surface
r	radial component
s	suction surface
x	axial component
y	component in y-direction
z	component in z-direction

TURBINE DESIGN AND APPLICATION

θ tangential component
0 }
1, 2, } mesh-point designations
3, 4 }

CHAPTER 6

Introduction to Boundary-Layer Theory

By William D. McNally

As shown in chapter 2, the pressure ratio across a turbine provides a certain amount of ideal energy that is available to the turbine for producing work. The portion of the ideal energy that is not converted to work is considered to be a loss. One of the more important and difficult aspects of turbine design is the prediction of the losses.

Before losses can be predicted, it is necessary to understand their causes. The primary cause of losses is the boundary layer that develops on the blade and end-wall surfaces. Other losses occur because of shocks, tip-clearance flows, disk friction (windage), flow incidence, and partial-admission operation. This chapter gives an introduction to boundary-layer theory, which is used to calculate the parameters needed to estimate viscous (friction) losses. Methods for determining the basic viscous loss and the associated trailing-edge and mixing losses are presented in the next chapter.

NATURE OF BOUNDARY LAYER

When a real fluid (such as air) flows past a turbine blade at normal velocities, the influence of viscosity on the flow is confined to a relatively thin layer in the immediate neighborhood of the blade. This layer is called the boundary layer. At the outer edge of this layer the flow is frictionless, and conditions there agree with those calculated with the use of ideal (frictionless, nonviscous) flow assumptions. At the wall, on the other hand, the velocity of the fluid is zero in all directions (no-slip condition).

It is the frictional, or viscous, forces in this thin layer that reduce the fluid velocity from its free-stream, frictionless value to zero at the wall.

A boundary layer on a turbine blade is illustrated in figure 6-1. The boundary layer develops from a small finite thickness at the stagnation point at the leading edge of the blade and grows along both the suction and pressure surfaces. The initial portion of the boundary layer is always laminar. In a laminar boundary layer, fluid layers parallel to the blade surface slide over each other. Any minute local fluctuations in velocity are sufficiently damped so that they have negligible influence on the smoothness of the overall flow. The velocity at a point is either steady with time or changes in some smooth way, as figure 6-2(a) indicates.

Most flows being ducted to a turbine, or entering it from a combustor, are turbulent in nature. The fluctuating components of velocity have a significant influence in this type of flow. With this overall flow, the boundary layer on the blades cannot remain laminar for any great distance. It usually passes through a transition region and becomes a turbulent boundary layer. In the transition region, weak disturbances in the flow are amplified, and this leads to the random fluctuations in velocity that are characteristic of turbulent flow. In the turbulent boundary layer, as in turbulent flow, the velocity at any point oscillates in a random fashion about a mean value, as figure 6-2(b) indicates.

Figure 6-1 also shows a separated region in the turbulent boundary layer. Separation can likewise occur in the laminar boundary layer. When a boundary layer separates, the fluid moves away from the blade surface. The manner in which this happens is illustrated in figure 6-3. As the free-stream velocity decreases along the rear portion of the suction surface of a turbine blade, static pressure correspondingly increases. This positive

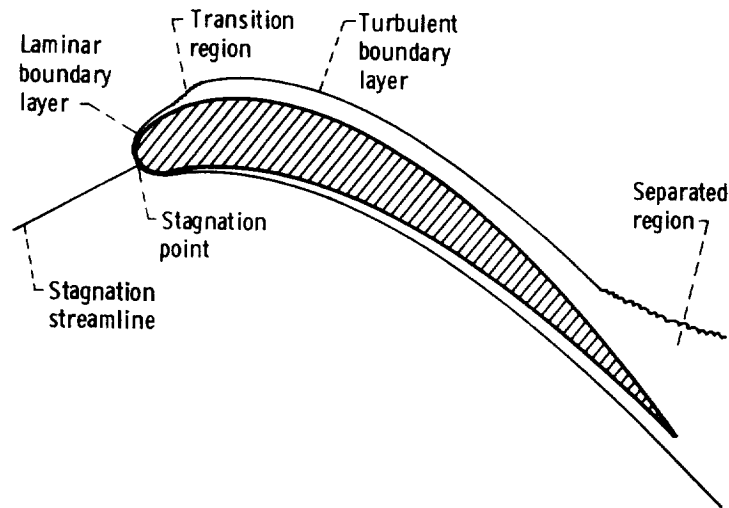
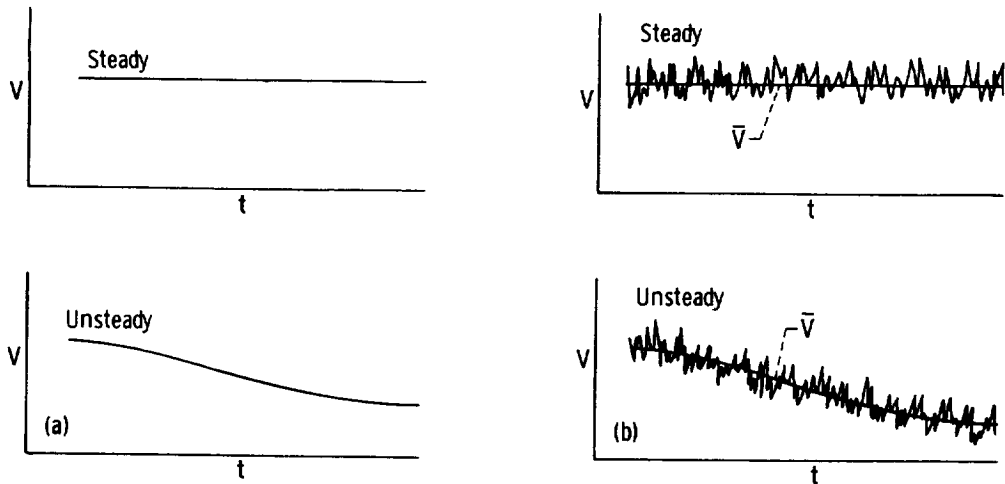


FIGURE 6-1.—Boundary layer on blade.



(a) Laminar flow.

(b) Turbulent flow.

FIGURE 6-2.—Variation of velocity with time at a point.

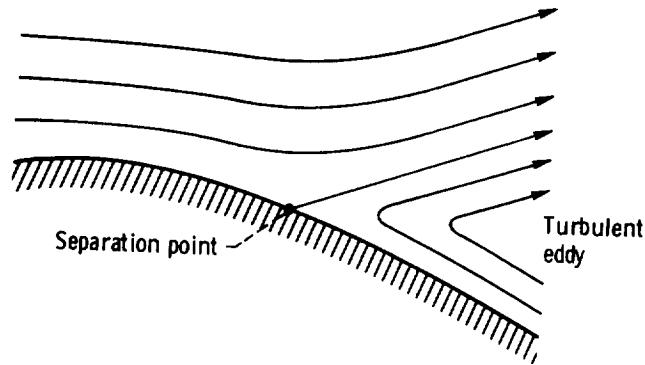


FIGURE 6-3.—Boundary-layer separation.

pressure gradient (adverse pressure gradient) retards the flow in the boundary layer and causes it to lose energy. The flow in the boundary layer can be retarded to such a degree that very close to the wall it moves in a direction opposite to that of the mean flow passing the blade. This is separation. The point at which the flow reverses itself is the separation point. The laminar boundary layer at the leading edge of a turbine blade can also separate and immediately reattach itself to the surface as a turbulent boundary layer. This is illustrated in figure 6-4.

Finally, it should be noted that both laminar and turbulent boundary layers can be either incompressible or compressible, depending on the level of the Mach number. Just as there are different equations to represent laminar and turbulent boundary-layer flow, there are different equations for the incompressible and compressible variations of each.

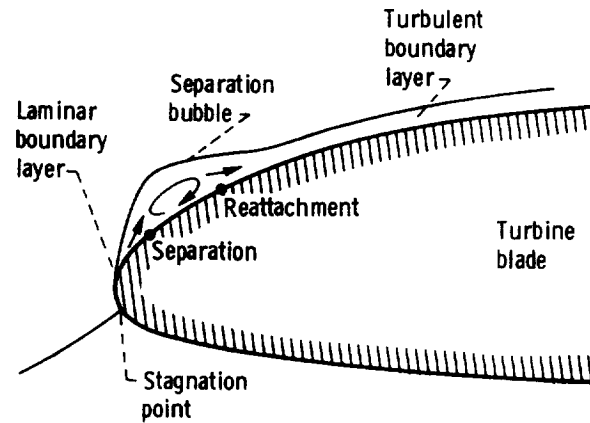


FIGURE 6-4.—Laminar separation and reattachment.

Boundary layers should be considered compressible if the free-stream relative Mach number exceeds values of 0.3 to 0.4. The boundary-layer equations for these various cases are derived and solution methods are discussed in this chapter.

DERIVATION OF BOUNDARY-LAYER EQUATIONS

The general equations of motion of viscous fluids are called the Navier-Stokes equations. In normal coordinate systems, there are three such equations, one for each of the coordinate directions. The boundary-layer equations can be derived from the Navier-Stokes equations. The Navier-Stokes equations themselves can be derived by applying the law of conservation of momentum to a fluid element. This exercise is lengthy, and will not be repeated here. References 1 and 2 both have the complete derivation, in two somewhat different forms.

There are various forms of the Navier-Stokes equations, depending on what assumptions are made during their derivation. The following equation represents the Navier-Stokes equations combined into vector form for a compressible fluid with constant viscosity:

$$\frac{d\mathbf{u}}{dt} = g\mathbf{f} - \frac{g}{\rho} \nabla p + \frac{\mu}{\rho} \nabla^2 \mathbf{u} + \frac{1}{3} \frac{\mu}{\rho} \nabla(\nabla \cdot \mathbf{u}) \quad (6-1)$$

where

- u** general velocity vector, m/sec; ft/sec
- t** time, sec
- g** conversion constant, 1; 32.17 (lbm) (ft)/(lbf) (sec²)
- f** general body force acting on a unit mass of fluid, N/kg; lbf/lbm

- ρ density, kg/m³; lbm/ft³
 p static pressure, N/m²; lbf/ft²
 μ dynamic viscosity, (N)(sec)/m²; lbm/(ft)(sec)

In this equation, \mathbf{u} represents a general velocity vector with components u , v , and w in the three coordinate directions x , y , and z , respectively.

$$\mathbf{u} = u\mathbf{i} + v\mathbf{j} + w\mathbf{k} \quad (6-2)$$

where \mathbf{i} , \mathbf{j} , and \mathbf{k} are the unit vectors in the three coordinate directions. The total, or substantial, derivative of \mathbf{u} is $d\mathbf{u}/dt$. In any of the coordinate directions,

$$\frac{d}{dt} = \frac{\partial}{\partial t} + u \frac{\partial}{\partial x} + v \frac{\partial}{\partial y} + w \frac{\partial}{\partial z} \quad (6-3)$$

In equation (6-1), the Laplacian operator ∇^2 is applied to the vector \mathbf{u} rather than to a scalar function. If the term $\nabla^2\mathbf{u}$ is expanded into simple vector quantities, equation (6-1) becomes

$$\frac{d\mathbf{u}}{dt} = g\mathbf{f} - \frac{g}{\rho} \nabla p + \frac{\mu}{\rho} \nabla(\nabla \cdot \mathbf{u}) - \frac{\mu}{\rho} [\nabla \times (\nabla \times \mathbf{u})] + \frac{1}{3} \frac{\mu}{\rho} \nabla(\nabla \cdot \mathbf{u}) \quad (6-4)$$

Expressing the ∇ operator in terms of gradients, curls, and divergences, which may be more familiar to the reader, equation (6-4) becomes

$$\frac{d\mathbf{u}}{dt} = g\mathbf{f} - \frac{g}{\rho} \text{grad } p + \frac{\mu}{\rho} \text{grad}(\text{div } \mathbf{u}) - \frac{\mu}{\rho} \text{curl}(\text{curl } \mathbf{u}) + \frac{1}{3} \frac{\mu}{\rho} \text{grad}(\text{div } \mathbf{u}) \quad (6-5)$$

In order to derive the boundary-layer equations, equation (6-1) has to be expanded into three scalar equations, one for each of the coordinate directions. The three resulting equations are

$$\begin{aligned} \frac{\partial u}{\partial t} + u \frac{\partial u}{\partial x} + v \frac{\partial u}{\partial y} + w \frac{\partial u}{\partial z} = g f_x - \frac{g}{\rho} \frac{\partial p}{\partial x} + \frac{\mu}{\rho} \left(\frac{\partial^2 u}{\partial x^2} + \frac{\partial^2 u}{\partial y^2} + \frac{\partial^2 u}{\partial z^2} \right) \\ + \frac{1}{3} \frac{\mu}{\rho} \frac{\partial}{\partial x} \left(\frac{\partial u}{\partial x} + \frac{\partial v}{\partial y} + \frac{\partial w}{\partial z} \right) \end{aligned} \quad (6-6)$$

$$\begin{aligned} \frac{\partial v}{\partial t} + u \frac{\partial v}{\partial x} + v \frac{\partial v}{\partial y} + w \frac{\partial v}{\partial z} = g f_y - \frac{g}{\rho} \frac{\partial p}{\partial y} + \frac{\mu}{\rho} \left(\frac{\partial^2 v}{\partial x^2} + \frac{\partial^2 v}{\partial y^2} + \frac{\partial^2 v}{\partial z^2} \right) \\ + \frac{1}{3} \frac{\mu}{\rho} \frac{\partial}{\partial y} \left(\frac{\partial u}{\partial x} + \frac{\partial v}{\partial y} + \frac{\partial w}{\partial z} \right) \end{aligned} \quad (6-7)$$

$$\frac{\partial w}{\partial t} + u \frac{\partial w}{\partial x} + v \frac{\partial w}{\partial y} + w \frac{\partial w}{\partial z} = \rho f_z - \frac{g}{\rho} \frac{\partial p}{\partial z} + \frac{\mu}{\rho} \left(\frac{\partial^2 w}{\partial x^2} + \frac{\partial^2 w}{\partial y^2} + \frac{\partial^2 w}{\partial z^2} \right) + \frac{1}{3} \frac{\mu}{\rho} \frac{\partial}{\partial z} \left(\frac{\partial u}{\partial x} + \frac{\partial v}{\partial y} + \frac{\partial w}{\partial z} \right) \quad (6-8)$$

where f_x , f_y , and f_z are the components of the body force \mathbf{f} .

Laminar Incompressible Boundary Layer

In order to derive Prandtl's boundary-layer equations for laminar incompressible flow, the following assumptions will be made:

- (1) Viscosity is a constant. This has already been assumed in the writing of the preceding equations.
- (2) Flow is incompressible. Since for incompressible flow the continuity equation is

$$\nabla \cdot \mathbf{u} = \text{div } \mathbf{u} = \left(\frac{\partial u}{\partial x} + \frac{\partial v}{\partial y} + \frac{\partial w}{\partial z} \right) = 0 \quad (6-9)$$

the final terms in equations (6-6) to (6-8) can be eliminated.

- (3) Flow is two-dimensional. This eliminates equation (6-8) from consideration, as well as all terms involving w or $\partial/\partial z$ in equations (6-6) and (6-7).

- (4) Flow is steady. This eliminates $\partial/\partial t$ terms.

- (5) Body forces are negligible in relation to inertia and viscous forces. Thus, f_x and f_y can be discarded from equations (6-6) and (6-7).

With these assumptions, the Navier-Stokes equations reduce to the following two equations for the x - and y -directions:

$$u \frac{\partial u}{\partial x} + v \frac{\partial u}{\partial y} = -\frac{g}{\rho} \frac{\partial p}{\partial x} + \frac{\mu}{\rho} \left(\frac{\partial^2 u}{\partial x^2} + \frac{\partial^2 u}{\partial y^2} \right) \quad (6-10)$$

$$u \frac{\partial v}{\partial x} + v \frac{\partial v}{\partial y} = -\frac{g}{\rho} \frac{\partial p}{\partial y} + \frac{\mu}{\rho} \left(\frac{\partial^2 v}{\partial x^2} + \frac{\partial^2 v}{\partial y^2} \right) \quad (6-11)$$

Likewise, the continuity equation becomes

$$\frac{\partial u}{\partial x} + \frac{\partial v}{\partial y} = 0 \quad (6-12)$$

In order to make equations (6-10) to (6-12) suitable for the analysis of boundary-layer flow, the equations are traditionally made dimensionless, and an order-of-magnitude check is performed on the various terms to show that some are negligible with respect to others. Figure 6-5 shows the velocities and coordinate directions pertinent to the boundary layer.

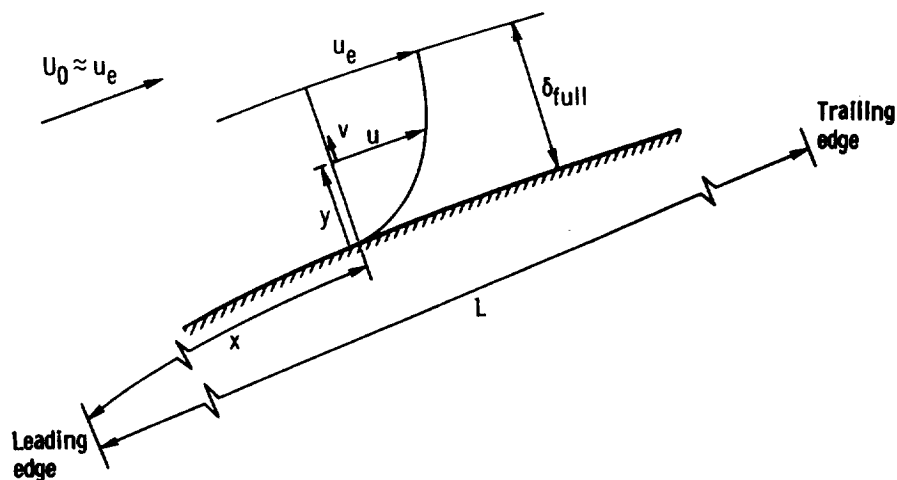


FIGURE 6-5.—Boundary-layer velocities and dimensions.

The following dimensionless parameters are defined:

$$X = \frac{x}{L} \quad (6-13a)$$

$$Y = \frac{y}{L} \quad (6-13b)$$

$$U = \frac{u}{U_0} \quad (6-13c)$$

$$V = \frac{v}{U_0} \quad (6-13d)$$

$$P = \frac{gp}{\rho U_0^2} \quad (6-13e)$$

$$Re = \frac{\rho L U_0}{\mu} \quad (6-13f)$$

where

- X dimensionless x -coordinate
- L characteristic length (in this case, the blade chord), m; ft
- Y dimensionless y -coordinate
- U dimensionless velocity in x -direction
- U_0 free-stream velocity upstream of blade, m/sec; ft/sec
- V dimensionless velocity in y -direction

TURBINE DESIGN AND APPLICATION

P dimensionless pressure
 Re Reynolds number

From figure 6-5, we see that since x is proportional to L , X is of order 1. And since y is proportional to the boundary-layer thickness $\delta_{f_{u1}}$, Y is of order $\delta_{f_{u1}}/L = \epsilon$, a quantity much less than 1. Likewise, since u is of order U_0 , $U = u/U_0$ is of order 1. And $V = v/U_0$ is of order ϵ , since velocities in the y -direction in the boundary layer are much smaller than those in the x -direction.

In order to put equations (6-10) to (6-12) in terms of dimensionless quantities, equations (6-10) and (6-11) are multiplied by L/U_0^2 , and equation (6-12) is multiplied by L/U_0 . The resulting dimensionless equations are

$$U \frac{\partial U}{\partial X} + V \frac{\partial U}{\partial Y} = -\frac{\partial P}{\partial X} + \frac{1}{Re} \left(\frac{\partial^2 U}{\partial X^2} + \frac{\partial^2 U}{\partial Y^2} \right) \quad (6-14)$$

$$U \frac{\partial V}{\partial X} + V \frac{\partial V}{\partial Y} = -\frac{\partial P}{\partial Y} + \frac{1}{Re} \left(\frac{\partial^2 V}{\partial X^2} + \frac{\partial^2 V}{\partial Y^2} \right) \quad (6-15)$$

$$\frac{\partial U}{\partial X} + \frac{\partial V}{\partial Y} = 0 \quad (6-16)$$

The order of magnitude of the various terms in these equations can now be compared with each other. Since X and U are of order 1, and Y and V are of order ϵ ,

$$\frac{\partial U}{\partial X} \approx \frac{1}{1} = 1 \quad (6-17a)$$

$$\frac{\partial U}{\partial Y} \approx \frac{1}{\epsilon} \quad (6-17b)$$

$$\frac{\partial V}{\partial X} \approx \frac{\epsilon}{1} = \epsilon \quad (6-17c)$$

$$\frac{\partial V}{\partial Y} \approx \frac{\epsilon}{\epsilon} = 1 \quad (6-17d)$$

$$\frac{\partial^2 U}{\partial X^2} \approx \frac{1}{1 \cdot 1} = 1 \quad (6-17e)$$

$$\frac{\partial^2 U}{\partial Y^2} \approx \frac{1}{\epsilon \cdot \epsilon} = \frac{1}{\epsilon^2} \quad (6-17f)$$

$$\frac{\partial^2 V}{\partial X^2} \approx \frac{\epsilon}{1 \cdot 1} = \epsilon \quad (6-17g)$$

$$\frac{\partial^2 V}{\partial Y^2} \approx \frac{\epsilon}{\epsilon \cdot \epsilon} = \frac{1}{\epsilon} \quad (6-17h)$$

Furthermore, the change in P with respect to X is of the same order of magnitude as the change of U with respect to X , so that $\partial P/\partial X$ is of order 1.

Relating these orders of magnitude to the terms in equations (6-14) to (6-16) yields

$$U \frac{\partial U}{\partial X} + V \frac{\partial U}{\partial Y} = -\frac{\partial P}{\partial X} + \frac{1}{Re} \left(\frac{\partial^2 U}{\partial X^2} + \frac{\partial^2 U}{\partial Y^2} \right) \quad (6-18)$$

$$(1)(1) + (\epsilon) \left(\frac{1}{\epsilon} \right) = -1 + (\epsilon^2) \left(1 + \frac{1}{\epsilon^2} \right)$$

$$U \frac{\partial V}{\partial X} + V \frac{\partial V}{\partial Y} = -\frac{\partial P}{\partial Y} + \frac{1}{Re} \left(\frac{\partial^2 V}{\partial X^2} + \frac{\partial^2 V}{\partial Y^2} \right) \quad (6-19)$$

$$(1)(\epsilon) + (\epsilon)(1) = -\epsilon + (\epsilon^2) \left(\epsilon + \frac{1}{\epsilon} \right)$$

$$\frac{\partial U}{\partial X} + \frac{\partial V}{\partial Y} = 0 \quad (6-20)$$

$$1+1$$

By examining equations (6-18) to (6-20), the following conclusions can be reached:

(1) In boundary-layer theory, it is assumed that the viscous terms $1/Re[(\partial^2 U/\partial X^2) + (\partial^2 U/\partial Y^2)]$ are of the same order of magnitude as the inertia terms $U(\partial U/\partial X) + V(\partial U/\partial Y)$. For this to be true in equation (6-18), $1/Re$ must be of order ϵ^2 , since $\partial^2 U/\partial Y^2$ is much larger than $\partial^2 U/\partial X^2$ and dominates the two terms in parentheses. Therefore, the Reynolds number must be relatively large.

(2) In equation (6-19), with $1/Re$ of order ϵ^2 and with $\partial^2 V/\partial Y^2$ dominating $\partial^2 V/\partial X^2$, the terms are of order ϵ . Therefore, unless $\partial P/\partial Y$ is to dominate, it too must be of order ϵ or less. Therefore, $\partial P/\partial Y$ is much smaller than $\partial P/\partial X$, and P can be considered a function of X alone. Therefore, $P = P(X)$ or $p = p(x)$, and $\partial P/\partial X = dP/dX$ or $\partial p/\partial x = dp/dx$. This allows us to assume that the pressure across the boundary layer in the

y -direction is essentially constant. It can be assumed equal to the potential flow pressure existing at the outside of the boundary layer.

(3) Since the first equation is of order 1, and the second equation is of order ϵ , the second equation can be neglected completely.

(4) In equation (6-18), $\partial^2 U / \partial X^2$ can be neglected because it is so small in comparison with $\partial^2 U / \partial Y^2$. This leaves the following dimensionless equations:

$$U \frac{\partial U}{\partial X} + V \frac{\partial U}{\partial Y} = -\frac{dP}{dX} + \frac{1}{Re} \frac{\partial^2 U}{\partial Y^2} \quad (6-21)$$

$$\frac{\partial U}{\partial X} + \frac{\partial V}{\partial Y} = 0 \quad (6-22)$$

These are Prandtl's boundary-layer equations in dimensionless form.

The boundary-layer equations in this form are useful in determining the influence of the Reynolds number on the size of the boundary layer for different fluids. From equation (6-21) we see that as Re increases in magnitude, the viscous-force terms $(1/Re)(\partial^2 U / \partial Y^2)$ will get smaller and smaller. The boundary-layer thickness will correspondingly decrease. So, as Re increases, δ_{fu} decreases. Furthermore, increasing Re corresponds to decreasing viscosity if $\rho L U_0$ is constant. So, as a general rule, the thickness of the boundary layer decreases as the viscosity decreases.

The boundary-layer equations can be put in terms of dimensional variables by multiplying equation (6-21) by U_0^2/L and equation (6-22) by U_0/L . The resulting equations are

$$u \frac{\partial u}{\partial x} + v \frac{\partial u}{\partial y} = -\frac{g}{\rho} \frac{dp}{dx} + \frac{\mu}{\rho} \frac{\partial^2 u}{\partial y^2} \quad (6-23)$$

$$\frac{\partial u}{\partial x} + \frac{\partial v}{\partial y} = 0 \quad (6-24)$$

These are Prandtl's boundary-layer equations for two-dimensional, laminar, incompressible flow. Density and viscosity are assumed constant and known. The pressure gradient along the blade surface, dp/dx , is also known from an ideal-flow solution. The remaining unknowns are u and v , and equations (6-23) and (6-24) are sufficient for their calculation.

It should be noted that the boundary-layer equations are not valid in the presence of shock waves (i.e., where instantaneous adverse pressure gradients of large magnitude occur). Just as flow phenomena in the boundary layer depend on mainly the Reynolds number, conditions in a shock wave depend on primarily the Mach number. Since the influence of Mach number is not included in the boundary-layer equations, they tell us nothing about the interaction of shock waves and boundary layers.

The boundary-layer equations are not completely reliable as separation is approached. One of the assumptions used in their derivation is that the velocity v is much smaller than u . Very close to the separation point, the boundary layer grows rapidly, and v begins to be of the same order as u . Nonetheless, the boundary-layer equations are generally used in calculations right up to the separation point, since the region where V is significant is very small, and little error in the location of the point of separation is incurred. However, these equations should not be used for detailed calculations in the neighborhood of a separated flow region.

The Navier-Stokes equations (6-6) to (6-8) used in the development of the boundary-layer equations were derived for an orthogonal system of coordinates in which the radius of curvature of each of the coordinate axes is quite large (i.e., where curvature effects are negligible). The question arises as to how the boundary-layer equations would change for flow over a curved wall. If a curvilinear orthogonal coordinate system (fig. 6-6) is introduced wherein the x -axis is in the direction of the curved wall and the y -axis is normal to it, a new set of Navier-Stokes equations can be derived for flow in such a system. These equations are given in reference 1. The terms in the equations are very dependent on the radius of curvature r at a position x along the blade surface. The relative orders of magnitude of the individual terms can be estimated in the same manner as was done previously. With the assumption that the boundary-layer thickness is small compared with the radius of curvature of the wall, and for the case where no large variations in curvature occur, so that $dr/dx \approx 1$, the same boundary-layer equations result as were obtained for flat walls. Therefore, the flat-plate boundary-layer equations may be applied to curved walls as well, provided there are no large variations in curvature, such as would occur near sharp edges.

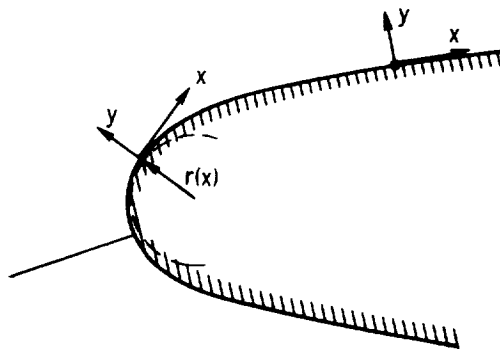


FIGURE 6-6.—Curvilinear coordinate system on a blade.

Laminar Compressible Boundary Layer

An order-of-magnitude analysis can also be performed to derive the equations for a compressible boundary layer. In the incompressible case, viscosity and density were assumed constant, temperature variations were neglected, and the energy equation was not used. For the compressible case, density is no longer constant, viscosity is considered a function of temperature, the equation of state is used to relate pressure and density to temperature, and, if the process is not isothermal, some form of the energy equation is required. The boundary-layer equations for compressible, nonisothermal, variable-viscosity flow will involve three parameters which can be related to temperature. These are viscosity, specific heat, and thermal conductivity.

There are several relations for viscosity as a function of temperature. The most common is probably Sutherland's relation (ref. 1)

$$\frac{\mu}{\mu_0} = \left(\frac{T}{T_0}\right)^{3/2} \frac{T_0 + S}{T + S} \quad (6-25)$$

where

- μ_0 dynamic viscosity at the reference temperature T_0 , (N)(sec)/m²; lbm/(ft)(sec)
- T absolute static temperature, K; °R
- T_0 reference temperature, K; °R
- S a constant, K; °R (for air, $S = 110$ K or 198° R)

A less complicated, but also less accurate, temperature-viscosity relation is the power law

$$\frac{\mu}{\mu_0} = \left(\frac{T}{T_0}\right)^\omega \quad 0.5 < \omega < 1.0 \quad (6-26)$$

where ω is a constant. For air, ω is approximately 0.65.

Specific heat and thermal conductivity can be related to temperature by least-squares polynomial-curve fits for the particular gas and temperature range involved. With these variables related to temperature, the unknowns in the compressible-boundary-layer problem reduce to u , v , ρ , and T . The four equations relating these variables will be the continuity equation, one component of the momentum equation, the state equation, and the energy equation.

The order-of-magnitude analysis of the continuity and momentum (Navier-Stokes) equations for compressible flow is almost identical to that for incompressible flow. For compressible flow with nonconstant viscosity, the equations analogous to (6-10) to (6-12) are the following:

$$\rho u \frac{\partial u}{\partial x} + \rho v \frac{\partial u}{\partial y} = -g \frac{\partial p}{\partial x} + \frac{\partial}{\partial x} \left[2\mu \frac{\partial u}{\partial x} - \frac{2}{3} \mu \left(\frac{\partial u}{\partial x} + \frac{\partial v}{\partial y} \right) \right] + \frac{\partial}{\partial y} \left[\mu \left(\frac{\partial u}{\partial y} + \frac{\partial v}{\partial x} \right) \right] \quad (6-27)$$

$$\rho u \frac{\partial v}{\partial x} + \rho v \frac{\partial v}{\partial y} = -g \frac{\partial p}{\partial y} + \frac{\partial}{\partial y} \left[2\mu \frac{\partial v}{\partial y} - \frac{2}{3} \mu \left(\frac{\partial u}{\partial x} + \frac{\partial v}{\partial y} \right) \right] + \frac{\partial}{\partial x} \left[\mu \left(\frac{\partial v}{\partial x} + \frac{\partial u}{\partial y} \right) \right] \quad (6-28)$$

$$\frac{\partial(\rho u)}{\partial x} + \frac{\partial(\rho v)}{\partial y} = 0 \quad (6-29)$$

If an order-of-magnitude analysis is performed on these equations similar to that for the incompressible-flow equations, the following boundary-layer equations result:

$$\rho u \frac{\partial u}{\partial x} + \rho v \frac{\partial u}{\partial y} = -g \frac{dp}{dx} + \frac{\partial}{\partial y} \left(\mu \frac{\partial u}{\partial y} \right) \quad (6-30)$$

$$\frac{\partial(\rho u)}{\partial x} + \frac{\partial(\rho v)}{\partial y} = 0 \quad (6-31)$$

The equation of state is also required for the solution of compressible boundary-layer flow. The state equation is

$$p = \rho RT \quad (6-32)$$

where R is the gas constant, in J/(kg)(K) or (ft)(lbf)/(lbm)(°R).

The final equation required besides the continuity equation, the momentum equation, and the equation of state, is the energy equation. The energy equation for a compressible boundary layer is derived from the energy equation for a perfect gas by means of another order-of-magnitude check. The following is the energy equation for compressible, two-dimensional steady flow of a perfect gas, written in full:

$$\rho c_p \left(u \frac{\partial T}{\partial x} + v \frac{\partial T}{\partial y} \right) = \frac{u}{J} \frac{\partial p}{\partial x} + \frac{v}{J} \frac{\partial p}{\partial y} + \frac{\partial}{\partial x} \left(k \frac{\partial T}{\partial x} \right) + \frac{\partial}{\partial y} \left(k \frac{\partial T}{\partial y} \right) + \frac{\mu}{gJ} \varphi \quad (6-33)$$

where

c_p specific heat at constant pressure, J/(kg)(K); Btu/(lbm)(°R)

J conversion constant, 1; 778 (ft)(lbf)/Btu

k thermal conductivity, W/(m)(K); Btu/(sec)(ft)(°R)

and

$$\varphi = 2 \left[\left(\frac{\partial u}{\partial x} \right)^2 + \left(\frac{\partial v}{\partial y} \right)^2 \right] + \left(\frac{\partial v}{\partial x} + \frac{\partial u}{\partial y} \right)^2 - \frac{2}{3} \left(\frac{\partial u}{\partial x} + \frac{\partial v}{\partial y} \right)^2 \quad (6-34)$$

If an order-of-magnitude check is performed on the above equations, the following boundary-layer energy equation results:

$$\rho c_p \left(u \frac{\partial T}{\partial x} + v \frac{\partial T}{\partial y} \right) = \frac{u}{J} \frac{dp}{dx} + \frac{\partial}{\partial y} \left(k \frac{\partial T}{\partial y} \right) + \frac{\mu}{gJ} \left(\frac{\partial u}{\partial y} \right)^2 \quad (6-35)$$

Equations (6-30), (6-31), (6-32), and (6-35) are the laminar boundary-layer equations for nonisothermal, two-dimensional, compressible flow of a gas obeying the ideal gas law.

Turbulent Boundary-Layer Solution Methods

It is desirable to have a turbulent boundary layer over the major portion of turbine blades. If the boundary layer is not turbulent, separation will probably occur on the blades, with a resulting decrease in their performance. Turbulent flow has irregular fluctuations (mixing or eddy motions) superimposed on the main fluid motion (see fig. 6-2). These fluctuations are so complex that closed-form solutions are not feasible at present. Yet, the mixing motion is very important, since the stresses in the fluid due to fluctuating components of velocity are often of greater magnitude than those due to the mean motion.

There are two approaches to the solution of turbulent boundary-layer flow. The first is the exact solution of the time-dependent, three-dimensional, Navier-Stokes equations. The three-dimensional equations are required, since two-dimensional calculations could never represent the stretching of eddies, which is a prime mechanism of turbulent flow. However, even the largest computers available at the present time cannot handle three-dimensional solutions of these equations on a small enough mesh to represent the fluctuating components of velocity of turbulent flow.

The second approach is to write the equations of continuity, momentum, and energy in terms of mean and fluctuating components of pressure, density, temperature, and velocity. In this approach, the time average of the u component of velocity, for example, is denoted by \bar{u} and the velocity of fluctuation by u' . So the velocities, density, pressure, and temperature are written as follows:

$$u = \bar{u} + u' \quad (6-36a)$$

$$v = \bar{v} + v' \quad (6-36b)$$

$$\rho = \bar{\rho} + \rho' \quad (6-36c)$$

$$p = \bar{p} + p' \quad (6-36d)$$

$$T = \bar{T} + T' \quad (6-36e)$$

The fluctuations in viscosity, thermal conductivity, and specific heat are

negligible and are not considered. So these three parameters are calculated as functions of the time-averaged value of temperature.

If the flow properties listed in equations (6-36) are substituted into the continuity, momentum, and energy equations for incompressible and compressible flow, a new set of stress terms arises in these equations. These are called the "apparent" turbulent stresses, or Reynolds stresses. They are of the form $\overline{\rho u'^2}$ and $\overline{\rho u'v'}$, where $\overline{u'v'}$ is the average over time of the product of u' and v' . These new terms in the equations add additional unknowns to the boundary-layer problem for which additional equations are not presently available. For this reason, empirical expressions or approximations are substituted for the Reynolds stress terms before the turbulent boundary-layer equations can be solved.

Turbulent Incompressible Boundary Layer

Substituting the relations of equations (6-36) into equations (6-10), (6-11), and (6-12), and then performing an order-of-magnitude analysis yields the following equations for turbulent, incompressible, boundary-layer flow:

$$\rho \bar{u} \frac{\partial \bar{u}}{\partial x} + \rho \bar{v} \frac{\partial \bar{u}}{\partial y} = -g \frac{d\bar{p}}{dx} + \frac{\partial}{\partial y} \left(\mu \frac{\partial \bar{u}}{\partial y} - \overline{\rho u'v'} \right) \quad (6-37)$$

$$\frac{\partial \bar{u}}{\partial x} + \frac{\partial \bar{v}}{\partial y} = 0 \quad (6-38)$$

These equations are analogous to equations (6-23) and (6-24) for laminar flow. Notice, however, the presence of the Reynolds stress term in the momentum equation. This adds a new unknown ($\overline{u'v'}$) to the original two (\bar{u} and \bar{v}), thereby making three unknowns with only two equations.

Turbulent Compressible Boundary Layer

Substituting the relations of equations (6-36) into equations (6-27), (6-28), (6-29), (6-32), and (6-33) and then performing an order-of-magnitude analysis yields the following equations for turbulent, compressible, boundary-layer flow:

$$\frac{\partial(\bar{\rho}\bar{u})}{\partial x} + \frac{\partial(\bar{\rho}\bar{v})}{\partial y} + \frac{\partial(\overline{\rho'v'})}{\partial y} = 0 \quad (6-39)$$

$$\bar{\rho}\bar{u} \frac{\partial \bar{u}}{\partial x} + \bar{\rho}\bar{v} \frac{\partial \bar{u}}{\partial y} + \overline{\rho'v'} \frac{\partial \bar{u}}{\partial y} = -g \frac{d\bar{p}}{dx} + \frac{\partial}{\partial y} \left(\mu \frac{\partial \bar{u}}{\partial y} - \overline{\rho u'v'} \right) \quad (6-40)$$

$$\bar{p} = \bar{\rho} R \bar{T} \quad (6-41)$$

$$\bar{p}c_p \left(\bar{u} \frac{\partial \bar{T}_t}{\partial x} + \bar{v} \frac{\partial \bar{T}_t}{\partial y} \right) + c_p \bar{\rho}' v' \frac{\partial \bar{T}_t}{\partial y} = \frac{\bar{u}}{J} \frac{d\bar{p}}{dx} + \frac{\partial}{\partial y} \left(k \frac{\partial \bar{T}_t}{\partial y} \right) + \frac{1}{gJ} \frac{\partial}{\partial y} \left[\left(\mu - \frac{k}{c_p} \right) \left(\bar{u} \frac{\partial \bar{u}}{\partial y} \right) \right] - \frac{\partial}{\partial y} [c_p \bar{\rho}' (v' T')] \quad (6-42)$$

where T_t is the absolute total temperature, in K or °R, and is defined as

$$T_t = T + \frac{u^2 + v^2}{2gJc_p} \quad (6-43)$$

We have now derived the basic boundary-layer equations for two-dimensional, laminar and turbulent, incompressible and compressible boundary-layer flow. We should note at this time that this is really only the starting point as far as boundary-layer solutions are concerned. These equations are only the basis for the many, many methods which presently exist for obtaining boundary-layer solutions under various circumstances.

SOLUTION OF BOUNDARY-LAYER EQUATIONS

After velocity profiles are discussed and the important boundary-layer parameters defined, some of the solution methods will be discussed. Included will be the flat-plate, incompressible solution, as well as compressible methods.

Velocity Profiles

One of the principal results obtained from most boundary-layer solutions is a description of the velocity profile in the boundary layer along the blade surface (fig. 6-7). The velocity profile describes mathematically

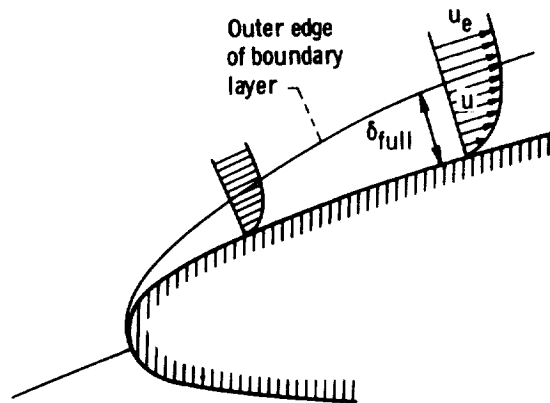


FIGURE 6-7.—Boundary-layer velocity profiles.

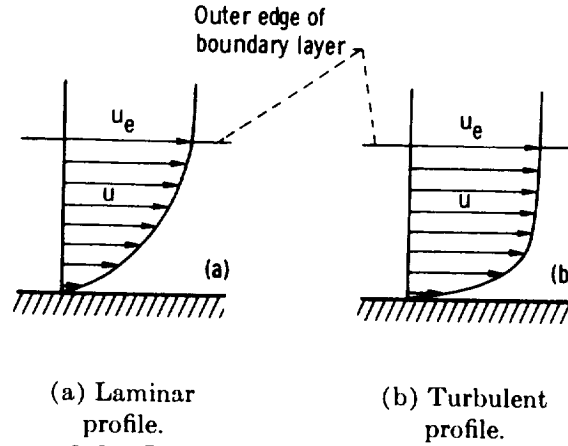


FIGURE 6-8.—Laminar and turbulent velocity profiles.

the dimensionless velocity u/u_e as a function of the dimensionless distance y/δ_{full} from the blade. The velocity u is the velocity in the boundary layer at a distance y from the surface, and the velocity u_e is the external free-stream velocity at a distance equal to the boundary-layer thickness, δ_{full} , from the surface. Alternately, δ_{full} is often defined as that distance from the blade where the velocity differs by 1 percent from the external velocity, u_e .

Velocity profiles for laminar flow (fig. 6-8(a)) tend to be parabolic in shape, while those for turbulent flow are blunted (fig. 6-8(b)). A commonly used mathematical expression for u/u_e in laminar flow is that originated by Pohlhausen (see ref. 1):

$$\frac{u}{u_e} = a \frac{y}{\delta_{full}} + b \left(\frac{y}{\delta_{full}} \right)^2 + c \left(\frac{y}{\delta_{full}} \right)^3 + d \left(\frac{y}{\delta_{full}} \right)^4 \quad (6-44)$$

The constants a , b , c , and d are defined in terms of a dimensionless shape parameter

$$\lambda = \frac{\delta_{full}^2}{\mu} \frac{du_e}{dx} \quad (6-45)$$

where

$$a = 2 + \frac{\lambda}{6} \quad (6-46a)$$

$$b = -\frac{\lambda}{2} \quad (6-46b)$$

$$c = -2 + \frac{\lambda}{2} \quad (6-46c)$$

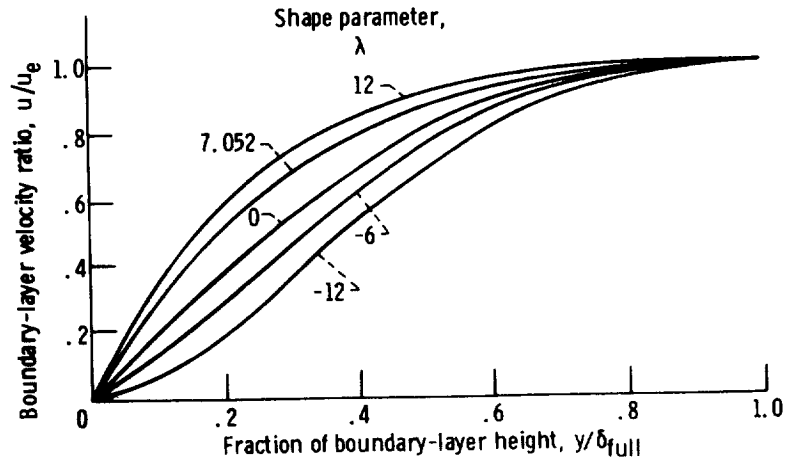


FIGURE 6-9.—Laminar velocity profiles.

$$d = 1 - \frac{\lambda}{6} \tag{6-46d}$$

Velocity profiles for various values of λ are shown in figure 6-9.

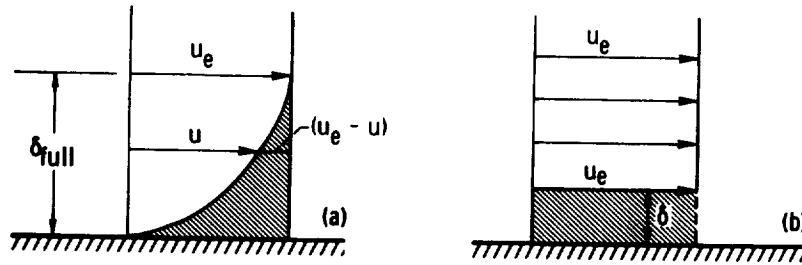
Velocity profiles for turbulent flow are often represented by the power law

$$\frac{u}{u_e} = \left(\frac{y}{\delta_{full}} \right)^{1/n} \tag{6-47}$$

Pipe-flow experiments show that the exponent n is a mild function of the Reynolds number and varies from 4 up to about 10. The value of $n=7$ is most appropriate for boundary-layer flow on a flat plate. The exponent n can be related to other boundary-layer parameters, namely the displacement thickness δ and the momentum thickness θ , which are described in the next section.

Definitions of Important Boundary-Layer Parameters

Solutions of the two-dimensional boundary-layer equations are most often obtained in terms of three important parameters. These are the displacement thickness δ , the momentum thickness θ , and the form factor H . In order to define these parameters, it is necessary to first define the thickness of the boundary layer, δ_{full} . The definition of boundary-layer thickness is rather arbitrary, since transition from the velocity inside the boundary layer to that outside it takes place asymptotically. This is of little importance, however, because the velocity in the boundary layer attains a value which is very close to the external velocity at a small distance from the wall. It is possible to define the boundary-layer thick-



(a) Actual velocity profile. (b) Equivalent profile for equal mass flow.

FIGURE 6-10.—Displacement thickness of a boundary layer.

ness as that distance from the blade where the velocity differs by 1 percent from the external velocity u_e .

The displacement thickness δ , for compressible boundary-layer flow, can be defined with the help of figure 6-10. As seen from figure 6-10(a), the decrease in mass flow within the boundary layer due to the influence of friction is given by

$$\text{Mass defect} = \int_{y=0}^{y=\delta_{full}} (\rho_e u_e - \rho u) dy \quad (6-48)$$

where ρ_e is the density, in kg/m^3 or lbf/ft^3 , in the free stream outside of the boundary layer. This integrated mass defect can be represented by a distance δ , the displacement thickness, as shown in figure 6-10(b). It is the distance by which the external potential field of flow is displaced outward as a consequence of the decrease in velocity in the boundary layer.

As figure 6-10 shows, the distance δ can be defined by the equation

$$\rho_e u_e \delta = \int_{y=0}^{y=\delta_{full}} (\rho_e u_e - \rho u) dy \quad (6-49)$$

Solving for δ gives

$$\delta = \frac{1}{\rho_e u_e} \int_{y=0}^{y=\delta_{full}} (\rho_e u_e - \rho u) dy = \int_{y=0}^{y=\delta_{full}} \left(1 - \frac{\rho u}{\rho_e u_e} \right) dy \quad (6-50)$$

The displacement thickness for incompressible flow reduces to

$$\delta = \frac{1}{u_e} \int_{y=0}^{y=\delta_{full}} (u_e - u) dy = \int_{y=0}^{y=\delta_{full}} \left(1 - \frac{u}{u_e} \right) dy \quad (6-51)$$

The loss of momentum in the boundary layer due to the presence of friction is given by

$$\text{Momentum defect} = \int_{y=0}^{y=\delta_{full}} \rho u (u_e - u) dy \quad (6-52)$$

This momentum defect from the momentum of purely potential flow can be represented by a distance θ , defined by the equation

$$\rho_e u_e^2 \theta = \int_{y=0}^{y=\delta_{full}} \rho u (u_e - u) dy \quad (6-53)$$

Solving for θ in this equation gives the definition of the momentum thickness for compressible boundary layers as

$$\theta = \frac{1}{\rho_e u_e^2} \int_{y=0}^{y=\delta_{full}} \rho u (u_e - u) dy = \int_{y=0}^{y=\delta_{full}} \frac{\rho u}{\rho_e u_e} \left(1 - \frac{u}{u_e}\right) dy \quad (6-54)$$

The momentum thickness for incompressible flow reduces to

$$\theta = \frac{1}{u_e^2} \int_{y=0}^{y=\delta_{full}} u (u_e - u) dy = \int_{y=0}^{y=\delta_{full}} \frac{u}{u_e} \left(1 - \frac{u}{u_e}\right) dy \quad (6-55)$$

The form factor H for both compressible and incompressible flow is defined as the ratio of displacement thickness to momentum thickness:

$$H = \frac{\delta}{\theta} \quad (6-56)$$

There are many other boundary-layer parameters besides δ , θ , and H for two-dimensional, and especially for three-dimensional, boundary layers. These three, however, are the principal parameters used in general boundary-layer studies.

Physical Interpretation of Separation

When separation of flow from a blade or a casing occurs, some of the retarded fluid in the boundary layer is transported away from the surface toward the main stream. When a region with an adverse pressure gradient exists along a surface, the retarded fluid particles cannot, in general, penetrate too far into the region of increased pressure because of their small kinetic energy. Thus, the boundary layer is deflected away from the surface and moves into the main stream. In general, the fluid particles behind the point of separation follow the pressure gradient and move in a direction opposite to the external stream. The point of separation is defined as the limit between forward and reverse flow in the layer in the immediate neighborhood of the wall. At separation,

$$\left(\frac{\partial u}{\partial y}\right)_{y=0} = 0 \quad (6-57)$$

Figure 6-11 illustrates separation occurring along a surface.

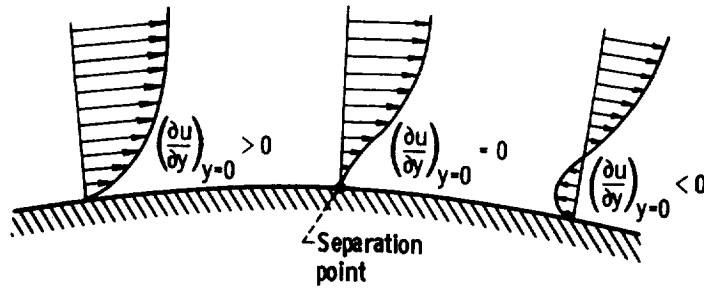


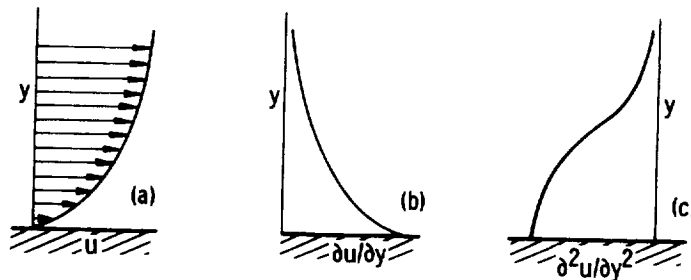
FIGURE 6-11.—Velocity gradients as flow undergoes separation.

By examining Prandtl's boundary-layer equations and considering the relation between pressure gradient dp/dx and velocity distribution $u(y)$, it is possible to infer that separation in a steady flow will occur only in the presence of an adverse pressure gradient (i.e., decelerated flow), $dp/dx > 0$. From equation (6-23), with the boundary conditions at the surface being $u = v = 0$, we have

$$\mu \left(\frac{\partial^2 u}{\partial y^2} \right)_{y=0} = \rho \frac{dp}{dx} \quad (6-58)$$

We can now relate velocity profiles to $\partial u / \partial y$, $\partial^2 u / \partial y^2$, and finally to dp/dx through equation (6-58). The equation indicates that in the immediate neighborhood of the wall, the curvature of the velocity profile, $\partial^2 u / \partial y^2$, depends only on the pressure gradient, dp/dx , and the curvature of the velocity profile at the wall changes its sign with the pressure gradient.

Figure 6-12(a) shows a velocity profile that would exist in a boundary layer subjected to a decreasing pressure. For such a profile, figure 6-12(b)



(a) Velocity profile.

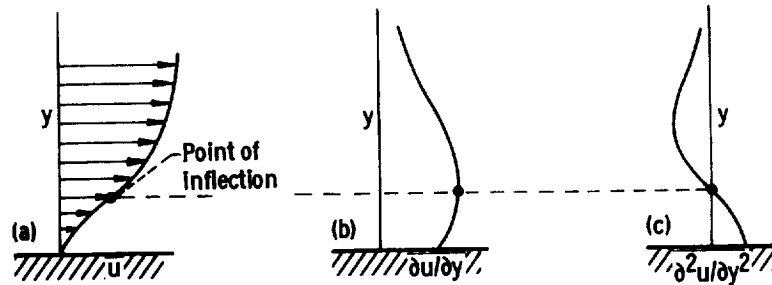
(b) Velocity gradient.

(c) Velocity-profile curvature.

FIGURE 6-12.—Velocity distribution in a boundary layer with pressure decrease.

indicates that $\partial u/\partial y$ is positive for all y and decreases as y increases. Furthermore, figure 6-12(c) indicates that $\partial^2 u/\partial y^2$, which is the slope of $\partial u/\partial y$, is negative for all y . From equation (6-58), we know that negative $\partial^2 u/\partial y^2$ corresponds to negative dp/dx . Consequently, a boundary layer subjected to a decreasing pressure (negative dp/dx) will have velocity profiles which are not indicative of impending separation (the form of fig. 6-12(a)).

Figure 6-13(a) shows a profile which would exist in a boundary layer with decelerated flow due to an increasing pressure (adverse pressure gradient). Here, figure 6-13(b) indicates that $\partial u/\partial y$ has a positive slope near the blade surface; that is, $\partial^2 u/\partial y^2$ is positive (fig. 6-13(c)). This corresponds to positive dp/dx . However, since in all cases $\partial^2 u/\partial y^2$ must be less than zero at some distance from the surface, there must exist a point for which $\partial^2 u/\partial y^2 = 0$. This is a point of inflection of the boundary-layer velocity profile. It follows that in a region of retarded potential flow



(a) Velocity profile.

(b) Velocity gradient.

(c) Velocity-profile curvature.

FIGURE 6-13.—Velocity distribution in a boundary layer with pressure increase.

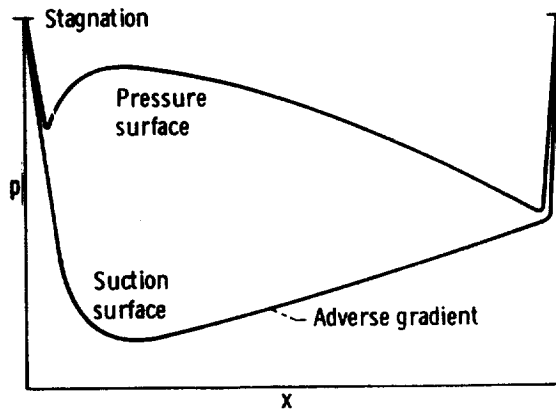


FIGURE 6-14.—Pressure distribution on a turbine blade.

(positive dp/dx), the velocity profile in the boundary layer will have a point of inflection. Since the velocity profile at the point of separation (with $\partial u/\partial y=0$ at the surface) must have a point of inflection, it follows that, with the assumptions used in deriving equation (6-23), separation can occur only when the potential flow is retarded (i.e., in regions of adverse pressure gradient).

Figure 6-14 indicates a typical pressure distribution on the surface of a turbine blade. The danger zone, as far as separation is concerned, is readily seen to be the rear portion of the suction surface, where the major part of the blade diffusion is taking place.

Laminar Incompressible Boundary Layer on a Flat Plate

Prandtl's boundary-layer theory was first reported in 1904 in Germany. It was later translated and published in 1928 as an NACA Technical Memorandum (ref. 3). The first mathematical solution of Prandtl's equations to be published was the flat-plate solution of Blasius in 1908. This German work was also later translated by NACA (ref. 4).

On a flat plate with steady flow at zero incidence, the velocity from the potential solution is constant. Therefore, $p(x)$ is constant and $dp/dx=0$. The boundary-layer equations, therefore, reduce to

$$u \frac{\partial u}{\partial x} + v \frac{\partial u}{\partial y} = \nu \frac{\partial^2 u}{\partial y^2} \quad (6-59)$$

where ν is the kinematic viscosity μ/ρ , in m^2/sec or ft^2/sec , and

$$\frac{\partial u}{\partial x} + \frac{\partial v}{\partial y} = 0 \quad (6-60)$$

The following are the boundary conditions:

$$\left. \begin{array}{ll} u=v=0 & \text{at } y=0 \\ u=u_\infty & \text{at } y=\infty \end{array} \right\} \quad (6-61)$$

With the use of a stream function ψ , Blasius transformed the partial differential equation (6-59) into the following ordinary differential equation:

$$f \frac{d^2 f}{dy^2} + 2 \frac{d^3 f}{dy^3} = 0 \quad (6-62)$$

where f is a normalized stream function

$$f(\eta) = \frac{\psi}{\sqrt{\nu x u_\infty}} \quad (6-63)$$

which depends on the dimensionless y -coordinate, η , where

$$\eta = \frac{y}{\sqrt{\frac{\nu x}{u_e}}} \quad (6-64)$$

This equation has the following boundary conditions:

$$\left. \begin{aligned} f = \frac{df}{dy} = 0 & \quad \text{at } \eta = 0 \\ \frac{df}{dy} = 1 & \quad \text{at } \eta = \infty \end{aligned} \right\} \quad (6-65)$$

Equation (6-62) cannot be solved exactly. Blasius obtained an approximate solution in the form of a power series expansion about $\eta=0$ and an asymptotic expansion for $\eta = \infty$, the two solutions being joined at a suitable point. More recently, Howarth (ref. 5) solved the Blasius equation (6-62) with a high degree of accuracy, and provided tabular values for f , df/dy , and d^2f/dy^2 as functions of η . Since $df/dy = u/u_e$, the solution gives the velocity profile of figure 6-15. This profile possesses a very small curvature at the wall and turns rather abruptly further from it in order

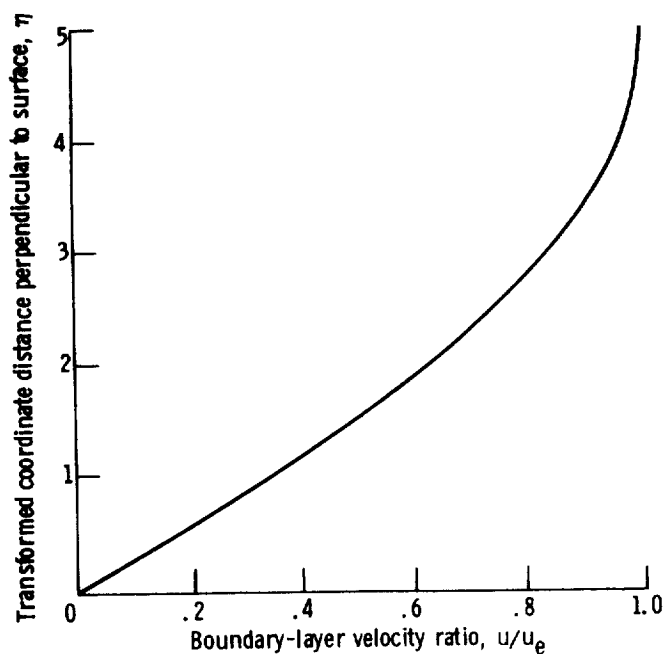


FIGURE 6-15.—Blasius-Howarth velocity profile for flow on a flat plate.

to reach the asymptotic value. At the wall itself, the curve has a point of inflection, since for $y=0$, $\partial^2 u / \partial y^2 = 0$.

From the order-of-magnitude analysis performed to obtain Prandtl's boundary-layer equations, we had the relation

$$\epsilon^2 \approx \delta_{full}^2 \approx \frac{1}{Re} \quad (6-66)$$

For a semi-infinite flat plate, the Reynolds number can be expressed as

$$Re_x = \frac{u_e x}{\nu} \quad (6-67)$$

In order to make equation (6-66) dimensionally correct, we can say

$$\frac{\delta_{full}^2}{x^2} \propto \frac{1}{Re_x} \quad (6-68)$$

or

$$\delta_{full} \propto \sqrt{\frac{\nu x}{u_e}} \quad (6-69)$$

The constant of proportionality can be obtained from Howarth's numerical solution and is equal to 5. So, for a semi-infinite flat plate at zero incidence in laminar flow, we obtain the useful relation for the boundary-layer thickness

$$\delta_{full} = 5.0 \sqrt{\frac{\nu x}{u_e}} \quad (6-70)$$

With the use of Howarth's solution to the Blasius equations, the following relations for other important boundary-layer parameters for laminar flow on a flat plate can also be obtained:

$$\delta = 1.72 \sqrt{\frac{\nu x}{u_e}} \quad (6-71)$$

$$\theta = 0.664 \sqrt{\frac{\nu x}{u_e}} \quad (6-72)$$

$$\frac{g\tau_w}{\rho u_e^2} = 0.332 \sqrt{\frac{\nu}{u_e x}} = \frac{0.332}{\sqrt{Re_x}} \quad (6-73)$$

$$D = \frac{1.328}{g} b \sqrt{\mu \rho l u_e^3} \quad (6-74)$$

$$C_f = 1.328 \sqrt{\frac{\nu}{u_e l}} = \frac{1.328}{\sqrt{Re_l}} \quad (6-75)$$

where

- τ_w shear stress on the surface, N/m²; lbf/ft²
 D total drag on both sides of flat plate, N; lbf
 b width of flat plate, m; ft
 l length of flat plate, m; ft
 C_f dimensionless drag or skin friction coefficient for flat plate
 Re_l Reynolds number based on plate length l

It should be noted that all of these relations are valid only for laminar flow; that is, they are valid only where $Re_l < 10^6$, a value that is indicative of laminar flow over the entire length of the plate. For $Re_l > 10^6$, transition to turbulent boundary layer will probably occur, and the expressions in equations (6-71) to (6-75) will be valid only from the leading edge of the plate to the transition point. If transition to turbulent boundary layer does occur, then the drag will be larger than that calculated by equation (6-74).

Integral Methods for Solving the Laminar-Boundary-Layer Equations

The two principal means of solving the laminar-boundary-layer equations are by integral methods and by finite-difference methods. Both means provide approximate solutions, since exact solutions are extremely cumbersome.

Integral methods are based on von Kármán's momentum integral formula. Von Kármán's original work was published in 1912 in Germany and was later translated by NACA (ref. 6). Von Kármán realized that it was not necessary to satisfy the boundary-layer equations for every fluid particle. Instead, he satisfied the boundary-layer equations close to the wall and in the region where external flow is approached by satisfying the boundary conditions. In the remaining region of fluid in the boundary layer, only a mean over the differential equation is satisfied. Such a mean is obtained from the momentum equation (eq. (6-23) or (6-30)) by integration over the boundary-layer thickness. If equations (6-23) and (6-30) are integrated from $y=0$ to $y=\delta_{fu}$, and if the definitions of displacement thickness (eq. (6-50)) and momentum thickness (eq. (6-54)) are introduced, the following equations result. For laminar, incompressible flow,

$$u_e^2 \frac{d\theta}{dx} + (2\theta + \delta) u_e \frac{du_e}{dx} = \frac{g\tau_w}{\rho} \quad (6-76)$$

For laminar, compressible flow,

$$u_e^2 \frac{d\theta}{dx} + (2\theta + \delta - M_e^2 \theta) u_e \frac{du_e}{dx} = \frac{g\tau_w}{\rho_e} \quad (6-77)$$

where the subscript e denotes conditions at the outer edge of the boundary layer.

Equation (6-76) or (6-77) leads to an ordinary differential equation for the boundary-layer thickness, provided that a suitable form is assumed for the velocity profile, u/u_e . This allows us to calculate the displacement thickness, δ , the momentum thickness, θ , and the shearing stress at the wall, τ_w . Pohlhausen was the first to use equation (6-76) to obtain a solution for incompressible boundary layers. His work was published in 1921 (refs. 7 and 1). The velocity profile assumed by Pohlhausen was discussed earlier in this chapter, under "Velocity Profiles." Although Pohlhausen's solution is probably the simplest, it is known to give poor results in regions of rising pressure. As a result, various authors have tried to improve and extend his method by assuming different families of velocity distributions.

A famous work among those which followed Pohlhausen's was that of Thwaites (ref. 8). Thwaites collected and compared all known velocity distributions from exact and approximate solutions for laminar incompressible flow. Thwaites' method does not require the solution of ordinary differential equations. He relates the wall shear, its derivative at the wall, and the form factor to one another without specifying a type of velocity profile. To do this, nondimensional forms of these quantities were defined and evaluated with the use of exact solutions for the laminar boundary layer. It developed that a nearly universal relation existed among these quantities for favorable pressure gradients. For adverse gradients, Thwaites selected a single representative relation. A unique correlation was chosen that reduced the solution of an incompressible problem to the evaluation of a single integral. Thwaites' method was extended to compressible fluids by Rott and Crabtree (ref. 9). They recognized that when heat transfer is negligible, and the Prandtl number is equal to 1, a transformation proposed by Stewartson (ref. 10) could be used to relate compressible to incompressible boundary-layer solutions.

One of the best integral methods to appear to date for the solution of laminar boundary layers is that of Cohen and Reshotko (refs. 11 and 12). Their method applies to compressible or incompressible flow over two-dimensional or axially symmetric surfaces. It handles arbitrary free-stream pressure distribution and performs well in areas of adverse pressure gradient. A surface temperature level may be specified, and heat transfer is calculated. Cohen and Reshotko's method is based on Thwaites' correlation concept. Stewartson's transformation (ref. 10) is first applied

to Prandtl's equations. The resulting nonlinear, first-order differential equations are expressed in terms of dimensionless parameters related to the wall shear, the surface heat transfer, and the transformed free-stream velocity. Then Thwaites' concept of a unique interdependence of these parameters is assumed. The evaluation of these quantities is then carried out by utilizing the exact solutions of reference 11. With the resulting relations, methods are derived for the calculation of all the important boundary-layer parameters. In 1960, Luxton and Young published a method (ref. 13) which is as general as Cohen and Reshotko's, but which allows the Prandtl number to have values slightly different from 1.

Finite-Difference Methods for Solving the Laminar-Boundary-Layer Equations

Finite-difference methods for solving the boundary-layer equations have recently come into prominence because of the development of digital computers. Smith and Clutter have done a considerable amount of work in developing this technique (refs. 14 and 15). Another recent reference of interest is that of Krause (ref. 16). These methods give very good results with relatively short running times on the computer.

Eddy-Viscosity and Mixing-Length Concepts in Turbulent Boundary-Layer Flow

Before referencing any of the current methods for solving turbulent boundary-layer flow, the concepts of "eddy viscosity" and "mixing length" should be discussed. These approximation concepts have been used in many of the methods developed to date to relate the Reynolds stresses produced by the mixing motion to the mean values of velocity components. By this means, the Reynolds stresses are given a mathematical form which, upon substitution into the governing equations, leads to differential equations containing only mean values of density, velocity, and pressure. These transformed differential equations constitute the starting point for the calculation of the mean boundary-layer flow.

Boussinesq first worked on this problem in 1877. In analogy with the coefficient of viscosity in Stokes' law for laminar flow

$$\tau_t = \frac{\mu}{g} \frac{\partial u}{\partial y} \quad (6-78)$$

where τ_t is the laminar shear stress, in N/m² or lbf/ft², he introduced a mixing coefficient, A_r , for the Reynolds stress in turbulent flow by putting

$$\tau_t = \frac{A_r}{g} \frac{\partial \bar{u}}{\partial y} \quad (6-79)$$

where τ_t is the turbulent shear stress, in N/m² or lbf/ft². In 1880, Reynolds introduced the concept of eddy, or virtual, viscosity, ϵ , where

$$\epsilon = \frac{A_r}{\rho} \quad (6-80)$$

Thus, the eddy viscosity is analogous to the kinematic viscosity $\nu = \mu/\rho$. Turbulent stress can then be expressed as

$$\tau_t = \frac{\rho}{g} \epsilon \frac{\partial \bar{u}}{\partial y} = -\frac{\rho}{g} \overline{u'v'} \quad (6-81)$$

With the use of this concept, terms in equations (6-37) and (6-40) such as

$$\frac{\partial}{\partial y} \left(\mu \frac{\partial \bar{u}}{\partial y} - \bar{\rho} \overline{u'v'} \right)$$

can be written as

$$\frac{\partial}{\partial y} \left[(\mu + A_r) \frac{\partial \bar{u}}{\partial y} \right]$$

A similar concept can be applied to the energy equation where an eddy, or a virtual, conductivity can be defined. The difficulty with applying the eddy-viscosity method is that A_r , and hence ϵ depend on velocity. It is, therefore, necessary to find empirical relations between these coefficients and the mean velocity.

In 1925, Prandtl introduced a completely different approximation for the Reynolds stresses. His argument is called Prandtl's mixing-length hypothesis, since the mixing length is somewhat analogous to the mean free path in the kinetic theory of gases. The main difference is that kinetic theory concerns itself with the microscopic motion of particles, whereas Prandtl's concept deals with the macroscopic motion of large clusters of fluid particles. Deriving Prandtl's expression for shear stress requires a good deal of discussion of his physical model of turbulent flow, all of which is contained in reference 1. His final expression is

$$\tau_t = \frac{\rho}{g} l^2 \left| \frac{d\bar{u}}{dy} \right| \frac{d\bar{u}}{dy} = -\frac{\rho}{g} \overline{u'v'} \quad (6-82)$$

where l is the mixing length, in m or ft.

On comparing Prandtl's expression (eq. (6-82)) with that of Boussinesq (eq. (6-81)), it appears that little has been gained. The unknown eddy viscosity ϵ of the first expression has merely been replaced by the unknown mixing length l of the second expression. However, Prandtl's equation (6-82) is generally more suitable for the calculation of turbulent motion than is equation (6-81). Turbulent drag is roughly proportional to the

square of velocity, and the same result is obtained from (6-82) if the mixing length is assumed to be independent of the magnitude of velocity. So, mixing length is a purely local function, although we cannot say it is a property of the fluid. It is far simpler to make assumptions about the mixing length l than about the eddy viscosity ϵ , and this constitutes the superiority of Prandtl's expression over that of Boussinesq.

Integral Methods for Solving the Turbulent Boundary-Layer Equations

Just as with the laminar-boundary-layer equations, there are both integral methods and finite-difference methods for solving the turbulent boundary-layer equations. Both of these provide approximate solutions, since exact solutions for turbulent flow are now impossible.

Gruschwitz was the first to propose a method for solving the equations for an incompressible turbulent boundary layer. His work was published in Germany in 1931. A rash of works followed, most of them making improvements to the calculational technique and empirical data used by Gruschwitz. Ludwig and Tillmann, whose work was published in Germany in 1949 and was translated by NACA in 1950 (ref. 17), proposed an empirical relation for the skin-friction term in the momentum integral equation. This relation is still used in many current methods. Stewartson's transformations (ref. 10) are likewise used in many methods for solving the turbulent-boundary-layer equations.

Maskell, in 1951 (ref. 18), proposed an improved method for incompressible turbulent boundary layers. He replaced the momentum equation by an empirically determined approximation which is directly integrable and thus determines the momentum thickness. A profile parameter is obtained from an empirical auxiliary differential equation. The Ludwig-Tillmann skin-friction formula is used to calculate the skin-friction distribution and to determine a separation point for flows with adverse pressure gradient.

Truckenbrodt, whose work was published in Germany in 1952 and was translated by NACA in 1955 (ref. 19), proposed solutions for both laminar and turbulent incompressible boundary-layer flows. The method is simple and, like Maskell's method, does not use the momentum integral equation. It applies to both two-dimensional and rotationally symmetrical flows. Because of its simplicity and relatively accurate results, Truckenbrodt's method is still used for incompressible turbulent boundary layers.

Compressible turbulent boundary layers were first treated adequately with the use of integral methods by Reshotko and Tucker in 1957 (ref. 20). Prior to their work, the Kármán momentum integral equation had been utilized with an assumed boundary-layer velocity profile, usually the power law, and one of several empirical skin-friction relations. When

pressure gradient was present, an auxiliary equation, usually the moment-of-momentum equation, was used. (This equation is obtained by multiplying the integrand of the momentum integral equation by a distance normal to the surface and then integrating with respect to that distance.) The momentum integral equation and the auxiliary equation were then solved simultaneously.

Reshotko and Tucker's method, applicable to compressible flow with heat transfer and pressure gradient, also uses the momentum and moment-of-momentum integral equations. These are expressed in incompressible form and are uncoupled with the use of Stewartson's transformation (ref. 10) and the results of Maskell (ref. 18). The Ludwig-Tillmann skin-friction relation is used in a form suitable for compressible flow with heat transfer through application of Eckert's reference-enthalpy concept (ref. 21). An approximation for the shear-stress distribution through the boundary layer and the power-law velocity profile are used to simplify the moment-of-momentum equation. Separation is located as the point where the skin friction, when extrapolated, becomes zero. This method, until several years ago, was the best available for compressible turbulent boundary layers. It is still widely used in many computer programs today.

One of the best integral methods available today for compressible turbulent boundary layers is that of Sasman and Cresci (ref. 22). It is simply an extension of the Reshotko-Tucker method. It uses somewhat the same analysis, but no attempt is made to uncouple the momentum and moment-of-momentum integral equations. These equations are solved simultaneously after introduction of boundary-layer shear-stress distributions obtained from recent numerical results of equilibrium turbulent boundary-layer analysis. The Sasman-Cresci analysis is better than that of Reshotko-Tucker at predicting separation in regions of adverse pressure gradient. McNally (ref. 23) has developed a computer program based on the Cohen-Reshotko (refs. 11 and 12) and Sasman-Cresci (ref. 22) techniques. An additional source of information on compressible turbulent boundary-layer analysis is the work of Herring and Mellor (ref. 24).

Finite-Difference Methods for Solving the Turbulent Boundary-Layer Equations

Finite-difference methods for solving the turbulent boundary-layer equations have recently begun to appear. Cebeci and Smith have done a large portion of this work to date (refs. 25, 26, and 27). Bradshaw, Ferriss, and Atwell have also developed methods for the turbulent boundary layer (refs. 28 and 29) based on the use of the turbulent energy equation. Patankar and Spalding have developed still another method for handling the turbulent boundary-layer equations (refs. 30 and 31). A great deal of work is going on in this field at the present time, and no method is yet

clearly superior to any of the others. Two relatively recent publications (refs. 32 and 33) compare many of the most prominent methods, both integral and finite difference, for solving the turbulent boundary layer.

CONCLUDING REMARKS

The selection of a method of solution suitable to a particular boundary-layer problem requires some familiarity with the various methods available. This can be achieved by studying some of the more recent references that have been mentioned herein. The present discussion of the methods of solution has been intended to show the historical development of solution techniques, the variety of methods available, and the complexity of the whole boundary-layer problem, especially where turbulent flows are involved.

REFERENCES

1. SCHLICHTING, HERMANN (J. KESTIN, TRANS.): *Boundary Layer Theory*. McGraw-Hill Book Co., Inc., any edition.
2. BIRD, R. BYRON; STEWART, WARREN E.; AND LIGHTFOOT, EDWIN N.: *Transport Phenomena*. John Wiley & Sons, Inc., 1960.
3. PRANDTL, L.: *Motion of Fluids with Very Little Viscosity*. NACA TM 452, 1928.
4. BLASIUS, H.: *The Boundary Layers in Fluids with Little Friction*. NACA TM 1256, 1950.
5. HOWARTH, L.: *On the Solution of the Laminar Boundary Layer Equations*. Proc. Roy. Soc. (London), Ser. A, vol. 164, no. 919, Feb. 18, 1938, pp. 547-579.
6. VON KÁRMÁN, TH: *On Laminar and Turbulent Friction*. NACA TM 1092, 1946.
7. POHLHAUSEN, K.: *Approximate Integration of the Differential Equation of the Limit Surface of Laminar Motion*. Zeit. f. Math. Mech., vol. 1, Aug. 1921, pp. 252-268.
8. THWAITES, B.: *Approximate Calculation of the Laminar Boundary Layer*. Aeronaut. Quart., vol. 1, Nov. 1949, pp. 245-280.
9. ROTT, NICHOLAS; AND CRABTREE, L. F.: *Simplified Laminar Boundary-Layer Calculations for Bodies of Revolution and for Yawed Wings*. J. Aeron. Sci., vol. 19, no. 8, Aug. 1952, pp. 553-565.
10. STEWARTSON, K.: *Correlated Incompressible and Compressible Boundary Layers*. Proc. Roy. Soc. (London), Ser. A, vol. 200, no. 1060, Dec. 22, 1949, pp. 84-100.
11. COHEN, CLARENCE B.; AND RESHOTKO, ELI: *Similar Solutions for the Compressible Laminar Boundary Layer with Heat Transfer and Pressure Gradient*. NACA TR 1293, 1956.
12. COHEN, CLARENCE B.; AND RESHOTKO, ELI: *The Compressible Laminar Boundary Layer with Heat Transfer and Arbitrary Pressure Gradient*. NACA TR 1294, 1956.
13. LUXTON, R. E.; AND YOUNG, A. D.: *Generalized Methods for the Calculation of the Laminar Compressible Boundary-Layer Characteristics with Heat Transfer and Non-Uniform Pressure Distribution*. R&M-3233, Aeronautical Research Council, Gt. Britain, 1962.

14. SMITH, A. M. O.; AND CLUTTER, DARWIN W.: Solution of the Incompressible Laminar Boundary-Layer Equations. AIAA J., vol. 1, no. 9, Sept. 1963, pp. 2062-2071.
15. SMITH, A. M. O.; AND CLUTTER, DARWIN W.: Machine Calculation of Compressible Laminar Boundary Layers. AIAA J., vol. 3, no. 4, Apr. 1965, pp. 639-647.
16. KRAUSE, EGON: Numerical Solution of the Boundary-Layer Equations. AIAA J., vol. 5, no. 7, July 1967, pp. 1231-1237.
17. LUDWIG, HUBERT; AND TILLMANN, W.: Investigations of the Wall-Shearing Stress in Turbulent Boundary Layers. NACA TM 1285, 1950.
18. MASKELL, E. C.: Approximate Calculation of the Turbulent Boundary Layer in Two-Dimensional Incompressible Flow. Rep. AERO 2443, Royal Aircraft Establishment, Nov. 1951.
19. TRUCKENBRODT, E.: A Method of Quadrature for Calculation of the Laminar and Turbulent Boundary Layer in Case of Plane and Rotationally Symmetrical Flow. NACA TM 1379, 1955.
20. RESHOTKO, ELI; AND TUCKER, MAURICE: Approximate Calculation of the Compressible Turbulent Boundary Layer with Heat Transfer and Arbitrary Pressure Gradient. NACA TN 4154, 1957.
21. ECKERT, E. R. G.: Engineering Relations for Friction and Heat Transfer to Surfaces in High Velocity Flow. J. Aeron. Sci., vol. 22, no. 8, Aug. 1955, pp. 585-587.
22. SASMAN, PHILIP K.; AND CRESCI, ROBERT J.: Compressible Turbulent Boundary Layer with Pressure Gradient and Heat Transfer. AIAA J., vol. 4, no. 1, Jan. 1966, pp. 19-25.
23. McNALLY, WILLIAM D.: FORTRAN Program for Calculating Compressible Laminar and Turbulent Boundary Layers in Arbitrary Pressure Gradients. NASA TN D-5681, 1970.
24. HERRING, H. JAMES; AND MELLOR, G. L.: A Method of Calculating Compressible Turbulent Boundary Layers. NASA CR-1144, 1968.
25. CEBECI, T.; SMITH, A. M. O.; AND MOSINSKIS, G.: Solution of the Incompressible Turbulent Boundary-Layer Equations with Heat Transfer. J. Heat Transfer, vol. 92, no. 1, Feb. 1970, pp. 133-143.
26. SMITH, A. M. O.; AND CEBECI, T.: Numerical Solution of the Turbulent-Boundary-Layer Equations. Rep. DAC-33735, Douglas Aircraft Co. (AD-656430), May 1967.
27. CEBECI, T.; AND SMITH, A. M. O.: A Finite-Difference Method for Calculating Compressible Laminar and Turbulent Boundary Layers. J. Basic Eng., vol. 92, no. 3, Sept. 1970, pp. 523-535.
28. BRADSHAW, P.; FERRISS, D. H.; AND ATWELL, N. P.: Calculation of Boundary-Layer Development Using the Turbulent Energy Equation. J. Fluid Mech., vol. 28, pt. 3, May 26, 1967, pp. 593-616.
29. BRADSHAW, P.: Calculation of Boundary-Layer Development Using the Turbulent Energy Equation. IX: Summary. Rep. NPL-Aero-1287, National Physical Lab., Jan. 30, 1969.
30. PATANKAR, S. V.; AND SPALDING, D. B.: A Finite-Difference Procedure for Solving the Equations of the Two-Dimensional Boundary Layer. Int. J. Heat Mass Transfer, vol. 10, no. 10, Oct. 1967, pp. 1389-1411.
31. PATANKAR, S. V.; AND SPALDING, D. B.: Heat and Mass Transfer in Boundary Layers. C.R.C. Press, 1967.
32. COLES, D. E.; AND HIRST, E. A., EDS.: Proceedings, Computation of Turbulent Boundary Layers—1968, AFOSR-IFP-Stanford Conference. Stanford Univ. Press, 1969.

TURBINE DESIGN AND APPLICATION

- 33. BERTRAM, MITCHEL H., ED.: Compressible Turbulent Boundary Layers. NASA SP-216, 1969.**

SYMBOLS

A_t	turbulent flow mixing coefficient, (N) (sec)/m ² ; lbm/(ft) (sec)
a	constant in eq. (6-44)
b	{ width of flat plate, m; ft constant in eq. (6-44)
C_f	skin-friction coefficient for a flat plate
c	constant in eq. (6-44)
c_p	specific heat at constant pressure, J/(kg) (K); Btu/(lbm) (°R)
D	total drag on flat plate, N; lbf
d	constant in eq. (6-44)
f	Blasius dimensionless stream function defined by eq. (6-63)
\mathbf{f}	general body force vector, N/kg; lbf/lbm
f_x	component of body force \mathbf{f} in x -direction, N/kg; lbf/lbm
f_y	component of body force \mathbf{f} in y -direction, N/kg; lbf/lbm
f_z	component of body force \mathbf{f} in z -direction, N/kg; lbf/lbm
g	conversion constant, 1; 32.17 (lbm) (ft)/(lbf) (sec ²)
H	form factor, defined by eq. (6-56)
\mathbf{i}	unit vector in the x -direction
J	conversion constant, 1; 778 (ft) (lbf)/Btu
\mathbf{j}	unit vector in the y -direction
k	thermal conductivity, W/(m) (K); Btu/(sec) (ft) (°R)
\mathbf{k}	unit vector in the z -direction
L	characteristic length (e.g., the blade chord), m; ft
l	{ Prandtl mixing length, m; ft length of flat plate, m; ft
M_∞	Mach number external to the boundary layer
n	exponent on the turbulent velocity profile, eq. (6-47)
P	dimensionless pressure, defined by eq. (6-13e)
p	static pressure, N/m ² ; lbf/ft ²
R	gas constant, J/(kg) (K); (ft) (lbf)/(lbm) (°R)
Re	Reynolds number based on L and U_0 , as defined by eq. (6-13f)
Re_l	Reynolds number based on l , as defined in eq. (6-75)
Re_x	Reynolds number based on x , as defined by eq. (6-67)
r	radius of curvature of blade surface, m; ft
S	constant in eq. (6-25), K; °R
T	absolute static temperature, K; °R
T_t	absolute total temperature, K; °R
T_0	reference temperature used in eq. (6-25), K; °R
t	time, sec
U	dimensionless velocity in x -direction, defined by eq. (6-13c)
U_0	free-stream velocity upstream of blade, m/sec; ft/sec
u	component of general velocity vector \mathbf{u} in the x -direction, m/sec; ft/sec

TURBINE DESIGN AND APPLICATION

\mathbf{u}	general velocity vector, m/sec; ft/sec
u_∞	free-stream velocity at the outer edge of the boundary layer, m/sec; ft/sec
V	dimensionless velocity in y -direction, defined by eq. (6-13d)
v	component of general velocity vector \mathbf{u} in the y -direction, m/sec; ft/sec
w	component of general velocity vector \mathbf{u} in the z -direction, m/sec; ft/sec
X	dimensionless x -coordinate, defined by eq. (6-13a)
x	$\left\{ \begin{array}{l} x\text{-coordinate, m; ft} \\ \text{coordinate parallel to boundary surface, m; ft} \end{array} \right.$
Y	dimensionless y -coordinate, defined by eq. (6-13b)
y	$\left\{ \begin{array}{l} y\text{-coordinate, m; ft} \\ \text{coordinate perpendicular to boundary surface, m; ft} \end{array} \right.$
z	z -coordinate, m; ft
δ	displacement thickness, m; ft
$\delta_{f,u,l}$	boundary-layer thickness, m; ft
ϵ	$\left\{ \begin{array}{l} \text{eddy viscosity defined by eq. (6-80), m}^2/\text{sec; ft}^2/\text{sec} \\ \text{a dimensionless quantity much less than 1} \end{array} \right.$
η	Blasius transformed y -coordinate defined by eq. (6-64)
θ	momentum thickness, m; ft
λ	dimensionless shape parameter defined by eq. (6-45)
μ	dynamic viscosity, (N)(sec)/m ² ; lbm/(ft)(sec)
μ_0	dynamic viscosity at reference temperature T_0 , (N)(sec)/m ² ; lbm/(ft)(sec)
ν	kinematic viscosity, m ² /sec; ft ² /sec
ρ	density, kg/m ³ ; lbm/ft ³
ρ_∞	free-stream density external to the boundary layer, kg/m ³ ; lbm/ft ³
τ_l	laminar shear stress, N/m ² ; lbf/ft ²
τ_t	turbulent shear stress, N/m ² ; lbf/ft ²
τ_w	shear stress at the wall, N/m ² ; lbf/ft ²
φ	function defined by eq. (6-34)
ψ	Blasius stream function, m ² /sec; ft ² /sec
ω	constant in eq. (6-26)

Superscripts:

—	time average
'	fluctuating component

CHAPTER 7

Boundary-Layer Losses

By Herman W. Prust, Jr.

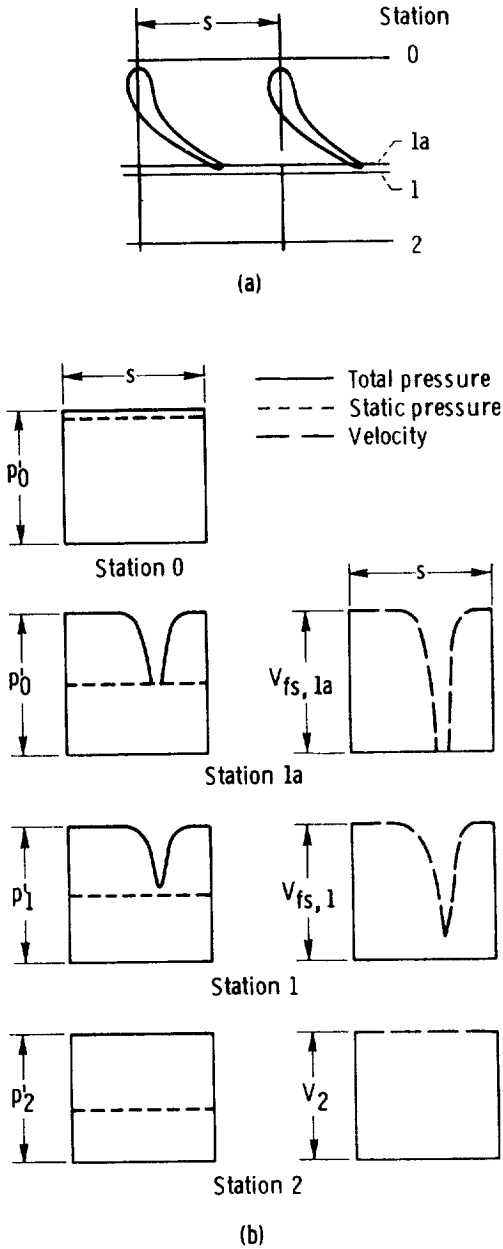
The primary cause of losses in a turbine is the boundary layer that builds up on the blade and end-wall surfaces. In particular, these losses are the friction loss resulting from the flow of the viscous fluid over the surfaces, the pressure-drag loss resulting from the flow of fluid past the blade trailing edge, and the loss downstream of the blades resulting from the mixing of the low-velocity boundary-layer fluid with the high-velocity free-stream fluid. Chapter 6 presented an introduction to boundary-layer theory, by means of which the surface boundary-layer buildup can be analytically described. This chapter covers analytical and experimental methods for determining the friction, trailing-edge, and mixing losses associated with the boundary layer. The theory presented herein refers primarily to two-dimensional blade-section boundary layers. Methods for obtaining three-dimensional blade plus end-wall losses from the two-dimensional results are also discussed.

A fundamental objective in blade-row design is to minimize the energy loss resulting from the flow of fluid through the blade row. Therefore, the final expressions for loss developed in this chapter are in terms of kinetic-energy loss coefficients. These coefficients express the loss in fluid kinetic energy as a fractional part of the ideal kinetic energy of the actual flow through the blade row. Efficiency based on kinetic energy can be obtained by subtracting these coefficients from unity, and this is consistent with the blade-row efficiency definition used in chapter 2.

Before proceeding with the discussion of boundary-layer parameters and loss coefficients, the blade-row station locations and associated pressure and velocity distributions will be introduced with the aid of figure 7-1. These pressure and velocity distributions and the associated dis-

cussion refer to an attached boundary layer only. A separated boundary layer, with its associated reversal of flow at the surface, is thicker, yields a higher loss, and cannot be analyzed in the same manner, if at all.

Figure 7-1(a) indicates the four station locations that will be referred



(a) Station locations.

(b) Pressure and velocity distributions.

FIGURE 7-1.—Station locations and associated pressure and velocity distributions.

to in this chapter. Station 0 represents the inlet to the blade row. At this station, a uniform total pressure p_0' is assumed, as indicated in figure 7-1(b). Station $1a$ is just within the trailing edge of the blade. The boundary layers developed on the blade surfaces result in velocity and pressure profiles as shown in figure 7-1(b). Velocity varies from the free-stream value $V_{fs,1a}$ to zero at the blade surfaces. There is, of course, no flow through the region of the solid trailing edge. Total pressure varies from the free-stream value $p'_{fs,1a} = p_0'$ to the static pressure p_{1a} at the blade surfaces. This static pressure is assumed constant across station $1a$, as is the flow angle α_{1a} . At station $1a$, only the surface friction loss has occurred.

Station 1 is just beyond the blade trailing edge, where the boundary-layer fluid has filled the void, but where little mixing with the free stream has occurred. This is indicated in figure 1(b) by the station-1 profiles showing flow throughout the entire wake region. Here too, static pressure and flow angle are assumed constant across the station. Between stations $1a$ and 1, the trailing-edge loss occurs. Station 2 is located at a distance sufficiently downstream of the blade row that complete mixing, with the associated mixing loss, has taken place. The velocity and total-pressure profiles are again uniform.

In order to simplify analysis and discussion, a number of variables have been assumed constant across the various stations. Uniformity of inlet conditions is a universal convenience that usually can be approached in component tests but seldom exists in actual applications. Experiments have shown that static pressure and flow angle do vary somewhat across both free stream and boundary layer at stations $1a$ and 1. In some instances, which will be later identified, this variation can be accounted for. Although some downstream mixing of the flow does take place, a completely uniform downstream state is merely a hypothetical convenience.

BOUNDARY-LAYER PARAMETERS

When a real fluid flows over a surface, a loss results due to both friction between the fluid and the surface and friction between the layers of fluid in the region adjacent to the surface. As shown by figure 7-2, the fluid velocity in the boundary-layer region varies from zero velocity on the surface to free-stream velocity V_{fs} at the full boundary-layer height δ_{full} . To describe the losses in flow, momentum, and energy resulting from the presence of the boundary layer, certain parameters are used. Some of these (displacement thickness, momentum thickness, form factor) were introduced in the last chapter and will be reviewed here; in addition, others specifically used for obtaining the desired kinetic-energy coefficients will be introduced and defined.

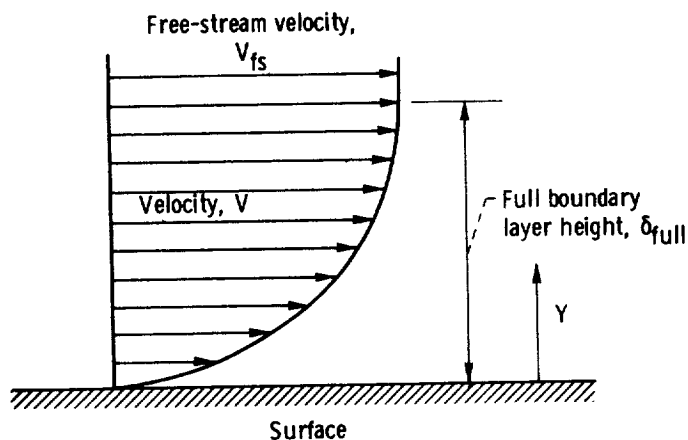


FIGURE 7-2.—Typical boundary-layer velocity profile.

The displacement thickness δ , which is indicative of the loss in mass flow, is defined by

$$\delta(\rho V)_{fs} = \int_0^{\delta_{full}} (\rho V)_{fs} dY - \int_0^{\delta_{full}} (\rho V) dY \quad (7-1)$$

where

- δ displacement thickness, m; ft
- δ_{full} boundary-layer thickness, m; ft
- V fluid velocity, m/sec; ft/sec
- ρ fluid density, kg/m³; lb/ft³
- Y distance in direction normal to boundary layer, m; ft
- $()_{fs}$ free-stream (ideal) conditions

Equation (7-1) states that the loss in mass flow of the fluid in the boundary layer is equal to the ideal flow which would pass through a length (or an area) equal to the displacement thickness. Solving for δ yields

$$\delta = \int_0^{\delta_{full}} dY - \int_0^{\delta_{full}} \frac{\rho V}{(\rho V)_{fs}} dY \quad (7-2)$$

The momentum thickness θ , which is indicative of the momentum loss, is defined by

$$\theta(\rho V^2)_{fs} = \int_0^{\delta_{full}} (\rho V V_{fs}) dY - \int_0^{\delta_{full}} \rho V^2 dY \quad (7-3)$$

where θ is the momentum thickness, in m or ft. Equation (7-3) states that the loss in momentum of the fluid in the boundary layer is equal to the

ideal momentum of the ideal flow which would pass through a length (or an area) equal to the momentum thickness. Solving for θ yields

$$\theta = \int_0^{\delta_{full}} \frac{\rho V}{(\rho V)_{fs}} dY - \int_0^{\delta_{full}} \frac{\rho V^2}{(\rho V^2)_{fs}} dY \quad (7-4)$$

The loss in kinetic energy can be similarly expressed in terms of an energy thickness defined by

$$\frac{1}{2} \psi (\rho V^3)_{fs} = \frac{1}{2} \int_0^{\delta_{full}} (\rho V V_{fs}^2) dY - \frac{1}{2} \int_0^{\delta_{full}} (\rho V^3) dY \quad (7-5)$$

where ψ is the energy thickness, in m or ft. Equation (7-5) states that the loss in kinetic energy of the fluid in the boundary layer is equal to the ideal kinetic energy of the ideal flow which would pass through a length (or an area) equal to the energy thickness. Solving for ψ yields

$$\psi = \int_0^{\delta_{full}} \frac{\rho V}{(\rho V)_{fs}} dY - \int_0^{\delta_{full}} \frac{\rho V^3}{(\rho V^3)_{fs}} dY \quad (7-6)$$

Ratios of the aforementioned thickness terms are also used as basic boundary-layer parameters. The form factor H is defined as

$$H = \frac{\delta}{\theta} \quad (7-7)$$

Substituting equations (7-2) and (7-4) into equation (7-7) and defining a dimensionless distance y as

$$y = \frac{Y}{\delta_{full}} \quad (7-8)$$

yields

$$H = \frac{\int_0^1 dy - \int_0^1 \frac{\rho V}{(\rho V)_{fs}} dy}{\int_0^1 \frac{\rho V}{(\rho V)_{fs}} dy - \int_0^1 \frac{\rho V^2}{(\rho V^2)_{fs}} dy} \quad (7-9)$$

An energy factor E is defined as

$$E = \frac{\psi}{\theta} \quad (7-10)$$

Substituting equations (7-6), (7-4), and (7-8) into equation (7-10) yields

$$E = \frac{\int_0^1 \frac{\rho V}{(\rho V)_{fs}} dy - \int_0^1 \frac{\rho V^3}{(\rho V^3)_{fs}} dy}{\int_0^1 \frac{\rho V}{(\rho V)_{fs}} dy - \int_0^1 \frac{\rho V^2}{(\rho V^2)_{fs}} dy} \quad (7-11)$$

Velocity profiles for turbulent flow are often represented by a power profile of the type

$$\frac{V}{V_{fs}} = y^n \quad (7-12)$$

where the value of the exponent n is most often between 0.1 and 0.25.

Note that this power profile is here expressed as y^n , while the same profile in chapter 6 (eq. (6-47)) is expressed as $y^{1/n}$. The exponent expressed as $1/n$ is consistent with general boundary-layer theory usage. The exponent expressed as n , however, is consistent with reference 1, wherein the equations that follow are derived. Therefore, the specific numerical value to be used for n will depend on the form being used for the exponent.

With this velocity profile, equations (7-9) and (7-11) can be integrated in series form, and the form and energy factors for turbulent flow can be expressed in terms of the exponent n and the free-stream critical velocity ratio V/V_{cr} . The resulting equations derived in reference 1 are

$$H = \frac{\frac{1}{n+1} + \frac{3A_{fs}}{3n+1} + \frac{5A_{fs}^2}{5n+1} + \dots}{\frac{1}{(n+1)(2n+1)} + \frac{A_{fs}}{(3n+1)(4n+1)} + \frac{A_{fs}^2}{(5n+1)(6n+1)} + \dots} \quad (7-13)$$

and

$$E = \frac{2 \left[\frac{1}{(n+1)(3n+1)} + \frac{A_{fs}}{(3n+1)(5n+1)} + \frac{A_{fs}^2}{(5n+1)(7n+1)} + \dots \right]}{\frac{1}{(n+1)(2n+1)} + \frac{A_{fs}}{(3n+1)(4n+1)} + \frac{A_{fs}^2}{(5n+1)(6n+1)} + \dots} \quad (7-14)$$

where

$$A_{fs} = \frac{\gamma-1}{\gamma+1} \left(\frac{V}{V_{cr}} \right)_{fs}^2 \quad (7-15)$$

and γ is the ratio of specific heat at constant pressure to specific heat at constant volume, and V_{cr} is the fluid velocity, in m/sec or ft/sec, at the critical (Mach 1) flow condition. For incompressible flow, where V/V_{cr} approaches zero, equations (7-13) and (7-14) reduce to

$$H_{inc} = 2n + 1 \quad (7-16)$$

and

$$E_{inc} = \frac{2(2n+1)}{3n+1} \quad (7-17)$$

Values of the form and energy factors for turbulent compressible flow are shown in figure 7-3 for V/V_{cr} varying from 0 to 1.4 and n varying from 0 to 1.5. It can be seen that the form factor varies much more than does the energy factor. For any constant exponent n , the energy factor is almost independent of V/V_{cr} .

The boundary-layer parameters just presented are general and can refer to a boundary layer on any type of body. They are directly useful in certain aerodynamic work. For instance, the drag of a body can be obtained directly from the momentum thickness. In turbine work, however, where the flow is confined to the physical boundaries of the blade row, it is simpler and more meaningful to express the losses as a fractional part of the ideal quantities that could pass through the blade row. The thickness parameters so expressed are herein termed "dimensionless thickness parameters" and are defined on the basis of zero trailing-edge thickness.

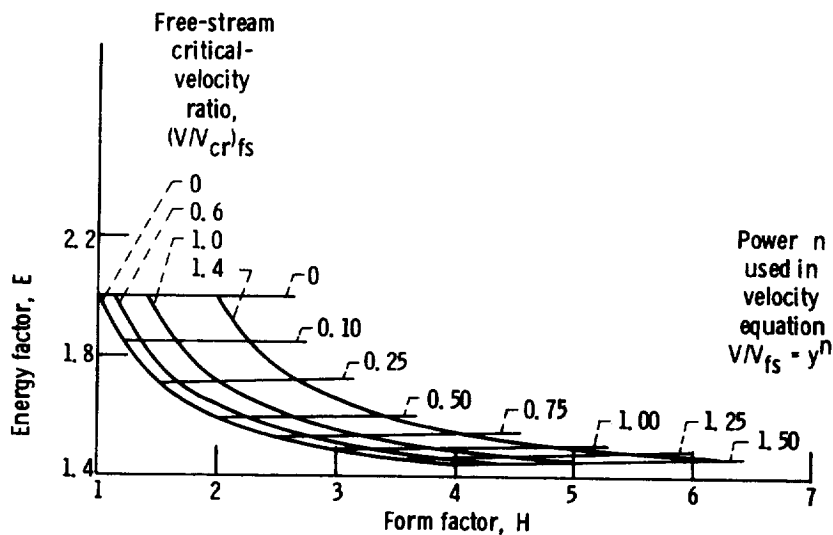


FIGURE 7-3.—Effect of compressibility on variation of energy factor with form factor.
(Data from ref. 1.)

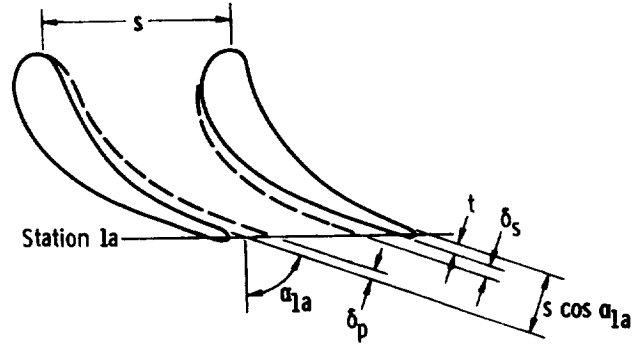


FIGURE 7-4.—Nomenclature for trailing-edge region.

These dimensionless thickness parameters must represent the sum of the suction- and pressure-surface thicknesses.

With the assumption that flow conditions in all channels are the same, the dimensionless thickness parameters are obtained by dividing the losses in flow, momentum, and energy for a single blade-row channel by the corresponding ideal quantities that could pass through one blade-row channel. The total losses for one channel, as indicated in figure 7-4, are composed of the suction-surface loss plus the pressure-surface loss, or

$$\delta_{tot} = \delta_s + \delta_p \quad (7-18)$$

$$\theta_{tot} = \theta_s + \theta_p \quad (7-19)$$

$$\psi_{tot} = \psi_s + \psi_p \quad (7-20)$$

where the subscripts *tot*, *s*, and *p* denote total value, suction-surface value, and pressure-surface value, respectively. Thus, in terms of the previously defined boundary-layer thicknesses, the dimensionless boundary-layer thicknesses are expressed as

$$\delta^* = \frac{\delta_{tot}(\rho V)_{fs}}{s \cos \alpha (\rho V)_{fs}} = \frac{\delta_{tot}}{s \cos \alpha} \quad (7-21)$$

$$\theta^* = \frac{\theta_{tot}(\rho V^2)_{fs}}{s \cos \alpha (\rho V^2)_{fs}} = \frac{\theta_{tot}}{s \cos \alpha} \quad (7-22)$$

$$\psi^* = \frac{\psi_{tot} \left(\frac{1}{2} \right) (\rho V^3)_{fs}}{s \cos \alpha \left(\frac{1}{2} \right) (\rho V^3)_{fs}} = \frac{\psi_{tot}}{s \cos \alpha} \quad (7-23)$$

where

- δ^* dimensionless displacement thickness
 θ^* dimensionless momentum thickness
 ψ^* dimensionless energy thickness
 s blade spacing, m; ft
 α fluid flow angle from axial direction, deg

Equations (7-21), (7-22), and (7-23) express the losses in flow, momentum, and energy, respectively, as fractions of their respective ideal quantities for the blade row if the trailing-edge thickness is assumed to be zero. These equations can be subscripted to apply at either station 1a, within the trailing edge, or station 1, beyond the trailing edge.

BLADE-ROW LOSS COEFFICIENTS

As mentioned previously, the losses are to be expressed in terms of kinetic-energy loss coefficients. In this section, methods for evaluating the friction, trailing-edge, and mixing losses and expressing them in terms of the kinetic-energy loss coefficients will be presented.

Surface-Friction Losses

The kinetic-energy loss coefficient \bar{e}_{1a} , defined as the loss in kinetic energy as a fraction of the ideal kinetic energy of the blade-row actual flow, can be expressed in terms of the boundary-layer dimensionless thicknesses as

$$\bar{e}_{1a} = \frac{\psi_{1a}^* s \cos \alpha_{1a} (\rho V^3)_{f,1a}}{(s \cos \alpha_{1a} - \delta_{1a}^* s \cos \alpha_{1a} - t) (\rho V^3)_{f,1a}} \quad (7-24)$$

where t is the blade-row trailing-edge thickness, in m or ft. (Refer to fig. 7-4 for the nomenclature in the region of the trailing edge of the blade.) Since this coefficient is referenced to station 1a, just within the blade-row trailing edge, it represents only the surface-friction loss. If a trailing-edge dimensionless thickness is expressed as

$$t^* = \frac{t}{s \cos \alpha_{1a}} \quad (7-25)$$

equation (7-24) reduces to

$$\bar{e}_{1a} = \frac{\psi_{1a}^*}{1 - \delta_{1a}^* - t^*} \quad (7-26)$$

In order to evaluate the loss coefficient \bar{e}_{1a} from equation (7-26), it is necessary to know the values of the dimensionless energy thickness ψ_{1a}^*

and the dimensionless displacement thickness δ_{1a}^* . These can be evaluated either experimentally or analytically, as will be discussed herein.

Experimental determination.—In determining experimental loss values, it is impractical to measure the density and velocity directly. Instead, pressure data are taken, and the density and velocity are related to pressure functions. The pressure data required for computing the friction loss consist of (see fig. 7-1) the upstream total pressure p_0' , the blade-exit static pressure p_{1a} , and the total-pressure loss survey data $p_0' - p_{1a}'$ for one blade space. Since the dimensionless boundary-layer thicknesses express the losses of the blade row as a fractional part of the ideal quantities which could pass through the blade row, the dimensionless displacement thickness can be expressed in terms of the flow across one blade pitch as

$$\delta_{1a}^* = \frac{s \cos \alpha_{1a} (\rho V)_{fs,1a} - t^* s \cos \alpha_{1a} (\rho V)_{fs,1a} - \cos \alpha_{1a} \int_0^s (\rho V)_{1a} du}{s \cos \alpha_{1a} (\rho V)_{fs,1a}} \quad (7-27)$$

where u is the distance in the tangential direction, in m or ft. Equation (7-27) simplifies to

$$\delta_{1a}^* = 1 - t^* - \int_0^1 \left(\frac{\rho V}{\rho_{fs} V_{fs}} \right)_{1a} d \left(\frac{u}{s} \right) \quad (7-28)$$

In a similar manner, the dimensionless momentum and energy thicknesses can be expressed as

$$\begin{aligned} \theta_{1a}^* &= \frac{\int_0^1 (\rho V V_{fs})_{1a} d \left(\frac{u}{s} \right) - \int_0^1 (\rho V^2)_{1a} d \left(\frac{u}{s} \right)}{(\rho V^2)_{fs,1a}} \\ &= \int_0^1 \left[1 - \left(\frac{V}{V_{fs}} \right)_{1a} \right] \left(\frac{\rho V}{\rho_{fs} V_{fs}} \right)_{1a} d \left(\frac{u}{s} \right) \end{aligned} \quad (7-29)$$

and

$$\begin{aligned} \psi_{1a}^* &= \frac{\int_0^1 (\rho V V_{fs}^2)_{1a} d \left(\frac{u}{s} \right) - \int_0^1 (\rho V^3)_{1a} d \left(\frac{u}{s} \right)}{(\rho_{fs} V_{fs}^3)_{1a}} \\ &= \int_0^1 \left[1 - \left(\frac{V}{V_{fs}} \right)_{1a}^2 \right] \left(\frac{\rho V}{\rho_{fs} V_{fs}} \right)_{1a} d \left(\frac{u}{s} \right) \end{aligned} \quad (7-30)$$

Assuming that the total temperature T' and the static pressure p_{1a} in

the boundary layer are the same as in the free stream, the density ratio $(\rho/\rho_{fs})_{1a}$ can be related to the pressure ratio p'_{1a}/p_0' as follows: From the isentropic relation,

$$\left(\frac{\rho}{\rho'}\right)_{1a} = \left(\frac{p}{p'}\right)_{1a}^{1/\gamma} \quad (7-31)$$

$$\left(\frac{\rho}{\rho'}\right)_{fs,1a} = \left(\frac{p}{p'}\right)_{fs,1a}^{1/\gamma} \quad (7-32)$$

Since $p'_{fs,1a} = p_0'$ and $\rho'_{1a}/\rho'_{fs,1a} = p'_{1a}/p_0'$ (from the ideal gas law, with $T'_{1a} = T'_{fs,1a} = T_0'$), division of equation (7-31) by equation (7-32) yields

$$\left(\frac{\rho}{\rho_{fs}}\right)_{1a} = \left(\frac{p_{1a}}{p_0'}\right)^{(\gamma-1)/\gamma} \quad (7-33)$$

The velocity ratio $(V/V_{fs})_{1a}$ can be related to the pressure ratios $(p/p')_{1a}$ and p_{1a}/p_0' as follows: From the total-temperature definition and isentropic relation, equations (1-51) and (1-52) of chapter 1, we can write

$$\frac{V^2}{2gJc_p T'} = 1 - \frac{T}{T'} = 1 - \left(\frac{p}{p'}\right)^{(\gamma-1)/\gamma} \quad (7-34)$$

where

- g conversion constant, 1; 32.17 (lbm) (ft)/(lbf) (sec²)
- J conversion constant, 1; 778 (ft) (lb)/Btu
- c_p specific heat at constant pressure, J/(kg) (K); Btu/(lb) (°R)

Subscripting equation (7-34) once for station 1a and again for free-stream values at 1a, dividing the first of these equations by the second, and recalling that $p'_{fs,1a} = p_0'$ and $T'_{fs,1a} = T'_{1a}$ yields

$$\left(\frac{V}{V_{fs}}\right)_{1a}^2 = \frac{1 - \left(\frac{p_{1a}}{p'_{1a}}\right)^{(\gamma-1)/\gamma}}{1 - \left(\frac{p_{1a}}{p_0'}\right)^{(\gamma-1)/\gamma}} \quad (7-35)$$

With the density and velocity ratios expressed in terms of the measured pressures by equations (7-33) and (7-35), it is now possible to integrate equations (7-28), (7-29), and (7-30) and evaluate the dimensionless boundary-layer thicknesses. Then, the kinetic-energy loss coefficient \bar{e}_{1a} can be computed from equation (7-26).

The kinetic-energy loss coefficient thus determined is a two-dimensional

coefficient; that is, it is based on data either from a two-dimensional cascade or from a constant radius of an annular cascade. (The annular cascade can be, and often is, the full stator or rotor from a turbine.) In order to obtain a three-dimensional loss coefficient for a blade row, data are taken at a number of radii sufficient to adequately cover the annulus, and the two-dimensional dimensionless boundary-layer thicknesses are calculated as shown previously for each radius. Three-dimensional boundary-layer thicknesses are then obtained by radial integration from hub to tip:

$$\delta_{1a,3D}^* = \frac{\int_{r_h}^{r_t} \delta_{1a}^* (\rho V)_{fs,1a} \cos \alpha_{1a} r dr}{\int_{r_h}^{r_t} (\rho V)_{fs,1a} \cos \alpha_{1a} r dr} \quad (7-36)$$

$$\theta_{1a,3D}^* = \frac{\int_{r_h}^{r_t} \theta_{1a}^* (\rho V^2)_{fs,1a} \cos \alpha_{1a} r dr}{\int_{r_h}^{r_t} (\rho V^2)_{fs,1a} \cos \alpha_{1a} r dr} \quad (7-37)$$

$$\psi_{1a,3D}^* = \frac{\int_{r_h}^{r_t} \psi_{1a}^* (\rho V^3)_{fs,1a} \cos \alpha_{1a} r dr}{\int_{r_h}^{r_t} (\rho V^3)_{fs,1a} \cos \alpha_{1a} r dr} \quad (7-38)$$

In terms of the measured pressures, these integrals are expressed as

$$\delta_{1a,3D}^* = \frac{\int_{r_h}^{r_t} \delta_{1a}^* (p_{1a})^{1/\gamma} \left[1 - \left(\frac{p_{1a}}{p_0'} \right)^{(\gamma-1)/\gamma} \right]^{1/2} \cos \alpha_{1a} r dr}{\int_{r_h}^{r_t} (p_{1a})^{1/\gamma} \left[1 - \left(\frac{p_{1a}}{p_0'} \right)^{(\gamma-1)/\gamma} \right]^{1/2} \cos \alpha_{1a} r dr} \quad (7-39)$$

$$\theta_{1a,3D}^* = \frac{\int_{r_h}^{r_t} \theta_{1a}^* (p_{1a})^{1/\gamma} \left[1 - \left(\frac{p_{1a}}{p_0'} \right)^{(\gamma-1)/\gamma} \right] \cos \alpha_{1a} r dr}{\int_{r_h}^{r_t} (p_{1a})^{1/\gamma} \left[1 - \left(\frac{p_{1a}}{p_0'} \right)^{(\gamma-1)/\gamma} \right] \cos \alpha_{1a} r dr} \quad (7-40)$$

$$\psi_{1a,3D}^* = \frac{\int_{r_h}^{r_t} \psi_{1a}^* (p_{1a})^{1/\gamma} \left[1 - \left(\frac{p_{1a}}{p_0'} \right)^{(\gamma-1)/\gamma} \right]^{3/2} \cos \alpha_{1a} r dr}{\int_{r_h}^{r_t} (p_{1a})^{1/\gamma} \left[1 - \left(\frac{p_{1a}}{p_0'} \right)^{(\gamma-1)/\gamma} \right]^{3/2} \cos \alpha_{1a} r dr} \quad (7-41)$$

The three-dimensional kinetic-energy loss coefficient is then obtained in a manner similar to equation (7-26):

$$\bar{e}_{1a,3D} = \frac{\psi_{1a,3D}^*}{1 - \delta_{1a,3D}^* - t_m^*} \quad (7-42)$$

where t_m^* is the trailing-edge dimensionless thickness at the mean radius and is used to represent the average value for the blade row.

Analytical determination.—The kinetic-energy loss coefficient \bar{e}_{1a} can also be evaluated with the use of analytically determined boundary-layer thickness parameters. While not as reliable as experimental values, analytical values are much less costly and time consuming to obtain. Analytical methods for calculating the basic boundary-layer parameters are discussed and referenced in chapter 6. The boundary-layer solutions are not simple, and the better methods require computer solution. Boundary-layer computer programs currently in use at the NASA Lewis Research Center include one (ref. 2) based on an integral method solution and another based on the finite difference method of reference 3.

An equation used in the study of reference 4 to compute turbulent boundary-layer momentum thickness was

$$\theta_{1a} = \frac{0.231}{\left(\frac{\rho V}{\rho' V_{cr}} \right)_{f_s, 1a} \left(\frac{V}{V_{cr}} \right)_{f_s, 1a}^{(1+H_{1a})}} \times \left\{ \frac{\int_0^l \left[\left(\frac{\rho V}{\rho' V_{cr}} \right)_{f_s} \left(\frac{V}{V_{cr}} \right)_{f_s}^{(1+H)} \right]^{1.268} \left(\frac{\mu}{\rho V} \right)_{f_s}^{0.268} (1 - A_{f_s})^{0.467} dx}{10^{0.678(2n+1)}} \right\}^{0.7886} \quad (7-43)$$

where

- A_{fs} parameter defined by equation (7-15)
 x distance along blade surface from forward stagnation point, m; ft
 l blade-surface distance from forward to rear stagnation point, m; ft
 μ viscosity, (N)(sec)/m²; lb/(ft)(sec)

The development of this equation is presented in reference 4. It is assumed that the boundary layer has a power-law velocity profile. In reference 4, the exponent n was obtained from the referenced equation

$$\frac{1}{n} = 2.6 \left[\left(\frac{\rho V}{\mu} \right)_{fs} x \right]^{1/14} \quad (7-44)$$

Equation (7-43) must be evaluated for both the suction and pressure surfaces of the blade. The free-stream velocities and densities required for equations (7-43) and (7-44) are those free-stream values adjacent to the blade-surface boundary layers. These can be obtained by any of the channel flow analysis techniques discussed in chapter 5.

Values of the form factor H as required in equation (7-43) and of the form factor H_{1a} and energy factor E_{1a} at station $1a$ for each surface can be obtained from equations (7-13) and (7-14). With θ_{1a} , H_{1a} , and E_{1a} known for both the suction and pressure surfaces, the various boundary-layer thickness parameters and the kinetic-energy loss coefficient \bar{e}_{1a} can be evaluated from the equations presented earlier in this chapter. For the turbine stator blade studied in reference 4, the analytical values, as calculated from equation (7-43), of the boundary-layer momentum thickness for the blade and for the two surfaces individually were reasonably close to the experimental values. In general, however, results obtained from equation (7-43) will not be as accurate as those obtained from the computer programs of references 2 and 3.

Three-dimensional boundary-layer parameters could be calculated directly from equations (7-36) to (7-38). The two-dimensional thickness parameters would have to be analytically determined at a number of radii sufficient to establish the variation over the blade length and would also have to be determined, somehow, over the end-wall surfaces. Such a procedure would require considerable effort, so the simplified method of reference 5 for predicting three-dimensional losses from two-dimensional mean-section losses is commonly used. Results obtained by this method have shown good agreement with experimental results.

In the method of reference 5, the following assumptions are made:
 (1) The average momentum loss for the blade surface can be represented by the dimensionless momentum thickness at the blade mean section;

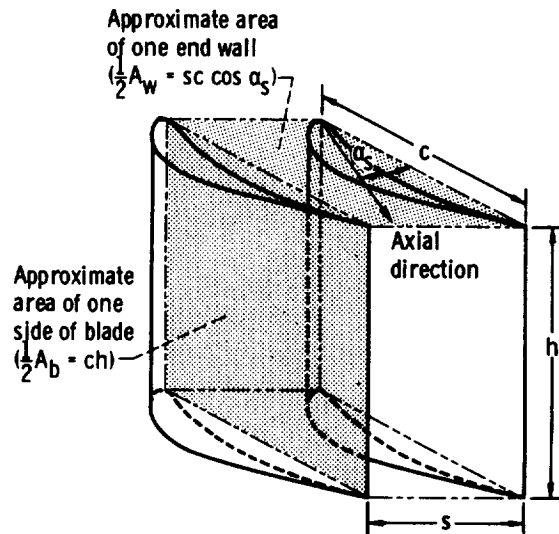


FIGURE 7-5.—Schematic diagram of equivalent two-dimensional blade used to calculate the effect of end-wall area on blade loss.

(2) the momentum loss per unit area on the inner and outer end walls is the same as the average momentum loss per unit area on the blade surface; and (3) the blade configuration can be satisfactorily approximated by an equivalent two-dimensional blade, as shown in figure 7-5, having a constant cross section, spacing, and stagger angle equal to those at the mean section of the given blade. The surface area of one equivalent blade (see fig. 7-5) is

$$A_b = 2ch \quad (7-45)$$

where

A_b total surface area (sum of suction-surface and pressure-surface areas) of one blade, m^2 ; ft^2

c blade chord, m ; ft

h blade height, m ; ft

The inner and outer end-wall area for one passage is

$$A_w = 2sc \cos \alpha_s \quad (7-46)$$

where

A_w total surface area of passage end walls (sum of inner and outer end-wall areas), m^2 ; ft^2

α_s blade stagger angle, deg

Now, taking the average momentum loss $\theta_{l_a, m}^*$ over the blade radial length

and modifying it to include the end-wall losses yields

$$\theta_{1a,3D}^* = \theta_{1a,m}^* \left(\frac{A_b + A_w}{A_b} \right) = \theta_{1a,m}^* \left(1 + \frac{s \cos \alpha_s}{h} \right) \quad (7-47)$$

The three-dimensional energy and displacement thickness parameters are then calculated as

$$\psi_{1a,3D}^* = E_{1a,m} \theta_{1a,3D}^* \quad (7-48)$$

and

$$\delta_{1a,3D}^* = H_{1a,m} \theta_{1a,3D}^* \quad (7-49)$$

Mean-section values are used for the energy and form factors. Although the energy and form factors were originally defined in terms of individual boundary-layer thicknesses, it is indicated in reference 4 that they can be satisfactorily used as is done in equations (7-48) and (7-49). The three-dimensional kinetic-energy loss coefficient is then obtained from equation (7-42).

Trailing-Edge Loss

The kinetic-energy loss coefficient \bar{e}_{te} that represents the loss associated with flow past the blade trailing edge can be determined either experimentally or analytically.

Experimental determination.—Experimental values of blade trailing-edge loss coefficient \bar{e}_{te} are obtained from differences between experimental two-dimensional loss coefficients \bar{e}_1 , which include both surface-friction loss and trailing-edge loss, and loss coefficients \bar{e}_{1a} , which include only the blade surface-friction loss. Thus,

$$\bar{e}_{te} = \bar{e}_1 - \bar{e}_{1a} \quad (7-50)$$

Loss coefficients \bar{e}_{1a} , which include only surface-friction loss, are obtained as described previously. Loss coefficients \bar{e}_1 , which include both surface-friction loss and trailing-edge loss, are determined in exactly the same manner except that the total-pressure loss and static pressure are measured at different locations. The surface-friction loss coefficients were based on data obtained just within the blade trailing edge at station $1a$, where the trailing-edge loss has not yet occurred. To determine the loss coefficients which include both surface-friction loss and trailing-edge loss, the measurements must be made at a location just downstream of the blade row, corresponding to station 1 in figure 7-1, where the trailing-edge loss, but little mixing, has occurred.

Analytical determination.—In reference 6, experimental drag coefficients are presented for a large number of surface discontinuities. Included in the reference are experimental data for sheet-metal joints of different

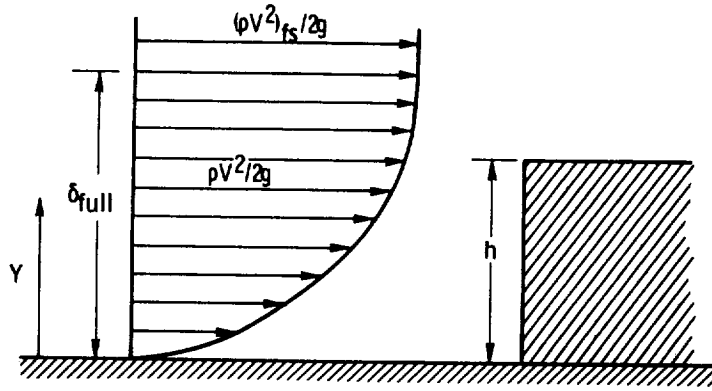


FIGURE 7-6.—Schematic diagram of body in boundary layer.

geometry, bolt and rivet heads of different geometry, and airfoil trailing edges. It is indicated that the pressure-drag loss due to the discontinuity behaves similarly regardless of the flow direction over the discontinuity. Therefore, the loss due to flow past a trailing edge will be treated analytically as if the loss were due to a body placed in the path of a boundary layer.

As indicated in reference 6, the drag of a small body of height h , equal to or less than the full boundary-layer height δ_{full} , placed in a turbulent boundary layer, as shown in figure 7-6, corresponds approximately to the effective dynamic pressure of the part of the boundary layer equal to the height of the body. Thus,

$$D = q_{eff} h C_D \quad (7-51)$$

where

- D drag on body, N/m; lb/ft
 h height of body, m; ft
 C_D drag coefficient

and the effective dynamic pressure q_{eff} is expressed as

$$q_{eff} = \frac{1}{h} \int_0^h \frac{\rho V^2}{2g} dY \quad (7-52)$$

Drag is related to momentum thickness as

$$D = \frac{\theta(\rho V^2)_{fs}}{g} \quad (7-53)$$

Therefore, a dimensionless momentum thickness θ_{te}^* representing the trailing-edge loss is obtained by combining equations (7-51) and (7-53) with a properly subscripted form of equation (7-22):

$$\theta_{ie}^* = \frac{q_{eff} h C_D}{s \cos \alpha_1 \frac{(\rho V^2)_{fs}}{g}} \quad (7-54)$$

The flow angle α_1 is related to the angle α_{1a} as discussed in chapter 4 (eqs. (4-26) and (4-27)).

Before equation (7-54) can be evaluated, the effective dynamic pressure must be determined. The ratio of the effective dynamic pressure to the free-stream dynamic pressure is equal to

$$\frac{q_{eff}}{q_{fs}} = \frac{1}{h} \int_0^h \left(\frac{\rho}{\rho_{fs}} \right) \left(\frac{V}{V_{fs}} \right)^2 dY \quad (7-55)$$

For turbulent flow, the variation of velocity in the boundary layer can be expressed with the use of the simple power profile presented previously. Combining equations (7-8) and (7-12) yields

$$\frac{V}{V_{fs}} = \left(\frac{Y}{\delta_{full}} \right)^n \quad (7-56)$$

Assuming that the total temperature and static pressure in the boundary layer and free stream are the same and using the ideal gas law and equation (1-64) of chapter 1 gives

$$\frac{\rho}{\rho_{fs}} = \frac{\frac{T_{fs}}{T_0'} \left[1 - \frac{\gamma-1}{\gamma+1} \left(\frac{V}{V_{cr}} \right)^2 \right]}{\frac{T}{T_0'} \left[1 - \frac{\gamma-1}{\gamma+1} \left(\frac{V}{V_{cr}} \right)^2 \right]} \quad (7-57)$$

Substituting equations (7-56) and (7-57) in equation (7-55) and using the parameter A_{fs} defined by equation (7-15) yields

$$\frac{q_{eff}}{q_{fs}} = \frac{1}{h} (1 - A_{fs}) \int_0^h \frac{1}{\left[1 - A_{fs} \left(\frac{Y}{\delta_{full}} \right)^{2n} \right]} \left(\frac{Y}{\delta_{full}} \right)^{2n} dY \quad (7-58)$$

Performing a binomial expansion and integrating then gives

$$\begin{aligned} \frac{q_{eff}}{q_{fs}} = (1 - A_{fs}) \left[\left(\frac{h}{\delta_{full}} \right)^{2n} \frac{1}{2n+1} + \left(\frac{h}{\delta_{full}} \right)^{4n} \frac{A_{fs}}{(4n+1)} \right. \\ \left. + \left(\frac{h}{\delta_{full}} \right)^{6n} \frac{A_{fs}^2}{(6n+1)} + \dots \right] \quad (7-59) \end{aligned}$$

Substituting equation (7-59) in equation (7-54) and using trailing-edge thickness t in place of body height h finally yields

$$\theta_{ie}^* = \frac{tC_D}{2s \cos \alpha_1} (1 - A_{fs}) \left[\left(\frac{t}{\delta_{full}} \right)^{2n} \frac{1}{2n+1} + \left(\frac{t}{\delta_{full}} \right)^{4n} \frac{A_{fs}}{(4n+1)} + \left(\frac{t}{\delta_{full}} \right)^{6n} \frac{A_{fs}^2}{(6n+1)} + \dots \right] \quad (7-60)$$

The boundary-layer thickness δ_{full} to be used in equation (7-60) should be the sum of the suction- and pressure-surface values.

Equation (7-60) is for compressible flow. In many cases, at least when n is not well known, the following simplified equation, which assumes incompressible flow and $n = 1/7$ (commonly used for turbulent flow), is adequate:

$$\theta_{ie}^* = 0.375 \sqrt[3]{\frac{t}{\delta_{full}}} \frac{tC_D}{s \cos \alpha_1} \quad (7-61)$$

The information in reference 6 indicates that the drag coefficient C_D can be set equal to 0.16 for a rounded trailing edge and 0.22 for a square trailing edge. The corresponding values reported in reference 7 and converted to the same basis as equation (7-61) are 0.14 for a rounded trailing edge and 0.22 for a square trailing edge. Frequently, δ_{tot} instead of δ_{full} will be available. In such a case, for incompressible flow,

$$\delta_{full} = \delta_{tot} \left(\frac{1}{n} + 1 \right) \quad (7-62)$$

and for compressible flow,

$$\delta_{full} = \frac{\delta_{tot}}{1 - (1 - A_{fs}) \left(\frac{1}{n+1} + \frac{A_{fs}}{3n+1} + \frac{A_{fs}^2}{5n+1} + \dots \right)} \quad (7-63)$$

Equations (7-60) and (7-61) give the fractional loss in blade-row momentum due to the blade trailing edge. To find the corresponding kinetic-energy loss coefficient, it is necessary to find the fractional losses in flow and kinetic energy. As a simple approximation, the form and energy factors, evaluated from equations (7-13) and (7-14) for compressible flow and from equations (7-16) and (7-17) for incompressible flow, are used to obtain

$$\delta_{ie}^* = H\theta_{ie}^* \quad (7-64)$$

and

$$\psi_{ie}^* = E\theta_{ie}^* \quad (7-65)$$

At station 1, which is just downstream of the blade trailing edge, fluid has flowed into the area behind the trailing edge and there is no longer a void due to trailing-edge blockage. Therefore, a kinetic-energy loss coefficient is obtained as

$$\bar{e}_{te} = \frac{\psi_{te}^*}{1 - \delta_{te}^*} \quad (7-66)$$

This loss coefficient expresses the loss in kinetic energy as a fraction of the ideal kinetic energy of the flow that would exist if the trailing-edge loss were the only loss. The trailing-edge kinetic-energy loss coefficient for incompressible flow is plotted against trailing-edge thickness in figure 7-7 for several values of the ratio of trailing-edge thickness to boundary-layer thickness. This figure is based on the momentum loss as expressed by equation (7-61). The flow loss associated with blade-surface friction is not included in equation (7-66). Therefore, this trailing-edge kinetic-energy loss coefficient is approximately, but not rigorously, additive with the surface-friction loss coefficient. Expression of the combined friction and trailing-edge loss in terms of a kinetic-energy loss coefficient is discussed in the next section.

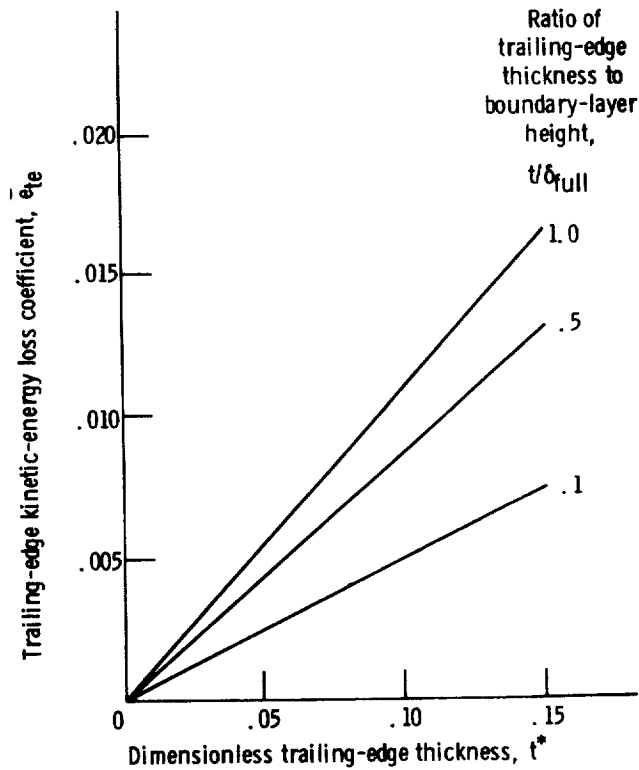


FIGURE 7-7.—Effect of trailing-edge blockage on kinetic-energy loss coefficient. Form factor $H = 1.3$; energy factor $E = 1.8$; drag coefficient $C_D = 0.16$.

Combined Friction and Trailing-Edge Loss

As stated in the discussion of the trailing-edge loss, the boundary-layer thickness parameters and a kinetic-energy loss coefficient expressing the combined friction and trailing-edge loss can be obtained by making the experimental measurements at a location corresponding to station 1, which is just downstream of the trailing edge. In this way, we obtain experimental values of δ_1^* , θ_1^* , and ψ_1^* from appropriately subscripted versions of equations (7-28), (7-29), and (7-30). The value of \bar{e}_1 is then obtained as

$$\bar{e}_1 = \frac{\psi_1^*}{1 - \delta_1^*} \quad (7-67)$$

Analytically, the boundary-layer thickness parameters at station 1 are obtained by adding the surface-friction loss to the trailing-edge loss. Before the friction and trailing-edge boundary-layer thickness parameters can be added, they must be expressed on the basis of the same ideal flow. The friction-loss dimensionless thicknesses at station $1a$ (δ_{1a}^* , θ_{1a}^* , ψ_{1a}^*) are expressed in terms of an ideal flow without trailing-edge blockage. However, there is a trailing-edge blockage at station $1a$, where the ideal flow with blockage must be comparable to the ideal flow at station 1, where there is no blockage. Therefore, the friction-loss boundary-layer thickness parameters are adjusted to account for the true (with blockage) ideal flow as follows:

$$\delta_{1,f}^* = \delta_{1a}^* \left(\frac{s \cos \alpha_{1a}}{s \cos \alpha_{1a} - t} \right) \quad (7-68)$$

$$\theta_{1,f}^* = \theta_{1a}^* \left(\frac{s \cos \alpha_{1a}}{s \cos \alpha_{1a} - t} \right) \quad (7-69)$$

and

$$\psi_{1,f}^* = \psi_{1a}^* \left(\frac{s \cos \alpha_{1a}}{s \cos \alpha_{1a} - t} \right) \quad (7-70)$$

where the subscript f refers to the loss due to surface friction. Adding the friction and trailing-edge loss parameters then yields the combined loss parameters at station 1:

$$\delta_1^* = \delta_{1,f}^* + \delta_{1e}^* \quad (7-71)$$

$$\theta_1^* = \theta_{1,f}^* + \theta_{1e}^* \quad (7-72)$$

and

$$\psi_1^* = \psi_{1,f}^* + \psi_{1e}^* \quad (7-73)$$

And the value of \bar{e}_1 is then obtained from equation (7-67).

After-Mix Loss

The after-mix loss is the total loss that includes the surface-friction loss, the trailing-edge loss, and the mixing loss. The after-mix loss coefficient \bar{e}_2 is determined as described in this section, and the mixing loss, if desired, is obtained by subtracting the previously determined \bar{e}_1 from \bar{e}_2 .

To determine the after-mix loss experimentally would require that the pressure measurements be made downstream of the blading where complete mixing has occurred. This is impractical for several reasons: (1) The length for complete mixing, while quite long, is unknown; (2) the after-mix loss would have to be corrected for side-wall friction for the mixing length, thus leading to possible error; and (3) after the flow had mixed, values of after-mix $p_0' - p_2'$ would be constant and small enough that the possibility of measurement error would be relatively large. For these reasons, values of after-mix loss are obtained analytically with the use of either experimentally or analytically determined before-mix (station 1) loss parameters.

The basic equations for determining the after-mix conditions are those for conservation of mass, momentum in the tangential direction, and momentum in the axial direction during mixing. Equating the mass flow rate before mixing (station 1) and after mixing (station 2) yields

$$\int_0^1 (\rho V)_1 \cos \alpha_1 d\left(\frac{u}{s}\right) = \cos \alpha_2 (\rho V)_2 \quad (7-74)$$

From conservation of momentum in the tangential direction we get

$$\int_0^1 (\rho V^2)_1 \sin \alpha_1 \cos \alpha_1 d\left(\frac{u}{s}\right) = \sin \alpha_2 \cos \alpha_2 (\rho V^2)_2 \quad (7-75)$$

and from conservation of momentum in the axial direction we get

$$g \int_0^1 p_1 d\left(\frac{u}{s}\right) + \int_0^1 (\rho V^2) \cos^2 \alpha_1 d\left(\frac{u}{s}\right) = gp_2 + \cos^2 \alpha_2 (\rho V^2)_2 \quad (7-76)$$

Although these equations are subscripted for two-dimensional flow, they can also be applied to three-dimensional flow by integrating radially.

If experimental survey data were available at station 1, the integrals in the above equations could be directly evaluated even with variations in static pressure and flow angle. These conservation equations could be written for any before-mix location at which data were available, and then used to evaluate the after-mix loss coefficient. In the case where the before-mix station is not station 1, it would not be possible to determine

the mixing loss completely by experimental means. In most cases, however, it is only the final after-mix loss that is desired, and survey measurements are usually made a little farther downstream of the trailing edge, where angle and pressure variations have somewhat damped out.

If static pressure and flow angle are constant across station 1, it is possible to express equations (7-74) to (7-76) in terms of the previously used boundary-layer parameters, as was done in reference 1. The analysis herein differs from that of reference 1 only in that the before-mix station used in reference 1 corresponds to station 1a herein. Equation (7-28) subscripted for station 1, where there is no trailing-edge void, can be written as

$$\int_0^1 (\rho V)_1 d\left(\frac{u}{s}\right) = (1 - \delta_1^*) (\rho V)_{fs,1} \quad (7-77)$$

Subscripting equation (7-29) for station 1 and combining it with equation (7-77) yields

$$\int_0^1 (\rho V^2)_1 d\left(\frac{u}{s}\right) = (1 - \delta_1^* - \theta_1^*) (\rho V^2)_{fs,1} \quad (7-78)$$

Substituting equations (7-77) and (7-78) into equations (7-74) to (7-76) yields the following equations for conservation of mass and momentum in terms of the boundary-layer parameters previously determined:

$$\cos \alpha_1 (1 - \delta_1^*) (\rho V)_{fs,1} = \cos \alpha_2 (\rho V)_2 \quad (7-79)$$

$$\sin \alpha_1 \cos \alpha_1 (1 - \delta_1^* - \theta_1^*) (\rho V^2)_{fs,1} = \sin \alpha_2 \cos \alpha_2 (\rho V^2)_2 \quad (7-80)$$

$$gp_1 + \cos^2 \alpha_1 (1 - \delta_1^* - \theta_1^*) (\rho V^2)_{fs,1} = \cos^2 \alpha_2 (\rho V^2)_2 + gp_2 \quad (7-81)$$

These equations, along with the ideal gas law and the conservation-of-energy equation ($T_1' = T_2'$), can be solved simultaneously as shown in reference 1 to obtain \bar{e}_2 , the after-mix kinetic-energy loss coefficient, for both compressible and incompressible flow.

For incompressible flow, the solution for \bar{e}_2 is

$$\bar{e}_2 = 1 - \frac{\sin^2 \alpha_1 \left(\frac{1 - \delta_1^* - \theta_1^*}{1 - \delta_1^*} \right)^2 + \cos^2 \alpha_1 (1 - \delta_1^*)^2}{1 + 2 \cos^2 \alpha_1 [(1 - \delta_1^*)^2 - (1 - \delta_1^* - \theta_1^*)]} \quad (7-82)$$

For compressible flow, no explicit solution was found, and the following steps are required to obtain \bar{e}_2 :

(1) The parameters C and D are computed from

$$C = \frac{(1 - A_{fs,1}) \frac{\gamma+1}{2\gamma} + \cos^2 \alpha_1 (1 - \delta_1^* - \theta_1^*) \left(\frac{V}{V_{cr}} \right)_{fs,1}^2}{\cos \alpha_1 (1 - \delta_1^*) \left(\frac{V}{V_{cr}} \right)_{fs,1}} \quad (7-83)$$

$$D = \left(\frac{V}{V_{cr}} \right)_{fs,1} \sin \alpha_1 \left(\frac{1 - \delta_1^* - \theta_1^*}{1 - \delta_1^*} \right) \quad (7-84)$$

(2) The quantity $(V_z/V_{cr})_2$ is obtained from

$$\left(\frac{V_z}{V_{cr}} \right)_2 = \frac{\gamma C}{\gamma + 1} - \sqrt{\left(\frac{\gamma C}{\gamma + 1} \right)^2 - 1 + \left(\frac{\gamma - 1}{\gamma + 1} \right) D^2} \quad (7-85)$$

(3) The density ratio $(\rho/\rho')_2$ is obtained from

$$\left(\frac{\rho}{\rho'} \right)_2 = \left\{ 1 - \left(\frac{\gamma - 1}{\gamma + 1} \right) \left[D^2 + \left(\frac{V_z}{V_{cr}} \right)_2^2 \right] \right\}^{1/(\gamma-1)} \quad (7-86)$$

(4) The total pressure ratio p_2'/p_0' is obtained from

$$\frac{p_2'}{p_0'} = \frac{\left(\frac{\rho V}{\rho' V_{cr}} \right)_{fs,1} \cos \alpha_1 (1 - \delta_1^*)}{\left(\frac{\rho V_z}{\rho' V_{cr}} \right)_2} \quad (7-87)$$

(5) The pressure ratio $(p/p')_2$ is obtained from

$$\left(\frac{p}{p'} \right)_2 = \left(\frac{\rho}{\rho'} \right)_2^\gamma \quad (7-88)$$

(6) Finally, \bar{e}_2 is obtained from

$$\bar{e}_2 = \frac{\left(\frac{p_0'}{p_2'} \right)^{(\gamma-1)/\gamma} - 1}{\left(\frac{p_0'}{p_2} \right)^{(\gamma-1)/\gamma} - 1} \quad (7-89)$$

Values of \bar{e}_2 include all the blade-row loss; that is, the frictional loss of the blade row, the trailing-edge loss, and the mixing loss. Values of \bar{e}_1

include all the blade-row losses except mixing loss. Therefore,

$$\bar{e}_{mix} = \bar{e}_2 - \bar{e}_1 \quad (7-90)$$

where \bar{e}_{mix} is the fractional loss in available energy due to mixing.

BLADE-ROW LOSS CHARACTERISTICS

In this section, experimentally and analytically determined losses of the various types considered will be presented and compared, and the effect of blade-row geometry on losses will be discussed.

Distribution and Comparison of Losses

Figure 7-8, taken from reference 8, compares experimentally and analytically determined values of kinetic-energy loss coefficients at three different angle settings for a given stator and at three stations representing different losses. The loss coefficient $\bar{e}_{1a,m}$, obtained just within the blade trailing edge, represents the surface-friction loss at the mean (arithmetic mean radius) section; the coefficient $\bar{e}_{1,m}$, obtained just beyond the trailing edge, represents the friction loss plus trailing-edge loss at the mean section; and the coefficient $\bar{e}_{2,3D}$ represents the total loss for the annulus including blade and end-wall friction, trailing-edge drag, and mixing. In general, agreement between the experimental and analytical loss coefficients is reasonably good.

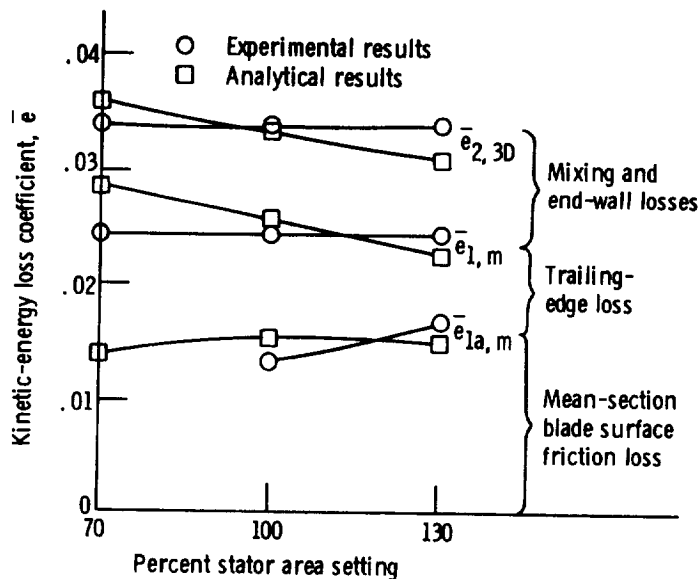


FIGURE 7-8.—Comparison of experimental and analytical loss coefficients for different stator area settings. (Data from ref. 8.)

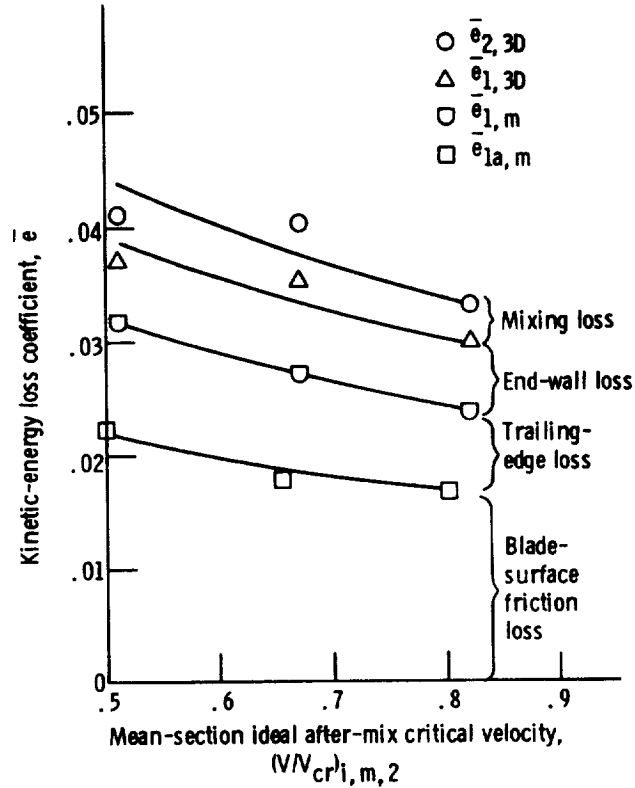


FIGURE 7-9.—Variation of loss coefficients with velocity. (Data from ref. 9.)

Figure 7-8 gives some idea of the distribution of losses in a stator blade row, but does not separate the mixing and end-wall losses. Figure 7-9, taken from reference 9, shows the variation in loss coefficient with velocity. Loss coefficient is seen to decrease slightly with increasing velocity. This figure also shows separately the mixing and end-wall losses, as well as the other blade-row losses.

In this particular case, the friction loss was about 2 percent of the stator ideal energy and about one-half of the total stator loss. The trailing-edge loss was about one-quarter of the total loss. In general, the trailing-edge loss will vary with trailing-edge blockage as was shown in figure 7-7. The end-wall loss, which was about 15 percent of the total loss for this case, will vary with the design, depending primarily on radius ratio and spacing. The mixing loss made up the remaining 10 percent of the total loss. The loss breakdown will, of course, vary with the stator design, but the comparison does indicate that each of the losses may be of consequence.

Effect of Blade-Row Geometry on Losses

A study of the effect of turbine geometry on turbulent-flow boundary-layer loss is presented in reference 10. In that study, the assumption was

made that the momentum loss per unit blade surface varies as the inverse of the chord Reynolds number to the m power:

$$\frac{\theta_{tot}}{c} \propto Re_c^{-m} \quad (7-91)$$

where Re_c is a Reynolds number based on blade chord c . Expanding equation (7-91) by multiplying and dividing by like terms, substituting into equation (7-22), and then using equation (7-47) to express the three-dimensional effect yielded an equation of the form

$$\theta_{3D}^* \propto \left(\frac{h}{s}\right)^m \left[1 + \frac{\cos \alpha_s}{\left(\frac{h}{s}\right)} \right] \left(\frac{\theta_{tot}}{c}\right)_{ref} \left(\frac{c}{s}\right)^{1-m} Re_h^{-m} \quad (7-92)$$

$$f\left(\frac{h}{s}\right) \quad f\left(\frac{c}{s}\right) \quad f(Re_h)$$

where Re_h is a Reynolds number based on blade height h . As indicated, the three-dimensional momentum thickness parameter can be expressed as a function of the geometric variables—height-to-spacing ratio h/s , blade solidity c/s , and height Reynolds number Re_h . The reference value of θ_{tot}/c , as explained in reference 9, is based on the minimum loss for a given solidity and, therefore, becomes a function of solidity. The exponent m is set equal to $\frac{1}{5}$ in the analysis.

In reference 10, the derivative of the dimensionless momentum thickness θ_{3D}^* with respect to each of the geometric variables was obtained in order to find the minimum-loss value of each variable in terms of the other variables (there is no minimum for height Reynolds number). With the optimum values known, the relative variations in momentum loss around the minimum values were then determined. The results of the analysis from reference 10 are shown in figures 7-10, 7-11, and 7-12. Also shown in each figure is the nature of the geometry variation associated with the change in each variable.

Figure 7-10 shows that a wide variation (50 percent or more) in h/s value around the optimum causes little increase in momentum loss. This results from the two counteracting effects of changes in chord Reynolds number and end-wall area. Figure 7-11 shows that the solidity of a blade may be varied considerably from optimum with some, but not excessive, loss. Comparison of the results in figures 7-10 and 7-11 shows that the loss is more sensitive to solidity than to the height-to-spacing ratio. The curve shape of figure 7-11 reflects also the counteracting influences of chord Reynolds number and end-wall area.

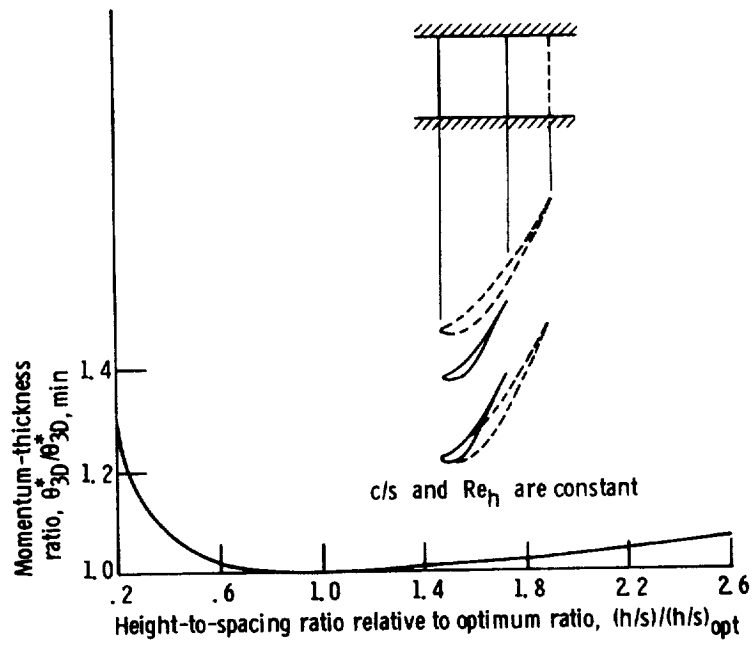


FIGURE 7-10.—Variation of momentum-thickness ratio with variation in height-to-spacing ratio. (Data from ref. 10.)

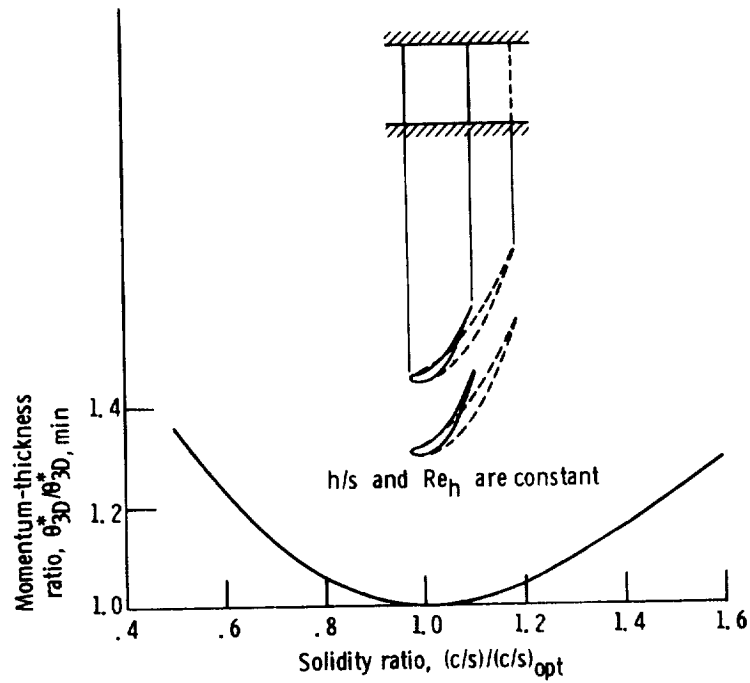


FIGURE 7-11.—Variation of momentum-thickness ratio with solidity ratio. (Data from ref. 10.)

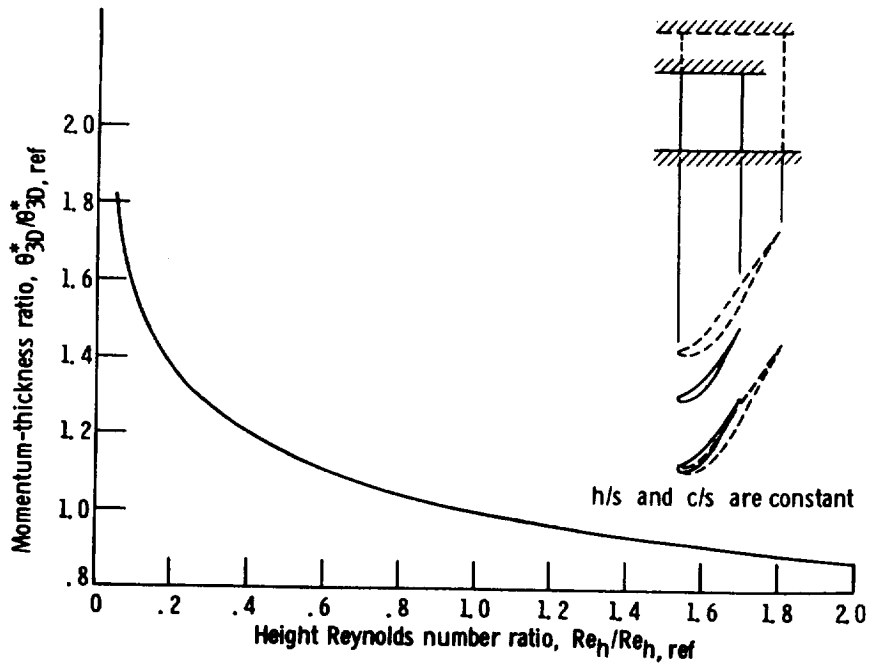


FIGURE 7-12.—Variation of momentum-thickness ratio with height Reynolds number ratio. (Data from ref. 10.)

Figure 7-12 shows the variation of momentum-thickness ratio with height Reynolds number ratio. While the figure indicates a change in Reynolds number due to change in geometry, the change in Reynolds number could also result from change in inlet flow conditions. The curve shape, then, results from the loss being inversely proportional to the Reynolds number to the $m = \frac{1}{5}$ power. These results show that an increase in height Reynolds number results in improved performance. The height Reynolds number is sometimes used in correlating the performance of different turbomachines.

REFERENCES

1. STEWART, WARNER, L.: Analysis of Two-Dimensional Compressible-Flow Loss Characteristics Downstream of Turbomachine Blade Rows in Terms of Basic Boundary-Layer Characteristics. NACA TN 3515, 1955.
2. McNALLY, WILLIAM D.: FORTRAN Program for Calculating Compressible Laminar and Turbulent Boundary Layers in Arbitrary Pressure Gradients. NASA TN D-5681, 1970.
3. PATANKAR, S. V.; AND SPALDING, D. B.: Heat and Mass Transfer in Boundary Layers. CRC Press, 1967.
4. WHITNEY, WARREN J.; STEWART, WARNER L.; AND MISER, JAMES W.: Experimental Investigation of Turbine Stator-Blade-Outlet Boundary-Layer Characteristics and a Comparison with Theoretical Results. NACA RM E55K24, 1956.

TURBINE DESIGN AND APPLICATION

5. STEWART, WARNER L.; WHITNEY, WARREN J.; AND WONG, ROBERT Y.: Use of Mean-Section Boundary-Layer Parameters in Predicting Three-Dimensional Turbine Stator Losses. NACA RM E55L12a, 1956.
6. HOERNER, SIGHARD F.: Fluid-Dynamic Drag. Midland Park, N.J., 1965.
7. PRUST, HERMAN W., JR.; AND HELON, RONALD M.: Effect of Trailing-Edge Geometry and Thickness on the Performance of Certain Turbine Stator Blading. NASA TN D-6637, 1972.
8. PRUST, HERMAN W.; MOFFITT, THOMAS P.; AND BIDER, BERNARD: Effect of Variable Stator Area on Performance of a Single-Stage Turbine Suitable for Air Cooling. V—Stator Detailed Losses with 70-Percent Design Area. NASA TM X-1696, 1968.
9. MOFFITT, THOMAS P.; PRUST, HERMAN W., JR.; AND BIDER, BERNARD: Effect of Variable Stator Area on Performance of a Single-Stage Turbine Suitable for Air Cooling. II—Stator Detailed Losses with 130-Percent Design Area. NASA TM X-1635, 1968.
10. MISER, JAMES W.; STEWART, WARNER L.; AND WHITNEY, WARREN J.: Analysis of Turbomachine Viscous Losses Affected by Changes in Blade Geometry. NACA RM E56F21, 1956.

SYMBOLS

A_b	surface area of one blade, m^2 ; ft^2
A_{f_s}	parameter defined by equation (7-15)
A_w	surface area of end walls for one passage, m^2 ; ft^2
C	parameter defined by equation (7-83)
C_D	drag coefficient
c	blade chord, m ; ft
c_p	specific heat at constant pressure, $J/(kg)(K)$; $Btu/(lb)(^\circ R)$
D	{ drag, N/m ; lb/ft parameter defined by equation (7-84)
E	energy factor
\bar{e}	kinetic-energy loss coefficient
g	conversion constant, 1 ; $32.17 (lbm)(ft)/(lbf)(sec^2)$
H	form factor
h	{ blade height, m ; ft height of body placed in boundary layer, m ; ft
J	conversion constant, 1 ; $778 (ft)(lb)/Btu$
l	blade surface distance from forward to rear stagnation point, m ; ft
m	exponent in equation (7-91)
n	turbulent boundary-layer velocity profile exponent
p	absolute pressure, N/m^2 ; lb/ft^2
q	dynamic pressure, N/m^2 ; lb/ft^2
Re_c	chord Reynolds number
Re_h	height Reynolds number
r	radius, m ; ft
s	blade spacing, m ; ft
T	absolute temperature, K ; $^\circ R$
t	trailing-edge thickness, m ; ft
u	distance in tangential direction, m ; ft
V	fluid velocity, m/sec ; ft/sec
x	distance along blade surface from forward stagnation point, m ; ft
Y	distance from surface normal to boundary layer, m ; ft
y	distance from surface normal to boundary layer expressed as fraction of boundary-layer thickness
α	fluid flow angle from axial direction, deg
α_s	blade stagger angle from axial direction, deg
γ	ratio of specific heat at constant pressure to specific heat at constant volume
δ	boundary-layer displacement thickness, m ; ft
δ_{full}	boundary-layer thickness, m ; ft

TURBINE DESIGN AND APPLICATION

θ	boundary-layer momentum thickness, m; ft
μ	viscosity, (N) (sec)/m ² ; lb/(ft) (sec)
ρ	density, kg/m ³ ; lb/ft ³
ψ	boundary-layer energy thickness, m; ft

Subscripts:

<i>cr</i>	critical flow conditions
<i>eff</i>	effective
<i>f</i>	friction
<i>fs</i>	free stream
<i>h</i>	hub
<i>i</i>	ideal
<i>inc</i>	incompressible
<i>m</i>	mean section
<i>min</i>	minimum
<i>mix</i>	mixing
<i>opt</i>	optimum
<i>p</i>	pressure surface
<i>ref</i>	reference
<i>s</i>	suction surface
<i>t</i>	tip
<i>te</i>	trailing edge
<i>tot</i>	total
<i>x</i>	axial component
0	blade-row inlet
1	just beyond trailing edge of blade row
1a	just within trailing edge of blade row
2	downstream uniform state
3D	three dimensional

Superscripts:

'	absolute total state
*	dimensionless value

CHAPTER 8

Miscellaneous Losses

By Richard J. Roelke

In the last chapter, the boundary-layer losses associated with the flow process in the blade channel were discussed. To determine the overall design-point efficiency of a turbine, other losses must also be considered; these include tip-clearance loss and disk-friction loss. In some instances, these losses represent a very small part of the turbine output and may be neglected; however, in other instances, these losses can be of such magnitude as to influence the selection of the turbine design point. The sum of these losses normally comprises all the losses that are considered in the design of a full-admission axial-flow turbine. If, however, a partial-admission turbine is being considered, there are additional losses that must be included. The partial-admission losses usually considered are the pumping loss in the inactive blade channels and the filling-and-emptying loss in the blade passages as they pass through the admission arc. Finally, a loss that occurs at off-design operation of any turbine is the incidence loss, which will also be covered herein.

TIP-CLEARANCE LOSS

Because a turbine must operate with some clearance between the tips of the rotor blades and the casing, some fraction of the fluid leaks across the tips, thus causing a reduction in turbine work output. This leakage loss is affected, first of all, by the nature of the tip geometry; that is, by the amount of radial clearance, by recesses in the casing, and by tip shrouds. For a given tip geometry, the amount of blade reaction affects the leakage loss, since a large pressure difference across the tip (high reaction) causes more higher-kinetic-energy flow to leak through the tip

gap from the pressure side to the suction side of the blade. With an unshrouded blade, this leakage flow not only causes a loss due to its own reduced work, but also causes an unloading of the blade, primarily in the tip region. Analytical evaluation of the drop in turbine efficiency caused by tip-clearance leakage is inherently difficult because of the complex flow problem. Several empirical expressions for clearance loss have been developed, and some of these are summarized in reference 1; however, they are rather complicated, and the author states that none is entirely satisfactory.

A number of tests have been made at the NASA Lewis Research Center to determine the effect of tip clearance and tip geometry on axial-flow impulse and reaction turbines. An examination of some of the results of these tests helps to obtain a better understanding of the tip-clearance loss. Figure 8-1 shows the angle traces at the blade exit of a 5-inch single-stage turbine (ref. 2). Two things to be noted from the angle traces are that the flow in the clearance space and near the tip was not fully turned,

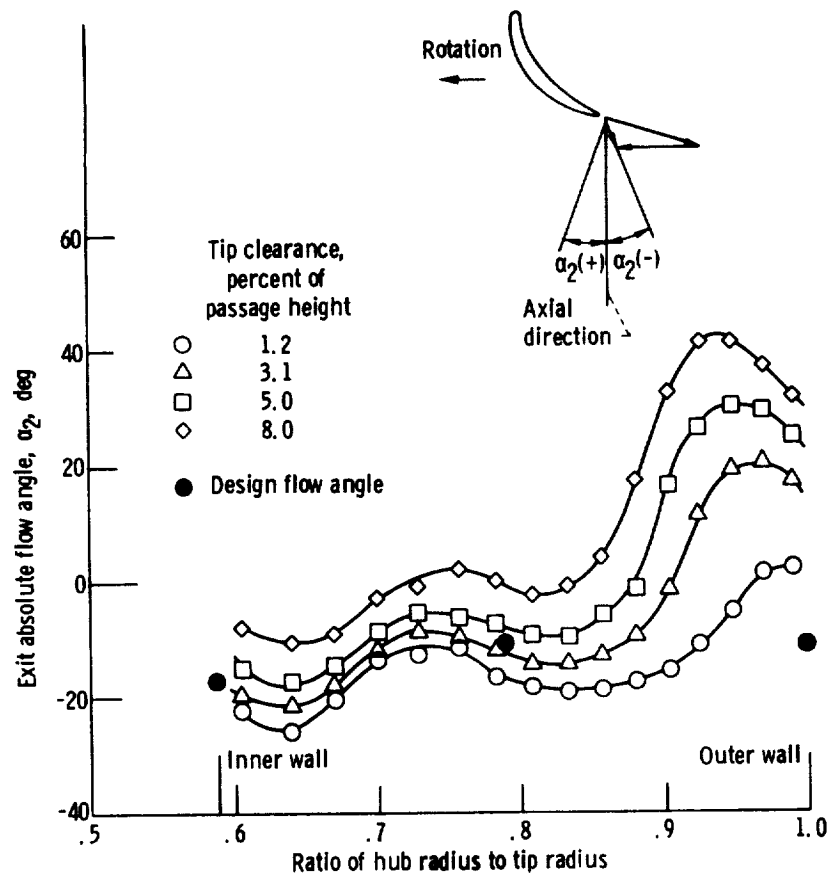


FIGURE 8-1.—Variation of exit flow angle with radius ratio for four rotor tip clearances. (Data from ref. 2.)

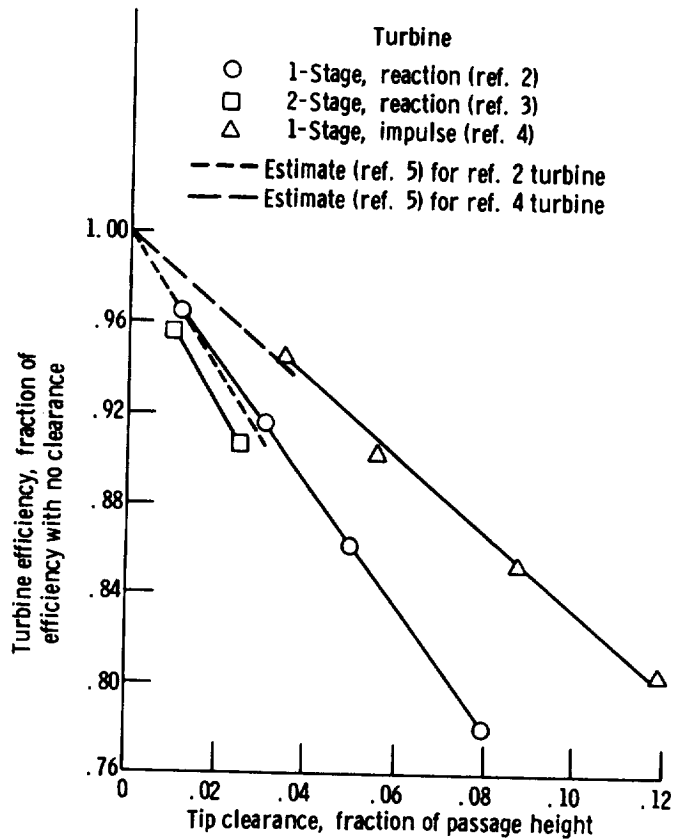


FIGURE 8-2.—Effect of tip clearance on efficiency.

even at the smallest clearance tested, and that underturning of the flow increased with increasing tip clearance, and this effect occurred all the way down to the hub. This underturning of the flow unloads the blade aerodynamically and results in lower turbine output and efficiency. The decrease in efficiency for this turbine, as well as for two others, is shown in figure 8-2.

The solid lines in figure 8-2 represent test results from single-stage (ref. 2) and two-stage (ref. 3) reaction turbines and from a single-stage impulse turbine (ref. 4). All turbines were unshrouded. The importance that the level of reaction plays in the clearance loss is clearly evident from the figure. For the same ratio of tip clearance to blade height, the losses in efficiency for the reaction turbines were about double that for the impulse turbine.

The dashed lines in figure 8-2 are estimates of the efficiency losses for the two single-stage turbines (refs. 2 and 4) as obtained from the curves published in reference 5 (as fig. 1.6) and reproduced here as figure 8-3. Extrapolation of the experimental data of figure 8-2 shows that figure 8-3 gives satisfactory estimates of tip-leakage loss for small tip clearances.

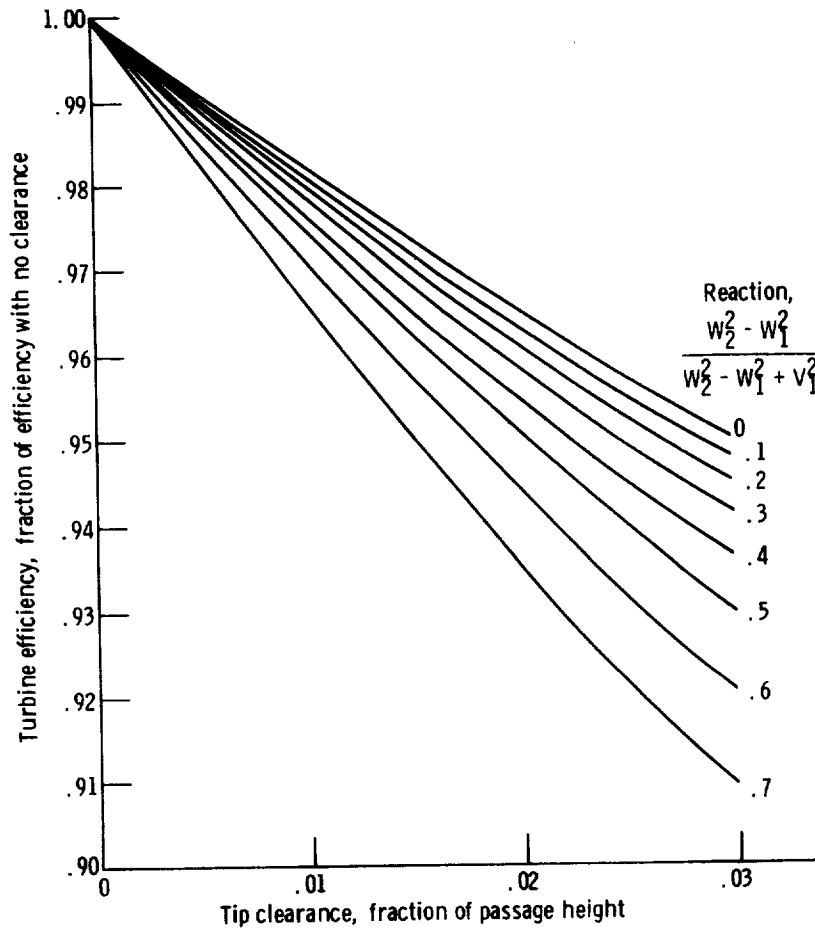
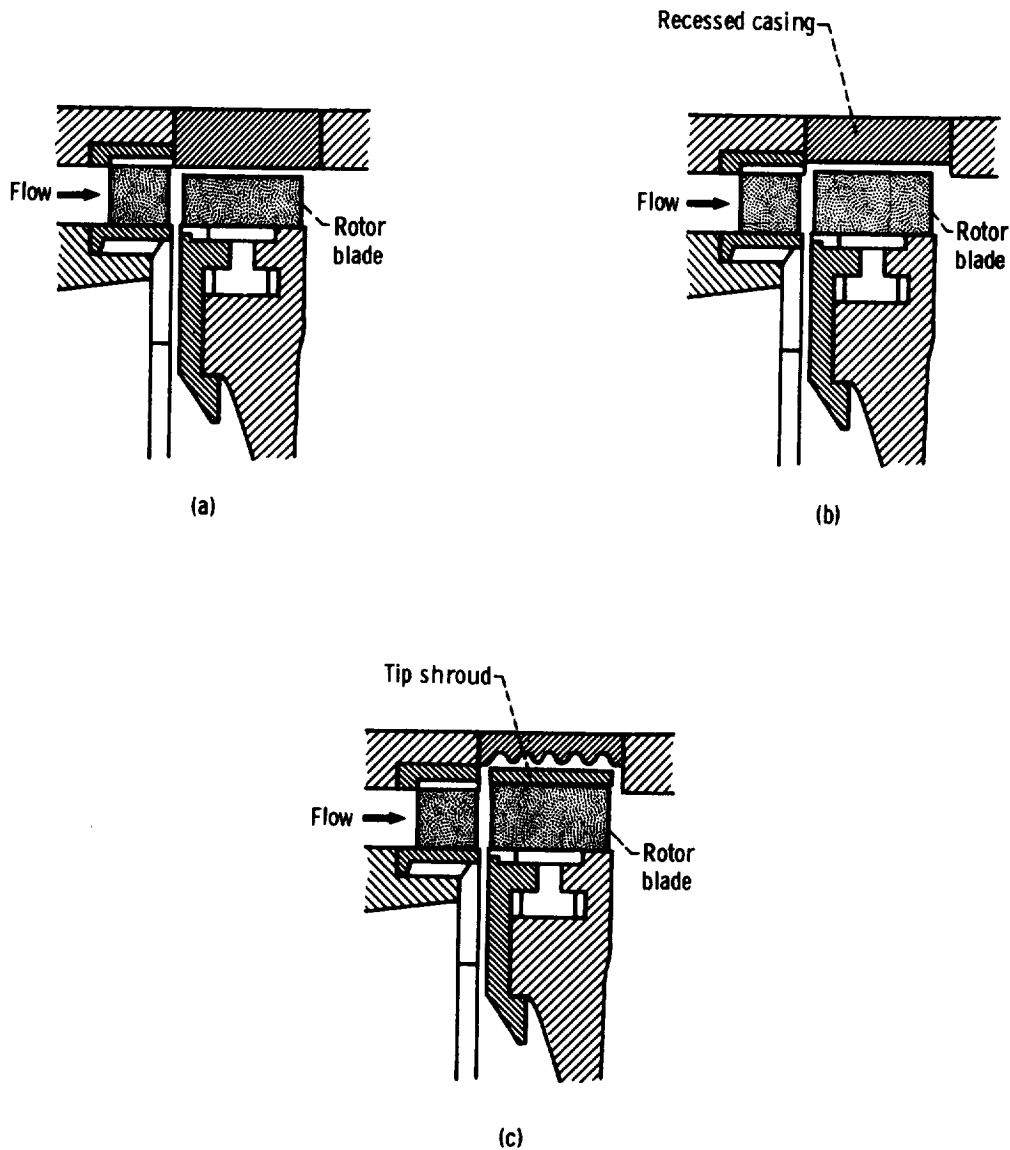


FIGURE 8-3.—Tip-clearance correlation for unshrouded blades. (Data from ref. 5.)

Reviewing the results shown in figures 8-2 and 8-3, it is apparent that the loss in efficiency increases with increasing reaction, and for moderate to large ratios of tip clearance to blade height, the loss is appreciable.

In addition to reducing the tip clearance, methods for reducing the tip-leakage losses include recessing the casing above the blade tip while increasing the blade height, and adding a tip shroud. These loss-reduction schemes can be used either individually or in combination. The single-stage impulse turbine of reference 4 was tested at several ratios of tip clearance to blade height, both without and with the recessed casing and the tip shroud. Figure 8-4 shows the three general configurations tested in reference 4, and the turbine-performance results are shown in figure 8-5. A clearer understanding of the performance characteristics is possible if the loss mechanisms are considered. The factors affecting turbine work for the reduced blade-height configuration as compared to a zero-clearance configuration consist of (1) reduced blade loading area, (2) clearance-gap leakage flow, (3) mixing of the leakage flow with channel throughflow,

MISCELLANEOUS LOSSES



(a) Reduced blade height (relative to zero-clearance blade height).

(b) Recessed casing.

(c) Shrouded rotor.

FIGURE 8-4.—Tip-clearance configurations investigated for impulse turbine (ref. 4).

and (4) blade unloading (as a result of flow going from the pressure side to the suction side). With the recessed-casing configuration, the blade extended to the passage outer radius and was of constant height as the clearance gap was changed by varying the amount of casing recess. Therefore, the reduced blade loading area was eliminated, and the leakage flow was reduced because of the indirect leakage path. With the shroud added to the blade, the blade unloading was eliminated, and the leakage flow was further reduced. Note from figure 8-5, however, that at tip-clearance

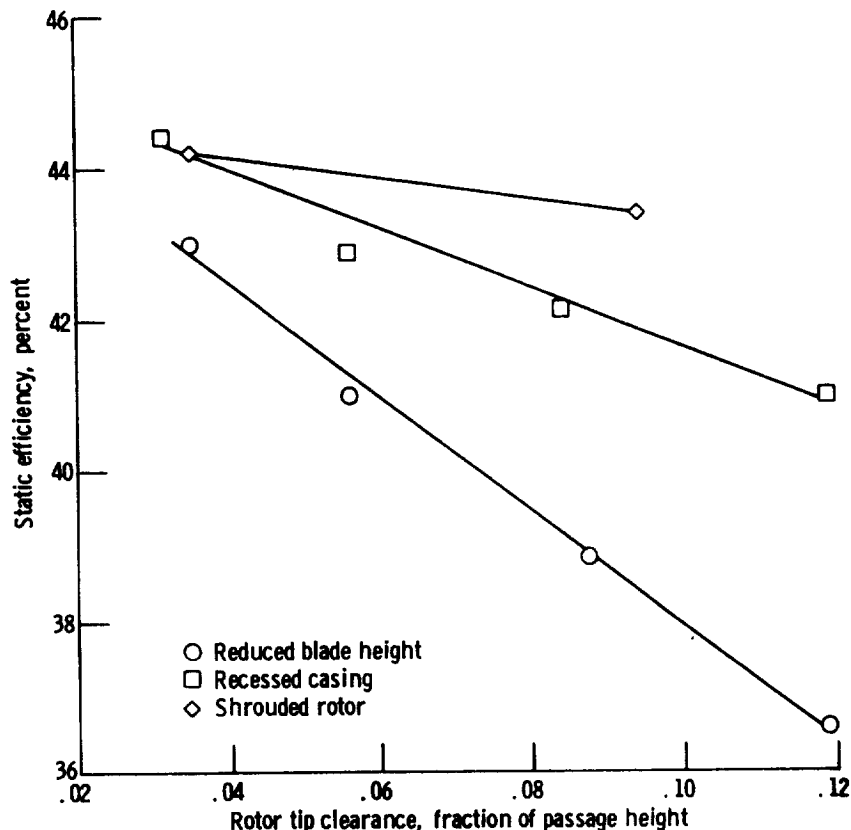


FIGURE 8-5.—Effect of tip-clearance configurations on turbine efficiency. (Data from ref. 4.)

fractions below some value, about 0.035 in this instance, the shroud no longer provides an increase in efficiency. This can be attributed to an increasing friction loss between shroud and casing as the clearance gap is decreased.

The comparative results shown in figure 8-5 for different blade-tip geometries are dependent upon that particular design and may not apply to other turbines. This is particularly true of the shrouded blade, since the leakage flow depends not only on the clearance span and pressure difference but also on the number of seals used. With respect to the recessed-casing configuration, it should be noted that the blade should not extend into the recess. If it does, the overlapping section will just be churning stagnant fluid and creating additional losses.

In summary, tip-clearance loss presents a complicated flow problem influenced by many factors and is not easily predicted with consistent accuracy. The clearance gap required for a turbine depends primarily on diameter (larger clearance for larger diameter) and, as seen previously, the loss increases as the ratio of clearance gap to blade height increases.

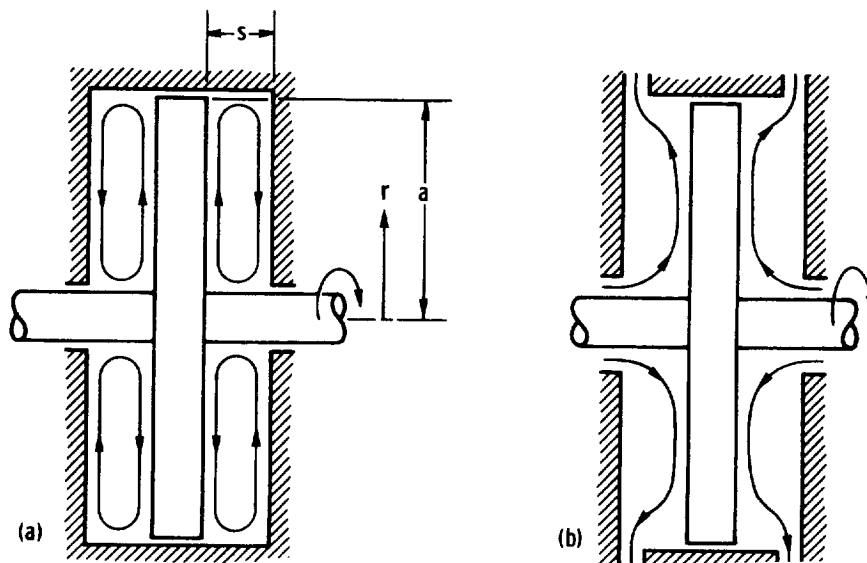
For any given diameter, therefore, the tip-clearance loss increases with increasing hub- to tip-radius ratio. It becomes increasingly difficult to maintain a desired small ratio of clearance gap to blade height as the turbine, and hence the blade height, becomes smaller. For a given radius ratio, therefore, the loss is more severe for small turbines and less severe for larger turbines. If tip leakage is considered to be a problem in a particular case, it might be worthwhile to carry out tests to evaluate the leakage effects.

DISK-FRICTION LOSS

The disk-friction loss (or windage loss) is due to the skin friction and circulation of fluid between the rotating disk and the stationary casing. In addition, some turbines for hot applications, for example aircraft engines, have a small steady stream of lower-temperature gas that bathes and cools the rotor disk. This cooling gas flows along the rotor-disk surface from near the engine centerline outward to the base of the blades. The qualitative nature of the flow patterns around rotor disks without and with throughflow of cooling gas are shown in figure 8-6. Equations for estimating the associated losses are presented herein.

No Throughflow

For the case with no throughflow, as in figure 8-6(a), the thin layer of fluid close to the rotating surface is thrown outward by centrifugal action



(a) Without throughflow.

(b) With throughflow.

FIGURE 8-6.—Flow patterns for rotating disks.

and returns via the stationary wall to the inner radius, thereby building up a continuous circulatory effect. Consider an element of area on one side of the disk

$$dA = 2\pi r dr \quad (8-1)$$

where A is the area, in m^2 or ft^2 , of one side of the disk, and r is the radius, in m or ft , of the area element dA . The fluid shear stress τ , in N/m^2 or lb/ft^2 , acting over this area at the radius r produces a resisting torque to the disk rotation of

$$\frac{dM_o}{2} = \tau 2\pi r^2 dr \quad (8-2)$$

where M_o is the resisting torque, in $N\cdot m$ or $lb\cdot ft$, for both sides of a disk in the case of no throughflow. The shear stress can be expressed as

$$\tau = \frac{C_f}{2g} \rho V_u^2 \quad (8-3)$$

where

- C_f fluid shear-stress coefficient
- g conversion constant, 1; 32.17 (lbm) (ft)/(lbf) (sec²)
- ρ density, kg/m^3 ; lb/ft^3
- V_u tangential component of fluid absolute velocity, m/sec ; ft/sec

At the disk surface, the fluid tangential velocity is

$$V_u = r\omega \quad (8-4)$$

where ω is the angular velocity, in rad/sec . By substituting equation (8-4) into (8-3), the total torque for both sides of the disk can be written as

$$M_o = \int_0^a \frac{2\pi}{g} C_f \rho \omega^2 r^4 dr \quad (8-5)$$

where a is the disk rim radius, in m or ft . Performing the integration yields

$$M_o = C_{M,o} \rho \frac{\omega^2 a^5}{2g} \quad (8-6)$$

where $C_{M,o}$ is a torque coefficient for the case of no throughflow. The disk-friction loss expressed as power is then the torque times the angular velocity:

$$P_{df} = \frac{M_o \omega}{J} = C_{M,o} \frac{\rho \omega^3 a^5}{2gJ} \quad (8-7)$$

where P_{df} is the disk-friction power loss, in W or Btu/sec , and J is a

conversion constant (equal to 1, or 778 (ft)(lb)/Btu). The form of equation (8-7) that is found in most handbooks is

$$P_{df} = K_{df} \rho N^3 D_r^5 \quad (8-8)$$

where

K_{df} disk-friction power-loss coefficient
 N rotative speed
 D_r disk rim diameter

A number of investigators have published values of the constant K_{df} in equation (8-8) to be used for different circumstances, while others have made small changes to the exponents to better fit the available data. The wide assortment of semiempirical equations used to predict this loss is, no doubt, due to variations of the test-apparatus geometry, the somewhat oversimplified model from which equation (8-7) is derived, and the existence of different types of flow that can occur in the space between the rotor and the casing. One thing that can be noted from equation (8-7) or (8-8) is that for a given blade speed, lower loss is obtained by having a smaller diameter and a higher rotative speed.

An extensive investigation has been conducted (refs. 6 and 7) to determine the effect of chamber proportions on disk friction and to present a clearer picture of the several modes of flow that may exist. In general, four modes of flow, or flow regimes, can exist in the axial space between the casing and the rotating disk, depending on the chamber dimensions and the flow Reynolds number. The torque coefficient $C_{M,o}$ was evaluated both theoretically and experimentally in each regime. A description of each regime and the associated equations for the torque coefficient are as follows:

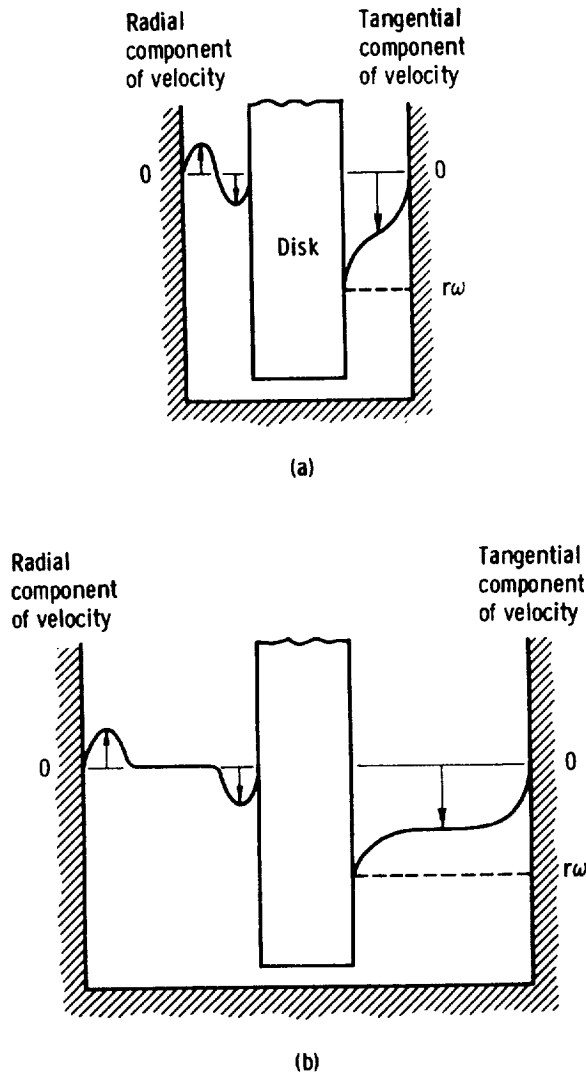
Regime I: Laminar Flow, Small Clearance. Boundary layers on the rotor disk and casing are merged, so that a continuous variation in velocity exists across the axial gap s . Figure 8-7(a) indicates the nature of the variations in the radial and tangential components of fluid velocity at a given radius in the gap. The best equation for torque coefficient, both theoretically and empirically, is

$$C_{M,o} = \frac{2\pi}{(s/a)R} \quad (8-9)$$

where s is the axial distance, in m or ft, between disk and casing, and R is the Reynolds number defined as

$$R = \frac{\omega a^2 \rho}{\mu} \quad (8-10)$$

where μ is the dynamic viscosity, in (N)(sec)/m² or lb/(ft)(sec).



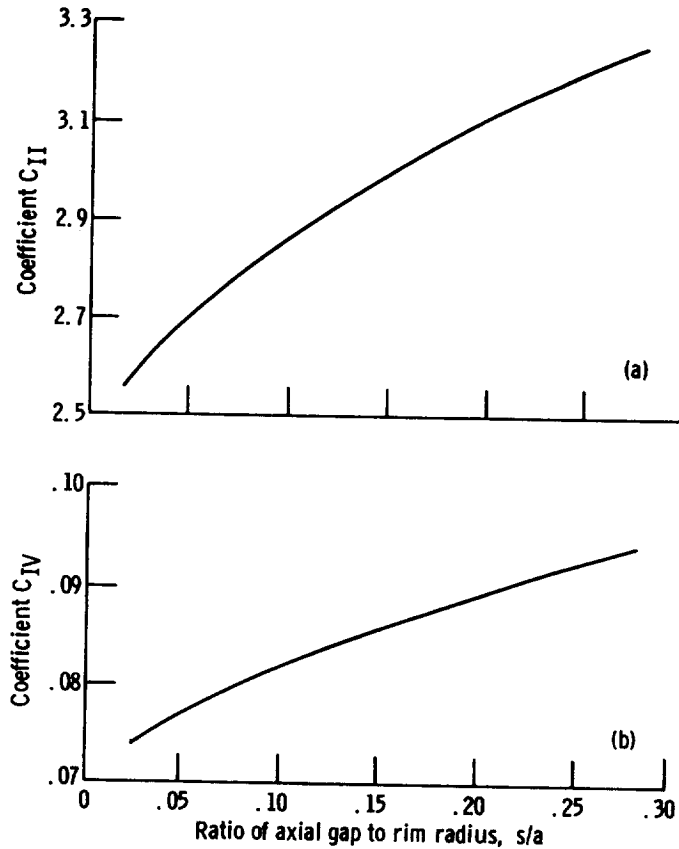
(a) Flow regimes I and III.
 (b) Flow regimes II and IV.

FIGURE 8-7.—Velocity patterns around rotating disks without throughflow.

Regime II: Laminar Flow, Large Clearance. The combined thickness of the boundary layers on the rotor and on the casing is less than the axial gap, and between these boundary layers there exists a core of rotating fluid in which no change in velocity occurs. Figure 8-7(b) shows the variations in the radial and tangential velocity components for this case. The best theoretical and empirical equations for torque coefficient are

$$C_{M,o} = \frac{C_{II}}{R^{1/2}} \quad (8-11)$$

where C_{II} is a function of (s/a) , as shown in figure 8-8(a), and



(a) Flow regime II.

(b) Flow regime IV.

FIGURE 8-8.—Evaluation of torque coefficients. (Data from ref. 6.)

$$C_{M,o} = \frac{3.70(s/a)^{1/10}}{R^{1/2}} \quad (8-12)$$

respectively.

Regime III: Turbulent Flow, Small Clearance. The turbulent counterpart of Regime I. The best theoretical and empirical equations for torque coefficient are

$$C_{M,o} = \frac{0.0622}{(s/a)^{1/4} R^{1/4}} \quad (8-13)$$

and

$$C_{M,o} = \frac{0.080}{(s/a)^{1/6} R^{1/4}} \quad (8-14)$$

respectively.

Regime IV: Turbulent Flow, Large Clearance. The turbulent counterpart of Regime II. The best theoretical and empirical equations for torque coefficient are

$$C_{M,o} = \frac{C_{IV}}{R^{1/5}} \tag{8-15}$$

where C_{IV} is a function of (s/a) , as shown in figure 8-8(b), and

$$C_{M,o} = \frac{0.102(s/a)^{1/10}}{R^{1/5}} \tag{8-16}$$

respectively.

The particular flow regime that exists at any Reynolds number can be determined by plotting torque coefficient against Reynolds number from equations (8-9), (8-11), (8-13), and (8-15), as shown in figure 8-9 for several values of s/a . The discontinuities (changes in slope) in the lines of figure 8-9 indicate transition from one regime to another. In this figure, the flow regimes are determined by matching the slopes of the lines with

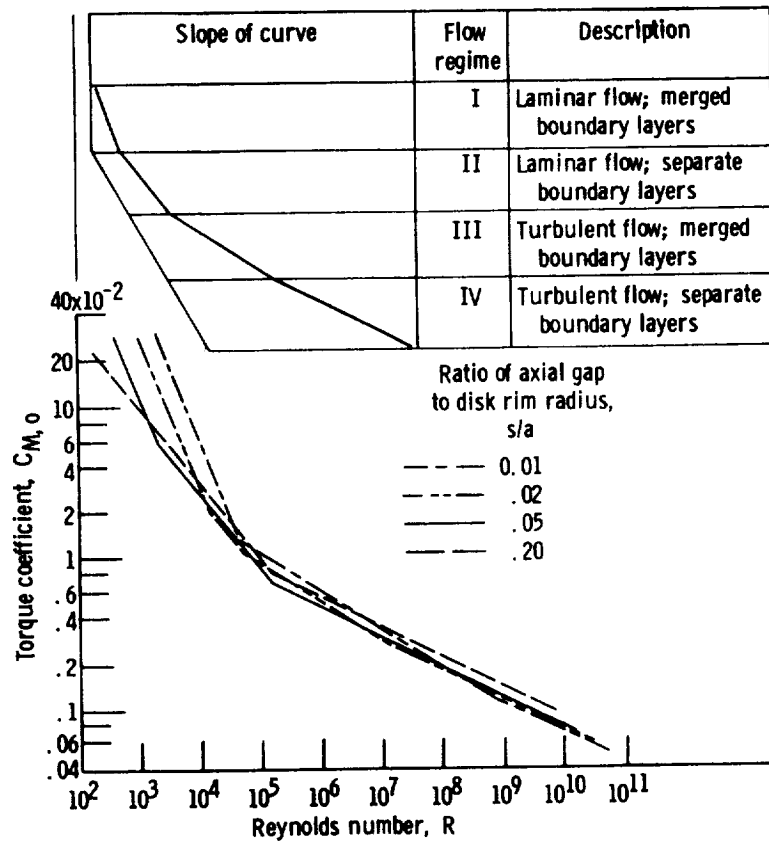


FIGURE 8-9.—Theoretical variation of torque coefficient with Reynolds number for no throughflow. (Data from ref. 6.)

those shown in the insert in the figure. Torque-coefficient values (ref. 6) determined experimentally with a 50.8-centimeter (20-in.) disk rotated in water and oil for several values of s/a verify the theory.

Throughflow

For the case of the rotating disk with throughflow, as in figure 8-6(b), the friction torque increases with the throughflow. This problem has been analyzed for low values of throughflow with regime-IV flow. In this case, it is assumed that the fluid enters the chamber near the centerline with no angular velocity and leaves at the rim with some angular velocity $K_o\omega a$. The symbol K_o represents the ratio of the angular velocity of the rotating core of gas to the angular velocity of the disk. The increase in torque, ΔM , over that without throughflow is the rate of change of angular momentum of the fluid flowing through the system:

$$\Delta M = 2\rho \frac{Q}{g} (K_o\omega a)a = 2\rho \frac{Q}{g} K_o\omega a^2 \quad (8-17)$$

where Q is the volumetric throughflow rate, in m^3/sec or ft^3/sec , in the clearance space on one side of the disk. The total torque for the throughflow case is then

$$M = M_o + \Delta M = \frac{C_{M,o}\rho\omega^2 a^5}{2g} + 2\rho \frac{Q}{g} K_o\omega a^2 \quad (8-18)$$

The value of K_o is approximately 0.45 for s/a ratios from 0.025 to 0.12.

An assessment of the power loss can be obtained by calculating the friction torque of the throughflow case compared to that of the no-throughflow case:

$$\frac{M}{M_o} = 1 + \frac{2\rho Q K_o\omega a^2}{\frac{1}{2} C_{M,o}\rho\omega^2 a^5} = 1 + \frac{4K_o}{C_{M,o}} \frac{Q}{\omega a^3} \quad (8-19)$$

Substituting equation (8-16) for $C_{M,o}$ yields

$$\frac{M}{M_o} = 1 + \frac{K_o R^{1/5}}{0.0255 (s/a)^{1/10}} \frac{Q}{\omega a^3} = 1 + 39.2 \frac{K_o}{(s/a)^{1/10}} \Upsilon \quad (8-20)$$

where Υ is a dimensionless throughflow number defined as

$$\Upsilon = \frac{Q}{\omega a^3} R^{1/5} \quad (8-21)$$

According to the data of reference 7, equation (8-20) predicts values that are somewhat high; moreover, the effect of s/a is not accurately

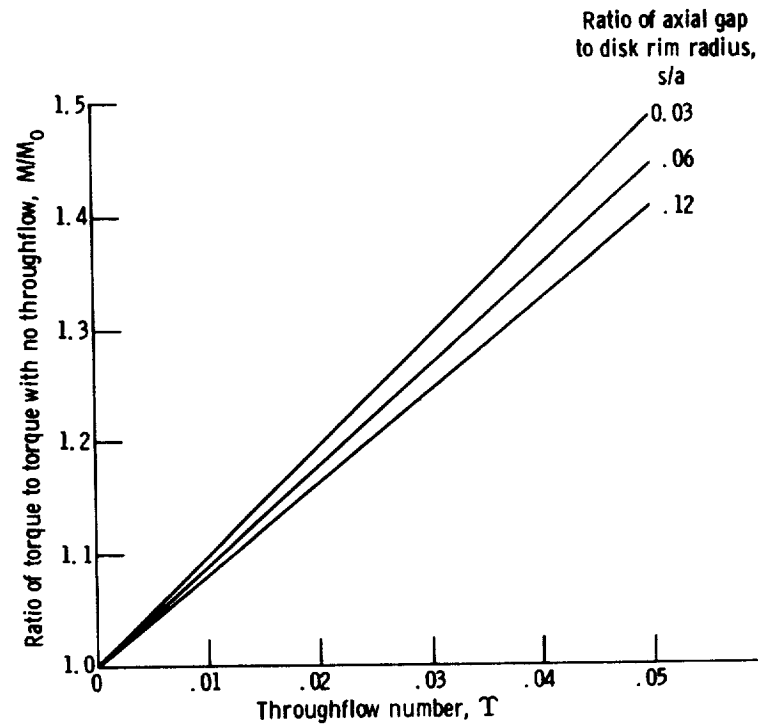


FIGURE 8-10.—Empirical variation of torque with throughflow number. (Data from ref. 7.)

given by $(s/a)^{1/10}$. Empirically, the test data are represented to within ± 5 percent by the relation

$$\frac{M}{M_0} = 1 + 13.9K_0 \frac{\tau}{(s/a)^{1/8}} \quad (8-22)$$

Equation (8-22) is plotted in figure 8-10 for several s/a values.

PARTIAL-ADMISSION LOSSES

Full-admission axial-flow turbines are used for most applications; however, unusual conditions sometimes arise for which a partial-admission turbine may be a better choice. If, for example, the design mass-flow rate is so small that a normal full-admission design would give very-small blade heights, then it may be advantageous to use partial admission. The losses due to partial admission with long blades may be less than the leakage and low Reynolds-number losses of the full-admission turbine having short blades. In addition, for a given rotative speed, partial admission allows the freedom of larger diameter and higher blade-jet speed ratios. Also, the use of partial admission may be a convenient way to reduce power output

of an existing full-admission turbine (physically block some of the stator passages). In general, partial-admission turbines have high specific-work output and low volumetric-flow rates.

As mentioned previously in this chapter, the partial-admission losses are the pumping loss in the inactive blade channels and the filling-and-emptying loss encountered as the blades pass through the active sector. This latter loss has been referred to as expansion, scavenging, or sector loss. The mechanisms of partial-admission losses are not clearly or fully understood, but they do result in a decrease in output power and efficiency when compared to the same turbine operating with full admission.

The pumping loss is that loss caused by the inactive blades rotating in a fluid-filled casing, and expressions for it are somewhat similar in form to, and often combined with, the expression for the disk-friction loss. These expressions all seem to trace back to reference 8, where the results of several experimental investigations are summarized. The equations for estimating pumping-power loss that resulted from these investigations showed that the effects of blade height and diameter on the pumping-power loss are quite uncertain, as evidenced by variations in the exponents on these terms. Further, the nature and location of obstructions (adjacent blade rows, casing wall, etc.) or lack of such in the vicinity of the three open sides of the blade channel were accounted for only by differences in the empirical loss coefficient. Therefore, it appears that a generally applicable expression for pumping-power loss is yet to be found.

The one equation perhaps most often used is

$$P_p = K_p \rho U_m^3 l^{1.5} D_m (1 - \epsilon) \quad (8-23)$$

where

P_p	pumping-power loss, W; (ft) (lb)/sec
K_p	pumping-power loss coefficient, $1/m^{1/2}$; (lbf) (sec ²)/(lbm) (ft ^{3/2})
U_m	blade mean-section speed, m/sec; ft/sec
l	blade height, m; ft
D_m	blade mean-section diameter, m; ft
ϵ	active fraction of stator-exit area

The value of the coefficient K_p as reported in reference 8 and converted to the units used herein is $3.63 \text{ l}/\text{m}^{1/2}$, or $0.0105 \text{ (lbf) (sec}^2\text{)}/\text{(lbm) (ft}^{3/2}\text{)}$, for an unenclosed rotor. For the same rotors enclosed, the coefficient values were one-quarter to one-half of the above values. More recently, the combined disk-friction and pumping losses for a single-stage rotor enclosed by the turbine housing were reported in reference 9. If a disk-friction loss estimated by equation (8-7) is subtracted from the combined losses of reference 9 and if the remaining loss is converted to the form of equation (8-23), the coefficient K_p is found to be $5.92 \text{ l}/\text{m}^{1/2}$, or $0.0171 \text{ (lbf) (sec}^2\text{)}/\text{(lbm) (ft}^{3/2}\text{)}$. This is significantly higher than the coefficients

reported in reference 8, and the difference is attributed to primarily the lack of an adequate loss model.

The other partial-admission loss shall herein be called the sector loss. Imagine a blade channel as it just starts to enter the active sector. It is filled with relatively stagnant fluid that must be pushed out by the high-momentum fluid leaving the nozzle. This scavenging will continue until the blade channel is completely within the active sector. As the blade channel passes out of the active sector, a second sector loss occurs. As the inlet to the blade channel is cut off from the nozzle active arc, less and less high-momentum fluid enters the channel. Since this fluid has the entire blade channel area to flow into, it is rapidly diffused as it flows through the rotor. These losses cause an overall decrease in the momentum of the fluid passing through the rotor, thus decreasing the available energy of the fluid. It was reported in reference 10 that this decrease in momentum may be found by multiplying the rotor-exit momentum by a loss coefficient

$$K_s = \left(1 - \frac{p}{3f}\right) \quad (8-24)$$

where p is the rotor-blade pitch, in m or ft, and f is the nozzle active arc length, in m or ft. Effectively, K_s is a rotor velocity coefficient that accounts for the sector loss.

The effect of the sector loss on turbine efficiency is determined as follows. With the use of equations (2-6) and (2-14), from volume 1, and the associated velocity diagram geometry, we can express the specific work of an axial-flow turbine as

$$\Delta h' = \frac{U_m}{gJ} (W_{u,1} - W_{u,2}) = \frac{U_m}{gJ} (W_1 \sin \beta_1 - W_2 \sin \beta_2) \quad (8-25)$$

where

- $\Delta h'$ turbine specific work, J/kg; Btu/lb
- W_u tangential component of relative velocity, m/sec; ft/sec
- W relative velocity, m/sec; ft/sec
- β fluid relative angle measured from axial direction, deg

The subscripts 1 and 2 refer to the rotor inlet and exit, respectively. For an impulse turbine (which most partial-admission turbines are), where $\beta_1 = -\beta_2$,

$$\Delta h' = \frac{U_m}{gJ} W_1 \sin \beta_1 (1 + K_w) \quad (8-26)$$

where K_w is the rotor relative-velocity ratio W_2/W_1 for the full-admission turbine. For the partial-admission turbine, applying the sector loss

coefficient yields

$$W_2 = K_w K_s W_1 \quad (8-27)$$

So, for the partial-admission turbine,

$$\Delta h'_{ra} = \frac{U_m}{gJ} W_1 \sin \beta_1 (1 + K_w K_s) \quad (8-28)$$

Since efficiency is

$$\eta = \frac{\Delta h'}{\Delta h_{id}} \quad (8-29)$$

where Δh_{id} is the turbine ideal specific work, in J/kg or Btu/lb, the efficiency of the partial-admission turbine with respect to that of the full-admission turbine is

$$\frac{\eta_{pa}}{\eta} = \frac{\Delta h'_{ra}}{\Delta h'} \quad (8-30)$$

Substituting equations (8-26) and (8-28) into equation (8-30) then yields

$$\eta_{pa} = \eta \frac{1 + K_w K_s}{1 + K_w} \quad (8-31)$$

The efficiency penalty expressed by equation (8-31) accounts for the sector loss only; the pumping loss discussed earlier will reduce the overall efficiency further. Equation (8-24) indicates that a partial-admission turbine rotor should have closely spaced blades to reduce the sector loss; however, as more blades are added to the rotor, the blade profile loss will increase. Also, the effect of the number of rotor blades on the pumping loss is not known. Therefore, the complete optimization of a partial-admission design cannot be done analytically at present.

In the study of reference 9, the efficiency of a small axial-flow turbine was determined over a range of admissions from 12 to 100 percent. The total loss due to partial-admission operation was taken as the difference between the full- and the partial-admission efficiencies. The blade pumping and disk-friction losses were measured separately and were subtracted from the total partial-admission loss to give what was called other partial-admission losses. These other losses include the sector loss and any loss due to leakage from the active sector to the inactive sector. The partial-admission losses of reference 9 are plotted against admission-arc fraction in figure 8-11. The combined pumping and disk-friction loss increased with decreasing arc fraction, while the other losses remained nearly constant over the range of arcs tested.

Predicted efficiencies (from ref. 10) are plotted against blade-jet speed

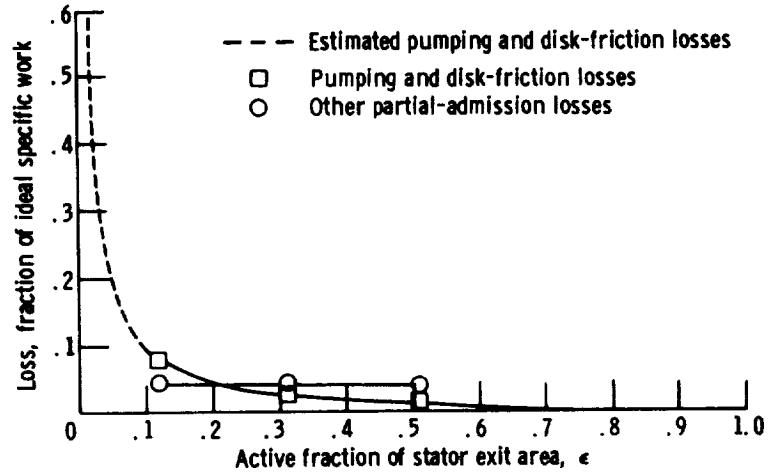


FIGURE 8-11.—Variation of partial-admission losses with active fraction of stator area. (Data from ref. 9.)

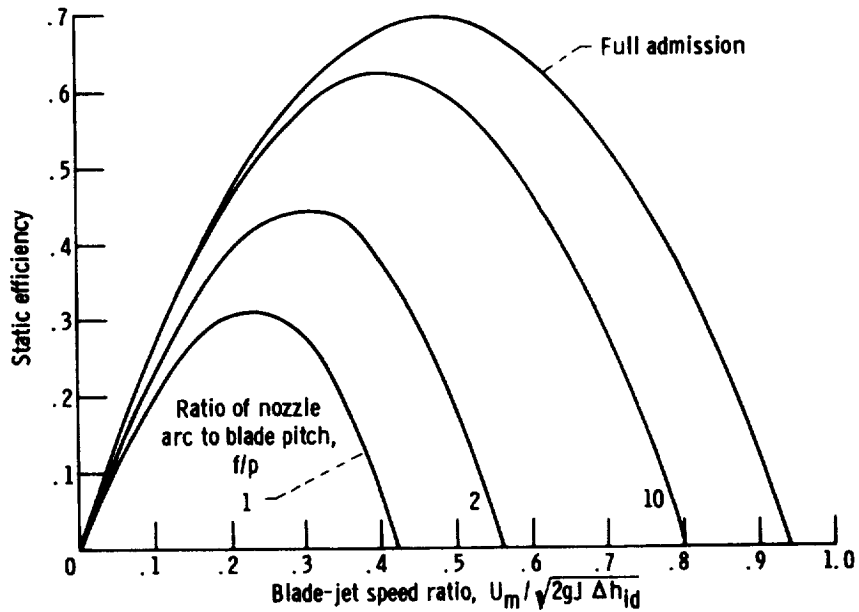


FIGURE 8-12.—Design-point performance of partial- and full-admission turbines. (Data from ref. 10.)

ratio (see discussion in vol. 1, ch. 2) in figure 8-12 for a particular turbine operating with full admission and with three different amounts of partial admission. The expected reduction in peak efficiency with reduced arc of admission is seen. The important thing to note from this figure is the reduction in optimum blade-jet speed ratio as admission arc is reduced. Aerodynamic efficiency is a maximum at a blade-jet speed ratio of 0.5,

irrespective of admission arc, and decreases with decreasing blade speed. Blade-pumping and disk-friction losses, which decrease with decreasing blade speed, become a larger part of the gross aerodynamic power as admission arc decreases. Therefore, as admission arc is reduced, the maximum net output power (aerodynamic power minus blade-pumping and disk-friction power) is obtained at lower blade speeds. Thus, for the design of a partial-admission turbine, the partial-admission losses must be factored into the design before an optimum or near-optimum blade-jet speed ratio can be selected.

INCIDENCE LOSS

The incidence loss is that loss which occurs when the gas enters a blade row (either stator or rotor) at some angle other than the optimum flow angle. Flow incidence would normally only occur at off-design conditions, since, theoretically at least, all gas and blade angles are matched at the design condition. The nomenclature used when speaking of incidence is shown in figure 8-13. The dashed line running through the blade profile is the camber line and defines the blade inlet angle. The incidence angle is defined as

$$i = \alpha - \alpha_b \quad (8-32)$$

where

- i incidence angle, deg
- α fluid flow angle from axial direction, deg
- α_b blade inlet angle from axial direction, deg

The fluid flow angle must be the absolute angle for stators and the relative angle for rotors. The incidence angle may be positive or negative, as indicated in figure 8-13. The sign of the incidence angle is important because cascade tests have shown that the variation of loss with incidence angle is different for positive and negative angles.

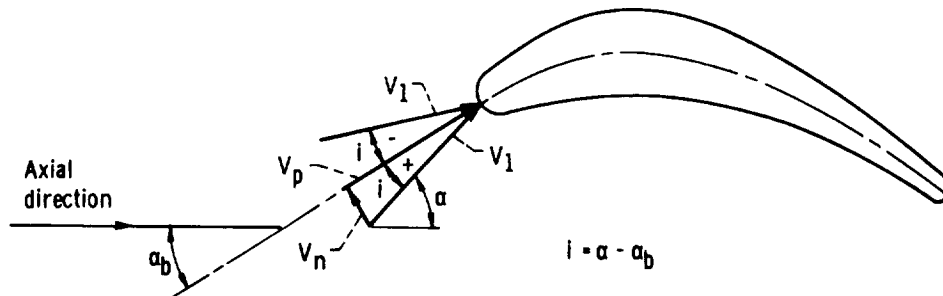


FIGURE 8-13.—Blade incidence nomenclature.

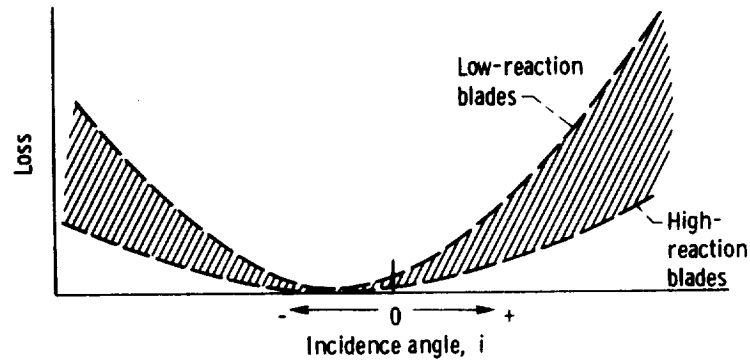


FIGURE 8-14.—Characteristics of blade incidence loss.

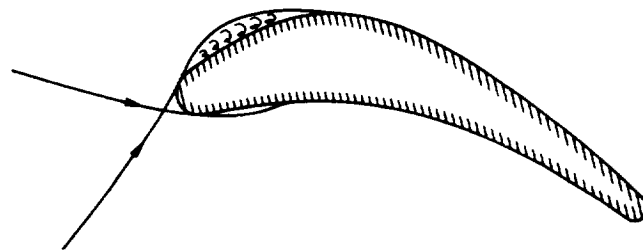


FIGURE 8-15.—Local flow separation on blade surface.

The general nature of the variation of incidence loss with incidence angle is shown by figure 8-14, which represents a summary of cascade test results. The loss curve is not symmetrical about the zero incidence angle, but shows a loss that is larger for positive incidence than for negative incidence. This may be due to some local separation on the suction surface at large positive incidence, as indicated in figure 8-15, and the lack, or smaller area, of separation at the same value of negative incidence. Also, blades in which the mean acceleration of the gas flow is large (high-reaction blades) have a wide range of incidence over which loss is low, whereas low-reaction blades have higher losses for the same incidence range.

Another thing to be noted from figure 8-14 is that the minimum loss does not occur at zero incidence, but at some small amount of negative incidence. This may be explained by the sketch of figure 8-16. The stagnation streamlines for two inlet flow angles are shown; one at zero incidence and the other at some small negative incidence with respect to the blade inlet angle. Both tests and theory show that the stagnation streamline curves upward as the flow impacts on the blade leading edge, and the true zero incidence occurs when there is some negative incidence

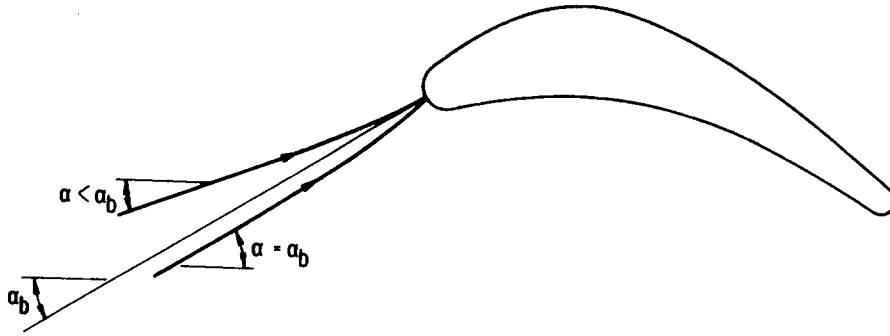


FIGURE 8-16.—Curvature of stagnation streamline at blade inlet.

relative to the free-stream flow. The incidence angle at minimum loss is usually -4° to -8° . Because of this, some turbine designers design their blades with a small amount of negative incidence, while others do not because of the small difference involved.

The magnitude of the incidence loss takes on importance when the off-design performance of a turbine must be predicted. A method for determining incidence loss based on test data is described in reference 11. An analytical method is described here with the aid of figure 8-13. The inlet velocity V_1 can be resolved into a component V_n normal to, and a component V_p parallel to the blade inlet direction (camber line at inlet). If it is assumed that the parallel component passes through the blade row without any entry loss and that the normal component is entirely lost, the recovered kinetic energy is

$$\frac{V_p^2}{2gJ} = \frac{V_1^2}{2gJ} \left(\frac{V_p}{V_1} \right)^2 = \frac{V_1^2}{2gJ} \cos^2 i \quad (8-33)$$

and the kinetic-energy loss due to incidence is

$$L_i = \frac{V_1^2}{2gJ} (1 - \cos^2 i) \quad (8-34)$$

In order to account for the differences in loss variation with positive and negative incidence, the effect of blade-row reaction, and the minimum loss not occurring at zero incidence, equation (8-34) has been generalized to

$$L_i = \frac{V_1^2}{2gJ} [1 - \cos^n (i - i_{opt})] \quad (8-35)$$

where i_{opt} is the optimum (minimum-loss) incidence angle. This type of equation has proved satisfactory when used in off-design performance

prediction methods such as that of reference 12. Where specific incidence-loss data are lacking, values of $n=2$ for negative incidence and $n=3$ for positive incidence have been used satisfactorily.

REFERENCES

1. HORLOCK, JOHN H.: Axial Flow Turbines. Butterworth Inc., 1966.
2. HOLESKI, DONALD E.; AND FUTRAL, SAMUEL M., JR.: Effect of Rotor Tip Clearance on the Performance of a 5-Inch Single-Stage Axial-Flow Turbine. NASA TM X-1757, 1969.
3. KOFSEY, MILTON G.; AND NUSBAUM, WILLIAM J.: Performance Evaluation of a Two-Stage Axial-Flow Turbine for Two Values of Tip Clearance. NASA TN D-4388, 1968.
4. KOFSEY, MILTON G.: Experimental Investigation of Three Tip-Clearance Configurations Over a Range of Tip Clearance Using a Single-Stage Turbine of High Hub- to Tip-Radius Ratio. NASA TM X-472, 1961.
5. HONG, YONG S.; AND GROH, F. G.: Axial Turbine Loss Analysis and Efficiency Prediction Method. Rep. D4-3220, Boeing Co., Mar. 11, 1966.
6. DAILY, J. W.; AND NECE, R. E.: Chamber Dimension Effects on Induced Flow and Frictional Resistance of Enclosed Rotating Disks. J. Basic Eng., vol. 82, no. 1, Mar. 1960, pp. 217-232.
7. DAILY, J. W.; ERNST, W. D.; AND ASHEDIAN, V. V.: Enclosed Rotating Disks with Superposed Throughflow: Mean Study and Periodic Unsteady Characteristics of the Induced Flow. Rep. R-54-16, Massachusetts Inst. Tech. (AROD-2500-2, AD-443060), Apr. 1964.
8. STODOLA, A. (LOUIS C. LOEWENSTEIN, TRANS.): Steam and Gas Turbines. Vol. I. McGraw-Hill Book Co., Inc., 1927. Reprinted by Peter Smith, 1945, pp. 200-201.
9. KLASSEN, HUGH A.: Cold-Air Investigation of Effects of Partial Admission on Performance of 3.75-Inch Mean-Diameter Single-Stage Axial-Flow Turbine. NASA TN D-4700, 1968.
10. STENNING, ALAN H.: Design of Turbines for High-Energy-Fuel Low-Power-Output Applications. Rep. 79, Dynamic Analysis and Control Lab., Massachusetts Inst. Tech., Sept. 30, 1953.
11. AINLEY, D. G.; AND MATHIESON, G. C. R.: An Examination of the Flow and Pressure Losses in Blade Rows of Axial-Flow Turbines. R&M-2891, Aeronautical Research Council, Gt. Britain, 1955.
12. FLAGG, E. E.: Analytical Procedure and Computer Program for Determining the Off-Design Performance of Axial-Flow Turbines. NASA CR-710, 1967.

SYMBOLS

A	area on one side of rotor disk, m^2 ; ft^2
a	disk rim radius, m ; ft
C_{II}	coefficient used to evaluate $C_{M,o}$ in regime II by equation (8-11)
C_{IV}	coefficient used to evaluate $C_{M,o}$ in regime IV by equation (8-15)
C_f	fluid shear-stress coefficient
$C_{M,o}$	torque coefficient with no throughflow
D	diameter, m ; ft
f	nozzle active arc length, m ; ft
g	conversion constant, 1; 32.17 (lbm) (ft)/(lbf) (sec ²)
$\Delta h'$	turbine specific work, J/kg ; Btu/lb
Δh_{id}	turbine ideal specific work based on ratio of inlet-total pressure to exit-static pressure, J/kg ; Btu/lb
i	incidence angle, deg
J	conversion constant, 1; 778 (ft) (lb)/Btu
K_{df}	disk-friction power-loss coefficient
K_o	ratio of rotating-core angular velocity to disk angular velocity
K_p	pumping power loss coefficient, $1/m^{1/2}$; (lbf) (sec ²)/(lbm) (ft ^{3/2})
K_s	sector loss coefficient
K_w	rotor velocity coefficient for full-admission impulse turbine
L_i	incidence loss, J/kg ; Btu/lb
l	blade height, m ; ft
M	frictional resistance torque for both sides of rotor disk, $N\cdot m$; $lb\cdot ft$
N	rotative speed, rad/sec ; rev/min
n	exponent in equation (8-35)
P_{df}	disk-friction power loss, W ; Btu/sec
P_p	pumping power loss, W ; Btu/sec
p	rotor-blade pitch, m ; ft
Q	volumetric throughflow rate, m^3/sec ; ft^3/sec
R	Reynolds number
r	radius, m ; ft
s	axial distance between rotor disk and casing, m ; ft
U	blade speed, m/sec ; ft/sec
V	absolute velocity, m/sec ; ft/sec
W	relative velocity, m/sec ; ft/sec
α	fluid flow angle from axial direction, deg
α_b	blade inlet angle from axial direction, deg
β	fluid relative angle measured from axial direction, deg
ϵ	active fraction of stator exit area
η	turbine static efficiency
μ	dynamic viscosity, (N) (sec)/ m^2 ; $lb/(ft) (sec)$
ρ	density, kg/m^3 ; lb/ft^3

TURBINE DESIGN AND APPLICATION

τ	fluid shear stress, N/m ² ; lb/ft ²
T	throughflow number defined by equation (8-21)
ω	angular velocity, rad/sec

Subscripts:

m	mean section
n	component normal to blade inlet direction
o	no throughflow
opt	optimum
p	component parallel to blade inlet direction
pa	partial admission
r	disk rim
u	tangential component
1	{ rotor inlet blade-row inlet
2	rotor exit

CHAPTER 9

Supersonic Turbines

By Louis J. Goldman

A supersonic turbine stage is defined as one that operates with a supersonic relative velocity entering the rotor. Supersonic turbines have potential application in systems where high-energy fluids (those having low molecular weights and, consequently, high expansion velocities) are used and/or where high pressure ratios are available. They have been used by NASA in rocket turbopump systems and have been studied for use in open-cycle auxiliary-power systems for space.

Supersonic turbines have the potential for large specific work outputs because of the high pressure ratio. For a given power level, this type of turbine would require a small amount of driving fluid and a small number of stages. It would, therefore, be light-weight and relatively simple. Because of high jet velocities, however, supersonic turbines generally operate at low blade-jet speed ratios (often less than 0.2). As indicated in chapters 2 and 3 (vol. 1), low blade-jet speed ratios correspond to low static efficiencies, primarily because of high exit-kinetic-energy losses. For systems where the primary design criteria are a minimum number of stages along with minimum fluid consumption, the ideal work available from the high pressure ratio could more than offset the lower turbine efficiency and may result in a supersonic turbine being the optimum design choice.

To keep the efficiency of supersonic turbines at the highest possible level, proper design methods must be used. Both supersonic stators and rotors are designed by the method of characteristics. In this chapter, supersonic turbine design and performance are discussed under the following headings: (1) method of characteristics, (2) design

of supersonic stator blades, (3) design of supersonic rotor blades, and (4) operating characteristics of supersonic turbines.

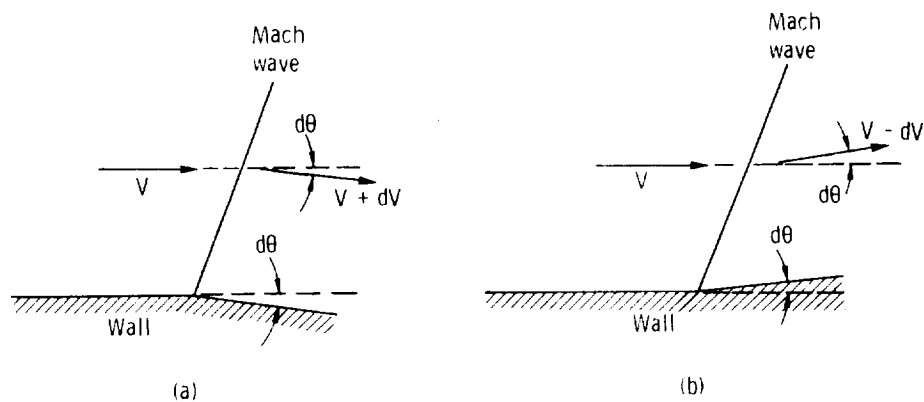
METHOD OF CHARACTERISTICS

The method of characteristics is a general method for solving a certain type (hyperbolic) of partial differential equation. The equations of motion for the two-dimensional supersonic flow of a perfect gas are of this type. Only this type of flow will be discussed in this chapter. Other types of supersonic flow (i.e., axially symmetric and certain non-steady flows) also can be handled by this method (see ref.1).

The method of characteristics can be developed in two ways: (1) by formal mathematical methods and (2) by simple dynamical considerations. The derivation based on dynamics stresses the physical processes involved. It will be the only one presented here. The mathematical derivation is useful in extending the method to other similar equations. Both developments are given in references 1 and 2.

Flow Along a Single Wall

The simplest supersonic flow field that satisfies the equations of motion (other than uniform parallel flow) is the flow through a single vanishingly weak standing wave. These waves, called Mach waves, can be considered to be very weak oblique shock waves. The entropy change through the wave is essentially zero. Examples of weak expansion and compression waves are shown in figure 9-1. As will be shown subsequently, an expansion wave is produced when the



(a) Expansion.

(b) Compression.

FIGURE 9-1.—Weak expansion and compression waves.

wall bends away from the flow, and a compression wave is produced when the wall bends toward the flow.

The bend (of angular magnitude $d\theta$) in the wall can be considered as a disturbance which produces the wave, which is required if the flow is to follow the wall. The bend in the wall may also be considered as a boundary condition to which one solution is a standing Mach wave with uniform flow fields on both sides of it. The importance of this solution can be appreciated when it is realized that any curved surface may be considered to be made up of a finite number of straight sections. The flow along a curved surface can, therefore, be approximated as the flow through a series of Mach waves. The dynamics of the flow through a weak expansion wave will now be discussed.

Consider the standing Mach wave included at an angle β to the direction of initial velocity V as shown in figure 9-2. The conservation of mass requires that

$$\frac{w}{A} = \rho V_n = (\rho + d\rho)(V_n + dV_n) = \text{constant} \quad (9-1)$$

where

w mass flow rate, kg/sec; lb/sec

A flow area along Mach wave, m^2 ; ft^2

ρ density, kg/m^3 ; lb/ft^3

V_n velocity component normal to Mach wave, m/sec; ft/sec

Neglecting second-order terms (i.e., $d\rho dV_n$) gives

$$\rho dV_n + V_n d\rho = 0 \quad (9-2)$$

Conservation of momentum in the tangential direction gives

$$\rho V_n V_t = (\rho + d\rho)(V_n + dV_n)(V_t + dV_t) \quad (9-3)$$

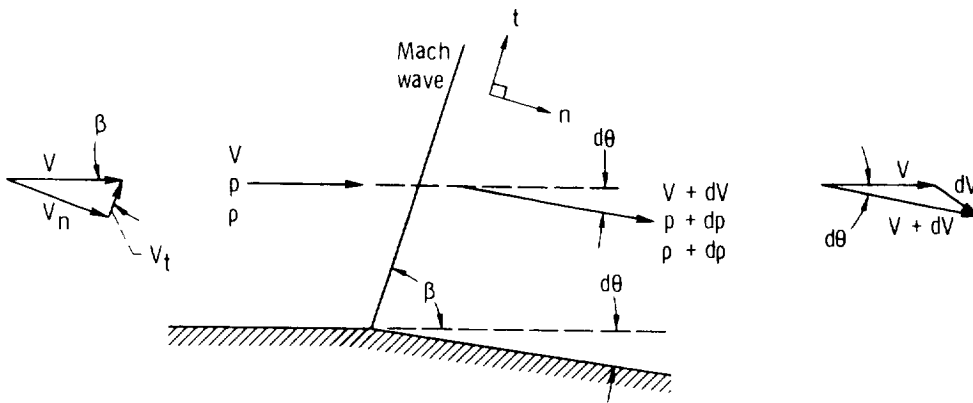


FIGURE 9-2.—Flow through a weak expansion wave, and associated nomenclature.

where V_t is the velocity component tangent to the Mach wave, in m/sec or ft/sec. Substituting equation (9-1) into equation (9-3) gives

$$\rho V_n V_t = \rho V_n (V_t + dV_t) \quad (9-4)$$

or

$$dV_t = 0 \quad (9-5)$$

This means that the tangential component of velocity remains constant as the flow crosses the wave. Consequently, the velocity change dV is equal to dV_n and is directed normal to the Mach wave.

Conservation of momentum in the normal direction gives

$$gp + \rho V_n^2 = g(p + dp) + (\rho + d\rho)(V_n + dV_n)^2 \quad (9-6)$$

where

g conversion constant, 1; 32.17 (lbm)(ft)/(lbf)(sec²)

p absolute pressure, N/m²; lb/ft²

Substituting equation (9-1) into equation (9-6) and expanding yields

$$0 = g dp + \rho V_n dV_n \quad (9-7)$$

Eliminating dV_n by using equation (9-2) results in

$$V_n^2 = g \left(\frac{dp}{d\rho} \right) \quad (9-8)$$

Equation (1-57) of chapter 1 (vol. 1) states

$$a = \sqrt{g \left(\frac{dp}{d\rho} \right)} \quad (9-9)$$

where a is speed of sound, in m/sec or ft/sec. Since the differential process being considered here is isentropic, substitution of equation (9-8) into equation (9-9) shows that

$$V_n = a \quad (9-10)$$

Therefore, the component of velocity normal to the Mach wave must be equal to the speed of sound. Noting from figure 9-2 that

$$V_n = V \sin \beta \quad (9-11)$$

gives

$$\sin \beta = \frac{V_n}{V} = \frac{a}{V} = \frac{1}{M} \quad (9-12)$$

where M is the Mach number. The angle β is called the Mach angle and has meaning only for $M \geq 1$.

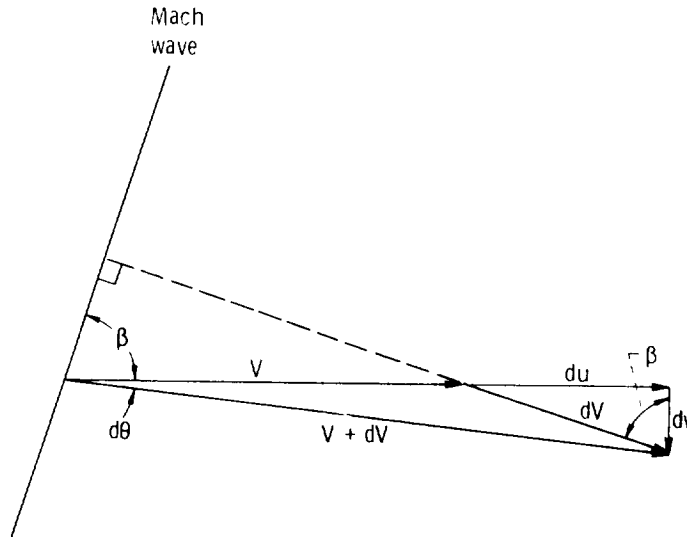


FIGURE 9-3.—Velocity diagram for flow through a weak expansion wave.

The relation between change in flow angle $d\theta$ and velocity change dV can be found from the velocity relations shown geometrically in figure 9-3. In the limit ($d\theta \rightarrow 0$),

$$du = dV \tag{9-13}$$

$$dv = V d\theta \tag{9-14}$$

and

$$\tan \beta = \frac{du}{dv} = \frac{dV}{V d\theta} \tag{9-15}$$

where

du component of dV parallel to initial velocity V , m/sec; ft/sec
 dv component of dV normal to initial velocity V , m/sec; ft/sec

Since, as can be determined from equation (9-12),

$$\tan \beta = \frac{1}{\sqrt{M^2 - 1}} \tag{9-16}$$

equation (9-15) becomes

$$\frac{dV}{V} = \frac{d\theta}{\sqrt{M^2 - 1}} \tag{9-17}$$

It is more convenient if dV/V is expressed in terms of the critical velocity ratio $M^* = V/V_{cr}$ rather than Mach number M . The critical velocity V_{cr} is equal to the speed of sound at the critical condition ($M=1$) and can be evaluated from equation (1-63) of chapter 1 (vol. 1). The relation between M^* and M is given by the equation

$$M = \sqrt{\frac{\frac{2}{\gamma+1} M^{*2}}{1 - \frac{\gamma-1}{\gamma+1} M^{*2}}} \quad (9-18)$$

where γ is the ratio of specific heat at constant pressure to specific heat at constant volume. Since V_{cr} is constant (because the total temperature is constant),

$$\frac{dV}{V} = \frac{dM^*}{M^*} \quad (9-19)$$

Substituting equations (9-18) and (9-19) into equation (9-17) gives, finally,

$$d\theta = \sqrt{\frac{M^{*2}-1}{1 - \frac{\gamma-1}{\gamma+1} M^{*2}}} \frac{dM^*}{M^*} \quad (9-20)$$

This is the differential relation between a change in flow angle and a velocity change through a single weak expansion wave. A similar relation could have been obtained for a single weak compression wave, except that equation (9-20) would have a minus sign.

Let us now consider the flow along a curved (convex) surface, as shown in figure 9-4. Assume that the surface is composed of a number of small bends, each producing a Mach wave. The relation indicated by equation (9-20) will be satisfied through each Mach wave provided the changes in θ are small. The combined flow field will, therefore, be a solution to the equations of motion for infinitesimal values of $d\theta$. This type of flow is called Prandtl-Meyer flow, or simple wave flow.

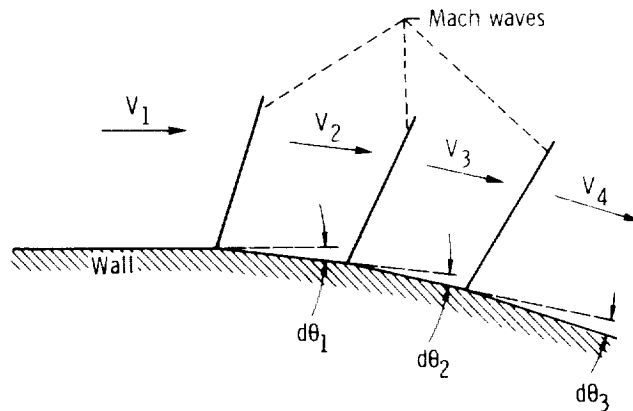


FIGURE 9-4.—Representation of flow along a convex wall.

If the number of segments approaches infinity, the flow field becomes continuous. Integration of equation (9-20) gives

$$\theta = \frac{1}{2} \sqrt{\frac{\gamma+1}{\gamma-1}} \arcsin [(\gamma-1)M^{*2}-\gamma] + \frac{1}{2} \arcsin \left(\frac{\gamma+1}{M^{*2}} - \gamma \right) + \text{constant} \quad (9-21)$$

If the constant is chosen such that $\theta=0$ when $M^*=1$ ($M=1$), the angle given by equation (9-21) is called the Prandtl-Meyer angle, and it is tabulated in many references (e.g., ref. 1). The Prandtl-Meyer angle is the angle through which the flow must turn in going from Mach 1 to the required Mach number and is often given the symbol ω (or ν). Therefore,

$$\omega = \frac{1}{2} \sqrt{\frac{\gamma+1}{\gamma-1}} \left\{ \frac{\pi}{2} + \arcsin [(\gamma-1)M^{*2}-\gamma] \right\} - \frac{1}{2} \left[\frac{\pi}{2} - \arcsin \left(\frac{\gamma+1}{M^{*2}} - \gamma \right) \right] \quad (9-22)$$

Note that the change in flow direction ($\Delta\theta$) in going from V_1 to V_2 is given by the change in the respective Prandtl-Meyer angles. That is,

$$\theta_2 - \theta_1 = \Delta\theta = \omega_2 - \omega_1 \quad (9-23)$$

The derivation has been for expansion waves. For compression waves, there would be a minus sign in equation (9-17). Therefore, the velocity decreases (M decreases) for flow through a compression wave. This means that the Mach angle β increases for flow along a concave wall, shown in figure 9-5. The Mach lines, there-

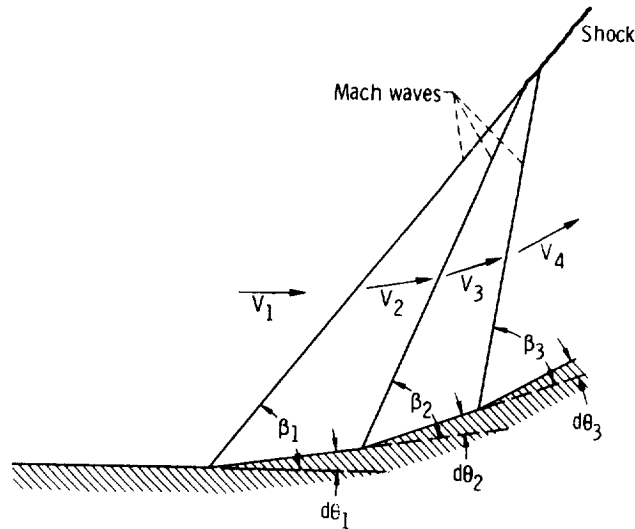


FIGURE 9-5.—Representation of flow along a concave wall.

fore, converge and form a shock as shown in the figure. The derived relations, of course, would be invalid in the shock region because of the entropy increase.

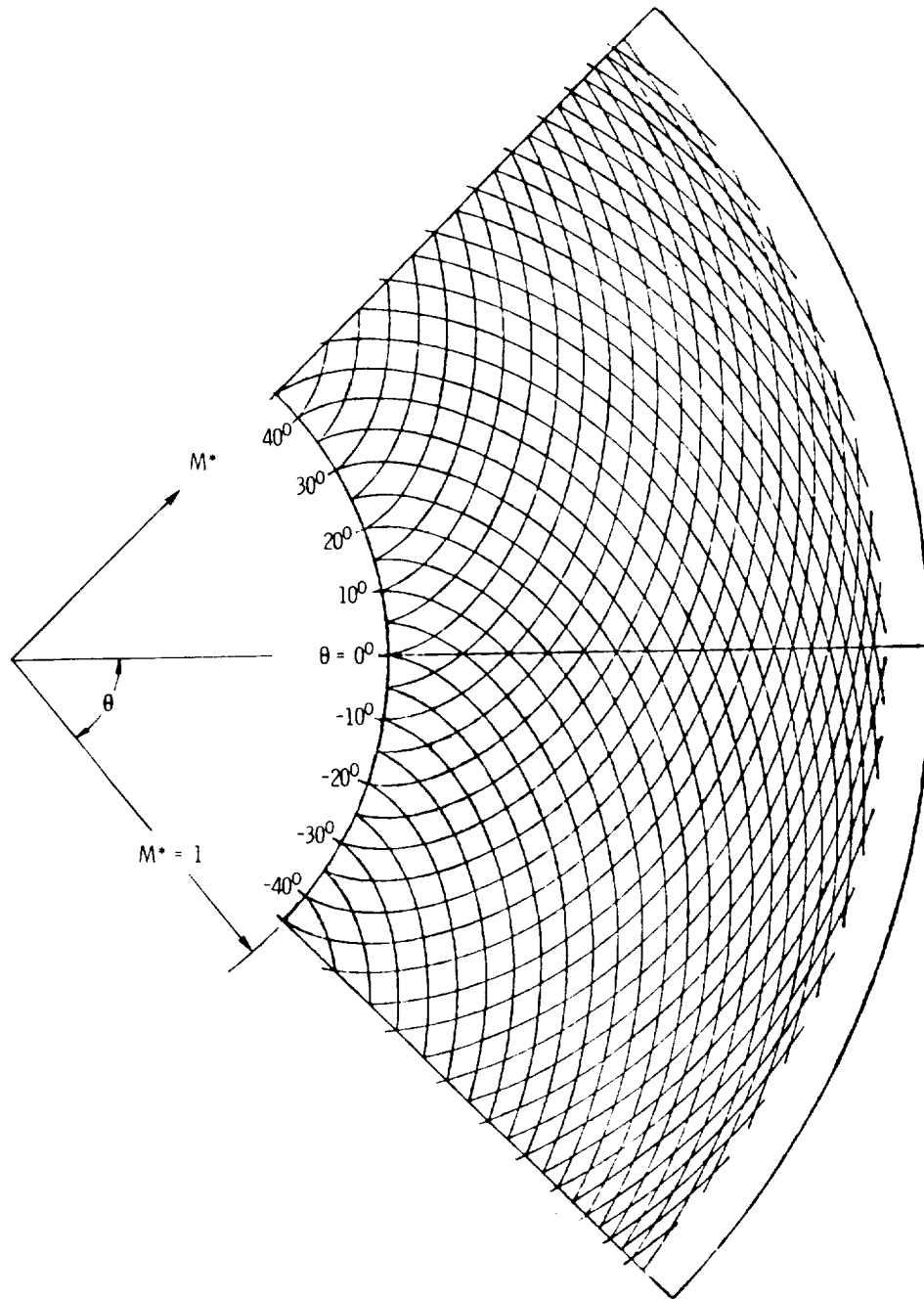
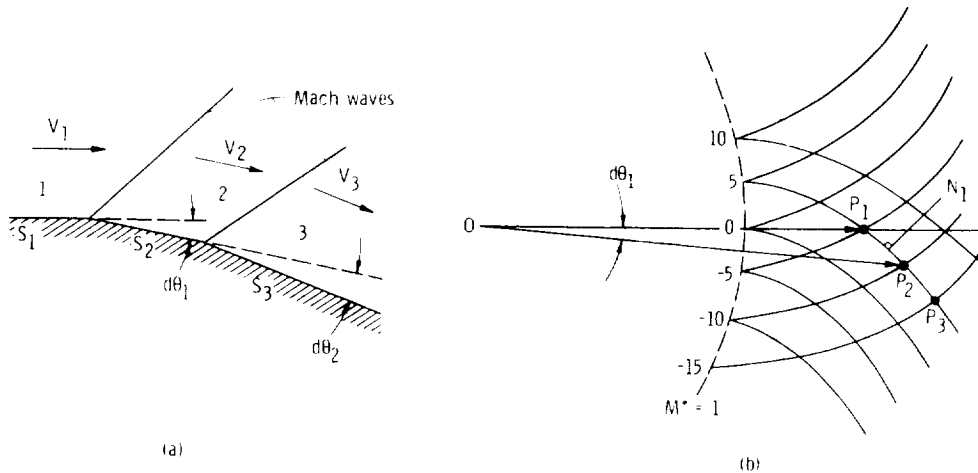


FIGURE 9-6.—Hodograph characteristic curves.

The relation between the flow angle θ and the critical velocity ratio M^* (eq. (9-21)) can be plotted on a polar diagram, as shown in figure 9-6. This type of diagram is called a hodograph plot. The curves of this plot are characteristic of the flow around any two-dimensional convex surface and are called hodograph characteristics. The value of the constant of equation (9-21) has been varied to generate these curves. The curves passing through $M^*=1$ at $\theta=0$ represent the variation of Prandtl-Meyer angle with critical velocity ratio as expressed by equation (9-22).

An important property of the hodograph characteristics is that the normals to the characteristics are parallel to the corresponding Mach wave in the physical plane. This allows the flow field to be constructed graphically and is best explained by a simple example. Consider the flow along a curved wall. After the wall is divided into a finite number of segments (fig. 9-7(a)), the initial point P_1 is located on the characteristic curve (fig. 9-7(b)) corresponding to V_1 (line OP_1 parallel to \vec{V}_1). Point P_2 is located in the hodograph diagram by drawing the line OP_2 parallel to \vec{V}_2 (or wall segment S_2). Note that P_2 must lie on the expansion characteristic curve through P_1 . The Mach wave separating V_1 and V_2 is found by drawing the normal (shown as N_1 in the figure) to the characteristic segment P_1P_2 . This direction is parallel to the Mach wave direction in the physical plane. The preceding process is continued through the additional segments.

The graphical procedure is, at best, cumbersome to use. The procedure may be made entirely numerical if it is recalled that the direc-



(a) Physical plane.

(b) Hodograph plane.

FIGURE 9-7.—Flow along convex wall.

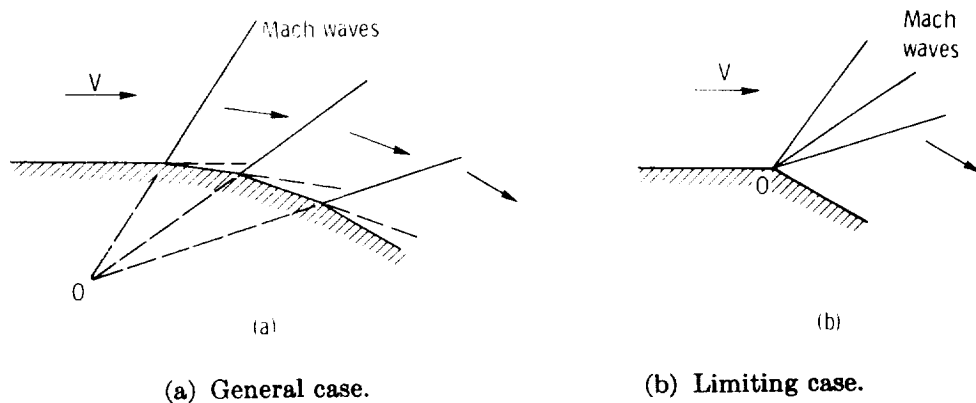


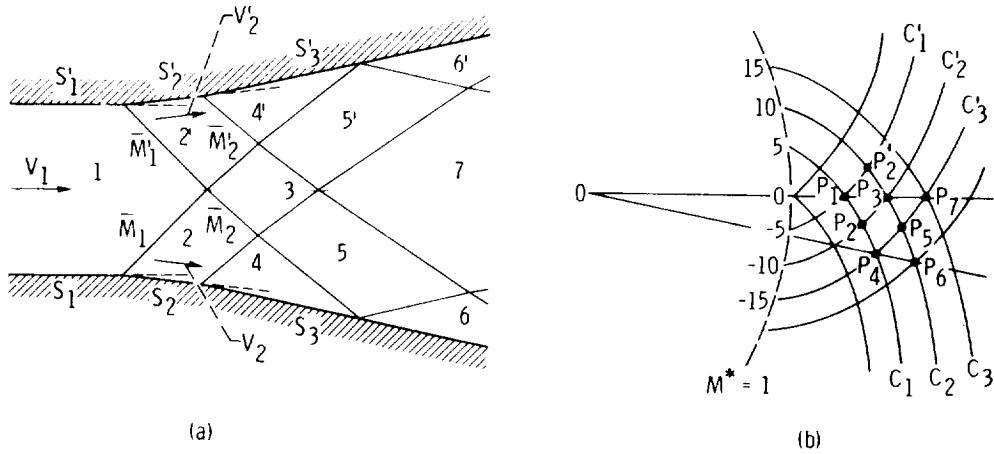
FIGURE 9-8.—Flow along convex wall with Mach waves intersecting at one point.

tion of the Mach wave is given by the Mach angle β . Since finite changes occur in the solution of practical problems, it is usually assumed that the waves lie at the Mach angle corresponding to the average speed between the two points, measured relative to the average direction of the flow between the two points. The flow past a wall may now be constructed completely numerically. The hodograph diagram, though, is still useful for visualization.

A special case of flow along a single wall occurs if the wall is so shaped that the Mach lines pass through a common point, as shown in figure 9-8(a). Now imagine that the wall approaches the common point O . The limiting case is represented by figure 9-8(b), where it is seen that a single large bend has replaced a number of small bends. This type of flow is often called corner-type flow, or flow around a corner, and as will be seen later, is important to the design of supersonic nozzles with sharp-edged throats. Equation (9-21) is still valid for this case.

Flow Between Two Walls

The method of solution used for the flow along a single wall can be generalized to handle the flow between two walls. Consider the initially uniform parallel supersonic flow bounded by two walls as shown in figure 9-9. Suppose that both walls are deflected outward the same amount. The flow is symmetric about the centerline of the channel. As before, the flow will be constructed by dividing the walls into a finite number of straight line segments, denoted here by S_1 and S'_1 , S_2 and S'_2 , and S_3 and S'_3 . The initial parallel flow field in region 1 is represented by the point P_1 in the hodograph diagram. The line OP_1 represents the direction and magnitude of the velocity \vec{V}_1 . The flow



(a) Physical plane.

(b) Hodograph plane.

FIGURE 9-9.—Flow between two walls.

in regions 2 and 2' (points P_2 and P'_2 in the hodograph diagram) can be determined, as before, for the flow through a weak expansion wave. The lines OP_2 and OP'_2 are parallel to \vec{V}_2 and \vec{V}'_2 , respectively.

The problem now is to determine what happens to the flow after the two initial Mach waves intersect. Flow fields 2 and 2' must be separated by another flow field, since \vec{V}_2 and \vec{V}'_2 are not in the same direction. Consider that the flow field 3 is separated from 2 and 2' by a continuation, in modified form, of the initial Mach waves \bar{M}_1 and \bar{M}'_1 . A jump from region 2 through any wave can satisfy the equations of motion only if the end point lies on a characteristic through P_2 ; that is, C_1 or C'_2 (since these curves represent eq. (9-21) graphically). Similarly, a jump from region 2' must lie on characteristic C'_1 or C_2 . To satisfy both sets of conditions, the end point of the jump representing the flow field 3 must be either point P_3 or P_1 in the hodograph plane. The end point being P_1 can be ruled out because this would mean that the extensions of the expansion waves are compression waves, which makes little physical sense. The end point being P_3 in the hodograph plane makes sense because it represents further flow expansion. The direction of the extensions \bar{M}_2 and \bar{M}'_2 of the initial Mach waves are given by the normals to the segments P'_2P_3 and P_2P_3 , respectively, in the hodograph plane. Because of the assumed symmetry of the flow, the velocity \vec{V}_3 is parallel to \vec{V}_1 . These procedures can be used to construct the flow field piecemeal until one of the waves advancing across the channel strikes the wall. A new type of solution is now required.

Consider the flow in field 4, which is parallel to the wall segment S_3 . The flow in field 5 is not parallel to the wall. Therefore, field 5 cannot extend the wall, and a new field 6 must separate it from the wall. The flow in field 6 is parallel to the wall and, therefore, point P_6 in the hodograph plane must lie on the extension of line OP_4 , because the flows in fields 4 and 6 are in the same direction. Also, P_6 must lie on one of the characteristics through P_5 , that is, C_2 or C'_3 . According to arguments similar to those used before, these conditions require that P_6 be located as shown in the hodograph diagram, where the wave between P_5 and P_6 is an expansion wave. In general, an expansion wave striking a solid boundary reflects as an expansion wave. The construction of the flow in the interior of the channel proceeds as before.

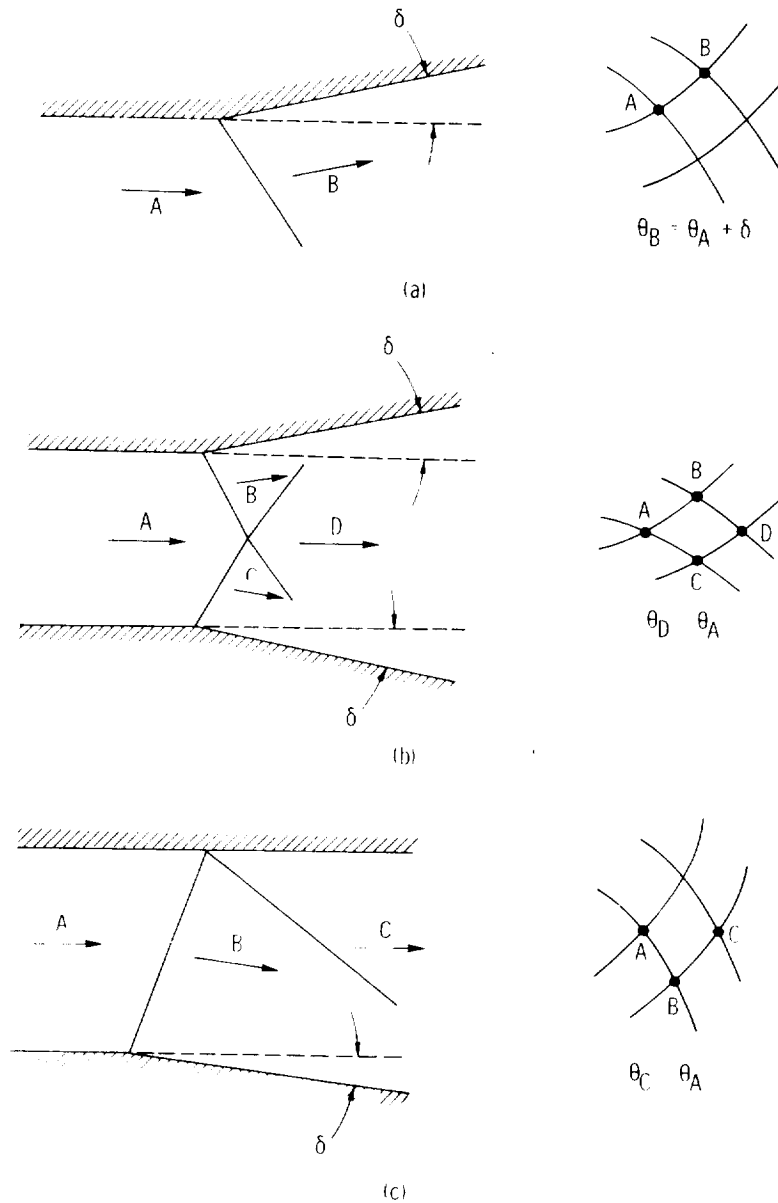
As seen from the foregoing discussion, the flow in the channel may be approximated by a number of small quadrilateral regions in each of which the velocity is constant. The sides of the quadrilaterals are the Mach waves. The equations of motion are satisfied in finite form across each wave and, therefore, are approximately satisfied throughout the entire flow field. This type of procedure is called the "field method," since the stream properties are found in small regions, or fields. Another calculation procedure, known as the "lattice-point method," is often used in supersonic flow problems. In this procedure, the stream properties are found at the intersections, or lattice points, of the Mach net. Both methods are, for most practical situations, identical. The "lattice-point method" will not be discussed further. Both methods are described in reference 1.

Summary of Elementary Flow Solutions

The flow solutions previously discussed, as well as others that are used for the design of supersonic stator and rotor blade sections, are summarized in figure 9-10. For each case, the physical situation is shown along with the hodograph solution. Figures 9-10(a), (b), and (c) show the previously discussed cases of a weak expansion wave, the intersection of expansion waves, and the reflection of an expansion wave from a solid boundary, respectively. In figure 9-10(c), the reflected wave is at a slightly smaller Mach angle than is the incident wave because of the higher Mach number associated with the flow across the reflected wave.

Figure 9-10(d) shows the cancellation of an expansion wave at a solid boundary. A bend at the proper location in the top wall is made in the same direction and of the same magnitude as the flow deflection produced by the wave. The boundary conditions are, therefore, satisfied without any additional (reflected) waves.

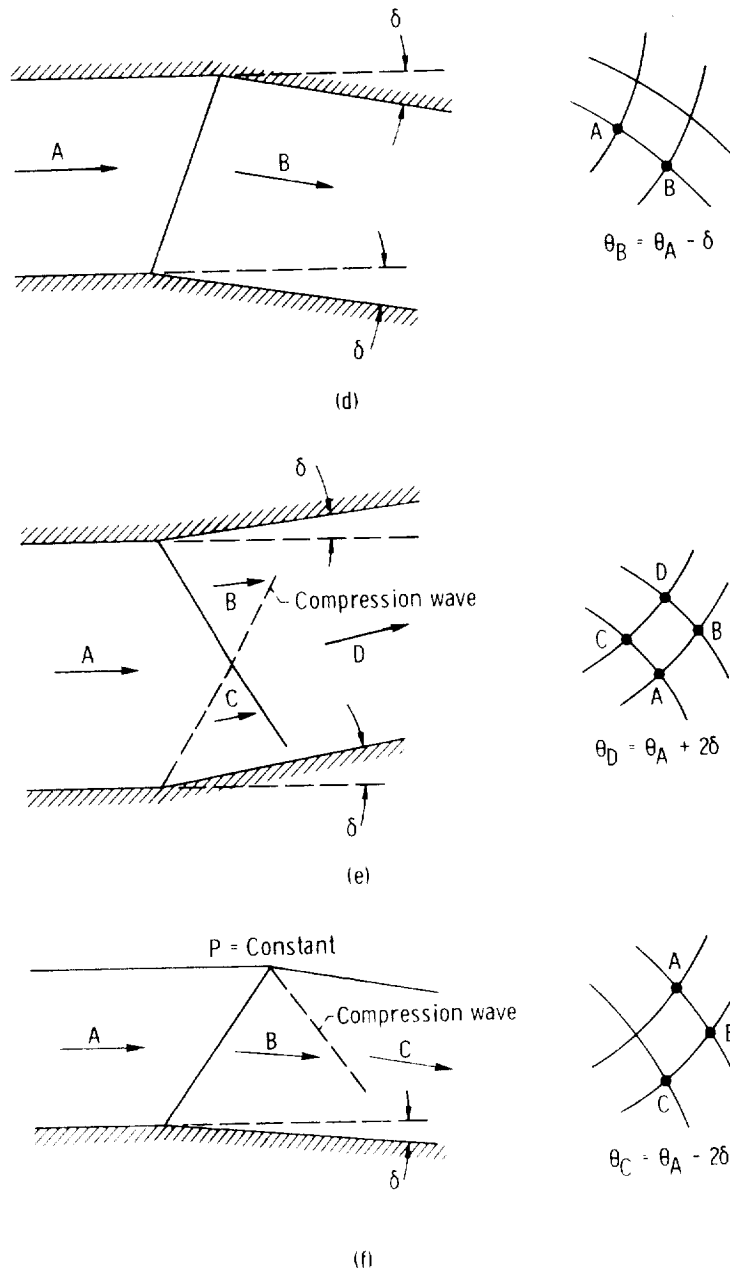
Figure 9-10(e) shows the solution for the flow field beyond the intersection of an expansion wave and a compression wave. The hodograph point representing region *D* must lie on the intersection of characteristic curves passing through *B* and *C*, as shown. Therefore, each wave continues unchanged in type beyond the intersection.



(a) Weak expansion wave.
 (b) Intersection of expansion waves.
 (c) Reflection of an expansion wave from a solid boundary.

FIGURE 9-10.—Elementary flow solutions.

TURBINE DESIGN AND APPLICATION



- (d) Cancellation of expansion wave at solid boundary.
- (e) Intersection of expansion and compression waves.
- (f) Reflection of expansion wave from a free boundary (constant pressure).

FIGURE 9-10.—Concluded.

A case that is not encountered in the design of supersonic blade sections, but may be of general interest, is shown in figure 9-10(f). This is the reflection of an expansion wave from a constant-pressure free boundary. The boundary condition requires that the pressure be

constant along the outside streamline. Since the flow is isentropic, the velocity magnitude of all the flow fields lying along the boundary must be equal. Therefore, field C must be as shown in the hodograph plane. In general, an expansion wave reflects from a free boundary (constant pressure) as a compression wave.

DESIGN OF SUPERSONIC STATOR BLADES

One of the most important uses of the method of characteristics is its application to the design of a channel to produce uniform, parallel flow at supersonic speeds. This is the basis of the design of two-dimensional nozzles for supersonic wind tunnels. This type of nozzle also has application to supersonic-turbine stator blades, since it is desired to have uniform parallel flow entering the rotor. Only the design of a stator based on this type of nozzle will be discussed here.

Nozzles Producing Uniform Parallel Flow

A supersonic nozzle that produces uniform, parallel flow is shown in figure 9-11. Since it is required that the flow be parallel and supersonic, the wall must first curve outward (AD) and then curve in again (DE), so that at the exit, the wall is again parallel to the initial flow. Point D is the point where the wall has its maximum slope. It is usually assumed that the flow at the throat is uniform, parallel, and sonic ($M=1$). Because of the nozzle symmetry, the nozzle axis is a streamline and may, for design purposes, be replaced by a solid boundary. Therefore, only one half of the nozzle need be designed.

The flow region $ABCD$ is called the expansion zone. The curved wall AD generates expansion waves which reflect off the centerline. The calculation procedure is the same as was discussed in the section

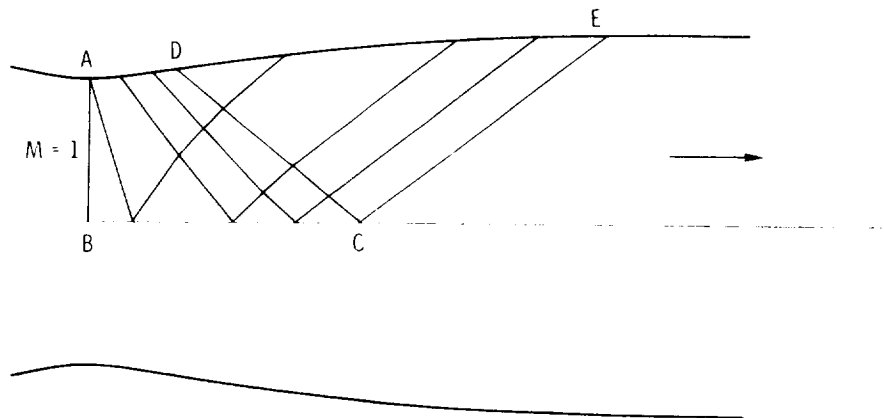


FIGURE 9-11.—Supersonic nozzle producing uniform, parallel flow.

“Flow Between Two Walls.” The region $DCED$ is called the straightening section, and the wall in this section is curved so that the incoming expansion waves are cancelled. The method of cancelling waves was seen in the section “Summary of Elementary Flow Solutions.” The flow past CE is uniform, parallel, and supersonic. The final Mach number depends on how much expansion occurs between A and D . For large exit Mach numbers, a nozzle of this type may be too long for supersonic turbine applications. In these cases, a limiting form of this type of nozzle is used.

A nozzle with a sharp-edged throat, shown in figure 9-12(a), produces uniform, parallel flow in the shortest possible length. It is a limiting form of the nozzle described previously (fig. 9-11), where points A and D coincide. The flow expands around the sharp edge (corner flow), producing waves that are reflected by the centerline. Cancellation of the reflected waves is again used to obtain uniform parallel flow at the exit. The hodograph diagram (fig. 9-12(b)) shows that one half of the expansion occurs as a result of the corner flow, and the other half as a result of the reflected waves. Therefore, the wall bounding region 2 is set at an angle equal to the Prandtl-Meyer angle ω_2 , which is half of the design exit Prandtl-Meyer angle ω_3 .

A computer program has been written (ref. 3) to design supersonic nozzles with sharp-edged throats by the method of characteristics. Only the supersonic portion of the nozzle is designed by the program. The input to the computer program includes the desired exit Mach number and the specific-heat ratio γ of the working fluid. The program output gives the coordinates of the nozzle. The program of reference 3 does not account for any flow losses.

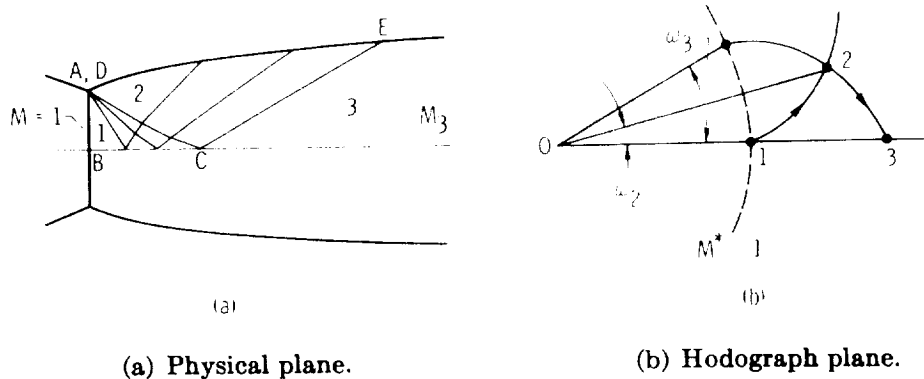


FIGURE 9-12.—Nozzle with sharp-edged throat.

Stator Nozzles

The sharp-edged-throat nozzle just discussed serves as the basis for the design of minimum-length (chord) supersonic stators. Additional considerations for a stator as compared to the nozzle previously

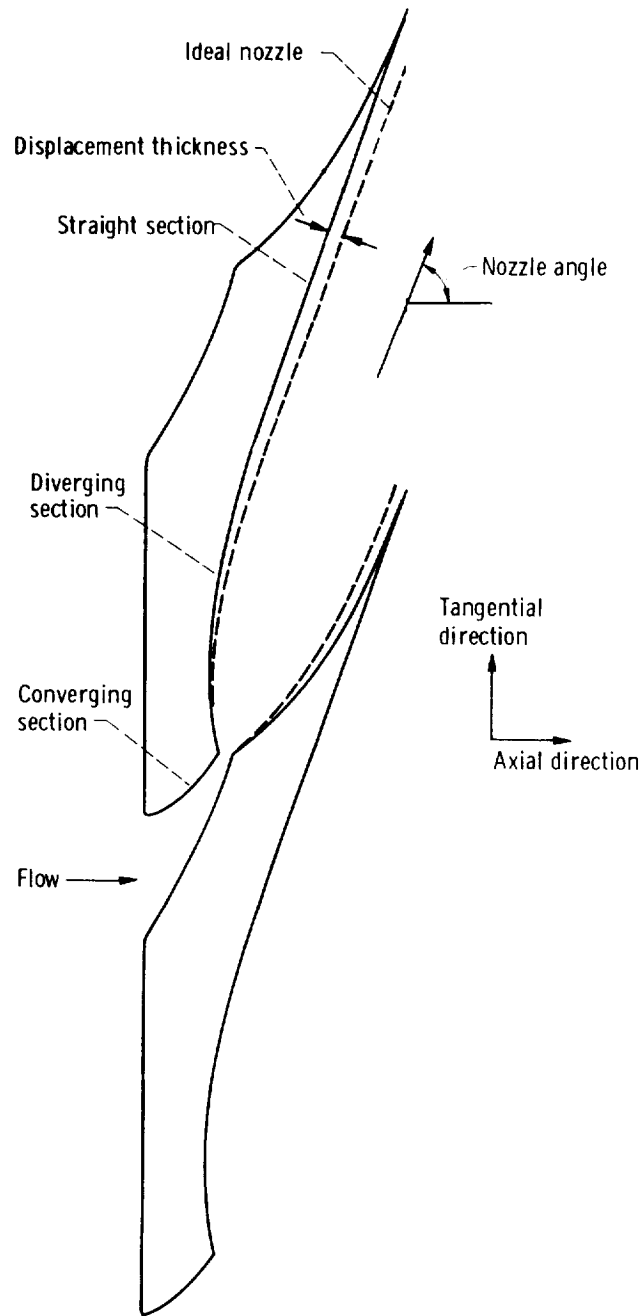


FIGURE 9-13.—Design of supersonic stator nozzle with sharp-edged throat.

discussed are the flow turning and the desire to include flow and energy losses.

A supersonic-turbine stator blade and channel section of the type being discussed herein is shown in figure 9-13 and will be referred to as a stator nozzle. The stator nozzle consists of three sections: (1) a converging (subsonic) section, (2) a diverging (supersonic) section, and (3) a straight section on the suction surface. The converging section accelerates the flow to sonic speed and can be designed by the methods of chapter 5 (vol. 2). In order to minimize losses, the converging section is designed to produce all of the turning of the flow. The diverging section accelerates the flow to the desired free-stream Mach number at the exit. This section is designed by the method of characteristics as previously discussed. The straight section on the suction surface completes the nozzle profile, and its length is determined by the required nozzle angle.

A computer program for the design of sharp-edged-throat supersonic stator nozzles, including a correction for losses, is presented in reference 4. An ideal (no loss) nozzle profile, indicated by the dashed lines in figure 9-13, is first designed by the method of characteristics. Boundary-layer parameters (displacement thickness, momentum thickness, etc.) are then computed for the ideal profile by methods discussed in chapter 6 (vol. 2). The final profile is then obtained by adding the local displacement thicknesses to the ideal nozzle coordinates as indicated in figure 9-13. The nozzle efficiency is obtained from the boundary-layer parameters as described in chapter 7 (vol. 2).

DESIGN OF SUPERSONIC ROTOR BLADES

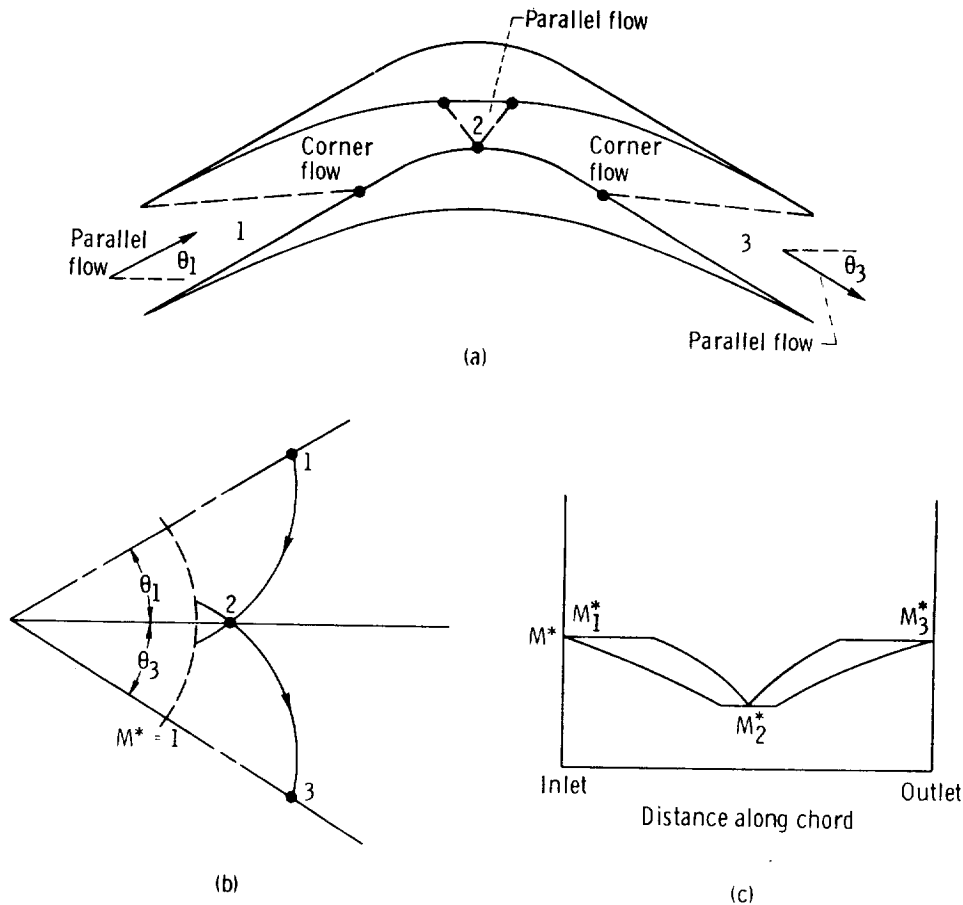
Two methods that have been proposed for the design of supersonic rotors are discussed herein. Both design methods use the method of characteristics. The channel is designed to prevent any shock formation caused by the convergence of compression waves. The flow entering the rotor passage is assumed to be uniform and parallel.

Corner-Flow Method

One method of designing supersonic rotor blades is given by Shapiro (ref. 1). A typical blade of this type is shown in figure 9-14(a). The entering uniform, parallel flow (region 1) undergoes a corner-type compression, resulting from flow along the concave lower (pressure) surface of the blade. The upper (suction) surface is curved so as to cancel the incoming compression waves. In region 2, parallel horizontal flow ($\theta=0$) is obtained. This parallel flow then undergoes a corner-type expansion, with waves being cancelled by the concave

surface, until uniform parallel flow of the desired Mach number occurs at the blade exit. Straight-line segments on the upper surface, parallel to the inlet and outlet flow directions, complete the blade profile.

For an impulse blade (as shown in fig. 9-14(a)), only one half of the blade needs to be designed, since it is symmetrical. The specification of corner flow makes this type of blade particularly easy to design, since only waves of one kind are present in any region. The hodograph diagram for this blade is shown in figure 9-14(b). Shown in figure 9-14(c) is the theoretical blade-surface velocity distribution, which is quite unusual. This type of velocity distribution is not very desirable, because the loading becomes zero in the middle of the blade. Another drawback of this design method is that for a given inlet Mach number,



(a) Blade and passage.

(b) Hodograph diagram.

(c) Blade loading diagram

FIGURE 9-14.—Supersonic rotor design by the corner-flow method.

the amount of flow turning is limited. The velocity in region 2 must be sonic (Mach 1) or higher. The maximum amount of flow turning is, therefore, equal to the sum of the inlet and exit Prandtl-Meyer angles. For reasonable Mach number levels (1.5 to 3.0), large amounts of flow turning (120° to 150°) would be impossible.

Vortex-Flow Method

Another method of designing supersonic rotor blades is described in reference 5. This method is based on establishing vortex flow within the passage. In a vortex-flow field, the product of velocity (also, therefore, critical velocity ratio M^*) and streamline radius is a constant throughout the field. A typical blade and passage designed by this method is shown in figure 9-15(a).

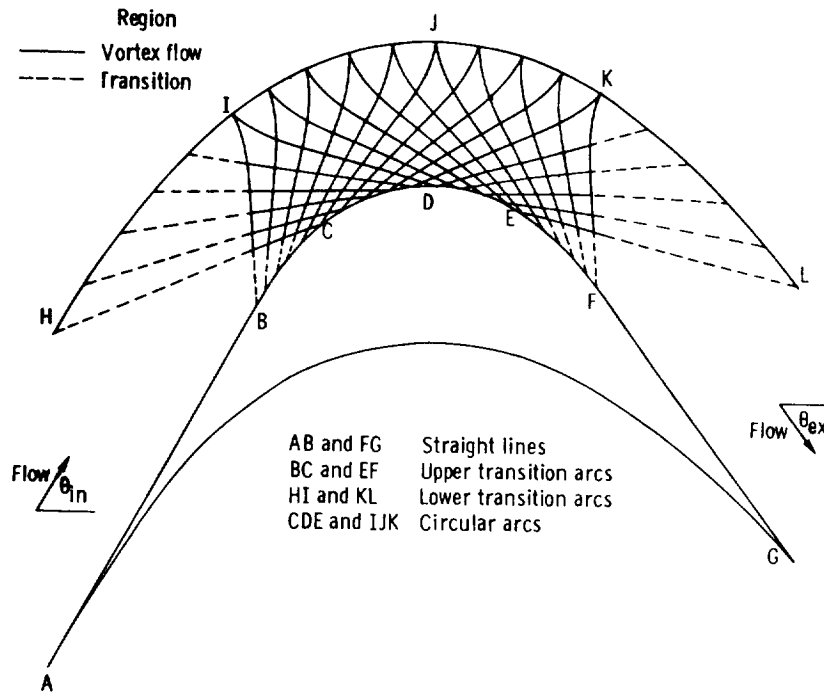
The blades consist essentially of three parts: (1) inlet transition arcs, (2) circular arcs, and (3) outlet transition arcs. The inlet transition arcs (lower and upper) convert the uniform parallel flow at the passage inlet into vortex flow by means of the compression waves generated by the lower transition arc and the expansion waves generated by the upper transition arc (see fig. 9-15(a)). The vortex-flow field begins where the compression and expansion waves first intersect. The concentric circular arcs turn and maintain the vortex flow. The outlet transition arcs reconvert the vortex flow into uniform parallel flow by cancelling the remaining waves generated by the circular arcs. Straight-line segments on the upper surface and parallel to the inlet and outlet flow directions complete the blade profile.

A hodograph diagram for this type of design is shown in figure 9-15(b). The flows along the blade surfaces are shown, with the letters corresponding to the locations indicated in figure 9-15(a). The constant-velocity flows along the circular arcs of the blade surfaces are represented by the circular arcs IK and BF on the hodograph diagram. In this type of design, there is no limit to the amount of flow turning obtainable in the rotor, because the circular arcs can provide any necessary degree of turning. The surface velocity distribution is shown on the blade-loading diagram, figure 9-15(c). This blade is seen to be quite highly loaded, especially as compared to the corner-flow design shown in figure 9-14.

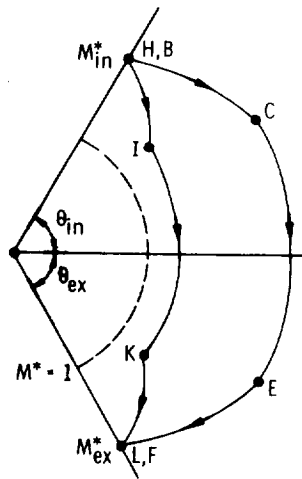
A computer program for designing rotor blades of this type by the method of characteristics is presented in reference 6. The computer program input includes the inlet and outlet flow angles, the inlet, outlet, and surface Mach numbers, and the specific-heat ratio of the gas. The output includes the rotor blade coordinates and a plot of the blade shape. An approximate method for obtaining the transition arcs without using the method of characteristics is described in

references 7 and 8. In this procedure, the vortex flow is established by making the curvature of the transition arcs one-half the curvature of the circular arcs. For very small curvatures, this method is correct.

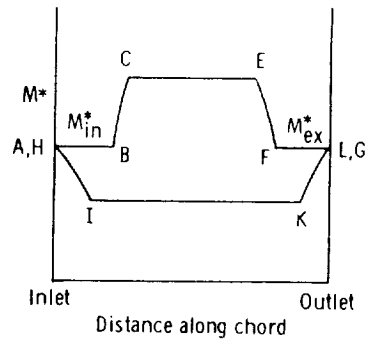
In this blade design, the lower- and upper-surface Mach numbers are specified. This permits blades of various shapes to be designed for



(a)



(b)



(c)

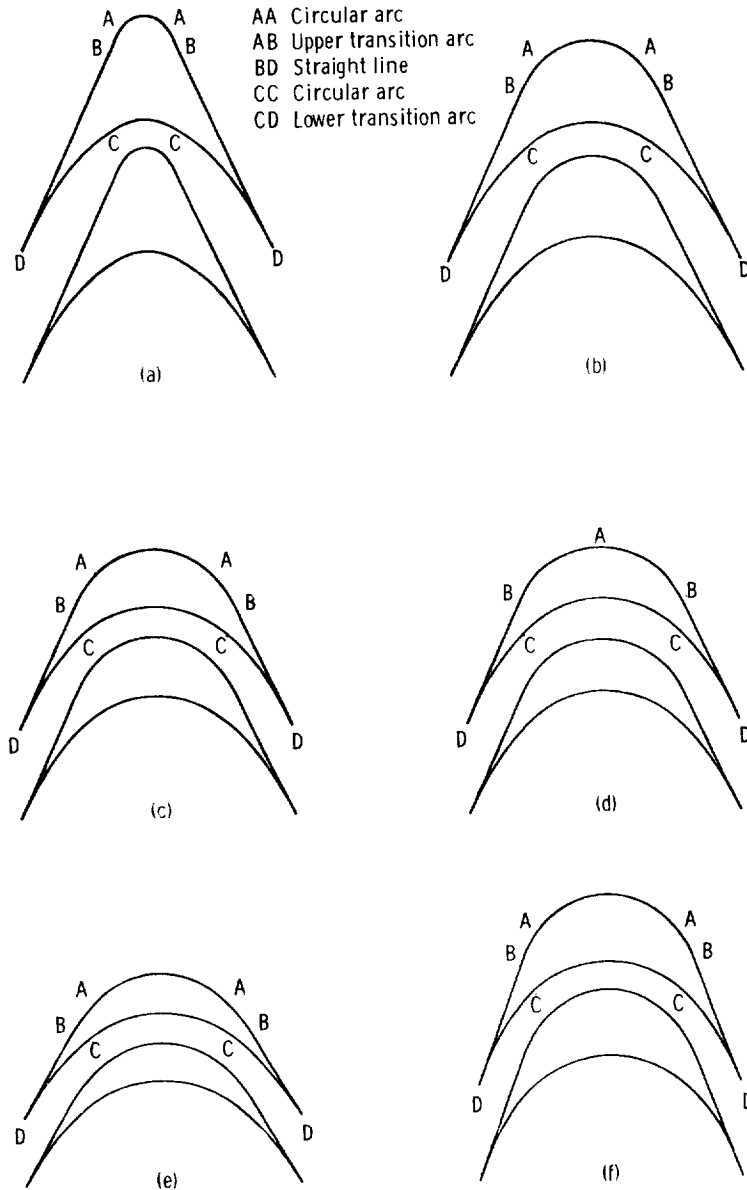
(a) Blade and passage.

(b) Hodograph diagram.

(c) Blade loading diagram.

FIGURE 9-15.—Supersonic rotor design by the vortex-flow method.

TURBINE DESIGN AND APPLICATION



- (a) Lower-surface Prandtl-Meyer angle, 0° ($M=1$); upper-surface Prandtl-Meyer angle, 59° ($M=3.5$); total flow turning angle, 130° .
- (c) Lower-surface Prandtl-Meyer angle, 18° ($M=1.7$); upper-surface Prandtl-Meyer angle, 59° ($M=3.5$); total flow turning angle, 130° .
- (e) Lower-surface Prandtl-Meyer angle, 21° ($M=1.8$); upper-surface Prandtl-Meyer angle, 59° ($M=3.5$); total flow turning angle, 120° .

- (b) Lower-surface Prandtl-Meyer angle, 12° ($M=1.5$); upper-surface Prandtl-Meyer angle, 59° ($M=3.5$); total flow turning angle, 130° .
- (d) Lower-surface Prandtl-Meyer angle, 18° ($M=1.7$); upper-surface Prandtl-Meyer angle, 104° ($M=10.7$); total flow turning angle, 130° .
- (f) Lower-surface Prandtl-Meyer angle, 21° ($M=1.8$); upper-surface Prandtl-Meyer angle, 59° ($M=3.5$); total flow turning angle, 140° .

FIGURE 9-16.—Turbine blade shapes at inlet Mach number of 2.5 (inlet Prandtl-Meyer angle of 39°) and specific-heat ratio of 1.4.

a given inlet Mach number. A number of blades designed by the program of reference 6 for an inlet Mach number of 2.5 are shown in figure 9-16. From the figure, it is seen that the upper-surface Mach number (cf. figs. 9-16(c) and (d)) has little effect on the blade shape, whereas the lower-surface Mach number (cf. figs. 9-16(a), (b), and (c)) and the flow turning (cf. figs. 9-16(e) and (f)) have significant effects. Guidance in the selection of a blade design is obtained by consideration of flow separation and supersonic starting problems, both of which will be discussed later in this chapter.

The previously discussed "method of characteristics" design procedure is only for the case of ideal (isentropic) flow. A computer program for the design of supersonic-turbine vortex-flow rotor sections, including a correction for losses, is presented in reference 9. The ideal (no loss) passage profile, indicated by the dashed lines in figure 9-17, is first designed by the method of characteristics. Boundary-layer parameters are then computed, and the final profile is then obtained by adding the local displacement thicknesses to the ideal profile as indicated in figure 9-17. Rotor profile loss coefficients are determined from the boundary-layer parameters as described in chapter 7 (vol. 2).

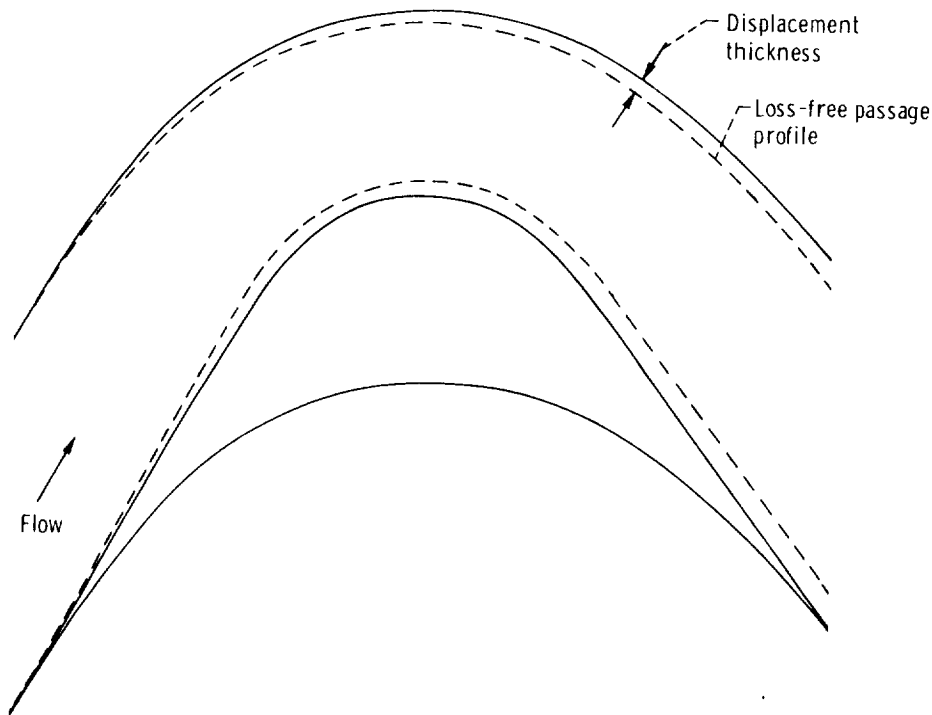


FIGURE 9-17.—Design of supersonic rotor blade section.

As seen from figure 9-15, adverse pressure gradients exist along transition arcs *HI* and *EF* within the rotor blade passages. The boundary-layer calculations give an indication of whether the pressure gradients are severe enough to cause flow separation. Flow separation results in large losses. If it is possible, it would be desirable to prevent separation. The separation criterion places limitations on the choice of the upper- and lower-surface Mach numbers.

OPERATING CHARACTERISTICS OF SUPERSONIC TURBINES

Supersonic Starting

Problems occur in the starting of supersonic diffusers because the diffuser must be able to swallow the shock that forms at the inlet

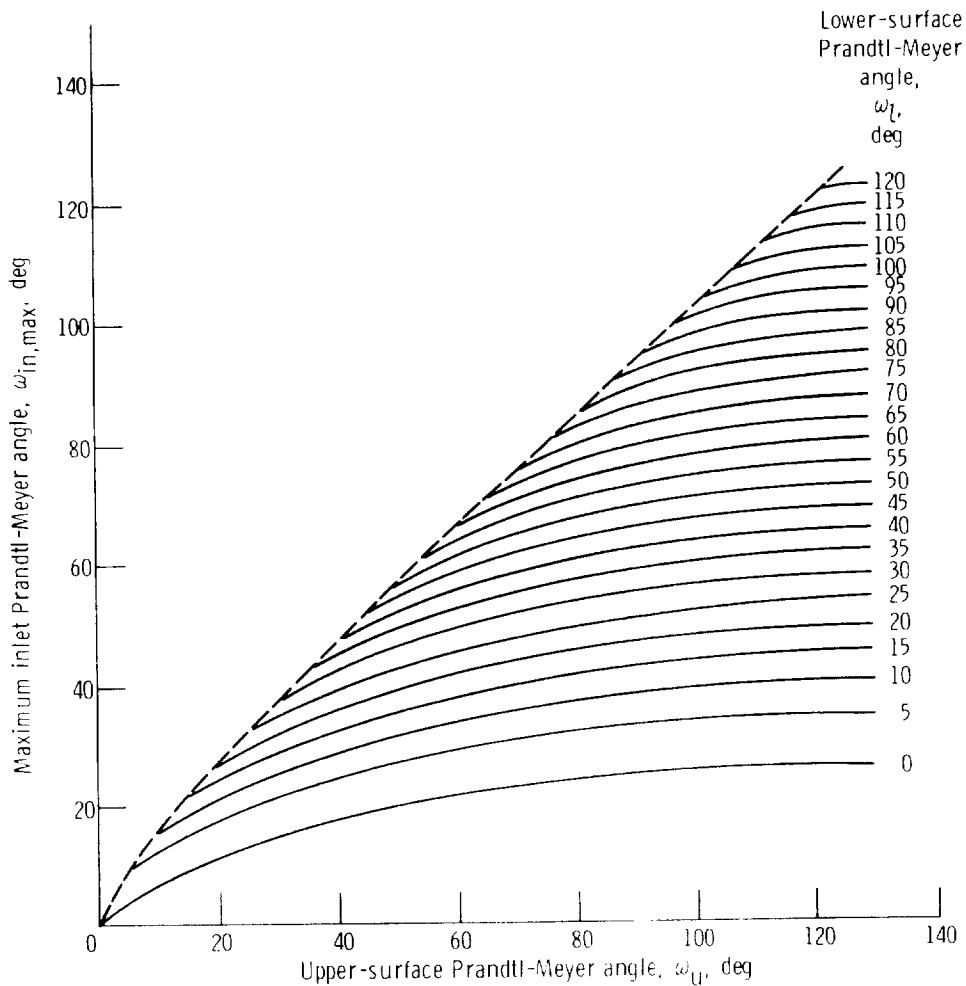


FIGURE 9-18.—Maximum Prandtl-Meyer angle for supersonic starting. Specific-heat ratio, 1.4.

during startup. Since the rotor blade passage is convergent-divergent in shape, similar problems would be expected to occur in the starting of supersonic turbines. As a first approximation, it is assumed that a normal shock spans the rotor blade passage at the instant of starting. The permissible contraction of the blade passage is set by this condition, since the passage must be large enough to permit the shock wave to pass through.

For specified flow Mach numbers along the circular-arc segments of the blade surfaces (often expressed in terms of the corresponding Prandtl-Meyer angles ω_u and ω_l), there exists a maximum value of the inlet Mach number (or inlet Prandtl-Meyer angle) for which supersonic flow can be established. The calculation procedure for determining this maximum value is given in reference 6. In figure 9-18, the maximum inlet Prandtl-Meyer angle for supersonic starting of vortex-flow rotor blades is plotted as a function of the blade-surface Prandtl-Meyer angles. In the usual design problem, the inlet Prandtl-Meyer angle is known from the velocity diagram, and the surface Prandtl-Meyer angles must then be determined in order to obtain the rotor blade

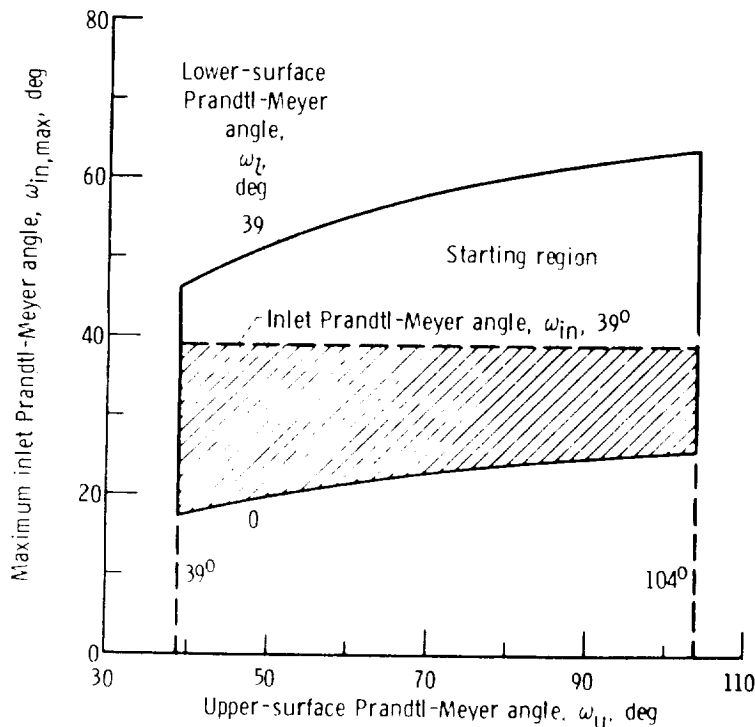


FIGURE 9-19.—Supersonic starting criterion applied to example turbine. Inlet Mach number 2.5; inlet Prandtl-Meyer angle, 39° ; inlet flow angle, 65° .

and passage profiles. To assure satisfactory starting for the given inlet conditions, the point representing the surface Prandtl-Meyer angles in figure 9-18 must lie on or above the ordinate corresponding to the inlet Prandtl-Meyer angle. In general, the supersonic starting condition places a severe restriction on the permissible design values of surface Mach numbers. This restriction is best seen from an example.

Suppose a blade is to be designed for the following conditions: (1) $\gamma=1.4$; (2) $M_{in}=M_{ex}=2.5$ ($\omega_{in}=\omega_{ex}=39^\circ$); and (3) $\theta_{in}=\theta_{ex}=65^\circ$. It is first noted that ω_i can vary from 0° to 39° , and that ω_u can vary from 39° to 104° . The 0° limit on ω_i is due to the fact that the flow must remain at least sonic; the 104° limit on ω_u is due to the fact that the inlet transition turning cannot exceed the inlet flow angle of 65° ($39^\circ+65^\circ=104^\circ$). In figure 9-19, the maximum inlet Prandtl-Meyer angle $\omega_{in, max}$ is plotted as a function of ω_u for this example. For clarity, only the bounds of ω_i and ω_u discussed previously are shown. The dashed line represents $\omega_{in}=39^\circ$, and the region shown crosshatched would not be permissible for design purposes because of supersonic starting considerations. Flow separation consideration will, in general, limit the maximum value of ω_u to much lower values than the limit indicated in the figure.

Supersonic Turbine Performance

Experimental performance data for supersonic turbines are reported in references 10 to 14. The variation in supersonic-turbine efficiency with blade-jet speed ratio (blade speed divided by ideal velocity corresponding to turbine inlet-total- to exit-static-pressure ratio) is illustrated in figure 9-20, which presents the data for the partial-admission turbine of reference 14. For any given speed, efficiency is maximum at about design pressure ratio and falls off rapidly as pressure ratio is decreased. The variation in maximum efficiency (circles in fig. 9-20) with blade-jet speed ratio is similar to that for a subsonic turbine. If this were a subsonic turbine, the efficiencies at the lower pressure ratios would have fallen on the envelope curve. The decrease in supersonic-turbine efficiency at the

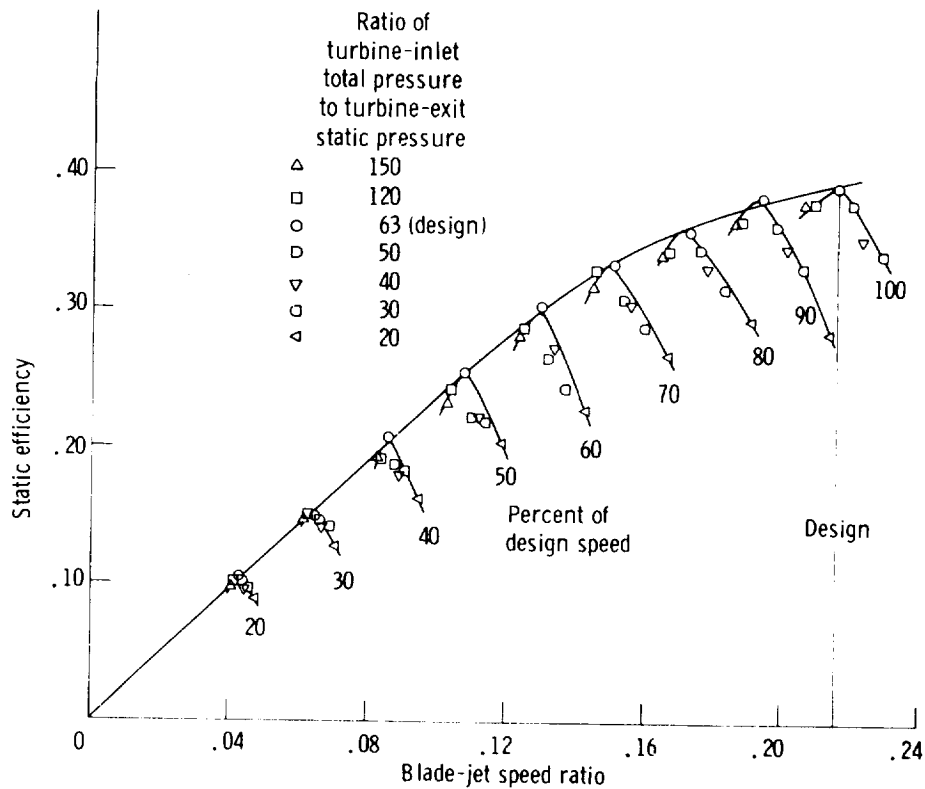


FIGURE 9-20.—Static efficiency of turbine as function of blade-jet speed ratio for constant speeds.

lower pressure ratios is due to the shocks occurring in the under-expanded stator nozzles.

The variation in static pressure throughout the stator nozzle of the turbine of reference 14 is shown in figure 9-21. The formation of the shock waves in the underexpanded nozzle is readily apparent. It can also be seen from this figure that at pressure ratios near design, the divergent section of the nozzle performed as expected, but the pressure did not remain constant in the straight section. There was some overexpansion followed by some compression. This same behavior was found in the data of reference 10.

TURBINE DESIGN AND APPLICATION

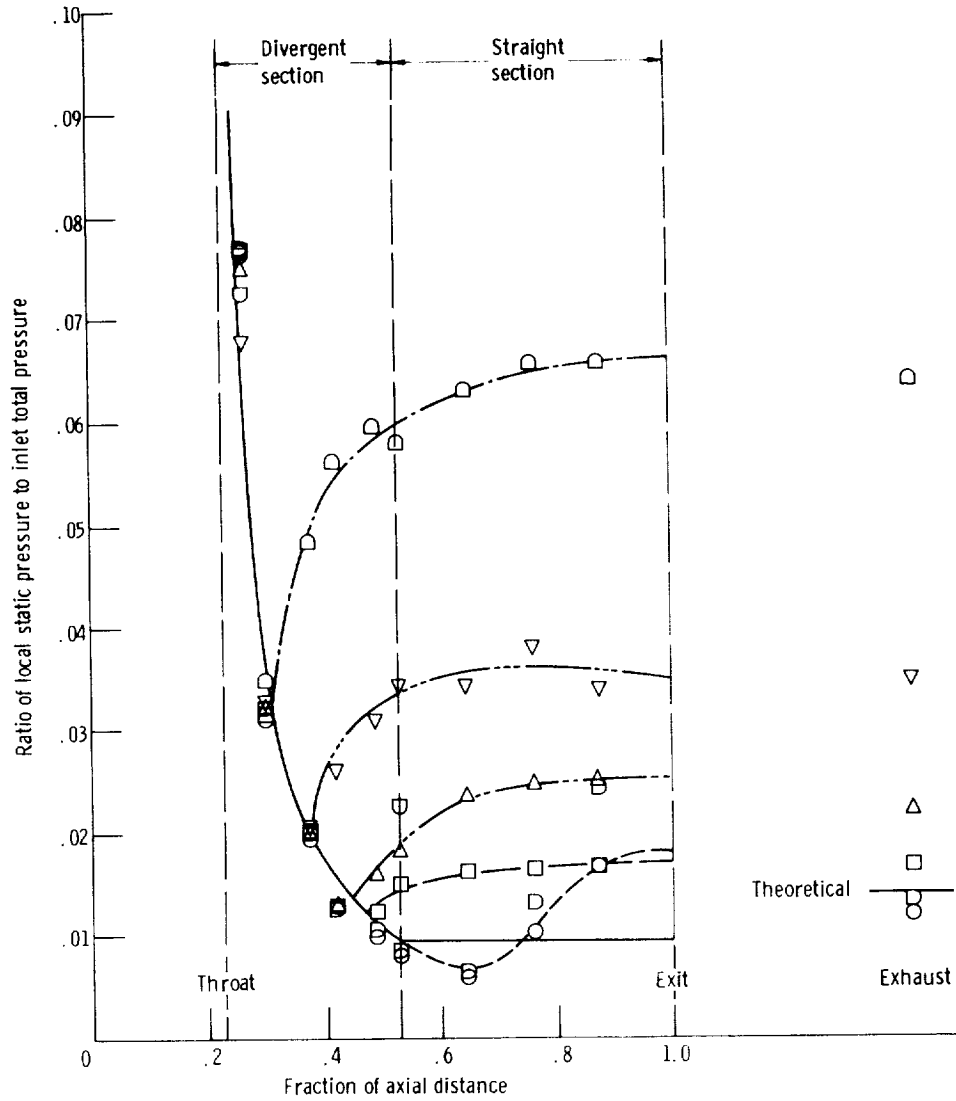


FIGURE 9-21.—Variation of nozzle pressure ratio with axial distance in nozzle for constant ratios of nozzle exit static pressure to inlet total pressure.

REFERENCES

1. SHAPIRO, ASCHER H.: The Dynamics and Thermodynamics of Compressible Fluid Flow. vol. 1. Ronald Press Co., 1953.
2. LIEPMANN, HANS WOLFGANG; AND PUCKETT, ALLEN E.: Introduction to Aerodynamics of a Compressible Fluid. John Wiley & Sons, 1947.
3. VANCO, MICHAEL R.; AND GOLDMAN, LOUIS J.: Computer Program for Design of Two-Dimensional Supersonic Nozzle with Sharp-Edged Throat. NASA TM X-1502, 1968.
4. GOLDMAN, LOUIS J.; AND VANCO, MICHAEL R.; Computer Program for Design of Two-Dimensional Sharp-Edged-Throat Supersonic Nozzle with Boundary-Layer Correction. NASA TM X-2343, 1971.
5. BOXER, EMANUEL; STERRETT, JAMES R.; AND WLODARSKI, JOHN: Application of Supersonic Vortex-Flow Theory to the Design of Supersonic Impulse Compressor- or Turbine-Blade Sections. NACA RM L52B06, 1952.
6. GOLDMAN, LOUIS J.; AND SCULLIN, VINCENT J.: Analytical Investigation of Supersonic Turbomachinery Blading. I—Computer Program for Blading Design. NASA TN D-4421, 1968.
7. STRATFORD, B. S.; AND SANSOME, G. E.: Theory and Tunnel Tests of Rotor Blades for Supersonic Turbines. R&M 3275, Aero. Res. Council, 1962.
8. HORLOCK, J. H.: Axial Flow Turbines: Fluid Mechanics and Thermodynamics. Butterworths, 1966.
9. GOLDMAN, LOUIS J.; AND SCULLIN, VINCENT J.: Computer Program for Design of Two-Dimensional Supersonic Turbine Rotor Blades with Boundary-Layer Correction. NASA TM X-2434, 1971.
10. MOFFITT, THOMAS P.: Design and Experimental Investigation of a Single-Stage Turbine with a Rotor Entering Relative Mach Number of 2. NACA RM E58F20a, 1958.
11. STABE, ROY G.; KLINE, JOHN F.; AND GIBBS, EDWARD H.: Cold-Air Performance Evaluation of a Scale-Model Fuel Pump Turbine for the M-1 Hydrogen-Oxygen Rocket Engine. NASA TN D-3819, 1967.
12. MOFFITT, THOMAS P.; AND KLAG, FREDERICK W., JR.: Experimental Investigation of Partial- and Full-Admission Characteristics of a Two-Stage Velocity-Compounded Turbine. NASA TM X-410, 1960.
13. JOHNSON, I. H.; AND DRANSFIELD, D. C.: The Test Performance of Highly Loaded Turbine Stages Designed for High Pressure Ratio. R&M 3242, Aero. Res. Council, 1962.
14. GOLDMAN, LOUIS J.: Experimental Investigation of a Low Reynolds Number Partial-Admission Single-Stage Supersonic Turbine. NASA TM X-2382, 1971.

SYMBOLS

A	flow area along Mach wave, m^2 ; ft^2
a	speed of sound, m/sec ; ft/sec
g	conversion constant, 1; 32.17 (lbm)(ft)/(lbf)(sec ²)
M	Mach number
M^*	critical velocity ratio (V/V_{cr})
p	absolute pressure, N/m^2 ; lb/ft^2
u	component of velocity parallel to initial flow direction, m/sec ; ft/sec
V	velocity, m/sec ; ft/sec
V_{cr}	critical velocity ($M=1$), m/sec ; ft/sec
v	component of velocity normal to initial flow direction, m/sec ; ft/sec
w	mass flow rate, kg/sec ; lb/sec
β	Mach angle, deg
γ	ratio of specific heat at constant pressure to specific heat at constant volume
δ	small change in flow direction, deg
θ	flow angle, deg
ν	Prandtl-Meyer angle, deg
ρ	density, kg/m^3 ; lb/ft^3
ω	Prandtl-Meyer angle, deg

Subscripts:

ex	rotor exit
in	rotor inlet
l	lower surface of blade
max	maximum
n	normal direction with respect to Mach wave
r	relative
s	isentropic
t	tangential direction with respect to Mach wave
u	upper surface of blade

CHAPTER 10

Radial-Inflow Turbines

By Harold E. Rohlik

Radial-inflow turbines are suitable for many applications in aircraft, space power systems, and other systems where compact power sources are required. Turbines of this type have a number of desirable characteristics such as high efficiency, ease of manufacture, sturdy construction, and reliability. There is a substantial amount of information on radial-inflow turbines in the literature. References 1 to 6 are general in nature and cover most areas of the design and performance of these machines. In this chapter, the radial-inflow turbine is described, and its features are compared with those of an axial-flow turbine. In addition, design geometry and performance, blade design, and off-design performance are discussed.

Figure 10-1 shows a section through a typical radial-inflow turbine. The flow enters the stator radially and leaves the rotor axially. This turning of the flow takes place in the rotor passage, which is relatively long and narrow. In axial turbines, the blade aspect ratio, which is the ratio of blade height to chord, varies from about 1 to as much as 8. Radial turbine rotor and stator blades, on the other hand, generally have aspect ratios from 0.1 to 0.5.

A torus, which is a doughnut-shaped plenum, or a volute (shown in fig. 10-2), which is a spiral flow passage, usually surrounds the stator inlet. The torus is fed by a radial inlet pipe, while the volute is fed by a tangential inlet pipe. In the case of a volute, a prewhirl (tangential component of velocity) is imparted to the gas before it enters the stator blade row. This results in stator blades with little or no camber. It can be seen from figure 10-2 that the overall diameter of a radial-inflow turbine is considerably larger than the rotor diameter.

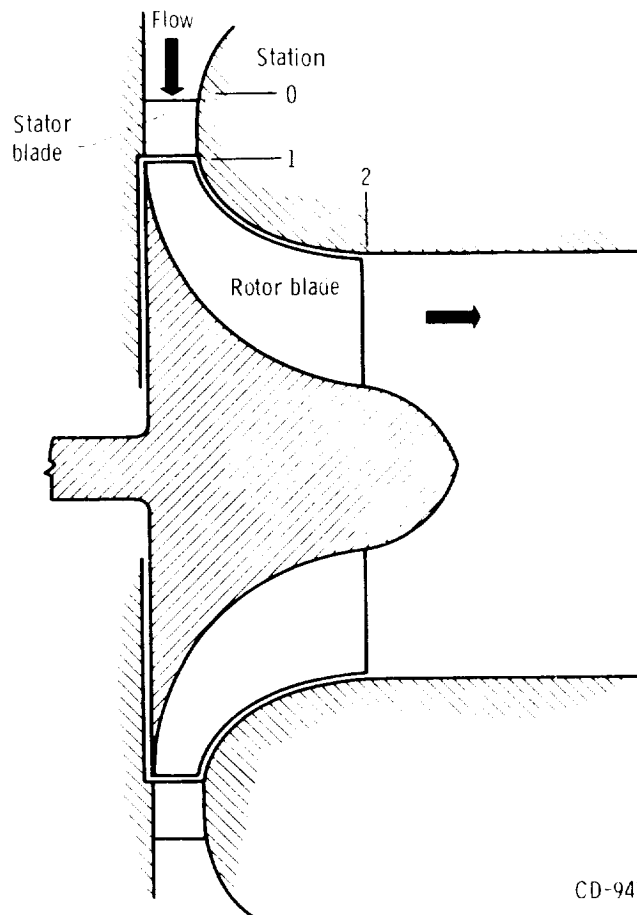


FIGURE 10-1.—Schematic cross section of radial-inflow turbine.

At the rotor inlet, where the flow velocity relative to the rotor has little or no tangential component ($W_u \approx 0$), the rotor blades are usually straight and radial. This straight section of the rotor blade generally is rather highly loaded, since angular momentum rV_u (where r is the radius, and V_u is the tangential component of absolute velocity) here varies with the square of radius. (Since $W_u \approx 0$, $V_u = U \alpha r$, where U is the blade speed. Therefore, $rV_u \propto r^2$.) At the rotor exit, the blades are curved to turn the flow, so that the exit absolute velocity has little or no whirl.

Figure 10-3 shows the blading more clearly. The stator blade shape shows that prewhirl is developed in the inlet volute. Also, the low solidity (ratio of chord to spacing) and low aspect ratio that are generally used in the stators of radial turbines can be seen. The turbine shown here has splitter, or partial, blades between the full blades in the rotor. They are used in the radial part of the flow passage

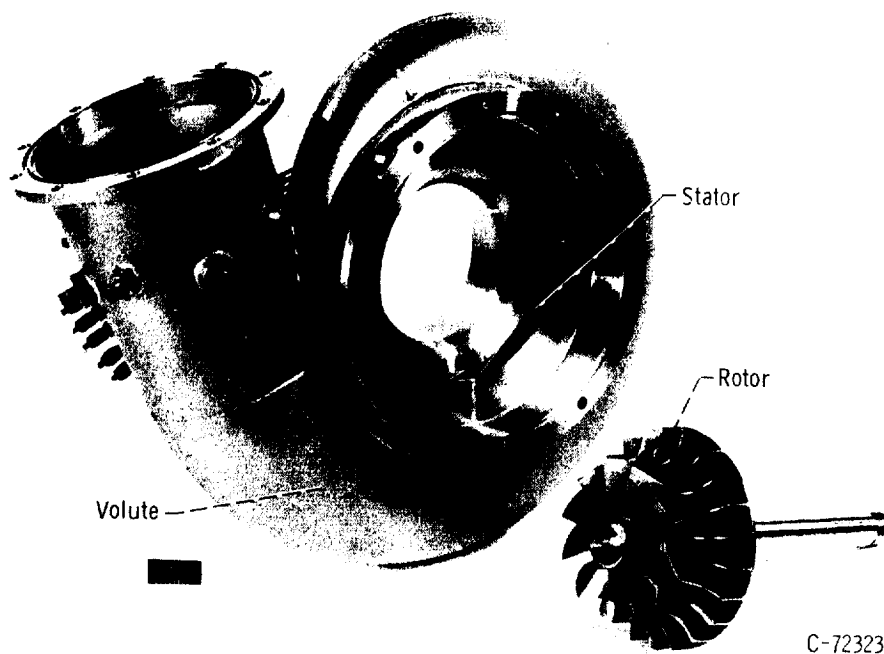


FIGURE 10-2.—Radial-inflow turbine.

to reduce the blade loading. Splitter blades are discussed further in the "BLADE DESIGN" section.

The expansion process in a radial turbine differs appreciably from that in an axial turbine because of the radius change in the rotor. The relative total temperature and pressure decrease with decreasing radius, as was discussed in chapter 2 of volume 1 (see eq. (2-31) and associated discussion). This is a distinct advantage for the radial turbine because it permits the use of a lower velocity level for a given overall expansion. This can be seen from the temperature-entropy diagram in figure 10-4, which shows the expansion through the rotor of a radial-inflow turbine. The change in relative total temperature T'' and the corresponding change in relative total pressure p'' are shown for the expansion. If this were an axial turbine ($T_1'' = T_2''$), the p_2'' line would be only slightly below the p_1'' line (as shown in fig. 2-8 of ch. 2), because the difference between p_1'' and p_2'' is due only to rotor losses. For the radial turbine, as shown in figure 10-4, the p_2'' line is farther removed from the p_1'' line because the difference is due to both the rotor losses and the change in radius. Therefore,

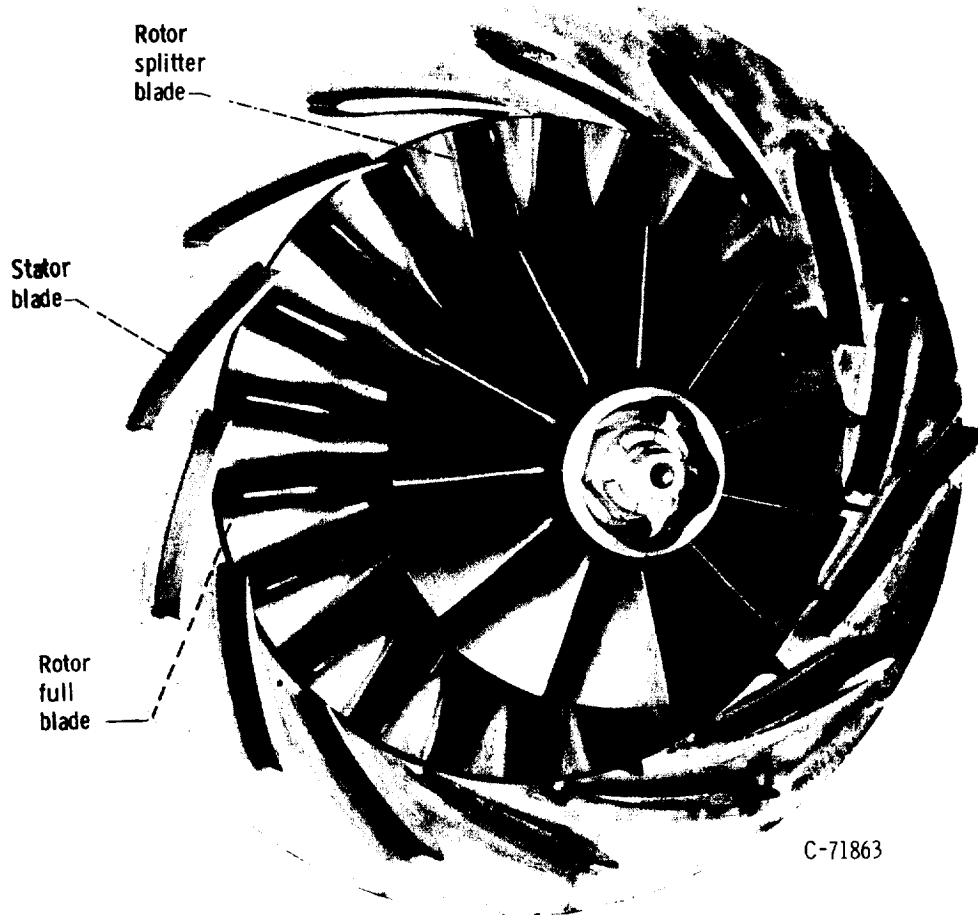


FIGURE 10-3.—Turbine stator and rotor assembly.

expansion from the same rotor inlet total pressure p_1'' to the same exit static pressure p_2 would require a higher relative velocity W_2 at the rotor exit in an axial turbine than in a radial turbine (larger vertical distance between p_2'' and p_2 for an axial turbine.) Since fluid friction losses in a rotor increase approximately with the square of the relative gas velocity, the advantage of a lower level of velocity is clear.

A radial-turbine velocity diagram is shown in figure 10-5 for a turbine with prewhirl in the inlet volute and a mean diameter ratio (exit-mean to inlet) of about 0.5. The difference between the blade speeds U_1 and U_2 is very evident. For a typical zero-exit-whirl velocity diagram, the relative kinetic energy W_2^2 leaving the rotor would be approximately three times as high if U_2 equaled U_1 , as in an axial turbine.

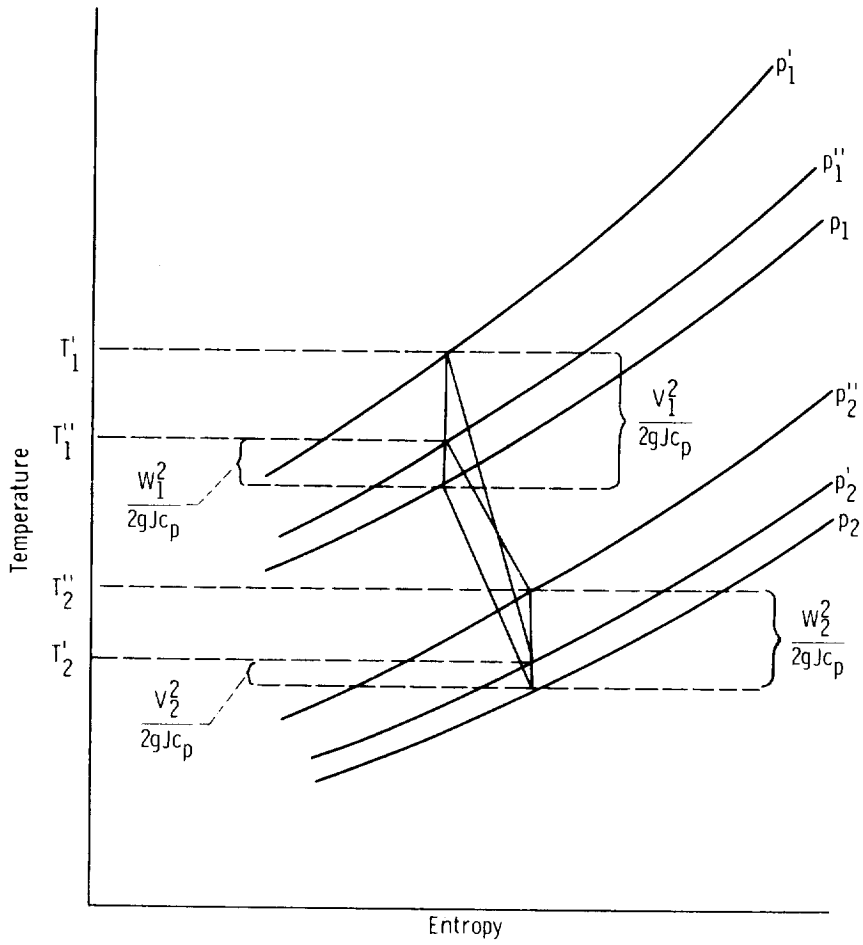


FIGURE 10-4.—Temperature-entropy diagram for a radial-inflow turbine rotor.

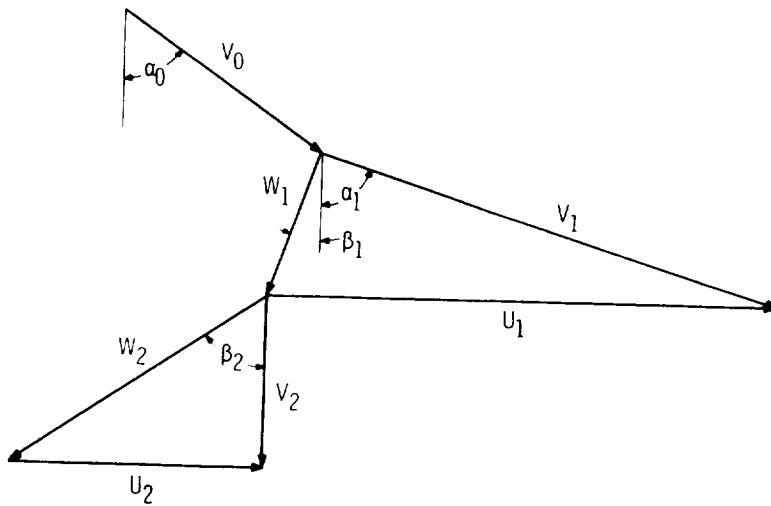


FIGURE 10-5.—Velocity diagram.

OVERALL DESIGN CHARACTERISTICS

Optimum Incidence

Since the blades are radial at the rotor inlet, the inlet flow angle β_1 shown in figure 10-5 is an incidence angle. There is some incidence angle that provides optimum flow conditions at the rotor-blade leading edge. This angle has a value sometimes as high as 40° with a radial blade. This optimum incidence condition is analogous to the "slip" factor in a centrifugal compressor, and is associated with the unloading of the blade near the tip and the distribution of mass flow in the rotor passage. Before the flow is influenced by the rotor blades, it is circumferentially uniform. Blade loading then produces a large static-pressure gradient across the passage, so that there is a streamline shift toward the suction surface. Stream-function flow analyses of this flow condition show that the streamline pattern properly locates the inlet stagnation point when there is an "optimum" angle β_1 . This pattern is shown schematically in figure 10-6. Note that the flow at the stagnation point is approximately radial. If this were not so, the flow would tend to separate from the suction surface near the leading edge, causing excessive loss. The relation between $V_{u,1}$ and U_1 has been studied analytically and experimentally in both compressors and turbines. It has

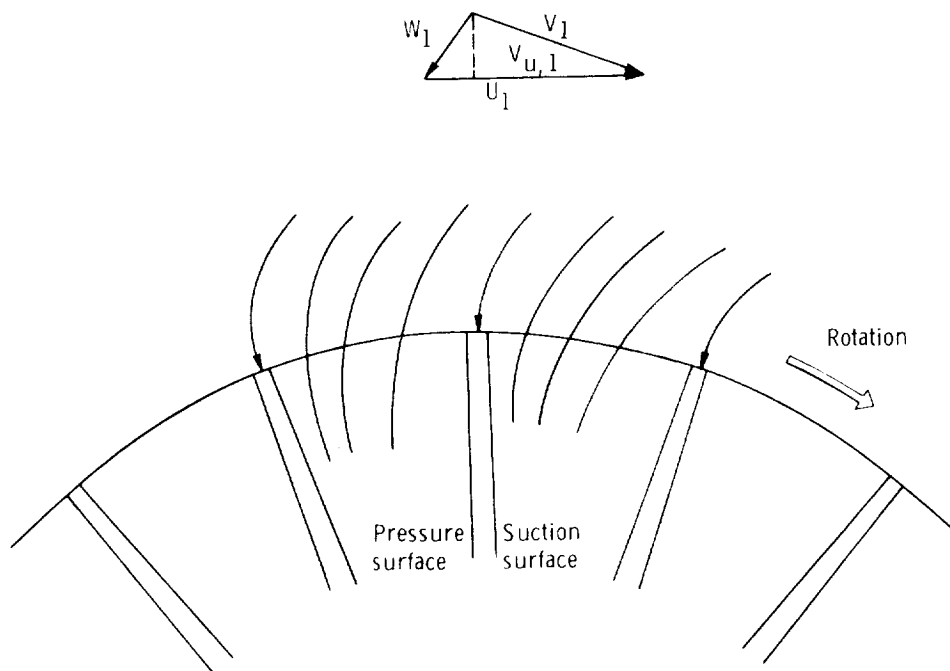


FIGURE 10-6.—Streamline flow at rotor inlet.

been determined that there is an optimum ratio of $V_{u,1}$ to U_1 . This optimum ratio depends on blade loading and, consequently, blade number and is often expressed as

$$\frac{V_{u,1}}{U_1} = 1 - \frac{2}{n} \quad (10-1)$$

where n is the number of blades (total of full blades plus splitter blades).

Effect of Specific Speed on Design Geometry and Performance

The specific speed parameter N_s (derived and discussed in ch. 2 of vol. 1) is given by the equation

$$N_s = \frac{NQ_2^{1/2}}{H^{3/4}} \quad (10-2)$$

where

- N rotative speed, rad/sec; rev/min
- Q_2 volume flow rate at turbine exit, m³/sec; ft³/sec
- H ideal work, or head, based on inlet and exit total pressures, J/kg;
 (ft)(lbf)/lbm

In its most commonly used form (with the stated U.S. customary units), it is not truly dimensionless. Specific speed is independent of size and may be considered as a shape parameter that expresses geometric and velocity-diagram similarity.

Analytical study.—The effect of specific speed on efficiency may be examined by substituting for N , Q_2 , and H as follows:

$$N = \frac{KU_1}{\pi D_1} \quad (10-3)$$

$$Q_2 = \pi D_2 h_2 V_2 \quad (10-4)$$

$$H = \frac{V_j^2}{2g} \left(\frac{\Delta h'}{\Delta h} \right)_{ia} \quad (10-5)$$

where

- K dimensional constant, 2π rad/rev; 60 sec/min
- D_1 rotor inlet (tip) diameter, m; ft
- D_2 rotor-exit mean-section diameter, m; ft
- h_2 rotor-exit passage height, m; ft
- V_2 rotor-exit fluid velocity (assumed to be in axial direction),
 m/sec; ft/sec
- V_j ideal jet speed, based on inlet-total to exit-static pressure
 ratio, m/sec; ft/sec
- g conversion constant, 1; 32.17 (lbm)(ft)/(lbf)(sec²)

$\Delta h'_{ia}$ ideal work based on inlet-total and exit-total pressures, J/kg;
Btu/lb

Δh_{ia} ideal work based on inlet-total and exit-static pressures, J/kg;
Btu/lb

These substitutions and some manipulation result in the following expression for specific speed:

$$N_s = (\text{Constant}) \left(\frac{\Delta h}{\Delta h'} \right)_{ia}^{3/4} \left(\frac{U_1}{V_j} \right)^{3/2} \left(\frac{V}{U} \right)_2^{1/2} \left(\frac{D_2}{D_1} \right)^{3/2} \left(\frac{h}{D} \right)_2^{1/2} \quad (10-6)$$

The terms of equation (10-6) are related to velocity-diagram characteristics and overall geometry. Any specific speed value can be achieved by an infinite number of combinations of these ratio terms. A large number of these combinations were examined analytically in reference 7 to determine optimum combinations over a wide range of specific speed.

The analysis of reference 7 related losses to mean-diameter flow properties, neglecting hub-to-shroud variations. The losses considered were those caused by the stator and rotor boundary layers, blade-to-shroud clearance, windage on the back of the rotor, and the exit kinetic energy. The number of rotor blades was varied with stator-exit flow angle α_1 (in degrees) according to the equation

$$n = 0.03 (\alpha_1 - 57)^2 + 12 \quad (10-7)$$

in order to provide the minimum number that would avoid separation. This was the total number of blades (full plus splitter) used in equation (10-1) to establish the rotor incidence angle. Other assumptions included a favorable reaction ($W_2 = 2W_1$), zero exit whirl ($V_{u,2} = 0$), a maximum limit of 0.7 for $D_{t,2}/D_1$, and a minimum limit of 0.4 for $(D_h/D_t)_2$.

The effects of geometry and velocity-diagram characteristics were examined by calculating the previously mentioned losses for a large number of combinations of stator-exit flow angle α_1 , stator-blade-height to rotor-inlet-diameter ratio h_1/D_1 , and rotor-exit to rotor-inlet diameter ratio $D_{t,2}/D_1$ at three rotor-tip critical velocity ratios (U/V_{cr})₁. The static efficiency was then plotted against specific speed. For the range of values used in the study, all of the calculated points fell in the shaded areas shown in figure 10-7. Stator-exit flow angle is seen to be a prime determinant of efficiency, which falls into a small region for each stator-exit flow angle. The boundaries of each region are set by the extreme values of input variables and by the assumed geometric limits. For any given value of specific speed, there can be a large variation in static efficiency, as much as 45 to 50 points for some values. The dashed curve is the envelope of all the computed static

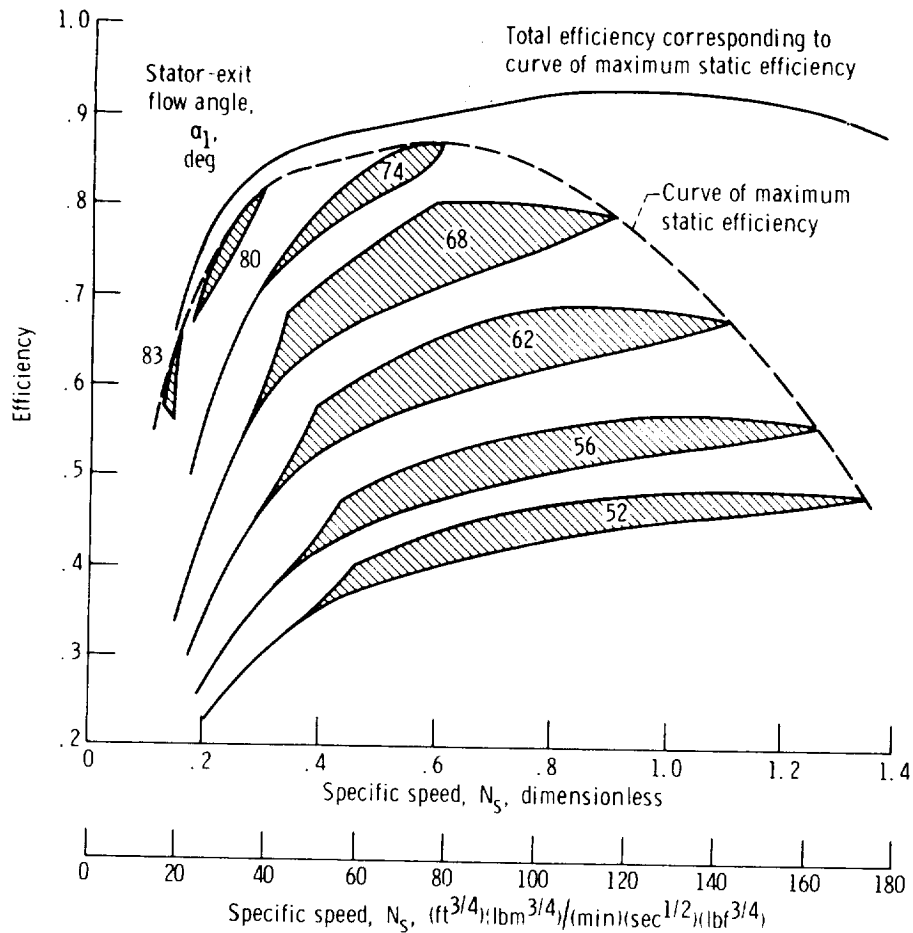


FIGURE 10-7.—Effect of specific speed on computed design-point efficiency. (Data from ref. 7.)

efficiencies, and the solid curve above it represents the corresponding total efficiencies. The computed values of efficiency do not necessarily represent achievable values, because there are many assumptions associated with the loss model used in the study of reference 7. The primary concern of that study, however, was to determine the optimum geometry and velocity ratios.

Most of the geometric and velocity ratios vary continuously along the envelope curves. The optimum values of some of these ratios as functions of specific speed are presented in figures 10-8 to 10-11. Figure 10-8 shows that the optimum stator-exit flow angle is large at low specific speed and decreases (opens to a larger flow area) with increasing specific speed. Figure 10-9 shows that the optimum ratio of stator-blade height to rotor-inlet diameter is small at low specific speed and increases with increasing specific speed until a maximum is reached at

TURBINE DESIGN AND APPLICATION

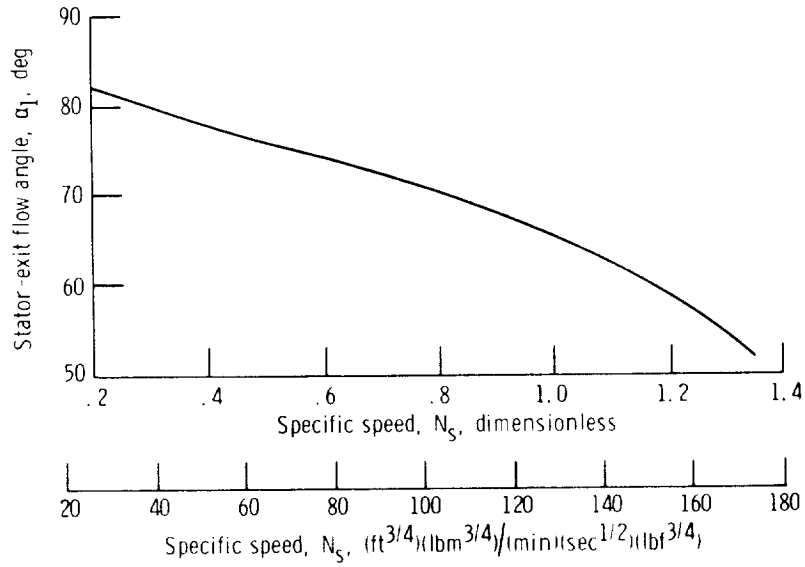


FIGURE 10-8.—Effect of specific speed on optimum stator-exit angle. (Data from ref. 7.)

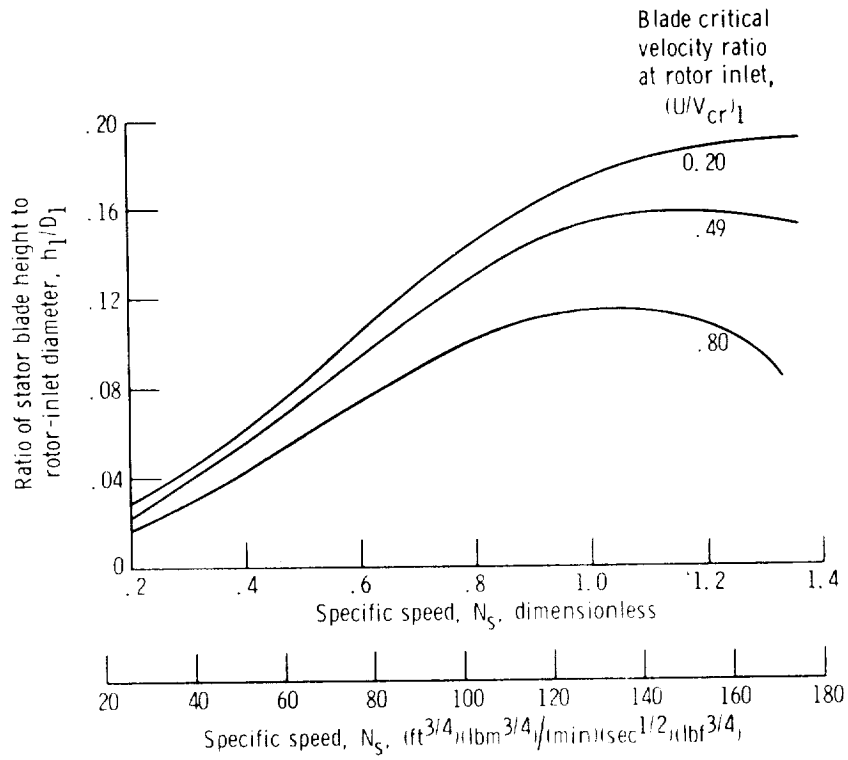


FIGURE 10-9.—Effect of specific speed and blade speed on optimum ratio of stator-blade height to rotor-inlet diameter. (Data from ref. 7.)

RADIAL-INFLOW TURBINES

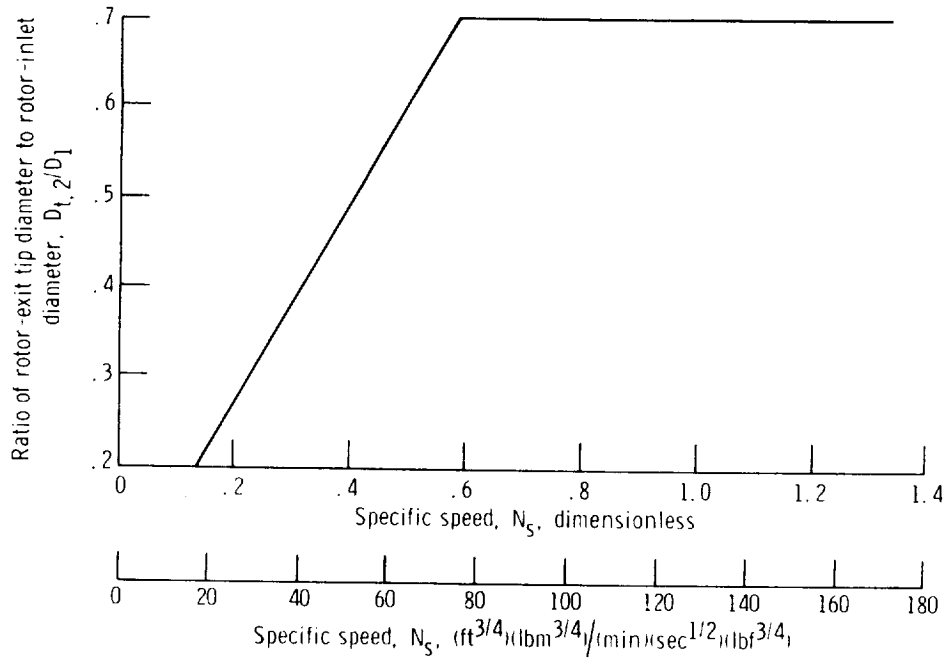


FIGURE 10-10.—Effect of specific speed on optimum ratio of rotor-exit tip diameter to rotor-inlet diameter. (Data from ref. 7.)

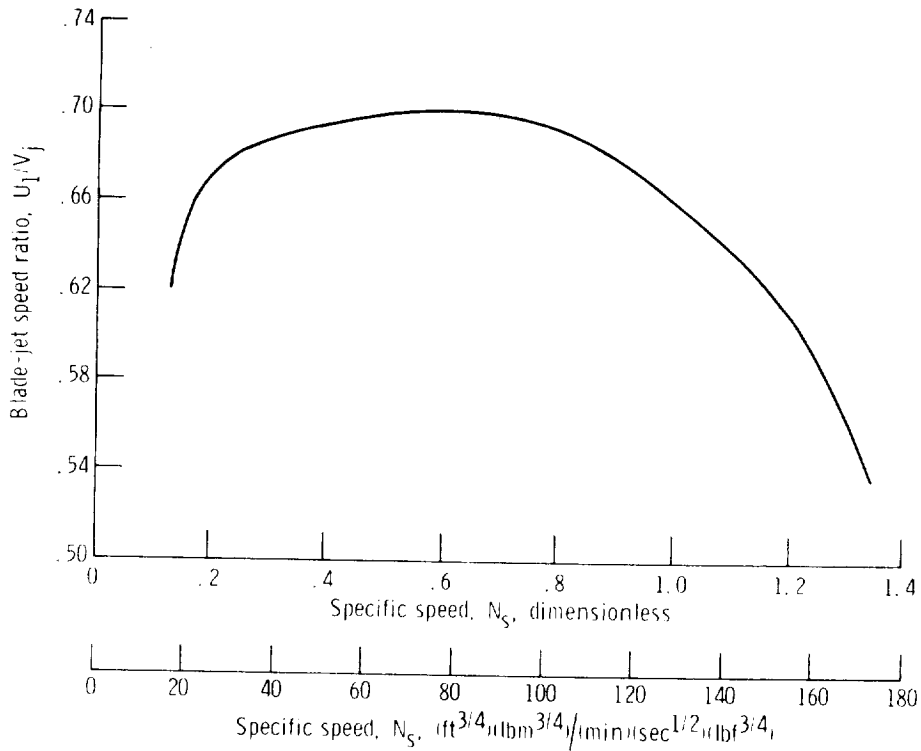
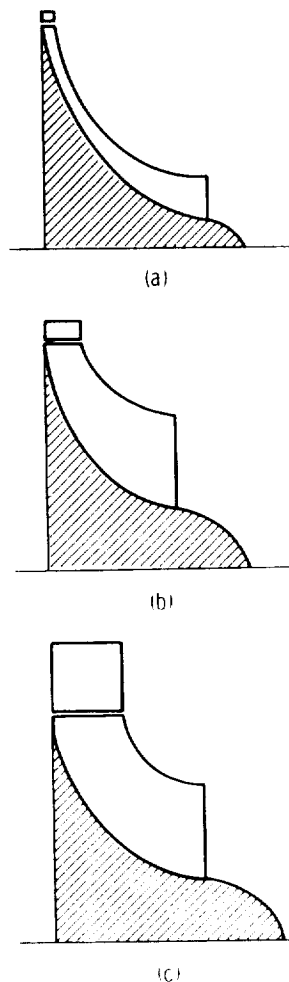


FIGURE 10-11.—Effect of specific speed on optimum blade-jet speed ratio. (Data from ref. 7.)

some value of specific speed depending on the overall level of velocity in the turbine. The only effect that compressibility has on the optimum geometric and velocity ratios is also shown in figure 10-9, where it is seen that higher velocity levels result in smaller ratios of stator-blade height to rotor-inlet diameter at any given specific speed. Figure 10-10 shows that the optimum ratio of rotor-exit tip diam-



- (a) Specific speed, 0.23; $30 \text{ (ft}^{3/4}\text{)(lbm}^{3/4}\text{)/(min)(sec}^{1/2}\text{)(lbf}^{3/4}\text{)}$. Stator-exit flow angle, 81° .
- (b) Specific speed, 0.54; $70 \text{ (ft}^{3/4}\text{)(lbm}^{3/4}\text{)/(min)(sec}^{1/2}\text{)(lbf}^{3/4}\text{)}$. Stator-exit flow angle, 75° .
- (c) Specific speed, 1.16; $150 \text{ (ft}^{3/4}\text{)(lbm}^{3/4}\text{)/(min)(sec}^{1/2}\text{)(lbf}^{3/4}\text{)}$. Stator-exit flow angle, 60° .

FIGURE 10-12.—Sections of radial turbines of maximum static efficiency.
(Data from ref. 7.)

eter to rotor-inlet diameter is small at low specific speed and increases rapidly with increasing specific speed until the imposed limit of $D_{t,2}/D_1=0.7$ is reached. It is seen from figure 10-11 that the optimum blade-jet speed ratio U_1/V_j varies with specific speed in a manner similar to the variation of static efficiency.

The optimum values shown in figures 10-8 to 10-11 can be used for the design of radial-inflow turbines. Sections of turbines with optimum geometries are shown in figure 10-12 for three values of specific speed. These sections show that specific speed is largely an index of flow capacity.

The design study of reference 7 also indicated the variation in the different losses along the curve of maximum static efficiency. This is shown in figure 10-13 for the range of specific speed covered. For low values of specific speed, the stator and rotor viscous losses are very

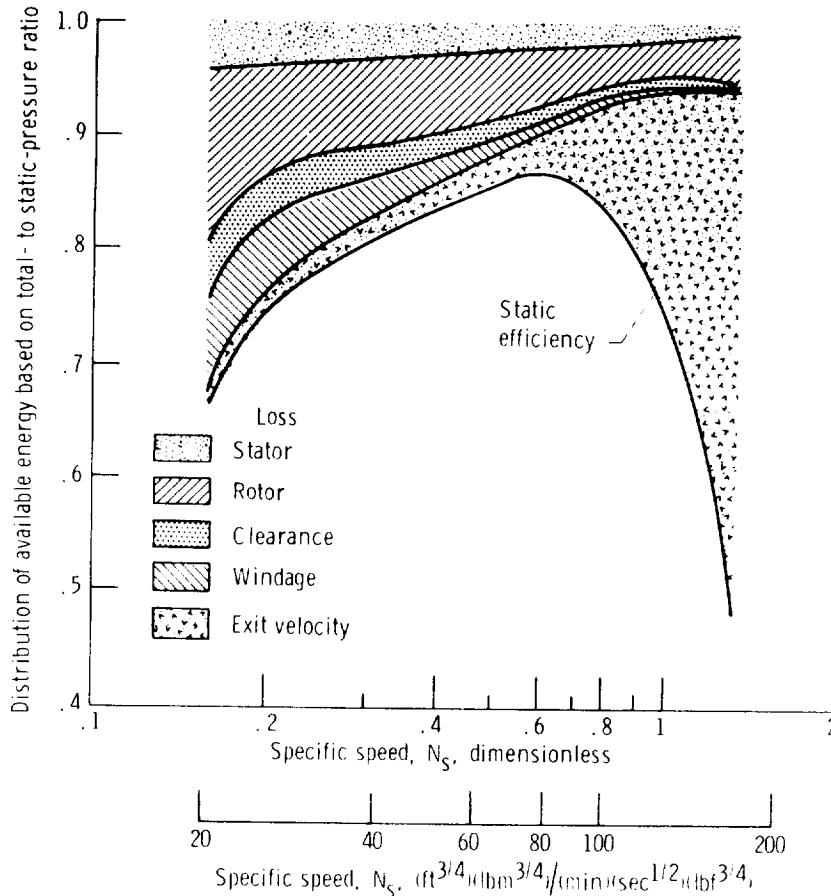
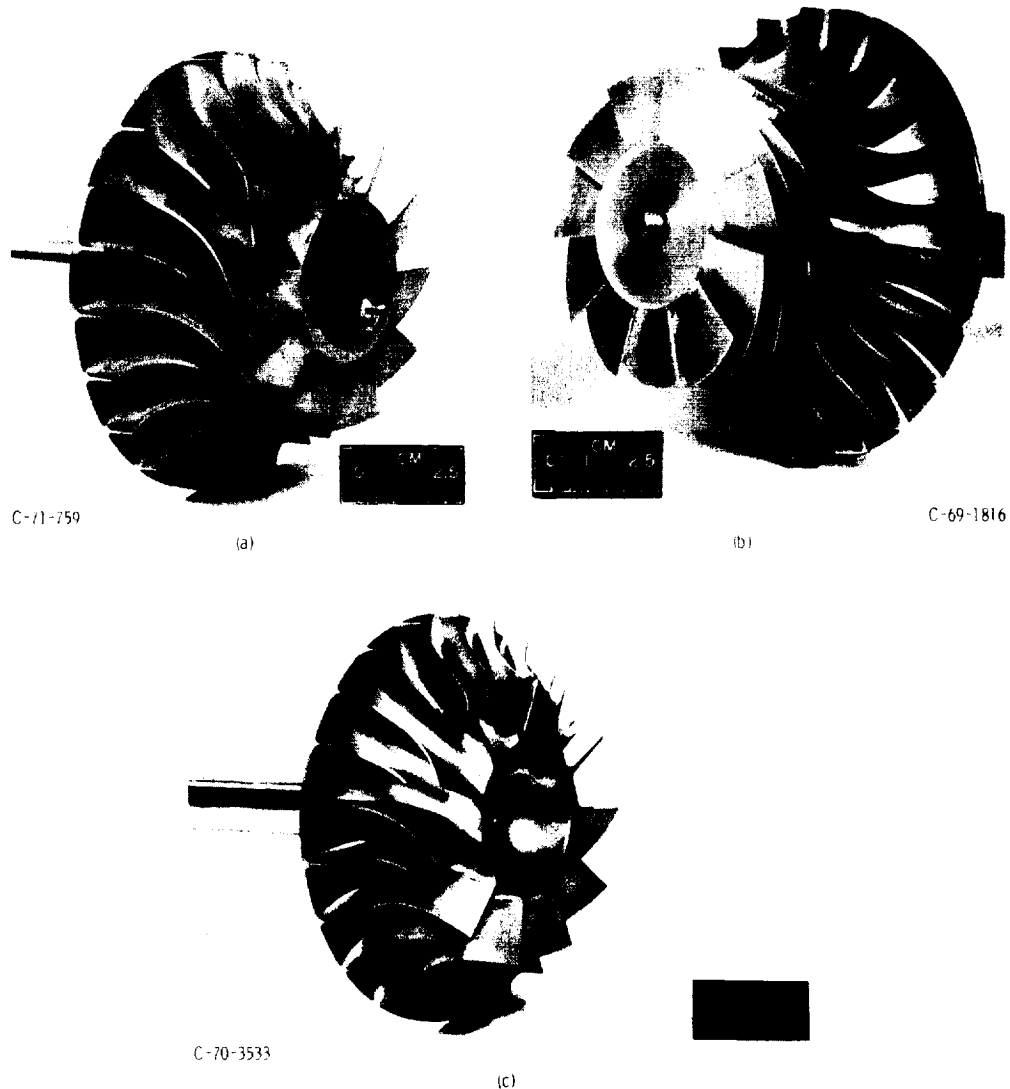


FIGURE 10-13.—Loss distribution along curve of maximum static efficiency. (Data from ref. 7.)

TURBINE DESIGN AND APPLICATION

large because of the high ratio of wall area to flow area. Also, the clearance loss is large because the blade-to-shroud clearance is a relatively large fraction of the passage height. The windage loss, which depends on primarily the diameter and rotative speed, is also large at low specific speed because of the low flow rate. As specific speed increases, the stator and rotor losses, clearance loss, and windage loss all decrease because of the increased flow and area. The exit kinetic-energy loss becomes predominant at high values of specific speed.



(a) Design rotor.

(b) Rotor with exducer extension.

(c) Cut-back rotor.

FIGURE 10-14.—Rotor configurations used in specific-speed study of reference 8.

Experimental study.—In order to determine experimentally the effect of specific speed on turbine efficiency, a turbine was modified (ref. 8) to accept a series of stator blade rows with different numbers of blades and different blade angles. The rotor was fitted with an extension for reduced area operation and was also cut back for increased area operation. These modifications were used to vary the stator throat area from 20 to 144 percent of the design throat area and to vary the rotor throat area from 53 to 137 percent. This allowed the turbine to be operated over a large range of specific speed. Figure 10-14 shows the rotor as designed, with the reduced-area extension, and cut back. Details of the geometry, test results, and internal velocity calculations are given in reference 8.

Performance was determined experimentally for 13 combinations of stator area and rotor area. Figure 10-15 shows the envelopes of the

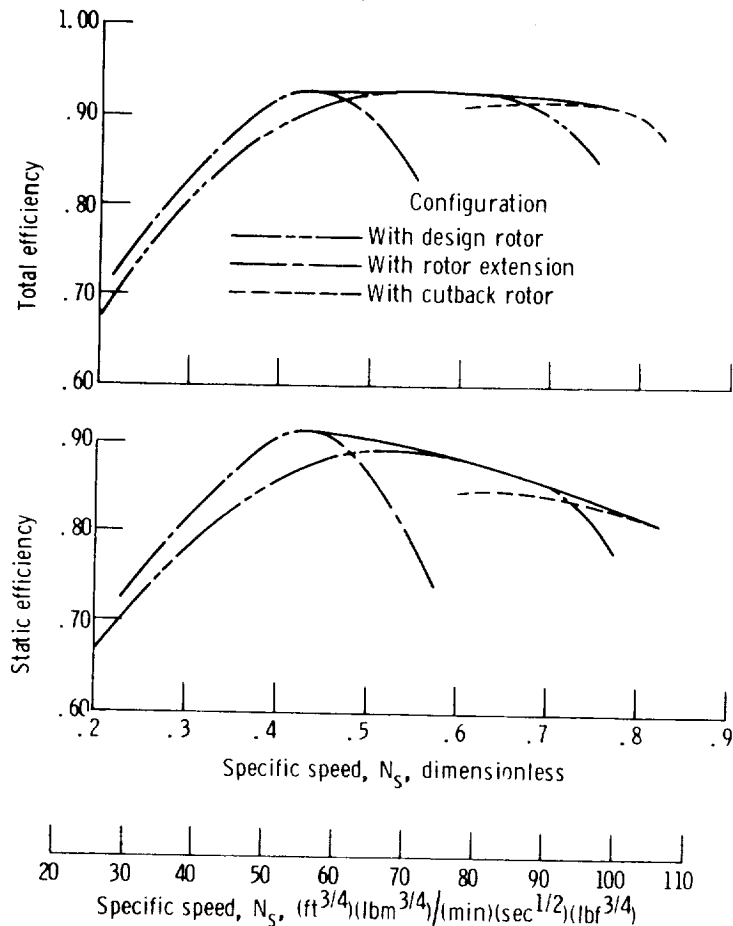


FIGURE 10-15.—Experimental variation of efficiency with specific speed. (Data from ref. 8.)

design-speed efficiency curves obtained with each rotor configuration, as well as the overall envelope curve. Specific speed for each stator-and-rotor combination was varied simply by varying overall pressure ratio at design speed. Note that total efficiencies over 0.90 were measured for specific speeds from 0.37 to 0.80 (48 to 103 $(\text{ft}^{3/4})$ $(\text{lbm}^{3/4})/(\text{min})(\text{sec}^{1/2})(\text{lbf}^{3/4})$). Maximum efficiencies were obtained when the ratio of stator throat area to rotor throat area was near the design ratio. Maximum static efficiencies of about 0.90 were measured in the specific speed range of about 0.4 to 0.5 (51 to 65 $(\text{ft}^{3/4})$ $(\text{lbm}^{3/4})/(\text{min})(\text{sec}^{1/2})(\text{lbf}^{3/4})$).

The investigation of reference 8 showed that a particular basic design could be used for a variety of applications (different specific speeds) and, even though the distribution of internal velocities is considerably off design, still yield high efficiency. Further, a radial turbine might be used to advantage in applications requiring variable stators. In this investigation, the volume flow rate varied by a factor of nearly three, with total efficiency remaining over 0.90. In addition, the parallel endwalls of the stator blade row minimize the potential for leakage.

Effect of Blade-to-Shroud Clearance

Clearance between the blade and the shroud must be adequate to avoid contact during speed and thermal transients, but it must be minimized to avoid loss of work due to flow bypassing the blades, generation of turbulence, and blade unloading. The efficiency loss due to blade-to-shroud clearance was one of the losses included in the previously discussed specific-speed analysis. For the losses shown in figure 10-13, the clearance loss was based on an average clearance as determined from constant values of rotor-inlet and rotor-exit clearance-to-diameter ratios.

The effects of blade-to-shroud clearance at the rotor inlet and at the rotor exit on radial-inflow turbine efficiency were determined experimentally in the study of reference 9. The results of these studies are presented in figure 10-16, which shows the effects of both inlet clearance and exit clearance. Increasing exit clearance causes a significantly greater loss in turbine efficiency than does a comparable increase in inlet clearance. It is the exit clearance that determines the fraction of the flow that is fully turned to the exit blade angle. Since it is the turbine stator that produces the rotor inlet whirl, design flow turning can be achieved even with a relatively large inlet clearance. With equal inlet and exit clearances (in terms of percent of passage height), there was about a 1-percent loss in efficiency for each percent increase in clearance.

RADIAL-INFLOW TURBINES

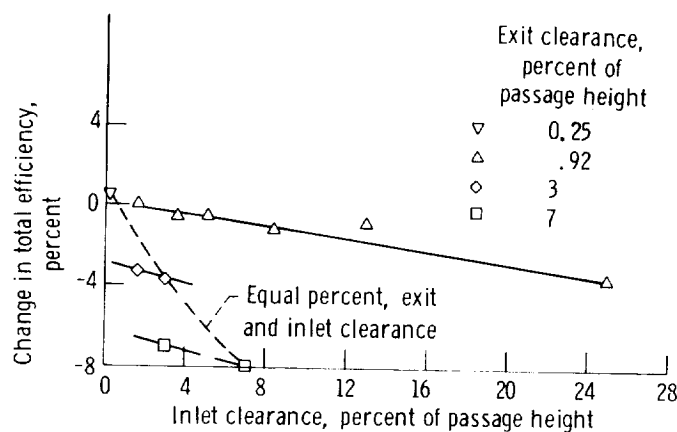


FIGURE 10-16.—Effects of inlet and exit clearances on total efficiency. (Data from ref. 9.)

An axial-flow turbine with the same flow conditions as a radial-inflow turbine would have a larger relative clearance (percent of rotor-exit passage height) than would the radial-inflow turbine. The larger rotor-exit diameter of the axial-flow turbine would result in a larger absolute clearance (since required clearance is largely a function of diameter) and a smaller passage height (in order to have same annulus area). This may be one of the reasons, along with the lower kinetic-energy level previously discussed, for the efficiency advantage of a radial-inflow turbine over a small axial-flow turbine for the same application.

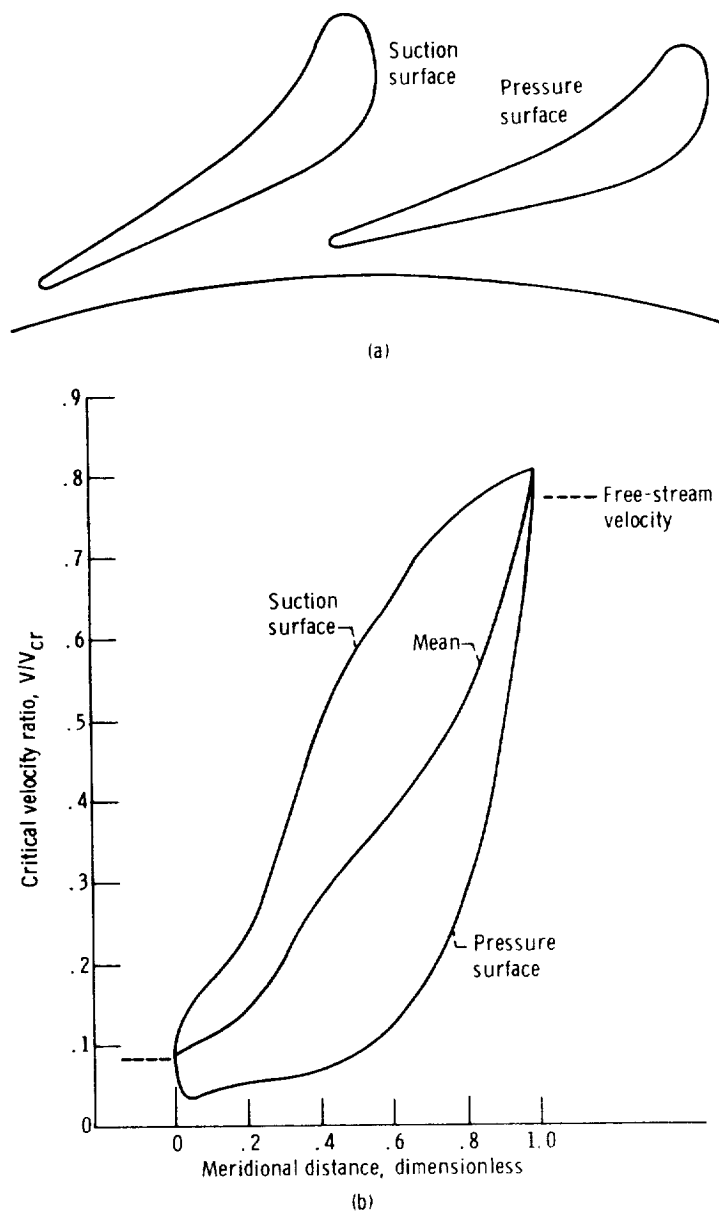
BLADE DESIGN

The curves (figs. 10-8 to 10-11) relating turbine geometry and velocity ratios to specific speed are useful in preliminary design studies for a particular turbine problem. They can be used to determine turbine size and shape, as well as the design velocity diagram. The next part of any design problem involves the examination of internal flow in order to determine the best stator and rotor blade profiles. The methods and computer programs discussed in chapter 5 (vol. 2) are used for this purpose.

Internal Flow Analysis

Stator.—Stator blade aerodynamic design is relatively straightforward. Typically, the blades have relatively little camber, long chords, and parallel endwalls. A long chord is usually specified because large blade profiles are easier to machine and because the small number

of blades (long chord means large spacing for a given solidity) means lower cost. Also, long chords are desirable because the stator blades serve as structural supports for the shroud. The aerodynamic penalty associated with the added endwall area (over that of short-chord



(a) Blades and passage.
 (b) Surface velocities.

FIGURE 10-17.—Stator blades with surface-velocity distributions.

blades) is small because of the high reaction and the resultant favorable boundary-layer conditions.

A two-dimensional flow analysis may be used for the stator because of the parallel or near-parallel endwalls. The stream-function method described in reference 10 provides satisfactory subsonic and transonic solutions. Input information for the computer program includes flow rate, fluid properties and conditions, inlet and outlet flow angles, and a complete specification of blade geometry. The calculated blade-surface velocities are examined for smooth acceleration and magnitude and rate of local decelerations. Successive trials are made with varying solidity, blade number, and distribution of blade curvature until satisfactory velocity distributions are obtained for the pressure and suction surfaces.

Figure 10-17(a) shows the stator blade and passage profiles for a radial-inflow turbine in which the flow entering the stator has no prewhirl. The calculated suction- and pressure-surface velocities are shown in figure 10-17(b). Except for a small deceleration at the pressure-surface leading edge, the flow accelerates continuously on both surfaces. The calculated velocities near the trailing edge may be used to determine whether the blade row can accomplish the design turning. If the suction and pressure surface velocity curves remain open at the trailing edge, the input value for the free-stream exit flow angle specifies more turning than the blades can provide. Conversely, if the curves cross before the trailing edge, the blades will provide more turning than is specified by the input flow angle.

Rotor.—The design of rotor blading is appreciably more difficult than that of stator blading because of adverse pressure gradients (decelerations) encountered and because of the three-dimensionality of the design. The computer program of reference 11 is particularly suitable for screening various combinations of shroud contour, hub contour, number of blades, blade thickness distribution, and blade curvature. This approach, which was developed specifically for radial-inflow turbines, uses the velocity-gradient method, with integration of directional derivatives along fixed arbitrarily located straight lines (called quasi-orthogonals) that intersect all streamlines in the meridional plane. A meridional-plane section with several of these quasi-orthogonals is shown in figure 10-18. A complete meridional solution of velocities and streamlines is obtained. Blade-surface velocities are then calculated approximately in the program of reference 11 with an equation based on irrotational absolute flow and a linear velocity distribution between blades. These blade-surface velocities are used to evaluate the various geometries primarily on the basis of obtaining smooth accelerations and avoiding severe decelerations.

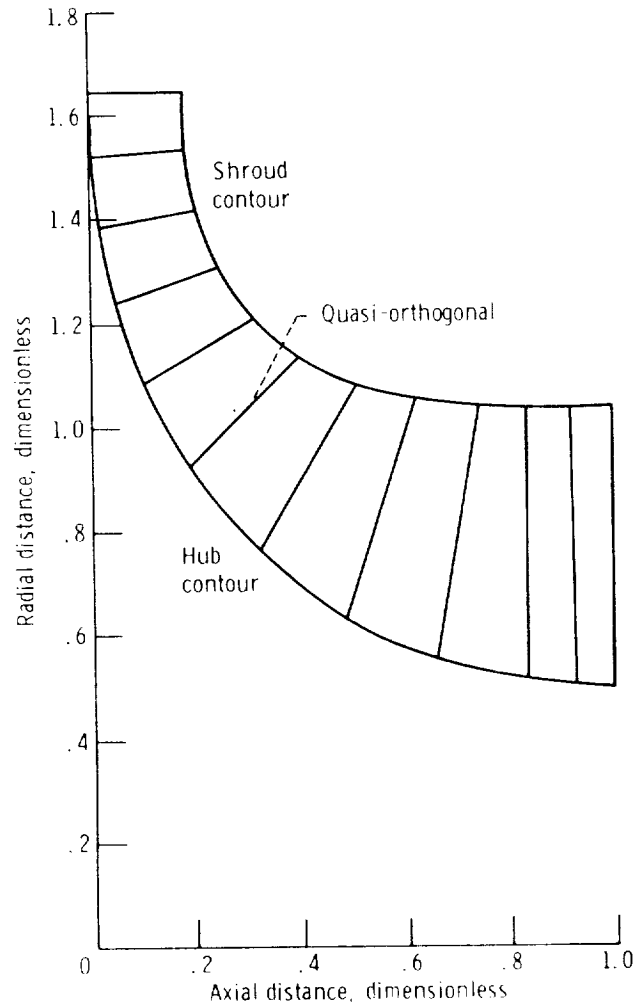
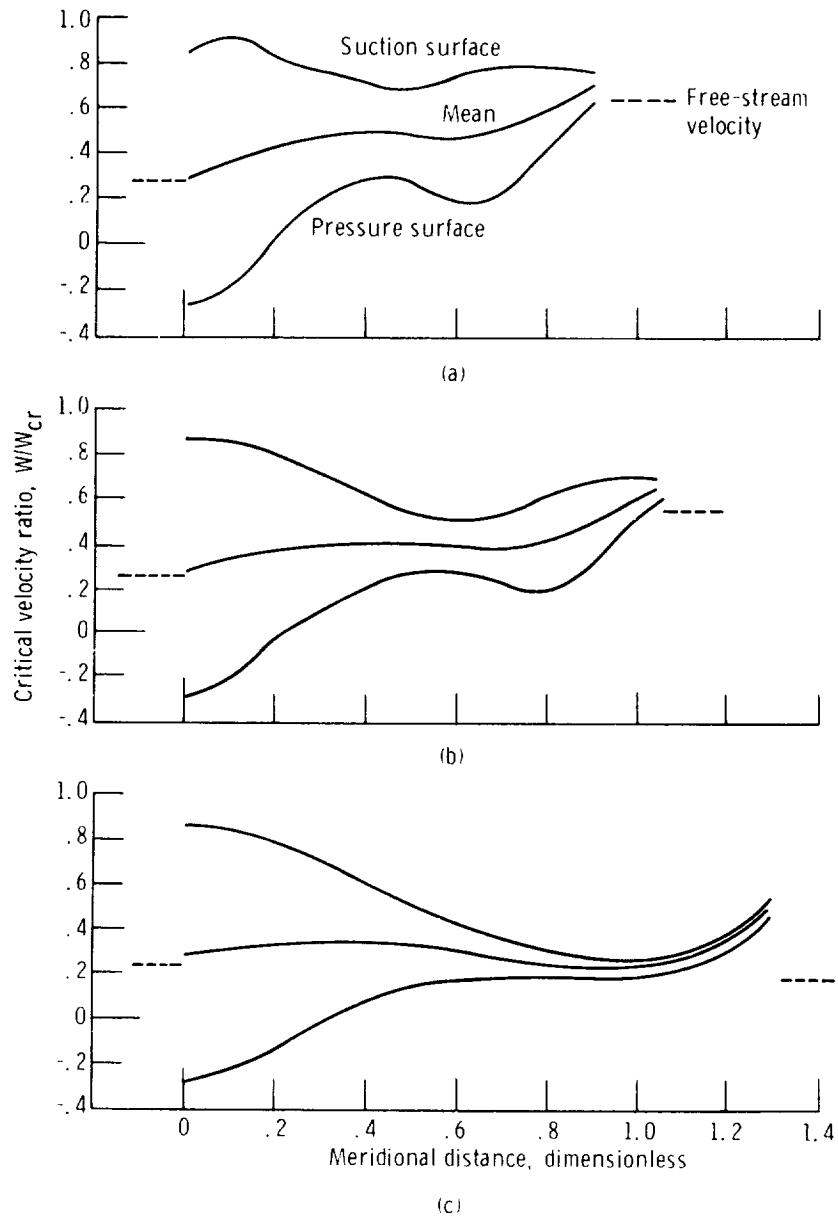


FIGURE 10-18.—Meridional section through radial-inflow turbine.

Blade-surface velocity distributions, as calculated from the meridional-plane solution of reference 11, at the hub, mean, and shroud sections of a radial-inflow turbine rotor are shown in figure 10-19. In figure 10-20 are shown the velocity distributions for the same blading, but as calculated by the stream-function method of reference 10. The surface velocities calculated from the meridional-plane solution agree fairly well with those of the stream-function solution over most of the blade. It can be seen, however, that an appreciable difference between solutions occurs at the leading and trailing edges. The linear velocity variation used in the meridional-plane solution method does not reflect the blade unloading that actually occurs in these regions. The stream-function method determines the blade surface velocities in a more rigorous manner. However, the meridional-

RADIAL-INFLOW TURBINES

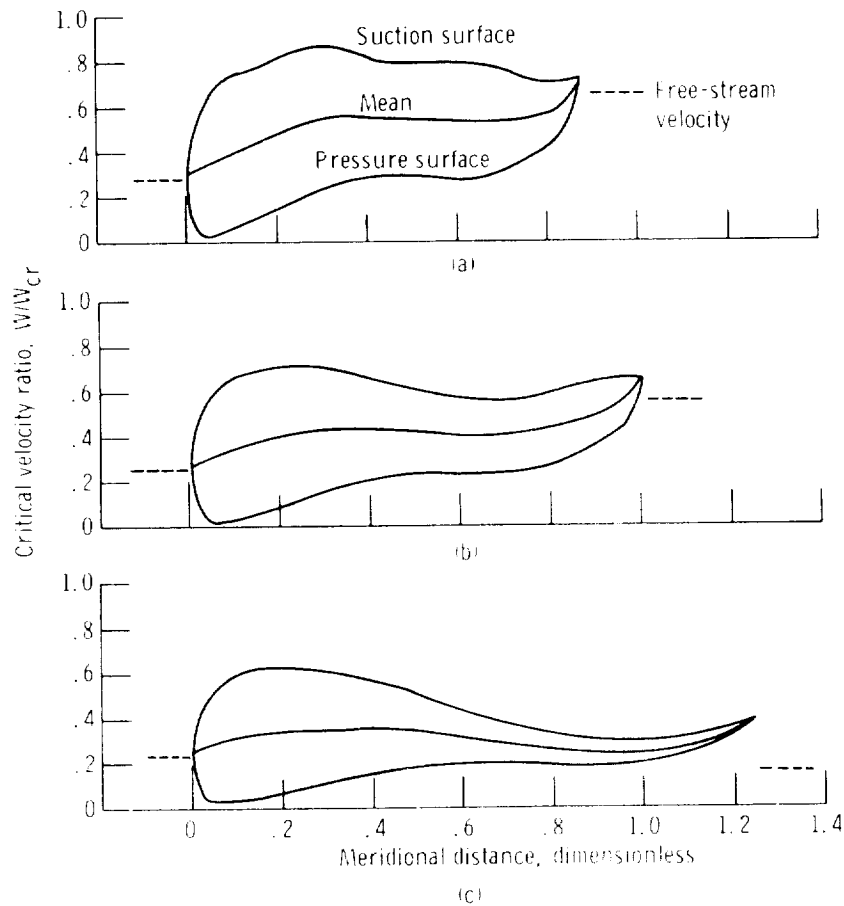


(a) Shroud section.
 (b) Mean (50-percent streamline) section.
 (c) Hub section.

FIGURE 10-19.—Rotor-blade surface-velocity distributions from meridional-plane solution.

plane program (ref. 11) is easier and quicker to use than the stream-function program (ref. 10) and, thus, provides a better means for rapid screening of the many design variables. A lesser difference occurs in the intermediate portion of the blade passage. In the meridional-

TURBINE DESIGN AND APPLICATION



(a) Shroud section.
 (b) Mean (50-percent streamline) section.
 (c) Hub section.

FIGURE 10-20.—Rotor-blade surface-velocity distributions from stream-function solution.

plane analysis, the flow is assumed to be circumferentially uniform, and the mean stream surface between the blades follows the prescribed mean blade surface. The stream-function solution considers blade-to-blade variations in the flow and defines a mean stream surface between blades that deviates from the mean blade surface. The distribution of blade loading, then, is also somewhat different.

Figures 10-19 and 10-20 illustrate the hub-to-shroud variations in the surface velocities and the blade loading, as well as the variations along the flow path. The blade is more heavily loaded along the shroud than elsewhere because of the lower solidity and the shorter flow path. Also, the shroud is a region of high flow. Therefore, the shroud is generally considered the most critical region and is examined most

carefully for favorable blade-surface velocity distributions. The loading near the rotor inlet, where the flow is nearly radial, is considerably higher than the loading near the rotor exit, where the flow is nearly axial. The high loading at the inlet is due primarily to the previously discussed rapid change in angular momentum ($rV_u \propto r^2$) in that section. This high loading near the inlet could be reduced by 50 percent through the use of splitters, which are discussed in the next section. The rear part of the hub surface shows a very low blade loading. This results principally from the long flow path and the great decrease in blade spacing from inlet to exit at the hub section. In this particular turbine, the blade spacing decreased by about 75 percent.

Splitter Blades

As indicated previously, the blade loading is highest at the rotor inlet, where the flow is radially inward. If this loading is excessive, as indicated by negative velocities calculated for the pressure surface and/or large decelerations on the suction surface, it can be reduced by using partial blades between the full blades in the radial part of the rotor. Such partial blades are shown in figure 10-3 and are commonly called splitter blades. When splitter blades are used, the reduced loading results in decreased boundary-layer losses per unit of surface area. However, there is now the additional surface area of the splitter blades to offset the reduced loss per unit area. A judgment must be made, therefore, as to whether the use of splitter blades will, on balance, be beneficial.

The effect of splitter blades on turbine performance was examined experimentally in the study of reference 12. A turbine designed with splitter blades was built and tested. The splitter blades then were removed, thereby doubling the blade loading in the upstream half of the rotor. Channel velocities were calculated for both cases. When the splitters were removed, calculated negative velocities on the pressure side of the blade indicated a reverse-flow eddy extending from the hub almost to the meridional 50-percent streamline, and a large increase in loading upstream of what had been the splitter trailing-edge location.

Turbine performance data (ref. 12) taken over a range of speed and pressure ratio showed very little difference in efficiency between the splitter and the no-splitter cases. The loss increase due to the loading increase when the splitters were removed was apparently offset by the reduced surface area. This result and the previously discussed effect of blade-shroud clearance indicate an insensitivity of efficiency to poor flow conditions near the rotor leading edge. The low inlet velocity and favorable rotor reaction in a radial-inflow turbine provide an appreciable margin of tolerance toward such conditions.

OFF-DESIGN PERFORMANCE

The performance characteristics of radial-inflow turbines are slightly different from those of axial-flow turbines. In an axial-flow turbine at all rotor speeds, the flow rate becomes zero only when the turbine pressure ratio (inlet-total- to exit-static-pressure) is one. In a radial-inflow turbine, however, this is only true at zero speed, as illustrated in figure 10-21. With rotation, the centrifugal force on the fluid within the rotor must be balanced by a pressure gradient directed radially inward. Therefore, there is some small pressure ratio across the turbine even with no flow (see fig. 10-21). This zero-flow pressure ratio increases with speed because of the increasing centrifugal force.

The variation of efficiency with blade-jet speed ratio, illustrated later in this section, for a radial-inflow turbine is very similar to that for an axial-flow turbine. The efficiency decrease as blade-jet speed ratio varies from the peak-efficiency point is slightly more rapid in the case of the radial-inflow turbine.

Prediction techniques for off-design performance are valuable in many situations. Estimated performance data can be useful in system studies to examine start transients and various operating conditions before any hardware is built. They can also be used to help select design modifications where system components may not be matched or to study the use of variable geometry. The approach in these off-design calculation methods is somewhat different from that used in design studies. In the off-design calculations, the geometry is

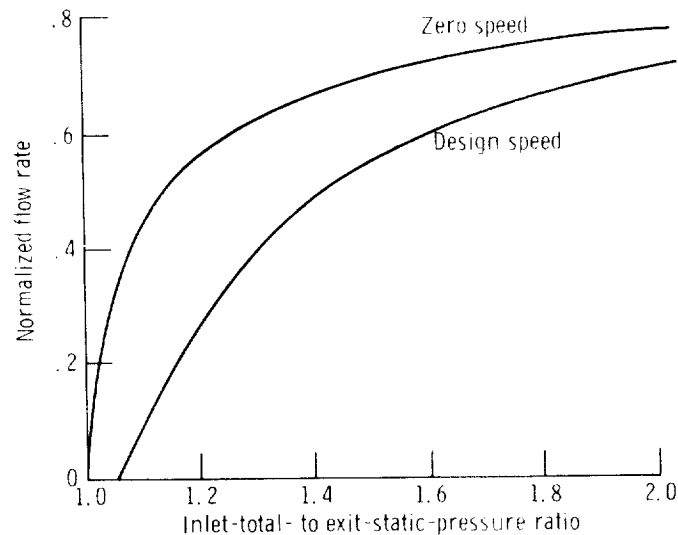


FIGURE 10-21.—Radial-inflow turbine flow characteristics.

fixed, the working-fluid inlet conditions are fixed, and the variables are blade speed and pressure ratio. Losses calculated for the stator and rotor depend on loss coefficients selected to force agreement between calculated and experimental or design values at the design operating point. Additional losses considered for subsonic flows are the rotor incidence loss and the exit kinetic-energy loss.

A radial-inflow turbine off-design performance calculation method developed at the NASA Lewis Research Center is described in reference 13, and the associated computer program is presented in reference 14. Figures 10-22 and 10-23 illustrate results obtained from a modified version of this computer program by presenting calculated performance over a range of speed and pressure ratio and comparing this with experimental performance. The mass flow estimation in figure 10-22 shows an accurate representation of the experimental variation of mass flow rate with pressure ratio. Total and static efficiencies plotted against blade-jet speed ratio are shown in figure 10-23. The calculated efficiencies are generally within 1 per-

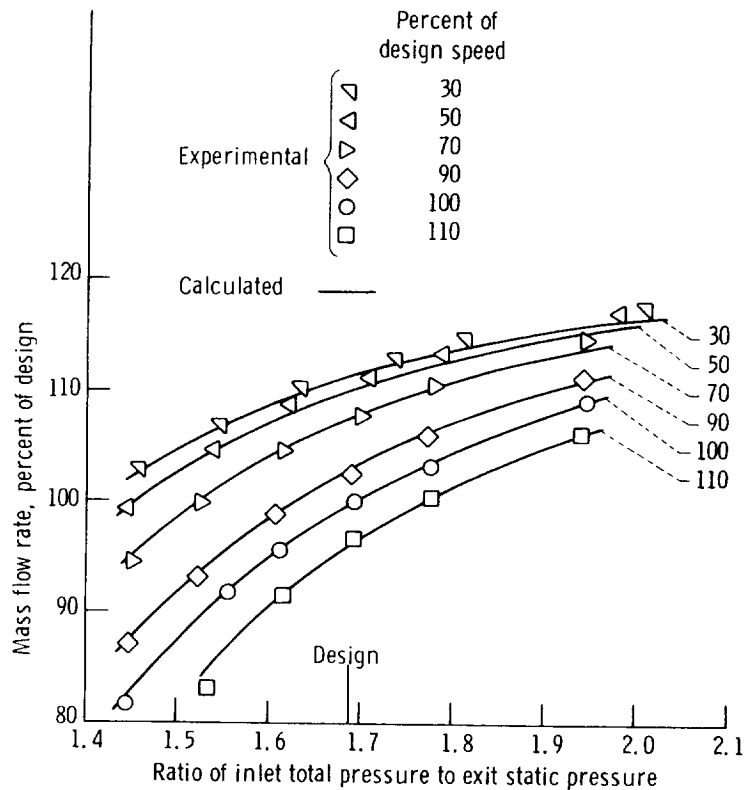


FIGURE 10-22.—Comparison of calculated and experimental flow rates for off-design operation.

TURBINE DESIGN AND APPLICATION

cent and at most 2 percent of the experimental values. The calculations are sufficiently accurate to provide a valuable tool in the examination of overall system performance prior to fabrication and testing of the various components.

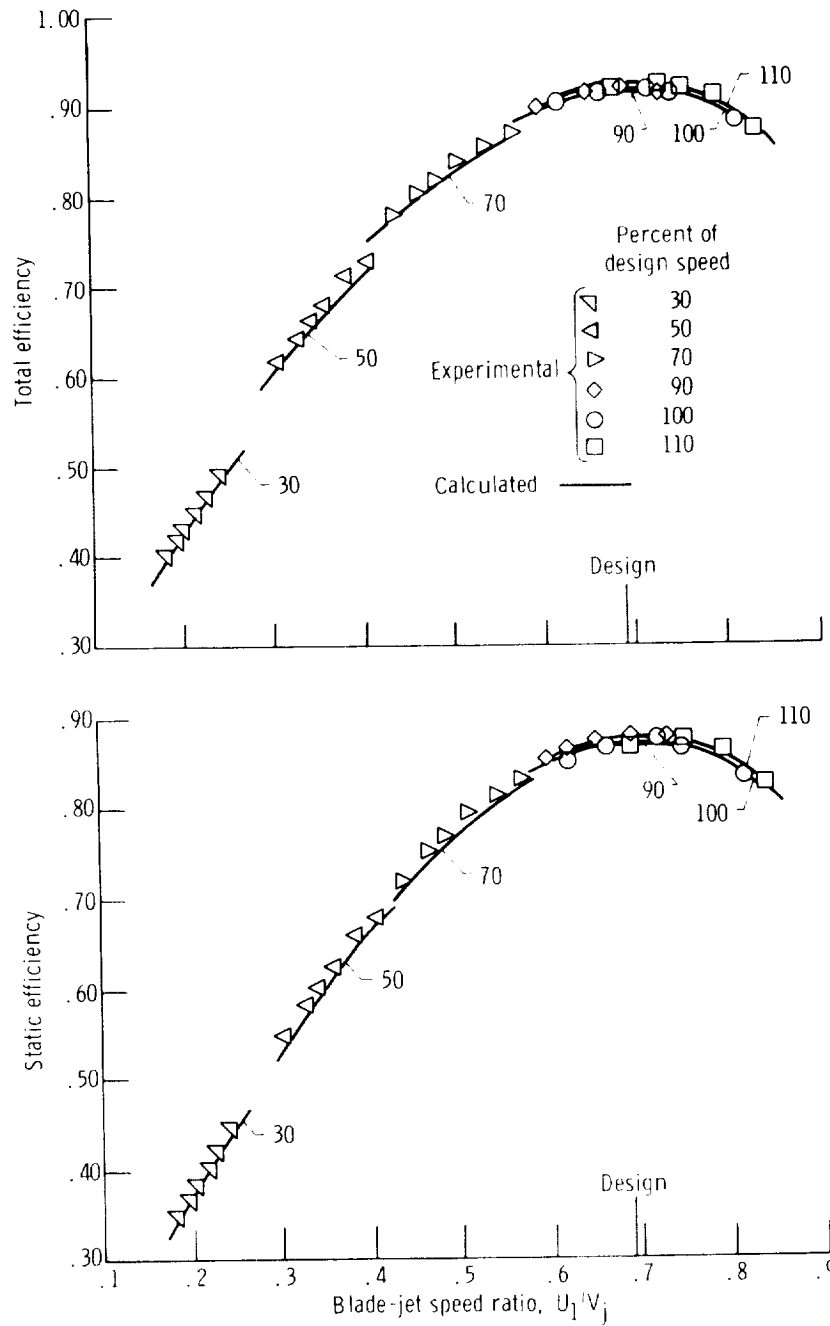


FIGURE 10-23.—Comparison of calculated and experimental efficiencies for off-design operation.

REFERENCES

1. SAWYER, JOHN W., ed.: Gas Turbine Engineering Handbook. Gas Turbine Publications, Inc., 1966.
2. SHEPHERD, D. G.: Principles of Turbomachinery. Macmillan Co., 1956.
3. RODGERS, C.: Efficiency and Performance Characteristics of Radial Turbines. Paper 660754, SAE, 1966.
4. LAGNEAU, J. P.: Contribution to the Study of Advanced Small Radial Turbines. Int. Note 38, von Karman Institute of Fluid Dynamics, Mar. 1970.
5. WOOD, HOMER J.: Current Technology of Radial-Inflow Turbines for Compressible Fluids. J. Eng. Power, vol. 85, no. 1, Jan. 1963, pp. 72-83.
6. HIETT, G. F.; AND JOHNSON, I. H.: Experiments Concerning the Aerodynamic Performance of Inward Flow Radial Turbines. Paper 13 presented at the Thermodynamics and Fluid Mechanics Convention, Inst. Mech. Eng., London, Apr. 1964.
7. ROHLIK, HAROLD E.: Analytical Determination of Radial Inflow Turbine Design Geometry for Maximum Efficiency. NASA TN D-4384, 1968.
8. KOFSEY, MILTON G.; AND NUSBAUM, WILLIAM J.: Effects of Specific Speed on Experimental Performance of a Radial-Inflow Turbine. NASA TN D-6605, 1972.
9. FUTRAL, SAMUEL M., JR.; AND HOLESKI, DONALD E.: Experimental Results of Varying the Blade-Shroud Clearance in a 6.02-Inch Radial-Inflow Turbine. NASA TN D-5513, 1970.
10. KATSANIS, THEODORE: Fortran Program for Calculating Transonic Velocities on a Blade-to-Blade Stream Surface of a Turbomachine. NASA TN D-5427, 1969.
11. KATSANIS, THEODORE: Use of Arbitrary Quasi-Orthogonals for Calculating Flow Distribution in the Meridional Plane of a Turbomachine. NASA TN D-2546, 1964.
12. FUTRAL, SAMUEL M., JR.; AND WASSERBAUER, CHARLES A.: Experimental Performance Evaluation of a 4.59-Inch Radial-Inflow Turbine With and Without Splitter Blades. NASA TN D-7015, 1970.
13. FUTRAL, SAMUEL M., JR.; AND WASSERBAUER, CHARLES A.: Off-Design Performance Prediction with Experimental Verification for a Radial-Inflow Turbine. NASA TN D-2621, 1965.
14. TODD, CARROLL A.; AND FUTRAL, SAMUEL M., JR.: A Fortran IV Program to Estimate the Off-Design Performance of Radial-Inflow Turbines. NASA TN D-5059, 1969.

SYMBOLS

c_p	specific heat at constant pressure, J/(kg)(K); Btu/(lb)(°R)
D	diameter, m; ft
g	conversion constant, 1; 32.17 (lbm)(ft)/(lbf)(sec ²)
H	ideal work, or head, based on inlet and exit total pressures, J/kg; (ft)(lbf)/lbm
h	passage height, m; ft
Δh_{ia}	ideal work based on inlet-total and exit-static pressures, J/kg; Btu/lb
$\Delta h'_{ia}$	ideal work based on inlet-total and exit-total pressures, J/kg; Btu/lb
J	conversion constant, 1; 778 (ft)(lb)/Btu
K	conversion constant, 2π rad/rev; 60 sec/min
N	rotative speed, rad/sec; rev/min
N_s	specific speed, dimensionless; (ft ^{3/4})(lbm ^{3/4})/(min)(sec ^{1/2}) (lb ^{3/4})
n	total number of blades (full plus partial)
p	absolute pressure, N/m ² ; lb/ft ²
Q	volume flow rate, m ³ /sec; ft ³ /sec
r	radius, m; ft
T	absolute temperature, K; °R
U	blade speed, m/sec; ft/sec
V	absolute velocity, m/sec; ft/sec
V_j	ideal jet speed, based on inlet-total- to exit-static-pressure ratio, m/sec; ft/sec
W	relative velocity, m/sec; ft/sec
α	fluid absolute flow angle measured from meridional plane, deg
β	fluid relative flow angle measured from meridional plane, deg

Subscripts:

cr	critical flow condition (sonic velocity)
h	hub
t	tip
u	tangential component
0	at stator inlet
1	at stator exit or rotor inlet
2	at rotor exit

Superscripts:

'	absolute total state
''	relative total state

CHAPTER 11

Turbine Cooling

By Raymond S. Colladay

The trend towards higher compressor pressure ratios and turbine-inlet temperatures to increase thrust and cycle efficiency has led to the necessity of cooling turbine blades, vanes, and end walls to meet life requirements. In this chapter, the term "vane" refers to a stator airfoil, while the term "blade" refers to the rotor airfoil. The hot combustor discharge gases enter the first vane row at peak temperatures frequently in excess of 1644 K (2500° F). In order to preserve the integrity of the turbine components in this hostile environment, air bled from the compressor is routed through the internal passages of the airfoils for cooling and then is dumped into the main gas stream at discrete locations around the blade or vane. This inevitably results in losses, both across the turbine and in the overall cycle thermodynamic efficiency. Consequently, very effective cooling schemes which utilize a minimum of air are required.

GENERAL DESCRIPTION

In any turbine cooling design, one must make a complete energy balance on the blade (or vane, or end wall) to arrive at a cooling configuration which meets a given metal temperature limit. The analysis can be broken up conceptually into three parts: (1) The prediction of the heat flux to the blade from the hot gas stream. This requires an understanding of the boundary-layer development over the airfoil, the location of the transition from laminar to turbulent flow, the potential-flow velocity distribution, and the temperature profile (pattern factor) of the gas leaving the combustor (or other heat

source). (2) A steady-state or transient heat-conduction analysis to provide a detailed map of metal temperatures for blade-stress predictions. And, (3) the prediction of complex internal coolant flow paths for convection-cooling calculations. To maintain closure on the energy balance, the entire heat transfer process—convection from hot gas to blade, conduction through the blade wall, and convection from blade to coolant—must be treated simultaneously.

Let us for a moment oversimplify the problem by considering a one-dimensional model of a turbine-blade wall on the suction or pressure surface (see fig. 11-1). The heat flux to the blade can be expressed as a product of a hot-gas-side heat-transfer coefficient and the temperature difference between the gas and the wall. The gas temperature is expressed as an effective gas temperature, which for convection cooling is the adiabatic or recovery temperature (the temperature the surface would reach if there were no cooling). For purposes of this illustration, let the adiabatic wall temperature be the total gas temperature. Therefore,

$$q = h_g(T_g' - T_{w,o}) \quad (11-1)$$

where

- q heat flux, W/m^2 ; $Btu/(hr)(ft^2)$
- h_g heat-transfer coefficient of hot gas, $W/(m^2)(K)$; $Btu/(hr)(ft^2)(^\circ R)$
- T_g' total temperature of hot gas, K ; $^\circ R$
- $T_{w,o}$ temperature of wall outer surface, K ; $^\circ R$

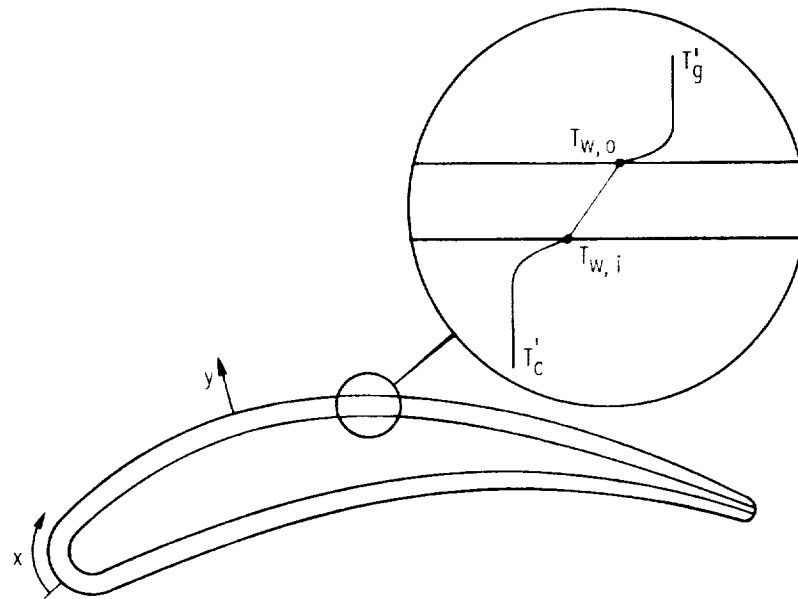


FIGURE 11-1.—Simplified one-dimensional model.

The heat removed from the wall, expressed in the same manner, is

$$q = h_c(T_{w,i} - T_c') \quad (11-2)$$

where

h_c heat-transfer coefficient of coolant, W/(m²)(K); Btu/(hr)(ft²)(°R)

$T_{w,i}$ temperature of wall inner surface, K; °R

T_c' total temperature of coolant, K; °R

The temperature drop through the wall is given by

$$q = -k_w \frac{dT}{dy} = \frac{k_w}{l} (T_{w,o} - T_{w,i}) \quad (11-3)$$

where

k_w thermal conductivity of wall, W/(m)(K); Btu/(hr)(ft)(°R)

y coordinate normal to wall surface, m; ft

l wall thickness, m; ft

The second equality holds only for constant thermal conductivity.

As is frequently done in a first-order design, let the heat-transfer coefficient h_x be approximated by a correlation for flow over a flat plate. For a turbulent boundary layer, the flat-plate local Nusselt number Nu is given by

$$Nu_x = \frac{h_x x}{k_g} = 0.0296 Re_x^{0.8} Pr^{1/3} \quad (11-4)$$

where

x distance along surface from leading edge of flat plate, m; ft

Re_x Reynolds number based on distance x

Pr Prandtl number

The Reynolds number is defined as

$$Re_x = \frac{\rho u_g x}{\mu} \quad (11-5)$$

where

ρ density, kg/m³; lb/ft³

u_g component of hot-gas velocity in x direction, m/sec; ft/sec

μ viscosity, (N)(sec)/m²; lb/(ft)(sec)

and the Prandtl number is defined as

$$Pr = K \frac{\mu c_p}{k_g} \quad (11-6)$$

where

K dimensional constant, 1; 3600 sec/hr
 c_p specific heat at constant pressure, J/(kg)(K); Btu/(lb)(°R)

For an ideal gas, equation (11-5) can be substituted into equation (11-4) to yield

$$h_x = \frac{k_g}{x} (0.0296) Pr^{1/3} \left[p_g' \sqrt{\frac{\gamma g}{RT_g'}} \frac{Mx}{\mu \left(1 + \frac{\gamma-1}{2} M^2\right)^{(\gamma+1)/2(\gamma-1)}} \right]^{0.8} \quad (11-7)$$

where

p_g' total pressure of hot gas, N/m²; lb/ft²
 γ ratio of specific heat at constant pressure to specific heat at constant volume
 g conversion constant 1; 32.17 (lbm)(ft)/(lbf)(sec²)
 R gas constant, J/(kg)(K); (ft)(lbf)/(lbm)(°R)
 M Mach number

On the coolant side, a number of cooling schemes can be used, but in general,

$$h_c = C Re_c^m Pr^n = C \left(\frac{w_c \mathcal{L}}{\mathcal{A}_c \mu} \right)^m Pr^n \quad (11-8)$$

where

C constant dependent on coolant-passage geometry
 Re_c Reynolds number based on characteristic length \mathcal{L}
 w_c coolant mass flow rate, kg/sec; lb/sec
 \mathcal{L} characteristic length for coolant passage, m; ft
 \mathcal{A}_c coolant-passage flow area, m²; ft²

For turbulent convection cooling, $m=0.8$ and $n=1/3$. Since efficient cooling is desired, internal laminar flow ($m=0.5$) should be avoided.

Now, consider the temperature profile through the blade wall, as depicted in figure 11-2, when the pressure p_g' and temperature T_g' of the hot gas are increased and the wall outer temperature $T_{w,o}$ is kept constant (going from state 1 to state 2 in fig. 11-2). From equations (11-7) and (11-1), the heat flux to the blade increases with pressure to the 0.8 power and it increases with increasing gas temperature. The increased heat flux raises the temperature drop through the wall (i.e., decreases $T_{w,i}$ for a fixed wall outer temperature $T_{w,o}$). At the same time, the compressor bleed air temperature increases (higher compressor pressure ratio), so the temperature difference ($T_{w,i} - T_c'$) available for convection cooling is sharply reduced. The heat flux q must be removed, otherwise the outer wall temperature will increase. Therefore,

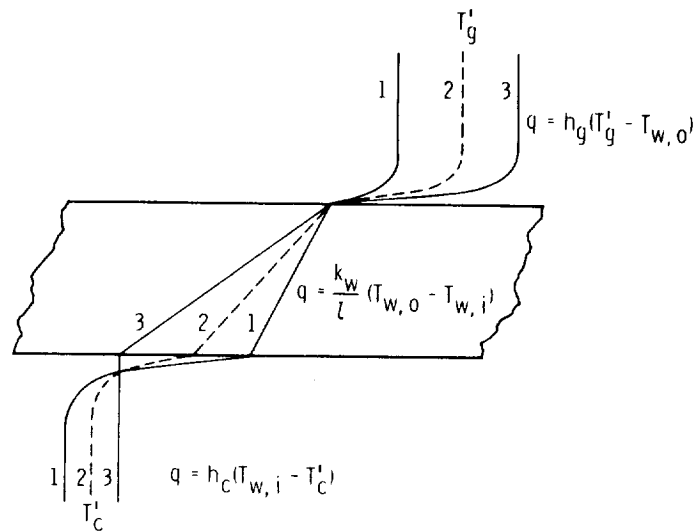


FIGURE 11-2.—Gas temperature and pressure effect on temperature drop through the wall.

h_c must be increased by increasing the coolant flow w_c . The limiting case, as seen from figure 11-2, is state 3, where the inside wall temperature and coolant temperature are equal; therefore, h_c must be infinite, and an infinite coolant flow is required. Of course, this condition is impossible to achieve.

Because of limited internal passage size and the restriction on the quantity of cooling air available and on its supply pressure, a limit to the capabilities of plain convection cooling is apparent. Figure 11-3 from reference 1 shows the highly nonlinear increase in cooling air required for convection cooling as pressure and temperature increase.

The limit in the application of advanced convection cooling is about 1644 K (2500° F) hot-spot turbine-inlet temperature and about 20 atmospheres pressure. To exceed these gas conditions while maintaining reasonable operating blade-metal temperatures, cooling designs must incorporate film or transpiration cooling. Figure 11-3 shows the potential savings in cooling air with the use of transpiration cooling or combined film and convection cooling as compared to convection cooling only. Figure 11-4 illustrates the basic methods for air-cooling turbine components (figs. 11-4(a) to (e)), and it also shows examples of blades cooled by one or more of these cooling methods (figs. 11-4(f) to (i)).

Film cooling is an effective way to protect the surface from the hot gas stream by directing cooling air into the boundary layer to provide a protective, cool film along the surface. The effective gas temperature

TURBINE DESIGN AND APPLICATION

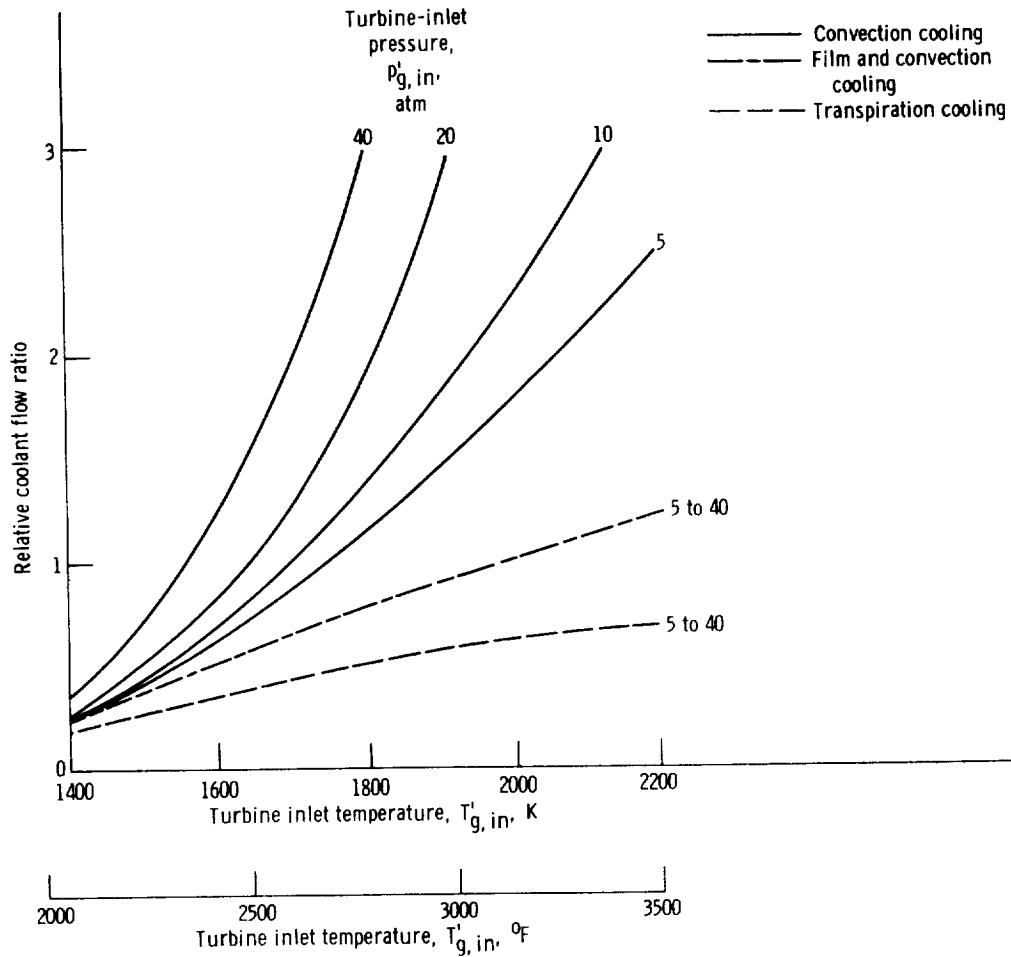


FIGURE 11-3.—Effect of turbine-inlet pressure and temperature on coolant flow requirements.

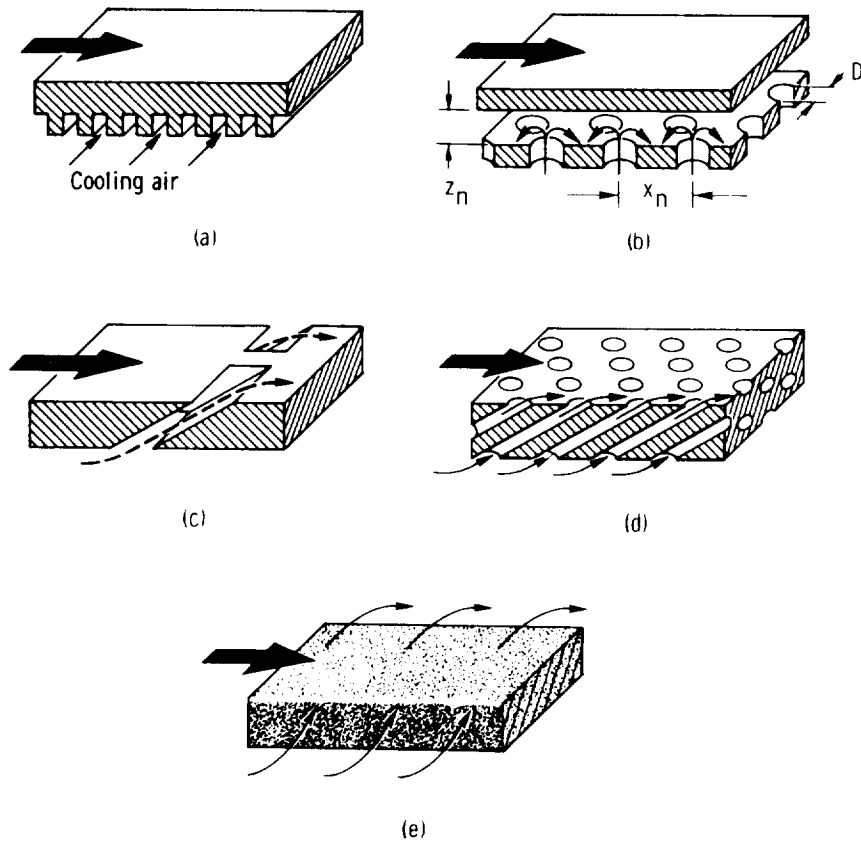
in equation (11-1) becomes the local film temperature, and the heat flux to the blade is then

$$q = h_g (T'_{film} - T_{w,o}) \quad (11-9)$$

where T'_{film} is the total temperature of the gas film, in K or °R. It is frequently assumed that the heat-transfer coefficient in this equation is the same as in the non-film-cooled case.

The injection of film air into the boundary layer causes turbine aerodynamic losses which tend to reduce some of the advantages of using higher pressures and temperatures. The aerodynamic and heat-transfer designs must be integrated to achieve an optimum configuration which ensures blade metal temperatures consistent with long-life objectives yet minimizes the loss in turbine efficiency.

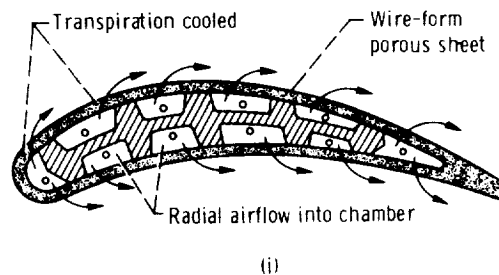
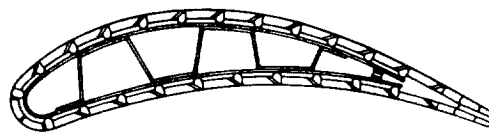
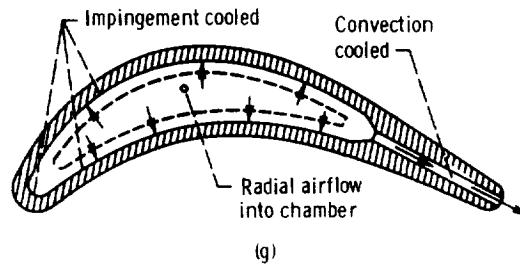
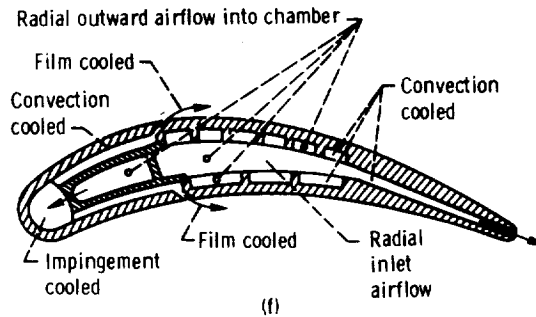
Transpiration cooling of a porous blade wall is the most efficient air-cooling scheme available, but it has significant drawbacks which currently limit its use to advanced designs operating under extreme heat-flux conditions. For efficient transpiration cooling, the pores should be small, which leads to problems of blockage due to oxidation and foreign contaminants. Also, the aerodynamic losses can be severe because of normal injection of cooling air into the boundary layer. To offset this latter point, however, it must be recognized that transpiration cooling requires less cooling air than other cooling schemes. A typical transpiration-cooled blade is shown in figure 11-4(i). Full-coverage film cooling from an array of discrete holes, as illustrated in figure 11-4(h), is an attempt to draw on some of the advantages of transpiration cooling without paying the penalties mentioned.



(a) Convection cooling. (b) Impingement cooling.
 (c) Film cooling. (d) Full-coverage film cooling.
 (e) Transpiration cooling.

FIGURE 11-4.—Methods for turbine blade cooling.

TURBINE DESIGN AND APPLICATION



- (f) Convection-, impingement-, and film-cooled blade configuration.
(g) Convection- and impingement-cooled blade configuration.
(h) Full-coverage film-cooled blade configuration.
(i) Transpiration-cooled blade configuration.

FIGURE 11-4.—Concluded.

HEAT TRANSFER FROM HOT GAS TO BLADE

Boundary-Layer Equations

General equations.—The transfer of heat to the blade is confined to the boundary-layer region very near the surface, where large velocity

and temperature gradients are present. Consequently, to describe the heat-transfer process, the following boundary-layer equations, introduced in chapter 6 (vol. 2), must be solved:

Conservation of mass

$$\frac{\partial}{\partial x} (\rho u) + \frac{\partial}{\partial y} (\rho v + \overline{\rho'v'}) = 0 \quad (11-10)$$

where

- v time-average value of velocity component in y direction,
m/sec; ft/sec
 $(\)'$ fluctuating component
 $(\)$ time-averaged quantity

Conservation of momentum

$$\rho u \frac{\partial u}{\partial x} + (\rho v + \overline{\rho'v'}) \frac{\partial u}{\partial y} = -g \frac{dp}{dx} + g \frac{\partial}{\partial y} \tau + g \rho B_x \quad (11-11)$$

where

- τ local shear stress, N/m²; lb/ft²
 B_x component of body force in the x direction, N/kg; lb/lbm

Conservation of energy

$$\rho u \frac{\partial H}{\partial x} + (\rho v + \overline{\rho'v'}) \frac{\partial H}{\partial y} = \frac{\partial}{\partial y} \left(\frac{1}{K} q + \frac{u\tau}{J} \right) + Q \quad (11-12)$$

where

- H total enthalpy, J/kg; Btu/lb
 J conversion constant, 1; 778 (ft)(lb)/Btu
 Q heat-generation term, W/m³; Btu/(sec)(ft³)

The dependent variables ρ , u , v , and H are time-average values (i.e., $\bar{\rho}$, \bar{u} , \bar{v} , and \bar{H} , as denoted in ch. 6), with the overbar being understood.

The solution of these equations requires appropriate expressions for the shear stress and heat flux through the hydrodynamic and thermal boundary layers. The laminar contribution to molecular diffusivity of heat and momentum is straightforward, but our limited understanding of turbulent flow requires the use of various assumptions in describing the turbulent counterpart. One such assumption, which bears little physical resemblance to the structure of turbulence but has persisted because of its simplicity and success in predicting turbulent transport processes, is Prandtl's mixing-length hypothesis for eddy diffusivity of heat and momentum. The shear stress and heat flux are expressed as the sum of the laminar and turbulent contributions:

$$\tau = \frac{\rho}{g} \left(\nu_L \frac{\partial u}{\partial y} - \overline{u'v'} \right) \quad (11-13)$$

and

$$q = K\rho \left(\alpha_L \frac{\partial h}{\partial y} - \overline{v'h'} \right) \quad (11-14)$$

where

- ν_L laminar component of momentum diffusivity (kinematic viscosity), m²/sec; ft²/sec
- α_L laminar component of heat diffusivity, m²/sec; ft²/sec
- h static enthalpy, J/kg; Btu/lb

The turbulent shear stress $\overline{u'v'}$ and heat flux $\overline{v'h'}$ are assumed proportional to the respective gradients in the mean flow variable; that is,

$$\overline{u'v'} = -\nu_T \frac{\partial u}{\partial y} \quad (11-15)$$

and

$$\overline{v'h'} = -\alpha_T \frac{\partial h}{\partial y} \quad (11-16)$$

where the subscript T denotes the turbulent component of momentum and heat diffusivity.

Equations (11-13) and (11-14) can then be written as

$$\tau = \frac{\rho}{g} (\nu_L + \nu_T) \frac{\partial u}{\partial y} = \frac{\rho}{g} \nu \frac{\partial u}{\partial y} \quad (11-17)$$

and

$$q = K\rho(\alpha_L + \alpha_T) \frac{\partial h}{\partial y} = K\rho\alpha \frac{\partial h}{\partial y} \quad (11-18)$$

The preceding boundary-layer equations assume temperature-variable properties and compressible, turbulent flows (inclusive of laminar flow where both ν_T and α_T approach zero). If the variation in specific heat c_p is neglected and there is no internal heat generation, the energy equation reduces to equation (6-42).

If temperature-variable properties are assumed at the onset of the analysis, all boundary-layer equations must be solved simultaneously. However, constant properties are frequently assumed, and experimental data are usually taken under approximately isothermal conditions. The final results are then corrected to account for temperature-variable properties. These corrections will be considered in a later section.

Integral equations.—As we saw in chapter 6 (vol. 2) with the momentum equation, it is often convenient to solve the boundary-layer equations from an integral approach in terms of integral parameters

such as momentum and displacement thicknesses rather than in terms of discrete velocity profiles. Just as the displacement and momentum thicknesses derive their meaning from the integral momentum equation, so the enthalpy thickness is a significant boundary-layer parameter for the integral energy equation. The enthalpy thickness Δ is defined as follows:

$$\Delta = \frac{\int_0^{\infty} \rho u (H - H_g) dy}{\rho_g u_g (H_{w,o} - H_g)} \quad (11-19)$$

Note that the subscript g refers to the free-stream value denoted by the subscript e in chapter 6. For low-velocity, constant-property flow,

$$\Delta = \frac{\int_0^{\infty} u (T' - T'_g) dy}{u_g (T_{w,o} - T'_g)} \quad (11-20)$$

The enthalpy thickness is a measure of the convected energy decrement caused by the boundary layer.

The integral energy equation can be derived either by integrating equation (11-3) or directly by balancing the transport of energy across the boundary of a control volume containing the hydrodynamic and thermal boundary layers (for details see ref. 2). In either case, the resulting integral energy equation for compressible flow with temperature-variable properties and mass transfer at the wall is

$$\frac{q}{K \rho_g u_g (H_{w,o} - H_g)} + \frac{\rho_c u_c}{\rho_g u_g} = \frac{d\Delta}{dx} + \Delta \left[(1 - M_g^2) \frac{1}{u_g} \frac{du_g}{dx} + \frac{1}{(H_{w,o} - H_g)} \frac{d}{dx} (H_{w,o} - H_g) \right] \quad (11-21)$$

Note that if we make restrictive assumptions of constant properties, zero pressure gradient, low-speed flow (incompressible), no mass flux at the wall, and constant temperature difference ($T_{w,o} - T'_g$) with x , then equation (11-21) reduces to its simplest form,

$$\frac{q}{K \rho u_g c_p (T_{w,o} - T'_g)} = \frac{d\Delta}{dx} \quad (11-22)$$

If a local heat-transfer coefficient $h_{g,x}$ is defined as

$$h_{g,x} = \frac{q}{(T_{w,o} - T'_g)} \quad (11-23)$$

then,

$$\frac{h_{g,x}}{K \rho u_g c_p} = \frac{d\Delta}{dx} = St_x \quad (11-24)$$

The group of variables on the left side is dimensionless and is called the local Stanton number St_x , which is also equal to

$$St_x = \frac{Nu_x}{Re_x Pr} \quad (11-25)$$

Notice from equations (6-72) and (6-75) that with similar assumptions, the integral momentum equation resulted in

$$\frac{C_{f,x}}{2} = \frac{d\theta}{dx} \quad (11-26)$$

For compressible flow, there is dissipation of kinetic energy into thermal energy by viscous shear within the boundary layer. This is characterized by an increase in the static temperature near the wall as shown in figure 11-5. The effective gas temperature $T_{g,e}$, or adiabatic wall temperature $T_{w,a}$, is the temperature the wall would reach if it were uncooled and is, therefore, a measure of the viscous heating in the boundary layer. This dissipation of kinetic energy is related to the recovery factor r defined by the following equation:

$$T_{g,e} = T_{w,a} = t_g + r \frac{u_g^2}{2gJc_p} \quad (11-27)$$

where t_g is the hot-gas static temperature, in K or °R. For laminar flow, the recovery factor can be approximated by $Pr^{1/2}$, while for a turbulent boundary layer, r is assumed to equal $Pr^{1/3}$. It is not surprising that the Prandtl number has an effect on the adiabatic wall temperature. The Prandtl number is the ratio of the viscosity (responsible for energy dissipation) to the thermal diffusivity (mechanism allowing heat to escape from the boundary layer). This would suggest that for a given free-stream kinetic energy, a high Prandtl number should lead to a high adiabatic wall temperature, and vice versa.

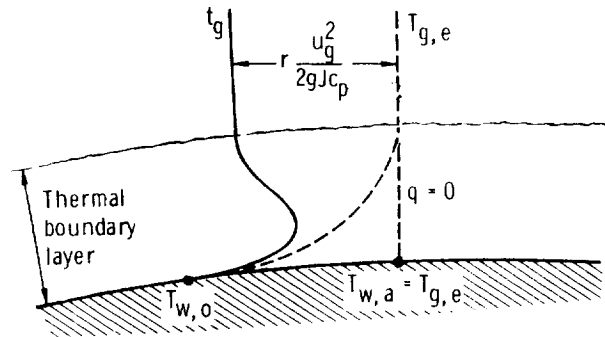


FIGURE 11-5.—Temperature distribution in a high-velocity boundary layer.

The heat flux to the blade is proportional to the temperature gradient (either effective or static gas temperature) at the wall:

$$q = -k_g \left. \frac{\partial t}{\partial y} \right|_{y=0} = -k_g \left. \frac{\partial T_{g,e}}{\partial y} \right|_{y=0} = h_{g,x} (T_{g,e} - T_{w,o}) \quad (11-28)$$

As we have already seen, it is convenient to express the heat flux in terms of the heat-transfer coefficient $h_{g,x}$ and the gas-to-wall temperature difference. The gas temperature in this case must always be the effective gas temperature, or the adiabatic wall temperature.

The problem in determining the heat flux to the blade is to find a suitable expression for the heat-transfer coefficient $h_{g,x}$. The objective is to design a cooling configuration which will yield a constant outer-wall temperature. In reality, however, the surface temperature is never constant. The effect that the actual varying surface temperature has on the thermal boundary layer can be accounted for in more refined design stages.

Solutions to Boundary-Layer Equations

First-order approximation.—The simplest approach to the solution is to assume that the heat-transfer coefficient on the suction or pressure side of the blade is approximated by a flat-plate correlation faired into a heat-transfer coefficient distribution around a cylinder in a crossflow for the blade leading-edge region. Though the flat-plate expression pertains, in a strict sense, only to zero-pressure-gradient flow, the results are accurate enough for a first-order approximation. In fact, often the flat-plate correlation yields results surprisingly close to those of more sophisticated analyses, primarily because the Stanton number St is relatively insensitive to pressure gradient.

For laminar flow over a flat plate with the thermal and the hydrodynamic boundary layers both beginning at the leading edge, the energy equation can be solved directly by means of the Blasius similarity solution discussed in chapter 6 for the velocity profile. With the wall temperature assumed to be constant, the result is

$$h_{g,x} = 0.332 \frac{k_g}{x} Re_x^{1/2} Pr^{1/3} \quad (11-29)$$

The turbulent counterpart is given by

$$h_{g,x} = 0.0296 \frac{k_g}{x} Re_x^{0.8} Pr^{1/3} \quad (11-30)$$

The local velocity $u_{g,x}$ is used in the Reynolds number.

For the heat-transfer coefficient $h_{g,le}$ in the leading-edge region, the following correlation is frequently assumed:

$$h_{g,lc} = a \left[1.14 \frac{k_g}{D} \left(\frac{\rho_g u_{g,\infty} D}{\mu} \right)^{1/2} Pr^{0.4} \left(1 - \left| \frac{\Phi}{90} \right|^3 \right) \right] \quad -80^\circ < \Phi < 80^\circ \quad (11-31)$$

where

- a augmentation factor
 D diameter of leading-edge circle, m; ft
 $u_{g,\infty}$ velocity of gas approaching leading edge, m/sec; ft/sec
 Φ angular distance from leading-edge stagnation point, deg

The bracketed term is the heat-transfer coefficient for a cylinder of diameter D (see fig. 11-6) in a cross-flowing, laminar free stream.

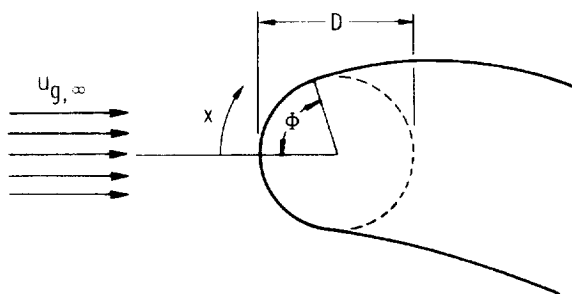


FIGURE 11-6.—Blade leading-edge geometry.

The term a is an augmentation factor used to adjust the coefficient to account for the highly turbulent mainstream flow approaching a vane or blade leading edge. Various magnitudes of the factor a , from 1.2 to 1.8, have been used. This amplification of heat flux is uniquely associated with large, favorable-pressure-gradient flows. The highly accelerated flow at the stagnation region stretches vortex filaments oriented with their axes in the direction of flow, thereby increasing the turbulent fluctuating velocities within the boundary layer. Kestin (ref. 3) has studied this phenomenon in detail, but as yet, no general correlation of stagnation heat transfer with turbulence scale and intensity is available.

Transition from laminar to turbulent flow will occur when the Reynolds number becomes sufficiently high to allow instabilities in the boundary layer to grow. For a flat plate with zero pressure gradient, it can generally be assumed that transition will take place in the Reynolds number range of 200 000 to 500 000, depending on free-stream turbulence and surface roughness. However, a Reynolds num-

ber based on the distance, x , from the leading edge (boundary-layer origin) is not a practical transition criterion, because it is not a local parameter. It is more convenient to use the momentum thickness, θ , as the characteristic length in the Reynolds number for determining transition, because the critical Reynolds number at a given point is then independent of the history of the boundary layer; that is, it is immaterial how the boundary layer developed in getting to the given state. For a strongly accelerated flow, the boundary layer never becomes turbulent. This fact is consistent with the use of θ but not with the use of x . A value of $Re_{\theta, crit} = 360$ is a "universal" critical Reynolds number corresponding to $Re_x = 300\ 000$ for a flat plate and $Re_D = 2000$ for pipe flow. For flow over a turbine blade with very high free-stream turbulence, a conservative value of $Re_{\theta, crit} = 200$ can be assumed.

An approximate expression for the momentum thickness variation on a turbine blade can be derived from the integral momentum equation from chapter 6 (eq. (6-76)) by making suitable assumptions as to the functional form of the local velocity profile through the boundary layer (see ref. 2). Upon integrating equation (6-76), the laminar momentum thickness as a function of a variable free-stream velocity is given by

$$\theta_L = \frac{0.67\nu^{0.5}}{u_g^3} \left(\int_0^x u_g^5 dx \right)^{0.5} + \theta_{stag} \quad (11-32)$$

where x is the surface distance measured from the stagnation point, in meters or feet. The momentum thickness θ_{stag} at the stagnation point of a cylinder of diameter D in a crossflow with an approach velocity $u_{g, \infty}$ is

$$\theta_{stag} = \frac{0.1D}{\sqrt{\frac{u_{g, \infty} D}{2\nu}}} \quad (11-33)$$

Turbulent or transitional flow, then, exists when the value of θ is such that $(\rho u_g \theta / \mu) > 200$. The value of x where this occurs is denoted as x_{crit} .

The turbulent momentum thickness is obtained in a similar manner by the equation

$$\theta_T = \left[\frac{0.016\nu^{0.25}}{u_g^{4.11}} \int_{x_{crit}}^x u_g^{3.86} dx + \theta_{L, crit}^{1.25} \left(\frac{u_{g, crit}}{u_g} \right)^{4.11} \right]^{0.8} \quad (11-34)$$

This assumes an abrupt transition from laminar to turbulent flow.

Integral method.—The solution of the integral equations of momentum and energy to obtain the heat flux to a blade is a more refined and accurate approach than the "flat-plate approximation" previously discussed. The penalty for more accuracy is, of course, the increased complexity of the computation. In many cases, the more sophisticated

methods are not warranted in the early stages of design. The integral method accounts for free-stream velocity variation more realistically, and the effect of a nonconstant surface temperature on $h_{g,x}$ can also be included. However, some assumptions must still be made in order to solve the integral equations.

Consider the integral energy equation (eq. (11-21)) with constant specific heat and no mass transfer across the wall boundary.

$$St_x = \frac{h_{g,x}}{K\rho_g u_g c_p} = \frac{d\Delta}{dx} + \Delta \left[\frac{1}{\rho_g} \frac{d\rho_g}{dx} + \frac{1}{u_g} \frac{du_g}{dx} + \frac{1}{(T_{w,o} - T_g')} \frac{d}{dx} (T_{w,o} - T_g') \right] \quad (11-35)$$

Ordinarily, the integral momentum equation would first have to be solved in order to evaluate the enthalpy thickness Δ in equation (11-20). Ambrok (ref. 4), however, proposed an approach whereby equation (11-35) could be solved independently of the momentum equation by making use of the fact that experimental data show the Stanton number to be a very weak function of pressure gradient. He proposed that the Stanton number can be written as a function of a local Reynolds number based on enthalpy thickness as the characteristic length, and that this function is independent of pressure gradient.

$$St_x = f(Re_\Delta) \quad (11-36)$$

If f is independent of pressure gradient, then the flat-plate solution should give us the functional form.

For turbulent flow over a flat plate, combining equations (11-4) and (11-25) yields

$$St_x = 0.0296 Re_x^{-0.2} Pr^{-2/3} \quad (11-37)$$

Recalling from equation (11-24) that for a flat plate

$$St_x = \frac{d\Delta}{dx} \quad (11-38)$$

the local Stanton number can be expressed in terms of the enthalpy thickness by combining equations (11-37) and (11-38) so as to obtain

$$St_x = (0.0296 Pr^{-2/3})^{1.25} (0.8 Re_\Delta)^{-0.25} \quad (11-39)$$

Hence, the function f from equation (11-36) is given by equation (11-39) for turbulent flow and; by assumption, for any arbitrary free-stream velocity variation. (The same argument holds for laminar flows.) Substituting equation (11-39) into equation (11-35) and integrating yields

$$St_x = \frac{h_{g,x}}{K\rho_g u_g c_p} = 0.0296 Pr^{-2/3} (T_g' - T_{w,o})^{0.25} I^{-0.2} \quad (11-40)$$

where

$$I = \int_{x_{crit}}^x \frac{\rho_g u_k (T_k' - T_{w,o})^{1.25}}{\mu} dx + \left[\frac{0.8 Re_\Delta (T_k' - T_{w,o})}{0.0296 Pr^{-2/3}} \right]_{x=x_{crit}}^{1.25} \quad (11-41)$$

The integration is performed numerically for $h_{g,x}$, with the critical enthalpy-thickness Reynolds number being evaluated from the laminar-boundary-layer equation. For further details, see reference 2.

Finite-difference solution.—The most accurate method of calculating the heat flux to a turbine blade is to solve all the boundary-layer equations simultaneously by a finite-difference approach. There are several good numerical programs available to do this. One of these was developed by W. M. Kays and uses the numerical procedure of Spalding and Patankar (ref. 5). In addition to the equations for the conservation of mass (eq. (11-10)), momentum (eq. (11-11)), and energy (eq. (11-12)), a fourth conservation equation, that of turbulent kinetic energy \mathcal{K} is also solved simultaneously with the others. Conservation of turbulent kinetic energy is given by

$$\rho u \frac{\partial \mathcal{K}}{\partial x} + (\rho v + \overline{\rho'v'}) \frac{\partial \mathcal{K}}{\partial y} = \rho \nu_T \left(\frac{\partial u}{\partial y} \right)^2 + \frac{\partial}{\partial y} \left[\rho (\nu_L + \nu_T) \frac{\partial \mathcal{K}}{\partial y} \right] - \mathcal{J}_T \quad (11-42)$$

where \mathcal{J}_T is a turbulent dissipation term, in W/m^3 or $Btu/(ft^3)(sec)$. The turbulent kinetic energy is defined as

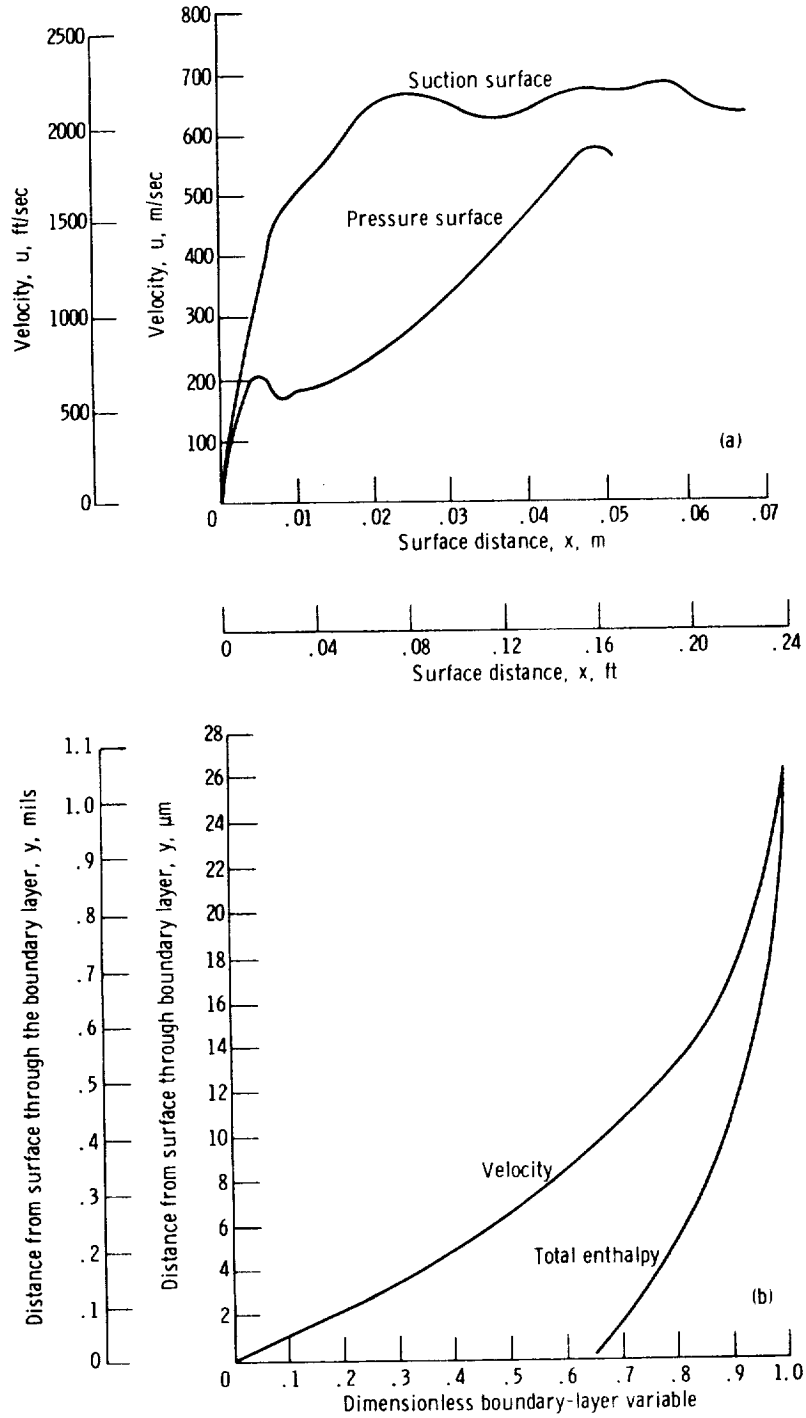
$$\mathcal{K} = \frac{1}{2gJ} (\overline{u'^2} + \overline{v'^2} + \overline{w'^2}) \quad (11-43)$$

where w' is the fluctuating component of velocity, in m/sec or ft/sec , in the direction perpendicular to the x - y plane. By including the turbulent-kinetic-energy equation, the mixing length is calculated locally in the boundary layer. Also, the effects of free-stream turbulence can be accounted for.

All properties are evaluated locally through the boundary layer with no restrictive or approximating assumptions made on the variation of surface temperature or velocity profile. Mass transfer at the wall (transpiration cooling) and local film cooling are also handled in a straightforward manner.

Figure 11-7 presents example results from computer plots showing the flexibility of the numerical approach for the case of a high-temperature, high-pressure turbine vane. The free-stream velocity profile is given in figure 11-7(a). The initial profiles through the boundary layer must be supplied as a boundary condition to get the integration started (fig. 11-7(b)), but from then on, profiles can be

TURBINE DESIGN AND APPLICATION

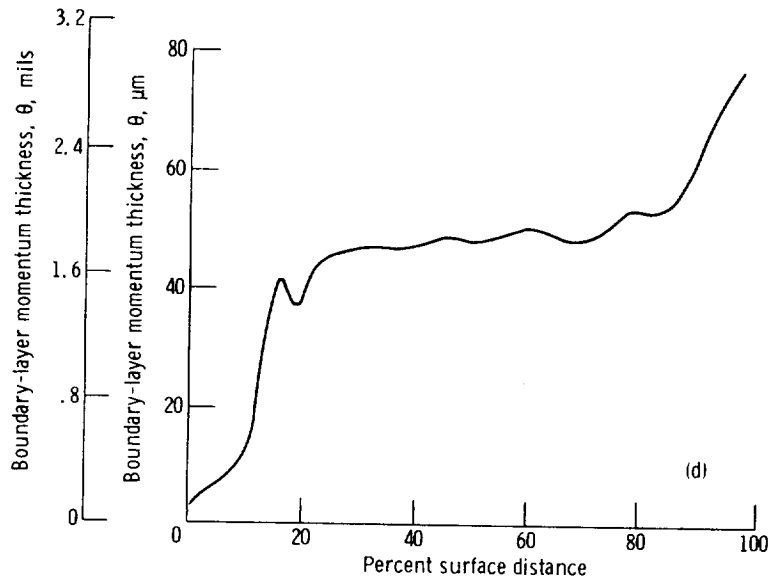
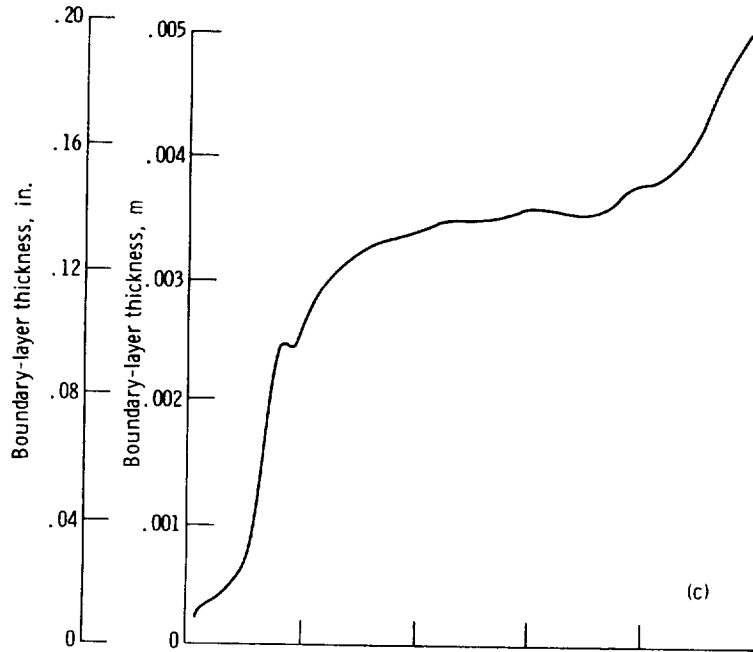


(a) Surface velocity profile.

(b) Initial profiles for finite-difference numerical boundary-layer program. Free-stream reference velocity, 30.87 m/sec or 101.28 ft/sec; free-stream reference enthalpy, 1.0447×10^6 J/(kg)(K) or 249.7 Btu/(lb)(°R).

FIGURE 11-7.—Boundary-layer development over a high-temperature, high-pressure turbine vane.

calculated through the boundary layer at discrete x locations. The boundary-layer thickness, momentum thickness, momentum-thickness Reynolds number, and heat-transfer coefficient are shown in figures 11-7(c) to 11-7(f), respectively. Notice that just upstream of the

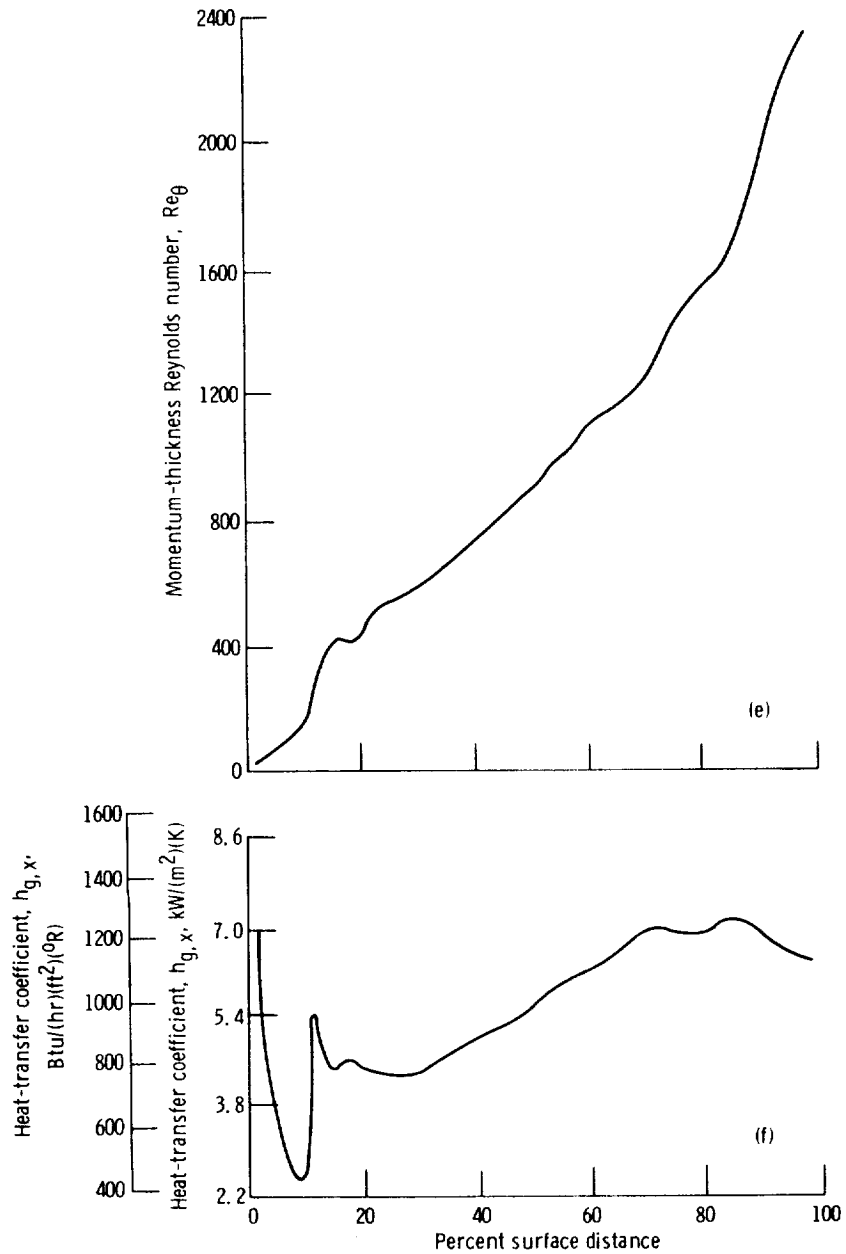


(c) Pressure-side boundary-layer thickness.
 (d) Pressure-side boundary-layer momentum thickness.

FIGURE 11-7.—Continued.

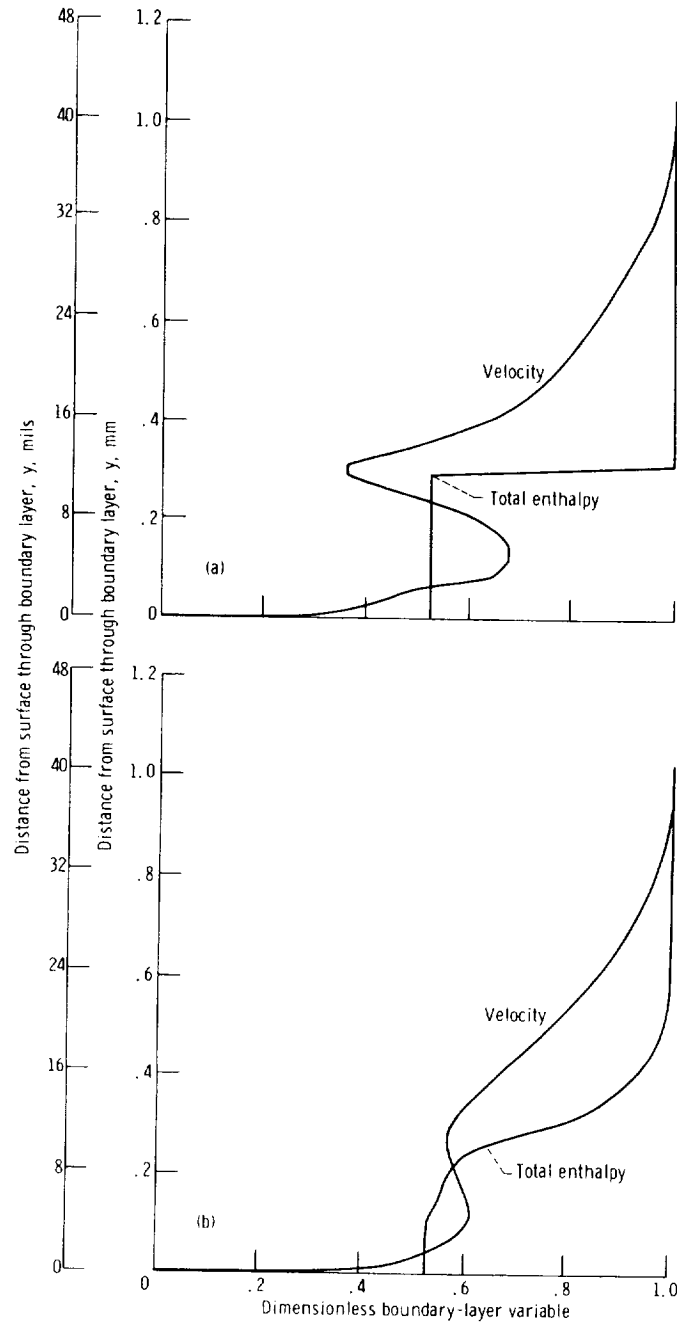
TURBINE DESIGN AND APPLICATION

20-percent surface distance location on the vane, the boundary-layer thickness (fig. 11-7(c)) and the momentum thickness (fig. 11-7(d)) increase rapidly and then decrease slightly over a short distance before continuing to increase. This "blip" is caused by the rapid



(e) Pressure-side momentum-thickness Reynolds number.
 (f) Pressure-side heat-transfer coefficient.

FIGURE 11-7.—Concluded.



(a) Initial profiles at slot. Free-stream reference velocity, 609.6 m/sec or 2000 ft/sec; free-stream reference enthalpy, 4.8189×10^6 J/(kg)(K) or 1151.75 Btu/(lb)(°R).
 (b) Three slot-widths downstream of slot. Free-stream reference velocity, 610.8 m/sec or 2004 ft/sec; free-stream reference enthalpy, 4.8189×10^6 J/(kg)(K) or 1151.75 Btu/(lb)(°R).

FIGURE 11-8.—Boundary-layer profiles along adiabatic wall with film cooling.

deceleration and acceleration of the mainstream flow resulting from the adverse-pressure-gradient region aft of the leading edge on the pressure side. Transition from a laminar boundary layer occurs at about the 10-percent location. Very little of the boundary layer is in a transitional state, as can be seen from figure 11-7(f).

Initial velocity and enthalpy profiles illustrating an example of film cooling are given in figure 11-8(a). About 3 slot widths downstream, the profiles have changed to the shapes shown in figure 11-8(b).

Temperature-Dependent Fluid Properties

The relations involving the dimensionless parameters Re , Pr , Nu , and St , discussed in earlier sections, contain gas properties ρ , k , μ , and c_p , which all vary with temperature. The temperature dependence of these transport properties causes a change in the velocity and temperature profiles (and, therefore, in the heat-transfer coefficient) compared to results obtained if properties were constant. Since large temperature variations occur across the boundary layer, at what temperature are the properties to be evaluated? Usually, constant-property analytical solutions (except in the finite-difference method) or the experimental data obtained with small temperature differences are corrected to account for property variation. Two schemes are in common use for the correction of constant property results; namely, the temperature-ratio method (for gases) and the reference-temperature method.

In the latter method, all transport properties are evaluated at the reference temperature:

$$T_{ref} = 0.5 T_{w,o} + 0.28 t_g + 0.22 T_{g,e} \quad (11-44)$$

The temperature-ratio method assumes

$$\frac{Nu}{Nu_{CP}} = \frac{St}{St_{CP}} = \left(\frac{T_{g,e}}{T_{w,o}} \right)^n \left(\frac{t_g}{T_{g,e}} \right)^m \quad (11-45)$$

The subscript CP refers to constant properties evaluated at the free-stream static temperature. For laminar flow, $n=0.08$ and $m=0.12$. For turbulent flow, $n=0.4$ and $m=0.6$, a much greater influence than in laminar flow.

CONDUCTION WITHIN THE BLADE WALL

Once the local heat-transfer coefficients on the hot-gas side and coolant side are known, the heat-flux boundary conditions for the heat-conduction problem are available. The blade or vane is broken up into a number of finite elements, as shown, for example, in figure

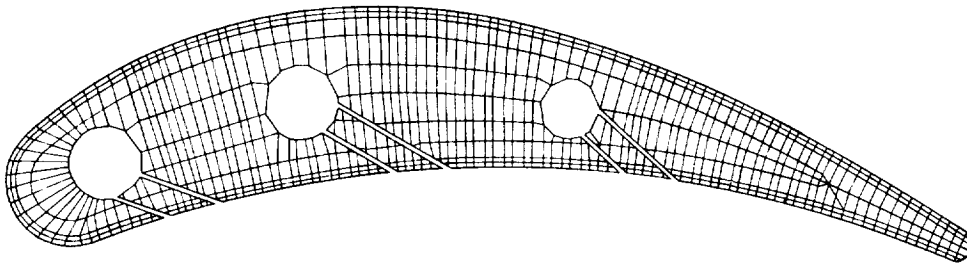


FIGURE 11-9.—Typical node breakdown for a turbine-blade conduction analysis.

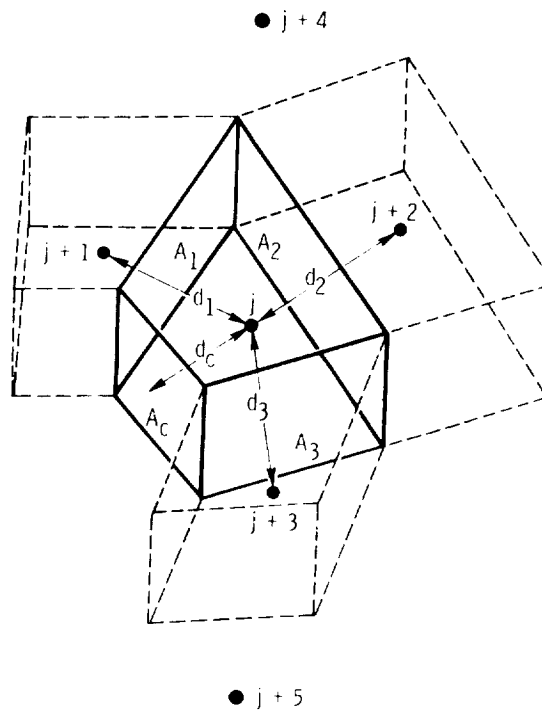


FIGURE 11-10.—Typical boundary element for heat-conduction analysis.

11-9, and an energy balance is written for each element. The result is a system of algebraic finite-difference equations, with the number of equations equal to the total number of elements. All equations must then be solved simultaneously by means of a high-speed, digital computer. Once such a conduction analysis is completed, a detailed temperature distribution throughout the blade is available for use in thermal-stress calculations.

Consider a typical boundary element from figure 11-10. Accounting

for all the energy transfer between the given element (the j^{th} element) and those adjacent to it (elements $j+1$ to $j+5$), including the fluid boundary, leads to the following algebraic equation (see fig. 11-10).

$$\frac{A_c}{\frac{d_c}{k_w} + \frac{1}{h_c}} (T_j - T_c')^m + \frac{k_w A_1}{d_1} (T_j - T_{j+1})^m + \frac{k_w A_2}{d_2} (T_j - T_{j+2})^m + \dots + \frac{k_w A_5}{d_5} (T_j - T_{j+5})^m = \frac{\rho c_p V_j}{\Delta(\text{time})} (T_j^{n+1} - T_j^n) \quad (11-46)$$

where

- A_i surface area between j^{th} element and element or boundary denoted by subscript i , m^2 ; ft^2
- d_i distance between j^{th} element and element or boundary denoted by subscript i , m ; ft
- V_j volume of j^{th} element, m^3 ; ft^3

The superscript m denotes time step n or $n+1$, depending on whether an explicit or implicit transient scheme is used.

A similar equation for every volume element must be written. The calculation may be either transient or steady-state, depending on how the equations are structured. If the element is allowed to reduce to an infinitesimal size, the energy balance at a point yields the familiar heat-conduction equation

$$\rho c_p \frac{\partial T}{\partial(\text{time})} = \frac{\partial}{\partial x} \left(k_w \frac{\partial T}{\partial x} \right) + \frac{\partial}{\partial y} \left(k_w \frac{\partial T}{\partial y} \right) + \frac{\partial}{\partial z} \left(k_w \frac{\partial T}{\partial z} \right) \quad (11-47)$$

where x , y , and z are the coordinate directions.

COOLANT-SIDE CONVECTION

There can be many internal flow geometries used to promote heat transfer by convection to the coolant, and for that reason, it would be impossible to discuss each convection-cooling scheme. Essentially, the problem is to determine the heat-transfer coefficient, h_c , and the local coolant temperature, T_c' , in the previously shown equation

$$q = h_c (T_{w,i} - T_c') \quad (11-2)$$

This is not, however, as simple as it sounds. The coolant flow path can be very complex, and the internal flow and pressure distribution must be known before the heat-transfer coefficient can be determined. An internal flow network is established, and conservation of momentum equations that describe the internal pressure distribution are solved

to determine the flow split between various parts of the blade. Since there is interaction between each of the three heat-transfer steps discussed (convection from hot gas to surface, conduction through the surface, and convection from surface to coolant), an iterative cycle between the three calculations must be made. After the percentage of air available for cooling a given region of the blade has been determined, empirical correlations for the particular convection scheme considered must be used to determine h_c .

Various methods are used to enhance coolant-side convection heat transfer. Fins can be added to the cooling passages to act as "turbulators" to keep the flow highly mixed and the boundary layers thin. They also help by increasing the convection surface area. One of the most effective convection methods is impingement cooling (fig. 11-4(b)), where small jets of cooling air are directed toward the inside wall of the blade, as seen in figures 11-4(b) and (g). One representative correlation from reference 6 for impingement cooling gives

$$Nu_{D, imp} = \varphi_1 \varphi_2 Re_D^m Pr^{1/3} \left(\frac{z_n}{D} \right)^{0.091} \quad (11-48)$$

where

$Nu_{D, imp}$	impingement-cooling Nusselt number based on hole diameter as characteristic dimension
z_n	distance between hole and wall, m; ft
D	hole diameter, m; ft

The power m on the Reynolds number and the coefficient φ_1 are both functions of the impingement-hole array geometry and the Reynolds number. A least-squares-curve fit of the data in reference 6 gives

$$m = a_1 \left(\frac{x_n}{D} \right)^2 + b_1 \left(\frac{x_n}{D} \right) + c_1 \quad (11-49)$$

and

$$\varphi_1 = \exp \left[a_2 \left(\frac{x_n}{D} \right)^2 + b_2 \left(\frac{x_n}{D} \right) + c_2 \right] \quad (11-50)$$

where x_n is the center-to-center distance, in meters or feet, between holes in the direction of flow, and the coefficients a , b , and c are given in table 11-I as functions of Re_D . The coefficient φ_2 is an attenuation factor to account for crossflow caused by the accumulation of fluid from multiple rows of impingement jets. It can be expressed as

$$\varphi_2 = \frac{1}{1 + a_3 \psi^{b_3}} \quad (11-51)$$

where a_3 and b_3 are given in table 11-I, and ψ for the i^{th} row of

TURBINE DESIGN AND APPLICATION

TABLE 11-I.—IMPINGEMENT-COOLING CORRELATION COEFFICIENTS

Coefficient	Reynolds number range, 300 to 3 000	Reynolds number range, 3 000 to 30 000
a_1	-0.0015	-0.0025
b_1	.0428	.0685
c_1	.5165	.5070
a_2	0.0126	0.0260
b_2	-.5106	-.8259
c_2	-.2057	.3985
a_3	0.4215	0.4696
b_3	.580	.965

impingement holes is defined as

$$\psi = \left(\frac{G_{cf}}{G_h} \right) \left(\frac{z_n}{D} \right) \tag{11-52}$$

where

- G_{cf} crossflow mass flux, kg/(sec)(m²); lb/(hr)(ft²)
- G_h impingement-hole mass flux, kg/(sec)(m²); lb/(hr)(ft²)

FILM AND TRANSPIRATION COOLING

As turbine-inlet temperature and pressure increase, it becomes apparent that convection cooling must be augmented by film cooling to reduce blade metal temperatures and conserve cooling air (as shown in fig. 11-3). The importance of combining both film and convection cooling in a given design is shown in figure 11-11. Here, blade surface temperatures are given for convection cooling only, film cooling only, and combined film and convection cooling, all for the same hot-gas and cooling-air conditions and the same percent coolant flow rate. Except in the immediate region of the film injection hole, the combined cooling yields a significantly lower wall temperature than does either film or convection cooling alone. Notice also that the average wall temperature for film cooling only is about the same as for convection cooling, but the wall temperature gradients are much higher because of the rapid decay of the protective film.

First, localized film cooling from rows of holes or slots will be discussed, then transpiration cooling and full-coverage discrete-hole film

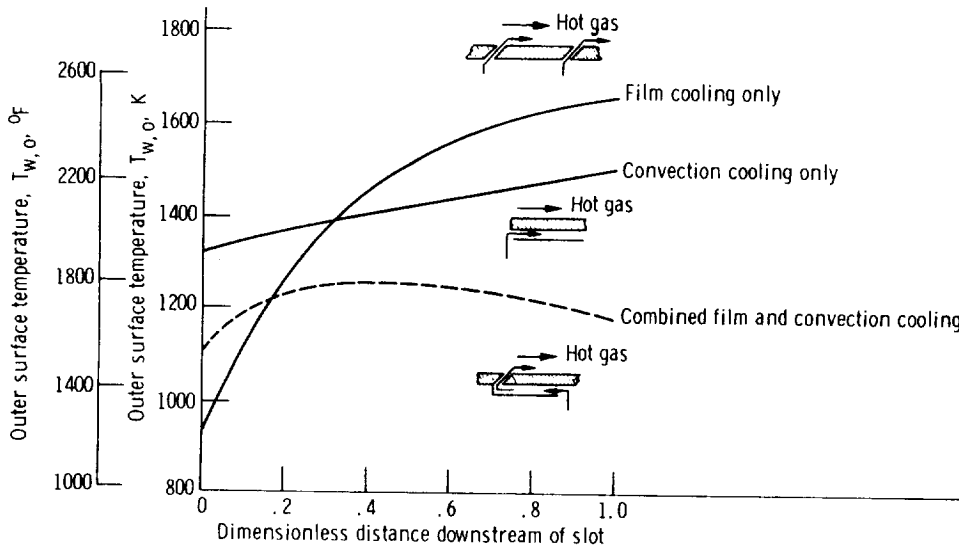


FIGURE 11-11.—Effect of combining film and convection cooling. Constant coolant flow rate.

cooling. To successfully analyze and model film cooling, the “non-film-cooled” heat-transfer coefficient must be known. Hence, the film-cooling analysis builds on the preceding discussion. In the following expression for the heat flux to the surface, the effective gas temperature becomes the film temperature T'_{film} :

$$q = \epsilon h_{g,x} (T'_{film} - T_{w,o}) \quad (11-53)$$

where $h_{g,x}$ is the heat-transfer coefficient without film cooling, and

$$\epsilon = \frac{(h_{g,x})_{film}}{h_{g,x}} \quad (11-54)$$

Very near the point of injection, the heat-transfer coefficient is altered somewhat by the injection itself, and ϵ is included to account for this. However, the effect is usually damped out rapidly, so ϵ is frequently assumed to be unity. The film temperature is sometimes called the adiabatic wall temperature with film cooling, because it is obtained from experimental data under adiabatic wall conditions (i.e., it is the temperature of an uncooled wall having a buffer film layer of cool air between it and the hot gas (see fig. 11-12)). The film temperature is correlated in dimensionless form by the film effectiveness η_{film} :

$$\eta_{film} = \frac{T_{g,e} - T'_{film}}{T_{g,e} - T'_{c,o}} \quad (11-55)$$

where $T'_{c,o}$ is the injected film temperature (coolant temperature at outer wall). The film effectiveness decays from a value of 1, at the

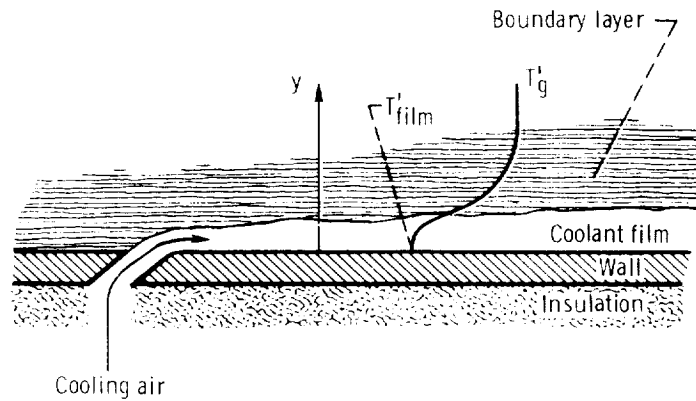


FIGURE 11-12.—Experimental determination of film temperature.

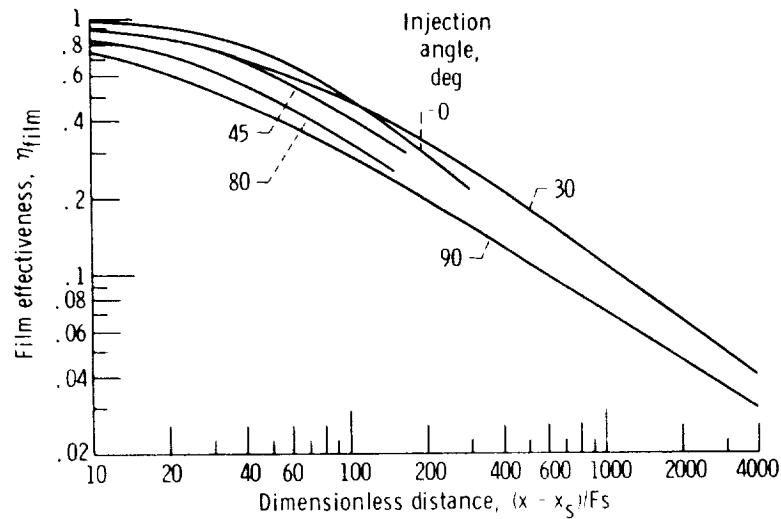


FIGURE 11-13.—Film-cooling effectiveness for slots.

slot, to zero, far downstream. Figure 11-13 gives experimental values of film effectiveness for film injection from slots as determined by a number of investigators. The distance downstream from the slot ($x - x_s$) is normalized by the slot width s and the mass-flux ratio F between the film air and the hot-gas stream. The indicated injection angle is with respect to the surface (0° is parallel to the surface, and 90° is perpendicular). As seen, the film effectiveness decreases with increasing injection angle.

The following expressions (from ref. 7) correlate turbine-blade slot film cooling reasonably well:

$$\eta_{film} = \exp \left\{ -2.9 \left(\frac{\rho_c u_c^2}{\rho_g u_g^2} \right)^{-n} \left(\frac{\rho_g u_g x}{\rho_c u_c s} \right) (Re_x)^{-0.2} \left[1 - \left(\frac{x_s}{x} \right)^{0.8} \right] \right\} \tag{11-56}$$

for small values of $(x - x_s)$, and

$$\eta_{film} = \frac{C \left(\frac{\rho_c u_c^2}{\rho_g u_g^2} \right)^n \left(\frac{\rho_c u_c s}{\rho_g u_g x} \right) (Re_x)^{0.2}}{1 - \frac{x_s}{x}} \tag{11-57}$$

for large values of $(x - x_s)$, where x_s is the location of the downstream edge of the slot, in meters or feet, measured from the stagnation point. Values for the coefficient C and the exponent n are $C=2.7$ and $n=0.21$ for a 30° injection angle, and $C=1.95$ and $n=0.155$ for a 15° injection angle.

Film effectiveness as a function of the downstream and lateral distances from the injection hole is presented in figure 11-14 (from ref. 8) for film cooling from a single hole and from a row of holes. For small lateral distances, up to about 1 hole diameter in this case, film effectiveness decreases with downstream distance, as previously shown

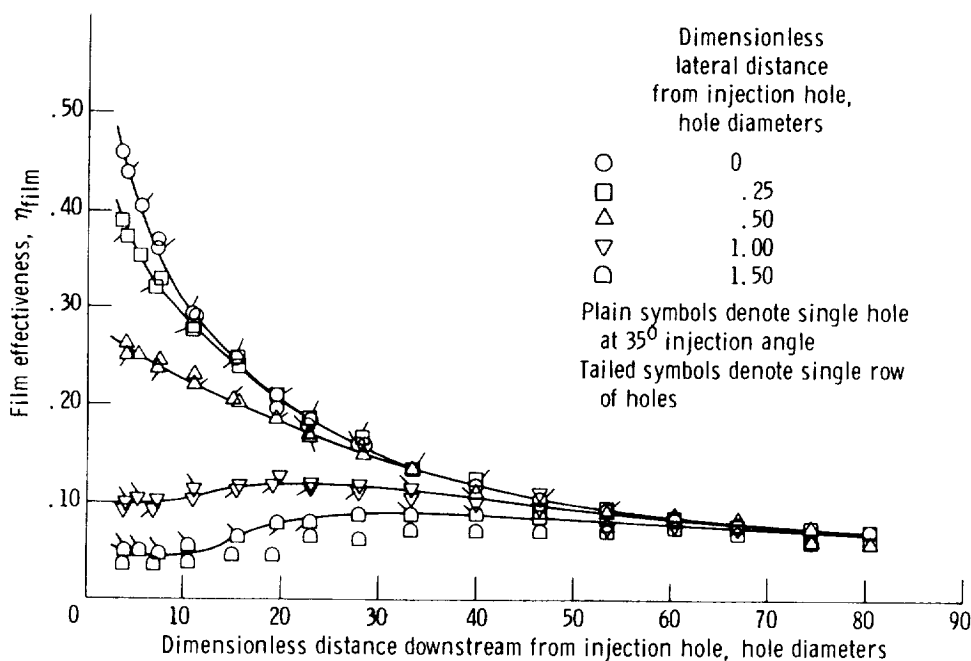


FIGURE 11-14.—Film-cooling effectiveness as function of dimensionless downstream and lateral distances from injection holes. Mass-flux ratio, 0.5; injection-hole diameter, 1.18 cm or 0.464 in.; gas velocity, 30.5 m/sec or 100 ft/sec; Reynolds number, 0.22×10^5 .

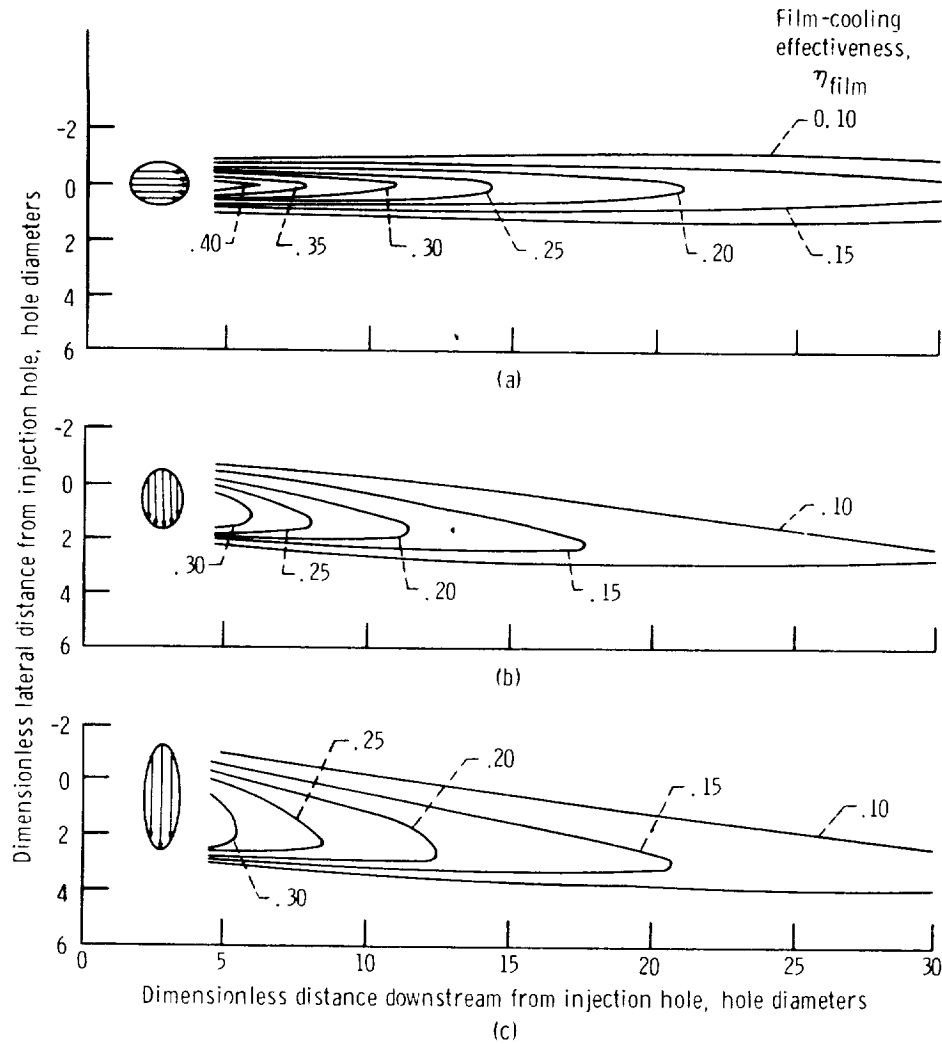
for slots, and the same values are obtained for single holes as for a row of holes. For larger lateral distances, effectiveness initially increases with downstream distance as a result of the spreading of the injected flow, and the values for the row of holes are larger than for the single hole because of the interaction of flows from adjacent holes. Notice also that η_{film} is not unity at the injection hole. This is due to entrainment of hot gases underneath the film jet as the jet separates from the surface. Very limited data are available for a staggered row of film-cooling holes. Frequently, the slot data are used for this case, with an effective slot width s defined such that the total area of the holes equals the area of the slot.

Figure 11–15 (from ref. 8) shows the spreading of a film layer from a single hole at various angles of injection. For a 35° injection angle in the direction of the main gas stream, the film spreads less than 2 hole diameters, giving very local film coverage. A compound angle of injection gives more lateral coverage, but the film does not persist as far downstream.

Transpiration cooling of a porous wall is one of the most effective methods of cooling available. With mass transfer from the wall into the boundary layer, it combines film cooling with efficient convection cooling. The porous wall serves as a very effective heat exchanger, where the heat conducted into the wall from the hot gas stream is continuously transferred to the coolant in counter flow as it passes through the small pores. However, there are problems in applying this method of cooling to turbine blades. The pores tend to be extremely small and, therefore, are subject to blockage due to oxidation or contaminants in the air. Also, from an aerodynamic-loss standpoint, a penalty is paid, since the film air is injected into the gas stream essentially normal to the boundary.

In order to alleviate these problems yet still obtain some of the characteristic advantages of transpiration cooling, full-coverage film cooling is used. In full-coverage film cooling, the cooling air issues from a large number of small, closely-spaced, discrete holes in the surface. This type of cooling lies in the spectrum between pure transpiration cooling on the one end, with essentially a continuous mass flux over the surface, and localized film cooling on the other end. The amount of heat transferred by convection to the cooling air flowing through the wall depends on the tortuosity of the internal flow passages. The wall may be constructed of simple, straight-through holes, with a low resultant convection effectiveness, or it may consist of a maze of interconnected flow passages, with a relatively high convection effectiveness.

Convection effectiveness η_{conv} is a term borrowed from heat-exchanger theory and is a measure of the ability of the wall (or blade



- (a) Injection angle, 35°; lateral injection, 90°.
- (b) Injection angle, 90°; lateral injection, 35°.
- (c) Injection angle, 90°; lateral injection, 15°.

FIGURE 11-15.—Lines of constant film-cooling effectiveness for single-hole injection. Mass-flux ratio, 0.5.

acting as a heat exchanger) to transfer heat to the cooling air by convection.

$$\eta_{conv} = \frac{T'_{c,o} - T'_{c,in}}{T'_{w,o} - T'_{c,in}} \quad (11-58)$$

Since an optimum design utilizes as much of the heat sink available in the cooling air as possible for convection cooling, η_{conv} values approaching the limit of 1 are desirable. However, the convection

effectiveness is usually limited by the cooling-air supply pressure available. As η_{conv} increases, so does the pressure drop through the wall.

Consider a one-dimensional model of the porous or perforated turbine blade wall in figure 11-16. An energy balance can be written on the solid metal matrix and on the cooling-air flow through the wall (see ref. 9). The resulting differential equations for local metal temperature through the wall, T_w , and local coolant temperature in the wall, T'_c , are

$$\frac{d^3 T_w}{dy^3} + \frac{h_V}{G_c c_p} \frac{d^2 T_w}{dy^2} - \frac{h_V}{k_{w,e}} \frac{dT_w}{dy} = 0 \quad (11-59)$$

and

$$T'_c = T_w - \frac{k_{w,e}}{h_V} \frac{d^2 T_w}{dy^2} \quad (11-60)$$

where

$k_{w,e}$ effective thermal conductivity of the porous wall, W/(m)(K);
Btu/(hr)(ft)(°R)

h_V internal volumetric heat-transfer coefficient, W/(m³)(K); Btu/
(hr)(ft³)(°R)

The boundary conditions are

$$h_c(T_{w,i} - T'_{c,in}) = k_{w,e} \left. \frac{dT_w}{dy} \right|_{y=0} \quad (11-61)$$

and

$$G_c c_p (T'_{c,i} - T'_{c,in}) = k_{w,e} \left. \frac{dT_w}{dy} \right|_{y=0} \quad (11-62)$$

In this case, as seen from figure 11-16, G_c is the mass flux per unit of surface area.

An overall energy balance gives, as a third boundary condition for the heat flux to the wall,

$$q = G_c c_p (T'_{c,o} - T'_{c,in}) = G_c c_p \eta_{conv} (T_{w,o} - T'_{c,in}) \quad (11-63)$$

Typical wall and coolant temperature profiles are shown in figure 11-16. They are both nonlinear with opposite signs in the second derivative, which is a consequence of the interaction of the coolant and matrix heat transfer.

The heat flux to the wall can also be written in terms of a hot-gas-side heat-transfer coefficient:

$$q = h_{t,x} (T_{g,e} - T_{w,o}) \quad (11-64)$$

This is somewhat different from the heat flux expression with local

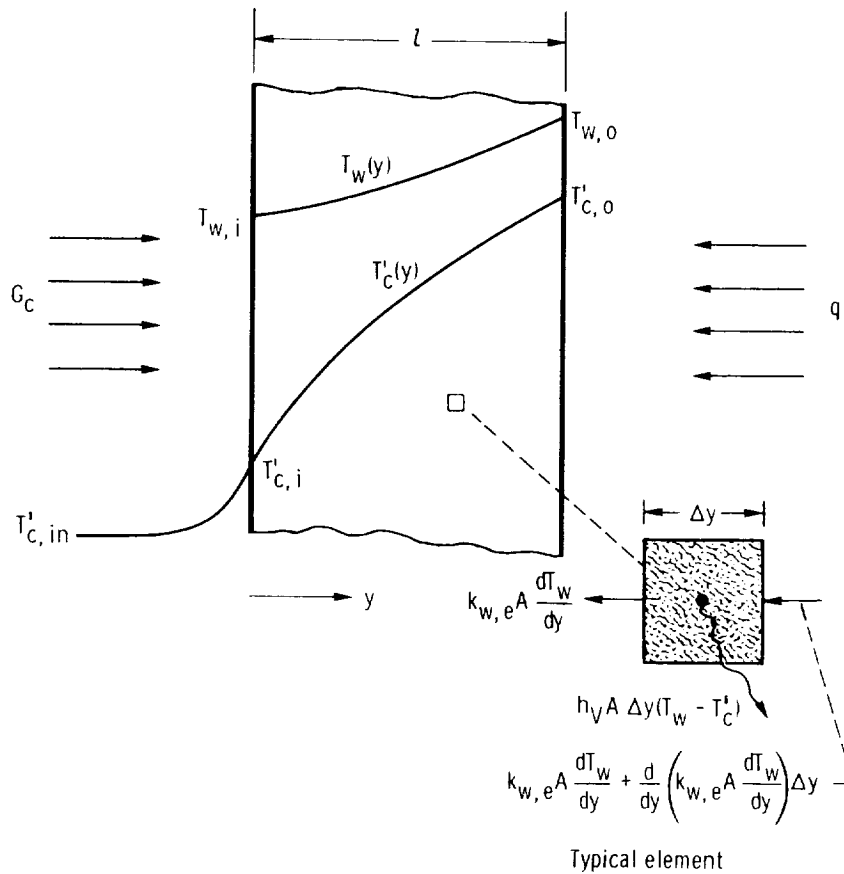


FIGURE 11-16.—Porous-wall temperature profile model.

film cooling in that the actual recovery gas temperature and a “reduced” heat-transfer coefficient $h_{t,x}$ due to blowing are used rather than the film temperature and the solid-blade heat-transfer coefficient $h_{g,x}$.

Consistent with the local one-dimensional model of the blade wall, which incidentally gives good results if the pressure gradient is not too large, we can write

$$\frac{h_{t,x}}{h_{g,x}} = \frac{St_{t,x}}{St_{g,x}} = \frac{F}{e^{F/St_{g,x}} - 1} f \quad (11-65)$$

where the correction factor f is a function of convection effectiveness as shown in figure 11-17 (from ref. 10), and F is the ratio of the coolant mass flux (surface averaged) to the hot-gas mass flux:

$$F = \frac{(\rho u)_c}{(\rho u)_g} \quad (11-66)$$

TURBINE DESIGN AND APPLICATION

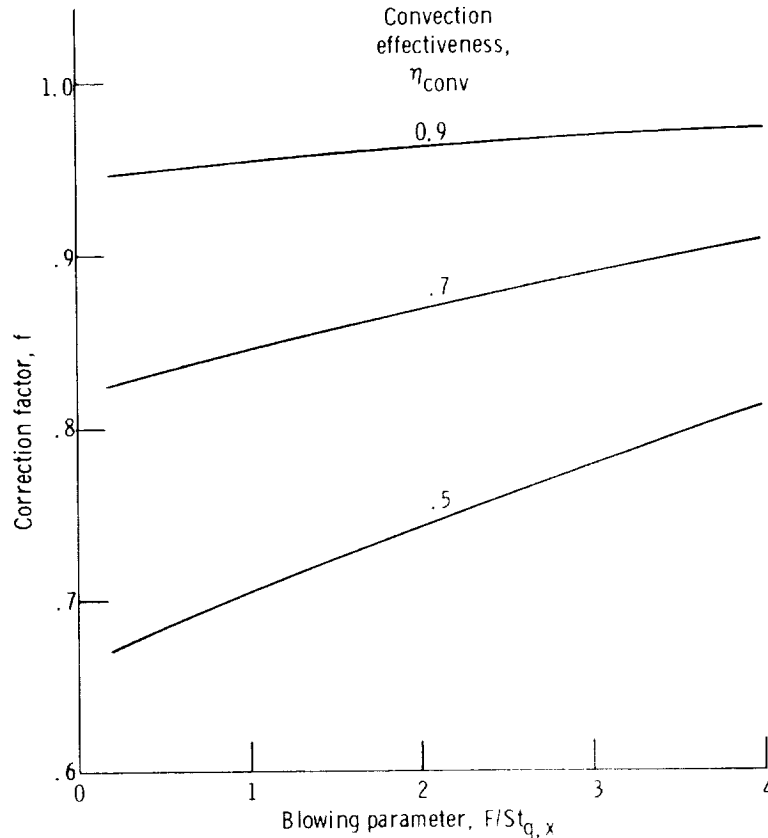


FIGURE 11-17.—Correction to equation (11-65) for wall convection effectiveness.

SIMILARITY

It is often of economic necessity to evaluate the heat-transfer performance of turbine components at conditions other than the actual engine environment. Generally, initial tests are conducted to evaluate heat-transfer and aerodynamic performance with actual-size prototype hardware at lower gas temperatures and pressures than the actual application. This practice raises a valid question as to whether a cooled blade configuration meeting design specifications at the test conditions will behave similarly under actual engine conditions. To answer this question, the various similarity parameters which are important in relating test performance to engine performance of an actual-size film-convection-cooled turbine blade are discussed.

The Mach number distribution and momentum-thickness Reynolds number distribution around the vane must be the same between engine and test conditions. Similarity in these two parameters is

essential to ensure the same relative distributions of heat-transfer coefficient and adiabatic wall temperature and the same point of transition from laminar to turbulent boundary layer.

Let superscript (t) refer to test conditions and superscript (e) refer to engine conditions. To ensure that the local Mach number distribution does not change between the two conditions, the equivalent mass flow must be the same in both cases. Therefore,

$$\frac{w_g^{(t)}}{w_g^{(e)}} = \frac{p_g'^{(t)}}{p_g'^{(e)}} \sqrt{\frac{(RT')_g^{(e)} \Gamma_g^{(t)}}{(RT')_g^{(t)} \Gamma_g^{(e)}}} \quad (11-67)$$

where Γ is an approximate correction (from eqs. (2-128) and (2-129)) for the variation of specific heat with temperature given by

$$\Gamma = \sqrt{\gamma} \left(\frac{2}{\gamma+1} \right)^{(\gamma+1)/2(\gamma-1)} \quad (11-68)$$

Since the local momentum-thickness Reynolds number must also remain unchanged between (t) and (e) conditions,

$$\frac{\left(\frac{\rho u \theta}{\mu} \right)_g^{(t)}}{\left(\frac{\rho u \theta}{\mu} \right)_g^{(e)}} = \frac{\theta_g^{(t)} \mu_g^{(e)} w_g^{(t)}}{\theta_g^{(e)} \mu_g^{(t)} w_g^{(e)}} = \frac{\theta_g^{(t)} \mu_g^{(e)} p_g'^{(t)}}{\theta_g^{(e)} \mu_g^{(t)} p_g'^{(e)}} \sqrt{\frac{(RT')_g^{(e)} \Gamma_g^{(t)}}{(RT')_g^{(t)} \Gamma_g^{(e)}}} = 1 \quad (11-69)$$

If the local film effectiveness is to remain unchanged between engine and test conditions, the coolant to hot-gas mass-flux ratio $(\rho u)_c/(\rho u)_g$, the coolant to hot-gas momentum ratio $(\rho u^2)_c/(\rho u^2)_g$ (or density ratio ρ_c/ρ_g), and the momentum-thickness to film-ejection-hole-diameter ratio θ_g/D must be the same in both cases. Since actual-size hardware is presumed, then

$$\frac{\left(\frac{\theta_g}{D} \right)_g^{(t)}}{\left(\frac{\theta_g}{D} \right)_g^{(e)}} = \frac{\theta_g^{(t)}}{\theta_g^{(e)}} = 1 \quad (11-70)$$

and equation (11-69) becomes

$$\frac{\mu_g^{(e)} w_g^{(t)}}{\mu_g^{(t)} w_g^{(e)}} = \frac{\mu_g^{(e)} p_g'^{(t)}}{\mu_g^{(t)} p_g'^{(e)}} \sqrt{\frac{(RT')_g^{(e)} \Gamma_g^{(t)}}{(RT')_g^{(t)} \Gamma_g^{(e)}}} = 1 \quad (11-71)$$

Equation (11-71) shows that the gas flow rate must vary directly with the viscosity and gives the functional relation between gas pressure and temperature which will provide the same Reynolds number and Mach number distributions for test and engine conditions. Parametric curves of equation (11-71) are shown in figure 11-18 for air.

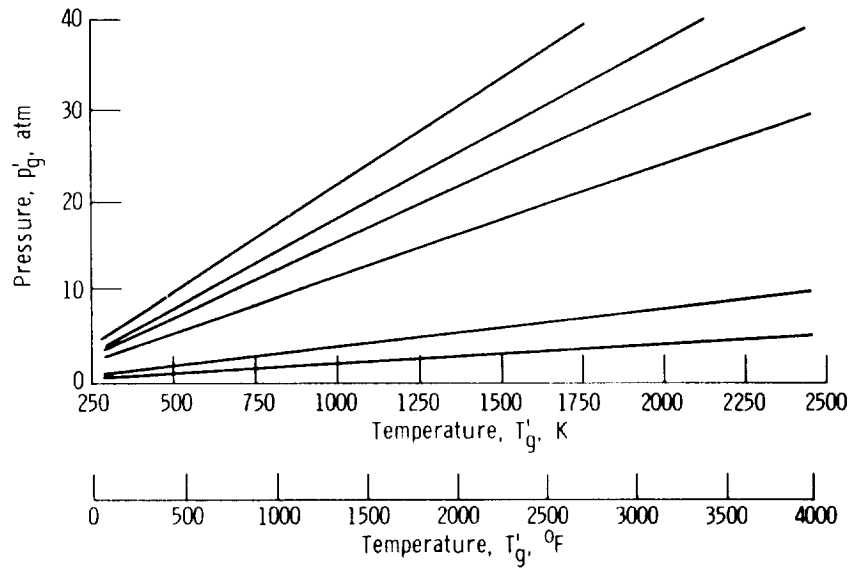


FIGURE 11-18.—Similarity curves of constant Mach number and momentum-thickness Reynolds number distributions around a turbine vane for air properties.

The cooling-air flow rate and temperature are then set by the coolant-to-gas mass-flux ratio and momentum ratio. Requiring

$$\left[\frac{(\rho u)_c}{(\rho u)_g} \right]^{(t)} = \left[\frac{(\rho u)_c}{(\rho u)_g} \right]^{(e)} \quad (11-72)$$

implies

$$\left(\frac{w_c}{w_g} \right)^{(t)} = \left(\frac{w_c}{w_g} \right)^{(e)} \quad (11-73)$$

and it is necessary that

$$\left(\frac{t_{c,o}}{t_g} \right)^{(t)} = \left(\frac{t_{c,o}}{t_g} \right)^{(e)} \quad (11-74)$$

to ensure equality of test and engine momentum ratios, since $p_{c,o} = p_g$.

Neglecting conduction in the plane of the wall compared to that in the direction normal to the wall, the film ejection temperature $T'_{c,o}$ is related to the supply coolant temperature by

$$\frac{(H_{c,o} - H_{c,in})^{(t)}}{(H_{c,o} - H_{c,in})^{(e)}} = \frac{q^{(t)} \mu_g^{(e)}}{q^{(e)} \mu_g^{(t)}} \quad (11-75)$$

where the viscosity ratio here represents the mass flow ratio (see eq. (11-71)). Satisfying equations (11-71) to (11-75) ensures that the hot-gas-side heat-transfer coefficient distribution around the vane will

have the same shape for both test and engine conditions. The heat-transfer coefficient in dimensionless Stanton number form is

$$St_g^{(t)} = St_g^{(e)} \left(\frac{Pr^{(e)}}{Pr^{(t)}} \right)_g^{2/3} \quad (11-76)$$

Since the Prandtl number cannot be set independently if all other similarity conditions discussed are met, the departure of the Stanton number ratio from unity depends on the Prandtl number ratio in equation (11-76).

On the coolant side, the heat-transfer coefficient in dimensionless Nusselt number form is given by

$$Nu_c^{(t)} = Nu_c^{(e)} \left(\frac{Pr^{(t)}}{Pr^{(e)}} \right)_c^{1/3} \left(\frac{\mu_g^{(t)} \mu_{c,o}^{(e)}}{\mu_g^{(e)} \mu_{c,o}^{(t)}} \right)^m \quad (11-77)$$

where m is the power on the Reynolds number for coolant-side convection. The viscosity factor in equation (11-77) is the test-to-engine coolant Reynolds number ratio. As with the Prandtl number, this factor cannot be set independently, although its departure from unity is small. In fact, if the viscosity over the full temperature range $t_g^{(e)}$ to $t_{c,o}^{(t)}$ could be approximated by a power law

$$\mu \propto t^\omega \quad (11-78)$$

then, by equation (11-74), the test-to-engine coolant Reynolds number ratio (based on the film-cooling hole diameter and the ejection temperature) would be 1. The same coolant Reynolds number for actual and simulated conditions is important to ensure the same pressure drop through the internal cooling air passages for the two conditions.

If the cooled blade is to perform the same during a test as it does in the engine, there must be some normalized outer wall temperature which remains invariant between test and engine conditions. The most convenient dimensionless wall temperature includes only those temperatures which are known, namely the coolant supply temperature $T'_{c,tn}$ and the effective gas temperature $T_{g,e}$. Hence, the dimensionless wall temperature φ , defined as

$$\varphi = \frac{T_{g,e} - T_{w,o}}{T_{g,e} - T'_{c,tn}} \quad (11-79)$$

or some similar grouping of these three temperatures, is commonly used as a measure of the cooling performance of a given blade design.

Strict equality in φ for test and engine is, however, impossible with actual hardware, since the temperature drop through the wall is not scaled properly because of the lower heat flux at reduced temperature and pressure. It is easier to cool the blade at the reduced conditions, because the driving potential for convection cooling ($T_{w,i} - T'_c$) is proportionately greater than at high temperature and pressure. How-

TURBINE DESIGN AND APPLICATION

ever, for properly scaled test conditions, the difference between $\varphi^{(t)}$ and $\varphi^{(e)}$ is well within the range of experimental accuracy in most cases.

An example of similarity states generated by solving equations (11-71) to (11-77) simultaneously is given in table 11-II for a high-pressure, high-temperature gas-turbine-engine environment. Air properties were used rather than those for a given fuel-air ratio gas. For a test condition using ambient cooling air, the dimensionless wall temperature $\varphi^{(t)}$ is 1 percent higher than what it would be in the actual engine.

Radiation can be a significant component of the total heat flux to a blade under high-temperature and high-pressure conditions and is not directly affected by film cooling with air. Since radiation cannot be conveniently simulated at the low-temperature and low-pressure test conditions, it must be accounted for in the heat-flux ratio $q^{(t)}/q^{(e)}$ in equation (11-75).

TABLE 11-II.—SIMILARITY STATES

(a) Takeoff condition

Gas total temperature		Gas total pressure, atm.	Coolant temperature		$\varphi^{(t)}/\varphi^{(e)}$
K	°F		K	°F	
¹ 2200	¹ 3500	¹ 33.7	¹ 848	¹ 1066	-----
367	200	4.3	145	-199	1.04
478	400	6.0	188	-122	1.03
589	600	7.7	230	-45	1.02
700	800	9.4	273	31	1.01
758	905	10.3	294	70	1.01
811	1000	11.1	315	107	1.01
922	1200	12.9	357	182	1.00
1033	1400	14.6	399	259	1.00
1144	1600	16.4	442	335	1.00
1255	1800	18.2	485	413	1.00
1367	2000	19.9	528	490	1.00
1478	2200	21.7	571	568	1.00
1589	2400	23.5	613	644	1.00
1700	2600	25.3	656	721	1.00
1811	2800	27.1	699	799	1.00
1922	3000	28.9	743	878	1.00
2033	3200	30.9	786	955	1.00
2144	3400	32.8	828	1030	1.00

¹ Reference condition.

TABLE 11-II.—Concluded

(b) Cruise condition

Gas total temperature		Gas total pressure, atm.	Coolant temperature		$\varphi^{(t)}/\varphi^{(e)}$
K	°F		K	°F	
¹ 2200	¹ 3500	¹ 13.8	¹ 801	¹ 983	-----
367	200	1.7	139	-209	1.03
478	400	2.5	180	-136	1.02
589	600	3.2	220	-64	1.01
700	800	3.9	259	7	1.01
799	978	4.5	294	70	1.01
811	1000	4.6	299	78	1.01
922	1200	5.3	338	148	1.00
1033	1400	6.0	378	220	1.00
1144	1600	6.7	417	291	1.00
1255	1800	7.4	458	364	1.00
1367	2000	8.2	498	437	1.00
1478	2200	8.9	539	510	1.00
1589	2400	9.6	579	582	1.00
1700	2600	10.4	619	655	1.00
1811	2800	11.1	660	729	1.00
1922	3000	11.8	702	804	1.00
2033	3200	12.7	743	878	1.00
2144	3400	13.4	782	948	1.00

¹ Reference condition.

REFERENCES

1. ESGAR, JACK B.; COLLADAY, RAYMOND S.; KAUFMAN, ALBERT: An Analysis of the Capabilities and Limitations of Turbine Air Cooling Methods. NASA TN D-5992, 1970.
2. KAYS, W. M.: Convective Heat and Mass Transfer. McGraw-Hill Book Co., Inc., 1966.
3. KESTIN, J.: The Effect of Free-Stream Turbulence on Heat Transfer Rates. Advances in Heat Transfer. Vol. 3. T. F. Irvine, Jr.; and J.P. Hartnett, eds., Academic Press, 1966, pp. 1-32.
4. AMBROK, G. S.: Approximate Solution of Equations for the Thermal Boundary Layer With Variations in Boundary Layer Structure. Soviet Phys.-Tech. Phys., vol. 2, no. 9, 1957, pp. 1979-1986.
5. SPALDING, D. B.; AND PATANKAR, S. V.: Heat and Mass Transfer in Boundary Layers. Chemical Rubber Co., 1968.
6. KERCHER, D. M.; AND TABAKOFF, W.: Heat Transfer by a Square Array of Round Air Jets Impinging Perpendicular to a Flat Surface Including the Effect of Spent Air. J. Eng. Power, vol. 92, no. 1, Jan. 1970, pp. 73-82.

TURBINE DESIGN AND APPLICATION

7. ARTT, D. W.; BROWN, A.; AND MILLER, P. P.: An Experimental Investigation Into Film Cooling With Particular Application to Cooled Turbine Blades. Heat Transfer 1970. Vol. 2. Ulrich Grigull and Erich Hahne, eds., Elsevier Publ. Co., 1970, pp. FC1. 7.1-FC1. 7.10.
8. GOLDSTEIN, R. J.; ECKERT, E. R. G.; ERIKSEN, V. L.; AND RAMSEY, J. W.: Film Cooling Following Injection Through Inclined Circular Tubes. Rep. HTL-TR-91, Minnesota Univ. (NASA CR-72612), Nov. 1969.
9. COLLADAY, RAYMOND S.; AND STEPKA, FRANCIS S.: Examination of Boundary Conditions for Heat Transfer Through a Porous Wall. NASA TN D-6405, 1971.
10. L'ECUYER, MEL R.; AND COLLADAY, RAYMOND S.: Influence of Porous-Wall Thermal Effectiveness on Turbulent-Boundary-Layer Heat Transfer. NASA TN D-6837, 1972.

SYMBOLS

A	surface area of one side of volume element, m^2 ; ft^2
\mathcal{A}	coolant-passage flow area, m^2 ; ft^2
a	augmentation factor, eq. (11-31)
a_1, a_2, a_3	coefficients in eqs. (11-49) to (11-51)
B_x	body-force component in x direction, N/kg ; lbf/lbm
b_1, b_2, b_3	coefficients in eqs. (11-49) to (11-51)
C	constants in eqs. (11-8) and (11-57)
C_f	friction coefficient, eq. (11-26)
c_p	specific heat at constant pressure, $J/(kg)(K)$; $Btu/(lb)(^\circ R)$
c_1, c_2	coefficients in eqs. (11-49) and (11-50)
D	diameter of leading-edge circle, impingement hole, or film-injection hole, m ; ft
\mathcal{D}	dissipation term in eq. (11-42), W/m^3 ; $Btu/(ft^3)(sec)$
d	distance between volume elements (see fig. 11-10), m ; ft
F	ratio of coolant mass flux to hot-gas mass flux
f	correction factor used in eq. (11-65)
G	mass flux, $kg/(sec)(m^2)$; $lb/(hr)(ft^2)$
g	conversion constant, 1; 32.17 $(lbm)(ft)/lbf)(sec^2)$
H	total enthalpy, J/kg ; Btu/lb
h	heat-transfer coefficient, $W/(m^2)(K)$; $Btu/(hr)(ft^2)(^\circ R)$
h_v	internal volumetric heat-transfer coefficient, $W/(m^3)(K)$; $Btu/(hr)(ft^3)(^\circ R)$
h	static enthalpy, J/kg ; Btu/lb
I	term defined by eq. (11-41)
J	conversion constant, 1; 778 $(ft)(lb)/Btu$
K	dimensional constant, 1; 3600 sec/hr
\mathcal{K}	turbulent kinetic energy, J/kg ; Btu/lb
k	thermal conductivity, $W/(m)(K)$; $Btu/(hr)(ft)(^\circ R)$
\mathcal{L}	coolant-passage characteristic length, m ; ft
l	wall thickness, m ; ft
M	Mach number
m	exponents used in eqs. (11-8), (11-45), and (11-48)
Nu	Nusselt number
n	exponents used in eqs. (11-8), (11-45), (11-56), and (11-57)
Pr	Prandtl number
p	pressure, N/m^2 ; lb/ft^2
Q	heat-generation term, W/m^3 ; $Btu/(sec)(ft^3)$
q	heat flux, W/m^2 ; $Btu/(hr)(ft^2)$
R	gas constant, $J/(kg)(K)$; $(ft)(lbf)/(lbm)(^\circ R)$
Re	Reynolds number
r	recovery factor, eq. (11-27)
St	Stanton number

TURBINE DESIGN AND APPLICATION

s	slot width, m; ft			
T	temperature, K; °R			
t	gas static temperature, K; °R			
u	component of gas velocity in direction along surface (x -direction), m/sec; ft/sec			
V_j	volume of j^{th} element, m ³ ; ft ³			
v	component of gas velocity in direction normal to surface (y -direction), m/sec; ft/sec			
w	<table> <tr> <td rowspan="2" style="font-size: 3em; vertical-align: middle;">{</td> <td>mass flow rate, kg/sec; lb/sec</td> </tr> <tr> <td>component of gas velocity in direction perpendicular to the boundary layer plane (x-y plane), m/sec; ft/sec</td> </tr> </table>	{	mass flow rate, kg/sec; lb/sec	component of gas velocity in direction perpendicular to the boundary layer plane (x - y plane), m/sec; ft/sec
{	mass flow rate, kg/sec; lb/sec			
	component of gas velocity in direction perpendicular to the boundary layer plane (x - y plane), m/sec; ft/sec			
x	distance along surface from leading edge, m; ft			
x_n	center-to-center distance between impingement holes in the direction of flow, m; ft			
y	coordinate distance normal to surface, m; ft			
z_n	distance between impingement holes and blade inner wall, m; ft			
α	heat diffusivity, m ² /sec; ft ² /sec			
Γ	specific heat ratio correction factor, eq. (11-68)			
γ	ratio of specific heat at constant pressure to specific heat at constant volume			
Δ	enthalpy thickness, m; ft			
ϵ	ratio of heat transfer coefficient with film cooling to heat transfer coefficient without film cooling			
η	cooling effectiveness			
θ	momentum thickness, m; ft			
μ	viscosity, (N)(sec)/m ² ; lb/(ft)(sec)			
ν	momentum diffusivity (kinematic viscosity), m ² /sec; ft ² /sec			
ρ	density, kg/m ³ ; lb/ft ³			
τ	local shear stress, N/m ² ; lb/ft ²			
Φ	angular distance from leading-edge stagnation point, deg			
φ	dimensionless wall temperature			
φ_1, φ_2	coefficients in eq. (11-48)			
ψ	term defined by eq. (11-52)			
ω	exponent in eq. (11-78)			

Subscripts:

a	adiabatic
CP	constant property
c	coolant
cf	crossflow
$conv$	convection
$crit$	critical, referring to transition from laminar to turbulent flow

D	with hole diameter as characteristic dimension
e	effective
$film$	film
g	hot gas at free-stream condition
h	hole
i	inner
imp	impingement
in	inlet
j	j th element
L	laminar
\mathcal{L}	with \mathcal{L} as characteristic length
le	leading edge
o	outer
ref	reference
s	downstream edge of slot
$stag$	stagnation
T	turbulent
t	transpiration
w	wall
x	{ local value { with x as characteristic length
Δ	with Δ as characteristic length
θ	with θ as characteristic length
∞	approaching leading edge

Superscripts:

(e)	engine condition
(t)	test condition
$'$	{ total state (referring to T and p) { fluctuating component (referring to $\rho, v, h, u,$ and w)

CHAPTER 12

Experimental Determination of Aerodynamic Performance

By Edward M. Szanca and Harold J. Schum

The preceding chapters have been concerned with primarily the theoretical aspects relating to turbines and turbine design. A great deal of consideration has been directed toward turbine blading, since, aerodynamically, the blading is the turbine. Associated hardware for the entire turbine assembly (rotor disks, shafting, bearings, casings etc.) is designed on the basis of mechanical criteria. Once the turbine is designed and built, it must be determined whether or not the aerodynamic design goals have been met. Only by testing the turbine can this be determined.

In addition to the overall performance of a turbine, a breakdown of the separate losses contributing to the overall loss is often desired. The stator loss can be obtained readily from experimental measurements, as discussed in chapter 7 (vol. 2). Rotor losses cannot be obtained easily from direct measurements; they are usually obtained indirectly from the stator loss and the overall performance measurements.

In developing a test facility and program, the researcher must determine which performance parameters he is interested in evaluating. The nature of the test facility, the instrumentation necessary to obtain the desired stator and/or overall performance parameters, and the manner in which these parameters vary with turbine operating conditions are the subject of this chapter.

TEST FACILITY AND MEASUREMENTS

The manner in which stator performance is expressed and computed is discussed in detail in chapter 7 (vol. 2) and will not be discussed herein. The parameters generally used to define turbine overall performance are mass flow rate, torque, specific work, and efficiency. These parameters are usually determined for ranges of rotative speed and pressure ratio in order to fully define the performance of the turbine. The mass flow rate, torque, rotative speed, inlet and exit pressures, and inlet temperature (needed to determine efficiency) are measured directly in the turbine test facility. Specific work is then calculated from the equation

$$\Delta h' = K \frac{\Gamma N}{Jw} \quad (12-1)$$

where

- $\Delta h'$ turbine specific work, J/kg; Btu/lb
- K conversion constant, 1; $\pi/30$ (rad)(min)/(rev)(sec)
- Γ torque, N-m; lb-ft
- N rotative speed, rad/sec; rev/min
- J conversion constant, 1; 778(ft)(lb)/Btu
- w mass flow rate, kg/sec; lb/sec

Efficiency is obtained by dividing the actual work $\Delta h'$ by the ideal work. Ideal work is a function of the turbine inlet total temperature and the pressure ratio across the turbine, as shown by equation (2-48b) or (2-49b) of chapter 2 (vol. 1). The inlet pressure is always the total pressure. The outlet pressure used to define ideal work, however, depends on the particular efficiency desired. Total efficiency is based on outlet total pressure and is most meaningful where all of the outlet velocity is useful or recoverable. Static efficiency is based on outlet static pressure and is most meaningful where all of the outlet velocity is lost. Rating efficiency is based on a pressure corresponding to the recovery of only the axial component of outlet velocity and, accordingly, is most meaningful where only the axial component of the outlet velocity is useful. Rating efficiency is not as commonly used as are the total and static efficiencies, which were discussed in chapter 2 (vol. 1).

In this section, a representative test facility will be described, and the types of devices generally used to make the required measurements will be discussed. Data acquisition and reduction systems will not be discussed in this chapter. These can vary from visual reading of manometers and gages with slide-rule computations to completely automatic electronic data acquisition with on-line computer process-

ing. A general discussion of data measurement, acquisition, transmission, and recording systems can be found in texts such as reference 1.

Description of Test Facility

A turbine test facility consists of the research turbine, a gas supply, an exhaust system, associated piping with control valves, a power absorber, and the instrumentation needed to make the desired measurements. A schematic diagram of a turbine test facility at the NASA Lewis Research Center is shown in figure 12-1. This facility, a photograph of which is shown in figure 12-2, is used to test single-stage or multistage turbines of about 76 centimeters (30 in.) in diameter. It is generally representative of most turbine test facilities and is used here as an example for this discussion. In such a facility, removal of the turbine rotor gives the room necessary to place survey instrumentation behind the stator and, thereby, transforms the rotating rig into a stator annular cascade.

Most turbine component testing is conducted with air at ambient temperature or slightly heated. This is commonly called cold-air

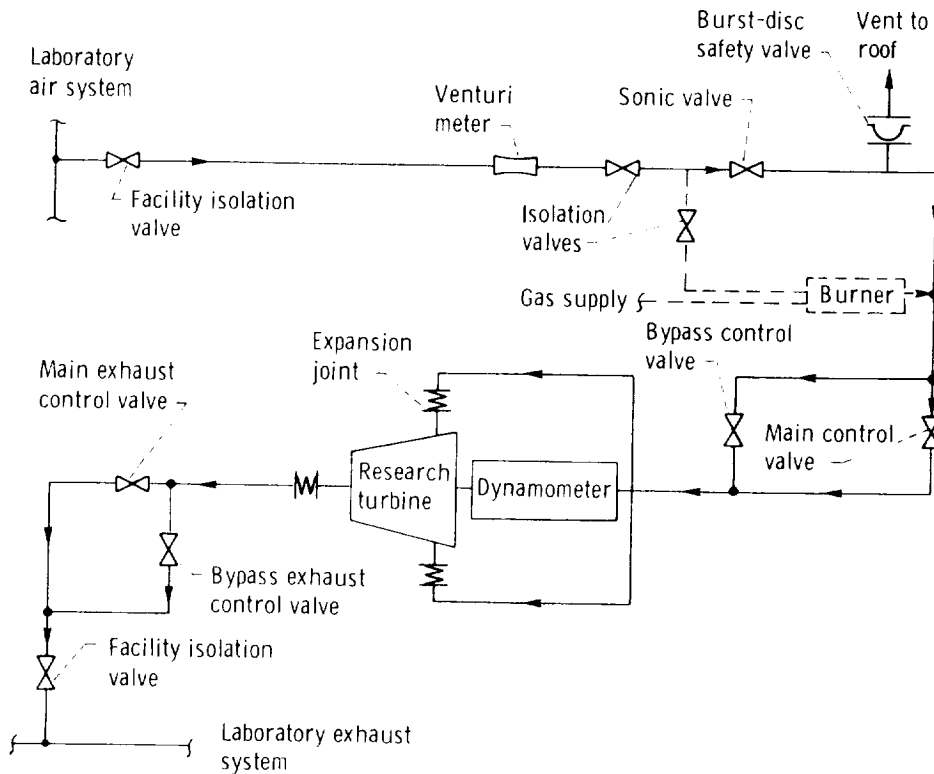


FIGURE 12-1.—Flow schematic of a turbine test facility.

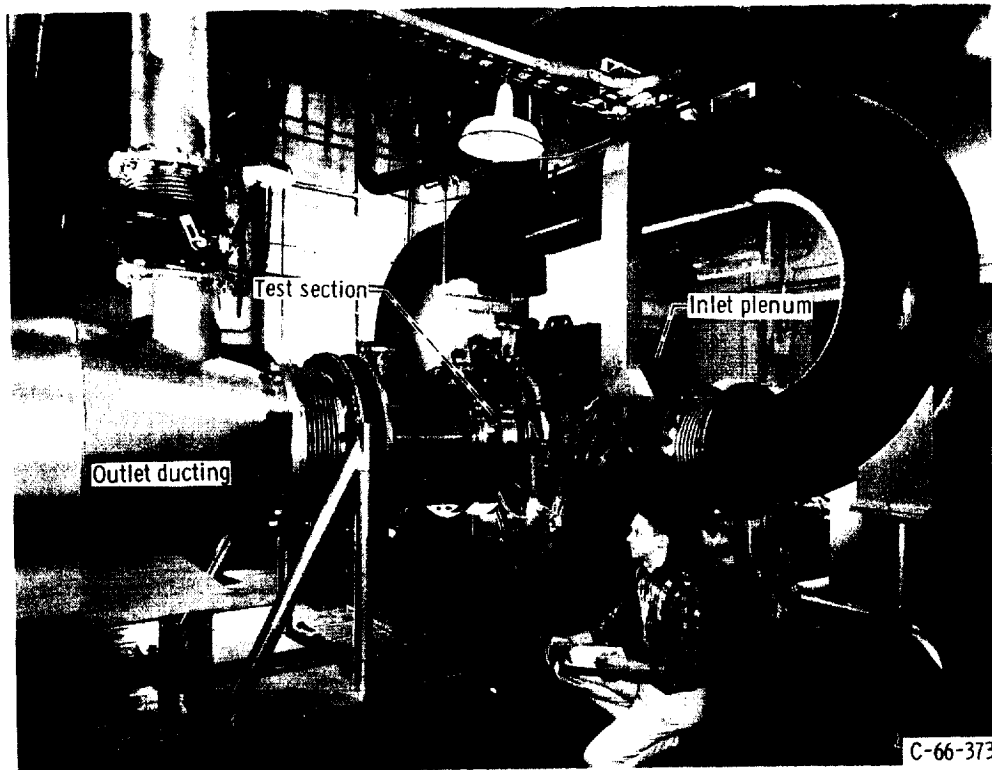


FIGURE 12-2.—Turbine test facility.

testing. Performance parameters are reported in terms of equivalent values based on standard sea-level conditions of pressure (10.133 N/cm^2 or 14.696 psia) and temperature (288.2 K or 518.7° R). This was discussed in chapter 2 (vol. 1). Using turbine-inlet test conditions of pressure and temperature near the standard values results in lower flow and power levels than would be encountered in an actual application and thereby facilitates testing. Yet, the model turbine velocity diagrams are similar to and the Mach numbers are the same as those of the actual turbine. Only Reynolds number, then, can present a dissimilarity; however, for the larger turbines, this effect of Reynolds number on turbine performance was found to be negligible. For smaller turbines, where Reynolds number effects are more important, turbine inlet pressure can be varied to obtain the proper Reynolds number.

Referring to figure 12-1, air for the turbine is supplied by the 27.6-N/cm^2 -gage (40-psig) air system of the laboratory. A calibrated venturi meter is located in a straight section of the 40.6-centimeter (16-in.) air-supply line for the purpose of metering the air flow. This

pipng is sized (as was all piping) such that the air velocities will not exceed 61 meters per second (200 ft/sec). Location of the air-metering device in the high-pressure supply line affords a relatively constant upstream pressure and may minimize the number of metering devices required for a range of flows. A further discussion of air-metering devices is presented in a subsequent section.

Downstream of the venturi meter is an isolation valve controllable by the turbine operator. A 30.5-centimeter (12-in.) sonic valve provides a high pressure drop to facilitate burner operation and automatic inlet-pressure control. A burst-disc safety valve and vent line provide protection from excessive pressure. Further downstream is the 50.8-centimeter (20-in.) main control valve used to establish the desired turbine-inlet pressure (for the example turbine, this was 76.2 cm (30 in.) of Hg absolute). The 15.2-centimeter (6-in.) bypass control valve permits fine control of the turbine-inlet pressure. The air then diverts into two 50.8-centimeter (20-in.) lines to provide dual entry of lower velocity air to the turbine entry plenum. (These lines can be seen in fig. 12-2.)

After passing through the turbine, the air is discharged to the altitude exhaust system of the laboratory through a 121.9-centimeter (48-in.) main control valve and a 40.6-centimeter (16-in.) bypass control valve. These valves permit the turbine operator to vary the pressure ratio across the turbine while the turbine-inlet pressure is maintained constant by automatic control. This type of pressure-ratio control has been most successful with small turbines. With large turbines, however, there is a slower response because of the large pipe volume between the turbine and the inlet control valve.

A burner installation is shown (in fig. 12-1) in phantom, because its use is optional. The purpose of the burner is to elevate the turbine-inlet temperature so as to avoid icing problems at the turbine exit. In this facility a single commercial jet-engine burner can, modified for operation with natural gas, is used. Some of the high-pressure air is bypassed to the burner and the heated air is then mixed with the remaining air. The desired turbine inlet temperature is maintained by controlling both the amount of bypassed air and the fuel flow. This particular burner has the capability to heat a maximum air flow of 23.6 kilograms per second (52 lb/sec) from ambient temperature to 422 K (300° F).

In general, burners using gasoline, jet fuel, or natural gas provide a relatively simple and inexpensive means of heating the air. However, combustion products are added to the air, and these must be accounted for in the performance calculations. Electrical heaters provide clean heat, but are generally used only where flow rates are low, because of the cost and complexity of large installations.

All turbines and test facilities must be designed with safety features. The following are some of the potentially unsafe conditions that must be guarded against by constant monitoring:

- (1) Low supply of turbine and dynamometer lubricating oil
- (2) Low pressures of turbine and dynamometer lubricating oil
- (3) High temperature in bearings
- (4) High temperature of dynamometer outlet water
- (5) Low pressure of dynamometer water supply
- (6) High temperature of turbine inlet gas
- (7) High (or low) temperature of turbine exit gas
- (8) High pressure of turbine inlet gas
- (9) High pressure of turbine exit gas
- (10) Overspeed of turbine rotor
- (11) Reduced clearance between rotor and casing
- (12) Excessive rig vibration
- (13) Excessive shaft orbit

Interlocks on some of the monitoring systems prevent turbine starting. Some monitors provide for only an audible alarm during operation. Others provide a signal to rapidly shut the valves in the inlet air line as well as in the heater gas system. This quickly stops rotor rotation in order to prevent damage to the turbine and facility.

Research Turbine

A schematic diagram of one of the research turbines used in this test facility is presented in figure 12-3. An enlarged view of the test section with instrumentation stations indicated is also shown. As stated previously, the air enters a plenum from two sides; the plenum was designed with as much volume as feasible to provide for minimum velocity and minimum pressure distortion. A screen is shown located upstream of a converging section to further ensure a symmetrical circumferential pressure distribution to the turbine blades. This screen has an approximate 50 percent effective area, giving a pressure drop of 2 dynamic heads.

A short, straight, annular passage is provided between the converging inlet section and the first row of blades for the purpose of installing turbine-inlet pressure and temperature measurement devices. The inlet measuring station (station 0 of fig. 12-3) is located about $1\frac{1}{2}$ blade chords upstream of the stator blades. Since the inlet velocity is low, the insertion of probes does not significantly disturb the flow entering the blading.

A straight, annular flow passage is also provided downstream of the turbine blades to measure the turbine-outlet air state (measuring station 2, fig. 12-3). Measurements are made about 2 blade-chord

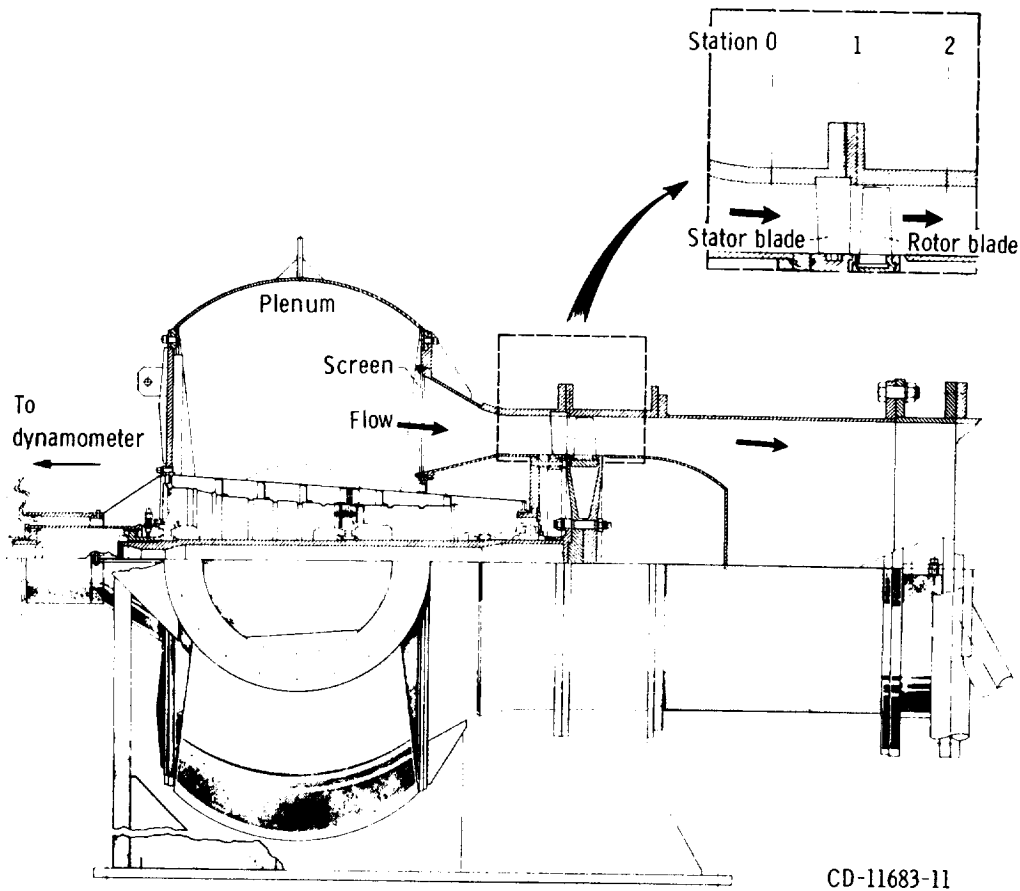


FIGURE 12-3.—Schematic diagram of turbine test section.

lengths downstream of the rotor, where the exit air is relatively stabilized and uniform.

Both the inlet and outlet sections of the test turbine are somewhat idealized as compared to an actual jet-engine turbine installation. The latter has a burner immediately preceding the turbine inlet, and a tail cone immediately following the last row of blades. Flow-passage diameters vary. Also, for the sake of engine weight saving, minimum axial length is required. Accurately measuring the state conditions before and after the turbine blading in varying area passages is extremely difficult, and this is the reason for the use of straight, annular flow passages in the test turbine.

Flow-Property Measurements

The flow-property measuring stations are located in the axial positions indicated in figure 12-3. There are numerous types and

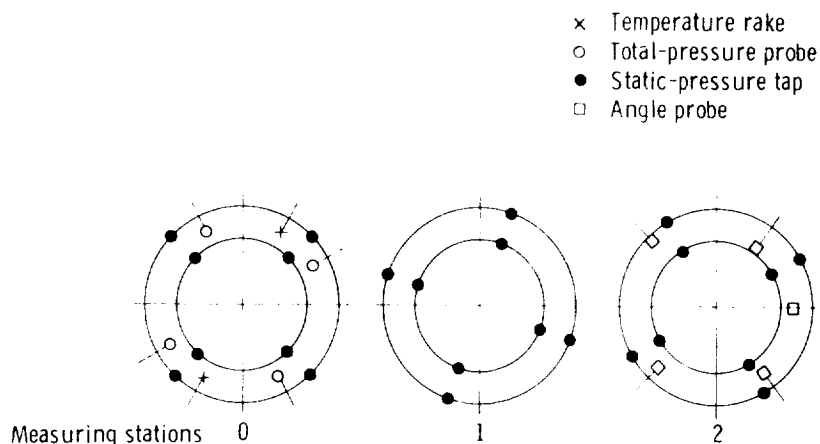


FIGURE 12-4.—Schematic diagram of turbine instrumentation.

variations of probes available to make the desired measurements. We will discuss primarily the instruments used in the example research turbine to obtain the desired measurements of pressure, temperature, and flow angle. The instrumentation located at the turbine inlet and outlet, as well as at the stator exit, is shown in figure 12-4.

In general, all turbine experimental investigations, irrespective of turbine size or number of stages, require the same overall data. The size of the turbine determines whether duplication of research instrumentation can be afforded. For large turbines, the relative size of the probes with respect to the flow passages can be considered negligible. In small turbines, the presence of the various probes with their associated blockage could have an effect on the turbine expansion process, and, therefore, on the values being measured. This consideration usually limits the number and size of probes.

Static pressure.—At each measuring station, as shown in figure 12-4, there are four static-pressure taps, diametrically opposed and 90° apart, on both the inner and outer walls. This multiplicity provides a check on the circumferential pressure distribution. In order to minimize the amount of instrumentation and data, multiple taps are often manifolded to provide a single reading. If the individual pressures differ, however, some flow circulation occurs and the observed pressure reading may not be the true average of the individual pressures.

As part of the stator performance test, it is often desired to determine the static-pressure distribution along the blade surface. As explained in a subsequent section, this information is used to calculate the blade surface velocities. Static-pressure taps are installed

EXPERIMENTAL DETERMINATION OF AERODYNAMIC PERFORMANCE

along the hub, mean, and tip sections of the blade. If the number of tubes that can be installed in any one blade is limited by the size of the blade, then the desired taps can be divided among two or more adjacent blades. For the research turbine being discussed, the blades are hollow and fairly large; thus, installing the taps presented no major problem. The pressure-tap hole size used is approximately 0.0254 centimeter (0.010 in.) in diameter. A small hole is desirable so as not to disturb the flow; however, too small a hole results in a long response time.

Inlet total pressure.—Four shielded total-pressure probes, 90° apart, are located at the inlet measuring station (see fig. 12-4) and are all immersed to the area center of the flow passage. One such probe is shown in figure 12-5(a). The shielding, which is about 0.48 centimeter (0.19 in.) in diameter and twice that in length, is such that pressure readings are relatively insensitive to yaw for some 40° . The unshielded probe shown in figure 12-5(b) is also commonly used for total-pressure measurement. This probe has an insensitivity to yaw for about 20° .

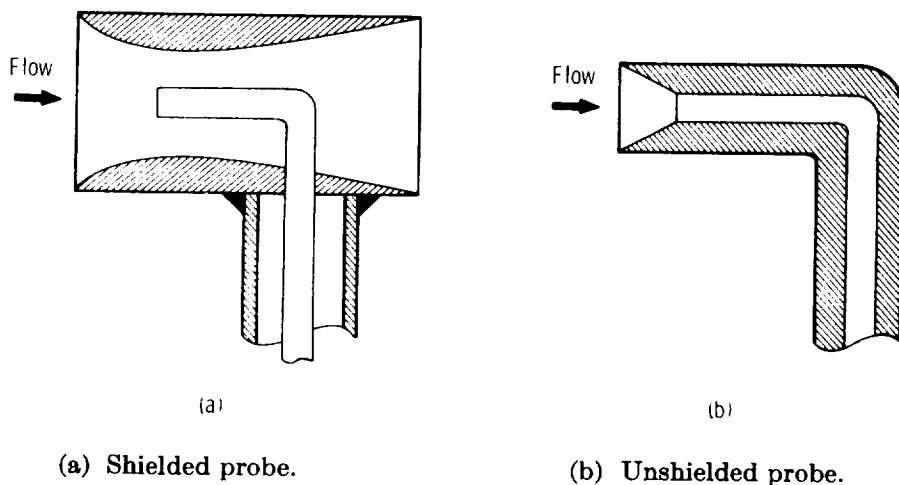


FIGURE 12-5.—Total-pressure probes.

The turbine-inlet total-pressure readings serve as a check on the circumferential pressure distribution and are used during turbine testing to establish and maintain a constant turbine-inlet total pressure. However, the turbine-inlet total-pressure value that is often used to define pressure ratio when reporting turbine performance is a value based on experimental measurements of mass flow rate, static

pressure, and total temperature and obtained by the following equation, with the flow angle α assumed to be zero at the turbine inlet:

$$p' = p \left[\frac{1}{2} + \sqrt{\frac{1}{4} + \frac{\gamma-1}{2g\gamma} \left(\frac{w}{pA_{an}} \right)^2 \frac{RT'}{\cos^2 \alpha}} \right]^{\gamma/(\gamma-1)} \quad (12-2)$$

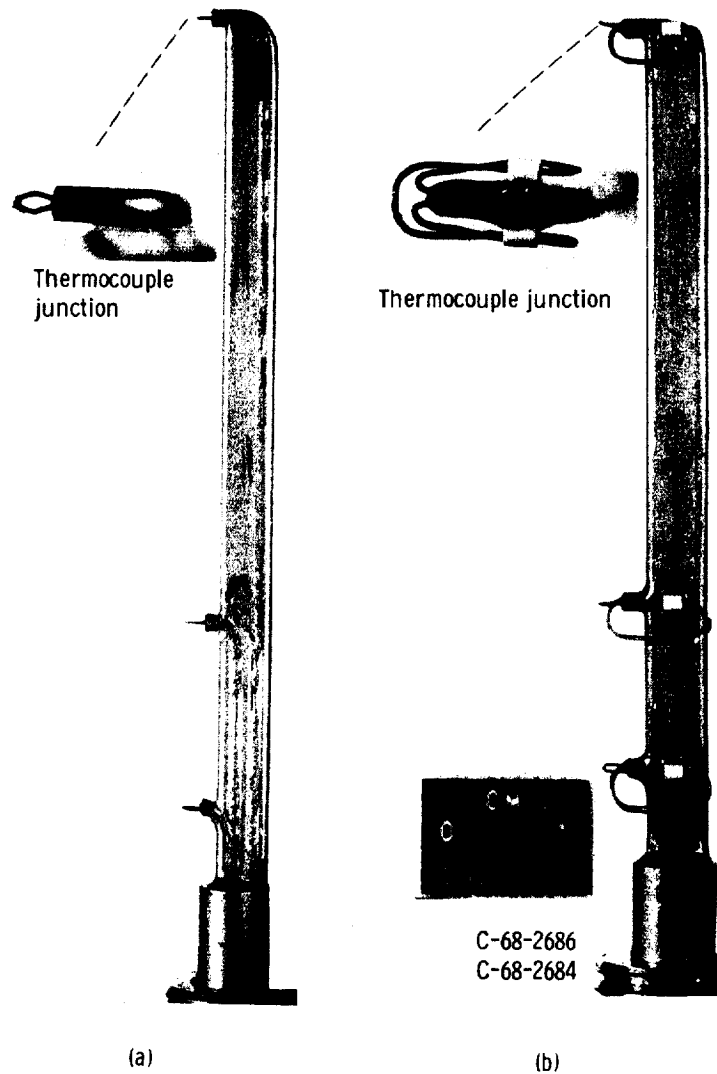
where

- p' total pressure, N/m²; lb/ft²
 p static pressure, N/m²; lb/ft²
 γ ratio of specific heat at constant pressure to specific heat at constant volume
 g conversion constant, 1; 32.17 (lbm)(ft)/(lbf)(sec²)
 A_{an} annulus area, m²; ft²
 R gas constant, J/(kg)(K); (ft)(lbf)/(lbm)(°R)
 T' total temperature, K; °R
 α flow angle measured from axial direction, deg

This calculated value of turbine-inlet total pressure is thought to be more representative of the true average value than is the experimental value.

Inlet temperature.—Two thermocouple rakes, spaced 180° apart, are located at the turbine inlet measuring station (see fig. 12-4). These rakes, which are of a type similar to that shown in figure 12-6(a), contain a number of thermocouples situated at the area center radii of equal annular areas. The particular rake shown in figure 12-6(a) was used to determine the temperatures at the center, the area-mean radius, and the wall of the outlet duct of a radial-inflow turbine. Provisions are made for individual readings as well as for the average of all the readings. The latter facilitates testing with the burner in operation, where a constant inlet temperature is maintained. Automatic fuel regulation to the burner is provided for this purpose.

Measurement of temperature at low Reynolds number can present a problem due to heat conduction effects. This problem did not exist for the large research turbine being used as an example herein, but was encountered in testing some small turbines as discussed in reference 2. A large amount of bare thermocouple wire must be exposed to the flow in order to make the conduction error negligible. The conventional thermocouple shown in figure 12-6(a) has a ratio of exposed wire length to diameter of about 12, which is inadequate for good accuracy at low Reynolds number. The modified thermocouple shown in figure 12-6(b) has a wire length-to-diameter ratio of about 170. This modified probe gives excellent results.



(a) Conventional type.

(b) Modified type.

FIGURE 12-6.—Thermocouple rake configurations.

Stator outlet.—During turbine testing, the only measurement made at the stator outlet is the previously mentioned static pressure. For stator performance testing, the rotor is removed, and a total-pressure survey probe is installed. Although it is desirable also to obtain stator-outlet radial and circumferential static-pressure surveys, the problems associated with conventional wedge probes, especially the effect of probe blockage on the value being measured, make such measurements



FIGURE 12-7.—Total-pressure survey probe installed in test facility.

unreliable. The required static pressures are obtained by interpolation from the values measured at the hub and tip wall taps. The total-pressure probe used in the test facility is shown in figure 12-7. This probe is fixed at an angle previously determined to be the average flow angle. Note that the probe has two sensing elements; these are required to obtain measurements at both the inner and outer walls.

The total-pressure survey equipment is shown in figure 12-8. The actuator provides for radial movement of the probe, and the motor-driven outer-wall saddle provides for circumferential movement. The probe shown in this figure does not have the same stem configuration as the previously shown probe (fig. 12-7) that was used in the example facility. Considerations regarding the effects of stem blockage, sensing

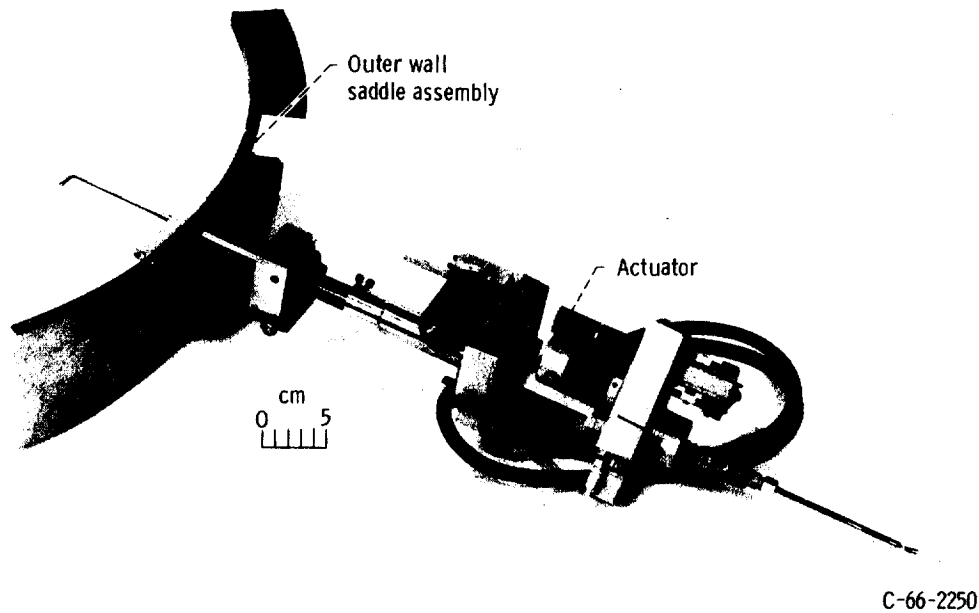


FIGURE 12-8.—Total-pressure survey equipment.

element diameter, and measurement distance behind the blade trailing edge are discussed in reference 3.

Although not used in the particular facility serving as the discussion example herein, optical laser techniques have recently come into use for directly measuring velocity magnitude and direction. A laser Doppler velocimeter, such as described in reference 4, allows the velocity measurements to be made without the use of flow-disturbing probes.

Turbine outlet.—Combination probes, with the type of sensing head shown in figure 12-9, capable of measuring total pressure, temperature, and flow angle are located at the turbine exit. Figure 12-4 shows that five of these combination probes are distributed circumferentially at measuring station 2. Each probe is located at the area center radius of one of five equal annular areas. In general, turbine size influences the number of probes permissible.

Measurement of flow angle is accomplished by means of a conventional self-balancing probe system. The probe shown is of a 3-tube design, with the center tube used to measure total pressure. The two side tubes are symmetrically located with respect to the center tube and are exposed to a pressure that ranges between the total pressure and the static pressure. The openings in the side tubes are in planes making an angle of 45° with the center tube. These side tubes are connected to the two sides of a diaphragm in a balance capsule. A

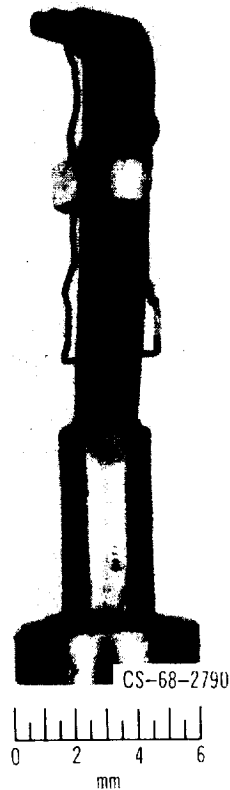


FIGURE 12-9.—Combination-probe sensing head.

differential transformer in the capsule is actuated by the diaphragm, so that an error signal is generated when the pressures in the side tubes of the probe are unequal. A servo-system operates to reduce the error to zero by pointing the probe into the flow.

Exit total-temperature and total-pressure measurements are generally not used for the primary determination of turbine efficiency, but they are used to determine values in order to check for gross discrepancies. It has been found that measurement of torque and use of equation (12-1) provides more reliable values of specific work than does measurement of exit total temperature. This is especially true if the temperature probe is in a fixed position and large variations in flow angle occur over the range of operating conditions. Even with a self-balancing probe, the exit passage would have to be surveyed and the results integrated in order for the specific work to be determined accurately.

Exit total pressure, which is used for the calculation of ideal work, is usually determined from equation (12-2). When the exit flow angle is small, use of equation (12-2) yields more reliable values of exit total pressure than does direct measurement. When the exit flow angle is

large, the radial variations in pressure and angle in the exit passage become large. In this case, unless integrated values can be obtained for use in equation (12-2), the choice between calculation and measurement of exit total pressure is not clear-cut.

Mass-Flow Measurement

Flows are usually measured with variable-head meters, which depend on the pressure differential caused by a constriction in the fluid pipe. The primary element is a restriction such as a venturi, nozzle, or orifice placed in the pipe through which the fluid is flowing. The secondary element may be a simple U-tube manometer or an intricate pressure recording device. Each of these meters has certain advantages and disadvantages, and the selection of any particular meter depends on the requirements and constraints of the particular application.

All of these variable head meters have the same basic equation for the computation of the rate of flow:

$$W = A_t M C E Y \sqrt{2g\rho_{in}(p_{in} - p_t)} \quad (12-3)$$

where

- A_t flow area of meter throat, m²; ft²
- M approach velocity factor
- C discharge coefficient
- E thermal expansion factor
- Y compressibility factor
- ρ_{in} density at meter inlet, kg/m³; lb/ft³
- p_{in} static pressure at meter inlet, N/m²; lb/ft²
- p_t static pressure at meter throat, N/m²; lb/ft²

The approach velocity factor is

$$M = \frac{1}{\sqrt{1 - \left(\frac{D_t}{D_{in}}\right)^4}} \quad (12-4)$$

where D is diameter, in m or ft.

The discharge coefficient C accounts for the difference between the actual flow rate and the theoretical flow rate and is significantly different for each type of meter. Although good approximations for discharge coefficients can be made from published data, a direct calibration of the meter should be made to assure accurate results. The thermal expansion factor E accounts for the fact that the meter throat area is usually determined from measurements obtained at room temperature, which usually is not equal to the temperature of the fluid flowing through the meter.

The compressibility factor for nozzles and venturi meters is

$$Y = \left\{ \frac{\gamma}{\gamma - 1} \left(\frac{p_t}{p_{in}} \right)^{2/\gamma} \left[\frac{1 - \left(\frac{p_t}{p_{in}} \right)^{(\gamma-1)/\gamma}}{1 - \frac{p_t}{p_{in}}} \right] \left[\frac{1 - \left(\frac{D_t}{D_{in}} \right)^4}{1 - \left(\frac{D_t}{D_{in}} \right)^4 \left(\frac{p_t}{p_{in}} \right)^{2/\gamma}} \right] \right\}^{1/2} \quad (12-5)$$

The derivation of equation (12-5), along with curves showing Y as a function of p_t/p_{in} and D_t/D_{in} , is presented in reference 5. For most concentric orifices having $(\Delta p/p_{in}) < 0.3$, the value of Y can be determined from the following empirical equation from reference 5:

$$Y = 1 - \left[0.41 + 0.35 \left(\frac{D_t}{D_{in}} \right)^4 \right] \frac{(p_{in} - p_t)}{p_{in}\gamma} \quad (12-6)$$

Venturi tube.—Figure 12-10 shows the important features of a venturi tube, which consists of a cylindrical entrance section, a converging section, a cylindrical throat section, and a diffuser section. The tubes are usually cast and have machined internal surfaces. The diffuser section usually is made with an included angle of about 7° with the object of accomplishing a maximum recovery of kinetic energy while minimizing friction loss. The total pressure loss from the venturi-tube inlet to exit is from 10 to 20 percent of the differential pressure between the inlet and the throat. The venturi tube has disadvantages in that it is bulky, difficult to construct (particularly so as to provide reproducibility), more expensive than other head meters, and requires a long, straight run of piping.

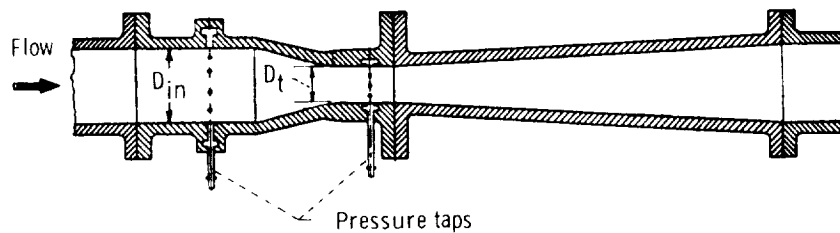


FIGURE 12-10.—Venturi tube.

Flow nozzle.—Figure 12-11 shows the shape of a commonly used flow nozzle. The flow nozzle approaches, to some extent, the venturi tube without the diffuser section. The high pressure recovery obtained with the venturi is thus lost, and the nozzle has a pressure loss of 30

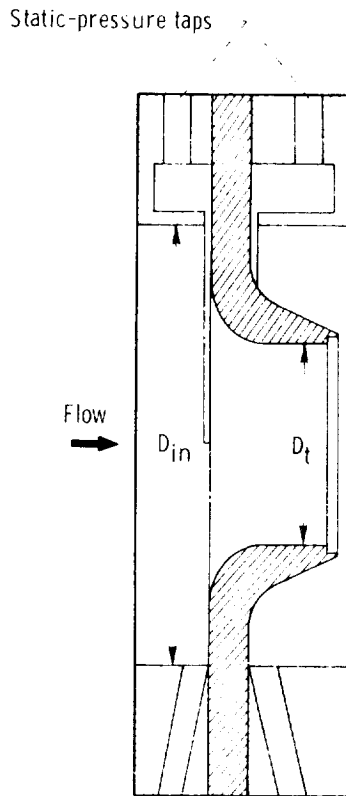


FIGURE 12-11.—Flow nozzle.

percent or more, depending on area ratio, of the differential pressure between the inlet and the throat. The flow coefficient (product of approach factor M and discharge coefficient C) for a nozzle is about 0.98.

Orifice.—The sharp-edged orifice (fig. 12-12) is probably the most widely used of the various head meters. Because of the inward flow of the streamlines on the upstream side of the plate, the minimum stream area occurs downstream from the orifice edge. This minimum area is known as the vena contracta, and it is at this area that the minimum pressure is obtained. The orifice has a pressure loss somewhat greater than that for a flow nozzle. The flow coefficient for an orifice is about 0.65. This low value is due to the effective minimum area being at the vena contracta rather than at the orifice itself.

It is possible to make, in most machine shops, an orifice with which published coefficients may be used. If the hole is carefully made according to specifications, a high degree of reproducibility of flow conditions is possible. The upstream edge must be sharp, and the axial length of the cylindrical portion must not exceed 5 percent of the in-

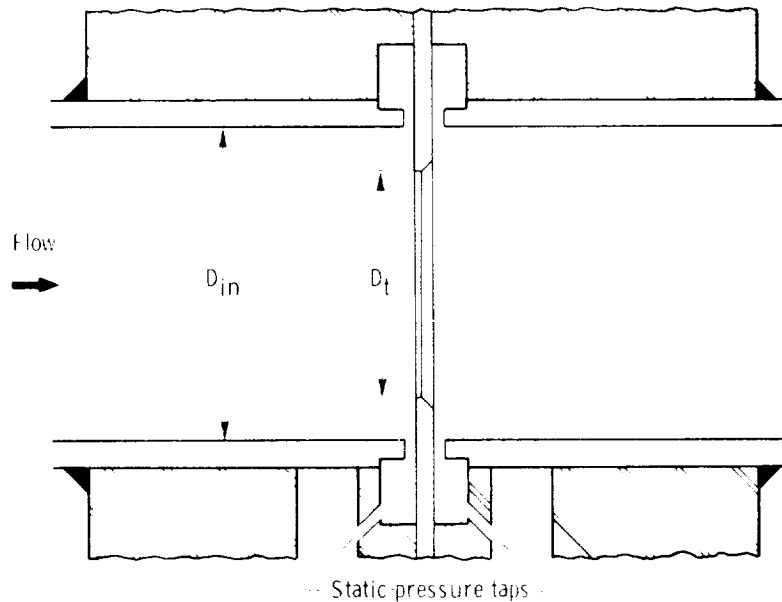


FIGURE 12-12.—Sharp-edged orifice.

side diameter of the pipe. Because it is possible to construct two or more orifices which will have the same coefficients when calibrated, the orifice is extensively used.

Torque Measurement

In turbine-component tests, an accurate measurement of torque produced by the turbine is of prime consideration in evaluating turbine performance. The devices most commonly used to determine turbine torque are cradled absorption dynamometers. Simply, the absorption dynamometer converts the energy supplied by the turbine into heat. This heat, in turn, is dissipated to the surroundings, where it generally serves no useful purpose. The dynamometer provides a load for the turbine, and this is used as the turbine speed controller.

Absorption dynamometers to be discussed in this section include (1) hydraulic, or fluid-friction, brakes; (2) electromagnetic brakes; (3) electric generators used as brakes; and (4) airbrakes. In addition, methods for measuring dynamometer force and types of torque meters other than absorption dynamometers are discussed.

Hydraulic dynamometer.—These units are frequently called water brakes, since the fluid is almost always water. A typical water brake is shown in figure 12-13, which shows clearly the cradle mounting generally used in dynamometer installations. The shaft is coupled

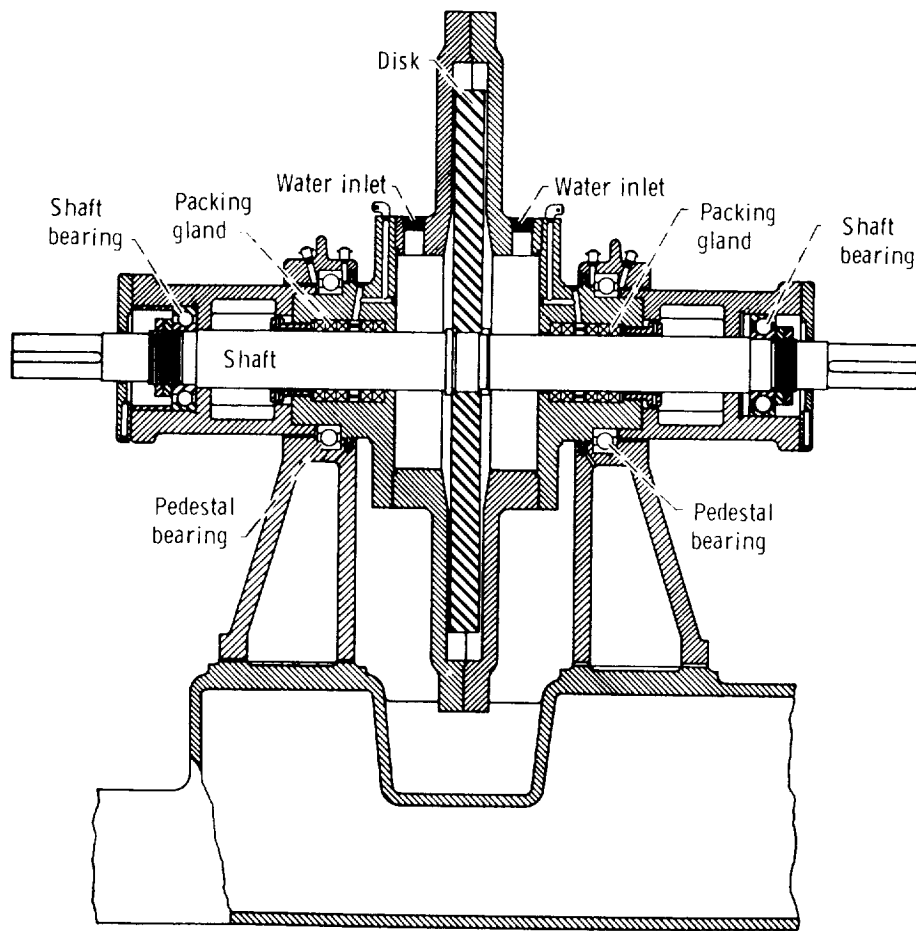


FIGURE 12-13.—Hydraulic dynamometer. (Courtesy of Murray Iron Works Co.)

directly to the test turbine and transmits the developed torque to the housing through the shaft bearings, the packing glands, and fluid friction on the disk. The housing is supported in the pedestal bearings so that it is free to rotate, within limits. As the shaft rotates, the housing tends to rotate with it. A scale attached to an arm on the housing permits determination of the turning moment, and the power absorbed may be computed.

Water fed into the disk compartment is thrown by centrifugal force to the periphery of the disk, where it forms a ring. As the discharge valves are closed or the inlet valves opened further, the water ring depth is increased; this results in greater frictional resistance between the disk and the housing, and a consequently increased absorption capacity of the brake. The amount of water circulated should be sufficient to prevent the formation of steam at any point, since such

action would cause momentary unloading. With a constant water level, the power-absorbing capacity of this brake varies almost as the cube of the speed. This characteristic (i.e., increase of torque with increase of speed, and vice versa) is typical of all fluid-friction and electrical-type dynamometers and makes them particularly desirable for testing nongoverned engines.

Some water brakes are provided with through-holes in the disk near the outer periphery. This tends to further increase the friction, and can increase power absorption by as much as an order of magnitude. Care must be exercised, however, because erosion of the disk can occur, particularly in the vicinity of these holes. Another way to increase power absorption capability is by staging; that is, by using more than one disk.

Eddy-current dynamometer.—The eddy-current dynamometer is shown in the two views of figure 12-14. In this device, the stator is supported on the pedestal bearings so that any torque may be transmitted by means of the torque arm and measured by the scale. The rotor is mounted on the shaft, which is supported in the stator in bearings. The stator carries a coil, which, when energized with direct current, magnetizes the stator and rotor. On the rotor are teeth with ends machined to produce a small air gap between them and the opposing face of the stator. The lines of force enter the rotor principally through the ends of the teeth, so that as the rotor is moved by the device being tested, the lines of force are caused to sweep through the

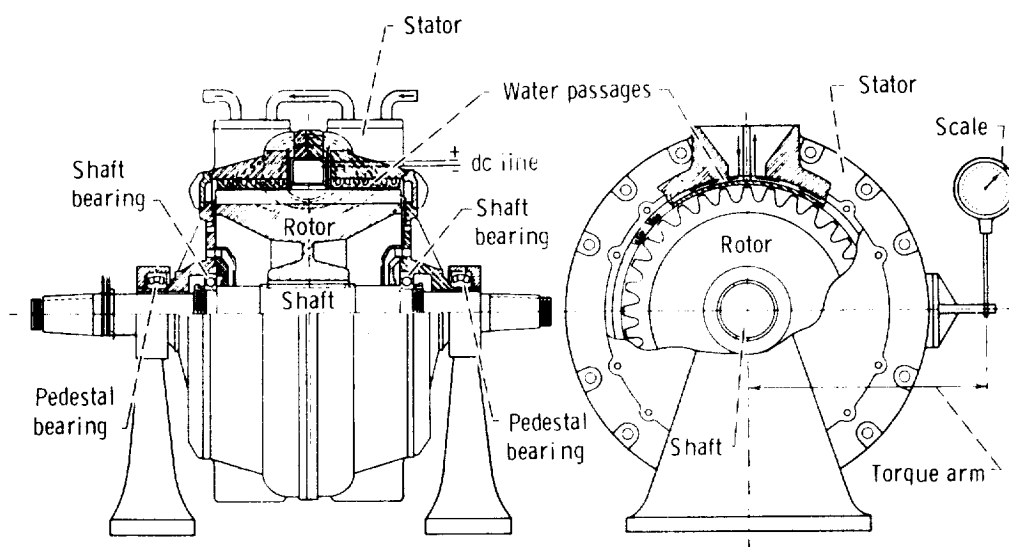


FIGURE 12-14.—Eddy-current dynamometer. (Courtesy of Mid-West Dynamometer and Engineering Co.)

iron of the stator. The magnetic attraction between the rotor and the stator causes the stator to try to turn with the rotor. The lines of force sweeping through the stator induce currents therein; this energy is dissipated to cooling water flowing through passages in the stator.

The dynamometer shown in figure 12-14 is called a dry-gap type, because the coolant water does not contact the rotor. A wet-gap eddy-current dynamometer is also commonly used. The wet-gap type has a cylindrical iron-core rotor, and the water flows from passages in the stator directly onto the rotor. Eddy-current dynamometers can be connected in series to give any required power absorption capability.

dc dynamometer.—A dc electric motor-generator, with frame or stator cradled, provides the most versatile dynamometer. It can be used to measure the power required to drive a device (testing a pump or a compressor) as well as to absorb the output of a prime mover (a turbine or a reciprocating engine). When it is driving, the unit acts as a motor; when it is absorbing energy, the unit acts as a generator. The driving capability permits the researcher to determine bearing, seal, and windage losses by removing the turbine rotor, driving the shaft, and measuring the torque as a function of speed. This frictional torque is then added to the torque measured during the turbine tests in order to obtain the true turbine torque. For the smaller turbines, the friction losses may represent an appreciable percentage of the total turbine power. For the larger jet-engine type turbines, these losses are generally small when compared to the total torque output, and hence, they can often be neglected.

Airbrake dynamometer.—The airbrake dynamometer is a type of power absorber that was developed at the NASA Lewis Research Center. It is used extensively for testing small turbines (less than about 19 kW (25 hp)). A cross-sectional view of the airbrake dynamometer is shown in figure 12-15. The airbrake consists of a throttle valve, an inlet collector, a stator, a rotor with either a paddle wheel or airfoil type blading, and flow straighteners to ensure axial entry and discharge of the air. After the air enters the inlet collector of the airbrake in an axial direction, it is accelerated through the stator, which gives it tangential momentum in a direction opposite to the direction of rotation of the rotor. The rotor removes tangential momentum from the air and, thereby, absorbs the research turbine power output. After leaving the rotor, the air passes through flow straighteners and is discharged from the airbrake in an axial direction. Therefore, the torque on the rotor is equal to the torque on the casing. The casing is cradled in air bearings, which are designed for radial and axial loads. A torque arm is attached to the casing for measurement of torque.

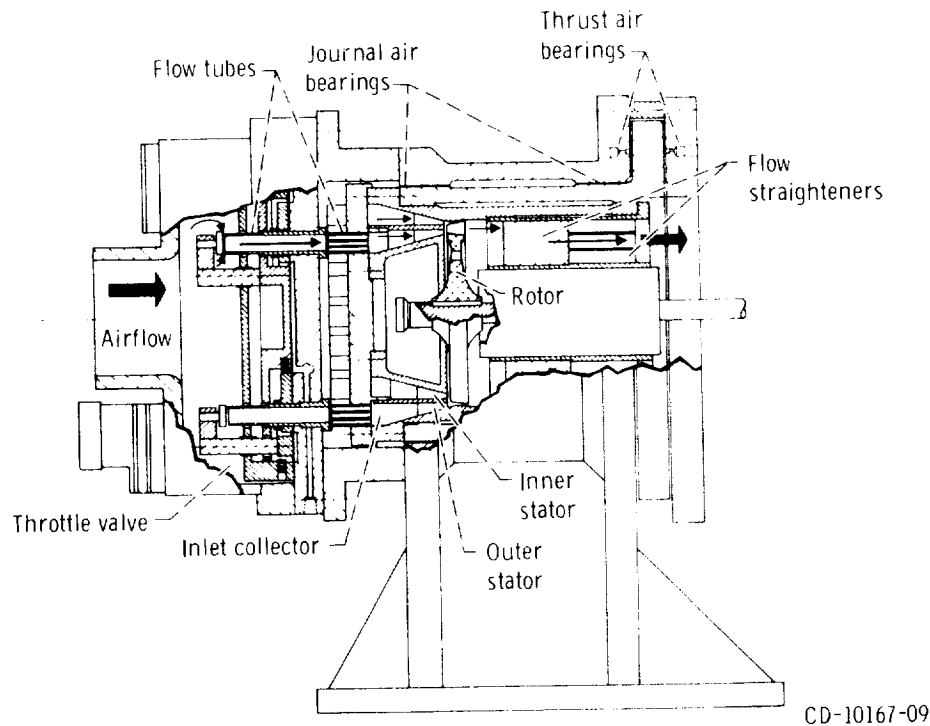


FIGURE 12-15.—Airbrake dynamometer.

It can be noted from figure 12-15 that the stator consists of two sections, an outer and an inner blade row, with independent valving for each blade row. This stator system is well adapted to measure extremely small turbine outputs at low inlet pressures. For example, a stator configuration can be used where one blade row can impart tangential momentum in the same direction of rotation as the rotor while the other stator blade row imparts tangential momentum in a direction opposite to the direction of rotation of the rotor. For this case, the rotor is of the paddle-wheel type design. Thus, the airbrake can be used to absorb turbine power or to drive the turbine. This driving capability, as was the case for the dc dynamometer, permits the measurement of bearing and seal frictional losses.

Measurement of dynamometer force.—The dynamometer force measurement can be obtained most simply by a spring-balance scale. Such a scale can be used because the displacements of the power absorber torque arm are very small. Because these scales indicate forces acting vertically, the torque arm should and does remain relatively horizontal, regardless of the magnitude of the force involved. The disadvantages of a spring-balance scale are that the reading is not readily remotely observable (low-power telescopes have been used), and available scales may not have the proper force range.

Hydrostatic devices with either a liquid (e.g., mercury) or a gas (e.g., air) as the fluid have been used to measure force. The principle of operation is that the force to be measured is impressed on the fluid, with the fluid being held in a confined space. The greater the force on the fluid, the greater becomes the pressure on the fluid. This fluid pressure can be calibrated in terms of the load or force required to produce it.

Most current turbine test facilities are equipped with calibrated strain-gage load cells to measure torque. These devices provide an electrical output signal which, with appropriate electronics, can provide direct torque readings on a digital voltmeter. This signal is particularly suitable for automatic digital data recording.

Strain-gage torquemeter.—Sometimes, in turbomachinery component testing, it is impractical to cradle the equipment as required for conventional torque measurement. The situation may arise wherein the turbine rotative speed is higher than the capability of the absorber, which would necessitate the use of an intermediate gear box. To circumvent this problem, a high-speed, strain-gage torquemeter, which operates on the principle that shaft torque and shaft surface strain are proportional, can be used. A bonded wire strain gage is mounted on the shaft, between the turbine and the power absorber. The fine wire has the property that its resistance is very nearly a unique function of the strain applied. Readings are transmitted through slip rings, onto brushes, and to appropriate electronic equipment, where the shaft torque is indicated. Problems encountered with this type of torquemeter include short brush life and the occurrence of induced voltages that interfere with the measurements.

Optical torquemeter.—An optical torquemeter basically consists of a shaft with polished parallel and flat reflecting surfaces at each end. A stationary optical unit measures the twist of the shaft. The optical system projects the illuminated image of a slit, by successive reflection from each of the reflecting surfaces on the shaft, onto two photocells separated by a hairline gap. Shaft twist produces unbalanced illumination on the two photocells. A servomechanism thereupon repositions the photocells to restore the null-balance condition. Photocell position is a measure of shaft twist.

Experience has indicated that the reflecting surfaces of the optical torquemeter must be kept highly polished to maintain accuracy. This may be difficult, because these surfaces are usually close to the turbine bearings and/or gearbox bearings and oil mist tends to cloud these surfaces. A higher intensity light source, such as a laser beam, may possibly facilitate accurate torque readings. The design of both the optical and the strain-gage torquemeters must provide for adequate torsional twist under load. Both systems have been operated in con-

junction with dynamometers, with good correlation. There are other types of torquemeters that are commercially available that also could be used for turbine testing.

Rotative-Speed Measurement

One of the simplest and most accurate measurements in turbine testing is that of rotative speed. The electric tachometer can be used to give a continuous indication of speed. A dc generator, with a permanent magnetic field and a rotating armature, is driven by the shaft the speed of which is to be measured. Since the field is constant, the voltage output of the generator is proportional to its speed. The usually remote indicator is a voltmeter graduated to read rotative speed.

For greater accuracy in speed measurements, a positively driven revolution counter should be used. A means is provided for engaging and disengaging it simultaneously with a timer. Commercial units, called chronotachometers, are available. These units are advantageous because they yield an average rotative speed for a given time (usually 1 minute).

The currently most accepted method of measuring speed is through the use of an electromagnetic or electronic pulse counter. It is particularly suited for high-rotative-speed machines. For this method, a sprocket with a given number of teeth is secured to the turbine shaft. An electronic pickup accurately counts the teeth (or impulses) for a given time and displays the count directly as rotative speed.

Rotative speed varies somewhat during turbine tests when the air supply pressure varies. Since mass flow rate and, therefore, power are directly proportional to pressure, an increase in supply pressure tends to drive the turbine faster. The absorber tends to correct for this, and there result accelerations and decelerations within the accuracy of the control system. It is, therefore, ideal to have a steady air supply to provide greater accuracy when taking data.

TURBINE PERFORMANCE

The performance characteristics of turbines are usually presented by means of performance maps. Such a performance map shows, on one figure, the turbine flow and work as functions of the operating conditions of speed and pressure ratio. Also shown on the map are contours of efficiency. The flow, work, and speed are shown in terms of equivalent conditions so that the map can be readily used for any inlet conditions of temperature and pressure. The concept and nature of equivalent conditions are discussed in chapter 2 (vol. 1).

In brief review, the equivalent conditions are

$$w_{eq} = w \frac{\sqrt{\theta}}{\delta} \epsilon \quad (12-7)$$

$$\Delta h'_{eq} = \frac{\Delta h'}{\theta} \quad (12-8)$$

and

$$N_{eq} = \frac{N}{\sqrt{\theta}} \quad (12-9)$$

where the subscript *eq* refers to the equivalent condition. The correction factors are defined as

$$\theta = \left(\frac{V_{cr,0}}{V_{cr,std}} \right)^2 \quad (12-10)$$

$$\delta = \frac{p'_0}{p'_{std}} \quad (12-11)$$

and

$$\epsilon = \frac{\gamma_{std} \left(\frac{2}{\gamma_{std} + 1} \right)^{\gamma_{std}/(\gamma_{std}-1)}}{\gamma \left(\frac{2}{\gamma + 1} \right)^{\gamma/(\gamma-1)}} \quad (12-12)$$

where the square of the critical velocity V_{cr} is

$$V_{cr}^2 = \frac{2\gamma}{\gamma+1} gRT' \quad (12-13)$$

The subscript *std* refers to the standard sea-level air conditions of pressure (10.133 N/cm² or 14.696 psia), temperature (288.2 K or 518.7° R), molecular weight (29.0), and specific heat ratio (1.4).

An example performance map is presented in figure 12-16. Equivalent specific work is plotted against the product of the equivalent mass flow and the equivalent rotative speed. This product conveniently spreads out the data because, as will be shown in the discussion to follow, there may be little or no variation in the mass flow rate with variations in rotative speed. Lines of constant pressure ratio (total pressure ratio in this case) and constant speed are presented on the map. Also, contours of efficiency are included for completeness.

Although a great deal of information can be obtained from the performance map, a better understanding of the turbine performance can be obtained if some of the performance parameters are plotted independently as functions of pressure ratio for a range of speed. The curves of this type to be presented in the following sections are not

TURBINE DESIGN AND APPLICATION

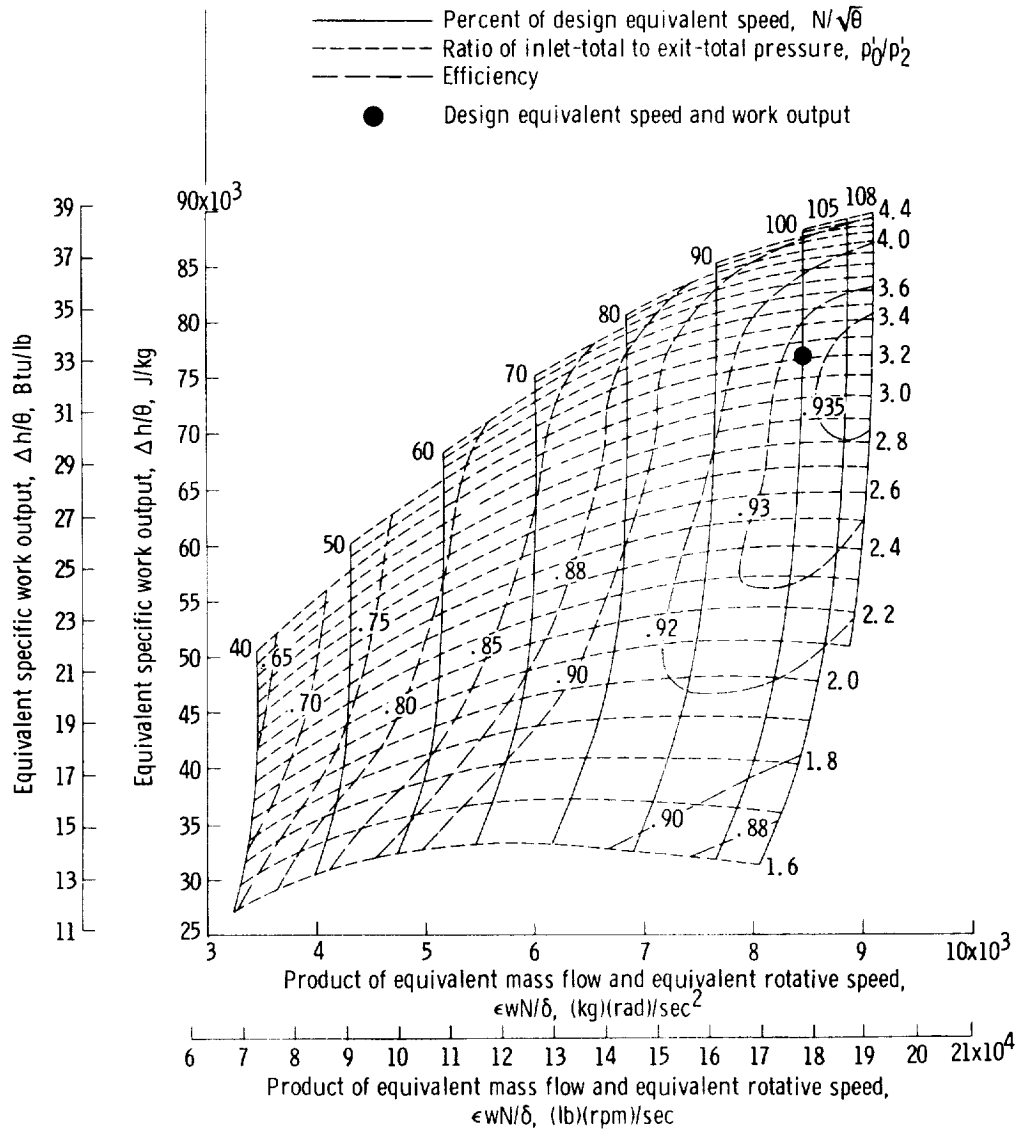


FIGURE 12-16.—Turbine performance map.

for the same turbine whose map is shown in figure 12-16, but were selected to illustrate certain points.

Mass Flow

Variations in mass flow rate with turbine pressure ratio and speed are shown in figures 12-17 and 12-18 for a single-stage turbine operated with two different stators. Figure 12-17 was obtained with a stator having a large stagger angle (small stator-throat area), and figure 12-18 was obtained with a stator having a small stagger angle

EXPERIMENTAL DETERMINATION OF AERODYNAMIC PERFORMANCE

(large stator-throat area). For both cases, the stator blades were identical, and the same rotor was used.

In both figures it can be seen that for a given speed, the mass flow rate increases as the pressure ratio increases until some maximum value is reached. A further increase in pressure ratio produces no increase in mass flow. The reason for this maximum in mass flow is that either the stator or the rotor has choked.

In figure 12-17, which is for the small stator-throat area, the maximum value of mass flow rate is unaffected by the rotational speed; this indicates that the stator is choked. In figure 12-18, the maximum mass flow rate is influenced by the rotational speed, which indicates that the rotor is choked. For the case of the choked rotor, the maximum mass flow rate increases with decreasing rotational speed. This is the usual behavior and is due to an increase in the rotor inlet relative total pressure with decreasing speed. In some cases, however, the occurrence of very large incidence losses causes a decrease in maximum flow with decreasing speed.

The foregoing discussion has been for the case of a single-stage turbine. In a multistage turbine, the flow variation shown in figure 12-17 would indicate a first-stage stator choke. A flow variation of

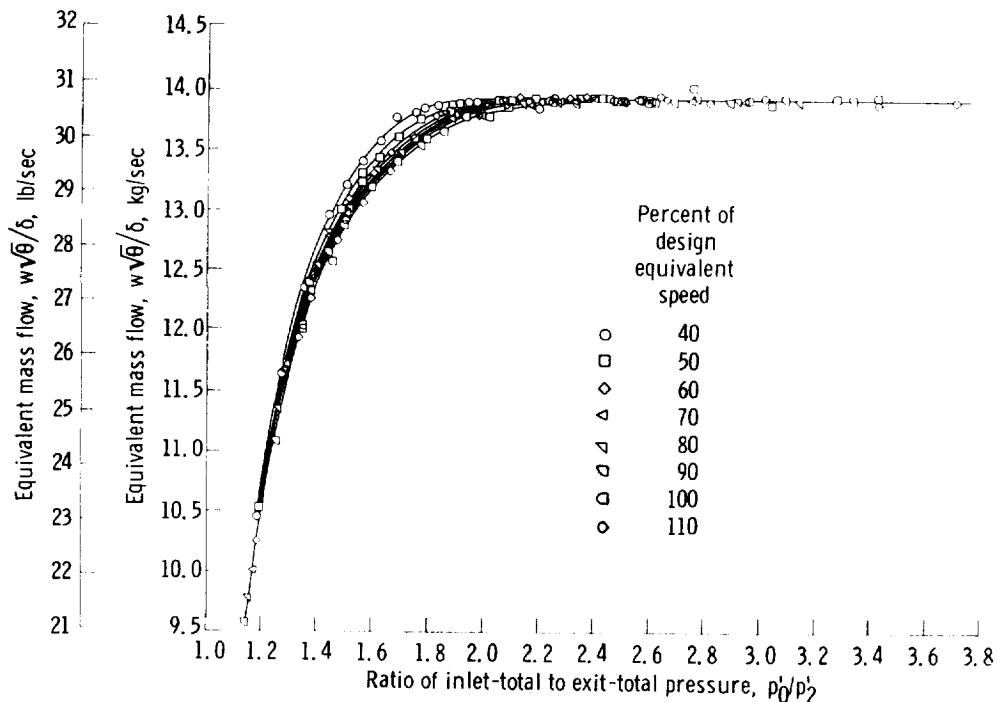


FIGURE 12-17.—Variation of equivalent mass flow with total-pressure ratio for turbine with small stator-throat area.

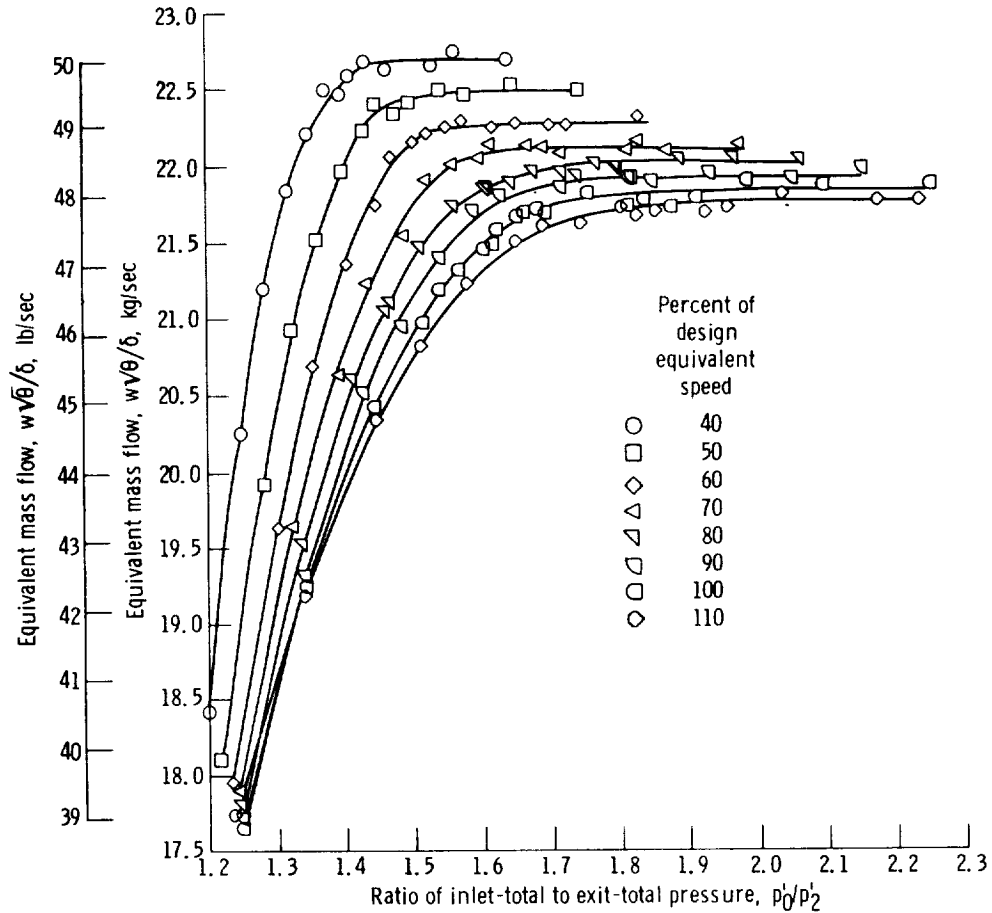


FIGURE 12-18.—Variation of equivalent mass flow with total-pressure ratio for turbine with large stator-throat area.

the type shown in figure 12-18 would indicate choking in some downstream blade row, either a rotor or a stator. To determine exactly where this choking occurred, static-pressure measurements between the blade rows would have to be obtained. Such data are illustrated in figure 12-19, where the variation in hub static pressure with turbine pressure ratio (at constant speed) is shown for each blade row exit of a two-stage turbine. As the turbine pressure ratio increases, choking in any given blade row is indicated by the static pressure upstream of that blade row remaining constant while the downstream static pressure continues to decrease. For the particular case illustrated in figure 12-19, choking occurs first in the second stator at a turbine pressure ratio of about 3.2. As turbine pressure ratio continues to increase, the second rotor then chokes at a turbine pressure ratio of about 3.7. It is, of course, the first choke that establishes the maximum flow rate for the turbine.

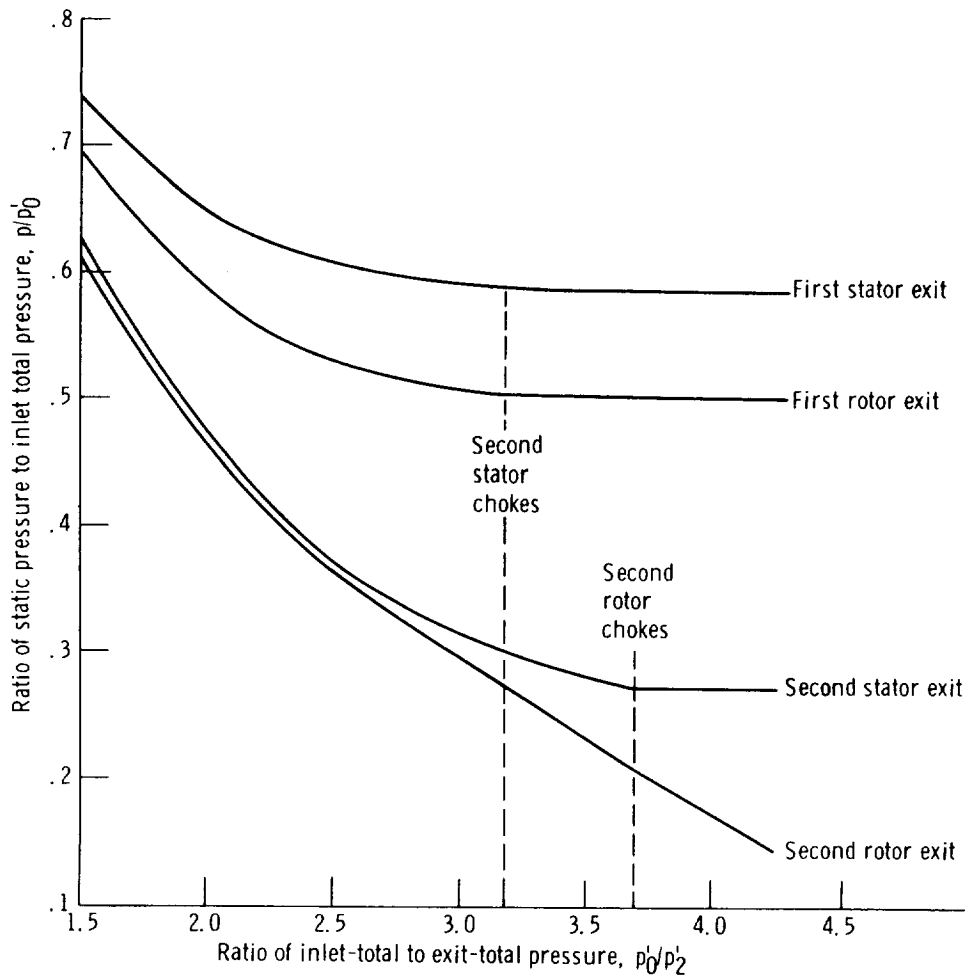


FIGURE 12-19.—Effect of turbine total-pressure ratio on hub static pressure in a two-stage turbine.

Torque

As indicated by equation (2-9) of chapter 2 (vol. 1), the torque should vary directly with the mass flow rate and with the change in tangential component of absolute velocity (ΔV_u) between rotor inlet and exit for any constant radius. The manner in which torque varies experimentally with turbine pressure ratio and speed is shown in figure 12-20. For a given speed, increasing the pressure ratio increases the torque due to a higher mass flow rate and higher values of ΔV_u resulting from the high velocities and increased turning (absolute) in the rotor. At a given pressure ratio, the torque decreases with increasing speed. This is due to a decrease in the amount of turning in the rotor (exit absolute flow angle becomes more positive as speed increases) and a possible decrease in mass flow rate.

TURBINE DESIGN AND APPLICATION

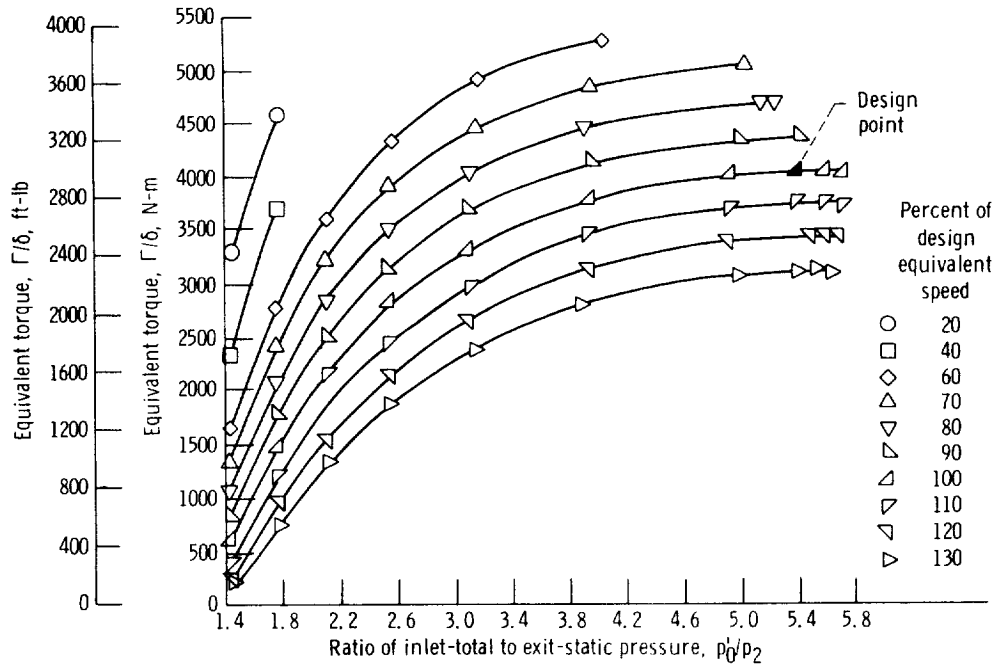


FIGURE 12-20.—Variation of equivalent torque with turbine pressure ratio and speed.

Figure 12-20 shows that as the pressure ratio increases for a given speed, the torque tends to level off and reach a maximum value. Above this limit, any further increase in pressure ratio results in no additional torque. This phenomenon is termed “limiting loading” and is indicated on a performance map by the lines of constant pressure ratio converging to yield a maximum value of equivalent specific work for each speed. In figure 12-16, limiting loading is being approached but has not been reached. Limiting loading occurs when the annulus area at the turbine exit is choked; that is, when the exit axial Mach number is unity.

The mass flow and torque curves just discussed can be plotted from measured data. These curves are then used to construct the turbine performance map. The usual procedure in constructing a performance map is to select the mass flow and torque at even increments of pressure ratio for the various speeds. Specific work, ideal specific work, and efficiency are then calculated, and the performance map can be drawn.

Efficiency

Another convenient and widely used method of presenting turbine

EXPERIMENTAL DETERMINATION OF AERODYNAMIC PERFORMANCE

performance is to plot efficiency as a function of blade-jet speed ratio ν , which is given by the equation

$$\nu = \frac{U}{\sqrt{2gJ\Delta h_{td}}} \quad (12-14)$$

where

U blade mean-section speed, m/sec; ft/sec

Δh_{td} ideal specific work based on ratio of inlet-total to exit-static pressure, J/kg; Btu/lb

This was discussed in chapter 2 (vol. 1), where a correlation was shown mathematically for an idealized case. For that case, efficiency was shown to vary parabolically with blade-jet speed ratio.

Experimentally obtained static efficiencies are plotted against blade-jet speed ratio in figure 12-21 for a two-stage axial-flow turbine over a

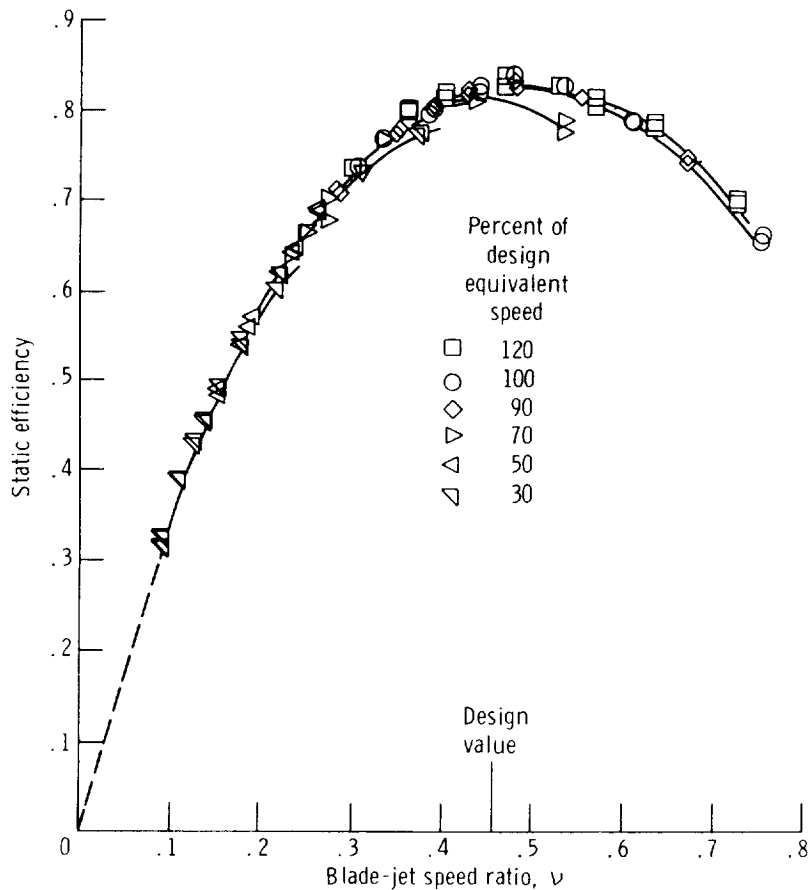


FIGURE 12-21.—Variation of efficiency with blade-jet speed ratio.

wide range of speed and pressure ratio. The total efficiencies for this turbine, because of the two stages and very low exit velocities, were only very slightly (1 or 2 percent) higher than the static efficiencies and are, therefore, not presented. Figure 12-21 shows that the blade-jet speed ratio serves very well to correlate turbine efficiency in a generalized manner for a real turbine as well as for an ideal turbine. It should be noted, however, that the correlation is not always as good as for the turbine represented by this figure. For operating conditions where limiting loading is approached, the speed lines tend to separate somewhat, especially at the lower blade-jet speed ratios.

Flow Angles

Although flow angles are not considered as turbine performance parameters, we should understand how they vary over the turbine

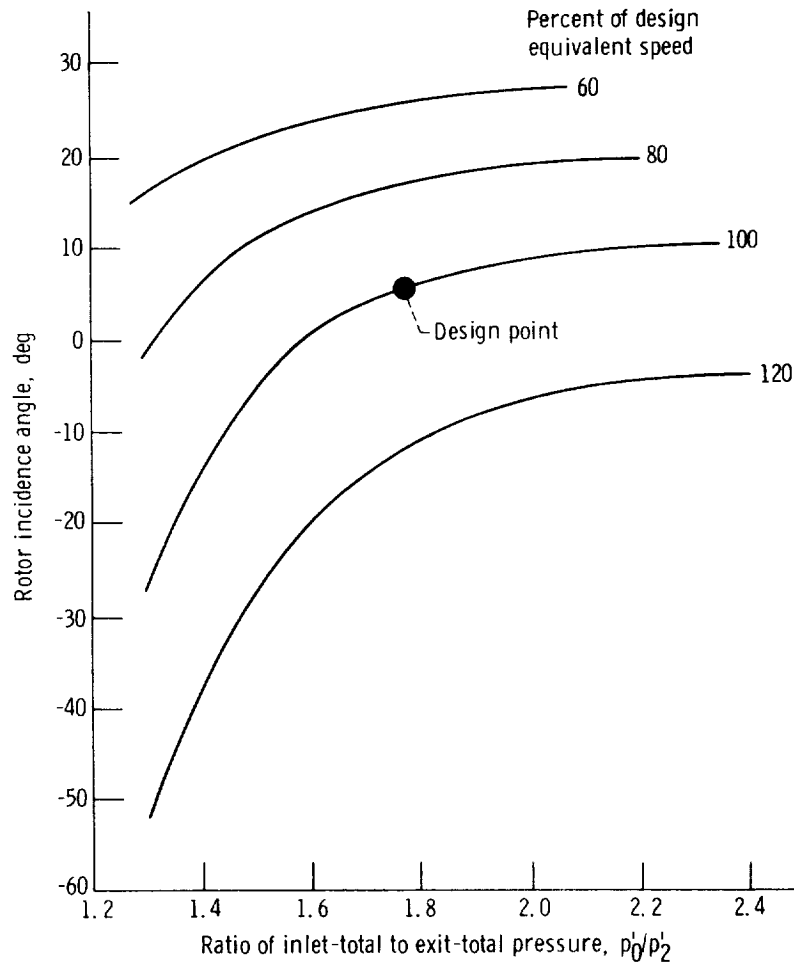


FIGURE 12-22.—Variation of rotor incidence angle with turbine pressure ratio and speed.

EXPERIMENTAL DETERMINATION OF AERODYNAMIC PERFORMANCE

operating conditions. The direction of the flow entering each blade row determines the incidence loss, which is an important contributor to off-design losses, as discussed in chapter 8 (vol. 2). The rotor inlet incidence angle, which is defined as the difference between the rotor-inlet relative flow angle and the rotor blade inlet angle, was calculated over a range of speed and pressure ratio for a typical single-stage turbine, and the resultant values are presented in figure 12-22. Flow angles are herein defined as being positive when the tangential component of the velocity vector is in the same direction as the blade velocity. The following generalized observations can be made from this figure: (1) a large variation in incidence angle occurs over the potential operating range of a turbine, (2) the change in incidence angle

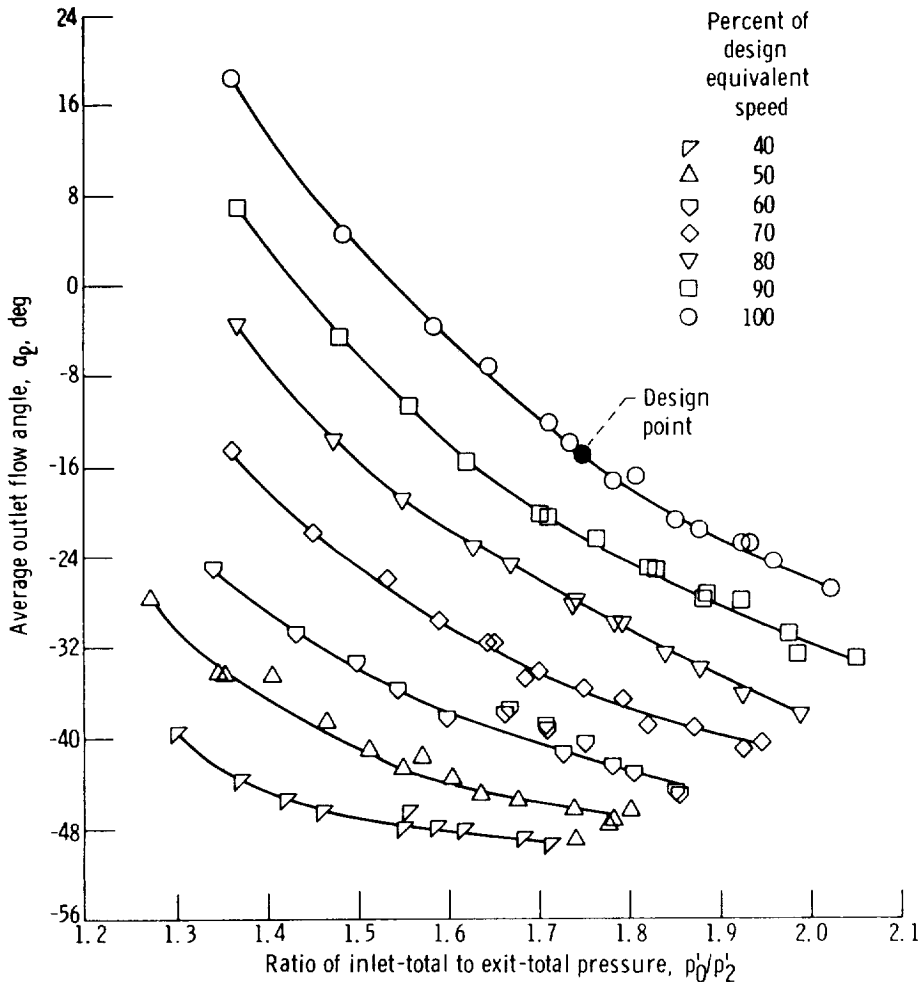


FIGURE 12-23.—Variation of outlet flow angle with turbine pressure ratio and speed.

with pressure ratio becomes greater as speed increases, and (3) the rotor incidence angle becomes more positive as the pressure ratio increases and speed decreases.

The turbine outlet flow angle is important with respect to the design of whatever component may be downstream of the turbine or to the amount of thrust that can be obtained from the outlet flow. Outlet flow angle is plotted over a range of speed and pressure ratio in figure 12-23 for the same single-stage turbine referred to in the last paragraph. The trends observed and generalizations made for the incidence angle also apply to the outlet flow angle, the only difference being that the change in outlet flow angle with pressure ratio and speed is in the direction opposite to that for rotor incidence angle.

Stator Loss

Stator loss is directly measurable in terms of total pressure by means of a total-pressure probe and survey equipment such as that previously shown in figures 12-7 and 12-8. A typical circumferential total-pressure loss survey taken at one radius just behind the stator trailing edge is shown in figure 12-24. It can be plainly seen that all of the loss occurs in the wake region. A composite of many such circumferential traces yields contours of stator total-pressure ratio such as shown in figure 12-25. The majority of the traces were concentrated near the hub and tip regions, where measurements were greatly affected by the end-wall boundary layers. The increased pressure loss with increasing critical velocity ratio (and flow) and the end-wall boundary-layer buildup can be noted. The total-pressure loss data can be converted to kinetic-energy loss coefficients as described in chapter 7 (vol. 2). Integration of the losses over the area of one full passage gives the total loss for the stator. Once the turbine and stator perform-

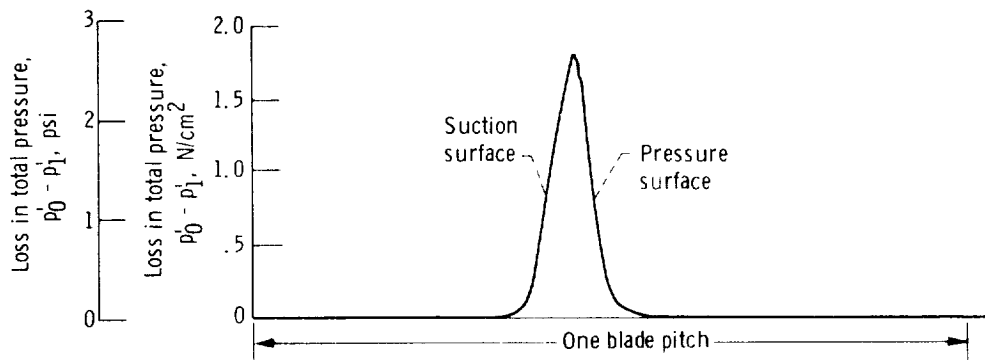


FIGURE 12-24.—Typical total-pressure loss survey data at blade exit.

EXPERIMENTAL DETERMINATION OF AERODYNAMIC PERFORMANCE

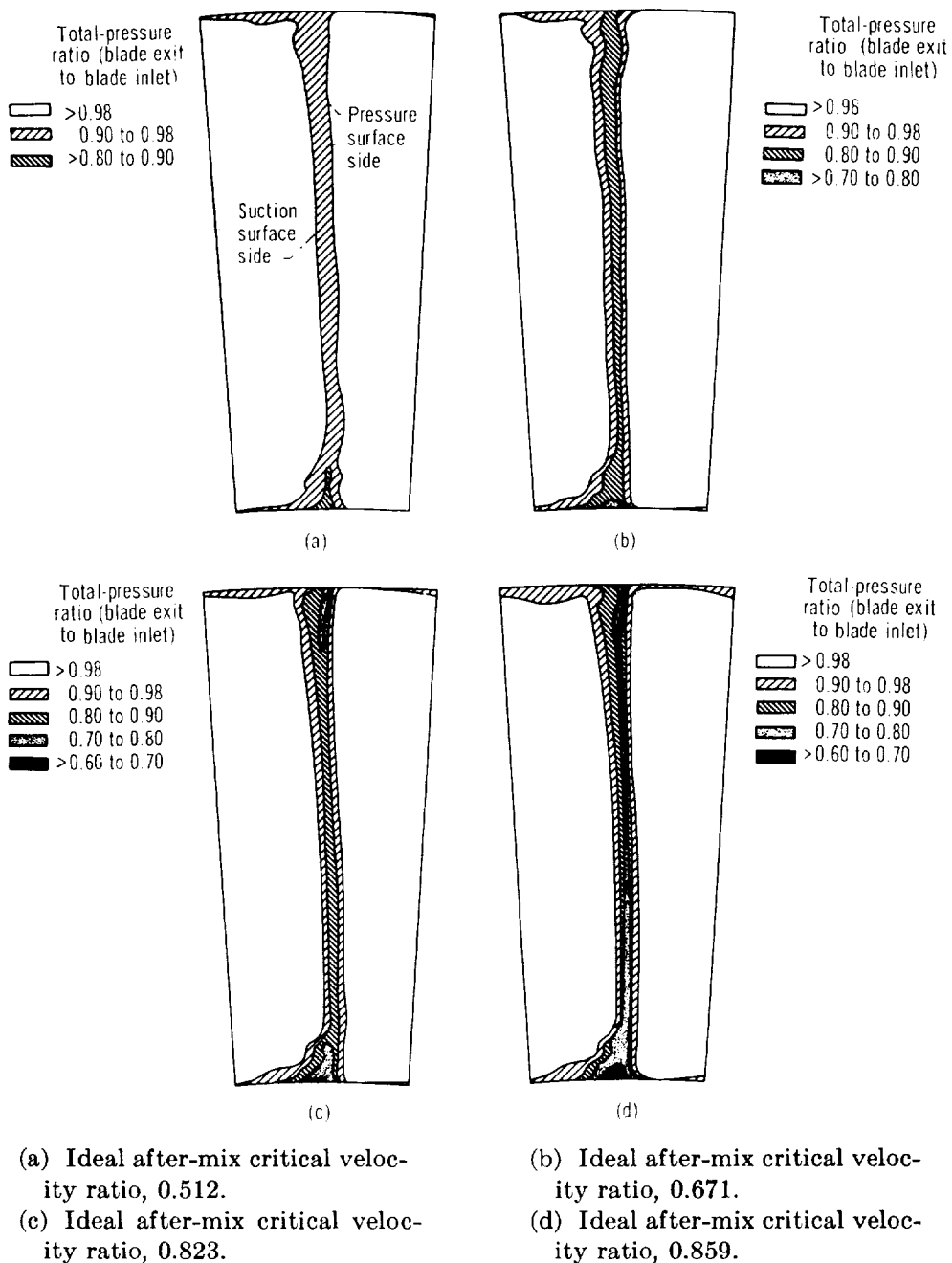


FIGURE 12-25.—Contours of total-pressure ratio from stator annular surveys.

ance have been obtained experimentally, a turbine loss breakdown can be made.

Surface Velocity

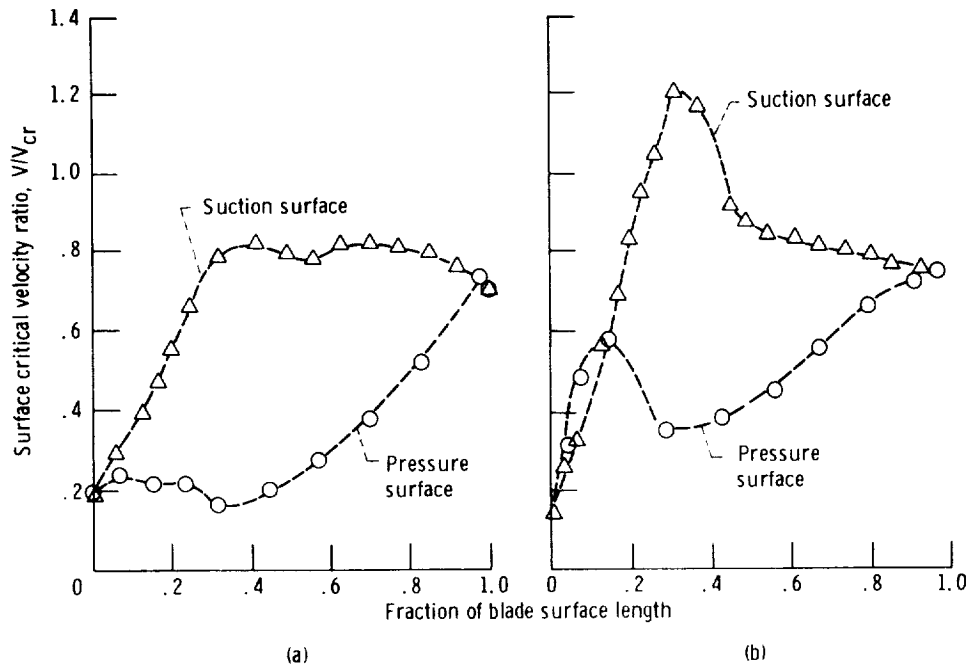
An important part of the blading design is the selection of the blade surface profiles that yield favorable surface velocity distributions.

Analytical methods for calculating surface velocities were discussed in chapter 5 (vol. 2). During the test program, it is of interest to determine whether the "designed for" surface velocities were actually achieved. To obtain the velocity distribution along a blade surface, static-pressure measurements are made along the blade surfaces in the manner discussed previously in the section on static-pressure measurements. With the static pressure distribution along the blade surfaces known, the velocity distribution can be determined from the relation

$$\frac{V}{V_{cr}} = \left\{ \frac{\gamma+1}{\gamma-1} \left[1 - \left(\frac{p}{p_0} \right)^{(\gamma-1)/\gamma} \right] \right\}^{1/2} \quad (12-15)$$

Figure 12-26 shows the experimentally determined surface velocity distributions for two stators tested under similar conditions. The distribution shown in figure 12-26(a) is considered to be a desirable one. Acceleration on the suction surface to the maximum velocity is smooth, and the maximum velocity is maintained subsonic. There are no large flow decelerations (diffusions) on either surface. The loading (force on blade) is well distributed along the blade.

Figure 12-26(b), on the other hand, shows a velocity distribution considered to be undesirable. Flow on the suction surface accelerates



(a) Desirable distribution.

(b) Undesirable distribution.

FIGURE 12-26.—Experimental surface velocity distributions.

EXPERIMENTAL DETERMINATION OF AERODYNAMIC PERFORMANCE

to a supersonic velocity ($V/V_{cr}=1.2$) and then undergoes a rapid deceleration back to a subsonic velocity. Such a deceleration causes a thickening of the boundary layer with an associated increase in loss and could possibly lead to separation of the flow off the suction surface. A deceleration is also observed on the pressure surface, but this is not as critical, because it is followed by an acceleration that would result in reattachment of any separated flow. In general, velocity distributions with sharp peaks and valleys should be avoided when the blades are being designed.

REFERENCES

1. DOEBELIN, ERNEST O.: Measurement Systems: Application and Design. McGraw-Hill Book Co., 1966.
2. FUTRAL, SAMUEL M.; KOSKEY, MILTON; AND ROHLIK, HAROLD E.: Instrumentation Used to Define Performance of Small Size, Low Power Gas Turbines. Paper 69-GT-104, ASME, Mar. 1969.
3. MOFFITT, THOMAS P.; PRUST, HERMAN W.; AND SCHUM, HAROLD J.: Some Measurement Problems Encountered When Determining the Performance of Certain Turbine Stator Blades from Total Pressure Surveys. Paper 69-GT-103, ASME, Mar. 1969.
4. WISLER, D. C.; AND MOSSEY, P. W.: Gas Velocity Measurements Within a Compressor Rotor Passage Using the Laser Doppler Velocimeter. Paper 72-WA/GT-2, ASME, Nov. 1972.
5. ASME RESEARCH COMMITTEE ON FLUID METERS: Fluid Meters, Their Theory and Application, 5th ed., The American Society of Mechanical Engineers, 1959.

SYMBOLS

A	area, m^2 ; ft^2
C	discharge coefficient
D	diameter, m ; ft
E	thermal expansion factor
g	conversion constant, 1; 32.17 (lbm)(ft)/(lbf)(sec ²)
Δh_{id}	ideal specific work based on ratio of inlet-total to exit-static pressure, J/kg ; Btu/lb
$\Delta h'$	turbine specific work, J/kg ; Btu/lb
J	conversion constant, 1; 778 (ft)(lb)/Btu
K	conversion constant, 1; $\pi/30$ (rad)(min)/(rev)(sec)
M	approach velocity factor, defined by eq. (12-4)
N	rotative speed, rad/sec ; rev/min
p	absolute pressure, N/m^2 ; lb/ft^2
R	gas constant, $J/(kg)(K)$; (ft)(lbf)/(lbm)(°R)
T	absolute temperature, K ; °R
U	blade mean-section speed, m/sec ; ft/sec
V	absolute gas velocity, m/sec ; ft/sec
ΔV_u	change in tangential component of absolute velocity between rotor inlet and exit, m/sec ; ft/sec
w	mass flow rate, kg/sec ; lb/sec
Y	compressibility factor, defined by eq. (12-5) or (12-6)
α	absolute flow angle, measured from axial direction, deg
Γ	torque, $N-m$; $lb-ft$
γ	ratio of specific heat at constant pressure to specific heat at constant volume
δ	ratio of turbine-inlet total pressure to standard sea-level pressure
ϵ	function of specific-heat ratio, defined by eq. (12-12)
θ	squared ratio of critical velocity based on turbine-inlet temperature to critical velocity based on standard sea-level temperature, defined by eqs. (12-10) and (12-13)
ν	blade-jet speed ratio, defined by eq. (12-14)
ρ	density, kg/m^3 ; lb/ft^3

Subscripts:

an	annulus
cr	critical condition (at Mach 1)
eq	equivalent
in	meter inlet
std	standard sea-level condition
t	meter throat
0	measuring station at turbine inlet

EXPERIMENTAL DETERMINATION OF AERODYNAMIC PERFORMANCE

- 1 measuring station at stator outlet
- 2 measuring station at turbine outlet

Superscript:

- ' absolute total state

REPORT DOCUMENTATION PAGE			Form Approved OMB No. 0704-0188	
Public reporting burden for this collection of information is estimated to average 1 hour per response, including the time for reviewing instructions, searching existing data sources, gathering and maintaining the data needed, and completing and reviewing the collection of information. Send comments regarding this burden estimate or any other aspect of this collection of information, including suggestions for reducing the burden, to Washington Headquarters Services, Directorate for Information Operations and Reports, 1215 Jefferson Davis Highway, Suite 1204, Arlington, VA 22202-4302, and to the Office of Management and Budget, Paperwork Reduction Project (0704-0188), Washington, DC 20503.				
1. AGENCY USE ONLY (Leave blank)	2. REPORT DATE June 1994	3. REPORT TYPE AND DATES COVERED Special Publication		
4. TITLE AND SUBTITLE Turbine Design and Application			5. FUNDING NUMBERS	
6. AUTHOR(S) A. J. Glassman				
7. PERFORMING ORGANIZATION NAME(S) AND ADDRESS(ES) Lewis Research Center Cleveland, OH 44135			8. PERFORMING ORGANIZATION REPORT NUMBER E-5666	
9. SPONSORING/MONITORING AGENCY NAME(S) AND ADDRESS(ES) National Aeronautics and Space Administration Washington, DC 20546			10. SPONSORING/MONITORING AGENCY REPORT NUMBER <u>NASA-SP-290</u>	
11. SUPPLEMENTARY NOTES Responsible person, Kestutis C. Civinskas, organization code 2760, (216) 433-5890.				
12a. DISTRIBUTION/AVAILABILITY STATEMENT Unclassified - Unlimited Subject Category - 7			12b. DISTRIBUTION CODE	
13. ABSTRACT (Maximum 200 words) NASA has an interest in turbines related primarily to aeronautics and space applications. Airbreathing turbine engines provide jet and turboshaft propulsion, as well as auxiliary power for aircraft. Propellant-driven turbines provide rocket propulsion and auxiliary power for space craft. Closed-cycle turbine engines using inert gases, organic fluids, and metal fluids have been studied for providing long-duration electric power for spacecraft. Other applications of interest for turbine engines include land-vehicle (cars, trucks, buses, trains, etc.) propulsion power and ground-based electrical power. In view of the turbine-system interest and efforts at Lewis Research Center, a course entitled "Turbine Design and Application" was presented during 1968-69 as part of the In-house Graduate Study Program. The course was somewhat revised and again presented in 1972-73. Various aspects of turbine technology were covered including thermodynamic and fluid-dynamic concepts, fundamental turbine concepts, velocity diagrams, losses, blade aerodynamic design, blade cooling, mechanical design, operation, and performance. The notes written and used for the course have been revised and edited for publication. Such a publication can serve as a foundation for an introductory turbine course, a means for self-study, or a reference for selected topics. Any consistent set of units will satisfy the equations presented. Two commonly used consistent sets of units and constant values are given after the symbol definitions. These are the SI units and the U.S. customary units. A single set of equations covers both sets of units by including all constants required for the U.S. customary units and defining as unity those not required for the SI units.				
14. SUBJECT TERMS engine design, turbine engines, aircraft engines, automobile engines, cooling			15. NUMBER OF PAGES 400	16. PRICE CODE A17
17. SECURITY CLASSIFICATION OF REPORT Unclassified	18. SECURITY CLASSIFICATION OF THIS PAGE Unclassified	19. SECURITY CLASSIFICATION OF ABSTRACT Unclassified	20. LIMITATION OF ABSTRACT Unlimited	